UNIVERSITY OF SOUTHAMPTON

A study on the sea level variations and the '*Milghuba*' phenomenon in the coastal waters of the Maltese Islands

by

Aldo F. Drago

Submitted for the degree of Doctor of Philosophy
School of Ocean and Earth Science

October, 1999

"This study is dedicated to
all those who believe in science
without understanding it"

DECLARATION

I hereby declare that the research and material presented in this thesis is the result of work done wholly by myself while I was in registered postgraduate candidature with the School of Ocean Science at the University of Southampton.

Signature: 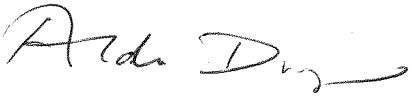

Date: 20/10/15

UNIVERSITY OF SOUTHAMPTON

ABSTRACT

FACULTY OF SCIENCE
SCHOOL OF OCEAN AND EARTH SCIENCE

Doctor of Philosophy

A STUDY ON THE SEA LEVEL VARIATIONS AND THE '*MILGHUBA*' PHENOMENON IN THE COASTAL WATERS OF THE MALTESE ISLANDS

by Aldo F. Drago

The phenomenology, generation and associated dynamics of short period seiche oscillations observed along the northern coast of the Maltese Islands are studied from a set of densely sampled, long term hydro-meteorological observations made at a permanent sea level gauge, together with simultaneous observations of bottom pressure recordings at offshore positions and across the Malta Channel. This coastal seiche, known locally as the '*milghuba*', manifests itself in conjunction with the occurrence of mesoscale atmospheric gravity waves travelling in the lower troposphere. The associated open sea waves excite the water bodies of the various inlets, bays and harbours into resonant oscillations which reach a range of up to 1m in Mellieha Bay.

Numerical experiments based on the free surface, non-linear Princeton Ocean Model (POM) in 2D mode explain the response characteristics of two adjacent wide-mouthed open embayments. The seiche-induced barotropic circulation and impact on the flushing of Mellieha Bay are studied by means of an advection-diffusion scheme implemented within POM.

Sea level signals on the synoptic, planetary wave and seasonal scales dominate the residual spectrum. A multiple regression model and a novel analytic technique based on the wavelet transform provide in combination a very effective means of studying the composition of the sea level signal and the dependence of its variability in time on one or more correlated parameters. Atmospheric pressure is the predominant factor determining the sea level variability at frequencies lower than 0.75cpd. In the upper synoptic frequency ($0.3 < f < 0.5$cpd) the response is very close to isostatic, with an average gain of 0.7. At other frequencies the overall response is non-isostatic implying that other factors besides mesoscale atmospheric pressure forcing contribute to the sea level variability. On account of the station's position close to the latitudinal axis of the Strait of Sicily, these signals are important in understanding the control of the Strait on intra-basin exchanges. Seasonal changes in the mean sea level show a major minimum in March and a major maximum towards the last months of the year. Besides the usual steric and direct meteorological effects, this variability is attributed to adjustments in the mass balance of the whole Mediterranean basin.

CONTENT

4. Generation of extreme atmosphere-induced seiche oscillations

5. Seiche dynamics in coastal embayments

LIST OF FIGURES

Chapter 1

Chapter 2

LIST OF TABLES

Chapter 2

Chapter 3

Chapter 4

Chapter 5

ACKNOWLEDGEMENTS

This work would not have been possible without the parallel endeavour to build the supporting structures for the undertaking in Malta of such research studies. The completion of this thesis has been accompanied by the establishment of the Physical Oceanography Unit which is now housed at the University of Malta, and is currently involved in numerous national and international projects. Under these circumstances it was not easy to find the time necessary for this study without stress and hardship, especially when the effort had to be added on top of my other demanding commitments at work.

The greatest sagrifice comes from my family. I am especially indebted to my wife Simone and my two boys, Roberto and Adrian, who have painstakingly supported me throughout the period of my studies. The largest price paid for this work is indeed the precious time that I have had reluctantly to take away from them. Special thanks must also go to my parents who have taught me to believe in my potentials since I was a child and to my father-in-law who has taken care of my family during my frequent visits to Southampton. A special remembrance goes also to my mother-in-law who would be certainly airing her praise to the four winds if she were still with us.

From the scientific point of view the support and direction received from a number of key people and numerous international acquaintances has guided me towards an optimal structure of my study with invaluable advice and comments. Despite his very busy schedule, my tutor Dr. S. Boxall, has been behind me throughout the study period, has encouraged my endeavours, smoothed all the accompanying problems, and has diligently supervised my fieldwork with visits in Malta especially during the initial stages. I am also grateful to Dr. Alexander Rabinovich of the Russian Academy of Sciences for his numerous suggestions, expert advice and for constantly feeding me with new publications on the subject. I wish also to thank staff members at the Proudman Oceanographic Laboratory who have helped me through the conduct of this work. A special thanks goes also to Dr. Salvatore Ferraro who initiated and subsequently fostered my interest on the study of sea level variability during a visit to the Italian CNR Institute in Trieste. The help of Dr. Salvo Mazzola of the Italian CNR Institute in Mazara del Vallo was also indispensable for the deployment of a bottom pressure gauge on the southern coast of Sicily during the Malta Channel Experiment.

My thanks also go to Mr. A. Xuereb and Mr. J. Bianco of the Hydrographic Office at the Malta Maritime Authority for kindly making available the sea level data in the Grand Harbour, and to Major J. Mifsud and Capt. A. Gauci of the Meteorological Office in Luqa for providing the atmospheric data and synoptic maps in Luqa.

I would also like to thank Rev. Prof. P. Serracino Inglott, President of the Malta Council for S&T, who has believed in my capabilities and who has concretely provided the means to support my initiatives in physical oceanography. I would like to finally thank Malta Freeport Co. Ltd. who sponsored my first year of studies, and the Oil Division who supported this work through the provision of the first water level recorder.

1. Introduction

1.1 General background

The quest to improve predictions of the residual circulation and to refine the skill of ocean forecasting numerical models in order to include mesoscale activity which contains energy at the synoptic time scale has in recent years accentuated the challenge to understand the interaction of the sea with the atmosphere. This consideration is indeed crucial for the Mediterranean sea where the tide is generally weak and the tidal circulation is greatly surpassed by the meteorologically forced motions. In the particular case of the Strait of Sicily, the synoptic variability and the mesoscale phenomena constitute very important components of the total flow. The signatures of these phenomena are captured by the sea level signals which carry a high level of variability at the synoptic, seasonal and interannual scales, and as in the rest of the Mediterranean, represent an energetic part of the sea level spectrum.

The Strait of Sicily is a large and dynamically active area connecting the eastern and western Mediterranean sub-basins. The general flow in the strait is mainly driven by the slow (vertical) Mediterranean thermohaline basin scale circulation. The region is known to contain a number of significant hydrodynamical processes and phenomena that span the full spectrum of temporal and spatial scales. The mesoscale processes are triggered by the synoptic scale atmospheric forcing. The heat and momentum fluxes at the air-sea interface represent the dominant factor in the mixing and pre-conditioning of the Mediterranean Atlantic Water (MAW) on its way to the Eastern Mediterranean.

The highly irregular bottom topography of the Strait takes the form of a submarine ridge which connects in the east and west to the respective Mediterranean basins only through a system of narrow sills. This ridge restrains the exchange between the two Mediterranean basins and has a controlling function, in addition to that at the Strait of Gibraltar, on the adjustment of the sea level in the Mediterranean to meteorological forcing. The ridge is characterised by a long-shaped NW-SE basin cutting deep into the continental shelf (Fig.1.1). The average depth of this intermediate basin is in the order of 500m. Owing to the nature of its different behaviour with respect to the main basins, it is generally considered as a third basin: the Central Mediterranean Basin. In contrast to the rest of the Mediterranean, the continental margins in the Strait are rather wide and shallow. On the African coast the shelf area covers more than a third of the areal extent of the Strait with water depths less

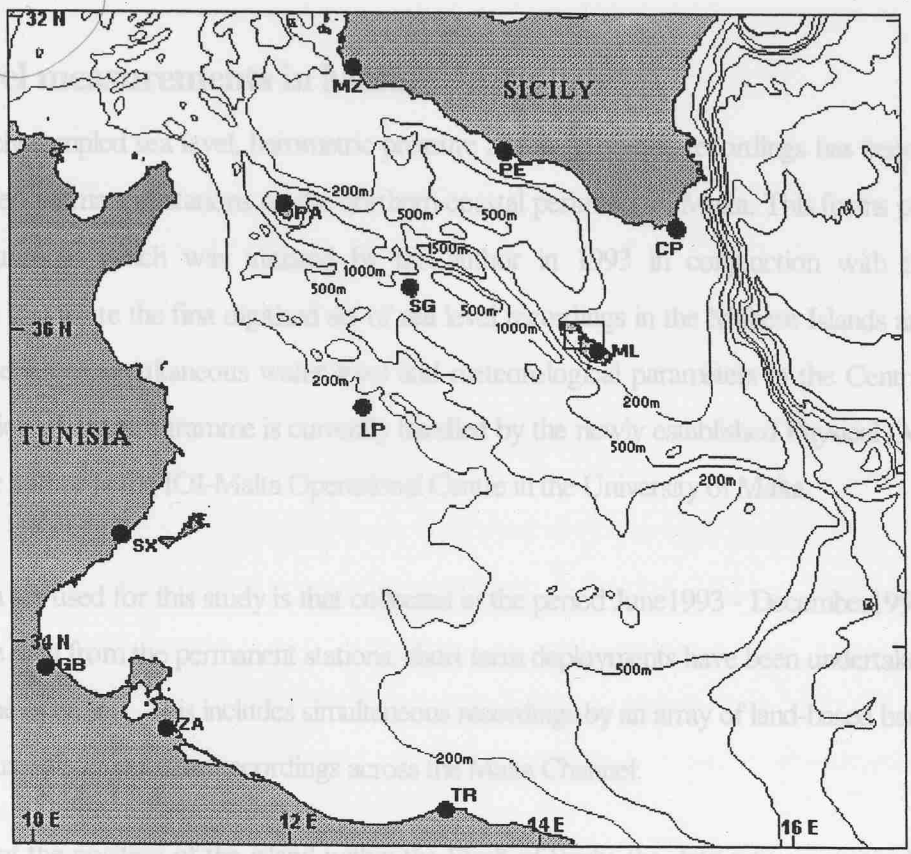

Gabes	= GB	Sfax	= SX
Zarzis	= ZA	Pantelleria	= PA
Lampedusa	= LP	Mazara del Vallo	= MZ
JANUS SG	= SG	Tripoli	= TR
Porto Empidocle	= PE	Malta	= ML
Capo Passero	= CP		

Fig. 1.1 The Central Mediterranean showing the sea level stations and the main isobaths.

than 30m in the Gulf of Gabes. Along the southern coast of Sicily the shelf takes the form of two disconnected and relatively shallow (< 200m) banks. The Maltese Archipelago, consisting of a group of small islands aligned in a NW-SE direction, is located close to the southeastern margin of the Sicilian shelf. The islands are thus located at an oceanographically strategic position in the middle of the exchange flow through the Strait, and act like a permanent station close to the shelf break.

1.2 Sea level measurements in Malta

A set of densely sampled sea level, barometric pressure and wind vector recordings has been collected at two recently installed permanent stations on the northern coastal perimeter of Malta. This forms part of an ongoing research programme which was initiated by the author in 1993 in conjunction with this study. These measurements constitute the first digitised set of sea level recordings in the Maltese Islands and are to date the longest time series of simultaneous water level and meteorological parameters in the Central Mediterranean. The continuation of this programme is currently handled by the newly established Physical Oceanography Unit manned by the author at the IOI-Malta Operational Centre in the University of Malta.

The main data set used for this study is that collected in the period June1993 - December1996 (43months). In addition to the data from the permanent stations, short term deployments have been undertaken, both along the coast and in the open sea. This includes simultaneous recordings by an array of land-based barographs and a set of simultaneous bottom pressure recordings across the Malta Channel.

On the merit of the position of the island within the Strait of Sicily, the data sets are particularly important for understanding the role of the strait in controlling the exchange between the two major basins of the Mediterranean Sea. With an internal Rossby radius of just a few tens of Kilometres on the shelf areas, mesoscale phenomena in the Strait of Sicily are impossible to detect and follow unless a detailed observation set is available in both time and space. Under such circumstances, sea level measurements become of great relevance as an indicator of the general dynamics of the sea (Wunsch, 1972) especially when measured, as in the case of Malta, at a location away from the continental mainland.

1.3 The 'Milghuba' phenomenon

The most remarkable feature in the analysis of the sea level data described above is the presence of a band of high frequency signals with periods ranging from several hours to as low as a few minutes. These non-tidal short period sea level fluctuations are an expression of a coastal seiche, known by local fishermen as the '*milghuba*'[1] . This phenomenon has now been observed to occur all along the northern coast of the Maltese

[1] The term '*milghuba*' comes from the Maltese verb '*laghab*' which means 'play'. The terminology refers to the 'play of the sea'.

archipelago and manifests itself with very short resonating periods of the order of 20 minutes in the adjacent coastal embayments. The phenomenology, generation and impact of the '*milghuba*' on the coastal dynamics constitute the major focus for this study.

Analysis of the full data set shows that weak seiching is present uninterrupted and appears as a background 'noise' on the tidal records. During random sporadic events the seiche oscillations can however become greatly enhanced and mask completely the astronomical signal. These large-amplitude sea level oscillations are accompanied by remarkable currents that are triggered by the sloshing water masses. While these seiche induced currents can be an important means for the flushing of coastal inlets and harbours, they can on the other hand be dangerous to navigation. Similar seiche oscillations have been reported in other parts of the world ocean, with the most recent studies being those conducted in Puerto Rico and the Philippines (Giese et al., 1982), in Nagasaki on the southern coast of Japan (Hibiya & Kajiura, 1982), at Capetown in South Africa (Shillington, 1984), at the Balearic Islands (Monserrat et al., 1991), and in the South Kuril Islands (Djumagaliev & Rabinovich, 1993). They are reported to cause severe damage to coastal areas, boats and port constructions. Due to their close relation with the behaviour of tsunami, research on seiches is considered to be important in disaster mitigation studies (Taku et al., 1992).

Reference to similar sea level variations (known as the '*Marrubbio*') on the southern coast of Sicily is found in the Italian 'Portolano' for ship navigation. Their occurrence is reported to be most frequent in May or June in association to southeasterly winds, and their crest-to-trough amplitudes reach as high as 1.5m. Literature on the '*Marrubbio*' is however very scarce and the only relevant publication is by Colucci & Michelato (1976). It is interesting to note that one of the first scientific studies on seiches by Sir George Airy (1878) refers precisely to the Grand Harbour in Malta. Since then the seiche phenomenon in Malta remained unstudied and this work is indeed the first dealing with these high frequency sea level oscillations in this region.

The large amplitude seiches in the Maltese Islands are mainly of an atmospheric origin. The simultaneous measurements of sea level and atmospheric pressure reveal the presence of pressure fluctuations of the order of a few millibars in coincidence with the occurrence of seiche events. These pressure signals are believed to be the surface expression of atmospheric wave disturbances that propagate in the lower troposphere as internal gravity waves. Their interaction with the open sea surface triggers the long period waves that subsequently force the seiches in the coastal areas. Part of this study focusses on the nature of these atmospheric waves and on those

factors that are important in the associated air-sea interaction. With an aim of developing a predictive capability of these events the study also attempts to identify the upper air conditions and the synoptic situations that most favourably trigger their occurrence.

1.2 Overview of the thesis

1.2.1 Aims and objectives

The overall objective of this work is to make an exhaustive and detailed analysis of the sea level signals collected in Malta and at the same time provide a broad and updated overview of current trends in the study of sea level variations particularly in the case of long period waves. This work also proposes new numerical techniques, in addition to more classical methods, for an improved analysis of data. It moreover makes use of robust finite difference numerical model applications to simulate the barotropic seiche dynamics in coastal areas. More specifically the main aims are to:

- identify and quantify the tidal and non-tidal signals composing the sea level spectrum in the vicinity of the Maltese Islands, and study their occurrence and variability in relation to the adjustment of the Mediterranean Sea to meteorological forcing and to other pertinent oceanographic processes;

- study the dependence of the low frequency variability on meteorological forcing by means of multiple regression analysis in the frequency domain;

- apply novel techniques of time series analysis such as that utilising the wavelet transform;

- study the phenomenology and generation of the 'milghuba' oscillations and of the long period wave field in general, including the incidence and amplification of these waves in coastal areas;

- assess the evidence and identify the conditions in favour of the triggering of large amplitude coastal seiches by atmospheric forcing;

- simulate the seiche-induced dynamics and the long-wave characteristics by means of finite difference numerical model applications;

1.2.2 Thesis structure

Further to this introductory Chapter, the thesis is divided into a total of four other chapters which specifically address different but inter-related aspects of the study. The extensive number of scientific publications consulted in this work are not reviewed in one place, but are instead referred to at appropriate places and in the context of the themes being tackled.

The general sea level characteristics and variability are treated in Chapter 2. The tidal signals are analysed by harmonic analysis and results compared to current tidal models for the Central Mediterranean Basin. The oscillations of non-tidal origin are studied in detail. The long series of observations are used to obtain information on the dependence of sea level variability, particularly at the synoptic and planetary wave time scales, on meteorological parameters. A novel method utilising wavelet analysis is used to assess the temporal development of the air pressure-sea level interaction. The validity of the wavelet transform is verified both as a means of decomposing and identifying the nature of a signal as well as a means of identifying the phenomenology in time space of one or more interdependent parameters. The combined use of a multiple regression model and the wavelet transform analysis is shown to permit a detailed analysis in both the frequency and time domains. The strong seasonal non-eustatic fluctuations in the mean sea level are treated at the end of the Chapter.

Chapters 3 - 5 deal more specifically with the '*milghuba*' phenomenon. The occurrence of strong seiche events is analysed in Chapter 2 by statistical techniques and their characterisation studied by means of visual classification methods, by spectral signatures as well as by a novel peaks analysis. The normal modes of barotropic oscillations of a number of coastal embayments and the Grand Harbour in Malta are calculated by solving the Helmholtz equation using a finite difference scheme. The method and corresponding code are presented and explained. Results are discussed with an aim of better understanding the response of the coastal embayments to forcing by long period waves in the open sea. Results are compared and verified against observations. The coupling between two adjacent embayments, Mellieha Bay and St. Paul's Bay, is also addressed. Observations of sea currents inside Mellieha Bay are used to quantify the role of seiche-induced water movements in the flushing of the bay. The Chapter closes by an account on the resonant oscillations of the outer shelf through the analysis of bottom pressure measurements at offshore stations including simultaneous recordings conducted on the southern coast of Sicily.

The study in Chapter 4 focusses on the identification of those atmospheric parameters that are responsible for the generation of extreme atmosphere-induced seiche oscillations. The generation mechanism for strong seiching is studied and compared to that causing ordinary background oscillations. This analysis is carried out by examining the response of an embayment to different atmospheric events as well as by comparing the response of different embayments to a given atmospheric perturbation. A set of simultaneous barograph measurements is used to study the generation of large-amplitude seiches by atmospheric gravity waves. Important atmospheric wave parameters and conditions favouring this interaction are assessed.

In Chapter 5 the Princeton Ocean Model (POM) in 2D mode is used to simulate the resonant periods and admittance function of Mellieha Bay and St. Paul's Bay by finite difference numerical methods. The model applications are used to obtain an improved understanding of the influence of the local topography and geometry in the amplification of long period waves incident into an embayment. The results of the model runs provide further insight into the role of leaky and bound waves in the excitation of oscillations in the embayment. An advection-diffusion transport model based on POM is furthermore written and applied to quantify the role of the seiche-induced circulation in flushing contaminants from Mellieha Bay.

The thesis ends by an overall summary together with an outline for future research directions in this field and new emerging opportunities for a more systematic observation of sea level in the Mediterranean Sea.

2. Sea Level variations along the Northern Coast of Malta

2.1 General introduction

2.1.1 Tides in the Mediterranean

Although the tides of the Mediterranean Sea are relatively weak with a typical range of 5 - 20cm, they have been an object of study since classical times. As reviewed by Grace (1931), the first theories treated the Mediterranean basins as separate closed entities and derived the equilibrium tide to each of them. Early twentieth century studies (Defant, 1961) already realised the importance of including the effects of the co-oscillation with the Atlantic tides through the Strait of Gibraltar. The broad outlines of the Mediterranean tide were established as being predominantly semidiurnal with standing wave regimes in four main basins that are separated by narrow nodal zones close to Alicante, Tunis and Crete, and with shallow-sea resonances at the head of the Adriatic and in the Gulf of Gabes. The syzigial excursions in Trieste and in the Gulf of Gabes reach 105cm and 216cm respectively (Mosetti & Purga, 1989). The M_2 tide alone has a remarkable amplitude of 48cm in Gabes.

On the basis of more recent studies it is clear that, contrary to earlier belief, the main Mediterranean tide is caused by the direct action of the tidal forces on the Sea itself. Extensive measurements of tidal currents around Gibraltar, demonstrate that forcing by the Atlantic tide could only account for 10% of the tidal motions in the Mediterranean basin (Candela et al, 1990). The phase relation between the barotropic tidal flow and the elevation in the strait corresponds to that of a standing wave, with the M_2 tide having no net energy flux through the strait. The important result is that the western Mediterranean does co-oscillate with the Atlantic tide, but all the dissipated energy must be provided by the action of the tidal forces on the whole Sea.

The diurnal constituents are generally weak except in the Adriatic where basin characteristics reinforce the amplitude of K_1, and f-values are higher than 0.5 (Manzella & Elliott, 1991). The tide in the Western basin is generally mixed, but f-values tend to decrease towards east where the contribution of the diurnal tide becomes progressively smaller. From tidal information obtained by harmonic analysis of observations at a large number of localities, Defant (1961) has explained the diurnal tide in the Mediterranean as the superposition of two

asynchronous waves, one originating from the co-oscillation with external Atlantic tide, while the other is the independent diurnal tide of the entire basin. The co-oscillation has two nodal lines: one in the Strait of Gibraltar itself, and the other in the Straits of Sicily and Messina. The independent tide is zero at Cadiz, increases in the western basin and then decreases steadily with a phase reversal at a nodal line in the Ionian Sea.

2.1.2 Tides in the Central Mediterranean

The general tidal pattern for the Mediterranean Sea as a whole gives nodal locations in the Strait of Sicily, and the magnitude of the tide in the region is thus generally small (Defant, 1961). The phase and amplitude of the four main tidal harmonic constituents for the main ports in the Central Mediterranean (Table 2.1) are based upon values from Mosetti & Purga (1989), Molines (1991) and Tsimplis et al. (1995). M_2 and S_2 are the semi-diurnal lunar and solar constituents respectively; K_1 and O_1 are the soli-lunar and the main lunar diurnal

Table 2.1

Harmonic constants for the Central Mediterranean Basin. Amplitudes in centimteres; phases in degrees, relative to UT

Station	Latitude	Longitude	M_2 cm /Deg	S_2 cm /Deg	K_1 cm /Deg	O_1 cm /Deg	Mean Spring Range	Mean Neap Range	Form Number
Gabes	33°53'	10°07'	51.1 79	36.4 107	2.5 349	0.5 81	175	29.4	0.034
Sfax	34°44'	10°46'	41.6 76	26.7 103	1.8 4	0.8 82	136.6	29.8	0.038
Zarzis	33°30'	11°07'	21.9 77	15.3 103	2.0 31	0.9 102	74.4	13.2	0.078
Pantelleria	36°47'	12°00'	1.6 31	1.9 42	1.3 184	1.4	7.0	0.6	0.771
Lampedusa	35°30'	12°30'	6.6 45	4.2 58	0.9 3	0.7	21.6	4.8	0.148
Mazara del Vallo	37°38'	12°35'	4.3 161	1.8 151	3.5 114	1.6 74	12.2	5.0	0.836
JANUS SG	36°10'	12°59'	4.8 50	3.1 57	0.5 78	0.9	15.8	3.4	0.177
Tripoli	32°54'	13°12'	11.1 60	5.4 75	2.0 13	0.6 121	33.0	11.4	0.158
Porto Empidocle	37°15'	13°30'	4.5 78	3.3 77	1.8 91	1.4 76	15.6	2.4	0.410
Malta	35°54'	14°31'	6.3 47	4.0 57	1.0 19	0.8 55	20.6	4.6	0.175
Capo Passero	36°41'	15°09'	6.7 62	3.5 67	1.9 52	0.9 46	20.4	6.4	0.275

Station locations are indicated in Fig. 1.1

constituents. Mean neap $2(M_2 - S_2)$ and spring $2(M_2 + S_2)$ tidal ranges and also the form number $(K_1 + O_1)/(M_2 + S_2)$ (Defant,1961) are included in Table 2.1. The values are in most cases derived from short series of tide gauge data. The constituents for Mazara del Vallo, the island of Pantelleria, the island of Lampedusa and an offshore mooring (SG) situated at approximately 20 nautical miles in the NNE of Linosa Island are taken from 9 months of bottom pressure measurements carried out during the JANUS Experiment (Astraldi et al., 1987).

The known longest historical sea level data set in the region refers to the Grand Harbour in Malta; these chart records are kept at the British Hydrographic Office and cover the period 1876-1926. The gauge was held in the French Creek except for a period of five years starting from 1903 when the measurements were transferred to Ricasoli. Unfortunately no records have been found after 1926.

In general there is a discrepancy in the phases of the constituents quoted by various sources and calculated from one or more years of this data from the Grand Harbour; the values in Table 2.1 are thus based on an analysis of 13 months of more recent data from May 1990 to May 1991 (Drago,1993). Besides the tabulated values, other important constituents in this port are N_2 (1.1cm; 48°), K_2 (1.3cm; 47°), and P_1 (0.2; 358°).

The tidal oscillations in the Strait of Sicily are dominated by the semidiurnal constituents with supplementary contributions from the diurnal constituents especially on the North African coast. M_2, S_2, K_2, N_2, K_1 and O_1 are the only components greater than 1cm (Purga et al., 1979). The higher frequency components are reported to be less than 1mm on the Sicilian coast (Mosetti et al., 1983). Notwithstanding their small size, the tides in this region denote a behaviour of particular interest. They are greatly connected with the hydrodynamics of the whole Mediterranean sea and their development is related to the influence of tidal co-oscillations. The basin morphology has also important effects and the relatively shallow bathymetry on the African shelf results in an amplification of the tide. The syzigial excursions in the Gulf of Gabes reach 216cm (Mosetti & Purga, 1989). The M_2 tide alone has a remarkable amplitude of 51cm in Gabes (Molines, 1991).

The diurnal tides are everywhere small and without nodes in the Strait (Manzella et al., 1988). The amplitude of K_1 is uniform with values of 3.1cm at Gabes and 2.1cm at Cape Passero. On the other hand the influence of the rotation of the earth causes strong transverse (North-South) oscillations that transform the nodal lines of the semidiurnal components in the region into amphidromies contra solem. On the basis of semi-empiric considerations, Sterneck (1915) had prognosticated an M_2 amphidromic point close to Pantelleria even before

tidal coastal data could provide a confirmation by means of field measurements. Numerical simulations of the barotropic tide (Mosetti & Purga, 1989 and Molines, 1991) have recently succeeded to reproduce these tidal features and to elaborate on the associated hydrodynamics.

2.1.3 Non-tidal sea level oscillations

Besides the influences of tidal origin, the sea level variability in the Strait of Sicily also depends on effects derived from interference by the general circulation, from mesoscale eddies propagating on the Sicilian shelf, from fronts and in particular from meteorological factors. The annual and semi-annual components Sa (365.3 days) and Ssa (182.6 days) are rather strong. Values for these long period constituents at Porto Empedocle and Cape Passero, along the southern coast of Sicily, exhibit a high spatial coherence, and give a contribution to the sea level variations that is in phase with the annual variations in atmospheric pressure (Mosetti & Purga, 1982). A direct inverse barometric effect is thus excluded at this scale. The dependence of the sea level on the atmospheric

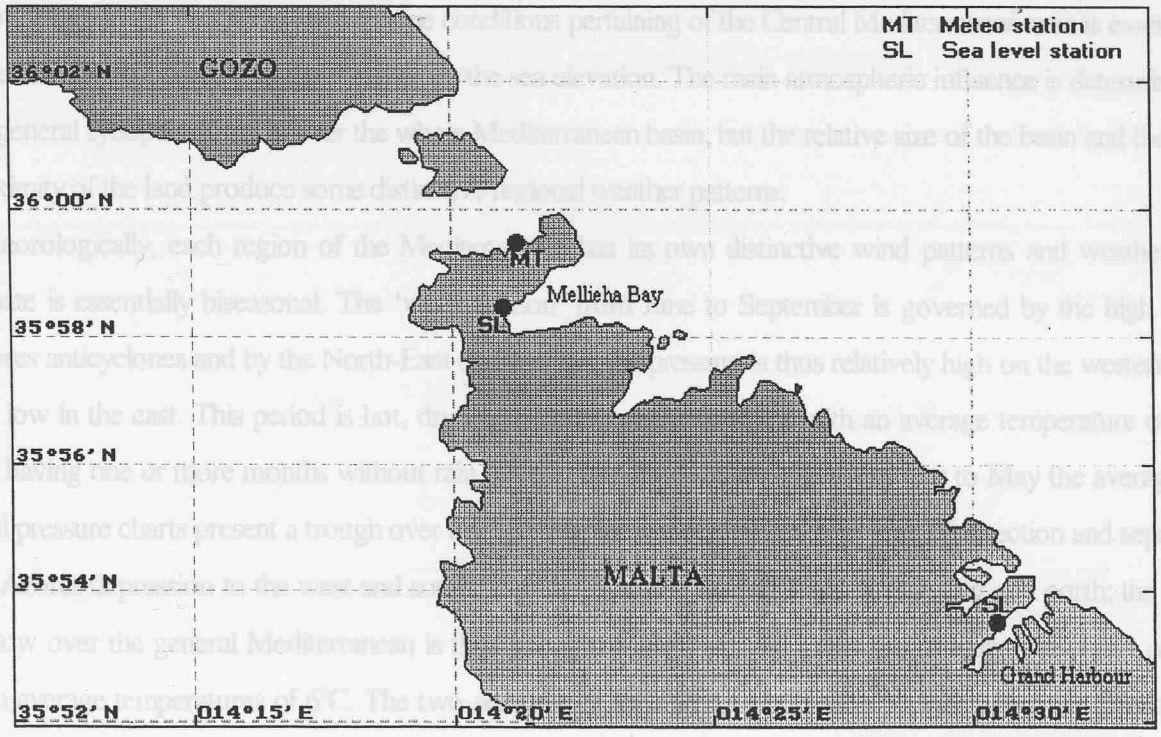

Fig. 2.1 Location of the hydro-meteorological stations.

pressure is a complex one and is directly modified by geostrophic gradients produced by different pressure regimes between the Western and Eastern Mediterranean basins.

The sea level and its variability in the Strait of Sicily is under studied. There are few if any long data sets especially on the African coast. Storm surges and seasonal sea level fluctuations in this region of the Mediterranean have not previously been studied. The only investigations relating to the low frequency variations are by Manzella et al. (1988), using bottom pressure measurements obtained during the Janus Experiment, and by Drago & Ferraro (1996) who analysed the sub-tidal signals from mean daily values of sea elevation in the Grand Harbour in Malta. The work presented in this chapter attempts to improve the knowledge on the full spectrum of sea level signals in the region through the analysis of the recent densely sampled sea level and meteorological data obtained from stations on the northwestern shore of Malta (Fig. 2.1).

2.1.4 Weather in the Central Mediterranean

Knowledge on the prevailing atmospheric conditions pertaining of the Central Mediterranean area is essential in understanding the forcing of the weather on the sea elevation. The main atmospheric influence is determined by the general synoptic situation over the whole Mediterranean basin, but the relative size of the basin and the close proximity of the land produce some distinctive regional weather patterns.

Meteorologically, each region of the Mediterranean has its own distinctive wind patterns and weather. The climate is essentially biseasonal. The 'warm season' from June to September is governed by the high of the Azores anticyclones and by the North-East depressions; the pressure is thus relatively high on the western basin and low in the east. This period is hot, dry and predominantly cloudless with an average temperature of 21°C and having one or more months without rain. During the 'cool season' from October to May the average sea-level pressure charts present a trough over the Mediterranean oriented in a NW and SE direction and separating the Azores depression to the west and south from the Eurasian thermal highs to the east and north; the winter airflow over the general Mediterranean is thus strongly convergent and gives rise to rainy and windy periods, with average temperatures of 6°C. The two seasons are separated by transition periods which are a mixture of the two main seasons and have no special characteristics of their own. In the eastern Mediterranean these transition periods normally take place in April and October/November; in the western Mediterranean they occur in May and October.

In winter, with the retreat of the sun south of the equator the general circulation of depressions entering from the Atlantic becomes predominant. These Atlantic depressions enter the Mediterranean by the Straits of Gibraltar and Spanish coasts or across the Bay of Biscay, travelling west to east and making the winter weather most unsettled with rain, sudden winds and agitation of the sea. The penetration of cold polar air from central and northern Europe also controls Mediterranean winter climate. The encounter of these frequent waves of cold air with the relatively warmer and moist air of the Mediterranean brings about vertical instability and the generation of depressions. The two main formation regions are the Gulf of Genoa and the region to the southeast of the Atlas Mountains. Both regions lie in the lee of predominantly northwesterly winds so that the depressions are initially lee lows. The lows in both regions may subsequently develop into vigorous circulations accompanied by considerable rainfall and frequently associated with gales. It is however important to note that whereas in the higher latitudes the warm sectors of frontal systems are usually associated with extensive layers of cloud, high humidities and precipitation, in the Mediterranean they may well be almost cloudless and quite dry. Occasionally the southern branch of the European jet stream overlies the Mediterranean latitudes and acts to intensify disturbances steering them eastwards along the main axis of the sea (Trewartha, 1962). The Mediterranean lows are however smaller in extent and less deep in comparison to the Atlantic lows; also anticyclones over the region

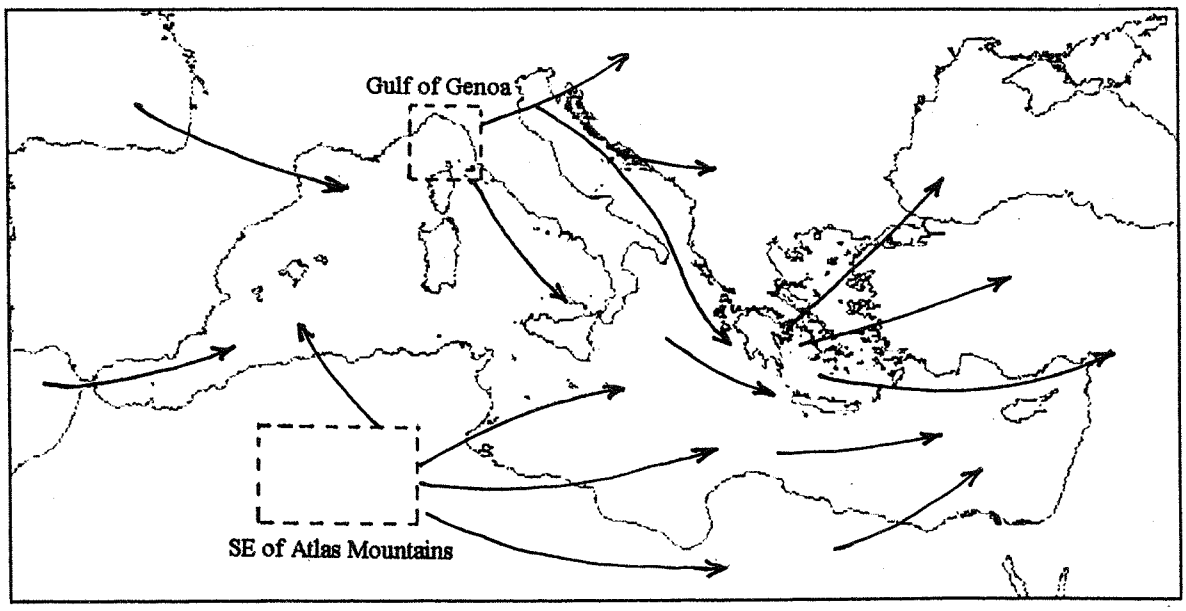

Fig. 2.2 Depression tracks and their main areas of formation

are not as intense as Siberian anticyclones, and the extreme range of pressure over the sea area is only from about 970 hPa to 1030 hPa. This makes the duration of bad weather associated with the Mediterranean lows shorter, but no less intense than disturbances of Atlantic origin.

Depressions also occur in the transition periods. In April/May the lows affecting the northern areas tend to be less vigorous than in winter, whereas the desert lows in the south are most vigorous and generally produce the strongest, dustiest Sciroccos, in the early transition period. In September/October the reverse is the case. Desert lows tend to be weaker and less frequent whereas north Mediterranean lows may become vigorous and produce gale or sometimes storm force winds in northern sea areas.

The track of an individual depression is generally determined by the airflow at levels well above the surface, but the topography of the land surface tends to steer their tracks parallel to the mountain ranges. Temperature is also important in that winter lows tend to remain over the warmer sea surface as long as possible. Fig. 2.2 shows the main tracks of the depressions which form in the Mediterranean. Their effect on the weather in the Sicilian Channel and the associated synoptic situations that can result in gales around the Maltese Islands is shown in Fig. 2.3. As in the rest of the Mediterranean, light to moderate winds prevail in this region for most of the time, but strong winds can be experienced almost throughout the year although their frequency is much less during summer when pressure gradients are usually less. Based on data collected at the Meteorological Office in Luqa from 1854 to 1986, the mean value of the wind speed according to both strength and frequency is 8.5 knots ($4.4 ms^{-1}$). The predominant wind speed is below 10 knots (Beaufort force less than 3) and the wind vector blows mainly from directions between 260° and 340°. The percentage frequency of calm is only 13%. The prevailing wind, especially during the winter months, is the northwesterly (Mistral) wind which blows on average about 103 days a year, usually in periods of three days. Due to the funnelling effect, the Mistral is also the strongest wind both locally and over the whole Sicilian Strait, and often reaches gale force. During summer the northerly and northeasterly winds become equally dominant to wind blowing from the northwest.

The Mistral is often associated with lows that develop over Northern Italy and move towards east down the Adriatic. As the accompanying cold front sweeps across the Central Mediterranean the southwesterly (Libeccio) or westerly wind switches abruptly to northwesterly and often intensifies to gale force as the low

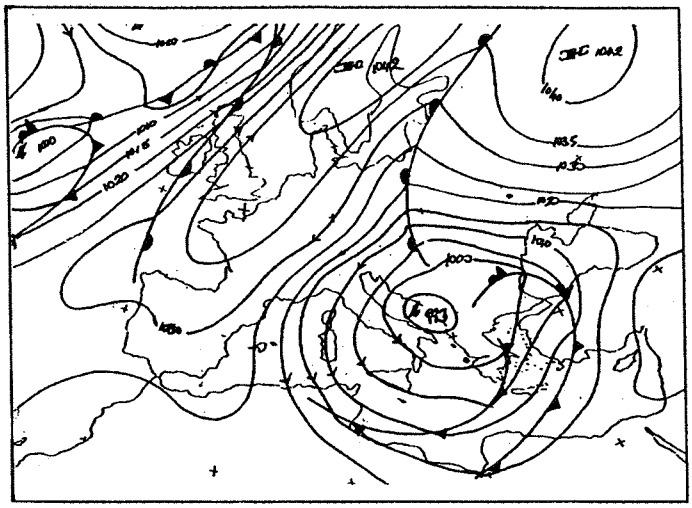

(a) Depression over the Adriatic producing northwesterly wind with gale force (21/1/98)

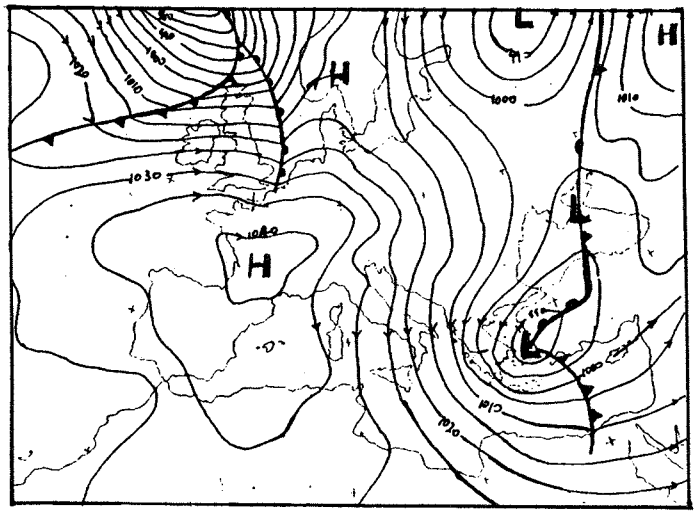

(b) Deep depression over the Aegean maintaining strong NW airflow over the Maltese Islands (29/1/94)

Fig. 2.3 (a),(b) Typical synoptic situations producing the most common strong winds in the Central Mediterranean.

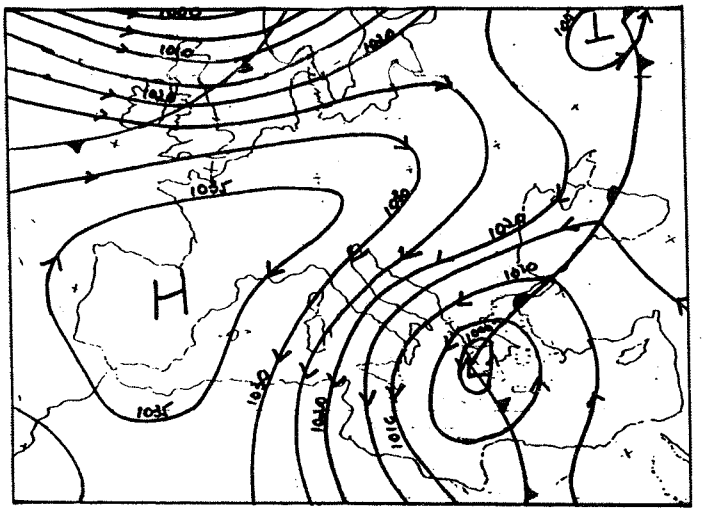

(c) Low over the South Ionian giving rise to strong occasionally gale force North to NE wind (14/1/95)

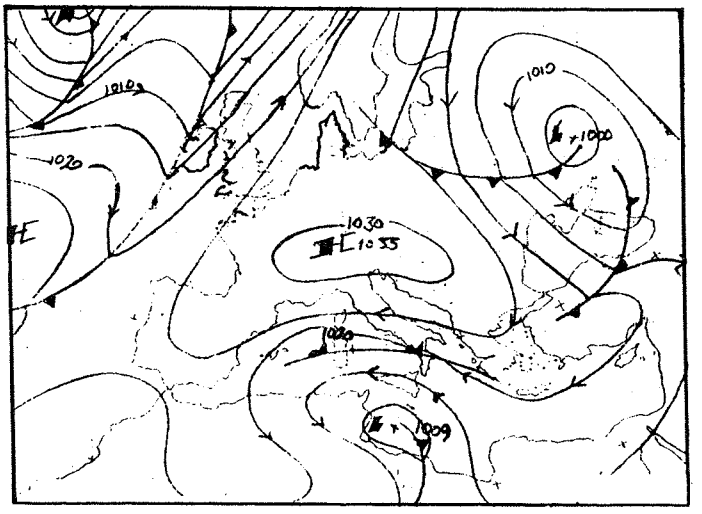

(d) Low pressure persisting to the SW of Malta accompanied with strong ENE wind and rough sea (30/12/92)

Fig. 2.3 (c),(d) Typical synoptic situations producing the most common strong winds in the Central Mediterranean.

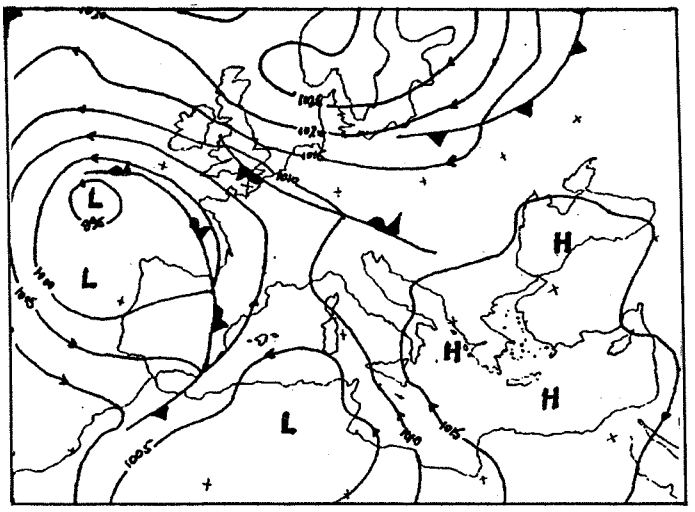

(e) Strong SE winds caused by low pressure over Tunisia and high over Greece (13/5/94)

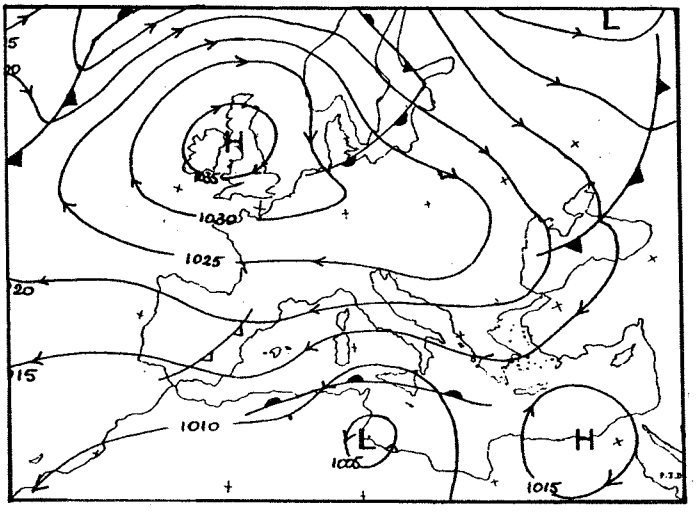

(f) A North African depression affecting the Maltese Islands with strong easterly wind (26/10/93)

Fig. 2.3 (e),(f) Typical synoptic situations producing the most common strong winds in the Central Mediterranean.

establishes itself over the North Ionian Sea or over Greece. The whole process can be repeated with the approach of a secondary front. A depression over eastern Algeria and Tunisia together with a high over Greece or the more extreme eastern areas of the Mediterranean can often produce strong pressure gradients over the Ionian and Central Mediterranean leading to strong southeasterly (Scirocco) winds of continental tropical origin. Such an event occurs mainly towards late winter or in the April/May transition and is occasionally accompanied by a heat wave with hot days and a rusty, cloudy sky loaded with Saharian dust that comes down with the drizzling rain. As the air flow passes over a large sea area, the associated moisture is relatively high and the Scirocco is usually much more wet compared to the dry Libeccio. Another meteorological situation, leading in this case to winds from the northeast (Gregale), is depicted in Fig. 2.3d and can become established during the 'cool season' especially during the period December to February. As a depression moves slowly towards east along the Libyan coast and becomes established over Benghazi, the contrast with the high pressure over Europe triggers the very strong Gregale which leaps down from the Greek and Balkan mountains and blows with a long duration and a long fetch piling up the sea all the way to the island of Djerba and the North African coast. This wind is not frequent but generally rises to gale force and is associated with heavy rain and poor visibility. During such meteorological conditions vigorous sea waves are usually set up in the Malta Channel. Significant wave heights of up to 6.5m have been reported off Malta on the occasion of gale winds from the northeast. These waves impinge orthogonally to the northern coast of the Maltese Islands and can hazardly penetrate the otherwise sheltered ports and embayments that stretch in parallel to their direction.

2.2 Materials and methods

2.2.1 Sea level measurements in Mellieha Bay

Since May 1993, densely sampled sea level data (at the variable rate of 30 or 60 samples per hour) have been collected at a permanent tide gauge installation positioned at the head of Mellieha Bay which is a small embayment on the northwestern coast of Malta (Fig. 2.1). The design and setting up of this sea level station by the author forms part of this work. It consists of an Endeco Type 1029/1150 differential pressure tide gauge which is clamped inside a small stilling well connected to the sea. The sensor is a highly accurate strain gauge with slight non-linearity, but ultra-high repeatability and with practically no long term drift. The pressure transducer is located in a subsurface case and at each recording it samples for a total of 49s in order to filter surface waves; records are logged onto a removable solid-state EEPROM cartridge situated in a topcase

recording unit. A thermistor bead bonded to the strain gauge is used to measure temperature and allows compensation for temperature effects on the transducer. The instrument measures absolute pressure; atmospheric pressure is compensated by means of a vented tube which passes through the topcase unit and terminates inside an environmental isolator in the form of a small exposed PVC tube with a bladder. The tide gauge datum is regularly checked for stability throughout the observation period. Sea levels are given from the zero of the tide gauge which is 2.6507m below BM No. 9541811 established by the Mapping Unit of the Malta Planning Directorate.

2.2.2 Collection of Meteorological Data

Meteorological parameters are also measured by Aanderaa sensors at a nearby automatic weather station in Ramla tal-Bir which is situated on the coastal strip overlooking the South Comino Channel. The sensors are positioned in an unobstructed location at a height of 20m from mean sea level. The data set consists of wind speed and direction, air pressure and temperature, relative humidity and net atmospheric radiation each measured at one or two minute intervals. The station is in operation since April 1994. Its design and setting up by the author forms also part of this work.

The anemometer measures the arithmetic mean of the wind speed with an accuracy of ± 2% of the reading and a threshold of $0.5ms^{-1}$. The wind direction sensor consists of a light wind vane pivoted on top of the housing, and magnetically coupled to a compass with a potentiometer ring inside the housing. Damping fluid in the vane shaft opposes rapid changes but permits light wind line-up so that an accuracy of ± 5° is achieved. Air pressure is measured by means of a miniature monolithic silicon pressure transducer with an accuracy of ± 0.2mb. Air temperature is measured to a resolution of 0.05°C by means of a 2000Ω platinum resistor which is protected by a radiation screen. The measurement of relative humidity is based upon the relationship between humidity and the length of a hygroscopic fibre. The variation of length gives rise to a force which is applied to a silicon beam whose deflection causes a change in resistance in two diffused resistors that form part of an electrical half-bridge. The accuracy of the measurement is ± 3%RH. The pyrgeometer employs a symmetrical high-sensitivity thermistor bridge that measures the temperature rise of a horizontal black surface. The symmetrical design ensures that the reading of the sensor is affected only by radiation (wavelength 0.3 - 60μm) and not by changes in ambient temperature. The accuracy of the measurement is ± 3% of the reading.

A 12-channel Aanderaa Sensor Scanning Unit model 3010 is used to read data from the sensor array. The unit has a built-in clock which triggers the measurement cycle at predetermined intervals. At each scan with a duration of 48 seconds, the unit measures in turn the input signal at each channel and transforms the readings into 10-bit data words. Channel 1 is reserved for a fixed reference reading which serves as a check on the performance as well as a station identifier. The remaining channels accept signals from the sensors. Data is recorded in the field by means of an electronic Data Storing Unit 2990 (DSU). This is a waterproof unit, based on CMOS RAM, and is capable of storing up to 64000 10-bit binary words. Data from the DSU is read by means of programme P3059 furnished by Aanderaa.

Meteorological data from this station is missing in the period between mid-October 1994 and mid-March 1995 due to sensor malfunction caused by the stray effect of a nearby lightning stroke. The data sets from this station constitute the first digitised measurements of hydro-meteorological parameters in Malta.

2.2.3 Other data sets

Short analogue records of hourly sea level data in the Grand Harbour and of 3-hour sampled air pressure at Luqa are provided by the Hydrographic Office of the Malta Maritime Authority, and by the local Meteorological Office respectively. Upon digitisation these data sets are also used in addition to the above data.

2.2.4 Processing of data

The software that comes with the instruments described in sections 2.2.1 and 2.2.2 is mainly used to communicate and configure or download data from the instruments. Processing of the collected data is simply limited to a listing in engineering units. A suite of MATLAB[1] macros have been thus developed as part of this work in order to quality check and edit data sets with efficiency. Other MATLAB macros are moreover written for preliminary processing (e.g. filtering of vector data, extraction of segments of data from larger data sets, re-formatting of data to prepare input files for other applications such as for tidal analysis, time location of maxima and minima, calculation of statistics, etc.), for management and archival, and for graphical presentation of data sets.

[1] MATLAB is an integrated technical computing environment that combines numerical computation, advanced graphics and visualisation, and a high level programming language. It is distributed by The MathWorks Inc., USA.

2.2.4.1 Data quality checks and editing

A MATLAB macro is written to check and edit raw data files consisting of listings of 10-bit words produced by Aanderaa instruments. Each record in the input raw data file is checked for consistency in the reference channel, in parameter values which must fit within a specified range, as well as in length in order to detect any missing fields. Consistency in time is verified by counting records between successive date/time labels in the file. Time jumps or gaps of one record are automatically compensated by interpolating missing values. If more than one record is found missing, the program exits with notification. The edited data file is accompanied by a log file which registers the changes made on the original data file. The edited data file is then transformed into engineering units by the programme P3059 supplied by Aanderaa Instruments.

A MATLAB macro is also written to append meteorological data files in chronological order. The output files consist of a series of combined files which give listings of the meteorological parameters in separate files. Before appending, the input files are checked for identical sampling intervals and for gaps between successive files. In the case of gaps less than 2 hours, missing values are linearly interpolation. Information on the processing is kept in a log file for reference.

The same treatment is applied by a similar MATLAB macro written for sea water elevation data files.

2.2.4.2 Further preparation of meteorological data

It is also appropriate to mention here that the atmospheric pressure must be reduced to its effective value at sea level. The variation in atmospheric pressure P with height h can be assumed to follow the hydrostatic equation: $\frac{dP}{dh} = -g\rho_{air}$, where g is the Earth's free gravitational acceleration. The equation of state for dry air $P = \rho_{air}RT$, where R is the specific ideal gas constant for dry air (R = [Universal gas constant] / [Molecular mass of dry air] = 8314.36 / 28.966 = 287.04 J Kg^{-1} K^{-1}) and T is the absolute air temperature, is also adopted. Moisture effects on the air density (ρ_{air}) are known to be significant only in the tropics at near surface levels and even then the maximum departure from the dry equation of state is only about 2%. Combination of the two equations gives:

$$\frac{1}{\rho_{air}}\frac{dP}{dh} = -\frac{g}{RT} \quad . \qquad (2.1)$$

If temperature is known as a function of height, this equation can be integrated. In the case of a constant temperature T throughout the vertical extent H_s joining the position of the sensor and the mean sea level,

$$\int_{P_o}^{P_{H_s}} \frac{dP}{P} = -\int_0^{H_s} \frac{g}{RT} dh \Rightarrow P_o = P_{H_s} e^{gH_s/RT}, \quad (2.2)$$

where P_{Hs} is the measured atmospheric pressure and P_o is its value reduced at mean sea level. Pressure variations must also be reduced by the same relation, that is:

$$\Delta p_o = \Delta p_{H_s} e^{gH_s/RT}. \quad (2.3)$$

With Hs=20m and an average air temperature of 295K, $\Delta p_o = 1.00226 \Delta p_{H_s}$.

Air pressure data are expressed in millibars and corrected to mean sea level using (2.2).

In the case of the wind data, the effect of the forcing is quantified by computing the wind stress components using the quadratic stress formulation with a drag coefficient of 0.0025.

2.2.4.3 Filters

Finite Impulse Response filters are used on the original data time series in two steps and with decimation to produce 10-minute series and hourly averaged values respectively. A cosine filter with 9 weighting factors, pass-band ending at 0.156 cycles/data interval (99% gain) and stop-band starting at 0.326 cycles/sampling interval (1% gain) is employed in the first step. A Doodson X_o filter (IOC-UNESCO, 1985) with 27 weighting factors and a half-gain at 0.39 cycles/hour is subsequently used to obtain the hourly values. The filter has thus no attenuation for periods higher than 4h and a half attenuation for a period of 2.5h. The Fortran code for these filtering routines is written as part of this work.

The mean sea level (MSL) is derived by applying the A24A24A25/(24^2*25) tide-killing filter (Godin, 1972) to the hourly data; this filter has a half-gain at a period of 2 days and thus retains only the longer period variations of the signal. A Fortran programme is written to apply this filtering process. Daily and monthly averages are calculated by taking the simple arithmetical mean of MSL over 24 hours or one month respectively.

2.2.4.4 Harmonic analysis

The data are also analysed by means of TIRA, a software developed at the Proudman Oceanographic Laboratory in Bidston, Birkenhead, U.K., for tidal harmonic analysis by a least squares procedure (Murray, 1964). TIRA allows analysis even in the presence of gaps. A few short gaps in the original data set are thus interpolated by using predicted values. Residuals prior to and after a data gap are linearly interpolated and used to estimate and add the non-tidal component to the predicted elevation during gaps.

In order to isolate the non-tidal higher frequency component in the data, the predicted tides are subtracted from the original records and further analysis is then performed on the residual series. This method is not suitable for data series that are not long enough to permit a reliable calculation of the tidal constituents. Moreover the sub-tidal frequencies are retained. An alternative technique is thus adopted especially in those cases where it is necessary to extract the supra-tidal frequency components from the rest of the signals.

2.2.4.5 Calculating residuals

The method consists of the repeated use of an Infinite Impulse Response (IIR) filter. In the first run an 8th order low pass Chebysev type I filter is utilised with a decimation factor of 2. The decimated series is successively filtered a second time utilising the same filter but with a decimation factor of 30. For each run the filter scans the data set in both the forward and reverse directions in order to remove any phase distortions; this effectively doubles the filter order. The resulting filtered series is next interpolated in two stages in order to re-establish the original sampling rate. The IEEE interpolation algorithm 8.1 is used. The method is automated by means of a MATLAB macro which has been expressly developed for this application. An IIR filter is preferred in order to enable the required

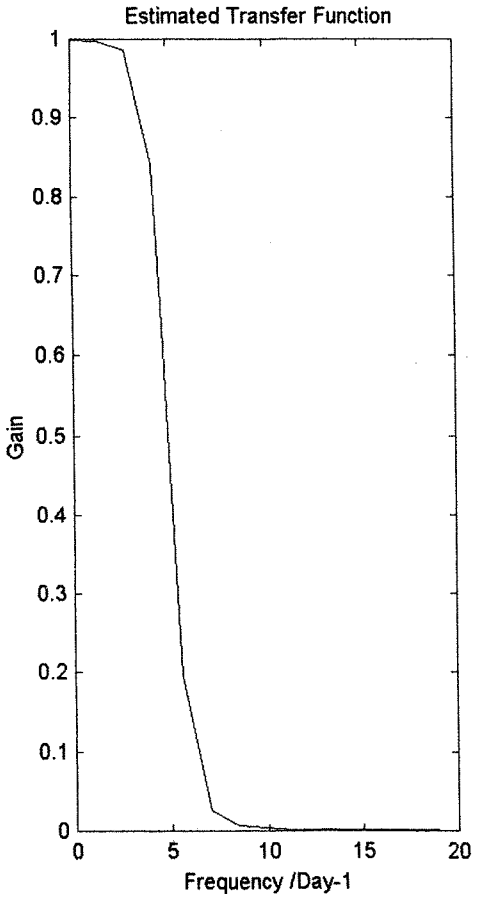

Fig. 2.4 Frequency response of smoothing filter

specifications to be met with much lower filter order than a corresponding Finite Impulse Response (FIR) filter. Provided that a sufficiently long run of data prior to the last measurement is memorised, the problem of the inherent non-linear phase distortion of the IIR filter is resolved by a non-causal, zero-phase filtering approach. Fig. 2.5 compares the plot of the low pass filtered interpolated series with that of the original data set. The high pass signal is obtained by subtraction. This very reliable filtering technique is furthermore achieved with minimal loss of data (just 59 records at each end). The overall frequency response is shown in Fig. 2.4 and has an attenuation of 50% at a frequency of 5cpd and a cut-off frequency at 10 cpd.

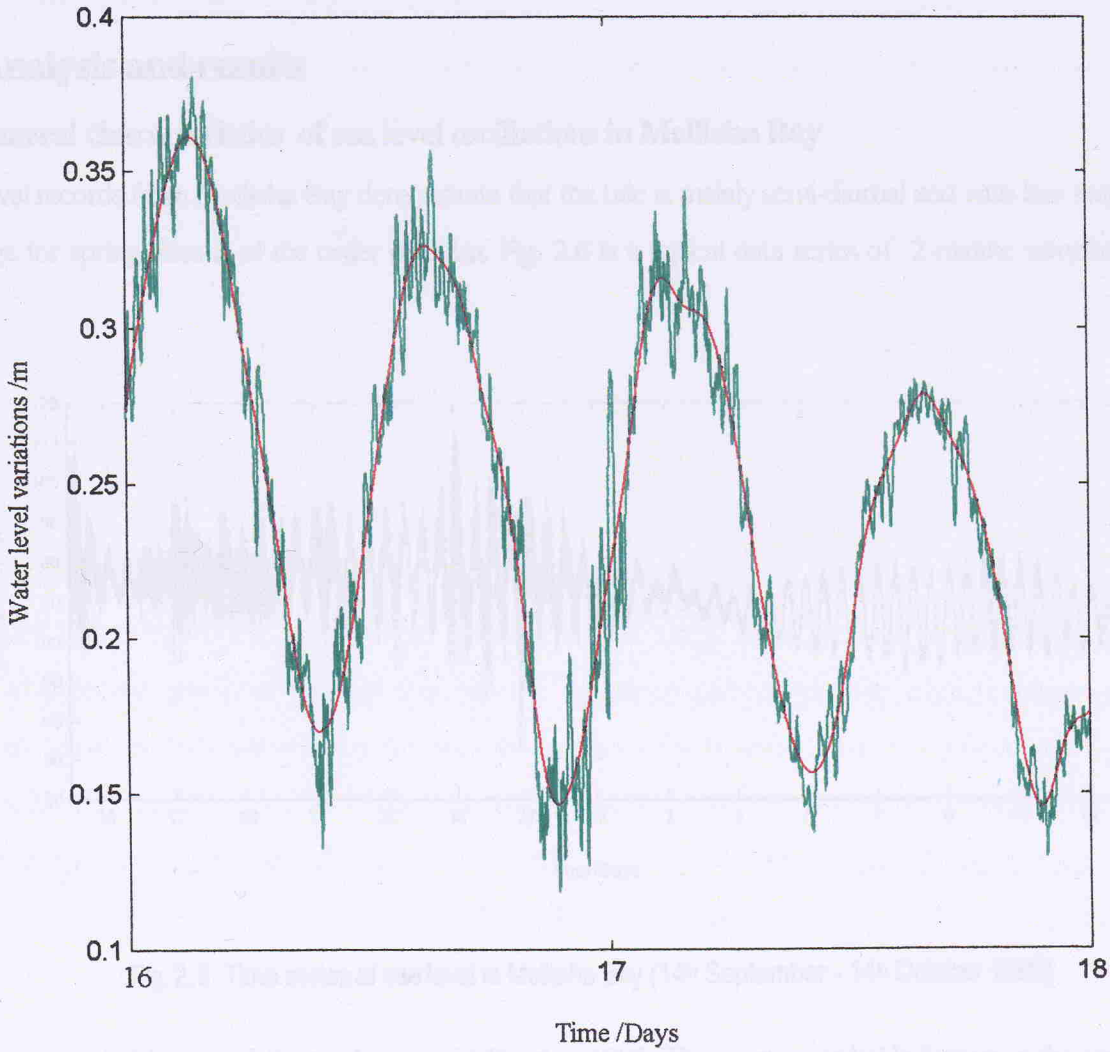

Fig. 2.5 Sample plot comparing the filtered low pass signal with the original data set

2.2.4.6 Energy distributions and power spectra

The sea level and meteorological data are also used to calculate energy distributions and power spectra. 50% overlapping segments are taken in each case. Trend and mean are removed and a Kaiser Bessel window (Harris, 1978) applied to each segment. The tapered segments are then subjected to Fast Fourier Transform (FFT) analysis to calculate the spectra by using the Welch method. In the case of spectra obtained from an average over a long series, the influence of transient effects is suppressed and the results thus determine the general phenomenology in the region of the measuring station.

2.3 Analysis and results

2.3.1 General characteristics of sea level oscillations in Mellieha Bay

Water level records from Mellieha Bay demonstrate that the tide is mainly semi-diurnal and with low amplitude. The range for spring tides is of the order of 0.2m. Fig. 2.6 is a typical data series of 2-minute sampled water levels

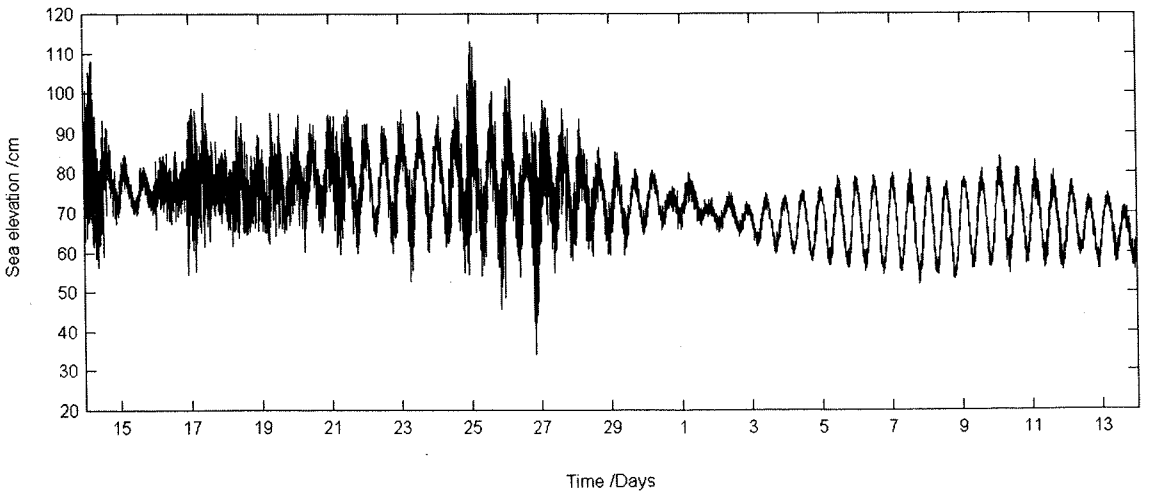

Fig. 2.6 Time series of sea level in Mellieha Bay (14th September - 14th October 1995)

covering the period from mid-September to mid-October 1995. The most remarkable feature in the trace is the presence of a band of high frequency signals. Spectral analysis (refer section 2.3.3) shows that these sea level oscillations have periods ranging from several hours to as low as a few minutes.

2.3.1.1 The coastal seiching phenomenon

The long term measurements presented in this work constitute the first digitised data set that permit the scientific study of these non-tidal short period sea level fluctuations which are the expression of a coastal seiche, known by local fishermen as the *'milghuba'*. This phenomenon has now been observed to occur all along the Northern coast of the Maltese archipelago and manifests itself with very short resonating periods of the order of 20 minutes in the adjacent coastal embayments. Analysis of the full data set shows that weak seiching is present uninterrupted and appears like a background 'noise' on the tidal records. During random sporadic events the seiche oscillations can become greatly enhanced and completely mask the astronomical signal. It is interesting to note that reference to similar sea level variations (known as the *'Marrubbio'*) on the southern coast of Sicily is found in the Italian 'Portolano' for ship navigation. Their occurrence is reported to be most frequent in May or June in association to south easterly winds, and their crest-to-trough amplitudes can reach as high as 1.5m. Literature on the *'Marrubbio'* is very scarce with the most relevant publication being that by Colucci & Michelato (1976) who quote typical periods of 14.6 minutes (main peak), 33.6 and 48 minutes (secondary peaks) in Porto Empidocle where the maximum seiche amplitude is however reported to reach only 35cm. The phenomenon is attributed to the free oscillations of the submarine basin overlooking the narrow strip of continental shelf on the Sicilian southern coast, that are triggered by rapid fluctuations in the wind direction and intensity during the passage of frontal meteorological systems.

2.3.1.2 The lower frequency oscillations

The longer period signals are better studied from the filtered hourly values. Fig.2.7 presents a representative record of observed, predicted (sum of tidal periodic variations) and non-periodic residual (observed minus predicted) water level fluctuations, together with the corresponding inverted barometric pressure for the period covering 18 March to 10th May, 1995. The smooth curve drawn upon the observed data gives the variation of MSL and shows the presence of long-period oscillations due to both long-period tidal constituents and meteorological influences. These signals have a periodicity of several days and are related to the large-scale cyclic atmospheric patterns in the region. The meteorological origin of these long-period variations is evidenced by the very consistent inverse relation between MSL and barometric pressure (Fig. 2.7).

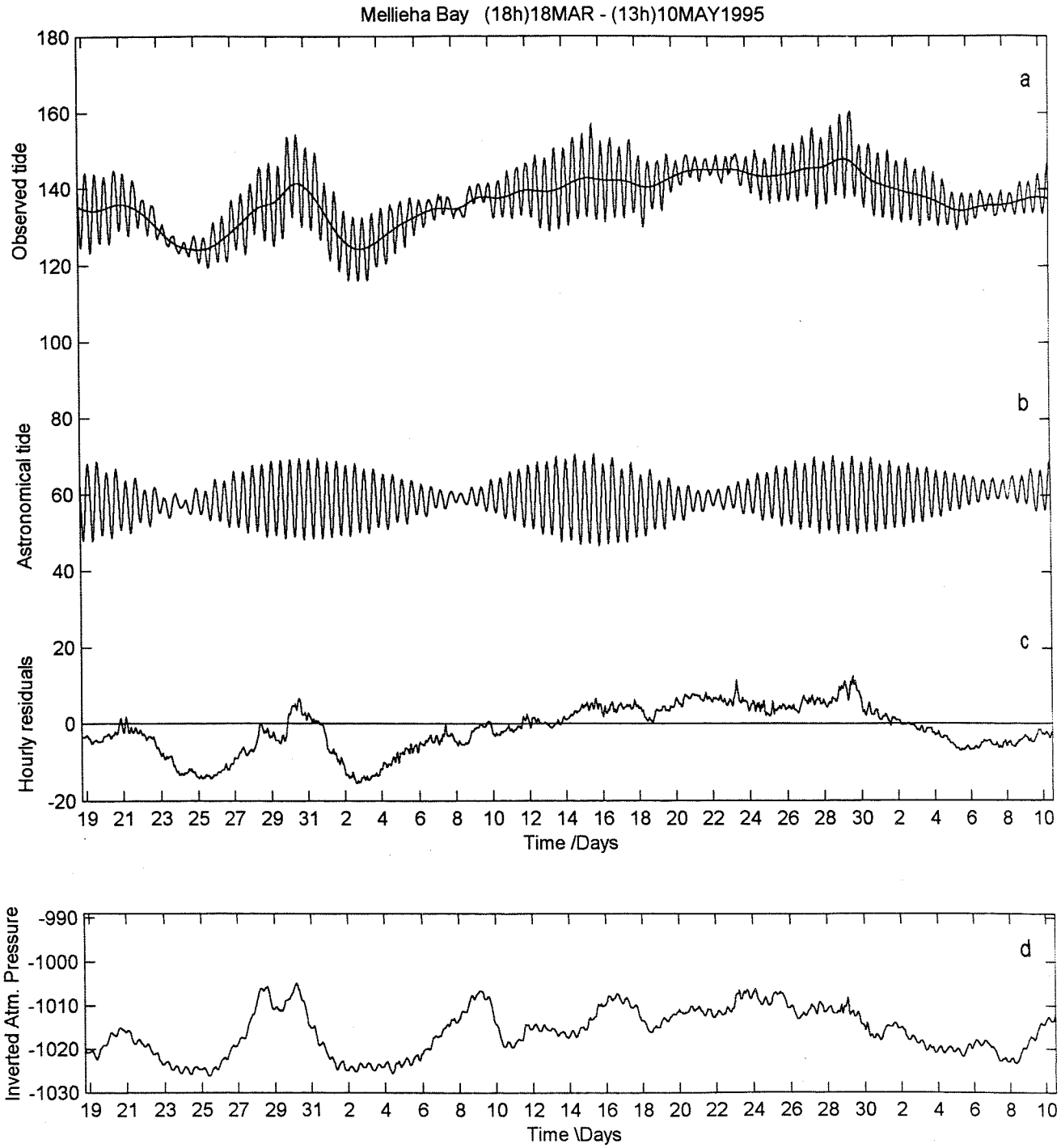

Fig. 2.7 Time series of (a) the observed tide and mean sea level, (b) the predicted astronomical tide and (c) the residual sea elevation in Mellieha Bay for the period 18th March - 10th May 1995; (d) is the inverted atmospheric pressure at MSL for the same period.

2.3.2 The tidal constituents

A linear least squares tidal analysis based on 61 constituents is performed on 43 months (June 1993 - December 1996) of hourly sea-level data from Mellieha Bay. TIRA is used for this analysis. Table 2.2 lists the amplitudes and phases of the harmonic constituents (with H > 1mm). The main constituent is M_2 , but the contribution of the solar radiation tidal input is high (S_2 is 62.4% of M_2), which is typical of the Mediterranean. The tide is predominantly semi-diurnal (Form Number = 0.15) and the main diurnal constituents K_1, O_1 and P_1 are relatively weaker in the region of the Maltese Islands compared to the Sicilian shore to the North. These diurnal constituents cause the minor diurnal inequalities.

Table 2.2
Tidal Harmonic constituents in Mellieha Bay with phases relative to GMT.

Harmonic Constituent	H /cm	g /Deg	Harmonic Constituent	H /cm	g /Deg	Harmonic Constituent	H /cm	g /Deg
Sa	8.85	201	pi1	0.30	149	nu2	0.19	064
Ssa	1.45	152	P1	0.26	051	M2	6.04	055
Mm	0.55	185	S1	0.58	281	L2	0.30	056
Mf	1.22	337	K1	0.70	053	T2	0.15	081
Msf	0.21	067	PSI1	0.27	057	S2	3.77	062
Q1	0.27	056	PHI1	0.15	056	K2	1.15	065
RO1	0.10	134	2N2	0.11	082	M3	0.10	169
O1	0.78	056	MU2	0.18	092	M4	0.15	271
chi1	0.17	253	N2	0.93	064	MS4	0.16	316

These results for Mellieha Bay are in good agreement with the values for the Grand Harbour in Table 2.1. The two locations are very close to one another and the differences, particularly in the phase, are probably more related to temporal changes. Changes in the tidal constituents between different locations can also however occur due to the presence of continental shelf waves which are known to propagate in the area. Besides producing an anomalous intensification of the tidal currents, these continental shelf waves are responsible for the appearance of small-scale variations in the harmonic constants (Rabinovich & Zhukov, 1984).

In the case of the Grand Harbour data, an analysis on separate months (May 1990 - May 1991) is also performed. From 29-day tidal analysis of successive months, Drago & Ferraro (1996) show that there is considerable variability in both the amplitudes and phase of the main constituents.

Table 2.3
Variability of the main Tidal Harmonic constituents in the Grand Harbour, Valletta (phases relative to GMT)

		M_2	S_2	N_2	K_1	O_1
Mean	**H (mm)**	62.6	39.3	11.0	10.7	8.3
Variance		2.6	3.3	2.3	1.8	1.8
Mean	**Phase (Deg.)**	47.3	57.6	50.4	24.1	52.3
Variance		3.3	4.3	14.4	9.0	16.4

The results are presented in Table 2.3. The constituents K_2 and P_1 are not included since they are derived constituents. For the N_2, K_1 and O_1 constituents, the standard deviation is of the order of 20% in the amplitude, and 23% in the phase. For M_2 and S_2 the variation is much less but not negligible. In the case of M_2, the amplitude fluctuates in the range 58mm to 67mm, and the phase in the range 42° to 53°. This variation can be attributed to the relative contributions of the equilibrium forcing and the tidal wave through Gibraltar in the propagation of the tide in the Mediterranean. A high-resolution, two-dimensional model of the whole basin (Tsimplis et al., 1995) has revealed that the incoming wave through the Strait of Gibraltar has an important influence on the tides in the whole Mediterranean Sea. In the Strait of Sicily the forcing at Gibraltar causes a wandering of the M_2 amphidrome to the eastern part of Sicily and gives rise to double amphidromes in the propagation of both K_1 and O_1 in the area between Malta and Sicily. Comparison of the constituents at different ports (refer Table 2.1) needs therefore to be reconsidered especially in those cases where the analysis is based on data sets of different length and different year or month. From the values in Table 2.1 it is however clear that for all the principal constituents the change in phase across the eastern side of the Central Mediterranean region is much more gradual with respect to the west. This is in agreement with tidal model results, but the phase differences between Malta and nearby Sicilian ports to the north suggest a relative spatial concentration of phase contours over the shallow continental shelf.

From a comparative analysis with simultaneous data in Mellieha Bay and the Grand Harbour, M_2 and S_2 are practically identical for both stations, except for a slight lead in Mellieha for the two constituents. The size of N_2

in the Grand Harbour is about half that in Mellieha Bay, whereas K_1 is stronger and about twice the size in Mellieha with respect to the Grand Harbour. The monthly variation in phase for N_2, K_1 and O_1 is quite high but coherent in the two stations. In Mellieha, N_2, K_1 and O_1 are consistently lagging with respect to the Grand Harbour. Differences in the higher frequency constituents, notably in M4 and MS4, are due to the different positions of the sea level gauges within the respective water bodies and the relatively shallow bathymetry in the inner part of Mellieha Bay.

2.3.3 Spectral analysis of sea level data

The characteristics of these sea level signals are obtained by spectral analytic techniques. Fig.2.8 a, b is a normalised power spectral density plot of the full 2-minute sampled data set from 1/6/93 to 2/1/97 plotted on a linear scale. Since the spectrum is obtained from an average over a long series, the influence of transient effects is suppressed and the results thus determine the phenomenology of the sea surface vertical movement in the region of this station. The Kaiser-Bessel spectral windows with 50% overlap are chosen to be 2^{17} records for the lower frequency range (Fig. 2.8a) and 2^{14} records for the higher frequencies (Fig. 2.8b). The different window sizes permit an optimal resolution for the long-period and short-period components respectively. The linear spectral plot gives a better visualisation of the relative distribution of energy. The corresponding logarithmic plots in Fig.2.9a-e display the same characteristics, but the components with smaller energy inputs are enhanced. In Fig.2.9a an additional frequency averaging is performed (Luther, 1982) in order to smooth the spectral estimates at the higher frequencies. In this case the degrees of freedom are 22 and 110 for the lower and higher frequency ends respectively of the spectrum.

2.3.3.1 Characterisation by frequency bands

Spectral analysis reveals three main frequency bands: (1) the low frequency (long-period) band (LB) in the range 0 to 0.8cpd (T(hours) > 30); (2) the tidal frequency band (TB) in the range 0.8 to 4.8cpd (30 > T(hours) > 5); (3) the long wave frequency (short-period) band (SB) in the range 4.8cpd and upwards (T(hours) < 5). The term 'long wave' is here associated to sea level fluctuations with periods intermediate between those of the long swell and of the astronomical tide. These spectra for these three frequency bands are drawn separately (Fig. 2.9b-e) for better visualisation. The tidal band is plotted for the observed (Fig. 2.9c) and the residual (Fig. 2.9d) data. The sea level variations are dominated by energy inputs from the low frequency signals and the semi-diurnal tidal components (Fig. 2.8), with a secondary contribution from the diurnal fluctuations.

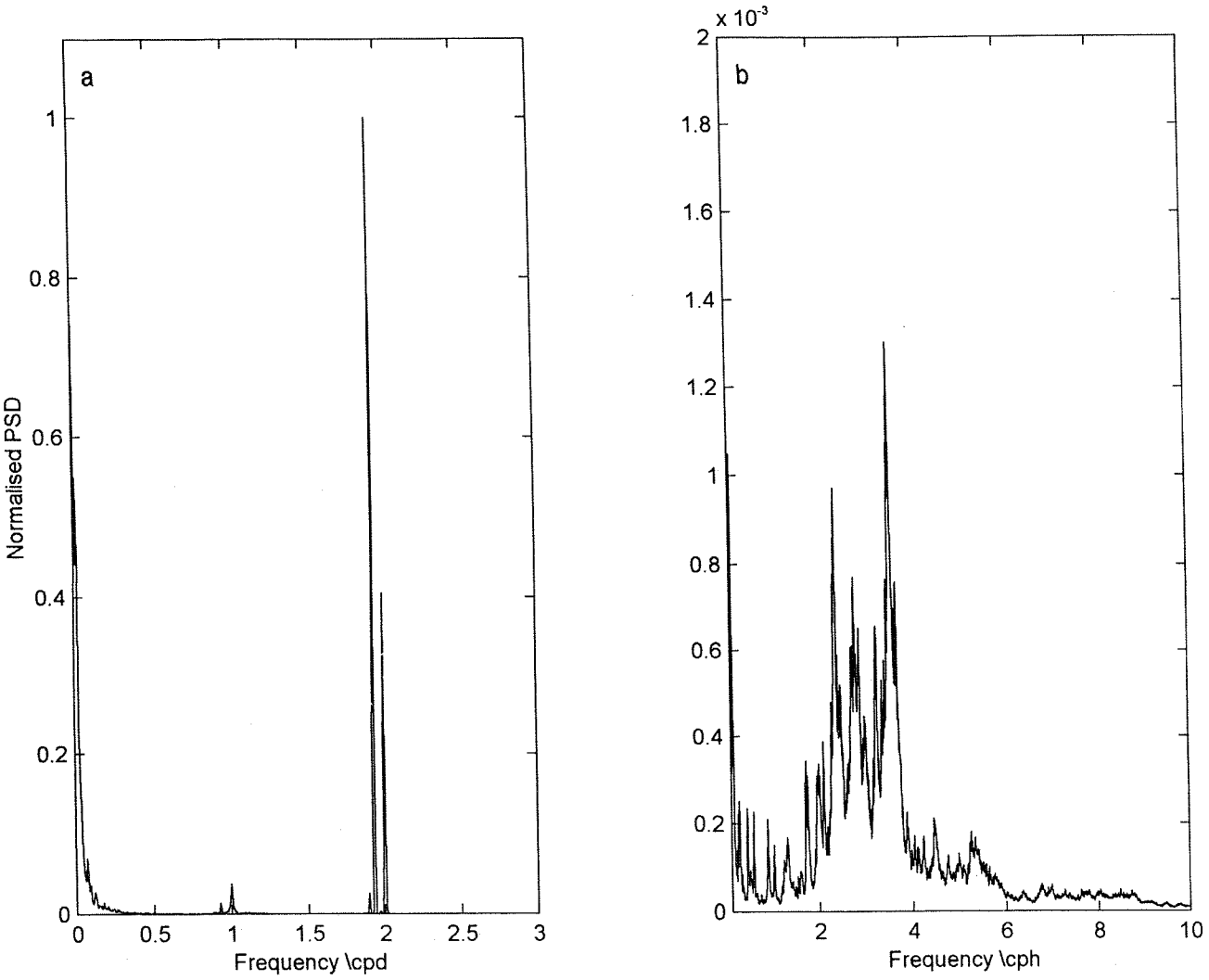

Fig. **2.8** Normalised power spectra on a linear scale calculated from 2-minute sampled sea levels in Mellieha Bay (1/6/93 - 2/1/97).
In (a) the 95% confidence factors, for 22 degrees of freedom are (B_{min} = 0.52; B_{max} = 2.5);
The spectrum normalisation factor is 0.2048m²/cpd.
In (b) the 95% confidence factors, for 176 degrees of freedom are (B_{min} = 0.85; B_{max} = 1.3);
The spectrum normalisation factor is 0.1572m²/cph.

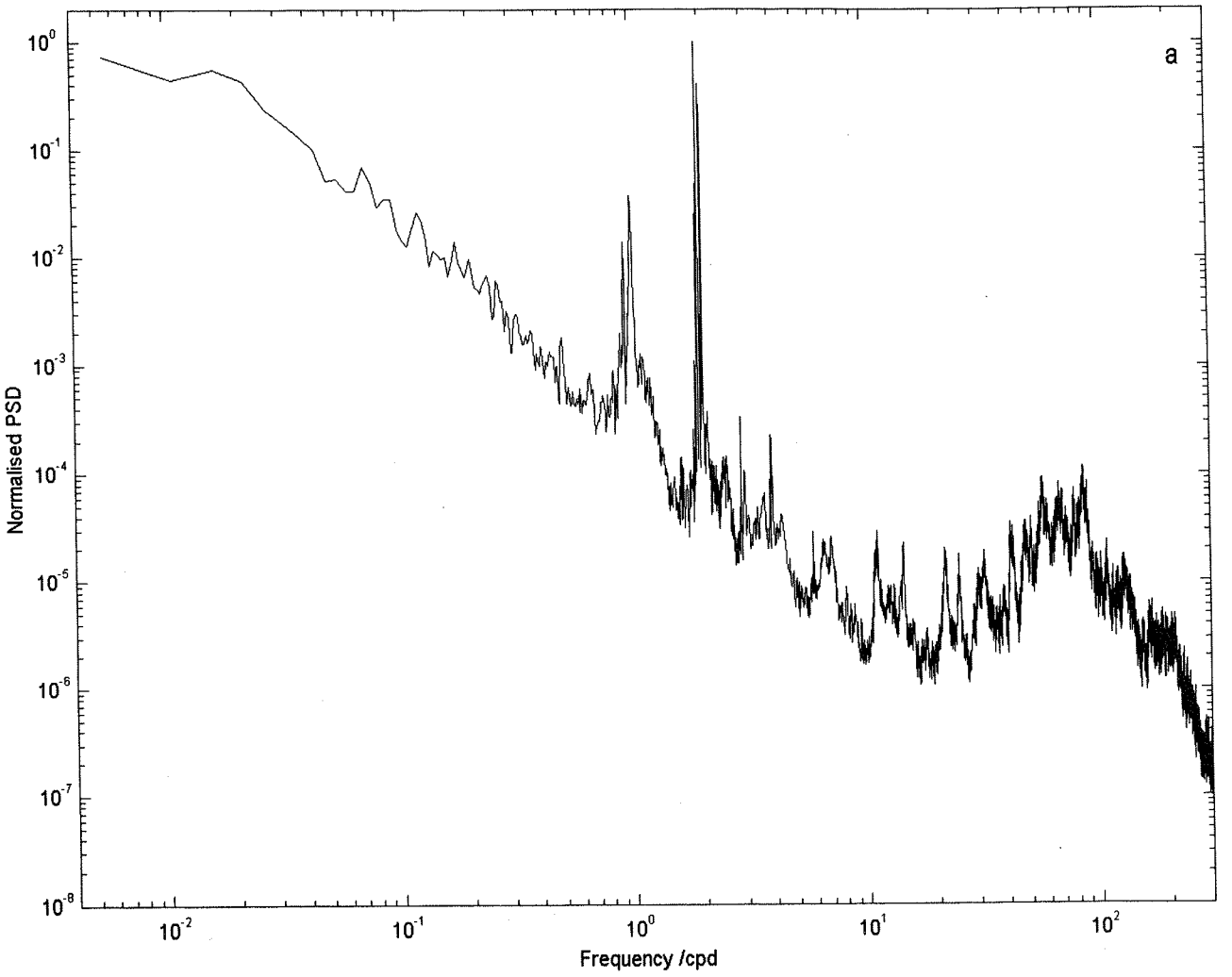

Fig. **2.9** (a) Normalised power spectrum on a logarithmic scale calculated from 2-minute sampled sea levels in Mellieha Bay (1/6/93 - 2/1/97).
Up to f = 3cpd, the spectrum is calculated with 22 degrees of freedom and 95% confidence factors B_{min} = 0.52 and B_{max} = 2.5).
For f > 3cpd, the spectrum is calculated with 110 degrees of freedom and 95% confidence factors B_{min} = 0.78 and B_{max} = 1.35).
The normalising factor is 0.2048m^2/cpd

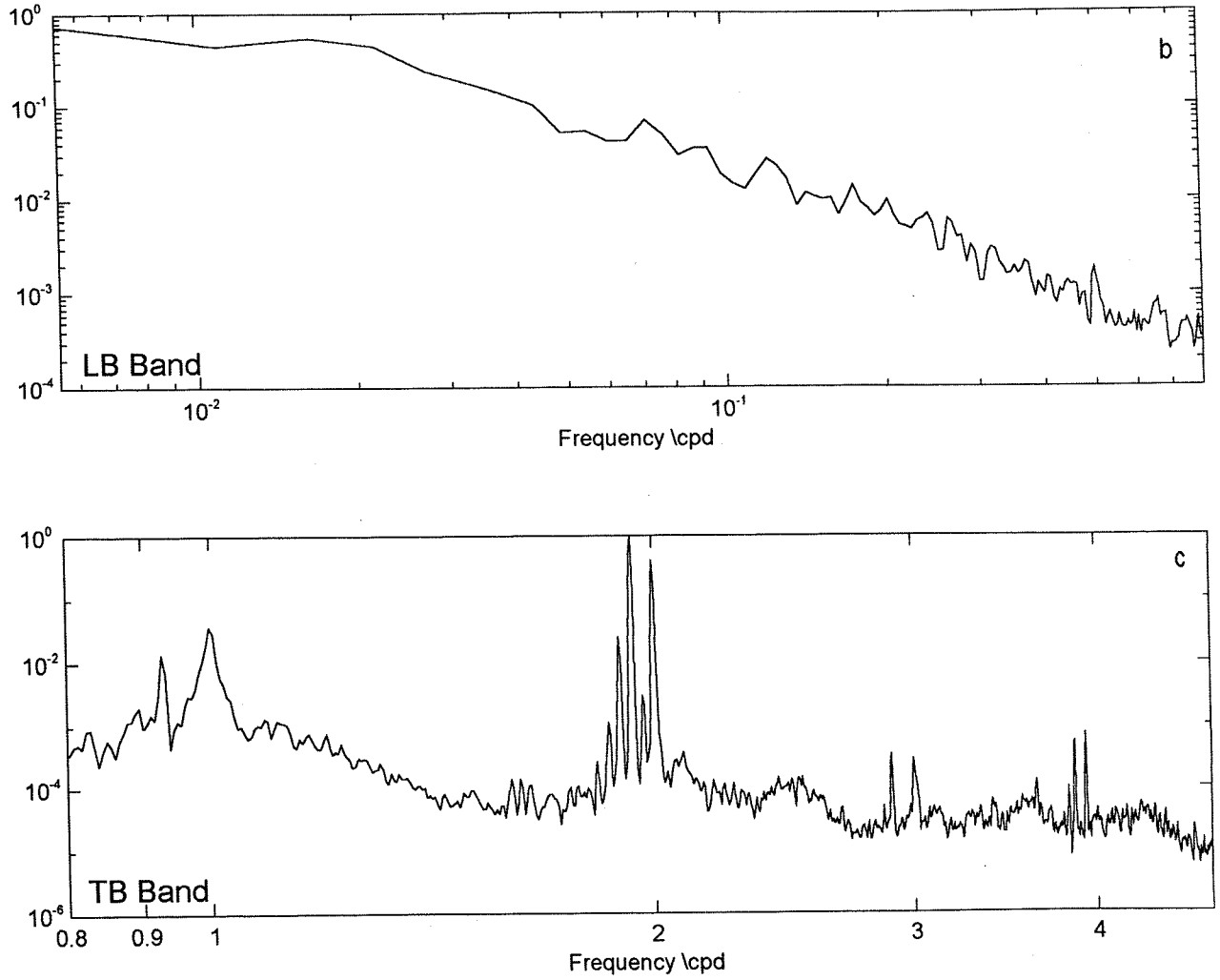

Fig. 2.9 Normalised power spectrum on a logarithmic scale for (b) the low frequency band; (c) the tidal band from observed sea levels.
The spectrum is calculated with 22 degrees of freedom and the 95% confidence factors are (B_{min} = 0.52; B_{max} = 2.5); the normalising factor is 0.2048m²/cpd.

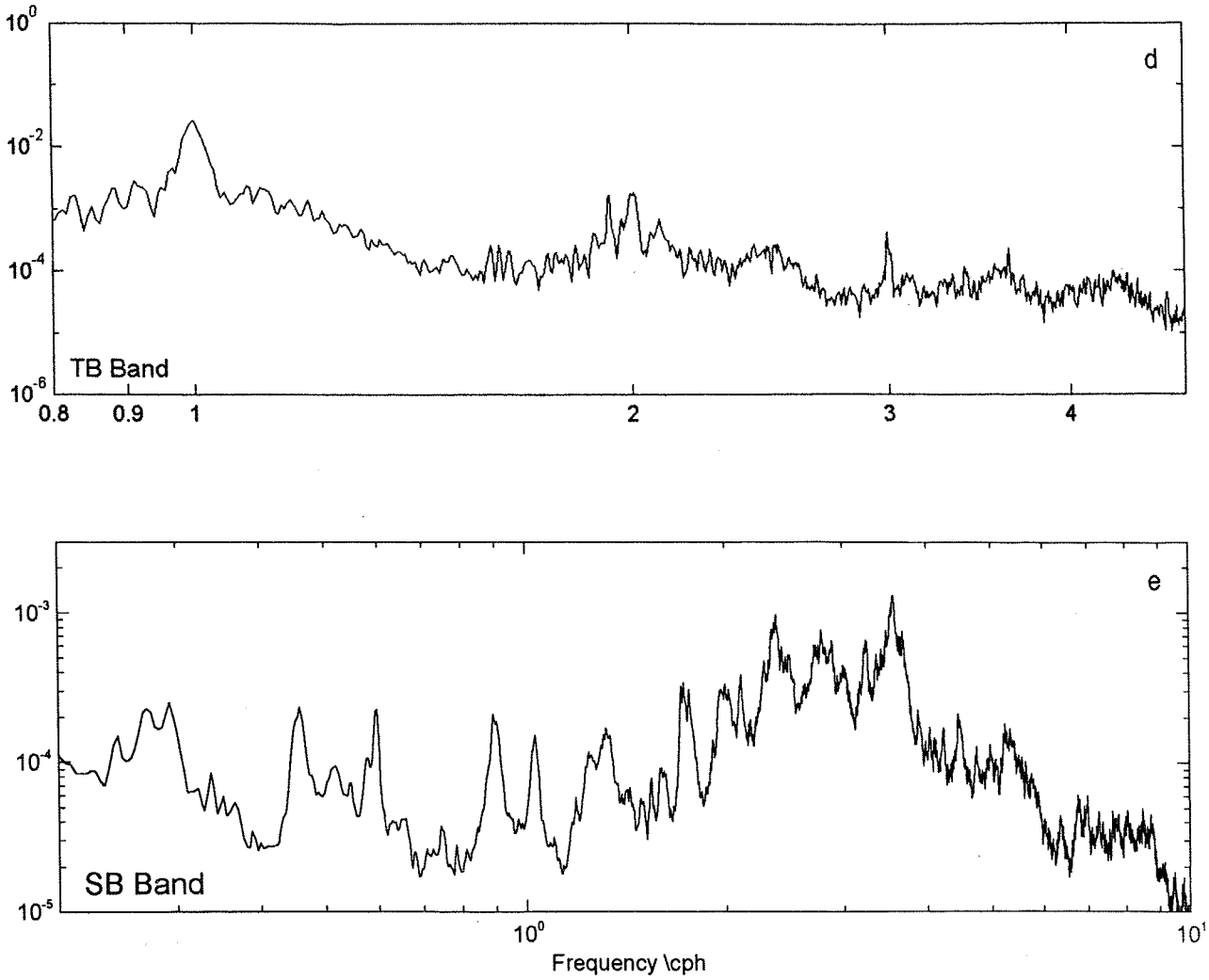

Fig. **2.9** Normalised power spectrum on a logarithmic scale for (d) the tidal band from residual levels, and (e) the short period band.
In (d), the spectrum is calculated with 22 degrees of freedom and the 95% confidence factors are (B_{min} = 0.52; B_{max} = 2.5); the normalising factor is 0.2048m²/cpd.
In (e) the spectrum is calculated with 110 degrees of freedom and the 95% confidence factors are (B_{min} = 0.78; B_{max} = 1.35); the normalisation factor is 0.1572m²/cph.

In the tidal frequency range, fluctuations are dominated by energy inputs of semi-diurnal frequency with weaker contributions from diurnal signals. Comparison between the two tidal energy density peaks yields a ratio of amplitudes of the order of 1:7 which agrees well with results from harmonic analysis of coastal tidal records. The peaks towards the higher frequency ends of the tidal range refer to the 1/3- and 1/4-diurnal contributions.

2.3.3.2 Energy distribution

The energy distribution at different frequencies is expressed as a percentage of the total energy in the records (Table 2.4). These percentages quantify the dominance of the low frequency inputs, proposed to be of large scale meteorological origin, which contribute for 57.3% of the total energy in Mellieha Bay. Tidal energy inputs (35.8%) mainly result from the semi-diurnal component (32.7%). The high frequency (greater than 4.8cpd) inputs, due to the coastal seiches, contribute only 6.6%. This figure is an average of seiche energy over the whole time span covered by the data series and greatly underestimates the real energy carried by the large amplitude seiches which are transient events lasting only for relatively short periods of time (from a few hours to a couple of days).

Table 2.4
Percentage energy distribution in Mellieha Bay

Frequency Band	%
Low frequency *(<0.8cpd)*	57.3
Diurnal *(0.8-1.2 cpd)*	3.0
Semidiurnal *(1.8-2.2 cpd)*	32.7
Quarter diurnal *(3.8-4.2 cpd)*	0.06
High frequency *(>4.2cpd)*	6.6
Other	0.36

2.3.4 Characterisation of the seiches

2.3.4.1 The seiche spectral peaks in Mellieha Bay

The broad 'hump' in the frequency range of 1 to 10 cph in the power spectrum (Fig. 2.9a and e) reveals a very interesting selective enhancement of a band of short-period signals in Mellieha Bay that explains the nature of its seiche oscillations. In this amplification process the response of the embayment is not restricted to the eigenperiods of its water body but spans a range of frequencies whose energy inputs are considerably increased above the background values. The characteristic eigenoscillations stand out as well-pronounced peaks upon this overall amplified response of the embayment. In particular, three sharp maxima with respective periods of 25.1, 21.2 and 16.8 minutes feature in the rather intricate spectrum.

Higher frequency maxima with frequencies above 4cph are an expression of the higher order bay modes. It is important to ascertain that this spectral structure in not contaminated by aliased signals. The energy density computed at a frequency f can have contributions from aliased frequencies $f \pm 2mN_f$ with m=1, 2, 3, etc. But the sampling interval (Nyquist frequency N_f of 30cph) in this case is sufficiently small to rule out effects due to aliasing. Contributions of the energy densities in the sea level at frequencies of 60, 90, 120,....cph are in fact known to be too small to be of any importance. The measured peaks of energy are thus real. The relation of these peaks to the bay modes of oscillation is discussed in Chapter 3.

2.3.4.2 Shelf resonances

The SB band (Fig. 2.9e) also presents a series of sharp, well-defined and equally energetic peaks on its lower frequency end. The main maxima have periods of 3.7, 2.2, 1.7, 1.1 hours, and 58, 46, 34.3, 29.5, 27.7, 25.1, 21.2 and 16.8 minutes. These peaks are analysed in detail in Chapter 3, section 6 where it is shown that they are related to shelf oscillations in the Malta Channel.

The mean energy densities in the lower SB band are considerably smaller than those in the tidal band. With a spectrum normalising factor of $1/0.1572 m^2\ cph^{-1}$, the mean peak densities measured from Fig. 2.9e are $(0.0002/0.1572) \times 100 \times 100 = 12.72 cm^2\ cph^{-1}$; an estimate of the mean wave amplitude A at these frequencies is obtained by scaling the power spectral density by the factor $fs=norm(w)^2/sum(w)^2$, where w is the Kaiser-Bessel window vector (size 8192). In this case fs=0.000184. Hence $A = 2(12.72 \times fs)^{1/2}$ which gives an estimate of 0.97mm.

2.3.5 Other oscillations of non-tidal origin

Spectral analysis of the residual sea level data allows the separate study of the non-tidal oscillations. The analysis is performed by two separate computations of energy spectra for (1) the whole time series (Fig. 2.9d), and (2) 27 successive 50% overlapped three-month periods in order to reveal any seasonal variability.

2.3.5.1 The diurnal residual

The most important result is a strong diurnal residual energy that covers a relatively broad band of spectral frequencies centred at 1cpd. This signal is probably related to the signature of baroclinic motions on the continental shelf. Measurements made during a physical oceanographic survey carried out in the NW coastal

area of Malta in summer 1992 have in fact revealed the presence of diurnal subsurface flows in the vicinity of the islands (Drago, 1997). These diurnal baroclinic currents are believed to be the expression of a topographically trapped wave that takes the form of an internal Kelvin-like waveform in the deeper sea away from the shelf break and is accompanied by shelf wave modes propagating over the continental platform. An associated vertical oscillation of the thermocline in the form of an internal tide has been quantified to have a crest-to-trough amplitude A of the order of 8m (Drago, 1997). From CTD casts taken during the same survey, the density profiles show that the seasonal pycnocline has a sharp gradient between 10 to 30m depth and acts as a clear interface between the surface mixed layer and the deeper layer. Taking the mean relative density difference between these upper and lower layers to be 0.3% (ρ_1 (upper) $\approx 1024.5 \mathrm{Kgm}^{-3}$; ρ_2(lower) $\approx 1027.5 \mathrm{Kgm}^{-3}$), the

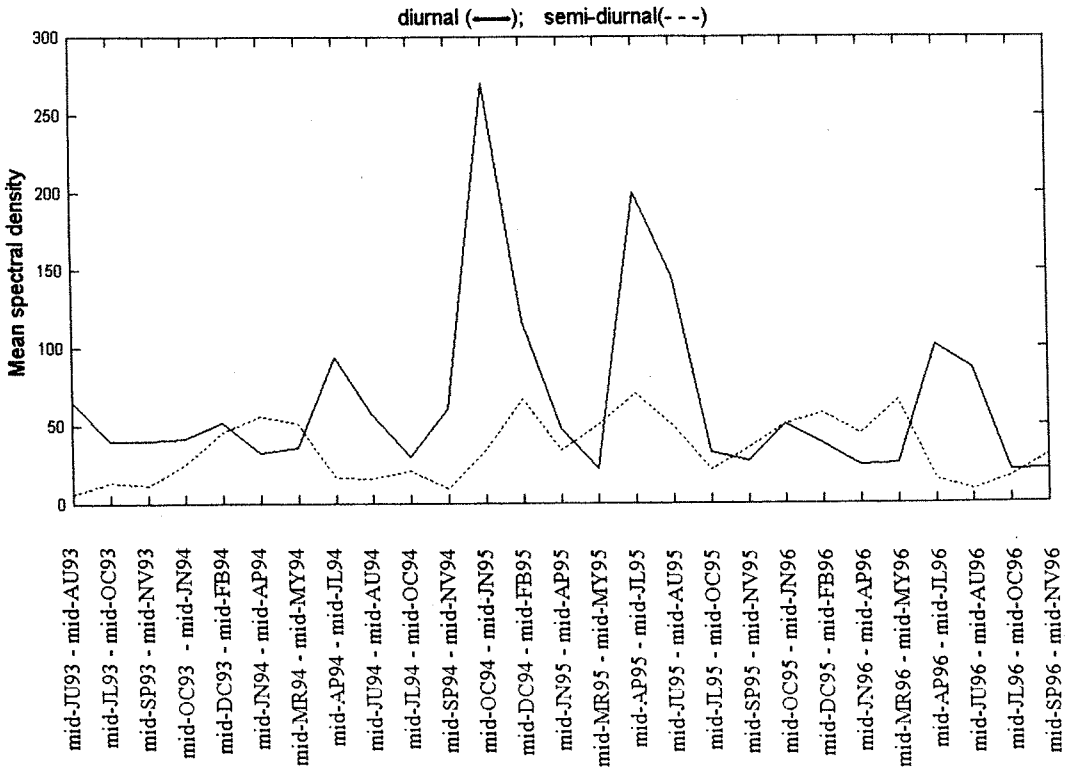

Fig.2.10 Variability of the (a) diurnal (solid) and (b) semidiurnal (dotted) residual energy calculated for successive 3-month half-overlapping periods.

free surface displacement accompanying this internal tide is given by $\Delta\eta = \frac{A}{2}\frac{\rho_2 - \rho_1}{\rho_1}$ and thus estimated to have an amplitude of the order of 1.2cm

The variability of the diurnal residual energy over the whole period of measurements (June 1993 - December 1996) is studied from a series of spectra calculated in each of successive 3-month half-overlapping periods. The energy carried in the frequency range of 0.978-1.022cpd is calculated for each spectral estimate. The relevant plot against time (Fig. 2.10a) shows a consistent pattern with peak energy during the periods spanning mid-October to mid-January and mid-April to mid-July respectively. This intra-seasonal variability of the diurnal signal is probably linked to dynamical processes that have a correlated temporal repeatability; there is as yet no sufficiently long hydrodynamical datasets to confirm this relationship. The variability of the semidiurnal residual energy calculated over the frequency range 0.48 - 0.52cpd is less pronounced. In particular, the semidiurnal residual can predominate over the diurnal residual during late winter and early spring.

2.3.5.2 Barotropic modes of the Mediterranean Sea

The energy peaks at 0.65 (Fig. 2.9b), 2.13 and 3.0cpd (Fig. 2.9d) are an expression of the lowest barotropic free modes for the Mediterranean Sea. By means of a depth-averaged model, Schwab & Rao (1983) obtained the spatial structure of these first three barotropic oscillations for the closed Mediterranean. All the three modes have a nodal zone in the Strait of Sicily and are not therefore expected to carry much energy in the region. The observed peaks agree closely to the computed periods which are 38.5h (1st mode), 11.4h (2nd mode) and 8.4h (3rd mode). More recently Candela & Lozano (1994) performed a computation of the interior basin modes with a higher (x5) grid resolution and taking into account exchange at the Strait of Gibraltar. The gravest gravitational mode is reported to have a frequency of 0.73cpd and refers to a gravitationally driven oscillation between the Western and Eastern basins through the Strait of Sicily. Note that the peak in the spectrum at 0.5 cpd remains unaccounted by any of these modes.

2.3.5.3 Variability in the low frequency range

The subtidal sea level signals are well resolved in the LB spectral band (Fig. 2.9b) by utilising a long window size of 65536 records (182days : 01hours : 04minutes). The sea-level is found to have significant variability in the 2.2 - 15days period (periods from tidal to several weeks). This is very typical of the whole Mediterranean basin where the sea level variability in the low frequency range represents an energetic part of the sea level spectrum.

This variability is greatly influenced by the weather. Sea level variations at time scales from one to ten days have been shown to be primarily due to surface pressure changes related to synoptic atmospheric pressure disturbances (Kasumovic, 1958; Mosetti, 1971; Papa, 1978; Godin & Trotti, 1975). Sea level variations at time scales from ten days to several weeks have been explained as being due to atmospheric planetary waves (Orlic, 1983; Lascaratos & Gacic, 1990).

The contribution of the wind is also important both with regard to its dynamic effects as well as to its effect on rate of evaporations and the difference in air-sea temperature.

The meteorological forcing on the sea level is discussed in the following sections. The synoptic variability and its dependence on the atmospheric pressure and the wind is studied in detail.

2.4 The dependence of the sea level variability on the atmosphere

Besides the effect of the tides and oceanographic factors such as water density and currents (both geostrophic and ageostrophic), the role of meteorology in determining the oscillations of the sea level has also to be taken into account. A sea level record indeed carries the superposed effects of a number of components. Its analysis and interpretation thus requires a knowledge of the dependence of the sea surface displacement on the local weather as well as on the tidal potential and on the hydrography. In view of the possible interdependence between components, such an analysis is not an easy task. It has however the benefit of relaying a great deal of otherwise inaccessible information on the related parameters themselves.

2.4.1 The response of sea level to atmospheric pressure

2.4.1.1 The inverted barometer (IB) effect

In the open ocean, a gradual increase in atmospheric pressure forces water out of the affected area and the sea level becomes lower so that any pressure gradients will tend to be neutralised. The more common term coined to describe this phenomenon is that of the "inverted barometer (IB) effect". Theoretically, an increase (decrease) of 1mb in atmospheric pressure should be accompanied by a 1 cm decrease (increase) in sea level, in which case the response is said to be isostatic. That is, the sea surface displacement $\Delta\eta$ in cm is given by $\Delta P / \rho g$, where $\Delta P = (P - \langle P \rangle)$ is the atmospheric pressure fluctuation about the mean pressure $\langle P \rangle$ in mb over the ocean and

ρ is the density of the ocean. Hence the inverted barometer factor (IBF) can be expressed as $\Delta\eta / \Delta P$ and is equal to unity in the case of an isostatic response. Equivalently, the barometer factor â defined in section 2.4.2.3 would at all frequencies be equal to -1.01cm/mb in the case of an isostatic response. If the sea level change is more than 1cm to 1mb, the response is called over-isostatic and IBF > 1; conversely it is called under-isostatic if the response is less than 1cm and IBF < 1.

The response of sea level to atmospheric forcing has always received great attention by scientists especially in relation to the impact of extreme low pressure systems travelling over coastal areas where they contribute, in addition to wind effects and tides, to destructive storm surges (Tsimplis, 1995). Further interest on the IB effect has been recently shown in connection with the attempt to exploit satellite altimetric measurements which can provide synoptic mapping of sea surface topography with increasingly improved accuracy (Larnicol et. al., 1995; Le Traon et. al., 1997), but which need to be corrected in order to account for the spatial variability of the atmospheric field.

The IB effect is however by no means easy to understand. An isostatic response is only expected when the pressure variations are sufficiently slow as to allow for the finite inertia of the affected water body. The spatial extent and speed of propagation of the forcing atmospheric pressure systems are thus important factors that control the associated displacements of the sea surface. Crepon (1975) showed that the response of a rotating fluid can only approach to isostasy if the spatial scale of the atmospheric disturbance is smaller than barotropic radius of deformation and in cases where the bottom friction is sufficiently large. This is further complicated by the finite dimensions and shape of the sea. Coastlines which can support Kelvin waves ease barometric adjustment.

In a closed basin, mass conservation requires $\langle P \rangle$ to be equal to the mean atmospheric pressure over the basin, and only a local adjustment to the spatial variations of the pressure field is expected. However, in the case of a semi-enclosed basin the restrictions in the flow imposed by both the bathymetry and the coastal configuration can lead to a non-isostatic response.

2.4.1.2 Application to the Mediterranean Sea

In the case of the Mediterranean where the Strait of Gibraltar restricts the flow from the Atlantic and the Strait of Sicily further provides a second restriction to the flow into the Eastern Mediterranean, the sea level cannot respond to the mean pressure over the basin unless there is an adequate adjustment at the straits. At low frequencies there is indeed enough time for the sea level to adjust and the straits are not expected to constrain the flow. In the case of high-frequency changes with spatial scales that are smaller than the basin scale dimensions, internal adjustment occurs without the need of flow through the straits. On the other hand, at intermediate frequencies control at the straits can restrain full adjustment and compel the response to deviate from a simple IB effect.

The work of Lacombe et. al. (1964) and Crepon (1965) has confirmed that this adjustment occurs at the Strait of Gibraltar. These results were the first to confirm that meteorological forcing by large scale patterns of atmospheric pressure and wind over the Atlantic and Mediterranean account for a significant part of the sub-tidal sea level variations and the associated flows in the strait on time scales of the order of days to months. Crepon (1965) observed that the records tend to be dominated by fluctuations with a period of about 10 days and in particular that both the sea level in the Western Mediterranean and the inflow through the Strait of Gibraltar were in phase with the inverted atmospheric pressure. However, mass continuity would require a correlation with the time derivative of pressure rather than the pressure itself. This apparent paradox has been resolved by making allowance for significant fluctuations in the flow through the Strait of Sicily in response to differences in sea level between the Eastern and Western Mediterranean basins. Garrett (1983) has proposed a two-basin, two-strait model based on geostrophic flow which explains the barotropic response of the Mediterranean to eastward travelling pressure systems particularly for periods of the order of 10 days. In this model, geostrophy (i.e. the Coriolis force) has control on the strait flow and the sea level difference between the adjoining seas is therefore limited by the cross-strait sea level difference caused by the Earth's rotation.

2.4.1.3 Garrett's model for the response of the Mediterranean to travelling pressure systems

The two main basins of the Mediterranean are respectively represented by channels of length L_1 and L_2 meeting at the Strait of Sicily where the origin x=0 is taken. The Western Basin is open to the Atlantic at the Strait of Gibraltar. The response of this twin basin to an atmospheric pressure system $p(\mathbf{x},t) = p(\mathbf{x})e^{-i\omega t} = p_a e^{i\mathbf{k}.\mathbf{x}}\, e^{-i\omega t}$

moving eastward with constant phase speed $c=\omega/k$ is required. The spatial average of the pressure at each basin is given by:

$$\langle p_1 \rangle = p_a \delta_1^{-1} \sin\delta_1 e^{-i\delta}{}_1,$$

$$\langle p_2 \rangle = p_a \delta_2^{-1} \sin\delta_2 e^{+i\delta}{}_2 \quad \text{where } \delta_i = \tfrac{1}{2}kL_i = \tfrac{1}{2}(\omega/c)L_i, \text{ for } i = 1,2. \qquad (2.4)$$

where $\langle\rangle$ denotes a spatial average over the respective basins so that $\langle p_1 \rangle$ and $\langle p_2 \rangle$.are only functions of time. The dimensionless parameter δ_i is related to the scale of the atmospheric pressure pattern with respect to the size of the respective basins.

Following Garrett & Toulany (1982), the volume flux $\mathrm{Re}\{Qe^{-i\omega t}\}$($=WH\mathrm{Re}\{ue^{-i\omega t}\}$), where u is the average current along the strait) through a shallow strait of depth H, width W and length L in response to a sea level difference $\mathrm{Re}\{\Delta\eta e^{-i\omega t}\}$ is given by the formula:

$$Q = gH\Delta\eta\{(-i\omega + \beta)(L/W) + f\}^{-1} \qquad (2.5)$$

where β is the coefficient of linearised bottom friction (i.e. friction $F = \beta u$). This equation can be applied to both the Strait of Gibraltar and Sicily. It is based on the assumption that each of the basins connected by the strait responds with regional coherence to changes in atmospheric pressure. This assumption applies for the Mediterranean which has a Rossby radius (approximately 1500 km) that is greater than the horizontal distance of an interior point to the closest coast, and any spatial variation in the subsurface pressure $p + \rho g\eta$ (p= local atmospheric pressure and η is the local sea level) would thus be quickly rendered uniform by surface gravity waves propagating rapidly in the form of Kelvin waves. This implies that at any position **x** in the basin:

$$p(\mathbf{x},t) + \rho g\eta(\mathbf{x},t) = \langle p \rangle(t) + \rho g\langle \eta \rangle(t) \qquad (2.6a)$$

Upon taking the atmospheric pressure to be measured in equivalent units of sea level, we can drop the factor ρg and write for each basin:

$$\eta_i = \langle \eta_i \rangle + \langle p_i \rangle - p_i, \; i = 1,2 \qquad (2.6b)$$

Appropriate values for H, W and L in (2.5) can only be determined by a numerical model of each strait. Garrett (1983) used the values H=250m and L/W=3 for both straits. The friction coefficient β is estimated by $C_d u_o/H$, where C_d approx 2.5×10^{-3} is the bottom drag coefficient, and u_o is an average speed taken to be 0.5 ms^{-1} in this case. This gives β approx 5×10^{-6} s^{-1}. At latitude 35°, $f = 8.4 \times 10^{-5}$ s^{-1} and the term $\beta(L/W)$ is only about f/6, and the effect of friction in this model is thus small. The term $i\omega(L/W)$ is more important since it is of the same order of f at a period of 2.5 days. Only in the case of sufficiently low frequencies can the volume flux be as

approximated by $Q = gH\Delta\eta/f$ and be therefore independent of the horizontal dimensions of the strait and of frequency.

On the basis of this model, the dimensionless parameter $\varepsilon_i = \omega f A_i (gH_i)^{-1}$, where i = 1,2, ($A_1$ and A_2 = respective horizontal areal extent of the Western and Eastern basins) defines a criterion on whether geostrophic control at any of the straits represents a constriction to the flow. This criterion can be expressed in terms of a time scale $T_i = A_i f/gH_i$ which establishes a limit above which flow constriction due to geostrophic control becomes less important. Taking the areal extent of the Eastern Mediterranean as $A_2 = 1.7 \times 10^{12}$ m^2 and the average depth of the Strait of Sicily as H_2 = 250m, results in a time scale T_2 of the order of one day. For the higher frequency synoptic time scales, the model thus predicts a significant non-inverse-barometric response of the Eastern Mediterranean.

2.4.1.4 Response at the Strait of Sicily

The flow from the Atlantic ocean into the western basin is given by:

$$Q_1 = gH_1 [f + (\beta - i\omega)(\mathbb{L}/W)]^{-1}[\eta_o(\mathbf{x}_1,t) - \eta_1(\mathbf{x}_1,t)] \qquad (2.7)$$

where $\mathbf{x}_1$ is a position in the strait (assumed to be much smaller in extent than that of the adjacent basins). The sea level $\eta_o(\mathbf{x}_1,t)$ just outside the strait in the Atlantic ocean can be expressed as the sum of an inverted barometer response $-p_o(\mathbf{x}_1,t)$ and an extra term $\eta'_o(t)$ for other oceanic effects on the sea level. Similarly, by 2.6b, $\eta_1(\mathbf{x}_1,t)$ is related to the spatial averages in the Eastern Mediterranean by:

$$\eta_1(\mathbf{x}_1,t) = \langle\eta_1\rangle + \langle p_1\rangle - p_1(\mathbf{x}_1,t)$$

Since $p_1(\mathbf{x}_1,t) = p_o(\mathbf{x}_1,t)$, then

$$Q_1 = gH_1 [f + (\beta - i\omega)(\mathbb{L}/W)]^{-1}[\eta'_o - \langle p_1\rangle - \langle\eta_1\rangle] = (\omega A_1/\varepsilon'_1)[\eta'_o - \langle p_1\rangle - \langle\eta_1\rangle] \qquad (2.8a)$$

where $\varepsilon'_1 = (\varepsilon_1/f)[f + (\beta - i\omega)(\mathbb{L}/W)]$. (2.8b)

Similarly the flow through the Strait of Sicily is given by:

$$Q_2 = gH_2 [f + (\beta - i\omega)(\mathbb{L}/W)]^{-1}[\eta_1(\mathbf{x}_2,t) - \eta_2(\mathbf{x}_2,t)] = (\omega A_2/\varepsilon'_2)[\langle\eta_1\rangle + \langle p_1\rangle - \langle\eta_2\rangle - \langle p_2\rangle] \qquad (2.9a)$$

where $\varepsilon'_2 = (\varepsilon_2/f)[f + (\beta - i\omega)(\mathbb{L}/W)]$. (2.9b)

By applying volume conservation for the two basins:

$$A_1 d\langle\eta_1\rangle/dt = Q_1 - Q_2 \; ; \; A_2 d\langle\eta_2\rangle/dt = Q_2 \,, \qquad (2.10)$$

and after some algebra we obtain:

$$\langle\eta_1\rangle = [(1 - i\varepsilon'_2)(\eta'_o - \langle p_1\rangle) - i\varepsilon'_1 R(\langle p_2\rangle - \langle p_1\rangle)]\, F \qquad (2.11a)$$

$$\langle\eta_2\rangle = [(\eta'_o - \langle p_1\rangle) - (1 - i\varepsilon'_1)(\langle p_2\rangle - \langle p_1\rangle)]\, F \qquad (2.11b)$$

where $F = [1 - \varepsilon'_1\varepsilon'_2 - i\varepsilon'_1(1+R) - i\varepsilon'_2]^{-1}$ and $R=A_2/A_1$. (2.11c)

At a point X in the Eastern Mediterranean just outside the Strait of Sicily, x=0 and hence $p_X=p_a$. From 2.6b, we have:

$$\eta_X = \langle\eta_2\rangle + \langle p_2\rangle - p_a\,. \qquad (2.12a)$$

Substituting for $\langle\eta_2\rangle$ by using 2.11b, $\langle p_2\rangle$ by using 1 and removing the forcing η'_o so that only direct forcing by the atmosphere is considered, we obtain from 2.12a:

$$\eta_X /(-p_X) = 1 - \delta_2^{-1} \sin\delta_2\, e^{+i\delta}{}_2 + (1 - i\varepsilon'_1)F\, \delta_2^{-1} \sin\delta_2\, e^{+i\delta}{}_2 + i\varepsilon'_1 F \delta_1^{-1} \sin\delta_1\, e^{-i\delta}{}_1 \qquad (2.12b)$$

The first two terms on the RHS give the local response to atmospheric pressure in the absence of flow through the Strait of Sicily; this response is zero at low frequency (i.e. as $\delta_2 \rightarrow 0$) and approaches the value of 1 at sufficiently high frequencies (i.e. as $\delta_2 \rightarrow$ infinity) when the scale of the atmospheric pressure system can be considered to be much less than the size of the Eastern Mediterranean basin.

The third and fourth terms are related to the effect imposed by the flow at the straits. As the frequency approaches zero, the third term tends to 1 and the fourth to term to zero; at high frequencies both terms vanish to zero since F tends to zero. This result implies that that the model predicts an isostatic response at low and high frequencies, with a non-isostatic response at intermediate frequencies.

2.4.1.5 The Candela model

More recently, Candela et. al. (1989) and Candela (1991) proposed a simple linear dynamical model with frictional control at the two straits. The model assumes a balance between acceleration, along-strait pressure gradient and friction. The frequency dependence of the sea level response to an input spectrum of atmospheric pressure is thus obtained by solving the following set of equations:

$$A_1 d\langle\eta_1\rangle/dt = Q_1 - Q_2 \qquad A_2 d\langle\eta_2\rangle/dt = Q_2 \qquad (2.13a)$$

$$\langle p_{s1}\rangle = \langle p_1\rangle + \rho g\langle\eta_1\rangle \qquad \langle p_{s2}\rangle = \langle p_2\rangle + \rho g\langle\eta_2\rangle \qquad (2.13b)$$

$$dQ_1/dt = -(A_G/\rho)\,[(\langle p_{s1}\rangle - \langle p_{so}\rangle)/L_1\,] - \lambda_1 Q_1 \qquad (2.13c)$$

$$dQ_2/dt = -(A_S/\rho)\,[(\langle p_{s2}\rangle - \langle p_{s1}\rangle)/L_2\,] - \lambda_2 Q_2 \qquad (2.13d)$$

where A_G, A_S are the section areas of the Straits of Gibraltar and Sicily respectively, λ_i is the friction coefficient for strait i , $\langle p_{si}\rangle$ is the mean subsurface pressure for basin i = 1,2 while the other symbols have the same

significance as above. < > again denotes a spatial average over a basin. $<p_{so}>$ is the subsurface pressure in the Atlantic just west of the Strait of Gibraltar. If the response of sea level in the Atlantic to atmospheric pressure is isostatic, $<p_{so}>$ can be set to a constant. The six unknowns (Q_1 , Q_2 , $<\eta_1>$, $<\eta_2>$, $<p_{s1}>$, $<p_{s2}>$) in the linear system of six equations can thus be solved at a given frequency by taking each variable proportional to $e^{-i\omega t}$. The model gives the mean sea level response $<\eta>$ to mean pressure $<p>$ for the respective basins. Assuming a local adjustment to spatial variations in the pressure within each basin, the response of sea level $\eta(\mathbf{x},t)$ at any position $\mathbf{x}$ and time t to pressure $p(\mathbf{x},t)$ is given by 2.6a :

$$\eta(\mathbf{x},t) = <\eta>(t) + [<p>(t) - p(\mathbf{x},t)]/ \rho g \qquad (2.14)$$

(Note that if $<\eta>(t) = - <p>(t)/ \rho g$, then $\eta(\mathbf{x},t) = - p(\mathbf{x},t)/ \rho g$ which yields the standard inverse barometer correction.)

The model has been used to correct TOPEX/POSEIDON altimetry data for atmospheric pressure effects (Le Traon & Gauzelin 1997). Comparison of TOPEX/POSEIDON with model predictions of mean sea level shows that a large part of the variance in mean sea level variations (50% in the Western Basin and 38% in the Eastern Basin) is actually explained by the model. The role of friction at the Strait of Gibraltar is also found to be much more well evidenced than in the Strait of Sicily. The model predicts that intermediate periods centred on 4 days should be under-isostatic. This non-isostatic response is corroborated by actual sea level gauge data. Several studies have in fact confirmed that the response is mainly under-isostatic for periods less than 15 days (Garrett & Majaess, 1984; Lascaratos & Gacic, 1990; Tsimplis & Vlakhis, 1994; Tsimplis, 1995).

2.4.1.6 Geostrophy vs friction

Although the Garrett (1983) and Candela (1991) analytical models are not able to fully explain the complex response of sea level to atmospheric forcing, they nonetheless both exhibit an amount of skill in explaining the deviation from the standard IB effect at high frequencies. It is however hard to reconcile the effects of geostrophy and friction on which the models are respectively based. Indeed the latter disregards rotation completely, but if the friction coefficient is taken equal to fW/L then the two models become equivalent. With L/W=3, this would require the friction coefficient to be 3×10^{-5}. In both models the geometric and bathymetric details are moreover simplified to uniform basins connected by one dimensional channels, while each basin is

assumed to have a spatially homogeneous sea surface height and no interior kinetic energy so that an integrated response of each basin is obtained.

2.4.1.7 Other models

A substantially refined model that takes into account the complex bathymetry of the Mediterranean, the role of the Atlantic Ocean, and that is able to resolve the sub-basin variability has been proposed by Candela & Lozano (1994). This numerical model simulates the barometric response of the Mediterranean Sea to observed atmospheric pressure derived from twice daily ECMWF (European Centre for Medium Range Weather Forecasts, Reading, England) analysis by using a space spectral representation of the shallow water equations on a β-plane with bottom friction. With respect to the Candela analytical model the predicted sea levels are closer to observations. On the other hand, the explained variance in the barotropic fluxes through the Strait of Gibraltar is practically the same as in the analytical model; this indicates that the specific geometric configuration of the system plays a minor role in determining transport.

2.4.2 Analysis of sea level and atmospheric pressure fields

2.4.2.1 Application of empirical orthogonal functions

Empirical orthogonal function (EOF) analysis is a very useful means of identifying space scales involved in the variability of a given field. One of the most significant EOF applications to both sea level and atmospheric pressure in the Mediterranean is that performed by Lascaratos & Gacic (1990) on datasets from selected stations in the Adriatic, Ionian and Aegean seas. The first two EOF modes of sea level and pressure respectively are reported to explain about 95% of the variance in the sub-tidal frequencies. The shape of the gain and phase spectra between atmospheric pressure and sea level for the combined modes in winter correspond very well with those obtained from the Garrett model. The first mode is predominant (90% of the variance) and represents variations of sea level and atmospheric pressure in the low frequency range of atmospheric planetary waves that occur with a spatial coherence over the entire region and with length scales that exceed the basin extent. The second mode is shown to be related to surface pressure changes induced by cyclonic activity and represents synoptic time scale variations for which the Adriatic Sea is out of phase with both the Ionian and Aegean Sea. Departures from the isostatic response at the first mode frequencies are shown to be mainly controlled by frictional effects on the flow rather than geostrophy at the Strait of Sicily. On the other hand, the unrestricted internal adjustment processes between the different basins in the area result in a response at the

second mode frequencies that is nearly barometric while geostrophic control at the Strait of Sicily introduces significant restriction at time scales of a few days.

A more comprehensive EOF analysis of atmospheric pressure in the Mediterranean is that carried out on six years (1985-1990) of twice daily ECMWF data covering the whole basin (Candela & Lozano, 1994). The variance is again explained in terms of the first two modes with a respective contribution of 65% and 16%. The first mode has a spatial structure of the same sign over the whole basin, with a maximum in the Ligurian Sea and a minimum in the Levantine basin. On the other hand the second EOF divides the Mediterranean in half with a node that is practically coincident to the longitude across Malta. The time variability of both EOFs is characterised by high pressure during winter and spring and low pressure in the summer and fall months. Their spectra are also concentrated at low frequencies and decrease monotonically with frequency without any discernable peaks.

The corresponding six-year time series of modelled response in sea surface height and transports are also submitted to an EOF analysis. The first four EOFs are found to account for about 47% of the response variability. Together they explain the phenomenology of the forced motion that mainly consists of an exchange between irrotational strait flow components and sub-basin secondary rotational circulations that take the form of eddies. These transformations occur as a result of vorticity contributions due to topography, β, and bottom stresses, in order of importance.

2.4.2.2 Sea level variability from space

Another study based on three years (October 1992 - October 1995) of atmospheric pressure data derived from ECMWF model analysis is described in Le Traon & Gauzelin (1997). In this case the mean pressure time series is submitted to coherence analysis with the corresponding three years of uncorrected mean sea level obtained from TOPEX/POSEIDON altimetry data. In comparison to sea level gauges, satellite altimetry is better commendable to quantitatively measure the mean sea level. As a matter of fact gauges measure the local response at a given place and will differ from the basin average response, particularly as a result of the wind effect which is likely to be averaged out in the mean sea level response for the basin. The study shows that variations in the mean atmospheric pressure over the Mediterranean can reach up to 15mb at high frequencies, especially during winter. There is also a marked seasonal signal, with winter being in general more anticyclonic.

In the range of frequencies $(60\text{days})^{-1}$ to $(6\text{days})^{-1}$, the overall variance in mean pressure is about ¼ that of mean sea level. This ratio is ½ for periods less than 50 days, and approximates to 1 for periods less than 25 days. The seasonal signal of the atmospheric pressure is thus less than that of the sea level. The mean sea level variability is well correlated to mean atmospheric pressure with the coherence remaining well above the 95% confidence limit at all frequencies although it drops considerably at periods between 20 and 30 days. The phase difference is always below that of a perfect inverse barometer effect (i.e. below 180°) and continues to decrease with frequency leading to an appreciable delay in the response of the sea level. A significant departure from an inverse barometer effect is registered at the higher frequencies.

2.4.2.3 Multiple regression analysis in the frequency domain

In cases where a variable is to be expressed in terms of two or more quantities which are also mutually interdependent, multiple regression analysis in the frequency domain can be adopted. The analysis is here described with an emphasis on the application to describe the effect of meteorological parameters on the sea elevation. This method is based on that described by Wunsch (1972) in his study of the Bermuda sea level, and has been applied by other authors (Garrett & Toulany, 1982; Garrett & Majaess, 1984; Tsimplis, 1995). The input signals are atmospheric pressure P, and the orthogonal set of wind components X (e.g. East-West or alongshore) and Y (e.g. North-South or cross-shore); the output is sea level η. If each signal is regarded as the sum of a number of sinusoidal components of different frequencies, and assuming linearity, the regressional model can be expressed at each frequency ω by:

$$\Gamma_{\eta}(\omega) = \hat{a}(\omega)\Gamma_{P}(\omega) + \hat{b}(\omega)\Gamma_{X}(\omega) + \hat{c}(\omega)\Gamma_{Y}(\omega) + N \qquad (2.15)$$

where Γ_i is the Fourier transform and $\Gamma_i(\omega)d\omega$ is the frequency component in the frequency band $\omega \rightarrow \omega + d\omega$ for each of the signals i=η, P,X and Y. The noise N is here a measure of the variability in sea level that is incoherent with P, X and Y. Each regression coefficient $\hat{a}, \hat{b}, \hat{c}$ is a function of frequency and explains the contribution of a particular input to the sea level response in the absence of the effect from other inputs. These complex coefficients are effectively frequency response functions; their phases represent the lag of the sea level response behind the respective meteorological forcing. The Fourier transforms of $\hat{a}, \hat{b}$ and $\hat{c}$ can be related to coefficients in a convolution representation of η in the time domain (Wunsch, 1972). To establish the model it is

necessary to optimise the values of the regression coefficients at each spectral frequency ω. This optimisation is carried out by a least squares determination of $\hat{a}, \hat{b}$ and $\hat{c}$. The cross-spectral estimate G of sea level η (the dependent variable) on an input (independent) variable such as atmospheric pressure P, is expressed in terms of a linear combination of auto- and cross-spectral estimates of the independent variable on the other inputs (e.g. the wind components, etc.). At each frequency ω, a set of simultaneous equations is thus obtained (Newland, 1993):

$$\begin{pmatrix} G_{P,P} & G_{P,X} & G_{P,Y} \\ G_{X,P} & G_{X,X} & G_{X,Y} \\ G_{Y,P} & G_{Y,X} & G_{Y,Y} \end{pmatrix} \begin{pmatrix} \hat{a} \\ \hat{b} \\ \hat{c} \end{pmatrix} = \begin{pmatrix} G_{P,\eta} \\ G_{X,\eta} \\ G_{Y,\eta} \end{pmatrix} \tag{2.16}$$

from which the regression coefficients can be determined. Following Garrett & Toulany (1982) the $(1-\alpha)$ confidence range for the amplitude and phase of the regression coefficients is given by:

$$\left|\Delta l_{i,\ \text{amplitude}}\right| = \sqrt{\frac{2(1-\alpha) f_{2,\upsilon-2} G_{NN} D_j}{\upsilon - 2}}$$

$$\Delta l_{i,\ \text{phase}} = \pm \sin^{-1} \frac{\left|\Delta l_{i,\ \text{amplitude}}\right|}{\left|l_{i,\ \text{amplitude}}\right|} \tag{2.17}$$

where $l_i = \hat{a}, \hat{b}, \hat{c}$ for i=1,2,3; D_j is the jth diagonal element of the inverse of the cross-spectral matrix **G** and $f_{2,\upsilon-2}$ is the value of the Fishers distribution with 2, υ -2 degrees of freedom. The auto-spectrum G_{NN} gives the residual variance associated with the component of η that remains unexplained by the model.

The relative importance of the inputs on the sea level can be analysed by comparing the amount of sea level variance that can be attributed to each of the inputs. Upon multiplying (2.15) by its complex conjugate on both sides, we obtain:

$$\begin{aligned}\Gamma_\eta \Gamma_\eta{}^* &= \hat{a}\hat{a}^* \Gamma_P \Gamma_P{}^* + \hat{b}\hat{b}^* \Gamma_X \Gamma_X{}^* + \hat{c}\hat{c}^* \Gamma_Y \Gamma_Y{}^* \\ &+ (\hat{a}^* \hat{b} \Gamma_P{}^* \Gamma_X + \hat{b}^* \hat{a} \Gamma_X{}^* \Gamma_P) \\ &+ (\hat{b}^* \hat{c} \Gamma_X{}^* \Gamma_Y + \hat{c}^* \hat{b} \Gamma_Y{}^* \Gamma_X) \\ &+ (\hat{a}^* \hat{c} \Gamma_P{}^* \Gamma_Y + \hat{c}^* \hat{a} \Gamma_Y{}^* \Gamma_P) + \textit{residual variance}\end{aligned} \tag{2.18}$$

where $\Gamma_i \Gamma_i{}^*$ is to be taken as the power spectrum for each of the signals i=η , P,X and Y while the cross terms are related to the cross-spectra of the input variables. The first three terms refer to the contribution to sea level variance by the separate inputs. The remaining three bracketed terms give the variance from the combination of inputs. Expressed in terms of the corresponding spectra (2.18) becomes:

$$\begin{aligned}S_{\eta\eta} &= \hat{a}\hat{a}^* S_{PP} + \hat{b}\hat{b}^* S_{XX} + \hat{c}\hat{c}^* S_{YY} \\ &+ (\hat{a}^* \hat{b} S_{PX} + \hat{b}^* \hat{a} S_{PX}{}^*) \\ &+ (\hat{b}^* \hat{c} S_{XY} + \hat{c}^* \hat{b} S_{XY}{}^*) \\ &+ (\hat{a}^* \hat{c} S_{PY} + \hat{c}^* \hat{a} S_{PY}{}^*) + \textit{residual variance}\end{aligned} \tag{2.19}$$

Dividing both sides of (2.18) by $\Gamma_\eta \Gamma_\eta{}^*$ and multiplying by 100 gives an estimate of the percentage variance by each term, as a function of frequency.

In the case of the response of sea level depending only on atmospheric pressure, the power spectrum of sea level is expressed by:

$$\Gamma_\eta(\omega) = \hat{a}(\omega)\Gamma_P(\omega) + \textit{noise}\,. \tag{2.20}$$

Hence

$$\hat{a}(\omega) = G_{P,\eta}(\omega) / G_{P,P}(\omega) = (C_{P,\eta}(\omega) + iQ_{P,\eta}(\omega)) / G_{P,P}(\omega), \tag{2.21}$$

where $G_{P,P}$ is the autospectrum of pressure, and $C_{P,\eta}$ and $Q_{P,\eta}(\omega)$ are, respectively, the co-spectrum and quadrature spectrum of pressure and sea level. â gives the response or 'admittance' of sea level per unit change

in atmospheric pressure. Its absolute value gives the gain or what is more commonly called the barometer factor which is expected to be -1.01 cm/mb for all frequencies.

2.4.2.4 Results from the Malta data sets

Analysis of the response of the residual sea level to barometric pressure and two orthogonal wind components is performed from hourly values of sea level, MSL pressure and wind data covering a period of 298 days 16 hours (0h 18th November 1995 - 15h 11th September 1996). Two methods of data analysis are applied: spectral analysis and multiple regression analysis. The first method consists of auto- and cross-spectral data examination between the various parameters. The multiple regression analysis is performed in the frequency domain. This combined analysis provides an estimation of the response functions of the sea level to the atmospheric disturbances and quantifies the relative contributions by the respective meteorological factors.

The comparative plot of the residual sea level and meteorological time series (Fig. 2.11) presents some very interesting first hand information. The residual sea level displays the presence of variability at different time scales. Sea level variations at a time scale of one month have the largest amplitudes and can reach peak-to-trough values of up to 0.35m. Higher frequency oscillations at time scales of several days (synoptic variability) appear on both the sea level and pressure time series, and are predominant during the winter months. These oscillations are related to natural periods of occurrence of cyclones in the region. Variations in the atmospheric pressure can reach up to 18mb at high frequencies, and are accompanied by equivalent variations in sea surface height. Both high and low frequency sea level oscillations in fact bear a distinct visual correlation with the inverted barometric pressure and extreme values of sea level are very well associated with extreme values of inverted pressure. It is also clear that the sea level and atmospheric pressure variance differs seasonally. The sea level signal shows however a greater variability than that implied by a simple barometric effect.

The two wind components are taken along the east-west and north-south with positive magnitude from the east and north respectively. Alternatively they are taken to correspond to a wind vector from directions 35° (positive cross-shore component) and 125° (positive along-shore component) with respect to north. These components are roughly coincident to a wind directed along the axis of Mellieha Bay and parallel to the northern foreshore coastline of the island respectively. The mean wind magnitude is 2.15 ms^{-1} from the west (N87°W). The wind data are characterised by frequent clockwise rotations of the wind direction which is indicative of the passage of

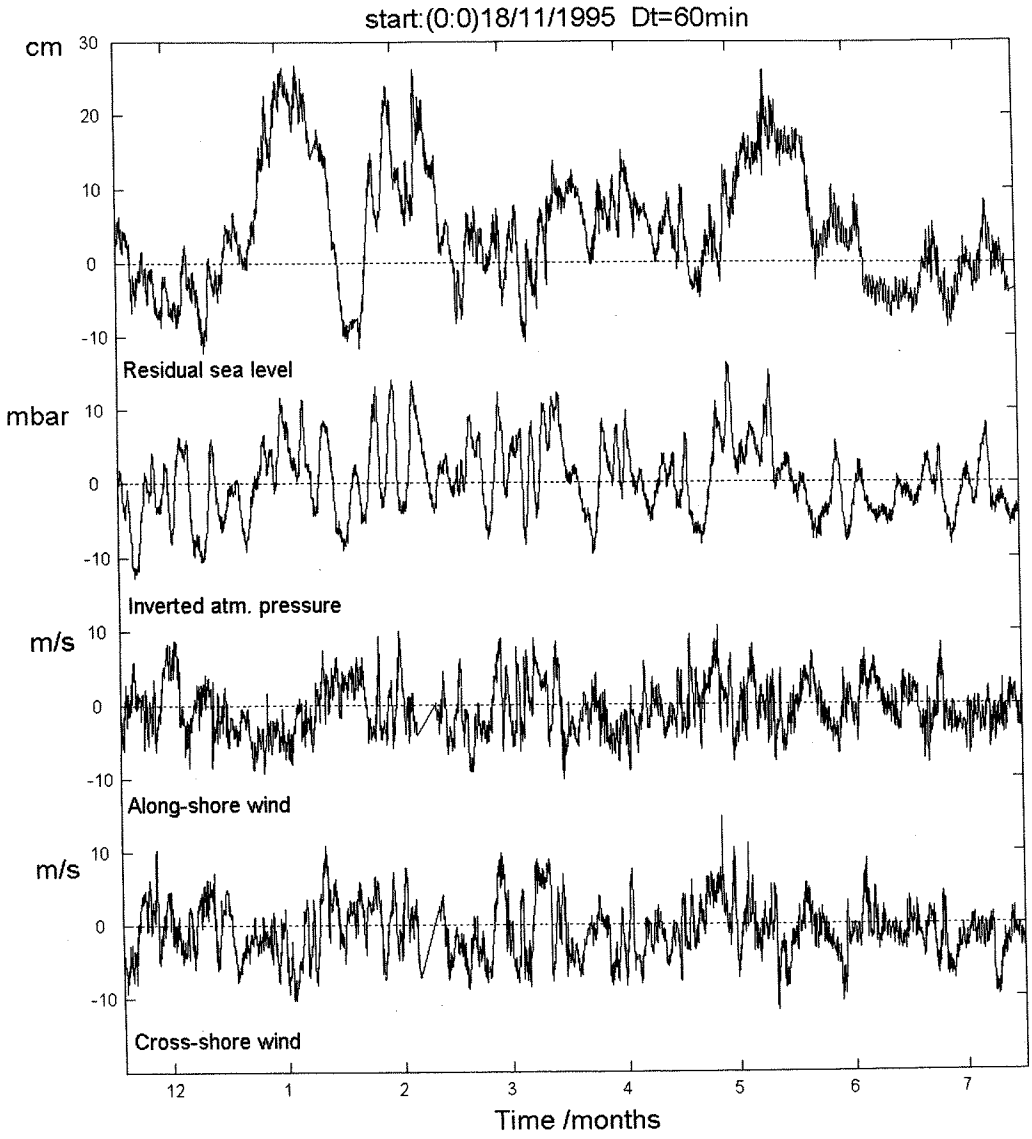

Fig. 2.11 Time series of (a) residual sea level in Mellieha Bay; (b) inverted barometric pressure fluctuations at MSL; (c), (d) along/cross-shore components of wind at Ramla station for the period mid-November 1995 to mid-July 1996.
(Residual sea level is measured relative to MSL; the positive along-shore wind component corresponds to a wind from S55°E; the positive cross-shore wind component corresponds to a wind from N35°E.)

fronts over the area (Fig. 2.12). During the occurrence of these pressure lows, the wind vector can typically rotate by 90° and subsequently attenuate very rapidly, or even undergo a complete reversal without losing in strength.

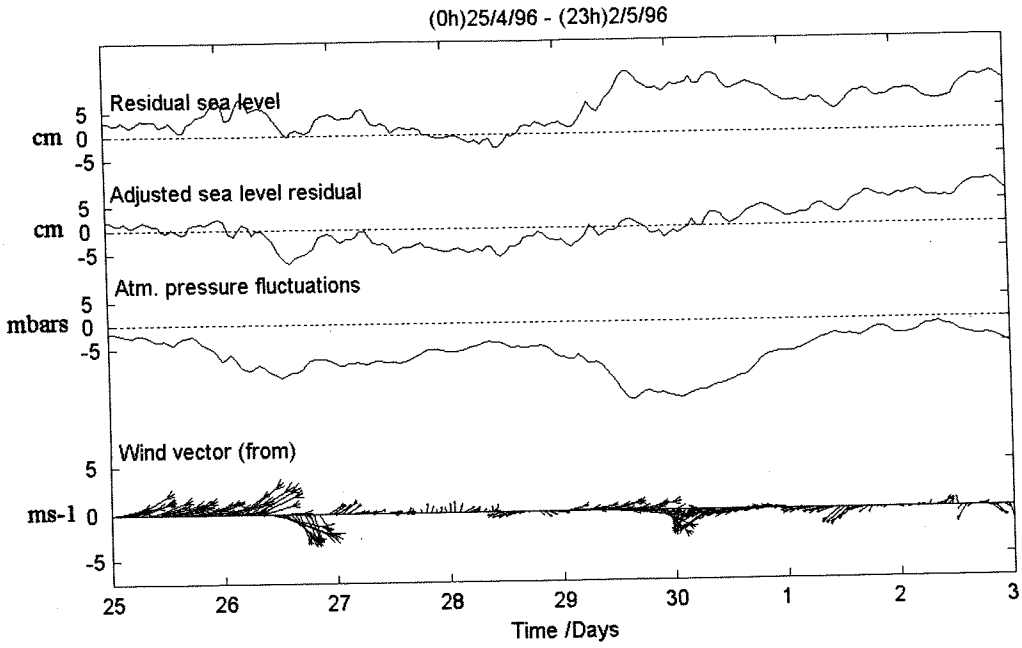

Fig. 2.12 Progress of changes in the wind vector in relation to atmospheric pressure fluctuations at MSL, the residual sea level and the adjusted sea level residual.
Adjusted sea level residual in cm = residual sea level in cm + (barometer factor * atmospheric pressure fluctuations in mbars)

The comparison is further investigated by means of auto- and cross-spectra of the data series which are computed from hourly values, after linear detrending and mean removal, by means of 13 50%-overlapping consecutive segments of 1024 points each. All the spectra (Fig. 2.13 and 2.14) show the 'red' shift of energy that is characteristic of geophysical processes. The prominent peak in the atmospheric pressure spectrum at the frequency of 2 cpd is due to the semidiurnal atmospheric tides. The diurnal maximum is less pronounced. At the higher frequencies, the atmospheric spectrum follows an $\omega^{-2.2}$ power law that is in good agreement with observations by Rabinovich & Monserrat (1996) and Kovalev et al. (1991) ($\omega^{-2.3}$), and only slightly steeper than that described by Herron et al. (1969) ($\omega^{-2.0}$). The spectrum has however a distinctive steeper gradient in the higher synoptic frequency range (0.2 - 1 cpd) where it follows an $\omega^{-3.2}$ power law decay. The pressure and wind spectra, especially the N-S component, exhibit a distinct flattening at periods greater than about 5 days. The sea

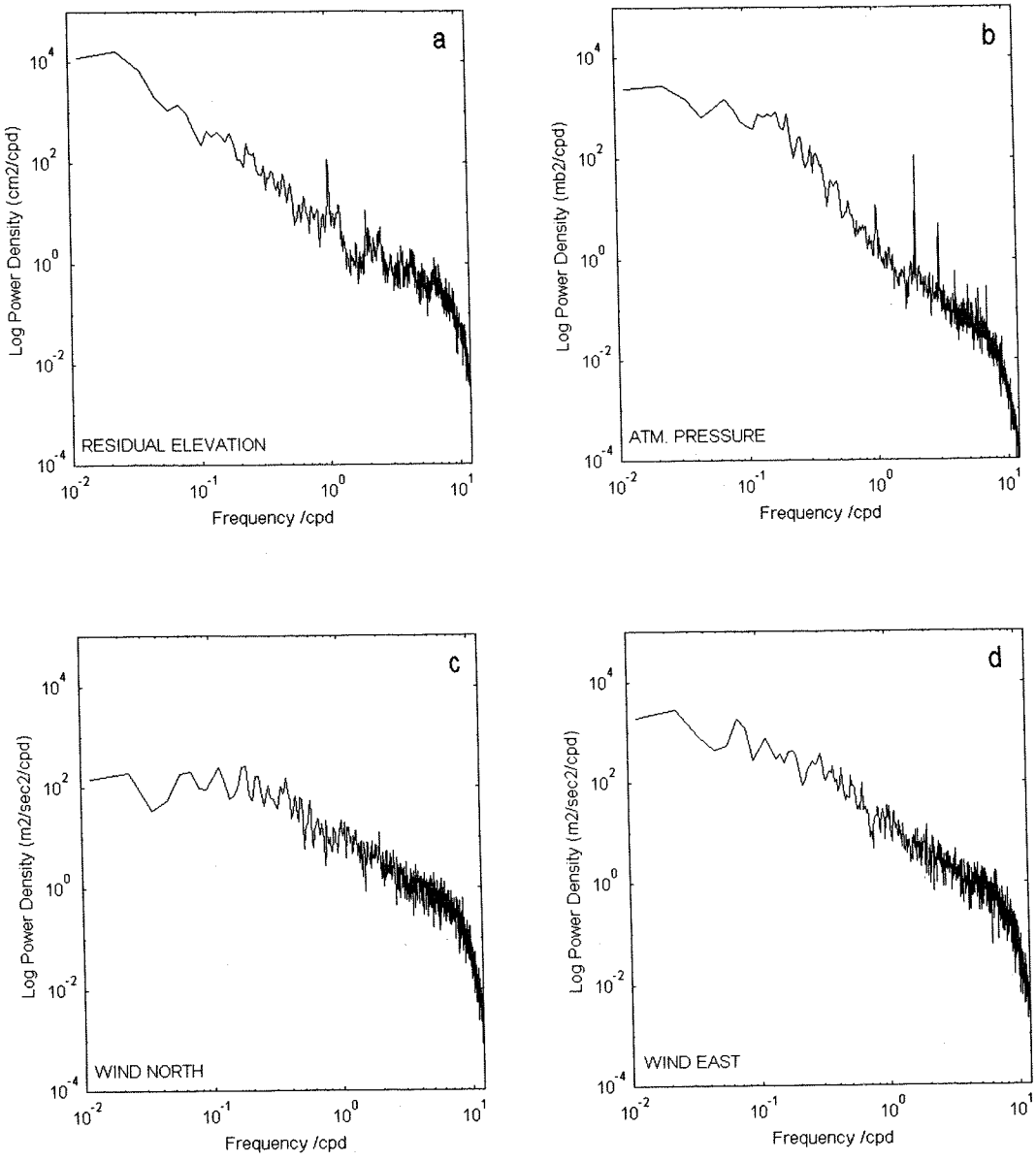

Fig. 2.13 General spectra for (a) residual sea elevation in Mellieha Bay, and (b) MSL atmospheric pressure and (c,d) wind components at Ramla Tal-Bir.
The 95% confidence factor, for 24 degrees of freedom is 5.0 dB (B_{min}=0.6; B_{max}=1.9).
Data used consists of hourly values from 18/11/95 - 11/8/96.

level spectrum has no such bounding limit on power at the lower frequencies and the spectrum has an almost constant slope for the full range of frequencies. The prevalence of the sea level spectrum over that of atmospheric pressure results in the power in sea level rising much more rapidly than that of pressure at periods longer than about 12 days, and in an increased divergence between the two spectra at the higher frequencies. At planetary time scales (several weeks), the sea level variance is close to seven times higher than that of pressure. The seasonal signal of the atmospheric pressure is thus less than that of the sea level.. At the synoptic time scale (0.05 - 0.5 cpd) the variances are equal at the lower frequency end, with variance in pressure become more

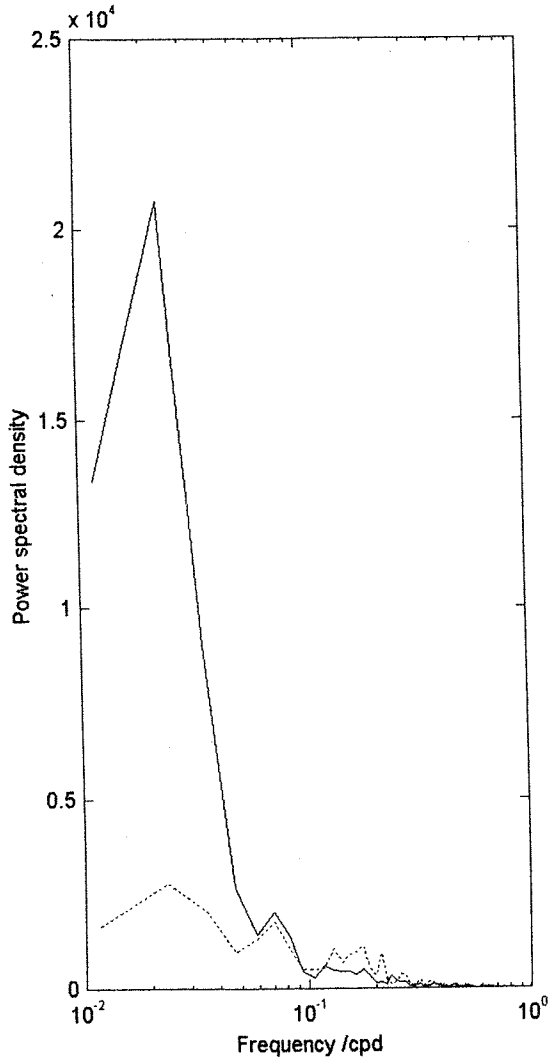

Fig. 2.14 Comparison spectra with semi-logarithmic scales for
(a) residual sea elevation in Mellieha Bay (solid), and
(b) MSL atmospheric pressure at Ramla Tal-Bir (dotted).
The 95% confidence factor, for 24 degrees of freedom is 5.0 dB (B_{min}=0.6; B_{max}=1.9).
Data used consists of hourly values from 18/11/95 - 11/8/96.

important with increasing frequency. The comparative plots of spectra on a semi-logarithmic scale (Fig. 2.14) shows that signals with frequencies higher than 0.5 cpd represent only a small fraction of the total variance in both residual sea level and atmospheric pressure.

The wind spectra exhibit a predominance of the EW component over the NS component in the synoptic frequency range (3:1) and especially for the lower frequencies (12:1).

2.4.2.5 Barometer factor from spectrum analysis

The significant dependence of sea level variability on atmospheric pressure in the synoptic and planetary wave scales is evidenced by the fairly high coherence between the residual sea level and atmospheric pressure fluctuations at these frequencies (Fig. 2.15). Coherence levels have an average of 0.7 for the response at frequencies lower than 0.5 cpd ($T > 2$ days). Coherence has a value of 0.6 for the lower frequencies, drops to 0.4 for frequencies centred on 0.14 cpd (T approx. = 7 days), and rises again to values close to 0.8 in the frequency range of 0.3 - 0.5 cpd ($2 < T < 3$ cpd) on average. The gain (barometer factor) and phase relationship bear a very similar dependence on frequency so that the response can be broadly classified into three bands of frequency (Fig. 2.16).

In the lower frequency planetary wave time scale ($f < 0.05$ cpd) the response is over-isostatic with a gain of about 1.5, and a lag of atmospheric pressure with respect to sea level a few tens of degrees less than 180°. This phase relationship is equivalent to that of an atmospheric pressure leading the inverted sea level by a few tens of degrees (i.e. an approximate phase difference of one day). This behaviour has been reported in other studies based on coastal data (Palumbo & Mazzarella, 1982; Pasaric & Orlic 1992; Tsimplis & Vlakhis, 1994) and is probably due to signals, such as from steric effects and wind, which can be correlated with atmospheric pressure. For periods higher than 25 days, Le Traon & Gauzelin (1997) have also found an over-isostatic response of the satellite-derived mean sea level to the ECMWF model analysis mean atmospheric pressure calculated over the whole Mediterranean.

In the lower synoptic frequency range ($0.05 < f < 0.3$ cpd) the pressure variance is higher than that of the residual sea level. The phase relationship remains less than 180° and a maximum delay of 70° in the response of the sea level is registered at a frequency slightly higher than 0.1 cpd. The response is thus well under-isostatic,

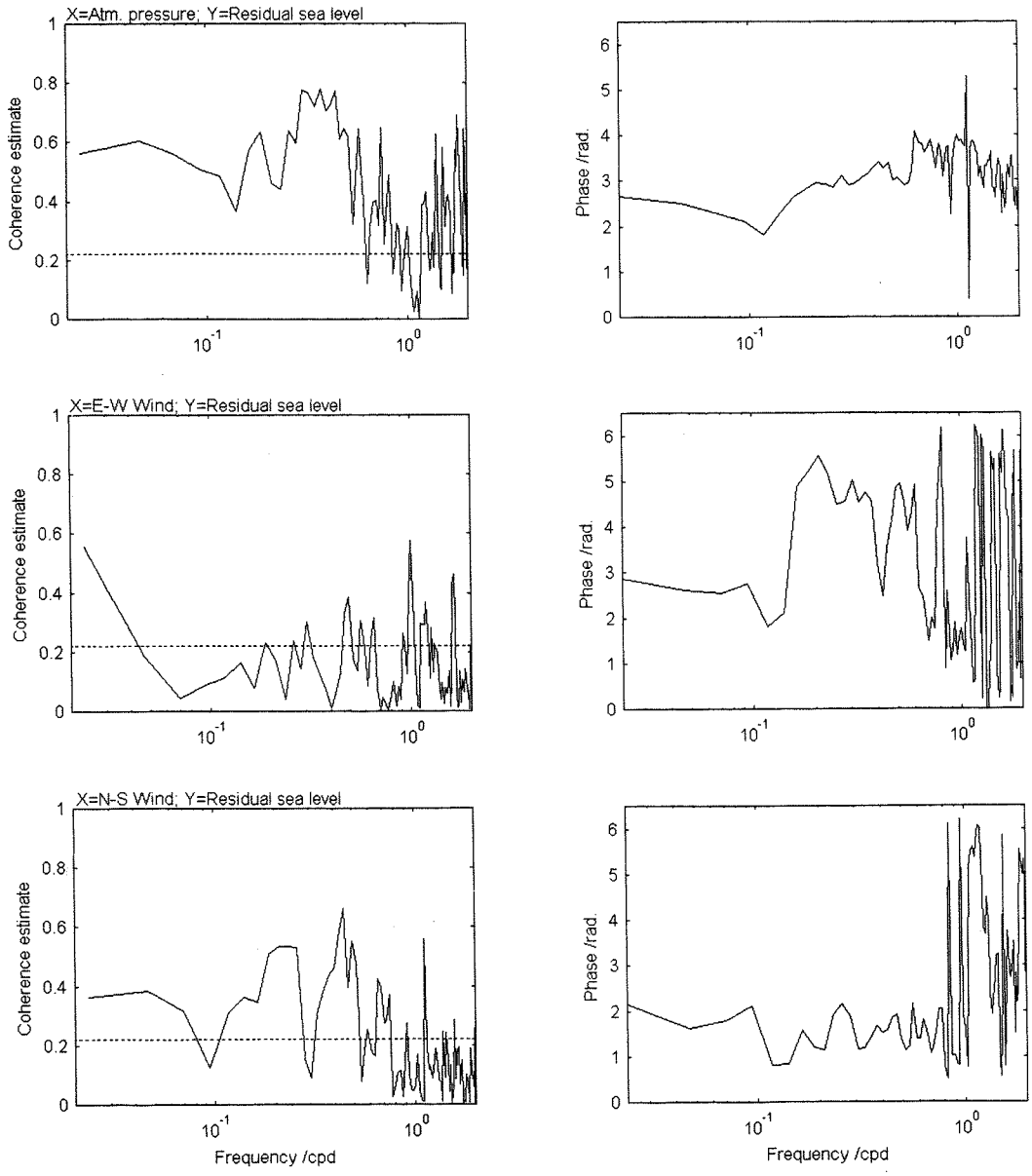

Fig. 2.15 Coherence and phase for residual sea level and (a) Atmospheric pressure at MSL, (b-c) E-W/N-S wind components for the period mid-November 1995 to mid-September 1996.
The phase indicates the lead of sea level with respect to the pressure or wind components. The dashed line indicates the level above which the coherence is significant at the 95% confidence level. With 24 degrees of freedom this is equal to 0.22.

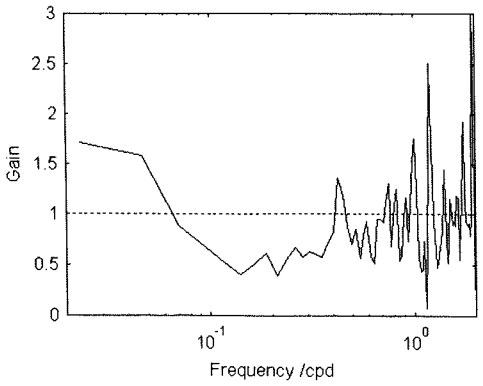

Fig. 2.16 Amplitude of the barometer factor as a function of frequency for the period mid-November 1995 to mid-September 1996.

and the equivalent sea level fluctuations are only about half the value expected for a perfect inverse barometer response. On the other hand the response is very close to isostatic in the upper synoptic frequency range ($0.3 < f < 0.5$ cpd). For this band of frequencies the sea level is highly correlated to pressure, and responds in antiphase to pressure with an average gain of 0.7.

For further higher frequencies ($f > 0.5$ cpd) the coherence is in general low except for a number of discrete frequencies. In particular, the sea level signals close to the diurnal frequency are uncorrelated to barometric pressure, which indicates that their origin has to be sought from other oceanographic influences.

It is not easy to see how these results can be used to explain the physical processes responsible for the non-isostatic response. It would certainly be necessary to measure the barometer factor at other sea level stations, particularly in the Central Mediterranean area, in order to assess the dependence of the response on the geographical position. Only then can one identify the extent to which discrepancies from the barometer effect can be related to special features of the bottom topography near individual stations with respect to the dependence on the larger scale dynamics of the strait. It is however interesting to note that these results corroborate the response models described above.

2.4.2.6 Effect of the wind

The non-isostatic values of the barometer factor can result from the omission of one or more variables that are closely correlated to atmospheric pressure. The wind is most likely to produce such an effect and cross-spectral estimates between wind and sea level are thus estimated. The wind components are taken along N-S and E-W

directions or alternatively by resolving along the cross-shore or along-shore directions. The sea level is taken either as the residual or as the adjusted residual sea level. The latter is calculated as the residual sea level added to (0.7*atmospheric pressure fluctuations in mb), where 0.7 is taken as the average barometer factor in the upper synoptic frequency range. Although the wind stress, rather than the wind itself, is expected to be related to the sea level through the dynamical equations, the coherence analysis between sea level and wind stress components did not give any significant difference from the coherence between sea level and the wind itself. Nonlinear relationships between wind and sea level are thus not investigated any further.

Sea level is not significantly coherent with E-W wind component except at frequencies below 0.05 cpd (Fig. 2.15). The sea level is however fairly coherent with the N-S wind over two main frequency bands within the synoptic range. This result does not necessarily indicate a causal relationship between sea level and this wind component since the meteorological variables can be intrinsically coherent between themselves. The coherence

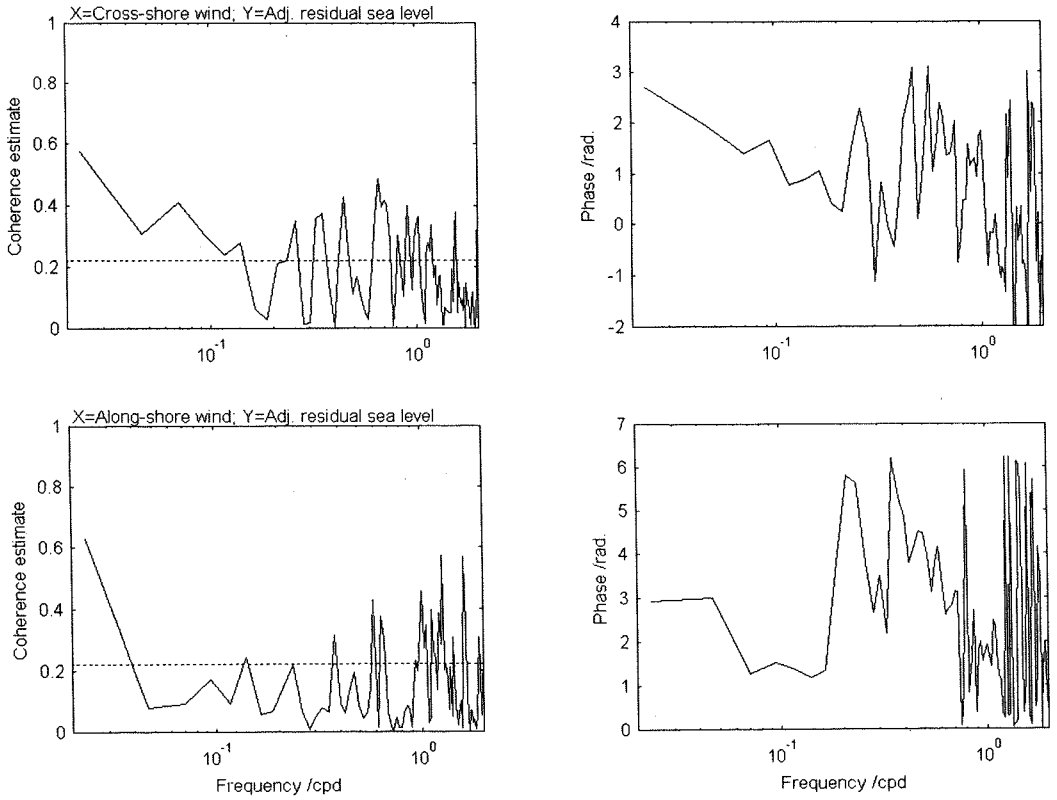

Fig. 2.17 Coherence and phase for the adjusted residual sea level and the Cross-/Along-shore wind components for the period mid-November 1995 to mid-September 1996.
The phase indicates the lead of sea level with respect to the wind components. The dashed line indicates the level above which the coherence is significant at the 95% confidence level. With 24 degrees of freedom this is equal to 0.22.

of sea level with pressure in combination with the coherence between the pressure and the N-S wind component (not shown) over the upper synoptic frequencies explains, in this case, the apparent coherence between sea level and the wind. The apparent direct forcing of sea level by the N-S wind in the upper synoptic range is thus not

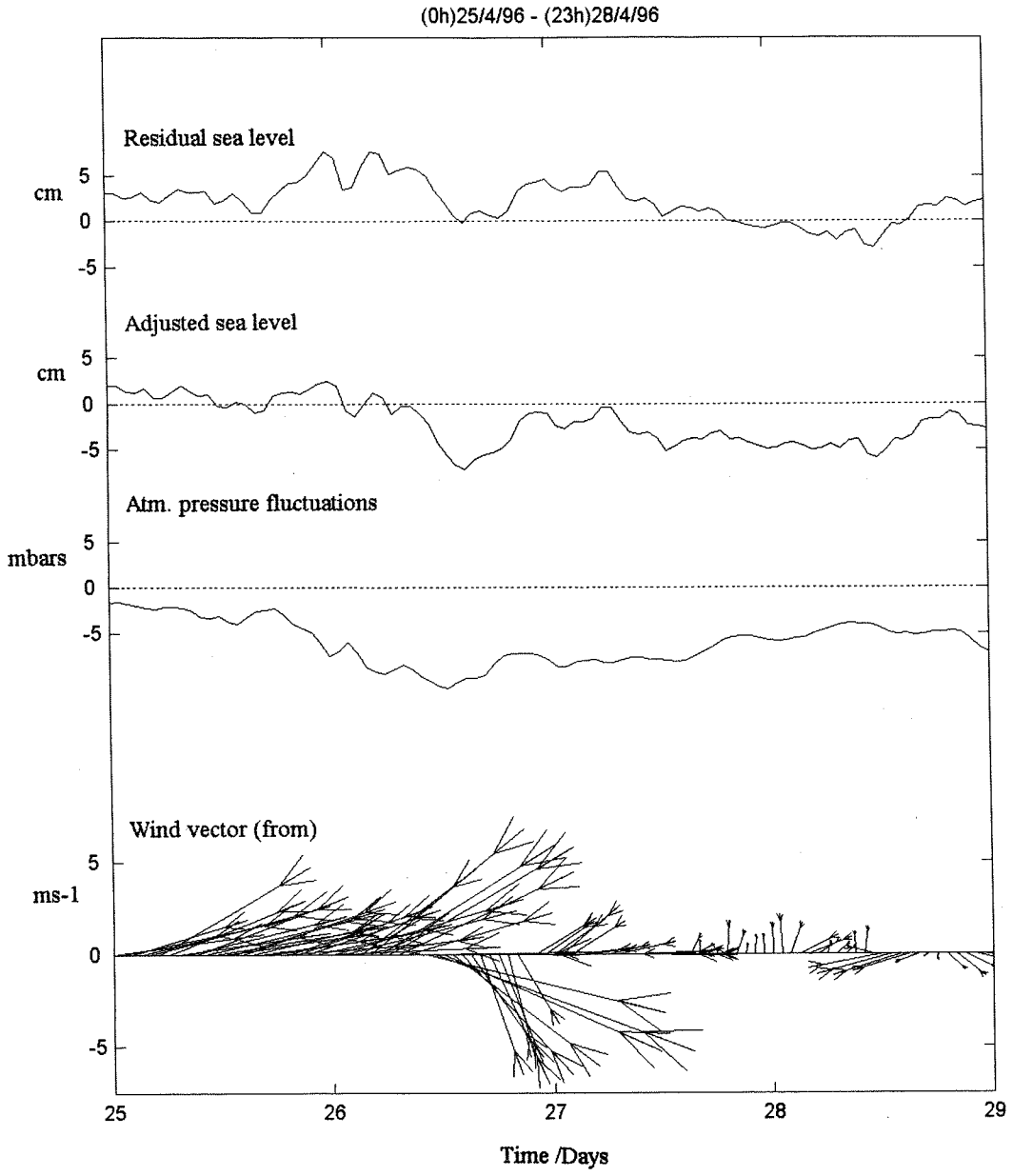

Fig. 2.18 Hourly averaged wind sticks compared with atmospheric pressure fluctuations (in mbars), the residual and adjusted residual sea level during the period 25-28th April 1996. Wind sticks indicate magnitude in m/s and direction of incidence with respect to North. Atmospheric pressure and sea level fluctuations are measured with respect to mean values calculated over the period mid-November 1995 to mid-September 1996.

real. This is further confirmed by the cross-spectral analysis with the adjusted residual sea level. Such ambiguities are removed by applying the multiple regression analysis described above.

Cross-spectra of the adjusted residual sea level with the wind are analysed in terms of the cross- and along-shore wind components. These component wind directions are taken with respect to the northern coast of Malta. Cross-shore components thus represent an axial wind with respect to Mellieha Bay, but are also perpendicular to the Sicilian southern coast. The analysis (Fig.2.17) shows that there is no band of frequencies with significant coherence except at the lower frequency end. On the planetary wave scale the adjusted sea level varies approximately in antiphase with the along-shore wind component and implies a general lowering of sea level in association to a southeasterly wind, and a rise in sea level with wind from the northwest. The phase with the cross-shore wind is less than 180° and presents a more complex relationship. At low frequencies there is a general lowering of sea level inside Mellieha Bay in association to a northeasterly (inshore) wind, whereas sea level rises on the occasion of southeasterly winds. This relationship with the axial wind is also observed at shorter time scales when the wind stick plots are compared to adjusted sea level on an event by event basis. When the wind blows from the sector bounded by directions 110° and 290° with respect to north, and in particular from the southwest (i.e. along bay axis towards the open sea) the sea level tends to rise; when the wind blows from the opposite sector and in particular from the northeast (i.e. along bay axis into the bay) the sea level tends to become lower. A typical case is shown in Fig. 2.18 where moderate but persistent Northeasterly winds during the 25th and 26th of April 1996 produced a gradual decrease in sea level that cannot be attributed to an effect of atmospheric pressure which is also decreasing. This behaviour does not of course comply with a direct local wind setup response within the bay itself whose dimensions are too small (about 3Km x 1Km) for any such effect to be sensible. The response must therefore be related to larger scale wind effects on the shelf water body especially within proximity to the shelf break.

2.4.2.7 Results of multiple regression analysis

The results of the multiple regression analysis are summarised in Figs.2.19 - 2.21. For convenience the residual sea level is inverted (negative); this is taken as the output. The isostatic response thus corresponds to 1cm/mb with larger and smaller values regarded as over-isostatic and under-isostatic respectively. The inputs are atmospheric pressure, and the along-/cross-shore wind components.

For all frequencies up to 0.75cpd, the overall explained variance is high and averages to about 75% of the total variance. The explained variance in the planetary wave and synoptic frequency ranges is mostly attributed to the direct effects of atmospheric pressure, except for an unexplained minimum around f = 0.12cpd where the along-shore wind component can explain close to 50% of the variability. For frequencies up to 0.1cpd the inverted residual sea level follows closely an ideal barometric response to atmospheric pressure except for the fact that the phase of atmospheric pressure with respect to the residual sea level is consistently a few tens of degrees less than 180°. For the very low frequencies (f < 0.05cpd) the explained variance is attributed to atmospheric pressure, along-shore wind and cross-shore wind in this decreasing order of magnitude. For these low frequencies the 95% confidence limits are rather large, but it is noted that the amplitude of the pressure coefficient is not significantly different from 1 so that the over-isostatic response deduced from the barometer factor cannot be attributed to atmospheric pressure.

A comparison of the pressure coefficient and phase from Fig. 2.19 and 2.20 with those of Fig. 2.15 and 2.16a shows that in the synoptic frequency range the allowance for the effect of wind does not lead to significant differences. The regression analysis is however able to quantify the relative importance of the inputs. The response in the range of frequencies centred around 0.08 cpd is particularly interesting; the atmospheric pressure explains up to 90% of the variance, but a good part of this variance is derived from the significant coupling of pressure with the wind components. For frequencies in the range 0.25 - 0.35cpd, the effect of atmospheric pressure is again predominant and contributes to approximately 60% of the sea level variance. At these frequencies the amplitudes of the wind coefficients are very low; this reconfirms the results in section 2.4.1.5 and the response clearly follows the inverted barometer effect.

The regression coefficients of the inverted residual sea level on the cross-/along-shore wind components are not significantly different from zero except for a number of discrete frequencies. In general, the wind does not therefore account for much of the sea level variance. In the synoptic frequency range the residual sea level leads the cross-shore wind component by $\pi/2$ radians while it lags by $\pi/2$ radians with respect to the along-shore wind component (note that the phase relationship with the *inverted* sea level has the opposite sign). This implies an increase in sea level in association to wind from the southwesterly (positive cross-shore wind component) or southeasterly (positive along-shore wind component) sectors. It is important to note that although these phase relationships are only meaningful when the corresponding amplitude values are significantly different from zero, these deductions are in agreement with results in section 2.4.2.6.

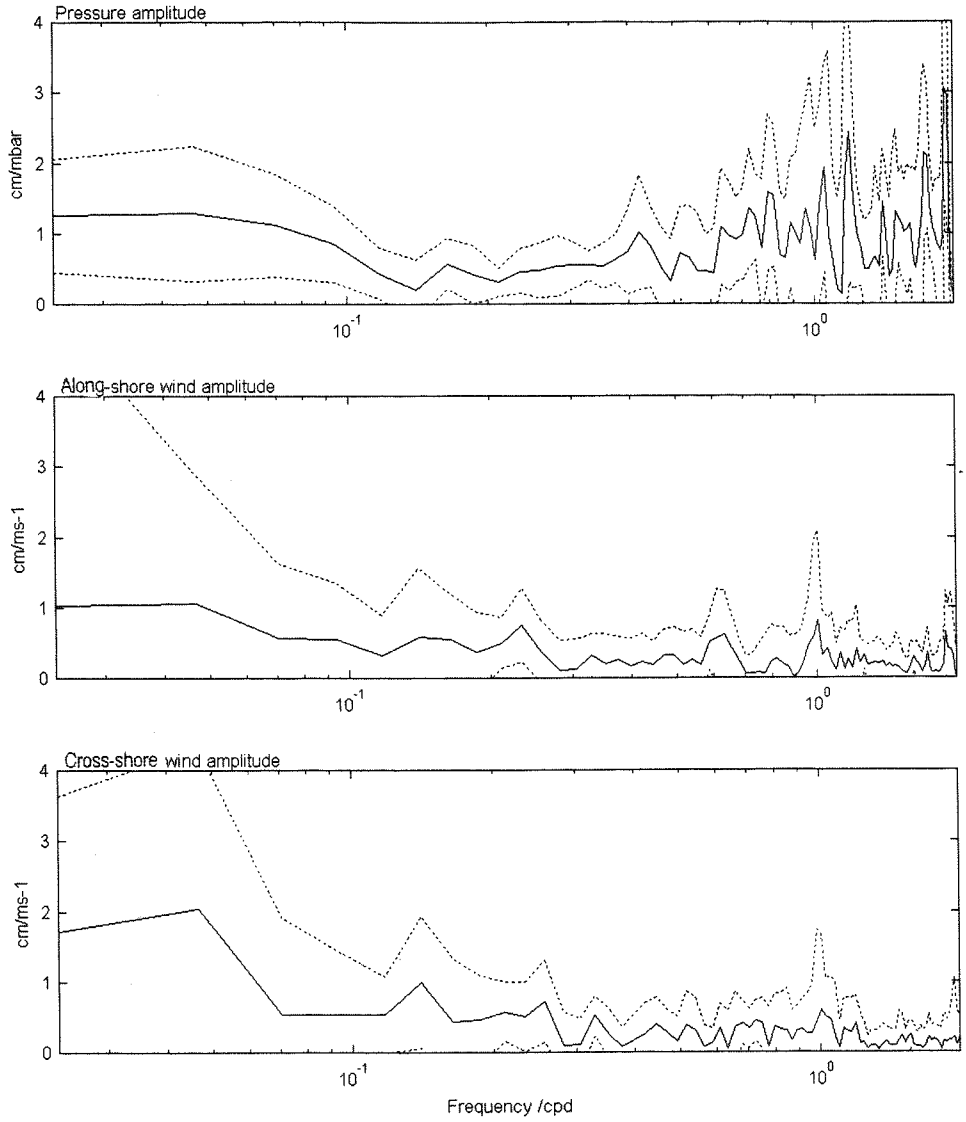

Fig. **2.19** Amplitude of the regression coefficients of inverted sea level on local atmospheric pressure and Cross-shore/Along-shore wind components in Ramla Station.

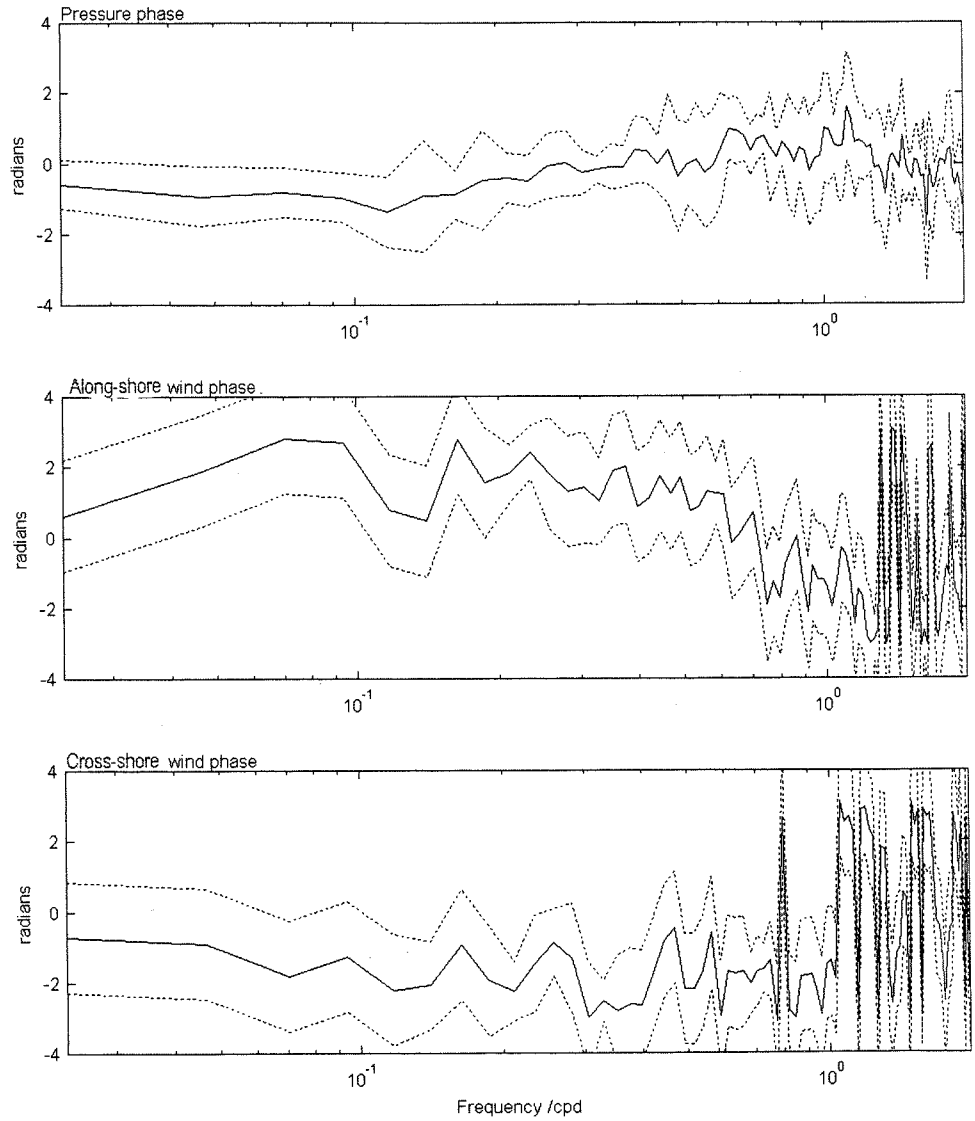

Fig. 2.20 Phase of the regression coefficients of inverted sea level on local atmospheric pressure and Along-/Cross-shore wind components in Ramla Station. The phase gives the lead in radians of the input on the respective output parameters.

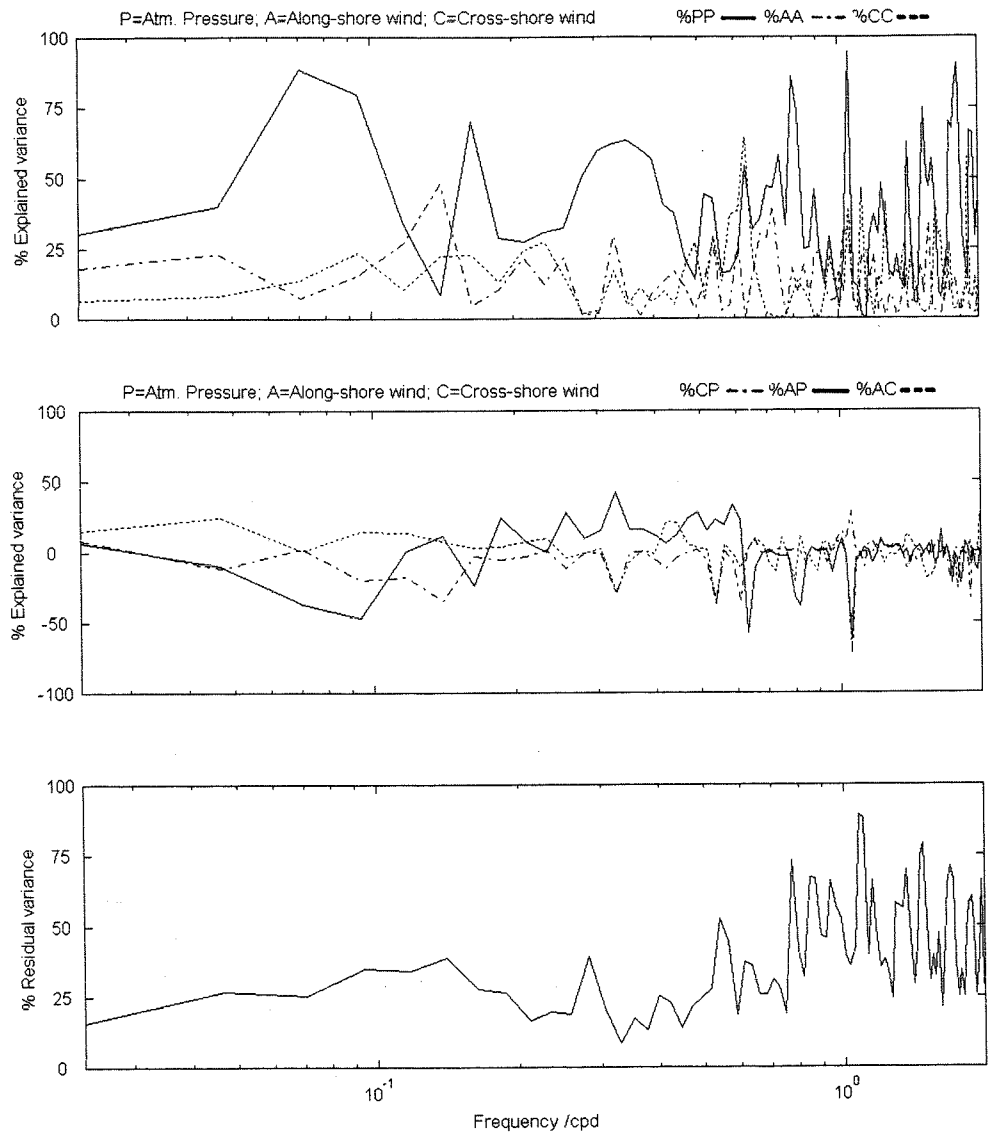

Fig. 2.21 Percentage of sea level variance accounted for by (a) the meteorological inputs (PP, AA and CC) and (b) their combinations (CP, AC and AP); (c) Residual variance due to part of sea level incoherent with atmospheric pressure and wind.

For frequencies higher than 0.8cpd, the variability is much harder to explain and the influence of other factors besides the direct effect of the weather parameters needs to be taken into account. At these frequencies the weather on average explains only half of the sea level variability. The interdependence of the input variables also becomes very low so that the respective effects on sea level can be treated separately.

2.5 Wavelet analysis

2.5.1 Wavelet vs Fourier analysis

One disadvantage with the statistical methods and conventional spectral analysis presented above is that they only provide time averaged results. Indeed Fourier analysis transforms the view of a signal from a time-based one to a frequency-based one. Time information is thus lost and the evolution in time of a signal cannot be identified. The methods assume that the signal is stationary so that its statistics do not change with time. In nature, it is known that processes are generally random. The spectral composition of a signal is indeed expected to vary continuously, and the changing relative contributions of its components may represent the most important features of the signal variability. Even the inter-dependence between a set of parameters, such as that of sea level and the weather parameters, may itself vary in time.

The application of the wavelet transform provides an effective method of analysing and synthesizing this variable structure of a signal in time and provides a means of localising events of interest at their exact temporal location. Wavelet theory (refer to Appendix 1 for a brief introduction on the subject) has been studied by mathematicians since the seminal papers by Daubechies (1987, 1988, 1990) and Mallat (1989). Although its application in signal processing is relatively new, wavelet analysis has already been successfully used in many engineering fields with applications in communications, geophysics, finance and medicine. It has proved to be a very powerful tool in speech and audio analysis and fingerprinting, in noise filtering, and in image and video digital compression. The present work is indeed the first application to time series of hydro-meteorological data. The method allows specific features of a signal to be localized in time by decomposing the signal into a family of basis functions, called wavelets.

In Fourier analysis a signal is broken up into smooth sinusoids of unlimited duration. Similarly, wavelet analysis consists in the breaking up of a signal into wavelets which are waveforms of effectively limited duration and

zero mean, but which tend to be irregular and asymmetric. Wavelet analysis is essentially a windowing technique with variable-sized regions. The analysis consists in shifting forward the wavelet in steps along the full signal and generating at each step a wavelet coefficient that measures the level of correlation of the wavelet to the signal in each section. When the full series is covered, a set of wavelet coefficients is generated that has the same consistency in time as that of the original signal. The variation in the coefficients indicates the changing level of similarity of the wavelet with the signal in time. This process is repeated with scaled (stretched) versions of the wavelet so that sets of wavelet coefficients at different scales are generated. This process produces a set of series of wavelet coefficients that are a function of scale and position. The lower scales refer to the compressed wavelet and are able to follow the rapidly changing details or high frequency component of the signal. The higher scales are composed from the stretched version of wavelet and the corresponding coefficients represent the slowly changing coarse features or low frequency component. The results can best be viewed by means of time-scale coefficient plots in which the x-axis represents position along the signal (time), the y-axis represents scale and the color or shade of grey represents the magnitude of the wavelet coefficients.

2.5.2 Continuous vs discrete wavelet transform

The analysis can either be carried out in continuous or discrete mode. The continuous wavelet transform operates at every scale, from that of the original signal up to some maximum scale determined by trading off the need for detailed analysis with available computation speed and power. During computation the analysing wavelet is also shifted smoothly over the full domain of the analysed signal so that the continuous wavelet transform is also continuous in terms of shifting. On the other hand the discrete wavelet transform calculates wavelet coefficients only at a determined subset of scales and positions. The discrete scales and positions are very often chosen on a dyadic (powers of two) basis. An efficient way to implement this scheme by using filters was developed by Mallat. The Mallat algorithm is essentially a filtering process and it decomposes the original signal into a series of approximations and details (refer to Appendix 1 for details). The approximations are the high-scale low frequency components of the signal. The details are the low-scale, high frequency components. The process consists of a number of successive filtering steps. The original signal is first decomposed into an approximation and an accompanying detail. The decomposition process is then iterated, with successive approximations being decomposed in turn so that the original signal is broken down into many lower-resolution components.

This analysis is carried out by means of the MATLAB Wavelet Toolbox which is a collection of wavelet analysis functions built on the MATLAB® Technical Computing Environment.

2.5.3 Application to the Malta data set

2.5.3.1 Results of the continuous wavelet transform analysis

Fig. 2.22b displays the results of the continuous wavelet transform analysis on hourly values of residual elevation obtained by using 148 integer scales and utilising a symlet wavelet of order 8 as a basis. The figure shows only the analysis covering the period 18/11/95 - 28/5/96. It is a time-scale plot of the signal in Fig. 2.22a where the x-axis represents position along the signal (time), the y-axis represents scale and the colour at each x-y point represents the magnitude of the wavelet coefficient at that point. A deep blue colour is assigned to the lowest negative magnitudes while a deep red colour is assigned to the highest positive magnitude. Zero magnitude corresponds to the shade of colour indicated by the arrow on the colourbar. The view of the signal by such a time-scale plot is different from the time-frequency Fourier view, but it is not unrelated.

Scales do not carry an exact engineering definition, like frequency. Although increasing scales can be taken to represent proportionately decreasing frequencies, a level of scale cannot be related to a single frequency and there is no strict relationship that binds the two quantities. Wavelet decomposition into scale coefficients thus constitutes a distinct method of viewing the components of a signal, and provides an alternative to signal decomposition by means of a time-frequency expression. Wavelet analysis gives instead a time-scale view of a signal and thus provides a method of expressing natural phenomena by utilising their very rudimentary multi-fractal basis.

Undoubtedly the greatest advantage of continuous wavelet transform analysis is its high resolution in time. It is however also able to resolve detail at scales where conventional methods would equivalently require a much longer data set. In the case of the sea level data analysis above, the synoptic frequency range is very well resolved by a wide range of scales covering the values from 40 and all the way up to 148. In comparison, an alternative Fourier frequency-time analysis with a running window of size N records and 50% overlap, would cover the same range of frequencies in just a few frequency segments each of width $1/(N\Delta T)$ cpd, and the frequency representation would only be calculated in time steps of $N\Delta T/2$ each. The continuous wavelet transform analysis is thus a very powerful tool compared to the classical power spectral techniques and is able to

give a high resolution in both signal detail composition and time with great efficiency on even a short time series of data.

A close view of Fig. 2.22 reveals how the analysis is able to follow in detail the synoptic time-scale structure contained in the original residual sea level signal. At each scale, a scan along the x-axis gives the undulating time series of wavelet coefficients and resembles very closely a modulated sinusoid with a central frequency representative of that scale. These undulations are exhibited by changes in colouration above and below the mean colour. In its totality of representation, the plot results in successive streaks of changing shades in colouration that vividly portray an animation of the time evolution at all scales. The successive appearance, lengthening and eventual shrinking and disappearance of the interleaved tongues follows the detailed temporal development of intensified events and eventual weakening at all scales of the residual sea level and thus provides an accurate study of the changing composition of the signal. The analysis reveals several interesting results. There are occasions where the intensified variation penetrates down to the lower scales such as in the case of the vigorous and very abrupt changes in residual sea level during the first quarter of February (X_1) and the beginning of March (X_2). Intensification is restrained to the higher scale components during summer. On other occasions, such as at Y_1 - Y_6, the variability concerns only a restricted number of scales. The selective reinforcement of scales is however different from one event to another and is by no means confined to any fixed or regular set of scales. It is also interesting to note the 'ripple' nature of the time-scale plot at the lower scales centred around the value of 20. This scale represents the diurnal oscillation. Analysis of the full data series from mid-1993 to 1996 shows that diurnal scales become invariably the predominant high frequency detail especially in the period mid-May to mid-November. During the rest of the months the diurnal signal is weaker and masked by other equally or more important signals from both lower and higher adjacent scales. This difference is clearly depicted in the comparison time-scale plots in Fig. 2.23a, b.

2.5.3.2 Dependence of synoptic variability on atmospheric pressure variations

The synoptic variability in the residual sea level is closely related to the corresponding atmospheric pressure fluctuations. A comparison between the coefficients derived from a separate continuous wavelet transform analysis on residual sea level and inverted atmospheric pressure fluctuations can provide qualitative and quantitative information on the relationship and its variation in time between the two quantities. The comparison is made by means of a correlation analysis on 9216 hourly averaged values of sea level and inverted pressure

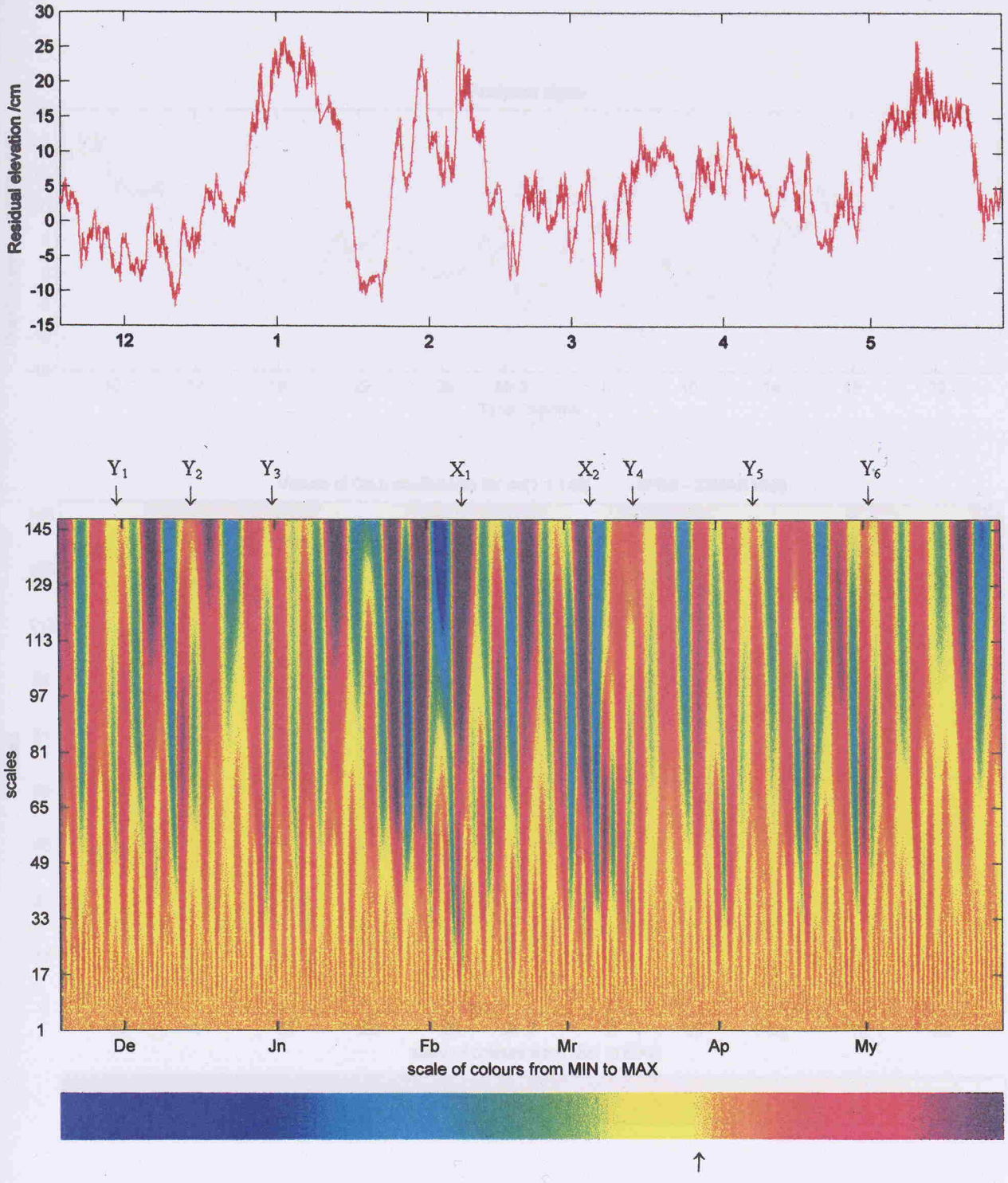

Fig.2.22 Analysis of synoptic scale variability by the continuous wavelet transform. The analysed signal in (a) is that of residual elevation. The wavelet coefficients are calculated at scales in the range [1:1:148] and their magnitude is displayed as a time-scale plot in (b). Magnitudes are plotted according to the horizontal colourbar which assigns a deep blue colour to the lowest negative magnitudes and a deep red colour to the highest positive magnitude. Zero magnitude corresponds to the shade of colour indicated by the arrow on the colourbar.

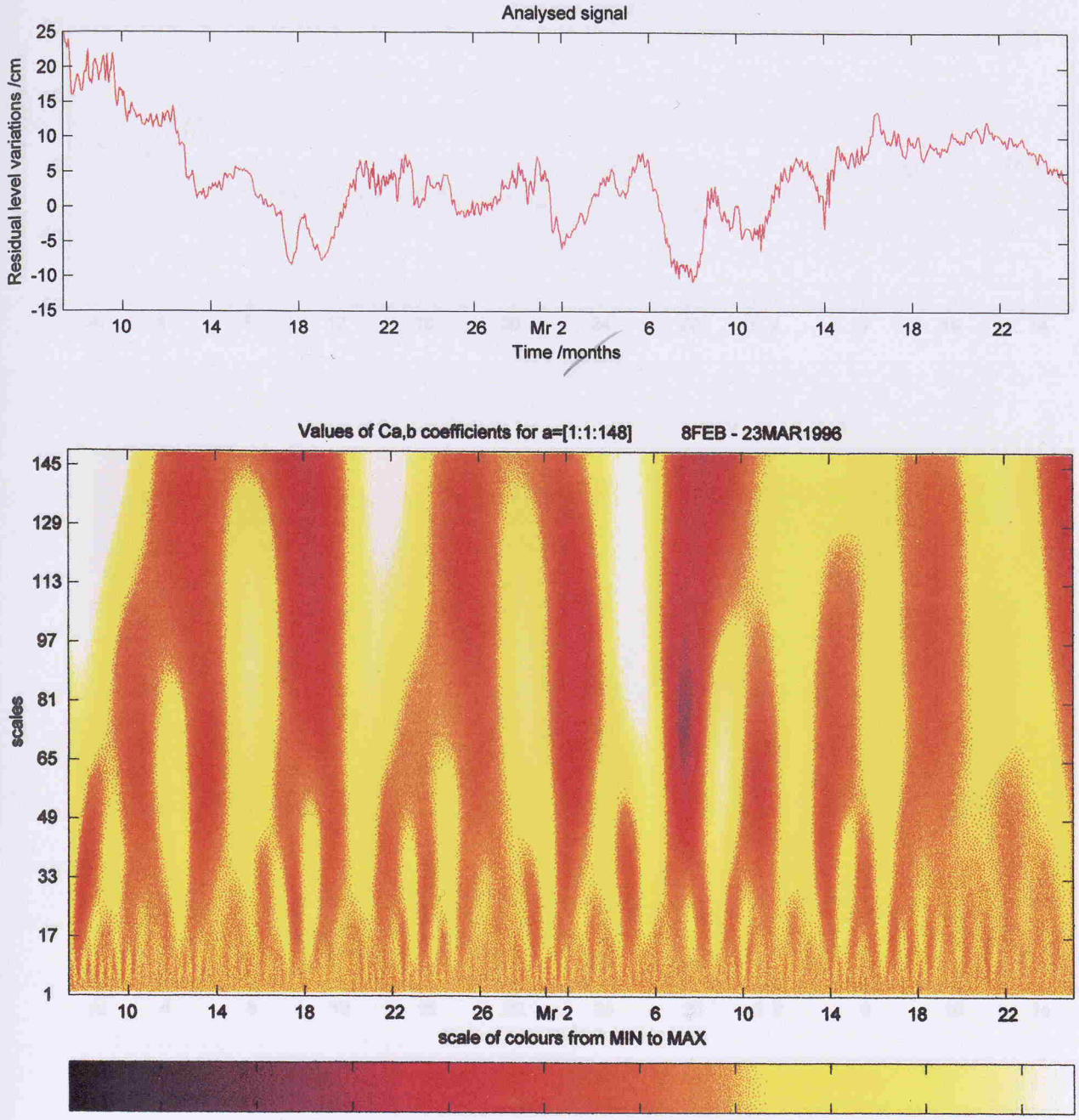

Fig.2.23 (a) Sample time series of residual sea level variations and the corresponding time-scale plots of the continuous wavelet transform coefficients for winter (8th February - 23rd March 1996).

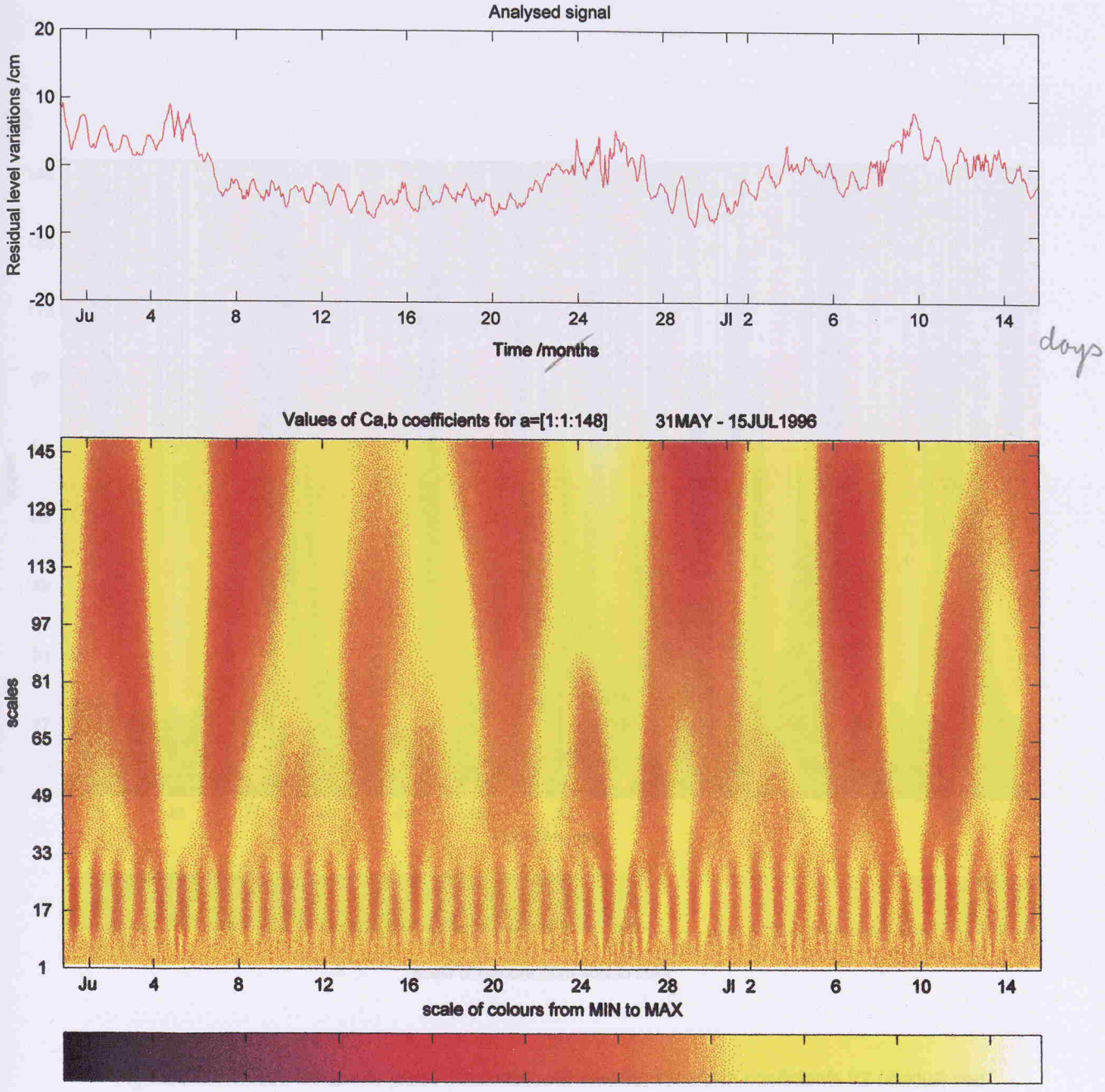

Fig. 2.23 (b) Sample time series of residual sea level variations and the corresponding time-scale plots of the continuous wavelet transform coefficients for summer (31st May - 15th July 1996).

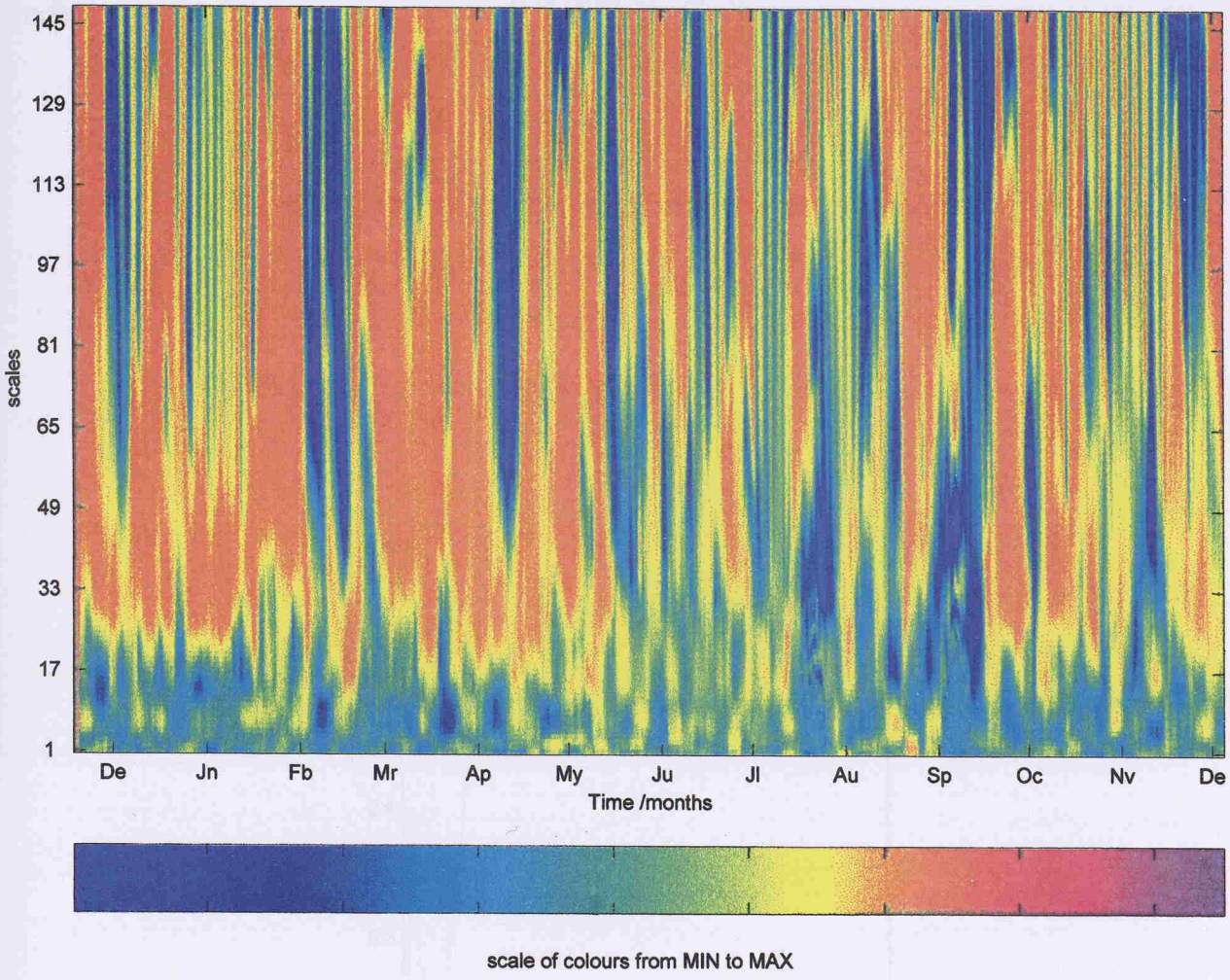

Fig. 2.24 Correlation factor r between the continuous wavelet transform coefficients for residual sea level and inverted atmospheric pressure fluctuations. Deep blue is equivalent to r = -1. Dark red is equivalent to r = +1. The continuous wavelet transform coefficients are calculated using 9216 hourly averaged values covering the period (0h) 18/11/95 to (0h) 5/12/96.

wavelet coefficients covering the period (0h) 18/11/95 to (0h) 5/12/96. At each scale, the pair of wavelet coefficient series are compared by calculating a running correlation coefficient using a window of size 100, which is displaced by one value at each step until the whole series of coefficients are covered. This is repeated at all the other scales so that a correlation time-scale map is obtained (Fig. 2.24). The colour scheme uses dark red for maximum positive correlation (r = +1) when the sea level and the inverted barometric pressure vary in perfect

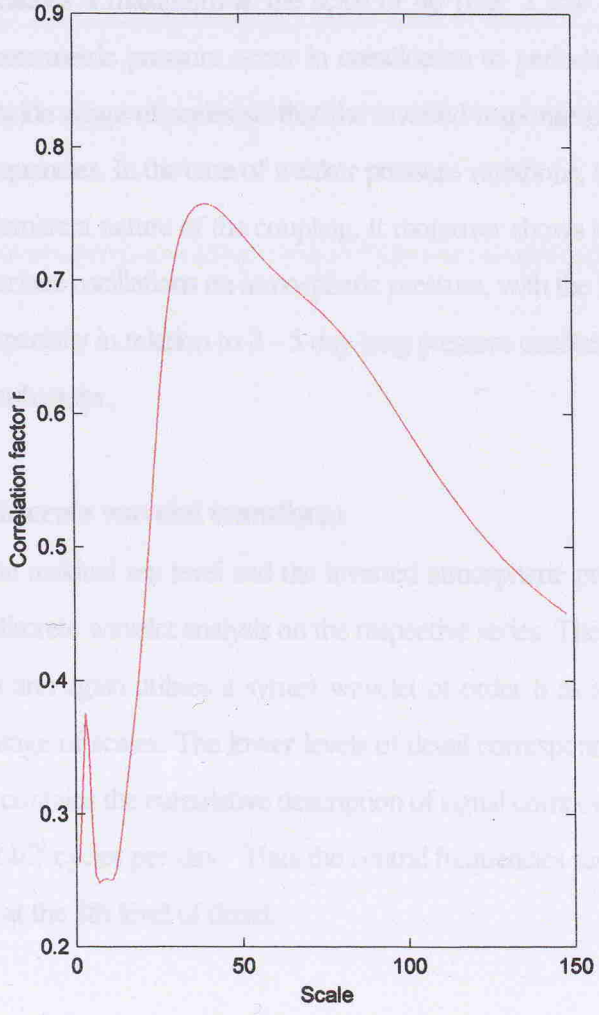

Fig. 2.25 Average correlation coefficient between residual sea level and inverted atmospheric pressure variations in the period (0h) 18/11/95 to (0h) 5/12/96.

phase; it is deep blue for maximum negative correlation (r = -1) when changes in sea level and inverted barometric pressure are in antiphase. Zero correlation (r = 0) implies a phase relationship that changes too rapidly to be significant.

The map in Fig. 2.24 clearly indicates that the response of the sea level to the barometric forcing is characterised by frequent and very dynamic interactions. The correlation is insignificant at the lower scales, but it can reach values close to r = +1 for scales higher than about 30. The average correlation worked out over the full period for each scale reaches a maximum at the scale of 40 (Fig. 2.25). Events of enhanced coupling between the sea level and barometric pressure occur in coincidence to periods of stronger fluctuations in the pressure field and covers a wide range of scales so that the inverted response of the sea level practically scans the full range of synoptic frequencies. In the case of weaker pressure variations, the correlation is negligible. The analysis thus reveals the intermittent nature of the coupling. It moreover shows the marked seasonal variation in the dependence of the sea surface oscillations on atmospheric pressure, with the interaction being more effective during the winter months especially in relation to 2 - 5 day long pressure oscillation trains that often accompany the passage of cyclonic perturbations.

2.5.3.3 Analysis by the discrete wavelet transform

The relationship between the residual sea level and the inverted atmospheric pressure variations can be further investigated by means of a discrete wavelet analysis on the respective series. The analysis is carried out up to the 8th level of detail (d1 - d8) and again utilises a symlet wavelet of order 8 as a basis. In terms of scales, each detail effectively covers a range of scales. The lower levels of detail correspond to the finer scales. In terms of frequency, a detail at level j contains the cumulative description of signal components with a central frequency at (sampling frequency)/2^j = 24/2^j cycles per day. Thus the central frequencies range from 12cpd at the first level of detail down to 0.094cpd at the 8th level of detail.

At each level, the time series of discrete wavelet transform coefficients is representative of the evolution in time of the signals in the range around the central frequency. The time series of these coefficients for the respective levels of detail in the period 18th November 1995 to 15th July 1996 are plotted in Fig. 2.26a, b for residual sea level variations and inverted atmospheric pressure fluctuations respectively.

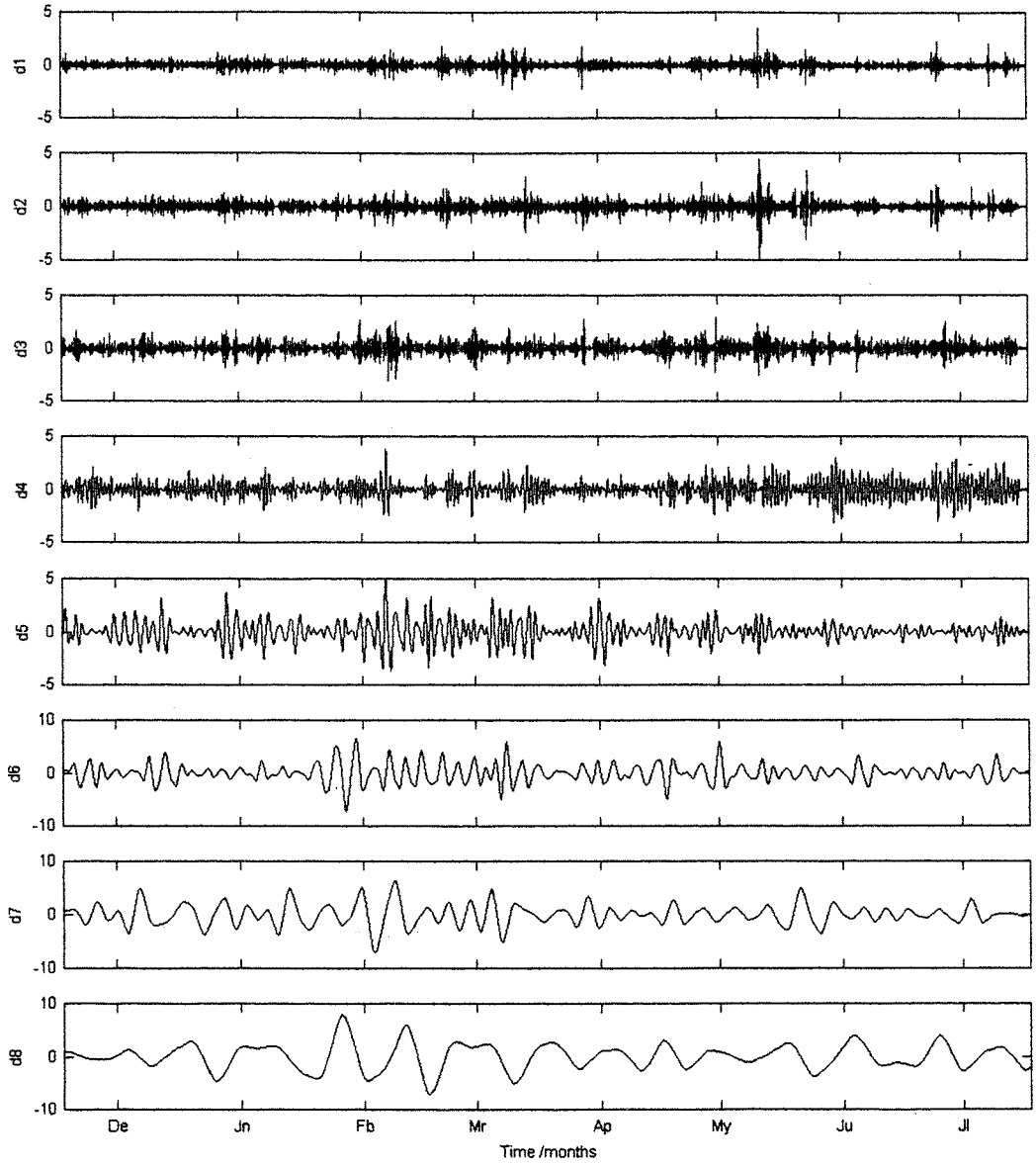

Fig.2.26 (a) Time series plot of the discrete wavelet transform detail coefficients for levels 1 to 8 in the period 18/11/95 to 15/7/96 for residual water level fluctuations.

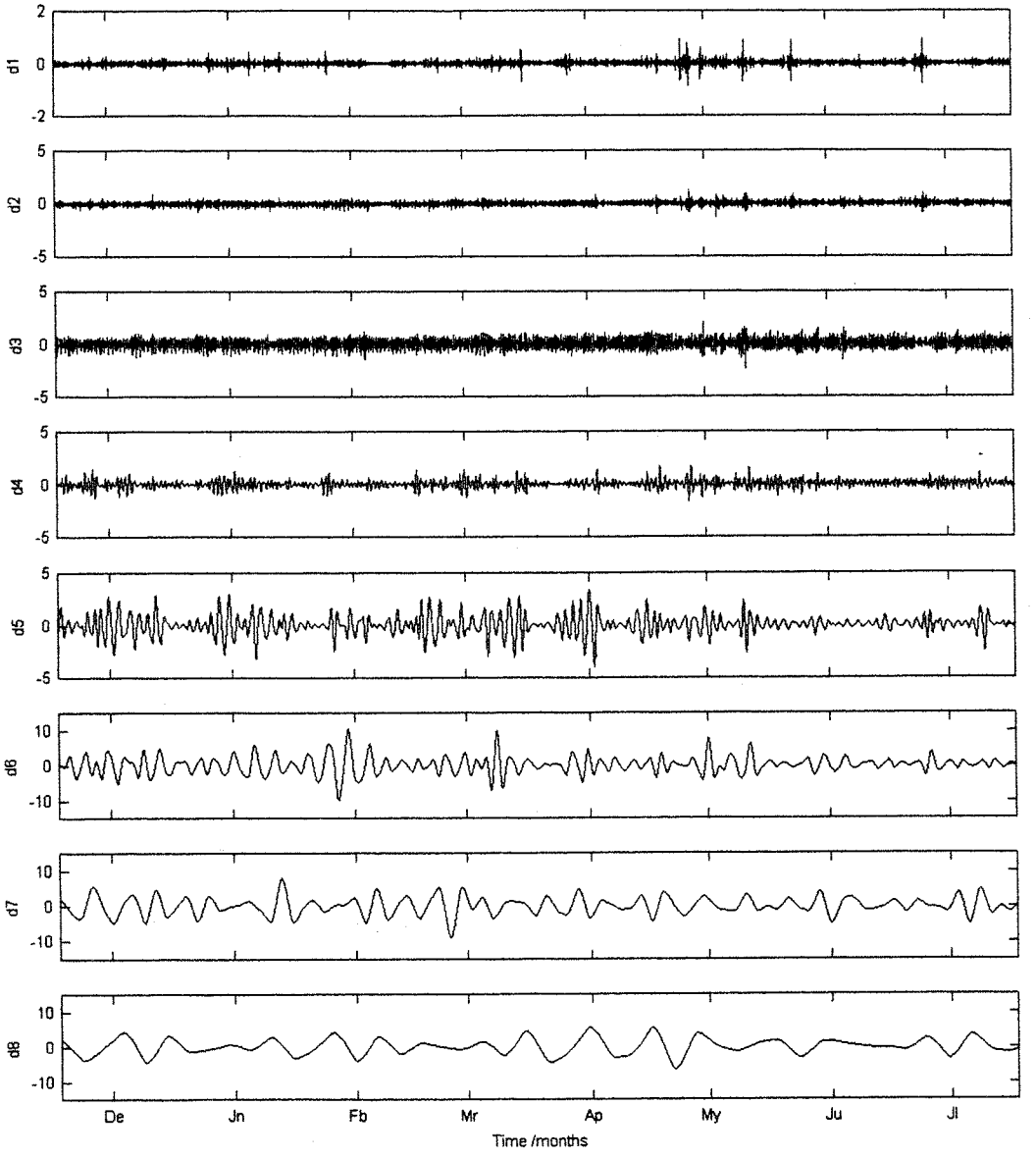

Fig.2.26 (b) Time series plot of the discrete wavelet transform detail coefficients for levels 1 to 8 in the period 18/11/95 to 15/7/96 for inverted atmospheric pressure fluctuations.

The main feature observed in the residual sea level details is that of the rapid variations in the amplitude of the coefficients. These variations are discontinuous in time. They are observed at all levels of detail, but do not generally occur at the same time although the correspondence between adjacent levels of detail is at times appreciable. The reinforcement of a detail is thus generally independent of the magnitude of the variations in the other levels of detail. This selective enhancement implies that the factors influencing the sea level signal at the different details may not necessarily be identical. The difference is particularly evident between the set d1 - d4 levels of detail and the remaining four higher levels d5 - d8. The amplitudes of the finer details are generally smaller except in the case of d4 which attains a very steady amplitude from May onwards. The variance of the finer details does not change with the seasons. On the other hand the upper levels of detail have higher amplitudes and are especially stronger during the winter months. The variability of the residual sea level is thus mainly explained by the higher levels of detail. This corroborates with the predominance of the sea level signals in the synoptic frequency range as discussed in the previous sections.

The difference between the two sets of details is even more evident in the atmospheric pressure field. The activity of the atmospheric pressure details at levels 1 and 2 is very low, whereas at level 3 it is pretty constant at an rms value below 0.5mb. The variability is principally explained by details d5 and d6, and to a lesser extent by d7 and d8. The reduced activity in barometric pressure fluctuations during summer is particularly evident in d5 and d6.

2.5.3.4 Inverted barometric effect by wavelet analysis

The correspondence between identical levels of detail for residual sea surface fluctuations and inverted atmospheric pressure can be used to study the validity of the IB condition and its dependence on the time and space scales. A perfect isostatic adjustment would signify a 1:1 relationship between the details. This correspondence is quantified both by cross-correlation analysis as well as by scatter plots and superimposed time series plots of the two sets of reconstructed detail coefficients. The scatter plot analysis in Fig. 2.27 shows that the correspondence is only significant at levels of detail 5 and 6 for which the correlation factor is 0.73 and 0.72 respectively. This linear dependence is much less evident for both higher and lower levels of detail (Table 2.5). The temporal development of this correspondence is investigated by the superposition of time series plots (Fig. 2.28) where it is noted that the atmospheric pressure anomaly and the sea level fluctuations at both details 5 and 6 can practically remain in phase for long periods (such as during the whole two months of April and May).

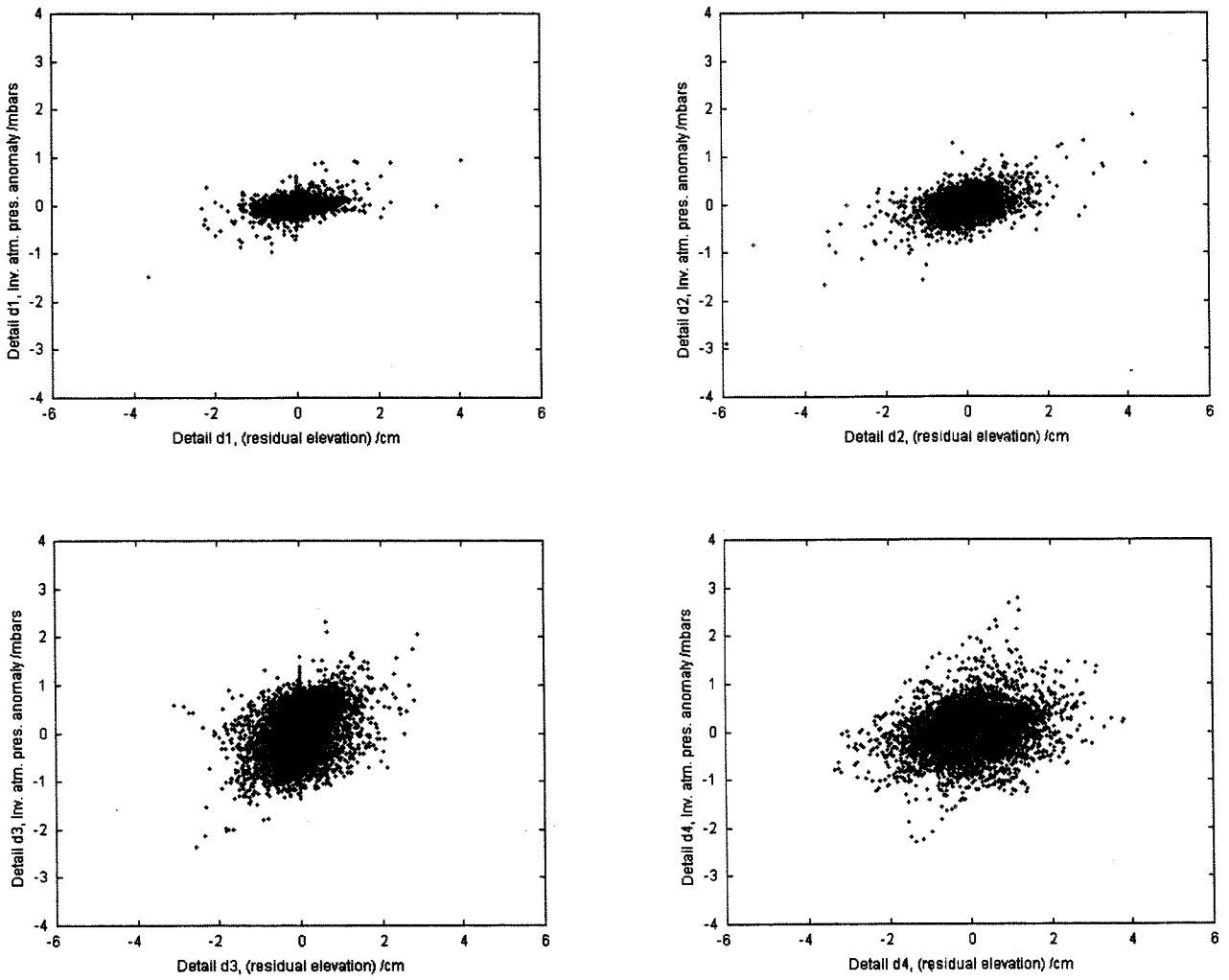

Fig.2.27 Scatter plots between the reconstructed details d1 - d4 for residual sea elevation and the inverted atmospheric pressure anomaly for the period 18th November 1995 - 5th December 1996.

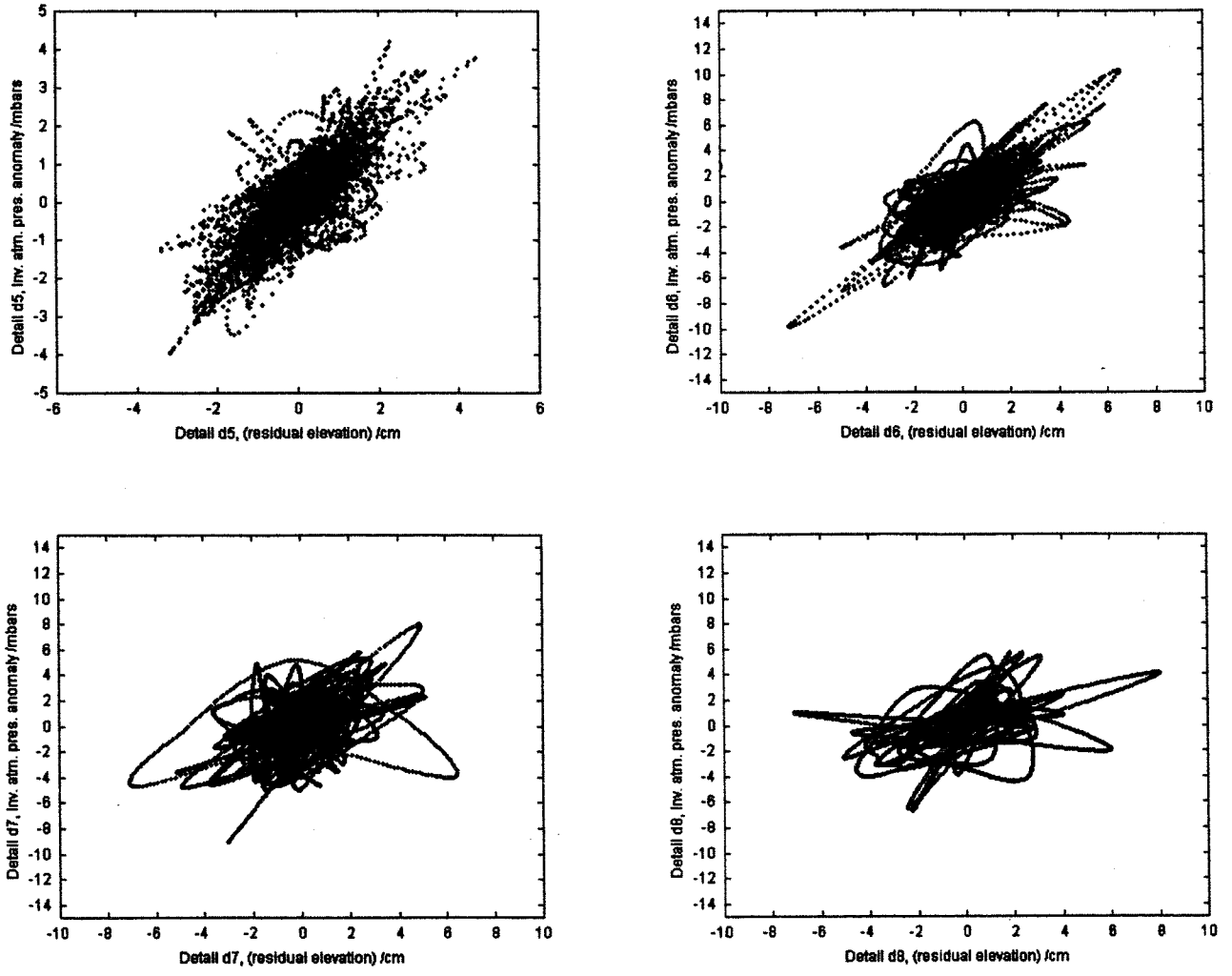

Fig.2.27 Scatter plots between the reconstructed details d5 - d8 for residual sea elevation and the inverted atmospheric pressure anomaly for the period 18th November 1995 - 5th December 1996.

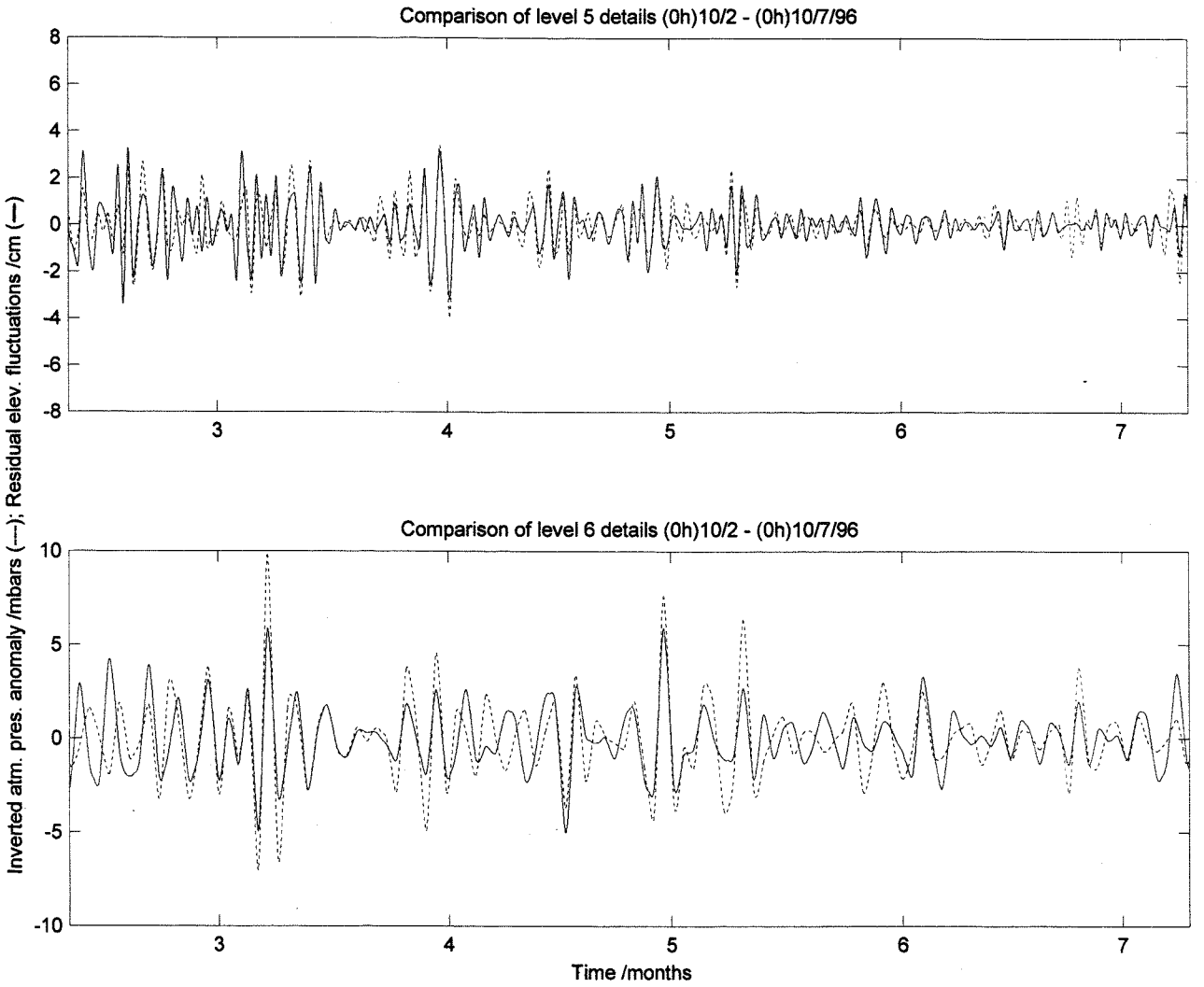

Fig. 2.28 Comparison time series plots for the reconstructed details (d5 and d6) of residual sea elevation (full line) and inverted atmospheric pressure anomaly (dotted line).

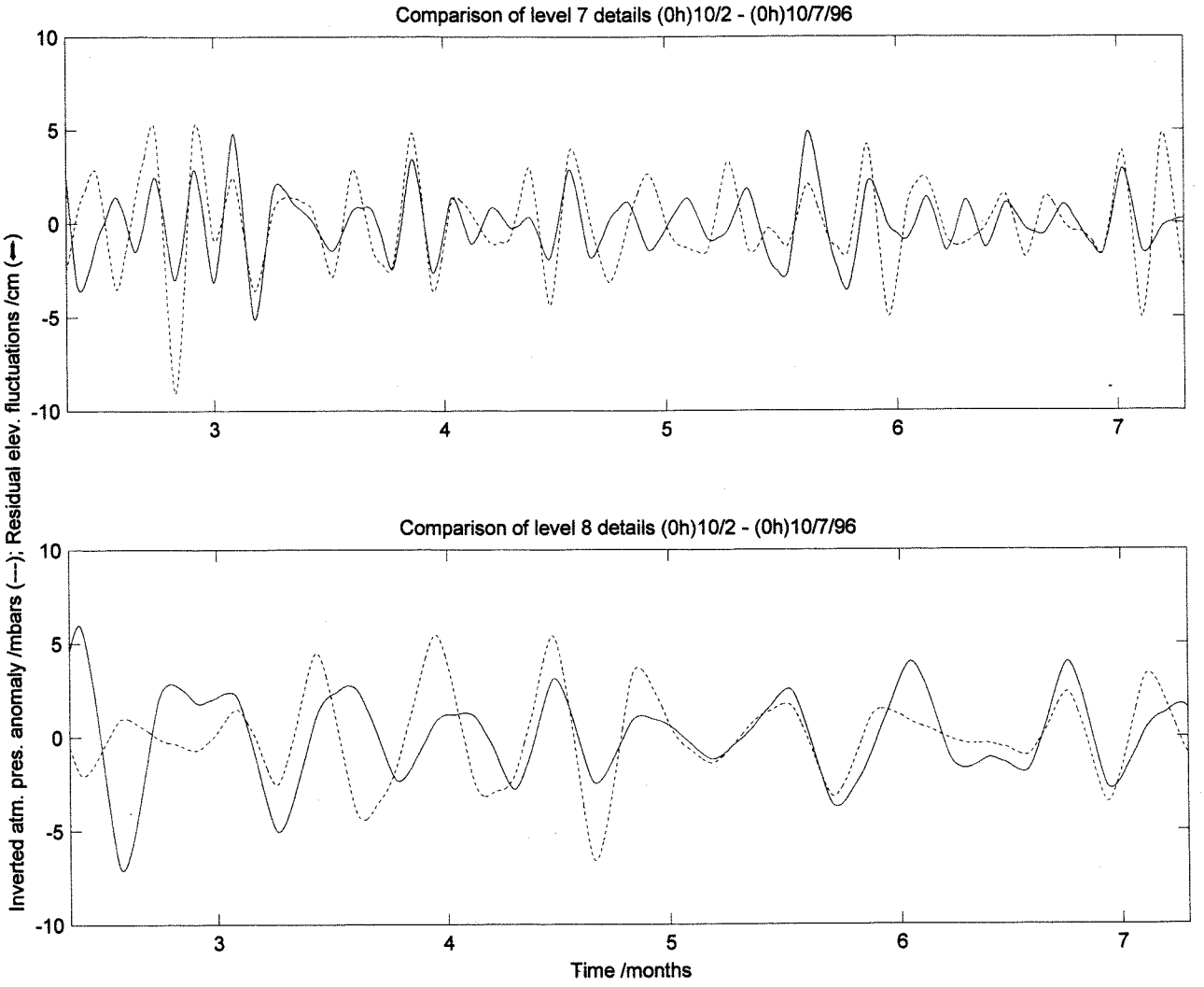

Fig.2.28 Comparison time series plots for the reconstructed details (d7 and d8) of residual sea elevation (full line) and inverted atmospheric pressure anomaly (dotted line).

At the 5th level of detail a close to isostatic response is particularly evident during the periods of stronger atmospheric pressure variations which regularly trigger the corresponding fluctuations in the residual sea level details. At the 6th level of detail the response is in general under-isostatic although there are periods, such as towards the end of

Table 2.5
Correlation between detail coefficients of residual sea level and inverted atmospheric pressure

Detail level	d1	d2	d3	d4	d5	d6	d7	d8
Correlation factor	0.300	0.359	0.356	0.215	0.726	0.718	0.400	0.471

February and in the first days of July, when the sea responds more vigorously than would be expected from a simple adjustment to atmospheric pressure anomalies. The results are a clear example of the very effective use of the wavelet transform in obtaining a detailed temporal analysis of one or more signals. The consistency of the correspondence is much less evident for the 7th and 8th levels of detail. At these levels other effects besides that of barometric pressure become important factors in affecting the variation in the sea surface displacement. In their varying development in time, the contribution of these effects can become predominant for certain periods. An investigation of these contributing factors on the sea level variability with respect to that of barometric pressure as their relative effect changes with time can be made by means of a comparison between wavelet transform approximations. The level 6 wavelet transform approximations $A(\Delta\eta_{res})$ of residual sea level and $A(-\Delta p)$ of inverted atmospheric pressure (Fig. 2.29) contain the cumulative contribution from details with levels higher than 6 and thus represent the low frequency signals of the two parameters. The comparison between these two approximations is made by means of the diagnostic $\chi = dA(\Delta\eta_{res})/dt - dA(-\Delta p)/dt$ which relates their respective variation in time. In the case of a perfect IB response, $\chi = 0$. In the case of a rise in sea level that is more rapid (or a fall that is slower) than expected from a simple response to a lowering (or increase) of atmospheric pressure, then $\chi > 0$. When the rise in level is slower (or the fall is more rapid) as compared to the IB response to an increase (or decrease) in atmospheric pressure, then $\chi < 0$. The diagnostic thus provides a quantitative measure of the relative importance of non-barometric effects.

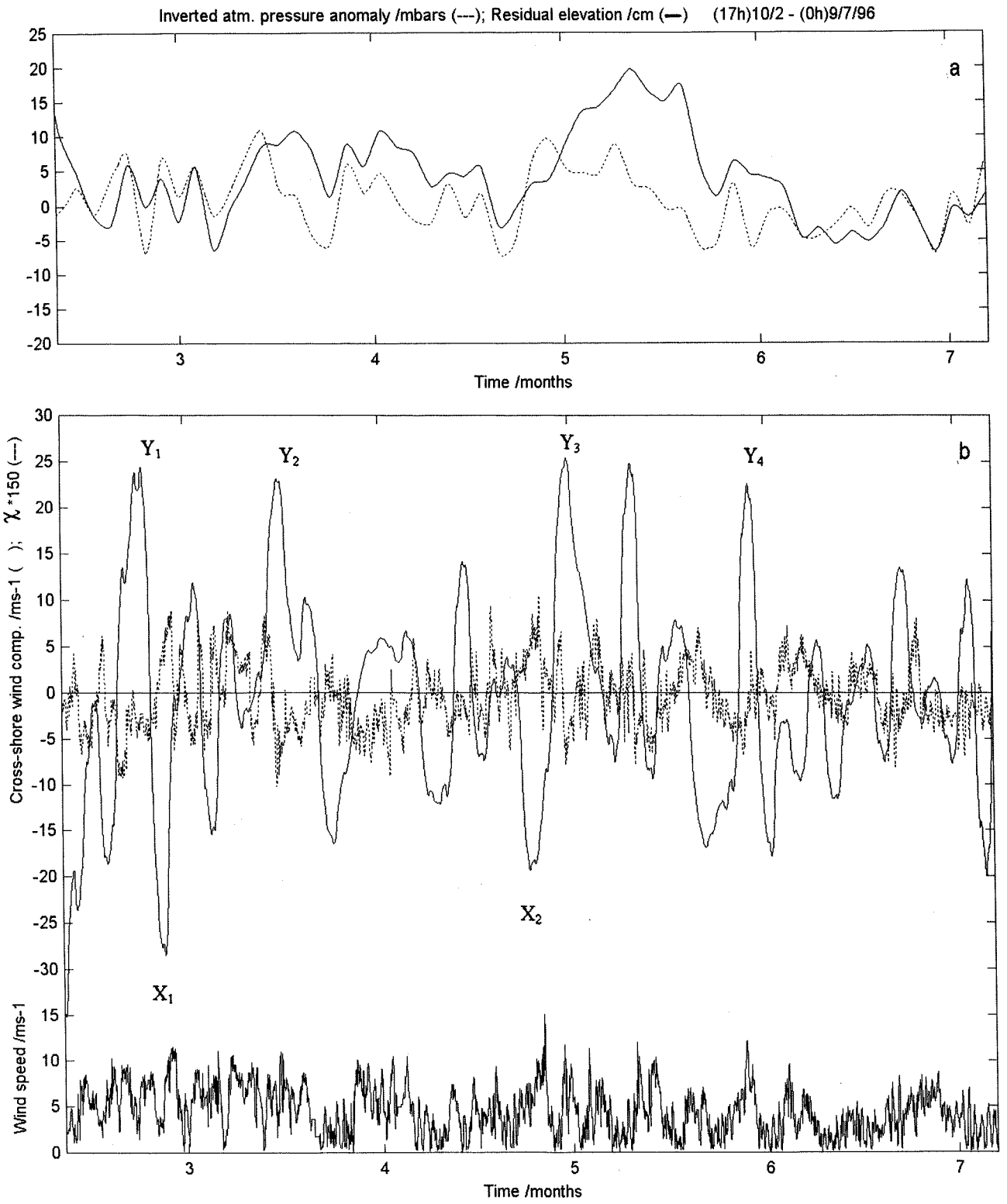

Fig. 2.29 (a) Time series of approximations at level 6 calculated for inverted atmospheric pressure (dotted line) and residual sea elevation (full line); (b) Comparison plot of $\chi = d[A(Dh_{res}) - A(Dp)]/dt$ and cross-shore wind component, (for χ: $\chi>0$ implies an accelerated rise/decelerated fall in sea, $\chi<0$ implies an accelerated fall/decelerated rise in sea level with respect to the inverted barometric effect; for wind : +ve component = onshore; -ve component = offshore); (c) Time series plot of wind speed. All plots cover the period 10th February to 8th July 1996.
Values of χ are multiplied by a factor of 150.

Fig. 2.29b is a time series plot of χ for the period 10th February to 8th July 1996. The values of χ are multiplied by a factor of 150 for better visualisation against the superimposed plot of cross-shore wind components. Positive peaks in χ refer to episodes of an accelerated rise (over-isostatic response) or a decelerated fall (under-isostatic response) in water level. Similarly the negative peaks refer to episodes of an accelerated fall (over-isostatic response) or decelerated rise (under-isostatic response) in water level. The variation of χ thus indicates the instantaneous disposition of the sea surface displacement above or below the level dictated by an IB response. In some cases these non-isostatic sea level effects can generally be related to the cross-shore wind. In particular the decelerated rise in sea level at X_1 (towards end of February) and X_2 (in the last week of April) are both related to an intensified onshore wind which does not allow the sea level to follow the simultaneous fall in atmospheric pressure. At Y_1, Y_2, Y_3 and Y_4 the peaking of an offshore wind does not allow the sea level to fall in adjustment to a rise in atmospheric pressure. These observations indicate a general tendency for the residual sea elevation to become lower on the occasion of onshore winds and higher when wind is offshore. This corroborates the results obtained in section 2.4.2.6. It is nevertheless noted that some fluctuations in χ occur on occasions when the wind is slack, and other effects besides those of wind and barometric pressure are thus involved in establishing the complex development of the sea level displacements in time.

2.5.4 Wavelet analysis - the way ahead

The analysis above is a clear demonstration of the very effective use of the wavelet transform in studying the composition of a signal. Wavelet analysis can lend itself as a valuable tool to identify the nature of variability carried by the signal and the dependence of the variability on one or more correlated parameters. In the application to sea elevation, the method allows a detailed study of the dependence of the sea level response on the weather variables as parameters change in time. The temporal development of the sea elevation can be modelled as a superposition of wavelet decompositions of the respective dependent parameters. This opens the way to alternative methods of forecasting and hindcasting sea elevations from a knowledge of the wavelet decompositions of the dependent parameters.

2.6 The seasonal variability

2.6.1 Seasonal changes in mean sea level

The seasonal variation in the mean sea level in Mellieha Bay is studied by 43 monthly averages of sea level data covering the period June 1993 to December 1996. The seasonal signal in the sea level is seen to be quite strong (Fig. 2.30) and is actually larger than the daily variation. Such seasonality is typical of the whole Mediterranean Sea. Emery et al. (1988) show that there are large variations in sea level changes in any given year across the Mediterranean. The magnitude of these sea level seasonal changes is in the order of tens of centimetres and

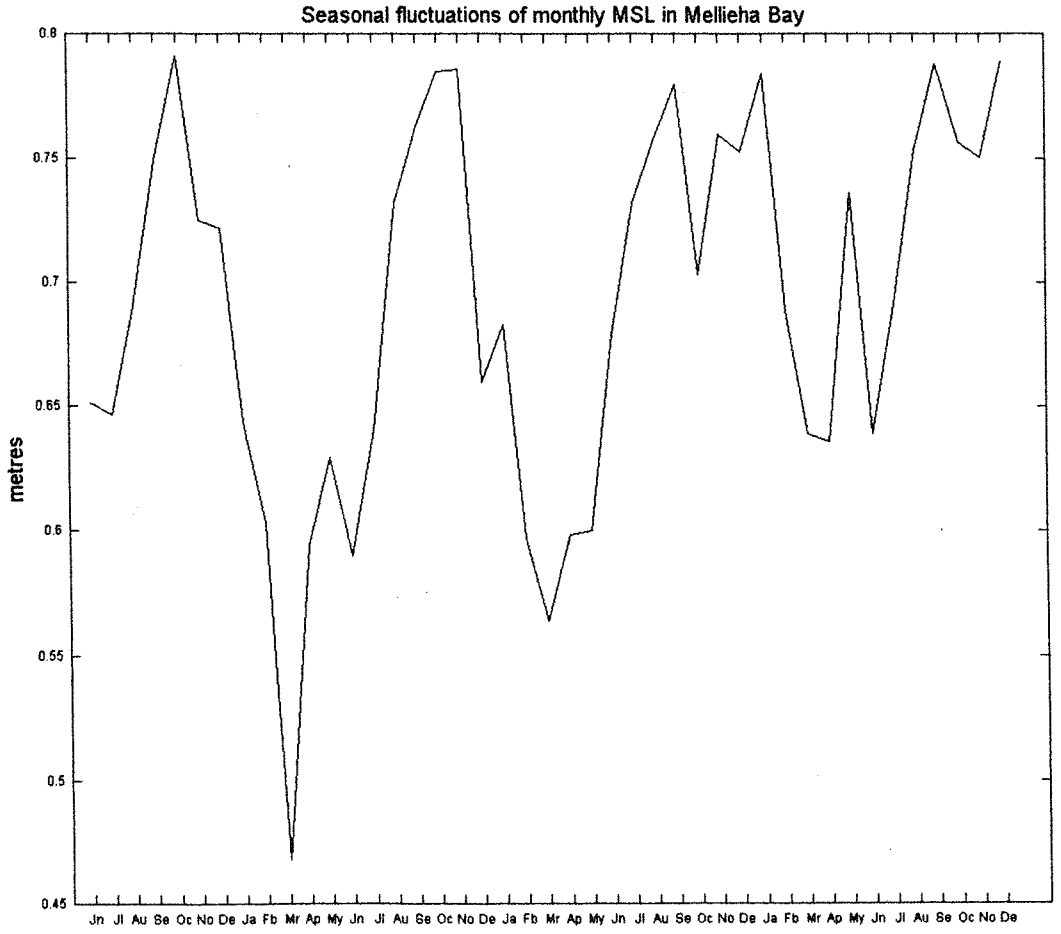

Fig.2.30 Monthly mean sea level in Mellieha Bay as a function of time (June 1993 - December 1996)

therefore greatly exceeds in size other effects on the sea level such as climate change (estimated to be in the order of a mm/year). Indeed this renders eustatic sea level determinations more difficult to detect. The range, pattern and regularity of the seasonal signal however varies widely for different locations in the Mediterranean and is often influenced by local effects such as temperature and periods of strong winds whose incidence can vary from year to year (Goldsmith, 1990). Mean sea level seasonality appears however to have a regional character. Similar seasonal patterns are exhibited by sea level measurements from stations in the same region. In general, seasonality in the West is less regular, but is not as sharp as in the southeastern Mediterranean. Analysis of sea levels derived from TOPEX/POSEIDON satellite altimetry data during 1993-94 show that the mean level variations in the western and eastern Mediterranean basins are about the same in magnitude, but have a phase lag which varies with time (Larnicol et al., 1995).

In the case of Mellieha Bay the records (Fig. 2.30, 2.31a) show that a sea level maximum generally occurs in October while a minimum occurs in March. The sharp lowering in the mean sea level after October is interrupted by a second maximum in December/January while the increase after March is temporarily halted by a secondary minimum in late Spring. The maximum range between the extreme levels is in the order of tens of centimetres. The three years are however not fully alike. Both the size and phase of the fluctuations as well as the occurrence of fast variations (such as the sharp rise in sea level in May 1996) are indicative of considerable interannual variability. A comparison with 13 months of sea level data covering the period May 1990 to May 1991 and obtained at a sea level station in the Grand Harbour (only within a few kilometres of distance from Mellieha Bay) further confirms that the seasonality is not very regular (Fig. 2.32a). During 1990/91 the rise to maximum sea level in October is more gradual, while the minimum in 1991 occurs in January rather than March. There seems thus to be a sensible phase shift in the seasonal signal with respect to the period 1995/96. This implies that in the case of local sea level variations with the longer time scales and with cycles in the order of tens of years, studies need to be based on longer time series of data so as to enable inferences on statistical averages that are better representative of the predominant seasonal signals.

2.6.2 Factors influencing the seasonal variability

The seasonal signal is also present, though less energetic, in the atmospheric pressure (Fig. 2.31b and 2.33b). After applying the IB correction the mean sea level still retains a large part of its variability and hence other

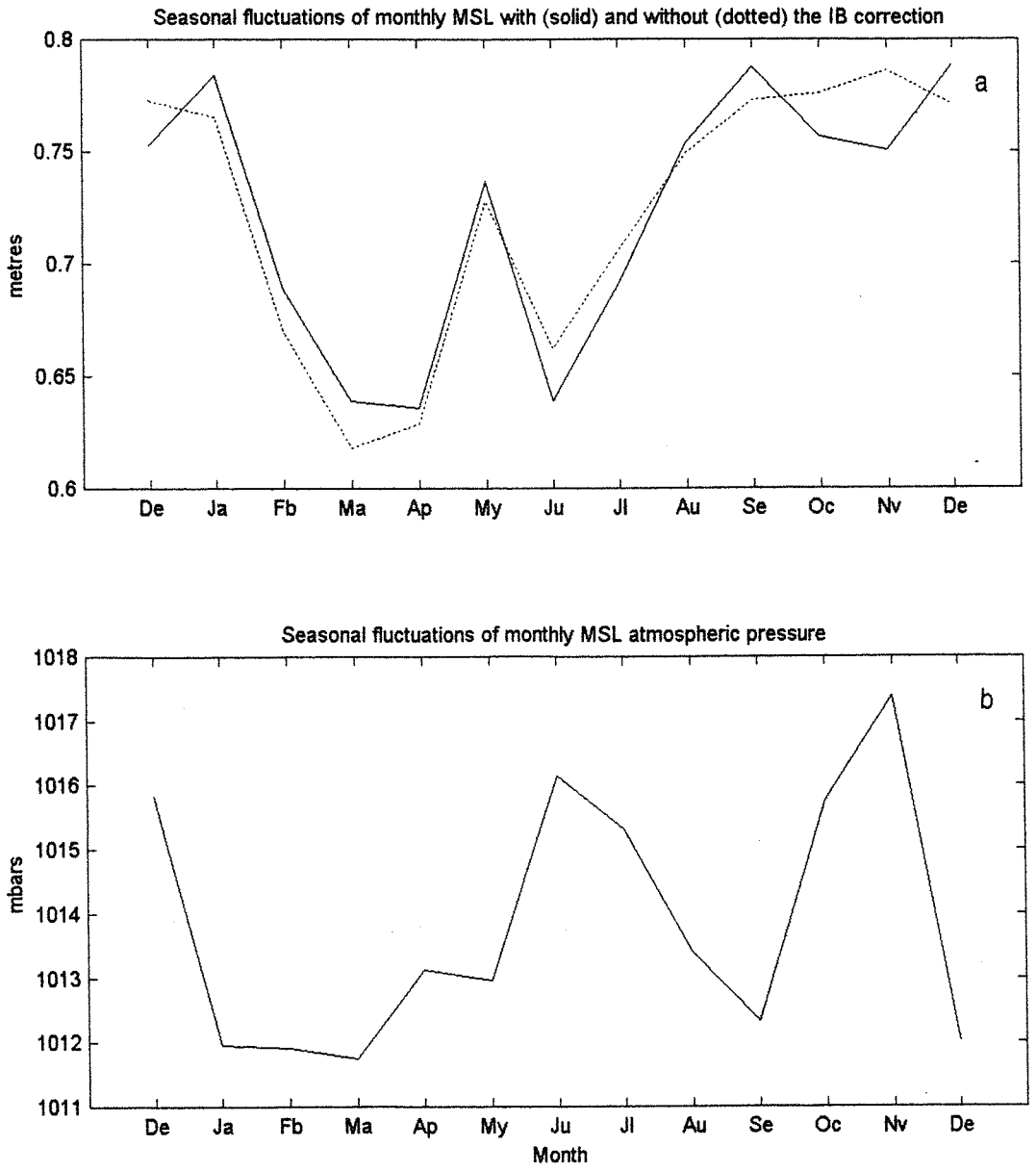

Fig. 2.31 (a) Monthly mean sea level in Mellieha Bay as a function of time with (dotted) and without (solid) the inverse barometer correction; (b) Monthly MSL atmospheric pressure at Ramla Station. (Period covered is December 1995 - December 1996)

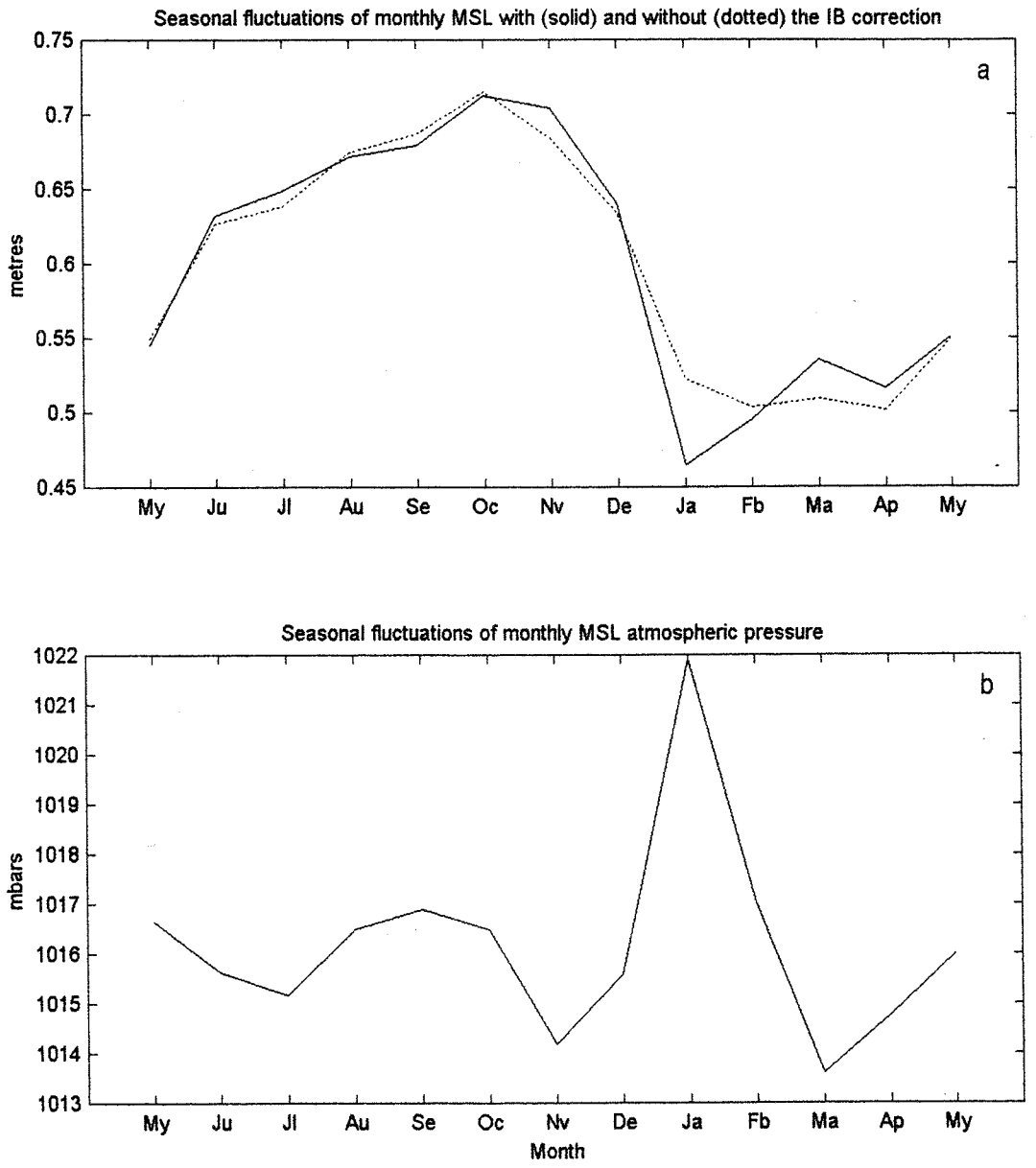

Fig. 2.32 (a) Monthly mean sea level in the Grand Harbour as a function of time with (dotted) and without (solid) the inverse barometer correction; (b) Monthly MSL atmospheric pressure at Luqa. (Period covered is May 1990 - May 1991)

factors besides the barotropic effect of barometric pressure are responsible for the sea level variations at this scale. As already mentioned, seasonal winds and the piling of water onshore as a result of storm surges can greatly contribute to the seasonal sea level Variations (Goldsmith & Gilboa, 1987). Other processes influencing sea levels include currents (Pirazzoli, 1987; Thompson & Pugh, 1986) and shelf waves (Hutchnance, 1987). Palumbo & Mazzarella (1982) have determined on various time scales the meteorological as well as the hydrographic and oceanic factors that can explain the seasonal cycle in the mean sea level. Sea water temperature and baroclinic phenomena such as steric effects which are related to the volume dilation and contraction of the sea surface layer in response to changes in heat fluxes are also important factors contributing to the seasonal oscillation. Following Gill & Niiler (1973), this effect can be quantified by:

$$d\eta/dt = (\alpha/\rho C_p)Q$$

where η is the sea level, α is the coefficient of thermal expansion, C_p is the specific heat capacity at constant pressure, and Q is the net heat flux. Using an ECMWF climatology of net surface heat fluxes for the Mediterranean, it is found that steric effects produce changes in the mean sea level that have the right phase compared to observations, but which are only about half in size to the actual variations (Larnicol et al., 1995). On the seasonal timescale, the Mediterranean is thus probably not in mass balance. In order to account for this discrepancy it seems necessary to hypothesize variations in the inflow and outflow at the Strait of Gibraltar. Ovchinnikov (1974) suggests that seasonal fluctuations in the inflow at the strait could well be in antiphase to the fluctuations in the outflow, thus resulting in a net barotropic flow and an associated expression in terms of mean sea level variations. On the basis of measurements made in the Bay of Naples, Palumbo & Mazzarella (1985) explain the seasonal cycle of mean sea level in terms of a mass balance that takes into account local evaporation and precipitation rates and Atlantic water inflow.

2.6.3 Relationship to basin water budgets and strait exchange

The response of the Mediterranean mean sea level to variations in the difference between evaporation and precipitation (E - P) in the basin is linked to the exchange at the seasonal scale at the straits. In the case of a barotropic adjustment to (E - P) variations, the basin has a very rapid response (gravity waves take less than a day to cross the whole Mediterranean) and the sea level is thus practically unaffected. On the other hand, when variations in (E - P) give rise to baroclinic processes, such as during the formation of deep waters and Levantine

Intermediate Water that are triggered by strong winter cooling and evaporation conditions, the associated vigorous vertical mixing processes are slower and an associated signature in the mean sea level is expected. These basin properties affect the nature of the exchange at the Strait of Gibraltar between the Mediterranean Sea and the Atlantic Ocean. On the basis of existing evidence, Garrett et al., (1990a) conclude that the hydraulically controlled flow in the Strait of Gibraltar is very close to the state of maximal exchange, but do not exclude a switching to a marginally sub-maximal state during the second half of the year. The main evidence supporting this seasonal pattern comes from the drop in the mean sea level along the strait from Cadiz to Malaga, which is found to change during the year becoming more enhanced during sub-maximal exchange conditions (Garrett et al., 1990b).

2.6.3.1 Sub-maximal vs maximal exchange

During sub-maximal exchange the density difference between the inflow and outflow is large; the budgets of the sea require only a slow exchange and the outflow is likely to be restricted to a thin layer above the bottom of the sill. If the sea becomes more mixed, the hydraulically controlled outflow becomes less dense; budgets will require greater flow rates and the outflow will occupy a thicker bottom layer in the strait; the exchange becomes maximal. The seasonal flips between the two states could thus be a consequence of wintertime replenishment of dense Mediterranean water followed by summertime draining of this water by the outflow. During sub-maximal exchange rapid adjustment through the strait to basin (E - P) variations is possible and no effect on the mean sea level is expected. On the other hand, the suppressed adjustment during maximal flow produces a direct response of the mean sea level to changes in (E - P).

Unfortunately knowledge on the seasonal variations in (E - P) in the Mediterranean is too scarce to confirm these suppositions. Whether the flow at Gibraltar is maximal or sub-maximal is still an open question. It is however certain that this simplified picture considering the Mediterranean as a single basin will have to be modified in order to include the more complex intra-basin interaction between the eastern and western Mediterranean through the Strait of Sicily. The mean sea level variations observed in Malta are found to be practically unrelated to the wind climate. The wind does not in fact have any significant seasonal character, being dominated by the westerly winds practically throughout the year. A great part of the seasonality is thus believed to be non-local in nature and to predominantly carry the signals deriving from differences of meteo-marine

parameters in the two basins. It is the intra-basin changes that in fact dictate the seasonality in the flow through the Strait of Sicily.

2.6.3.2 Intra-basin differences

Taking the example of the atmospheric pressure field, very different behaviours are observed between the two basins. From data reported by the Koninklijk Netherlands Meteorological Institute (1957) and by the Meteorological Office in London (1964), the western basin is characterised by a minimum in April. This is followed by a rise until July, with the pressure remaining practically constant until January when it starts to decline again until April. The range is on average 6mb. In the eastern basin a deeper minimum occurs at mid-July and is followed by a sharp rise until November. The range is about 10mb. The pressure remains approximately at the same levels during winter, with a maximum in January, after which it begins to fall until mid-July. With respect to these two characterisations, the observations in Malta (Fig. 2.31b and 2.32b) show that the atmospheric pressure field has a marked interannual variability and follows a mixed behaviour as the two pressure regimes are respectively pushed eastwards or westwards over the Central Mediterranean. This will have a local effect on the sea level, but most importantly the difference in pressure over the two basins will govern the flow through the Strait of Sicily and thus produce other indirect non-local effects on the sea level. These considerations render the measurements in Malta particularly important. Simultaneous observations at a number of locations in this part of the Mediterranean can certainly reveal key aspects on the exchange between the two basins.

A hydraulic control may also pertain to the flow in the Strait of Sicily. This can be dictated by discrepancies in the mass balance of the respective basins and may not necessarily have the same state of flow as that in the Strait of Gibraltar. It can be envisaged that the exchange condition through the two straits may in fact be different. Different factors that have a control on the strait exchange may moreover be expected to not simply play a disconnected role but to be indeed dynamically and mutually linked to one another. For example, the sea level drop across the straits may not simply be consequential of the state of flow, but may actually act as a forcing agent that dictates, possibly together with a number of other factors, the transition between marginally sub-maximal and maximal exchange strait flows.

2.7 Conclusions

The sea level data collected at the coastal station in Mellieha Bay on the northwestern coast of Malta gives a small tidal amplitude in the vicinity of the islands. The mean spring tidal range is only 20.6cm and is reduced to 4.6cm during neap tide. Water level variations are dominated by energy inputs from oscillations of non-tidal origin. These variations are mainly due to the prevailing meteorological and oceanographic conditions in the region. Although variations in atmospheric pressure associated with mesoscale meteorological phenomena produce a predominant effect on the sea level in the synoptic and sub-synoptic time scales, the response of the sea is non-isostatic and other factors contribute to its variability. It is not easy to identify the physical processes responsible for such a response. It would certainly be necessary to obtain simultaneous measurements at other sea level stations, particularly in the Central Mediterranean area, in order to assess the dependence of the response on the geographical position. Only then can one identify the extent to which deviations from the inverse barometer effect can be related to local effects as compared to the dependence on the larger scale dynamics of the Strait of Sicily acting as a connection between the two major basins of the Mediterranean Sea.

Analysis of the data by means of a multiple regression model and the wavelet transform provides a comprehensive study of the response of the sea level to atmospheric disturbances. The results of the multiple regression analysis confirm the predominant contribution of atmospheric pressure in determining the variability of the sea level for frequencies lower than 0.75cpd. The mid-synoptic frequency range is an exception where the unexplained variance rises to 30%. The pressure coefficient is exceptionally low at a frequency close to 0.12cpd at which the variability is mainly explained by the alongshore wind component. The direct wind effect is otherwise generally much smaller than that of barometric pressure. An inverse barometer response is followed most closely in the upper synoptic frequency range. For lower frequencies the residual sea level consistently lags the inverted atmospheric pressure by a few tens of degrees. In the planetary wave time scales effects from factors which are correlated to atmospheric pressure may erroneously be misinterpreted as an over-isostatic response of the sea level to barometric pressure.

The wavelet analysis allows a very effective study of the composition of a signal and the dependence of its variability in time on one or more correlated parameters. In the application to sea elevation, the analysis has described the intermittent nature of the sea level response to the weather variables. The position and extent of the frequency range at which the response approximates to the inverted barometer effect is found to depend on

the amplitude of the atmospheric pressure fluctuations. During the stronger pressure variations, the inverted response of the sea level occurs at practically the full range of synoptic frequencies and even lower. It is shown that the temporal development of the sea elevation can be modelled as a superposition of wavelet decompositions of the respective dependent parameters. This opens the way to alternative methods of forecasting and hindcasting sea elevations from a knowledge of the wavelet decompositions of the dependent parameters.

The phenomenology of the sea level oscillations in the synoptic frequency band expressed by the analysis are hard to explain on a theoretical basis. Synoptic variability is usually attributed to the effect of localised moving wind stresses as well as to moving large-scale weather systems. In the latter case, the dynamic effect of a moving atmospheric disturbance on a rotating ocean can give rise to quasi-geostrophic gradient-eddy motions on the shelf which are controlled by the conservation of potential vorticity over the variable bottom topography of the shelf-continental slope. The excitation of shelf waves by a moving cyclone is explained by two main mechanisms: (i) a resonance condition between the cyclone velocity and the maximum phase velocity of one or several shelf modes, and (ii) the scattering of the associated meteorological tide at the coastal irregularities, this mechanism being most effective close to the maximum frequency of each shelf mode (Kulikov & Shevchenko, 1992). For a semi-limited ocean and a shelf of constant width and uniform alongshore bathymetry these generation mechanisms of shelf waves would result in the excitation of oscillations at discrete frequencies whose values depend on the dispersion characteristics of the shelf modes. In the present analysis, the time-dependent coastal phenomena pertaining to the shelf area in the vicinity of the Maltese Islands is more complex and the records of the residual sea level do not exhibit any particular affinity to a consistent or preferred set of signals. The overall sea level signal contains contributions from the direct (isostatic) response to pressure, from the elevation due to any shelf wave activity as well as from oceanic effects from the deeper ocean. The general west to east direction of atmospheric disturbances over the Sicilian shelf is indeed opposite to that in which shelf waves would be expected to propagate. The Sicilian shelf has moreover a complicated configuration with variable width and highly different depth gradients. The termination of the shelf at both the eastern and western extremities may very well be unable to support the longer synoptic wavelengths. The variability in the synoptic range of frequencies, particularly in the lower frequency end, may thus be more intimately connected with dynamic features that occur in the deeper areas beyond the shelf area, and which are controlled by exchange

mechanisms through the strait. Further understanding on these factors necessitates an adequate database of hydro-meteorological data for the region that is sufficiently extensive in both spatial coverage and duration.

Seasonal changes in the mean sea level show a major minimum in March and a major maximum towards the last months of the year. Besides the usual steric and direct meteorological effects, this variability is attributed to adjustments in the mass balance of the whole Mediterranean basin.

Long period waves with periodicities that are in agreement to the theoretical natural periods of Mellieha Bay are also observed. They are attributed to large amplitude coastal seiche motions known locally as the *'milghuba'*. The detailed study of the phenomenology, generation and dynamical properties of these extreme seiche oscillations forms the basis of the subsequent chapters in this thesis.

3. The response of semi-enclosed water bodies to the '*Milghuba*'

3.1 Introduction

3.1.1 The main coastal embayments in the Maltese Islands

The coastline of the Maltese Islands, in particular along its northern segment, is characterised by a number of embayments and inlets (Fig. 3.1). They generally consist of elongated shallow (≈ 25m) semi-enclosed areas, a couple of Kilometres in extent and relatively sheltered areas, especially from the predominant NW winds. The embayments are very suitable sites for ports, yacht marinas, ship building and other maritime activities. Particularly in the case of the Grand Harbour and Marsamxett Harbour the complex system of creeks has been

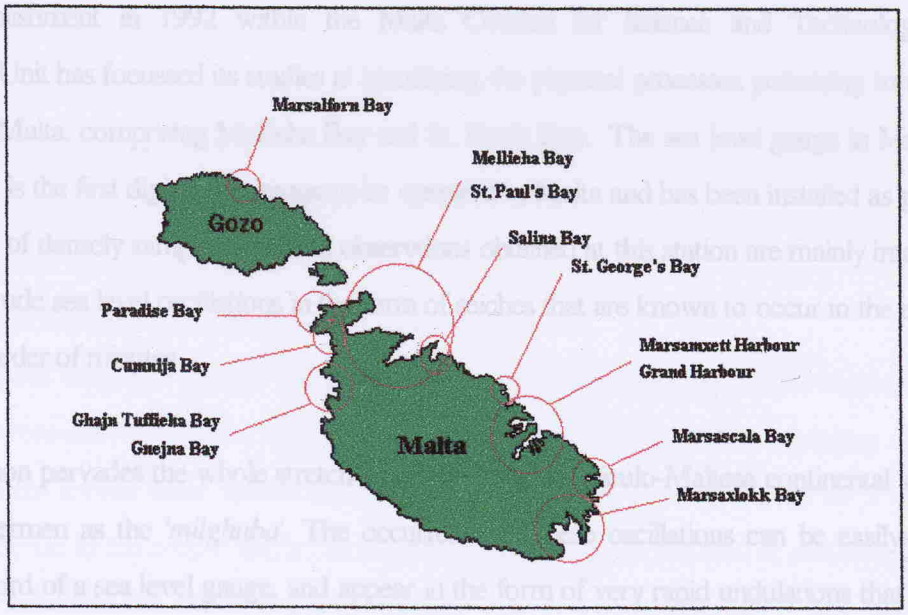

Fig. 3.1 Main embayments and inlets on the coast of the Maltese Islands

exploited for the construction of docks. In some cases coastal development has been accompanied by alterations in the morphology of the embayments resulting from dredging, sea reclamation, building of breakwaters, quays and other structures. In the case of Marsaxlokk bay, a traditionally focal location for fishing vessels, recent developments such as the building of a new power station and the establishment of the Malta Freeport terminals for the handling of heavy cargo and containers, have encroached on a considerable length of the shoreline and drastically changed this part of the island with subsequent alterations in the hydrodynamic response and wave impact patterns of the bay as well as an increased pressure on the health of the marine environment. In the case of Mellieha Bay and St. Paul's Bay, the axial orientation of the embayments and their relatively wide extent at their open mouths, makes them vulnerable to the NE winds that blowing over a large fetch can often reach gale strengths with associated devastating waves reaching the coast especially during storms. These two bays have also been the centre of the local fish-farming industry in the past ten years; at the head of Mellieha Bay, there is also the largest sandy beach of the island.

3.1.2 The effect of the seiche in the embayments

Since its establishment in 1992 within the Malta Council for Science and Technology, the Physical Oceanography Unit has focussed its studies at identifying the physical processes pertaining to the northwestern coastal area of Malta, comprising Mellieha Bay and St. Paul's Bay. The sea level gauge in Mellieha Bay (refer section 2.1.2.1) is the first digital tide gauge to be operated in Malta and has been installed as part of this study. The time series of densely sampled sea level observtions obtained at this station are mainly intended to monitor the large-amplitude sea level oscillations in the form of seiches that are known to occur in the embayments with periods of the order of minutes.

This phenomenon pervades the whole stretch of coast facing the Siculo-Maltese continental shelf. It is locally known by fishermen as the *'milghuba'*. The occurrence of these oscillations can be easily detected from a continuous record of a sea level gauge, and appear in the form of very rapid undulations that often completely mask the general variation of the sea level caused by the astronomical tide. The main subject of this chapter is to describe the existence, nature and origin of these oscillations. The generation of large amplitude seiches by atmospheric forcing is dealt in more detail in Chapter 4.

Generally speaking the seiche has a small amplitude, but sporadic intensified events are quite common, practically throughout the year. The displacements of the waterline associated with these events are easily visible to the eye, often uncovering a considerable portion of the shallow seabed in their regressional phase. In the Grand Harbour, the seiche is able to penetrate the protection of the breakwater. For severe events, these high frequency oscillations may cause flooding of wharves, disruption of sea activity, and loss of property. Damage at the ship dock gates has been reported due to the seiche. Ship loading/unloading operations can be delayed or even potentially hazardous. A tragic incident in 1982 concerned the toppling over of a barge crane which caused two deaths and other casualties. Although there are no records to prove it, the incident is believed to be the result of a rapid change in the level of the sea. The horizontal displacements associated to the seiche oscillations can also have adverse effects on moored vessels with stress on mooring lines and fender systems. The seiche-induced currents, especially the constricted flow at the harbour entrance, can be detrimental to navigation.

The periods of these seiche oscillations are similar to those of tsunami waves. Their transformation as they approach the coastal areas and their amplification in bays and harbours can be equally disastrous. Due to this close relation with the behaviour of tsunami, research on seiches is thus also important in disaster mitigation studies (Taku et al., 1992). Studies on the amplification of seiches are important in the design of coastal defences which are usually based on a 1:10,000 year storm surge level.

3.1.3 Forced oscillations in semi-enclosed coastal domains

The term 'harbour seiches' refers to the non-tidal transient oscillations of a semi-enclosed body of water resulting either from direct forcing or from the response to an external stimulation impinging at the open mouth. Although the term applies more specifically to port areas that are often protected by a rather narrow and restricted connection to the deeper sea, it can in general be also used in the case of embayments and gulfs with much wider mouths that are often comparable to their size. In a more generalised way 'coastal seiches' also include water level oscillations occurring at an open straight coast. The periods of these oscillations fall between wind waves and swell on the one hand and tides on the other, and range from a few minutes up to a few hours. They are thus classified as long period waves.

Long period oscillations in bays and harbours are usually associated with waves in the adjacent sea outside the harbour. The external broad-banded spectrum produces the forcing signal which can be realised as a combination of sinusoids with a spectrum of frequencies. The waves arriving from the open sea enter through the open sea boundary, propagate to the coastal area and are reflected from the coastal boundaries. They are subject to various deformations due to diffraction, refraction, shoaling and frictional losses of energy. Moreover part of their energy is radiated back to the sea through the open boundary. A preferential response occurs at periods that match the natural modes of the harbour. Oscillations within the harbour at these natural frequencies continues to increase in magnitude until there is a balance between energy input and energy losses such as those owing to friction, flow separation, boundary absorption, and radiation from the harbour mouth.

Seiches have been observed along many exposed coasts in the world ocean. Their amplification in bays and harbours is however linked to a number of inter-dependent factors, and large amplitude seiches are known to occur only in a number of places and under special conditions. Nagasaki, on the southern coast of Japan, periodically experiences very strong half-hourly oscillations, with heights exceeding 3m, which are termed '*abiki*' (Honda et al., 1908; Hibiya & Kajiura, 1982). In the Balearic Islands, the '*rissaga*' is a particularly troublesome 10-minute oscillation occuring mainly in summer. It is particularly strong in the elongated, shallow and narrow-mouthed Ciutadella Harbour on Menorca Island (Monserrat et al., 1991) where wave heights can exceed 3m for extreme events. A similar phenomenon, known locally as '*Seebar*', is observed on tha coast of the Baltic Sea, with episodes of waves reaching heights of 1-2m even during calm weather (Defant, 1961; Wilson, 1972). Other strong manifestations of seiches occur at Capetown in South Africa (Shillington, 1984), Los Angeles in the US (Giese & Chapman, 1993), in the South Kuril Islands (Djumagaliev & Rabinovich, 1993), and on the southern coast of Sicily where the sea level oscillations are known as the '*marubbio*' (Colucci & Michelato, 1976). The '*milghuba*' is believed to be an expression of the same phenomenon in the Maltese coastal sea.

3.1.4 Review of studies on the triggering of seiches

One of the first scientific studies on seiches is that by Sir George Airy (1878), better known for his mathematical theory on small-amplitude water waves. He observed that the frequent appearance of 21-minute sea level oscillations on the tidal records in the Grand Harbour in Malta is similar to the records of seiches in the Lake of Geneva, published in 1876 and 1877 by F. A. Forel. The origin of seiches has been attributed to a variety of processes. Forel (1892) and Chrystal (1908-1909) list a number of agents that can be responsible for seiches in

lakes. The most important are those of meteorological origin. By matching theory and observations, Wilson (1972) shows that moving atmospheric pressure variations are particularly inducive to energizing seiches in lakes. The same sources of excitation apply also to seiches in coastal areas. In the open sea, the forcing agent is able to act over a wide expanse of sea and the related sea disturbances can thus be much higher. This energy impinging on the mouth of a bay or the entrance of a harbour is subsequently responsible for the triggering of seiche oscillations in semi-enclosed areas. Examples on the generation of coastal seiches by meteorological perturbations especially due to the sea level adjustments related to cyclonic forcings exist in the literature (e.g. Munk et al., 1956; Darbyshire & Darbyshire, 1964; Wilson, 1972; Tintore' et al., 1988).

From studies (Derbyshire, 1963) on the seiches in a harbour in Table Bay on the west coast of Cape Peninsula, it is also evident that the forced waves in the harbour can be effectively caused by surf beats, a phenomenon closely related to swell, and which occurs all along the coastal area outside the harbour. Spectral analysis shows that the maximum height of the 2-minute seiche in the harbour coincides very well with the greatest surf beat activity. Surf beats consist of infragravity motions, with time scales of about 30-300s, occurring primarily in the surf zone. They occur in association to incident groups of short waves which carry a locked second order lower frequency component that is released when the incident waves break (Longuett-Higgins & Stewart, 1962). In a three-dimensional context, surf zone energy at surf beat frequencies results from certain combinations of group frequency and longshore wave number that cause the resonant excitation of edge waves (Bowen & Guza, 1978).

Deep-sea surface waves generated by submarine seismic crustal movements can also produce seiching in coastal waters. These disturbances give rise to tsunamis (e.g. Matuzawa et al., 1933; Wilson, 1971). Historical records show that the incidence of tsunamis in the Mediterranean, though not comparable to that in the Pacific Ocean, is quite frequent (Ozsoy et al., 1982). According to Van Dorn (1965), at least 23 large tsunamis had been reported in total in the Mediterranean. In Malta, the only recorded tsunami is that associated to the Messina Straits earthquake on 28th December 1908. This is the most devastating earthquake in Italy in recent history, leaving some 60,000 fatalities. The earthquake was accompanied by a disastrous tsunami which wiped out all the eastern coast of Sicily (Tinti & Giuliani, 1983). The tsunami wave reached the Maltese Islands some 55 minutes afterwards. The local newspapers (e.g. *'Malta'*, 29th December, 1908) report exceptional high sea levels in Msida Creek and Marsaxlokk Bay. In Msida seaside resorts and storage houses were inundated with

damage to property and merchandise. In Marsaxlokk, on the southeastern tip of the island, the impact must have been stronger and fishing boats were crashed against the quay. The tsunami was accompanied by a strong seiche in the Grand Harbour where the sea level gauge recorded sea level fluctuations with a maximum crest-to-trough excursion of 2 feet 11.8 inches (= 0.91m). The seiche persisted until late evening. These sea level registrations constitute the only useful records for this tsunami.

Studies carried out in Puerto Rico and the Philippines demonstrate that coastal seiches can also result from the response over the continental shelf to forcing by deep-sea internal solitary waves (Giese et al., 1982, 1990; Giese & Hollander, 1987; Chapman & Giese, 1990; Giese & Chapman, 1993). The origin of the internal waves by strong currents flowing over a shallow submarine topography may occur very far away; as they travel towards the coast their interaction with the shelf at the shelf break causes some transfer of energy into coastal seiches. The effectiveness of this interaction depends on the shelf break topography and the deep sea stratification. Giese et al. (1994) attribute the seasonal character of the 'rissaga' phenomenon in Cuitadella Harbour to a possible linkage with the strong stratification of the Mediterranean Sea during summer.

3.2 Basic characteristics of the seiche in Mellieha Bay

3.2.1 Seasonal characteristics

The characteristics of the seiche in Mellieha Bay are here investigated on the basis of sea level observations, sampled at 30 or 60 recordings per hour, at the bay head during the period June 1993 - December 1996. This data set is not long enough for a statistically significant description of the phenomenon on an inter-annual scale. It is however possible to obtain a good indication on the seasonal incidence. In Fig. 3.2 the running variance of the sea elevation is used as an indicator of seiche activity. The variance is calculated from the high-pass filtered data series, sub-sampled every two minutes, and using a running window of 21 records. The running variance gives a measure of the sea level energy carried by the signals resolved by the window size. It also gives information on the persistence in time of a particular seiche event. A sharp and high peak in the running variance time series plot is thus representative of a transient and strong seiche event.

The variance σ^2 is related to the mean square amplitude a_{rms} by $\sigma^2 = a_{rms}^2/2$, where $a_{rms}^2 = \langle H^2 \rangle/4$, H being the crest-to-trough wave height. A variance level of $124cm^2$ is thus taken to represent a wave height of 32cm. This level is taken as a threshold for identifying a significant seiche event. On this basis 49 seiche events are

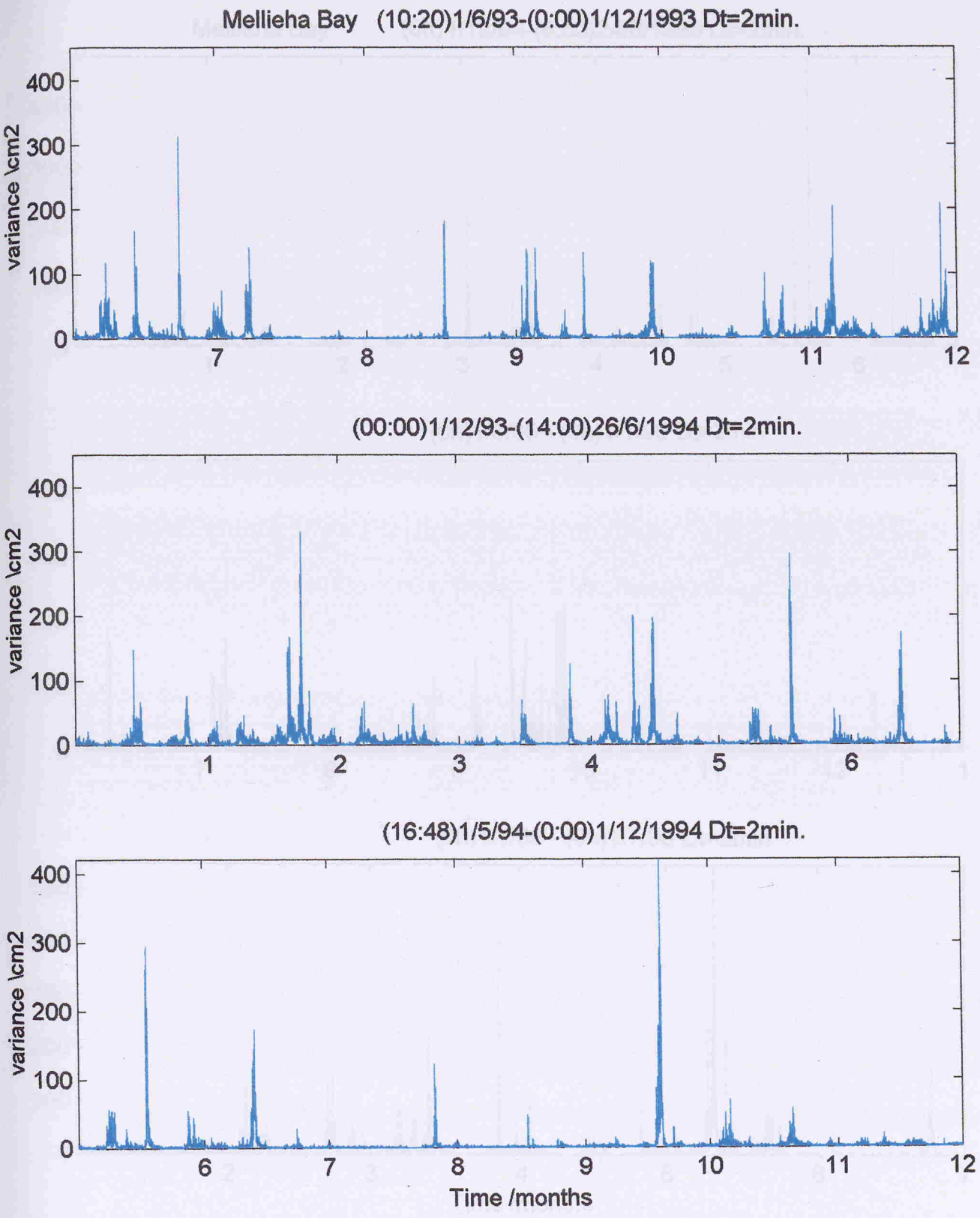

Fig. 3. 2 Time series of running variance of sea level in Mellieha Bay (June 1993 - December 1996).

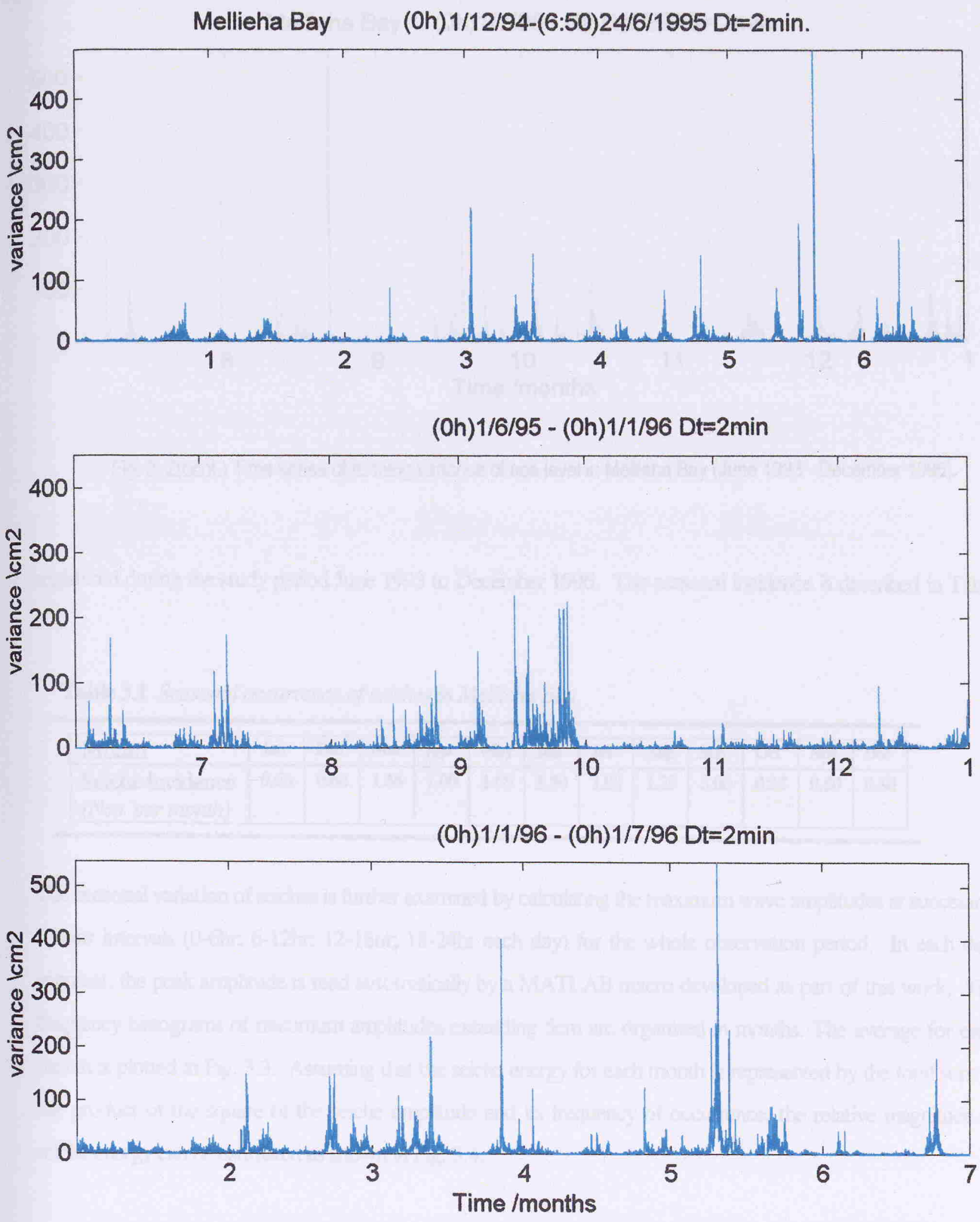

Fig. 3. 2(cont.) Time series of running variance of sea level in Mellieha Bay (June 1993 - December 1996).

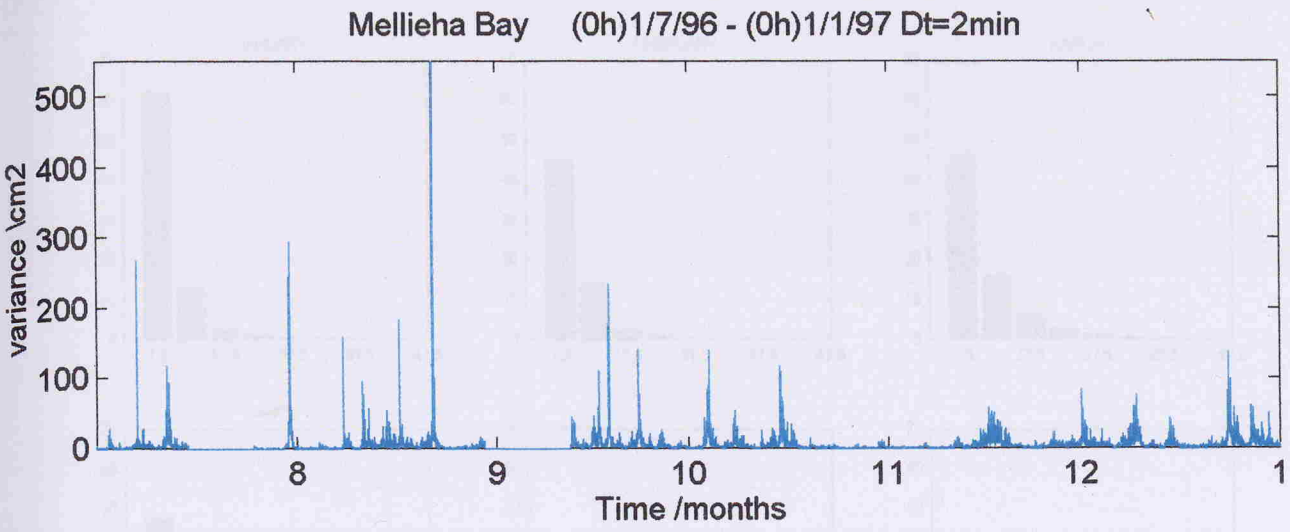

Fig. 3. 2(cont.) Time series of running variance of sea level in Mellieha Bay (June 1993 - December 1996).

registered during the study period June 1993 to December 1996. The seasonal incidence is described in Table 3.1.

Table 3.1 *Seasonal occurrence of seiches in Mellieha Bay*

Month	**Jan**	**Feb**	**Mar**	**Apr**	**May**	**Jun**	**Jul**	**Aug**	**Sep**	**Oct**	**Nov**	**Dec**
Seiche incidence *(Nos. per month)*	**0.66**	**0.66**	**1.66**	**1.00**	**1.66**	**1.50**	**1.00**	**1.25**	**3.00**	**0.25**	**0.50**	**0.50**

The seasonal variation of seiches is further examined by calculating the maximum wave amplitudes at successive 6-hour intervals (0-6hr; 6-12hr; 12-18hr; 18-24hr each day) for the whole observation period. In each data segment, the peak amplitude is read automatically by a MATLAB macro developed as part of this work. The frequency histograms of maximum amplitudes exceeding 5cm are organised in months. The average for each month is plotted in Fig. 3.3. Assuming that the seiche energy for each month is represented by the total sum of the product of the square of the seiche amplitude and its frequency of occurrence, the relative magnitude of seiche energy can be estimated as shown in Fig. 3.4.

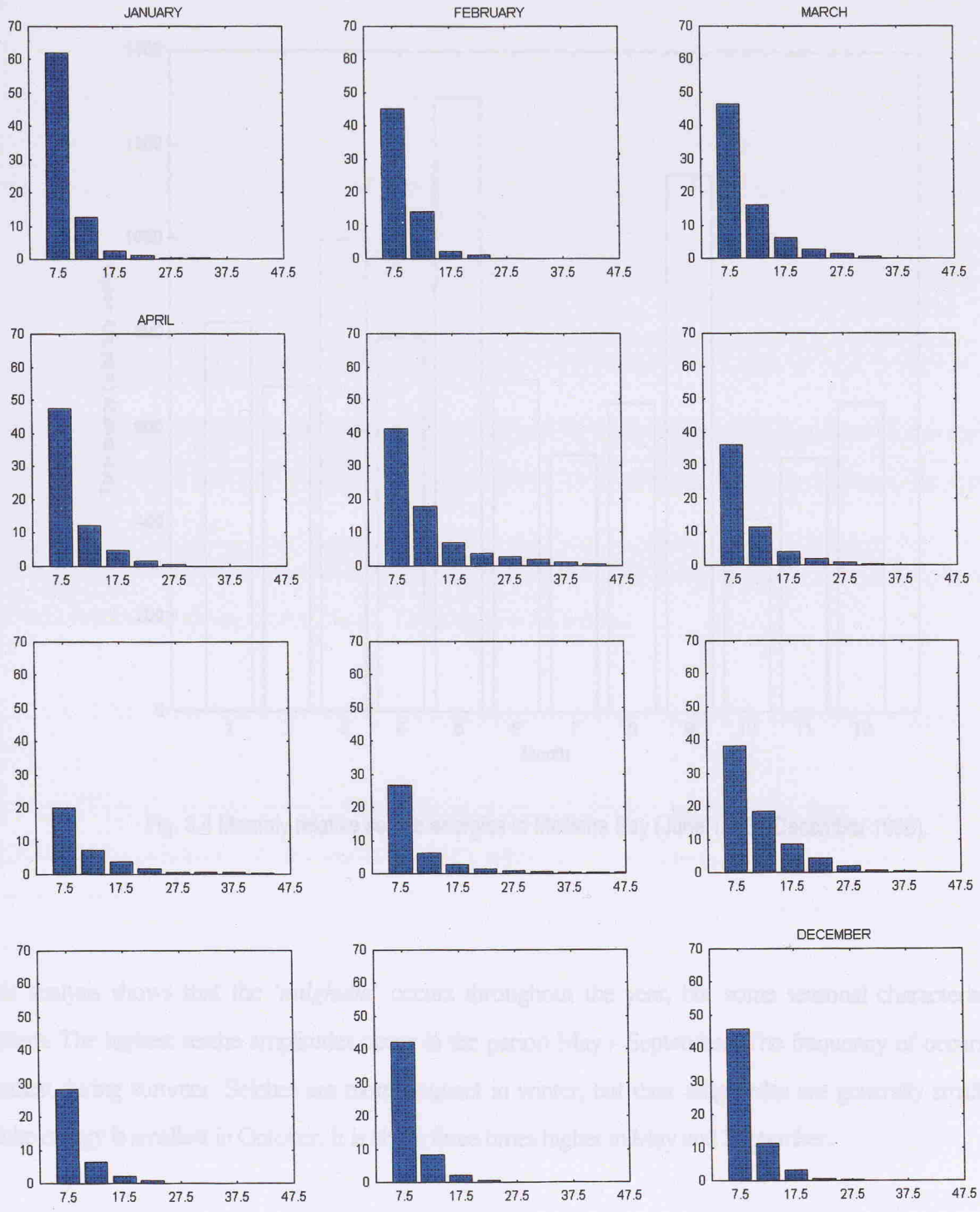

Fig. 3.3 Monthly frequency histograms of seiche maximal amplitudes exceeding 5cm in Mellieha Bay (June 1993 - December 1996).

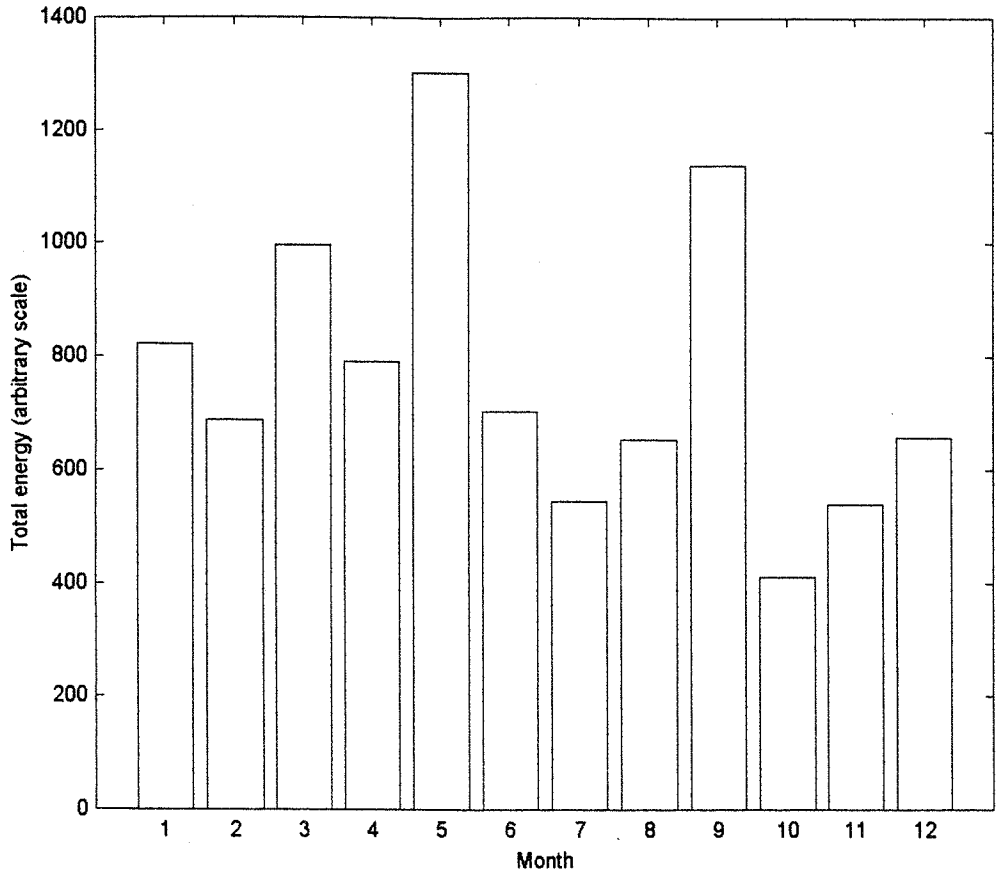

Fig. 3.4 Monthly relative seiche energies in Mellieha Bay (June 1993 - December 1996).

This analysis shows that the '*milghuba*' occurs throughout the year, but some seasonal characteristics are evident. The highest seiche amplitudes occur in the period May - September. The frequency of occurrence is smallest during summer. Seiches are more frequent in winter, but their amplitudes are generally smaller. The seiche energy is smallest in October. It is about three times higher in May and September.

During the summer months, in particular July and August, the seiche is very sharp, with a duration that can often be as short as a few cycles. The associated sea level fluctuations have a tsunami-like nature, starting with an abrupt and large impulse that subsequently decays after a few oscillations. Seiches during this time of year are particularly strong . On several occasions, seiche heights close to 1m have been recorded. The most spectacular

is that on 22nd August 1996 with an excursion in sea level of 1.3m. In other periods of the year the seiche height does not generally reach these extremes. The seiches are however much more persistent, lasting even for days on some occasions. The cumulative seiche energy is thus much higher. A short buildup period generally preceeds these seiche events. The seiche then develops as a succession of random intensifications which follow closely one another resulting in a series of bursts of large amplitude fluctuations. On the basis of this seasonal characterisation, it thus appears that stratification is not a prerequisite for the generation of seiches. The presence of stratification may however play a role in the nature and temporal development of a seiching event.

3.2.2 Power spectra of seiches

The twelve data segments listed in Table 3.2 are analysed to study the spectral signature of the sea level oscillations in Mellieha Bay. The data segments are divided into four separate sets according to the type and amplitude of the oscillations.

According to Rabinovich & Monserrat (1996) a classification of seiches can be based on a visual analysis of the recorded observations during strong events. Three types are identified:

- *Impulsive* (Type A) consisting of a strong initial oscillation(s) followed by a fast or slow decay of the seiche heights;
- *Resonant* (Type B) consisting of a gradual build up of seiche height to a maximum oscillation, followed (sometimes) by a period of sustained excitation, and a subsequent gradual reduction;
- *Complex* (Type C) consisting of a mixture of consecutive abrupt and gradual amplifications and reductions of seiche oscillations.

This classification has been found very useful for the relationship to the different mechanisms of seiche generation. For example, Type A resembles the record observed in the case of tsunami waves impinging in a coastal area. This classification scheme is however quite subjective and conditioned by the fact that in reality oscillations rarely resemble the ideal cases typified by cases A and B. The characteristics of a seiche event can also be expressed in terms of a number of parameters which can be utilised for a statistical study of the seiches. The most important parameters are the:

- *mean seiche period* - The seiche period is here defined as the time interval between the occurrences of two successive maxima in elevation of the sea surface. The mean seiche periods related to different strong events at

the same recording station may not necessarily coincide and will depend on the forcing mechanism responsible for the particular events. The distribution of mean seiche periods associated to a number of events is however centred around a value that is characteristic of the geometry of the oscillating water body.

- *Maximum fluctuation range* - The maximum excursion in elevation during a strong seiche event is certainly the most relevant parameter concerning the impact of the oscillations on the coastal areas. The distribution of this parameter over a number of events can be shown to follow a statistical trend in which the level of occurrence diminishes regularly with increasing maximum range of fluctuation.

- *Seiche event duration* - The duration of a seiche event is defined as the time interval in which the water level excursion is above a prescribed limiting value. This limiting value will vary with location. The median value of level excursions can be used as the best threshold to time delimit a seiche event.

The four sets of data segments have been chosen on the basis of the criteria outlined above. The three examples in set 1 are typical short duration large amplitude seiching events of the impulsive type Fig 3.5a-c. Set 2 are also examples of large amplitude oscillations, but the duration is much longer Fig. 3.5d-f. Set 3 represent seiches of the mixed type with medium range seiche heights below 0.4m. Set 4 typifies data intervals of background seiching with very low amplitude oscillations.

Table 3.2 *Selected seiching events in Mellieha Bay*

SET	**Central date of event and seiche type**		
	I	II	III
1	7 July 1996 impulse; large amplitude	17 August 1996 impulse; large amplitude	22 August 1996 impulse; large amplitude
2	19 September 1994 mixed; large amplitude	20 May 1995 impulse + resonance; large amplitude	10 May 1996 mixed; large amplitude
3	17 September 1995 mixed; medium amplitude	24 June 1996 mixed; medium amplitude	11/12 July 1996 mixed; medium amplitude
4	1/2 October 1995 weak	3/4 January 1996 weak	10/11 June 1996 weak

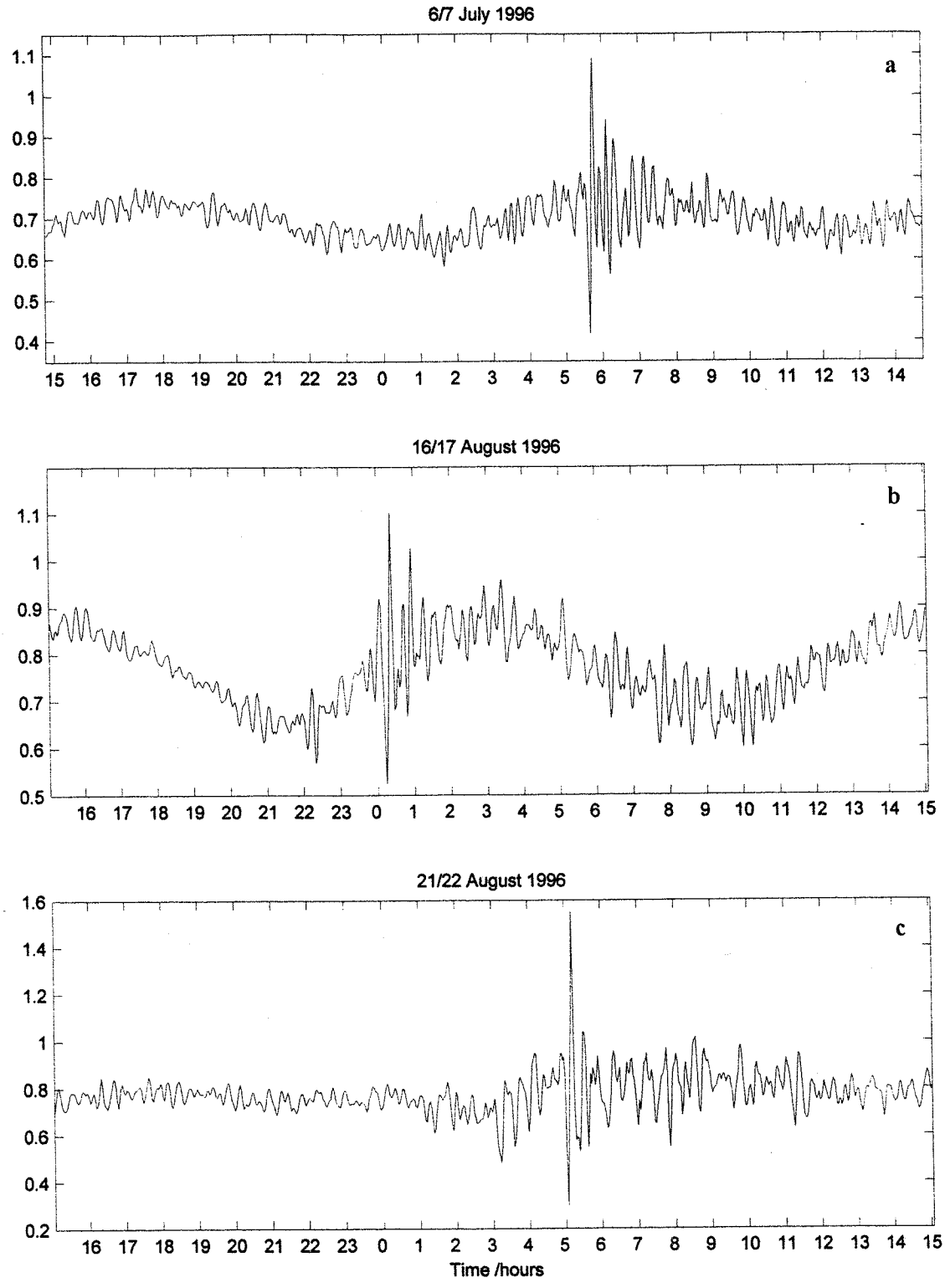

Fig. 3.5 (a-c) Typical examples of seiches in Mellieha bay with large amplitude and short duration, SET 1, (I, II,and III).

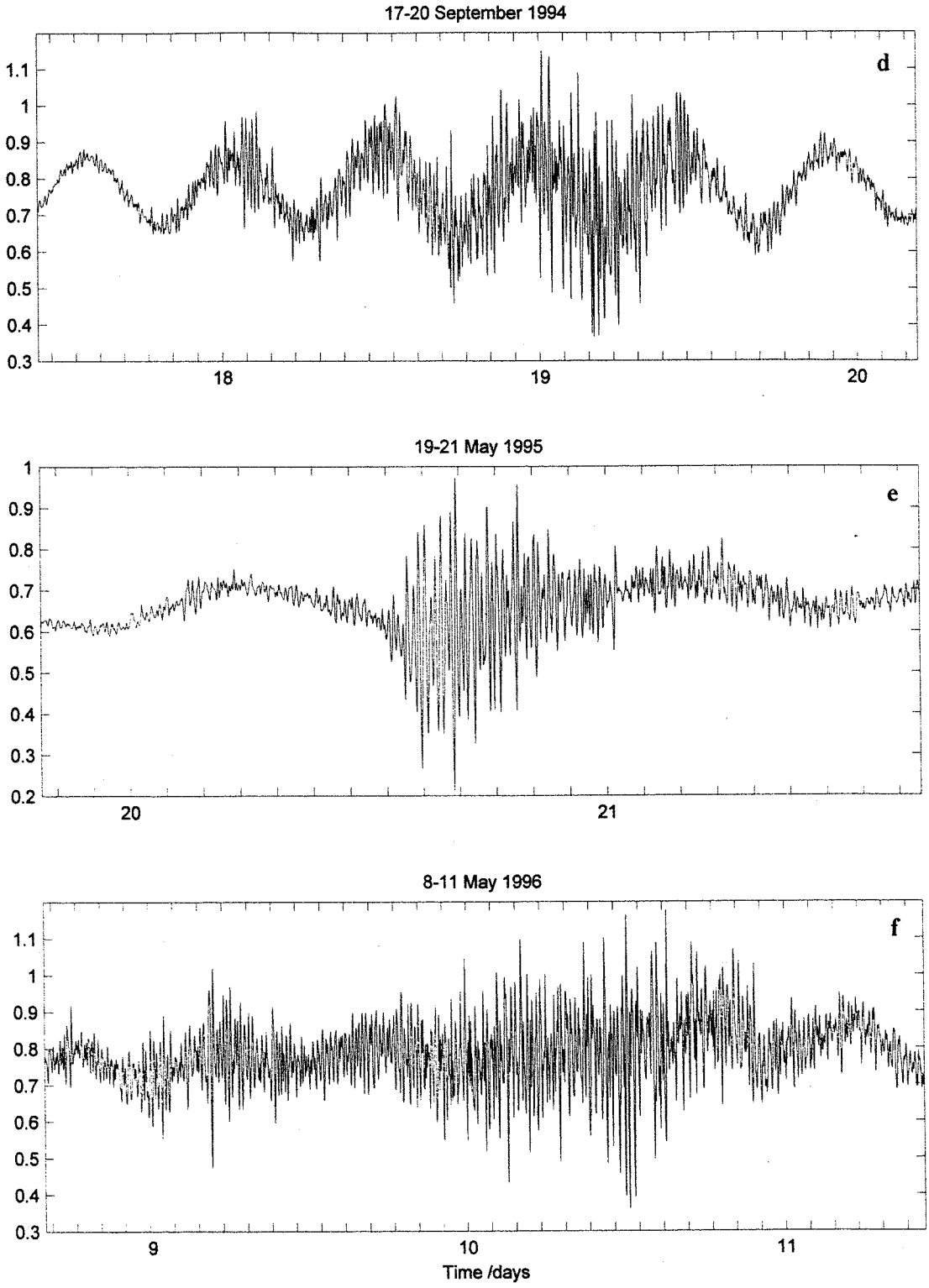

Fig. 3.5 (d-f) Typical examples of seiches in Mellieha bay with large amplitude and long duration, SET 2, (I, II and III).

For each data segment the spectral analysis is performed on 1280 points (after high pass filtering and detrending). A narrow spectral window of 256 points with 50% overlap is used. The resulting number of degrees of freedom is 20 and a reasonable significance level is thus achieved even though the data segment is short.

The results are plotted in Fig. 3.6 a-d. They present the particularly interesting case of Mellieha Bay with a wide entrance and possible coupling to the adjacent embayment. The bathymetry beyond its open mouth is furthermore complicated by a shallow bank offshore. Seiches are also amplified by the shoaling effect of the shallow sand bank at its head. The intensity and character of the observed seiche oscillations are thus highly unpredictable.

In the respective spectra, the peak P with the longest period (T = 16.6min) is the fundamental mode (as verified by numerical computation in section 3.4.7.1). The other main peaks with longer periods relate to oscillations involving the shelf area immediately adjacent to the bay. Generally speaking the twelve spectra are fairly similar to one another, although their power levels and relative energy distribution are different. The fundamental spectral peak is in general the most prominent except during the larger amplitude events when the lower frequency signals become more energetic and can even supercede the fundamental mode. The fundamental period is very stable with only slight frequency shifts of about 4%. It corresponds to a Merian along-axis extent that exceeds the actual physical dimensions of the bay. The volume of the excited water body is thus dictated by the bathymetry outside and in the immediate vicinity of the bay.

At times water level records in the bay take the form of quite regular oscillations, especially during periods when excursions are strong; at other times the seiching is irregular and is characteristic of a coastal configuration in which fractional areas are not as fixed as in the case of a cul-de-sac or small bay that is suddenly terminated. The main lower frequency peaks have periods T = 21.5 (X) and 25.5min (Y). They both have a stable frequency but a highly variable intensity. Their quality factor Q (calculated at frequency ω_o by $Q \approx \omega_o / \Delta\omega$, where $\Delta\omega$ is the peak half-width) is comparable to that of the fundamental mode. Q values tend to be higher in the case of the larger amplitude seiching events. Other lower frequency peaks are unstable and vary considerably from one seiche event to another.

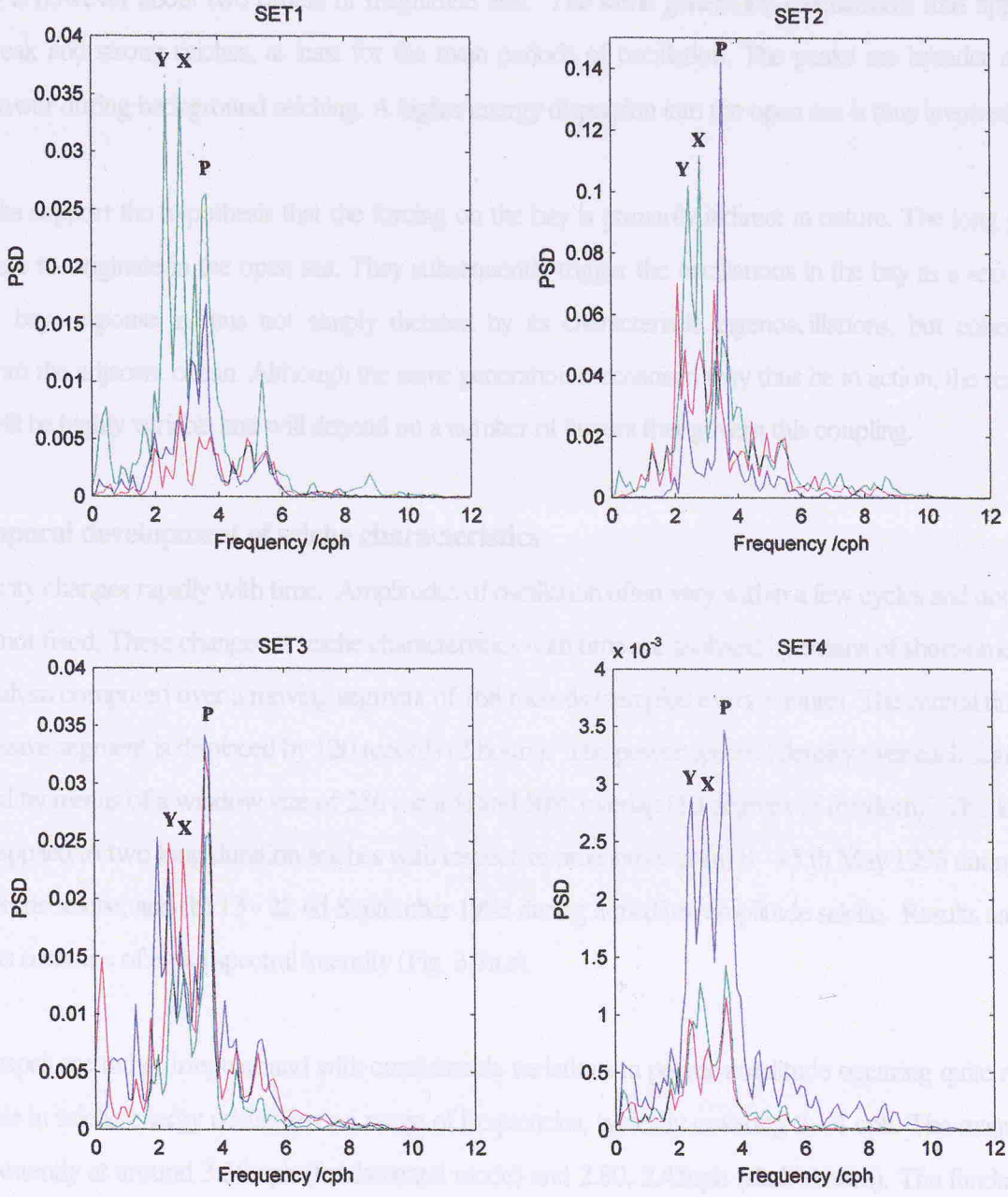

Fig. 3.6 Typical examples of power spectra of seiches in Mellieha bay with (a) large amplitude and short duration, SET 1, (b) large amplitude and long duration, SET 2, (c) medium amplitude, SET 3, and (d) background level, SET 4. For each set, case I is plotted in red, case II is plotted in blue, and case III is plotted in green. The 95% confidence factor, for 18 degrees of freedom is 6.1 dB (B_{min}=0.57; B_{max}=2.2).

It is important to note that the same spectral characteristics are observed during background seiching levels. The energy is however about two orders of magnitude less. The same generation mechanisms thus apply for both the weak and strong seiches, at least for the main periods of oscillation. The peaks are broader and Q values are lower during background seiching. A higher energy dispersion into the open sea is thus involved.

These results support the hypothesis that the forcing on the bay is primarily indirect in nature. The long period waves appear to originate in the open sea. They subsequently trigger the oscillations in the bay as a secondary effect. The bay response is thus not simply dictated by its characteristic eigenoscillations, but concerns a coupling with the adjacent ocean. Although the same generation mechanism may thus be in action, the resulting response will be highly variable and will depend on a number of factors that govern this coupling.

3.2.3 Temporal development of seiche characteristics

Seiche activity changes rapidly with time. Amplitudes of oscillation often vary within a few cycles and dominant signals are not fixed. These changes in seiche characteristics with time are analysed by means of short-time spectral analysis computed over a moving segment of 768 records (sampled every minute). The central time of each successive segment is displaced by 120 records (2 hours). The power spectral density over each segment is calculated by means of a window size of 256 records and 50% overlap (10 degrees of freedom). This kind of analysis is applied to two long duration seiches with respective time intervals (a) 8 - 15 th May 1996 during a large amplitude seiche, and (b) 13 - 22 nd September 1995 during a medium amplitude seiche. Results are displayed as contours of equal spectral intensity (Fig. 3.7a,c).

Spectral shapes are rather irregular and with considerable variations in power amplitude occuring quite rapidly. The increase in seiche energy occurs over a range of frequencies, typically covering 2 - 4 cph. The main peaks occur consistently at around 3.56 cph (fundamental mode) and 2.80, 2.45cph (shelf modes). The fundamental mode is the most stable and its peak period does not change significantly. The gravest mode of the bay does not thus depend on the forcing conditions except for the magnitude of the oscillations which changes from one event to another. The shelf mode periods are more variable, indicating a possible dependence on the direction of incidence of the long period waves in the adjacent open sea. Following Snodgrass et al. (1962), the predominant period of leaky waves on a step type continental shelf of width L is given by $(4L / c_o)\mathrm{Cos}\phi_o$,

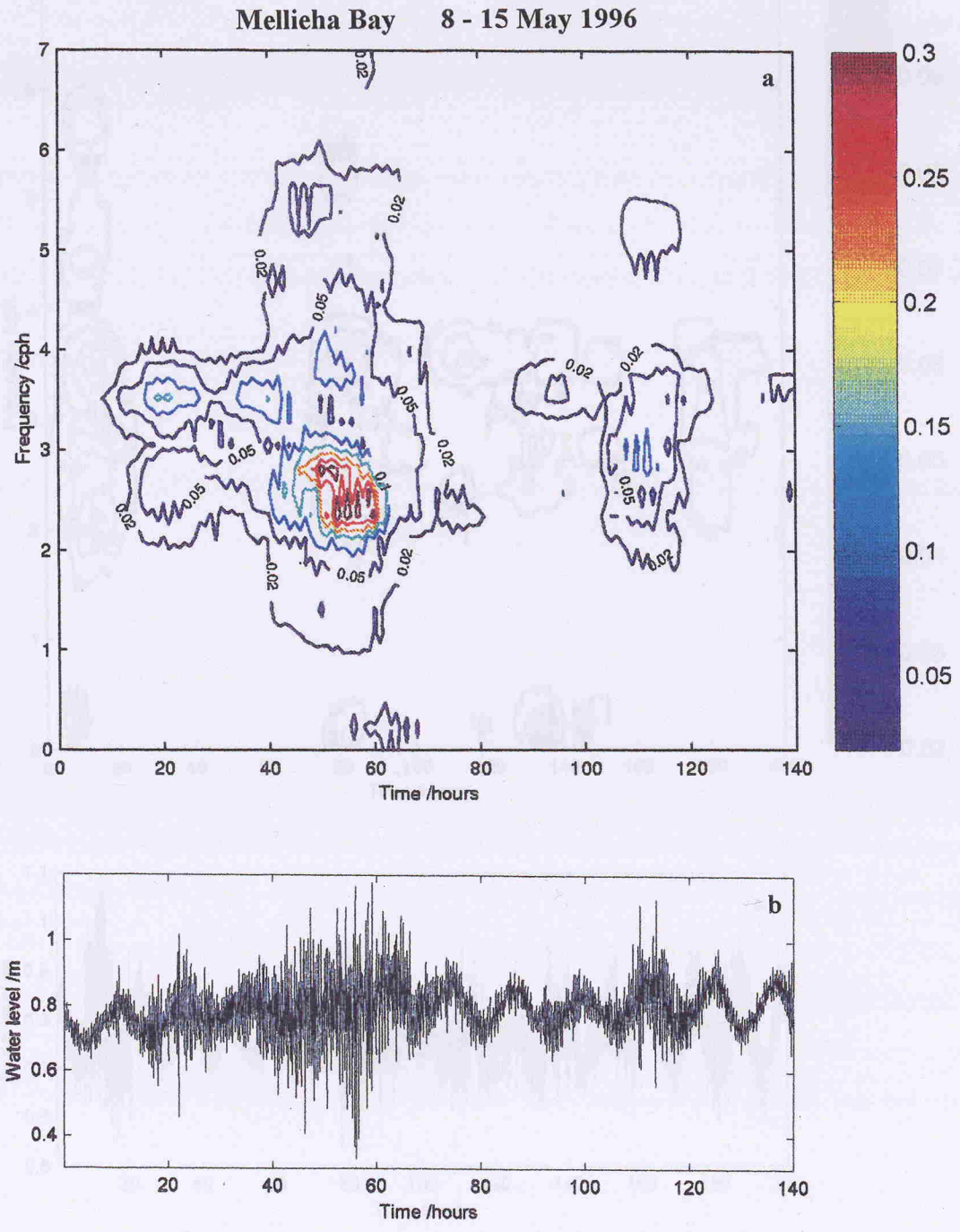

Fig. 3.7 Power density contours obtained by short-time spectral analysis (a) on times series of 1-minute sampled sea level records in Mellieha Bay from 5 - 8th May 1995 (b). The colorbar shows the range of spectral magnitudes in $m^2\ h^{-1}$. The 95% confidence factor for each short-time spectral estimate with 10 degrees of freedom is 8 dB (B_{min}=0.48; B_{max}=3.0).

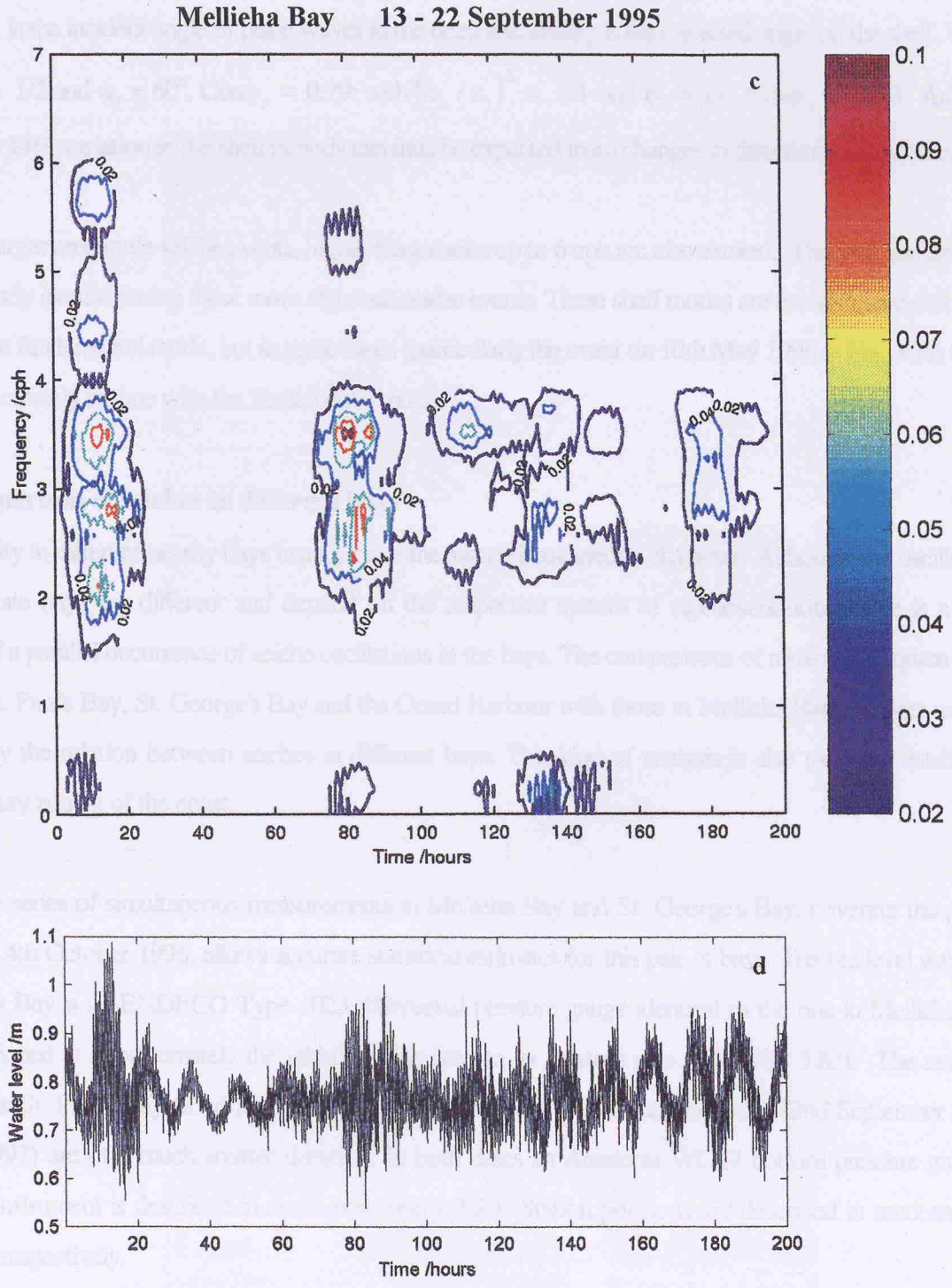

Fig. 3.7 Power density contours obtained by short-time spectral analysis (c) on times series of 1-minute sampled sea level records in Mellieha Bay from 13 - 22nd September 1996 (d). The colorbar shows the range of spectral magnitudes in $m^2 h^{-1}$. The 95% confidence factor for each short-time spectral estimate with 10 degrees of freedom is 8 dB (B_{min}=0.48; B_{max}=3.0).

where $\mathrm{Cos}\phi_o = [1-(c_o / c_1)^2 \mathrm{Sin}\phi_1]^{1/2}$, c_o and c_1 are the respective long wave phase speeds on the shelf and open sea, ϕ_1 is the incident angle of plane waves in the deep sea, and ϕ_o is the refracted angle on the shelf. With $(c_o / c_1)^2 = 1/2$ and $\phi_1 = 60°$, $\mathrm{Cos}\phi_o = 0.79$; with $(c_o / c_1)^2 = 1/4$ and $\phi_1 = 45°$, $\mathrm{Cos}\phi_o = 0.93$. An approximate 14% variation in the shelf periods can thus be expected from changes in direction of incidence.

During the larger amplitude seiche events, higher frequencies up to 6 cph are also excited. The shelf modes are also particularly intense during these more vigorous seiche events. These shelf modes are usually enhanced in parallel to the fundamental mode, but in some cases (particularly the event on 10th May 1996 in Fig. 3.7a) they dominate alternately in time with the fundamental mode.

3.2.4 Comparison of seiches in different bays

Seiche activity in different nearby bays usually have the same simultaneous character. Although the oscillations in the separate bays are different and depend on the respective system of eigenoscillations, there is a clear indication of a parallel occurrence of seiche oscillations in the bays. The comparisons of root-mean-square wave heights in St. Paul's Bay, St. George's Bay and the Grand Harbour with those in Mellieha Bay, are here used to further study the relation between seiches in different bays. This kind of analysis is also useful to establish a seiche intensity zoning of the coast.

A long time series of simultaneous measurements in Mellieha Bay and St. George's Bay, covering the period 5th April to 4th October 1996, allows accurate statistical estimates for this pair of bays. The sea level station in St. George's Bay is an ENDECO Type 1023 differential pressure gauge identical to the one in Mellieha Bay, and is positioned at approximately the middle of the bay on its western side (refer Fig. 3.8c). The sea level recordings in St. Paul's Bay (23rd March to 9th April, 1996) and the Grand Harbour (22nd September to 1st October, 1997) are of a much shorter duration. In both cases an Aanderaa WLR7 bottom pressure gauge is used. This instrument is described in detail in section 4.3.2.1. Station positions are described in sections 3.4.4 and 3.4.7.4 respectively.

For each high-pass filtered data series, the rms wave height is calculated at each of successive 2-hour overlapping data segments with 1-hour shift. The resulting time variation of rms wave heights in Mellieha Bay

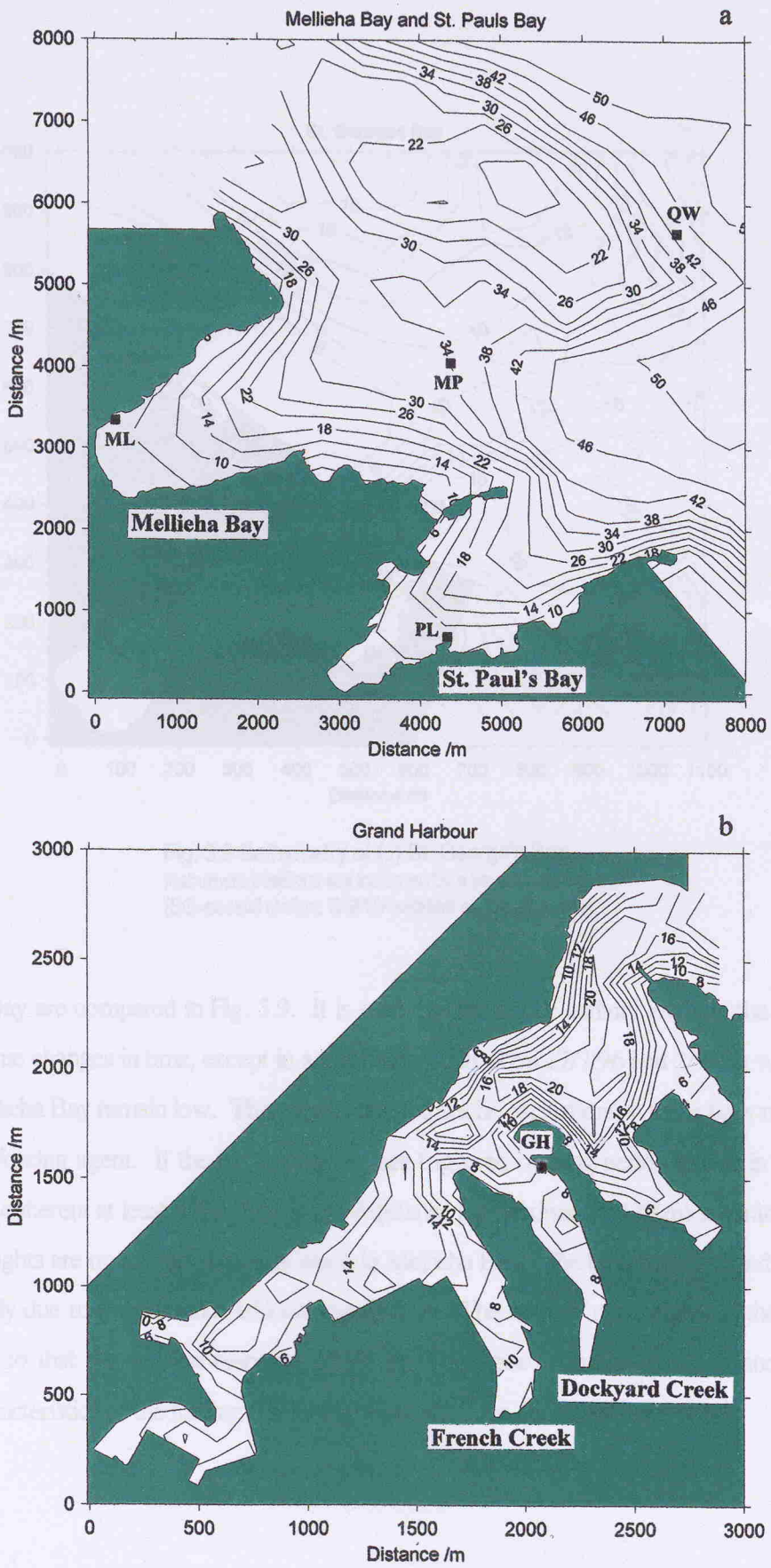

Fig. 3.8 Bathymetry of (a) Mellieha Bay and St. Paul's Bay, and (b) the Grand Harbour. Instrument positions are indicated by a small black square. (ML=Mellieha coastal station; MP=Melpaul station; QW=Qawra station; PL=St.Pauls Bay station; GH=Grand Harbour coastal station.)

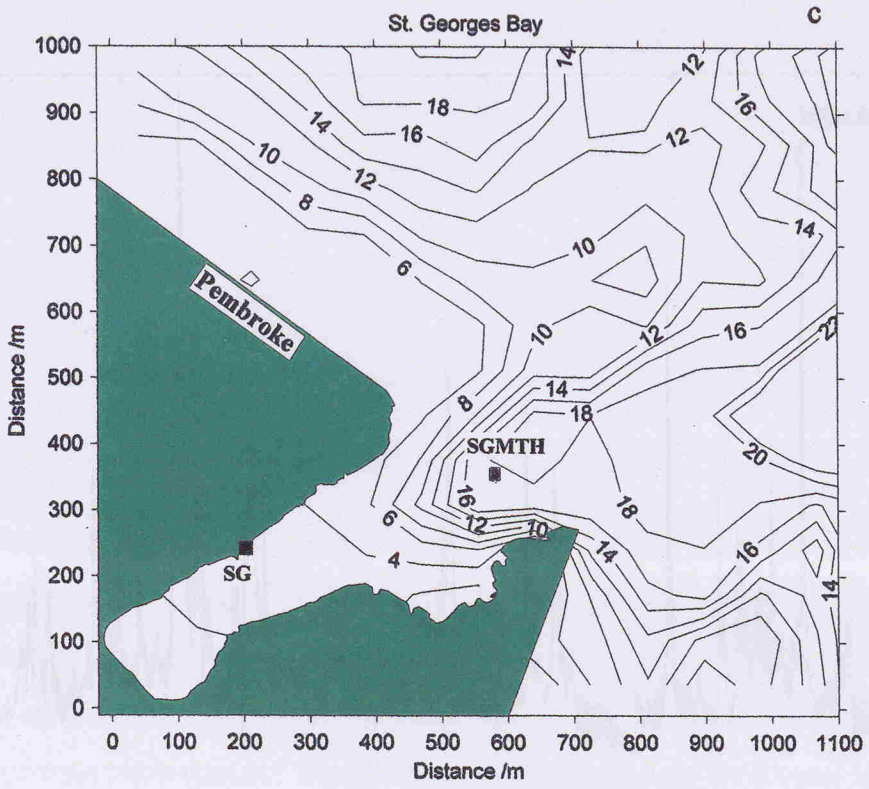

Fig. 3.8 Bathymetry of (c) St. George's Bay.
Instrument positions are indicated by a small black square.
(SG=coastal station; SGMTH=station at mouth of bay).

and St. George's Bay are compared in Fig. 3.9. It is seen that the seiche activity levels in the two bays follow very closely the same changes in time, except in a few cases (such as on 17/7/96 and 2/9/96) when the sea level fluctuations in Mellieha Bay remain low. This implies that the seiche oscillations in these bays must be related to the same external forcing agent. If the bay oscillations are triggered by long period waves in the open sea the latter must thus be coherent at least within the range of distance (approximately 12Km) separating the two bays. Peak rms wave heights are on average twice as much in Mellieha Bay. The bays thus respond differently to the same forcing mainly due to the influence of local topography. The ratio of rms heights in the two bays is not however constant so that the relative response of the bays changes from one event to another, possibly in relation to the characteristics of the forcing (such as spatial coherence, incidence, etc).

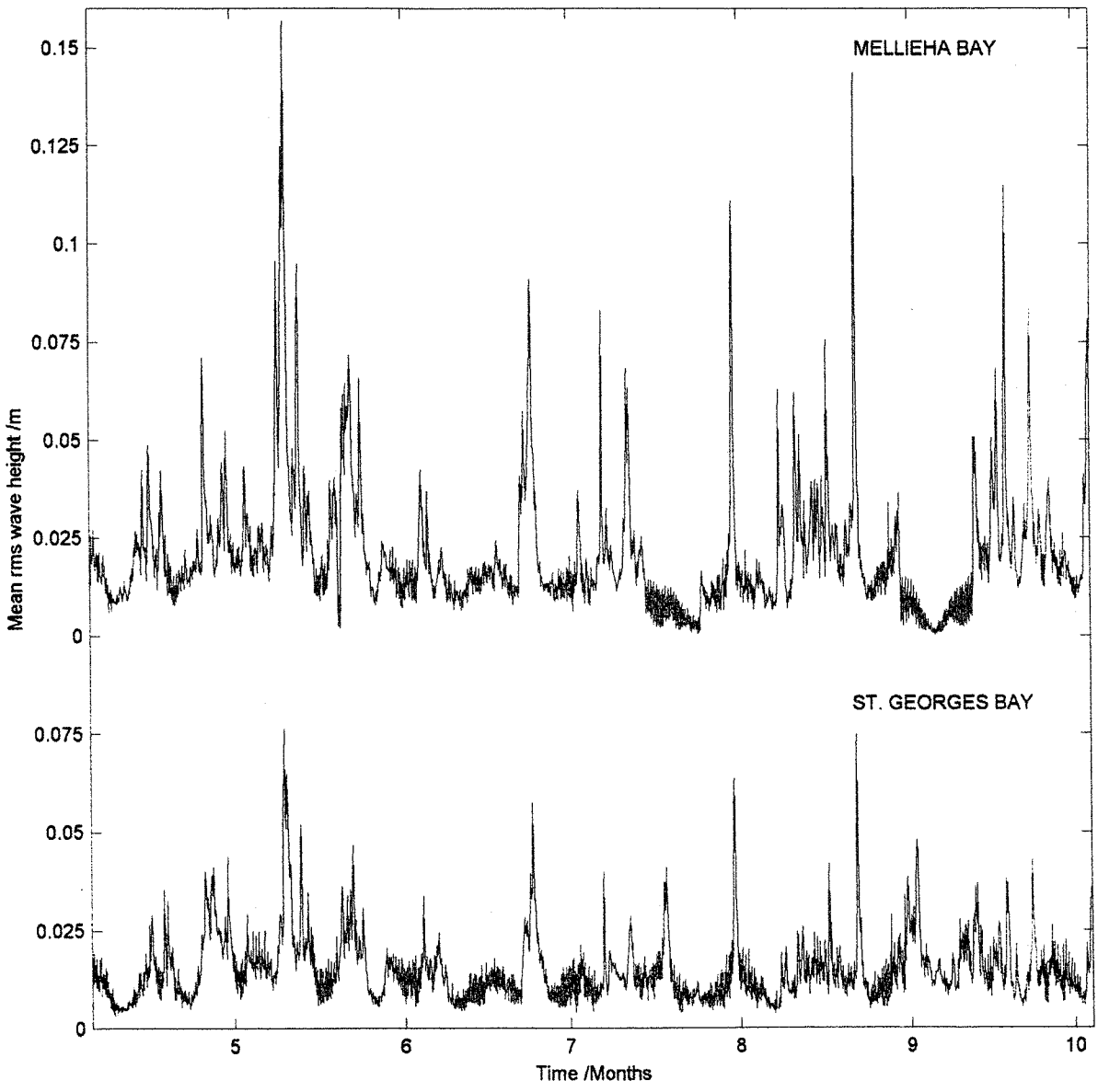

Fig. 3.9 Time series of mean rms seiche heights in Mellieha Bay and St. George's Bay during April - September 1996.

Correlation coefficients and regression ratios for different pairs of bays are estimated from scatter plots of the 2-hour time averaged rms wave heights (Fig. 3.10). These statistical estimates are summarised in Table 3.3. The correlation between Mellieha Bay and St. Paul's Bay is very high indicating a response of the two bays as a combined system. The difference in amplitudes reflects the different positions of the instruments within the respective bays.

Table 3.3 *Correlation and regression of rms seiche heights*

MELLIEHA BAY - ST. GEORGE'S BAY	r = 0.74	$\sigma_{ML} = 1.40\ \sigma_{SG}$
MELLIEHA BAY - ST. PAUL'S BAY	r = 0.97	$\sigma_{ML} = 1.53\ \sigma_{PL}$
MELLIEHA BAY - GRAND HARBOUR	r = 0.25	$\sigma_{ML} = 1.26\ \sigma_{GH}$

The correlation is also significantly high and the regression coefficients are sufficiently stable for Mellieha Bay and St. George's Bay. Although St. George's Bay is much smaller, the response of the bays is very similar. In particular, it is shown that although seiche heights are in general enhanced in elongated, narrow-mouthed and shallow inlets, the seiche can also be large in wide open-mouthed embayments. The estimates presented in Table 3.3 concern the whole data set. If estimates are repeated separately for low and high rms wave heights, it is found that for background oscillations ($\sigma_{ML} < 6$cm) r = 0.55 and $\sigma_{ML} = 1.23\ \sigma_{SG}$, whereas for the larger amplitude oscillations ($\sigma_{ML} > 6$cm) r = 0.80 and $\sigma_{ML} = 1.98\ \sigma_{SG}$. The relatively low correlation for background seiches is due to the occurrence of sea level fluctuations with high frequency components in St. George's Bay, during periods of calm in Mellieha Bay. The relative amplification of seiche oscillations in Mellieha Bay with respect to that in St. George's Bay is also higher during *'milghuba'* events compared to that during periods of background seiching. This implies that although the same mechanisms may apply for the generation of both background seiches and *'milghuba'* waves, supplementary mechanisms (such as due to the nonlinear interaction of wind waves) are in action in the smaller embayment which also faces a steeper bathymetry in the adjacent open sea area.

On the other hand the correlation with the Grand Harbour is low. During the short set of observations, the seiche is higher in the Grand Harbour on 23rd September, while it is subsequently higher in Mellieha Bay on the successive day. The sea level trace is also very smooth in the Grand Harbour when weak sea level oscillations are registered in Mellieha Bay. The available short data set does not allow a detailed analysis and it is not

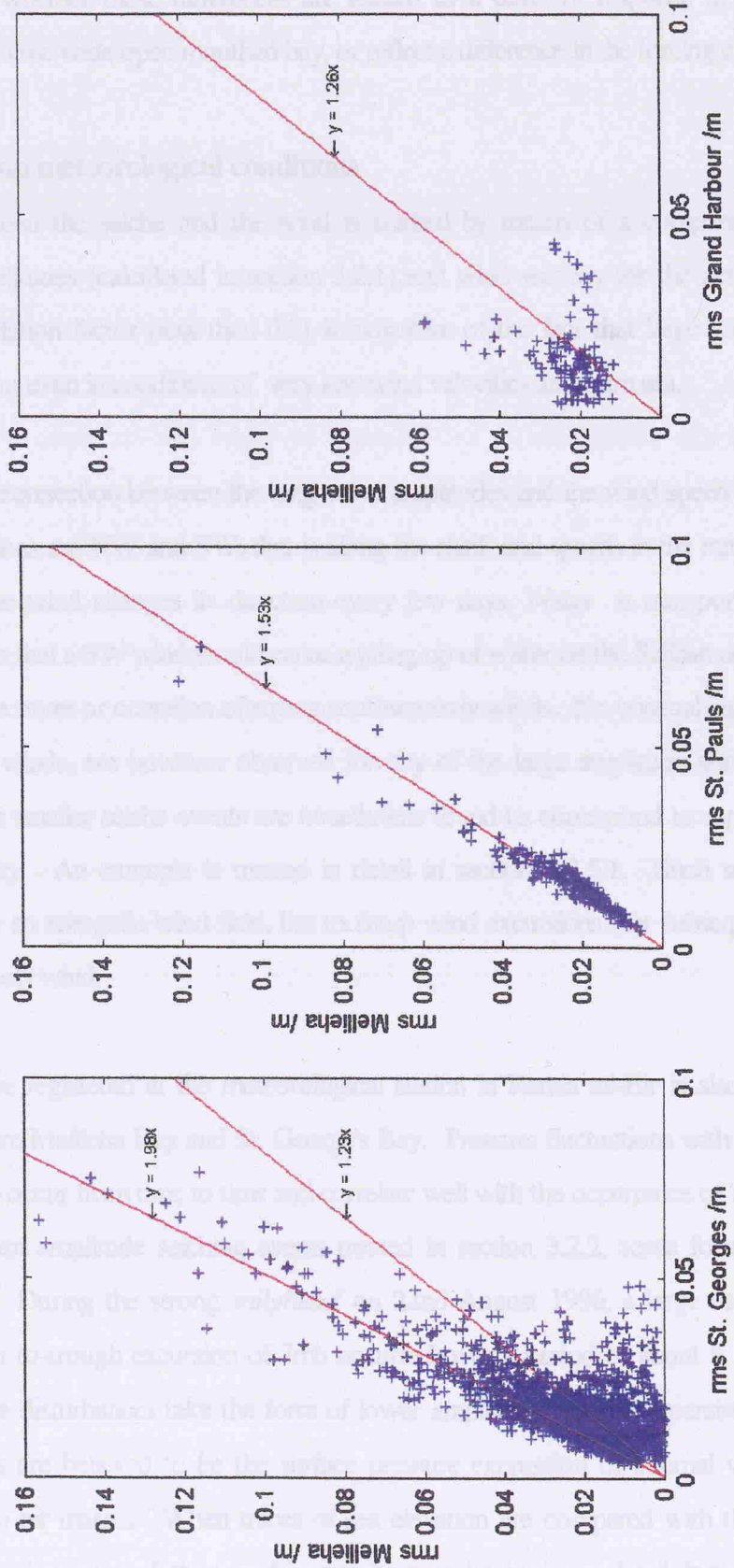

Fig. 3.10 Scatter plots of two-hour time-averaged rms seiche heights for various pairs of sea level stations. Regression lines are indicated in red.

possible to ascertain whether these differences are related to a different response of the narrow mouthed harbour with respect to the wide open mouthed bay, or reflect a difference in the forcing characteristics.

3.2.5 Dependence on meteorological conditions

The correlation between the seiche and the wind is studied by means of a comparative analysis between maximum seiche amplitudes (calculated in section 3.2.1) and wind velocity for the period June 1994 - June 1996. The low correlation factor (less than 0.2) is indicative of the fact that large amplitude oscillations in Mellieha Bay can occur even in conditions of very low wind velocities and calm sea.

There is no apparent connection between the long wave amplitudes and the wind speed or direction. The most common wind directions are NW and SW, that is along the shelf, and speeds in the range 7-10 ms^{-1} are quite usual. On average the wind changes its direction every few days. Water is transported to the right in the northern hemispere so that a SW wind would cause a piling up of water on the Sicilian coast. Oscillations might be associated with the onset or cessation of strong southwesterly winds. No unusual changes of this nature, or exceptionally strong winds, are however observed for any of the large amplitude seiche events discussed in Section 3.2.2. Some smaller seiche events are nonetheless found to correspond to rapid fluctuations in wind direction and intensity. An example is treated in detail in section 3.2.5.1. Such seiching events are not necessarily related to an energetic wind field, but to sharp wind excursions that subsequently veer to a steady easterly or southeasterly wind.

Atmospheric pressure registered at the meteorological station in Ramla tal-Bir is also compared with water elevation records from Mellieha Bay and St. George's Bay. Pressure fluctuations with amplitudes generally of the order of 1 - 2 mb occur from time to time and correlate well with the occurrence of *'milghuba'* events. In all the large and medium amplitude seiching events treated in section 3.2.2, some form of atmospheric wave activity is observed. During the strong *'milghuba'* on 22nd August 1996, a large oscillation in atmospheric pressure with a crest-to-trough excursion of 7mb occurred over a period of about 6 hours. More often the atmospheric pressure disturbances take the form of lower amplitude, but more persistent oscillations. These pressure fluctuations are believed to be the surface pressure expression of internal waves on the boundary surface between two air masses. When traces of sea elevation are compared with the pressure fluctuations observed in the same time interval, they are found to be completely uncorrelated, but periodicities of the same

order are present in both. The relation between these pressure perturbations and the occurrence of long period waves in the sea is treated in detail in Chapter 4.

3.2.5.1 Dependence on the wind field

The seiche event on 26/7/94 is taken as a case study to study the dependence of sea level oscillations in Mellieha Bay on the wind. The time series of water elevation (Fig. 3.11) shows that fluctuations reaching a maximum range of 33cm occur at 13:30GMT. Seiching during this time of the year is not very frequent, but when it occurs it is usually rather strong and of a short duration. Sea level oscillations in Mellieha Bay often occur in coincidence to large amplitude high frequency fluctuations of the atmospheric pressure. On this occasion the surface pressure observations do not however indicate any significant activity and the relation of this seiching event to atmospheric waves, at least locally, can thus be excluded. On the other hand, the wind vector during this day can be distinguished from the preceeding and subsequent days (when seiching is only at background values) and is characterised by sharp changes in both the wind direction and intensity (Fig. 3.12). The wind magnitude is not particularly strong although the measurements on land could very well underestimate the wind strength over the open sea areas. The seiche events do not thus seem to be related to an energetic wind field but rather to sharp rotations of the wind vector. The wind stick plot in Fig. 3.13 compares the rapid changes in the wind vector with the onset of seiche pulses which mainly occur at 04:30GMT, 10:30GMT, 13:00GMT, 16:30GMT and 21:00GMT. The 3rd and 4th seiche pulses have the largest amplitudes and occur in close coincidence to the two ESE wind gusts which are particularly evident from the E-W wind component time series plot (Fig. 3.12b).

The relation between the sea surface oscillations and the wind is studied in more detail by taking the running variance of sea elevation and the squared wind vector excursion $\left|\Delta\vec{W}\right|^2$ as diagnostics. The variance is calculated over a moving window of 21 records. The variance plot Fig. 3.14c indicates the variation of seiche intensity with time. The squared wind vector excursion is calculated by $\left|\vec{W}(t+\Delta t)-\vec{W}(t)\right|^2$ where $\vec{W}(t)$ and $\vec{W}(t+\Delta t)$ are the wind vectors at successive sampling times. This diagnostic can better follow the episodes of sharp changes in the wind since it takes both the wind direction and intensity into consideration and does not thus alert those changes in wind direction that occur during periods of slack. This diagnostic can either be calculated from the raw wind vector observations which retain the high frequency changes in the wind field, or

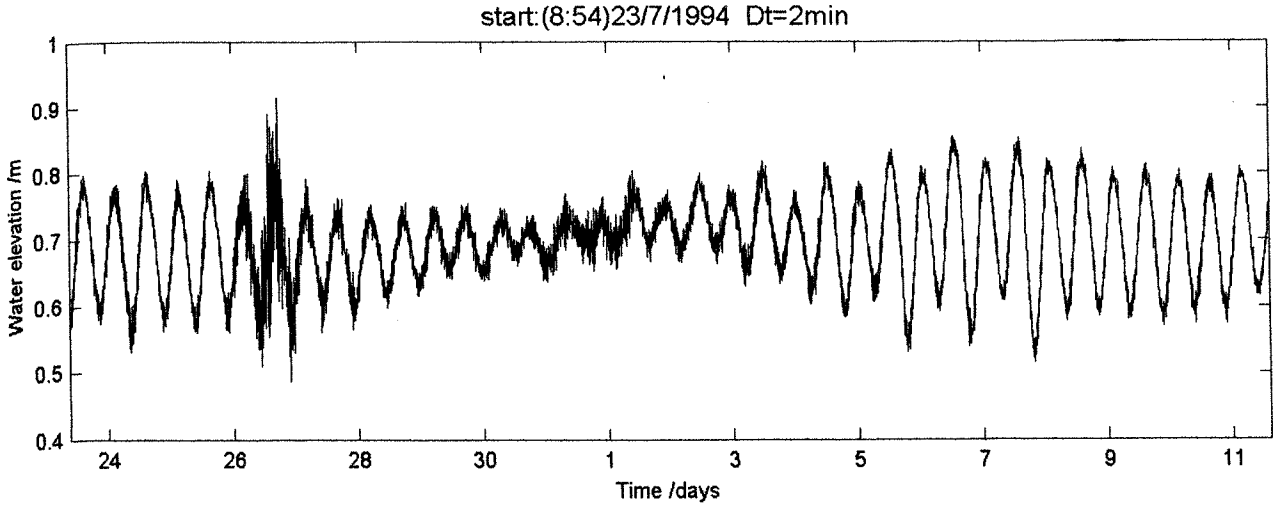

Fig. 3.11 Time series plot of sea level at the coastal gauge in Mellieha Bay from 08:54GMT 23rd July to 14:36GMT 11th August 1994.

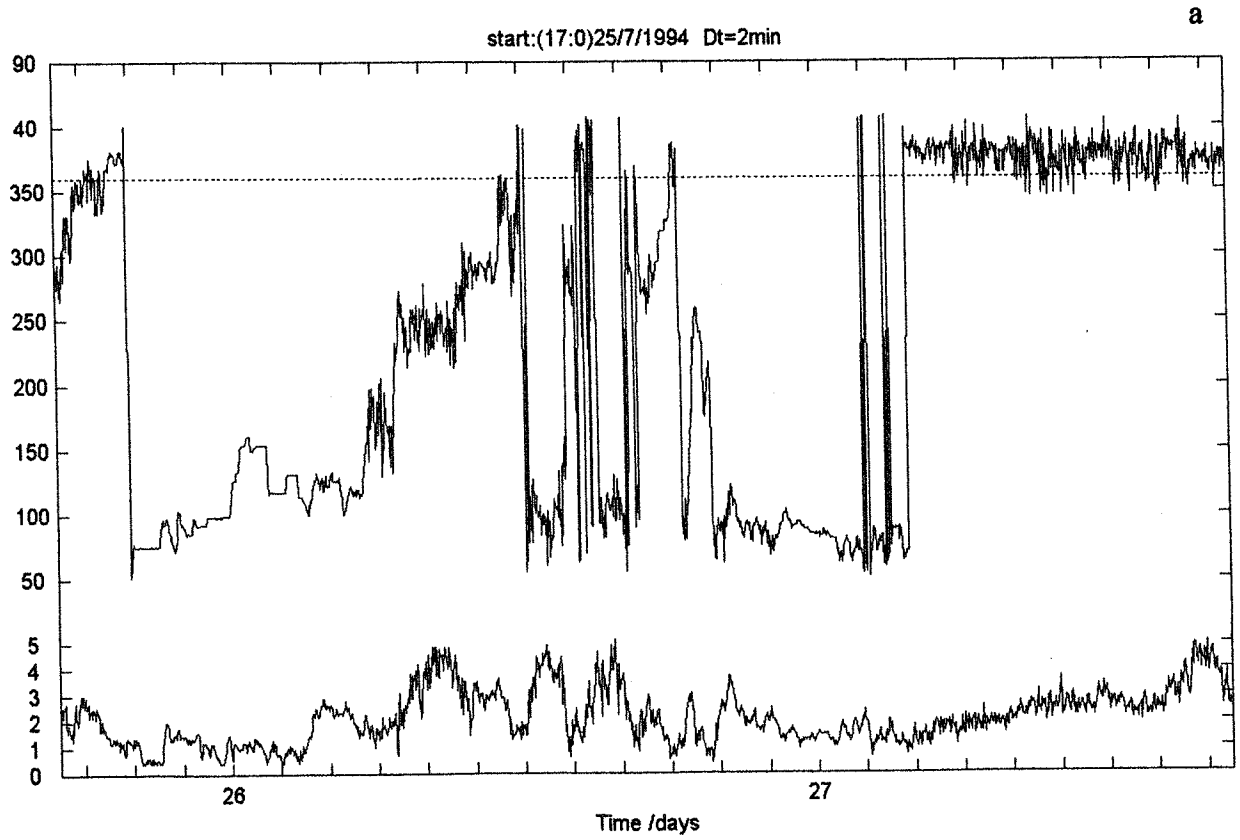

Fig. 3.12a Time series plot of 2-minute sampled measurements at Ramla tal-Bir Station of wind direction (in degrees with respect to North) and speed for the period 17:00GMT 25/7 - 17:00GMT 27/7/94.

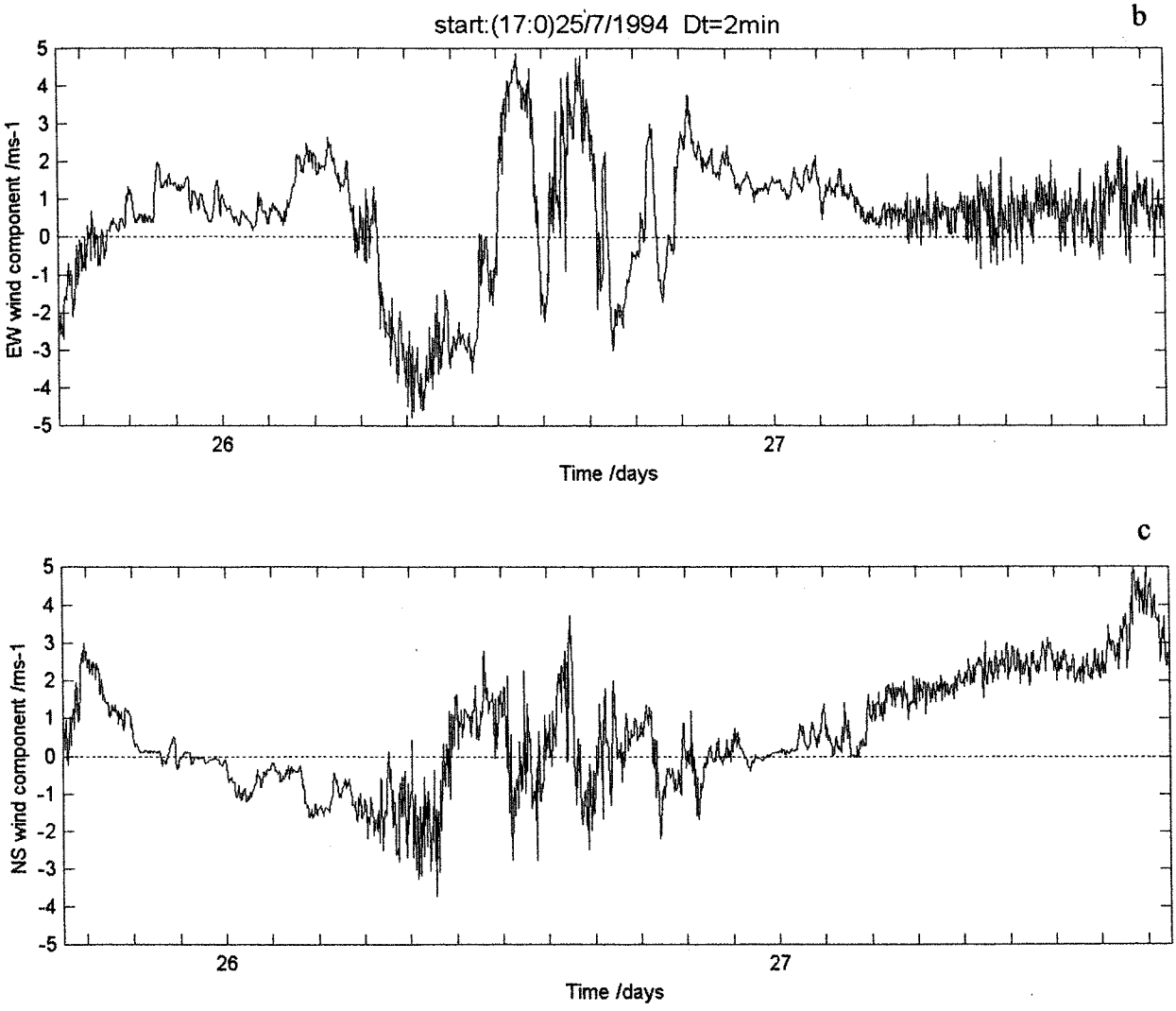

Fig. 3.12 b,c Time series plot of 2-minute sampled measurements at Ramla tal-Bir Station of East-West and North-South wind components for the period 17:00GMT 25/7 - 17:00GMT 27/7/94.

from the filtered wind vector series. The latter is obtained by filtering the E-W and N-S wind component series and subsequent recombination to produce the filtered wind direction and magnitude. The raw and the filtered square wind vector excursions are compared to the sea level variance in Fig. 3.14. The wind activity in the late morning of the 26th and on the 27th November is primarily turbulent in nature and does not coincide to an enhanced period of seiching. The sea level oscillations are thus not related to the turbulent fraction of the wind, but rather to the steady and sharp variations of the wind vector. The peaks in the filtered square wind vector

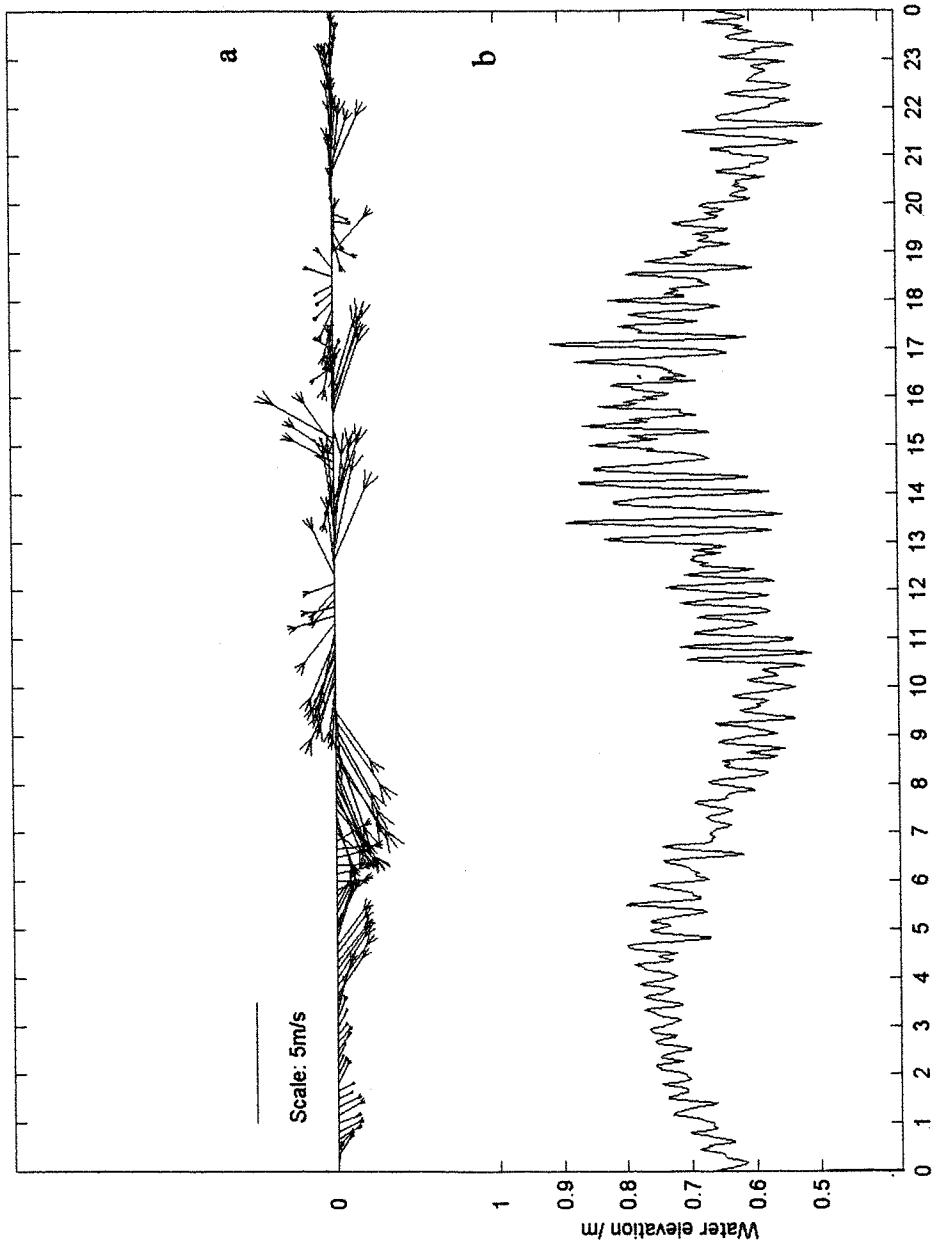

Fig. 3.13 Comparative plot of (a) 10-minute vector averaged wind sticks at Ramla tal-Bir, and (b) 2-minute sampled water elevation in Mellieha Bay during 26th July 1994.

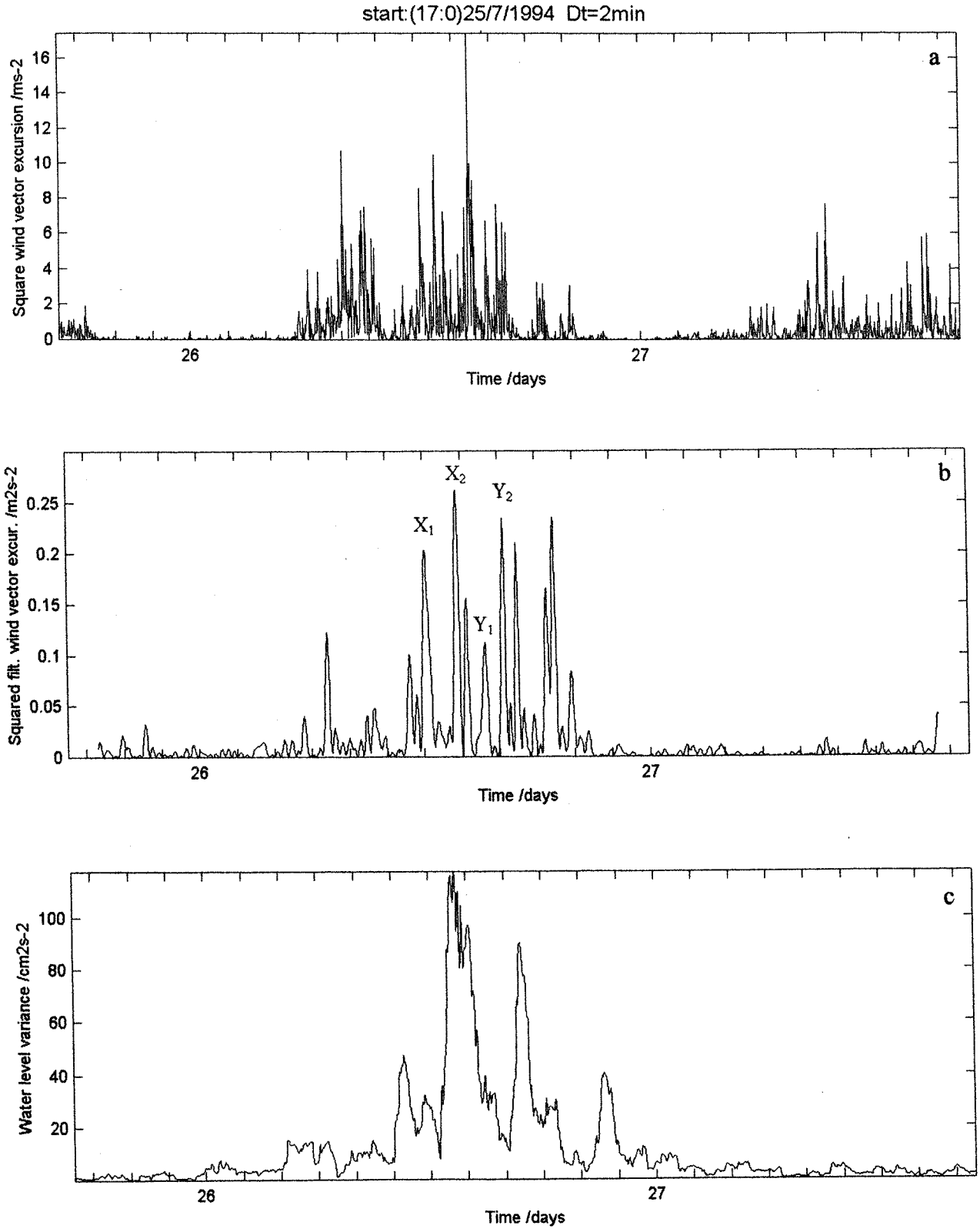

Fig. 3.14 Comparative plot of the (a) unfiltered and (b) low pass filtered squared wind vector excursions at Ramla tal-Bir with (c) the running variance of sea levels in Mellieha Bay during the period 17:00GMT 25/7 - 17:00GMT 27/7/94.

excursion indicate the occurrence of these consistent and sustained changes in the wind. They are certainly compatible to the enhanced period of sea level activity. In particular, peak X_1 indicates the rapid veering of the wind vector from WNW to ESE, and marks the onset of the first gust from ESE. After a slight period of slack wind, the subsequent ESE gust is indicated by the interval between peaks Y_1 and Y_2. The onset of the major seiche pulse at 13:00GMT occurs during the period between X_1 and X_2. On the other hand, the subsequent seiche intensification starting at 16:30GMT occurs after Y_2, that is after cessation of the ESE gust. It should however be pointed out that a simple relation between the local wind and the sea level activity is indeed unexpected since the wind will have a high variability in space especially close to the land. Measurements made from one observation point cannot thus represent the horizontal patterns of the wind field. The observations are however able to ascertain the dependence of the sea level oscillations on the supra-synoptic wind field variations.

3.2.6 Peaks analysis

3.2.6.1 Narrow band random processes

As described in Appendix 2, the probability distribution for the response of a linear time invariant system depends on the probability distribution of the excitation. The relationship is however by no means simple. There is no general method for obtaining the output probability distribution for a linear system except for the special case when the input probability distribution is Gaussian (Normal). If two random variables x_1 and x_2 are Gaussian, it is known that their sum $x = x_1 + x_2$ is then also Gaussian. This special property can be applied to show that the response y(t) of a linear system will be a Gaussian process if the excitation x(t) is Gaussian. The output of a linear system subjected to Gaussian inputs is therefore Gaussian and if the respective mean values, variances and covariances are known, the output probability distributions can be calculated by the probability density function $p(y) = \frac{1}{\sqrt{2\pi}\sigma_y} e^{-y^2/2\sigma_y^2}$.

For non-Gaussian processes the theory becomes much more complicated. This difficulty can however be surmounted if the system responds in such a manner that it has at least one resonant frequency at which large amplitudes are generated from small inputs. Such systems are not uncommon in nature and the resonating basin is one such example. The frequency response function $H(\omega)$ for such a resonant system transforms a broad band input signal into an output spectrum that is confined to a narrow band of frequencies in the vicinity of the

resonant frequency. The response is then a narrow banded random process and the output y(t) resembles a sine wave of slowly varying amplitude and phase. In such cases the system will approximate to a Gaussian response even though the excitation may not be Gaussian.

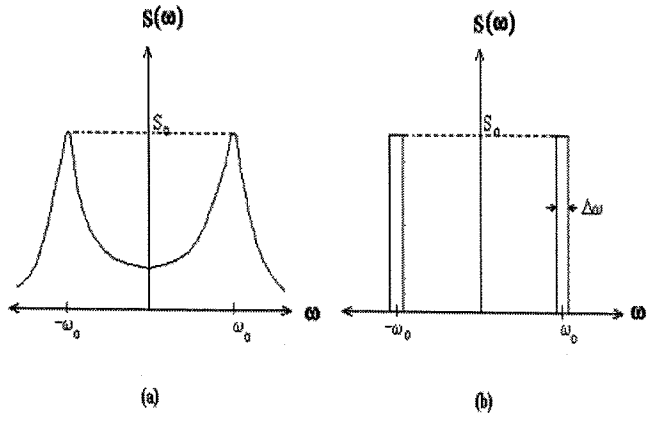

Fig. 3.15 Narrow band response of a resonant system (a) real; (b) idealised

Fig. 3.15a is a typical spectrum for a narrow banded process. This spectrum can be idealised into the form depicted in Fig. 3.15b with very sharp cut-offs above and below the resonant frequency. The idealised process includes only a very narrow band of frequencies $\Delta\omega$. If S_o is the peak spectral density, the variance is given by

$$\sigma^2 = \int_{-\infty}^{\infty} S(\omega)d\omega = 2S_o\Delta\omega \qquad (3.1)$$

For such a process the Rayleigh distribution can be applied to determine the probability distribution of peaks. The probability that any peak chosen at random, is greater than level a is

$$\text{Prob}\{\text{Peak value} > a\} = \int_a^{\infty} p(a)\mathrm{d}a \qquad (3.2a)$$

where $p(a) = \frac{a}{\sigma^2} e^{-a^2/2\sigma^2}$ is the Rayleigh probability density function. Hence

$$\text{Prob}\{\text{Peak value} > a\} = e^{-a^2/2\sigma^2} \qquad (3.2b)$$

The expected maximum peak value is approximated by

$$\langle a_{max} \rangle = \sigma\left\{\sqrt{2\ln(T/T_m)}\right\}, \text{ where } T_m = 2\pi\sqrt{\frac{\int_0^\infty S(\omega)d\omega}{\int_0^\infty \omega^2 S(\omega)d\omega}} \text{ is the mean period.}$$

If a_o is the median peak height for which the probability is 1/2, a_o can be expressed in terms of the variance by $a_o = \sigma\sqrt{2\ln 2}$. Upon substitution in (3.2b), we get

$$\text{Prob}\{(\text{Peak value}/a_o) > a/a_o\} = e^{-(\ln 2)(a/a_o)^2} \qquad (3.3)$$

3.2.6.2 The Weibull distribution

These equations pertain to a narrow band Gaussian process with very sharp and narrow frequency bands. The Rayleigh distribution strictly applies to cases where only one peak corresponds to each zero crossing. For a more general narrow band spectrum such as the one in Fig. 3.15a, the presence of high frequency components introduce irregularities in the smooth form of the sine wave approximation. The more general Weibull distribution of peaks, which is not based on a Gaussian assumption for the underlying narrow band process may then be more appropriate.

The Weibull distribution function is very similar to the Rayleigh distribution, but the exponent 2 in (3.3) is replaced by a constant k. Thus

$$\text{Prob}\{\text{Peak value} > a\} = e^{-(\ln 2)(a/a_o)^k}$$

$$\Rightarrow \ln[\text{Prob}\{\text{Peak value} > a\}] = -(\ln 2)(a/a_o)^k$$

$$\Rightarrow \ln[-\ln[\text{Prob}\{\text{Peak value} > a\}]] = \ln(\ln 2) + k\ln a - k\ln a_o \qquad (3.4)$$

Hence the slope of the graph $\ln[-\ln[\text{Prob}\{\text{Peak value} > a\}]]$ against $\ln a$ gives the Weibull exponent k.

3.2.6.3 Application to a statistical analysis of seiche excursions

A similar analysis can be applied to the sea water level excursions instead of the peaks in elevation. An excursion is here defined as the peak-to-peak difference in elevation which measures the vertical displacement in elevation between a maximum and a successive minimum or between a minimum and a successive maximum that are connected by a zero crossing. In both cases the excursion is taken to be positive. For a process that is statistically identical for both positive and negative displacements, it is appropriate to presume that the foregoing theory with regard to peaks applies equally well to excursions.

The statistical analysis on water level excursions described in the previous section is applied to several seiching events recorded in Mellieha Bay. The results are typified by the three cases in Fig 3.16a-c which treat a moderate amplitude and persistent seiche in (a), a relatively short duration resonant type seiche in (b), and a period of very weak seiching in (c). The straight line plots of ln[-ln[Prob{Excursion > a}]] against ln a confirm that the response of the bay close to its gravest mode approximates to a narrow banded process. There is however a distinct change in slope in the graphs which signifies that the characteristic Weibull exponent k depends on the magnitude of the seiching. Table 3.4 gives the general decrease of the mean Weibull exponent as we go towards stronger seiche events. The Gaussian assumption and the Rayleigh distribution can only approximate a medium sized seiche. As the seiche oscillations build up there is a distinct reduction in the value of k at $\ln(a) \approx 2.8$. The incidence of large excursions is then greater than that given by a Rayleigh distribution.

Table 3.4 *Classification of seiches by the Weibull exponent*

SEICHE EXCURSION	WEAK less than 5cm	MEDIUM between 5 and 17cm	STRONG more than 17cm
WEIBULL EXPONENT k	2.5 - 3	2 - 2.5	1 - 1.5

The probability density for the occurrence of large excursions is greater for the case when k is closer to 1 than when k=2 or higher (Fig. 3.17b). For the weaker oscillations the probability density function is closely centred symmetrically about the median value.

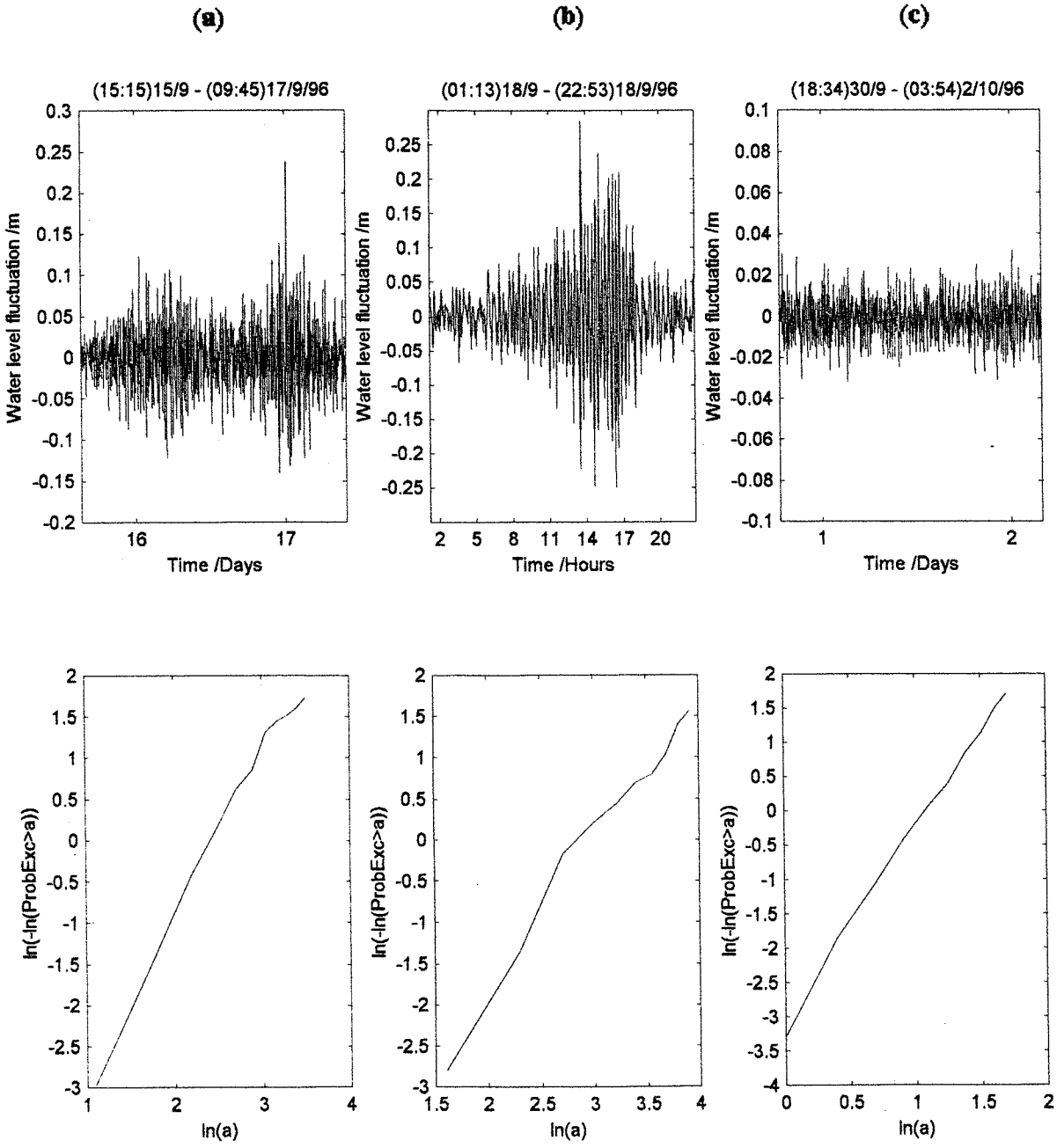

Fig. 3.16a-c Calculation of the Weibull exponent for three cases of sea level fluctuations in Mellieha Bay.

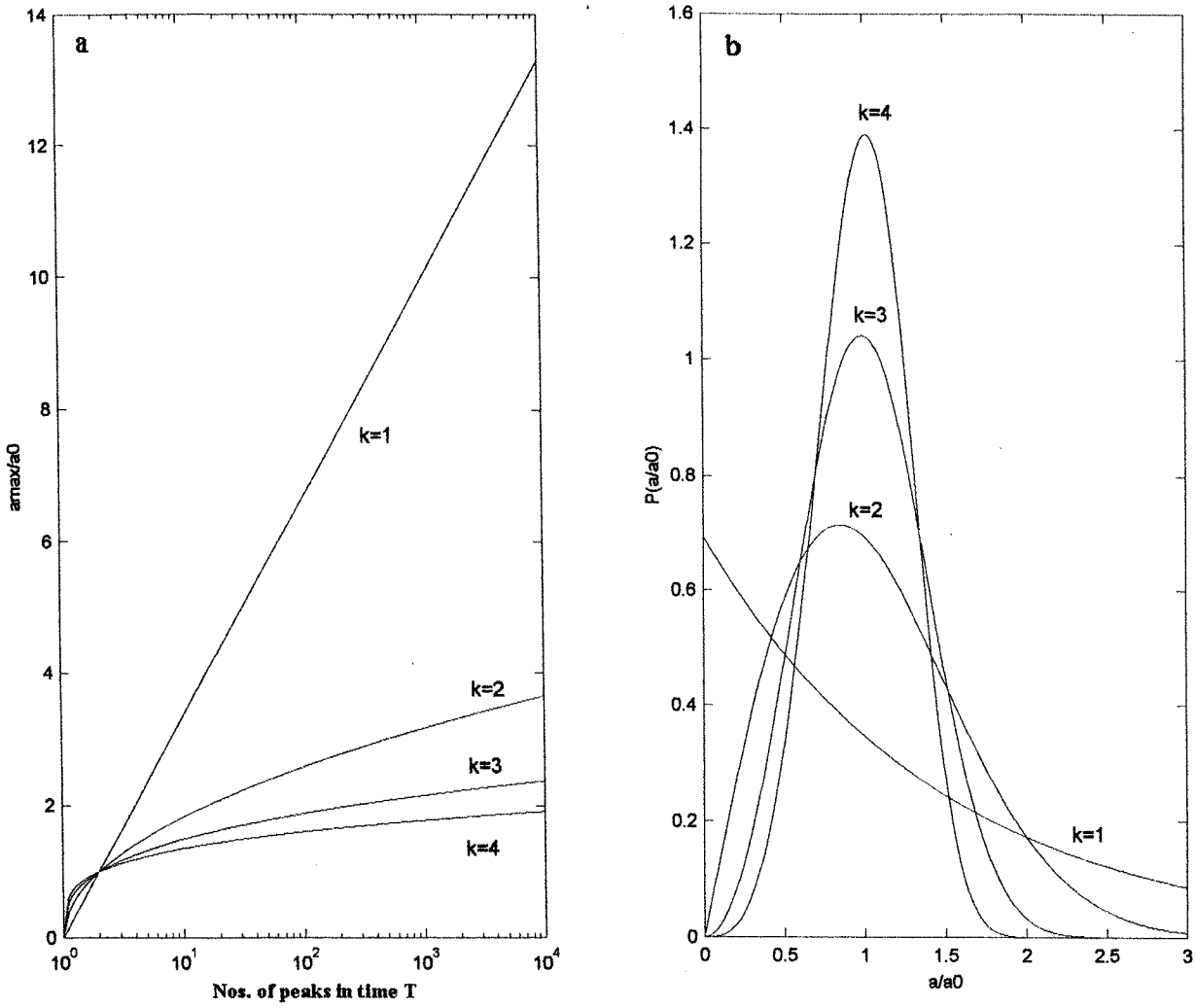

Fig. 3.17 (a) Plot of the ratio a_{max}/a_o against the number of excursions in time T and, (b) the Weibull probability density function ($P(a/a_o) = k\ \ln(2)\ (a/a_o)^{k-1}\ e^{-\ln(2)\ (a/a_o)^{k-1}}$) for different exponents k.

The highest excursion a_{max} that is expected in a given time extent T is a very useful estimate in practical cases. For any narrow band process in which there is one full cycle for every positive slope crossing of the zero axis and for which a Weibull distribution is applicable, a_{max} is given by:

$$\left(\frac{a_{max}}{a_o}\right) = \left\{\frac{Nos.\ of\ Excursions\ in\ time\ T}{\ln\ 2}\right\}^{1/k} \qquad (3.5)$$

Fig. 3.17a shows a plot of the relative maximum excursion a_{max}/a_o versus the number of excursions in a given time T (on a logarithmic scale) for several values of k. During weak seiching, when k is in the range between 2.5 and 3, only one peak in 100 is expected to exceed twice the size of the median excursion. The water level excursions in this case are all very similar in size. During a strong seiche event the smaller value of k signifies that the incidence is much higher, and one in about eight excursions is in this case expected to reach twice the median excursion.

3.3 A method to calculate normal modes of basin oscillations

The response of a water body to a disturbance can be numerically examined from a wave-theoretical approach in which the propagation of energy from an initial localised source is followed in both time and space. Such an approach leads to the computation of spectra at any location of the domain, which should match observations. The spatial characteristics of the basin oscillations, namely the location of nodes and peaks, is however better studied by means of a modal approach.

This method consists in calculating the normal mode solutions of an irregular basin with a variable depth by solving an eigen-equation that yields a discrete set of eigenperiods that are characteristic of the basin. The corresponding eigenvectors give the water height distributions and the spatial structure associated with each eigen-oscillation. The aim of this section is to apply this method to obtain the main natural periods and normal modes of oscillation of some coastal embayments along the perimeter of the Maltese Islands. This knowledge is important in understanding the behaviour of long waves in coastal regions.

3.3.1 General introduction to the calculation of normal modes of oscillation

For embayments and harbours of regular shapes the natural frequencies can be obtained by means of analytic techniques. For the most simple cases of elongated orthogonal basins with constant depth, Merian's formula (Defant A., 1961) can be used. For oblong basins with variable width and depth, complete theoretical investigations have been proposed by Chrystal G.(1904, 1905), Hidaka K. (1936), Defant A. (1961) and Proudman J. (1914); such cases are treated by 1-D models and with the assumption that the oscillations have no horizontal cross-components so that the motion of the water is always parallel to the axis along the 'talweg' of

the basin. The impedance theory of Neumann extended these considerations to cases where an irregularly shaped basin can be considered as a 'parallel' and/or 'series' combination of canals.

For basins with real topography numerical techniques have to be adopted. Theoretical analysis of two-dimensional bay oscillations in the case of simple geometries and uniform depths are given, among others, by Ippen & Goda (1963), Carrier et al., (1971) and Momoi (1970). Loomis (1966) and Hwang & Tuck (1970) have proposed numerical methods for bays with an arbitrary shape. Platzman (1975) applied the resonance iteration method to calculate the normal modes of Lake Superior and the Gulf of Mexico. This was superceeded by a computationally more efficient method, based on the Lanczos process, which was applied to the Atlantic and Indian Oceans. More recently Rabinovich & Levyant (1990) proposed a method based on the numerical conformal mapping of a basin with complex geometry onto a circle or ring and subsequent solution of the eigenvalue problem by the Ritz method. This method has been successfully applied to compute the theoretical seiches in Malokurilskaya Bay in Shikotan Island. It has also been generalised for the case of rotating water bodies with application to the Caspian Sea (Levyant & Rabinovich, 1994).

In this study a simpler finite difference method is proposed. This method is well suited to study the oscillations in basins of arbitrary shapes provided that the size of the grid cells can resolve its geomorphological details. The method consists in numerically solving the Helmholtz equation in the given domain by applying an implicit centered second order finite difference scheme and transforming it into an eigenvalue problem. After transformation of the eigenmatrix into Hessenberg form, it is subsequently solved by the QR method.

The earth's rotation is not taken into account since the applications concern small basins with natural periods of just a few minutes. For convenience, frictional stresses at the boundary bottom and sloping surfaces are also removed. This may lead to an underestimate of the periods of the higher modes which are related to oscillatory motions in the shallow parts of the basins.

3.3.2 Governing equations

The amplitude of long waves is usually small compared to wind waves. They normally have a height (i.e. double amplitude) of just a few tens of centimetres. Their small relative depth (ratio of water depth to wavelength) ensures that the vertical acceleration of water particles is negligible compared to the gravitational acceleration,

and the curvature of the trajectories of water particles is small. Consequently the vertical motion of water particles has no effect on the pressure distribution and the hydrostatic assumption is valid. The shallow water theory can thus be applied. The long wave equations of motion are:

$$\partial u/\partial t + u\partial u/\partial x + v\partial u/\partial y - fv = -g\partial \eta/\partial x + \nabla_H.\left(K_H \nabla_H u\right) + \partial/\partial z\left(K_M \partial u/\partial z\right)$$

$$\partial v/\partial t + u\partial v/\partial x + v\partial v/\partial y + fu = -g\partial \eta/\partial y + \nabla_H.\left(K_H \nabla_H v\right) + \partial/\partial z\left(K_M \partial v/\partial z\right) \quad (3.6)$$

in which, $\nabla_H \equiv \partial/\partial x + \partial/\partial y$, η is the water elevation referred to the still water level and with plane coordinates (x,y), $\underline{u} = (u, v, w)$ is the velocity field, g is the acceleration due to gravity, f is the Coriolis parameter, K_M and K_H are the vertical and horizontal eddy viscosity functions.

The dimensions of both K_M and K_H are L^2T^{-1}. Hence $o[K_H] \propto o[L].o[u]$ and $o[K_M] \propto o[H].o[u]$ where L and H are the horizontal and vertical flow field dimensions. Since $o[L] >> o[H]$, then $o[K_M] << o[K_H]$. The orders of magnitude of the horizontal and vertical momentum diffusion terms can now be compared:

$$o\left[\partial/\partial x\left(K_H \partial u/\partial x\right)\right] \propto o[L].o[u]^2/o[L]^2 \propto o[u]^2/o[L];$$

$$o\left[\partial/\partial z\left(K_M \partial u/\partial z\right)\right] \propto o[H].o[u]^2/o[H]^2 \propto o[u]^2/o[H]$$

so that the second expression dominates. The horizontal momentum diffusion terms in (3.6) can thus be neglected.

The horizontal velocity of water particles can be assumed to be uniform over the depth with steep gradients developing only near the seabed. This permits the simplification of the equations into a 2-dimensional version by integrating vertically. The depth averaged velocity $(U, V) = \frac{1}{(H+\eta)} \int_{-H}^{\eta} (u, v)\, dz$, where H(x,y) is taken to be the depth. Upon integrating the equations of motion (1), we obtain:

$$\partial U/\partial t + U\partial U/\partial x + V\partial U/\partial y - fV = -g\partial \eta/\partial x - F/H$$

$$\partial V/\partial t + U\partial V/\partial x + V\partial V/\partial y + fU = -g\partial \eta/\partial x - G/H \quad (3.7)$$

where (F,G) are the components of the frictional force acting on unit surface.

The equation of continuity is:

$$\partial \eta / \partial t + \partial HU / \partial x + \partial HV / \partial y = \text{forcing terms} \qquad (3.8)$$

The forcing terms can take the form of $\frac{\partial \eta_b}{\partial t}$ in the case of a tsunamogenic source, with $\eta_b(x, y, t)$ referring to sea bottom deformation. Alternatively the forcing can result from atmospheric pressure fluctuations in the form $\frac{1}{\rho g}\frac{\partial P}{\partial t}$, where P is the atmospheric pressure and ρ is the density of air.

If the velocity in the bottom boundary layer is assumed to follow a logarithmic decay, the bed friction can be formulated upon a quadratic dependence of bottom drag according to

$$\frac{\kappa \underline{U}|\underline{U}|}{H+\eta} \qquad (3.9)$$

where $\kappa = g/C^2$ is the bottom friction coefficient expressed in terms of the Chezy bed friction coefficient C. The bottom friction coefficient is related to the more familiar Manning's roughness parameter $n = \sqrt{\kappa\ (H+\eta)^{1/3}}$.

In cases where η / H is sufficiently small, the denominator in (3.9) can be approximated by $H(1+\eta / H) \approx H$. The friction term can thus be expressed in the linearised form $r\underline{U}$, where the linear friction coefficient r is a suitable average in space and time of $\frac{\kappa|\underline{U}|}{H+\eta}$.

The equations of motion can be further simplified by removing the non-linear terms. These terms do not contribute directly to the modification of the original harmonics; they however create net displacements out of oscillatory ones and double interactions.

If the variation in time of the free surface is assumed sinusoidal so that the time t can be eliminated by introducing $e^{i\sigma t}$, equations (3.7) and (3.8) become:

$$\begin{aligned} KU - fV + g\eta_x &= 0 \\ fU + KV + g\eta_y &= 0 \\ i\sigma\eta + (HU)_x + (HV)_y &= \text{forcing terms} \end{aligned} \qquad (3.10)$$

where $i\sigma + r = K$ and the derivation with respect to x and y is indicated by their indices. By eliminating U and V, we obtain the differential equation for η

$$(gH\eta_x)_x + (gH\eta_y)_y + \frac{gf}{K}(\eta_y H_x - \eta_x H_y) - i\sigma\frac{(f^2 + K^2)}{K}\eta = \text{forcing terms} \qquad (3.11)$$

This equation can be solved in a given domain Γ, when the vertical displacement η or the normal components of the velocity are given for an arbitrary line of demarcation. In the case of a semi-enclosed domain, this line of demarcation separates the basin from the adjacent open sea.

In cases where the extent of the domain is small the Coriolis effect can be dropped. In seeking the free periods of the basin (forcing terms = 0) with no friction (r = 0) so that $K = i\sigma$, and assuming that the free surface elevation follows a simple trigonometric variation in time $\eta = Ae^{i\sigma t}$, we obtain what is known as the Helmholtz equation:

$$\frac{\partial}{\partial x}\left[gh\frac{\partial A}{\partial x}\right] + \frac{\partial}{\partial y}\left[gh\frac{\partial A}{\partial y}\right] + A\sigma^2 = 0 \qquad (3.12)$$

where $A(x, y)$ gives the amplitude of oscillation at the point (x, y).

3.3.3 Boundary conditions

The solution must satisfy certain boundary conditions along the perimeter of the domain. The eigenperiods of the lower modes depend significantly on the boundary conditions adopted. At a coastal boundary $h\frac{\partial A}{\partial n} = \frac{i\sigma}{g} q_n$, where n is the unit vector normal to the boundary and directed into the domain and q_n is the normal influx through unit width of the boundary (taken as zero in this case). At an open boundary, a

radiation condition should ideally be applied. However this condition cannot be easily incorporated in the eigenvalue problem (Geller et. al. 1985). At an open boundary the formation of nodes is assumed so that the eigenvector and the water height are zero ($A = 0$).

3.3.4 Finite difference formulation and solution

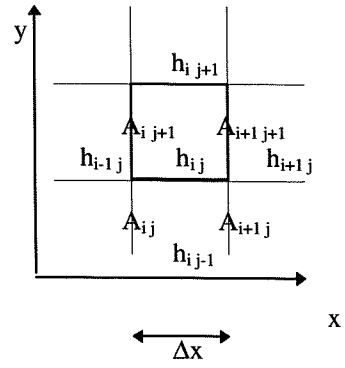

Fig.3.18 Computational molecule

In order to solve the problem, the domain with any complex geometry is divided up into a number of small square grid cells of size Δx; by using an implicit centered second order scheme, the Helmholtz equation is transformed into a finite difference form in which the depth h(i, j)is specified at the centre of each cell and the wave amplitudes $A_\Gamma(x,y)$ corresponding to the Γ mode of oscillation are defined at the grid nodes (i, j). For the grid node (i, j), the Helmholtz equation gives:

$$A_{i+1\,j}\left[\frac{h_{i\,j}+h_{i\,j-1}}{2}\right]+A_{i\,j+1}\left[\frac{h_{i\,j}+h_{i-1\,j}}{2}\right]+A_{i\,j-1}\left[\frac{h_{i\,j-1}+h_{i-1\,j-1}}{2}\right]$$
$$+A_{i-1\,j}\left[\frac{h_{i-1\,j}+h_{i-1\,j-1}}{2}\right]-A_{i\,j}\left[h_{i\,j}+h_{i-1\,j-1}+h_{i-1\,j}+h_{i\,j-1}\right]=\lambda_\Gamma A_{i\,j} \qquad (3.13)$$

where $\lambda_\Gamma = -\sigma_\Gamma^2\Delta x^2/g = -(4\pi^2\Delta x^2)/(gT_\Gamma^2)$ is the eigenvalue corresponding to the mode of oscillation with period T_Γ. For each mode there are N such equations, N being the number of internal grid points. This set of equations connects the N unknown wave amplitudes $A_{i\,j}$ which can be conveniently renumbered as A_n with node number n=1,N.

The resulting coefficients matrix M has dimensions NxN and satisfies the eigenvalue equation $MX = \lambda X$ which is subsequently solved to give for each mode Γ, the eigenvalue λ_Γ and the eigenvector $\{A_{1\Gamma}, A_{2\Gamma}, \ldots\ldots A_{N\Gamma}\}$ corresponding to the mode.

The EISPACK routines are used to convert the real matrix M to Hessenberg form by successive unitary (orthogonal) similarity transformations. The eigenvalues and eigenvectors are found by the QR-method.

This is currently the preferred computational technique for matrix eigenproblems. The QR-method was introduced in the early 1960s (Francis, 1961,1962) and has been studied extensively since then. It is an iterative method which produces a sequence of matrices that have the same eigenvalues as the original matrix. The limit of this sequence is a matrix whose structure yields an easy evaluation of the eigenvalues. The eigenvectors of the original matrix are derived from the final matrix of the sequence by utilising the recorded successive matrix members in the iteration process.

A basic notion in this iterative method is that of a similarity transformation, which for any (n x n) matrix M, is given by the correspondence $M \rightarrow P^{-1} MP$, where P is an n x n nonsingular matrix. If $Q = P^{-1} MP$, then Q and M are similar and for an eigenpair $(\lambda, \underline{x})$ of M, then $(\lambda, P^{-1}\underline{x})$ is an eigenpair for Q so that a similarity transformation preserves eigenvalues while eigenvectors are easily related. If P is unitary ($P^{-1}=P'$, the conjugate transpose) we have what is called a unitary similarity transformation; furthermore, if P is real and unitary the transformation is orthogonal.

By Schur's Theorem (Stewart 1973), for any arbitrary (n x n) matrix M (complex or real) there exists a unitary matrix P such that P'MP is upper triangular. This is the basis of the QR-method which applied to a complex matrix M produces, by means of unitary similarity transformations, a sequence of similar matrices which converge to an upper triangular matrix U. The eigenvalues of M are the diagonal elements of U; the eigenvectors are obtained by using the eigenvalues, U ,and the set of intermediate similarity transformations.

3.3.5 Amplitude of horizontal water movement

The particle velocity components at a specified location (x,y) in the domain are:

$$u = \frac{\partial \xi_{(x)}}{\partial t} \qquad v = \frac{\partial \xi_{(y)}}{\partial t} \tag{3.14}$$

where $\xi_{(x)}$ and $\xi_{(y)}$ are the particle displacements in the x- and y- directions respectively.

Now from eq. 3 with f=0 and β =0, combined with (3.14) we obtain

$$i\sigma \frac{\partial \xi_{(x)}}{\partial t} = -g\frac{\partial [A(x,y)\text{Cos } \sigma t]}{\partial x}$$
$$i\sigma \frac{\partial \xi_{(y)}}{\partial t} = -g\frac{\partial [A(x,y)\text{Cos } \sigma t]}{\partial y} \qquad (3.15)$$

which, upon integration over a suitable time interval, gives

$$\xi_{(x)} = \frac{g}{\sigma^2}\frac{\partial A}{\partial x} \qquad \xi_{(y)} = \frac{g}{\sigma^2}\frac{\partial A}{\partial y} \qquad (3.16)$$

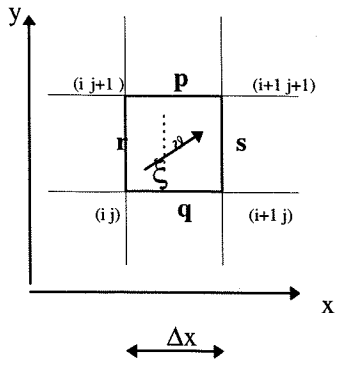

Fig. 3.19 Calculation of horizontal displacements

The displacements ($\xi_{(x)}$, $\xi_{(y)}$) are evaluated at the centre of each grid cell. In the case of the x-component, the finite difference formulation of the gradient on the right-hand side of (3.16) is first obtained at p and q respectively, from the vertical amplitudes at the nodes; the displacement at the grid cell centre is given as an average of the values at p and q.

$$\xi_{(x)} = \frac{g}{2\sigma^2}\left\{\frac{(A_{i+1\,j+1} - A_{i\,j+1})}{\Delta x} + \frac{(A_{i+1\,j} - A_{i\,j})}{\Delta x}\right\} \qquad (3.17a)$$

Similarly in the case of the y-component:

$$\xi_{(y)} = \frac{g}{2\sigma^2}\left\{\frac{(A_{i\,j+1} - A_{i\,j})}{\Delta y} + \frac{(A_{i+1\,j+1} - A_{i+1\,j})}{\Delta y}\right\} \qquad (3.18b)$$

and the magnitude and orientation of ξ is given by:

$$|\xi| = (\xi_{(x)}^2 + \xi_{(y)}^2)^{1/2} \qquad \vartheta = \tan^{-1}\left(\frac{\xi_{(x)}}{\xi_{(y)}}\right) \qquad (3.19c)$$

3.3.6 Implementation of the method

The array elements of the Helmholtz matrix M are assigned by means of a FORTRAN code which was written as part of this work. The program reads the geometry of the domain from an input file which contains information on:

- lateral domain boundaries defined for grid cells and internal grid nodes;
- bathymetry expressed as the value equal to the interpolated depth at the centre of a grid cell;
- information on the boundary grid points.

A perimeter with any number of open/closed curved boundary segments is allowed. The condition of full reflection at a coastal boundary is expressed at a fictitious coastal point (such as p in Fig. 3.20) just outside the domain according to the relation $A_p = A_s = A_q + (A_r - A_q)L / \Delta x$.

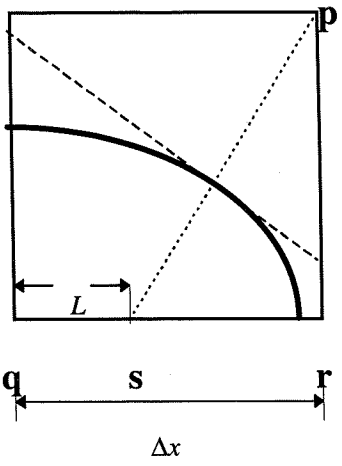

$$A_p = A_s = A_q + (A_r - A_q)L / \Delta x$$

Fig. 3.20 Reflection condition at a curved coastal boundary

The solution of the eigen-problem and the post-processing of the solution is made in the MATLAB environment. A number of M-files were developed in MATLAB to:

- read and solve the eigenmatrix,
- select and plot eigenvectors.

In plotting mode, the program allows choice from several options including:

(1) plotting coloured contour maps of elevation with a colourbar that assigns shades of blue/red to -ve/+ve elevations;

(2) plotting of elevation vs distance along any chosen transect;

(3) plotting of 2D/3D elevation maps filled with coloured flat shading according to a chosen colourbar;

(4) display of displacements superimposed over either contour plots or the meshed grid of the domain.

3.4 Eigenoscillations of small coastal embayments

The method described in the previous section is first applied to a rectangular embayment in order to test the validity of the calculations against analytical values. The method is subsequently used on four embayments on the northern coastal stretch of Malta. These are Mellieha Bay, St. Paul's Bay, St. George's Bay and the Grand Harbour (Fig. 3.8). The Grand Harbour is used as a test case in order to verify the skill of the method in calculating the eigenperiods of highly irregular shaped domains.

3.4.1 Bathymetry

No digitised bathymetry of the Maltese coastal sea exists except for the major harbours. The detailed bathymetry of the embayments and adjacent sea area was thus translated in digital form by means of a hand digitiser. This was carried out as part of this work and consisted in the digitisation of more than 15,000 sounding points. The data was obtained from survey maps supplied by the UK Hydrographic Office. The maps contain very dense soundings made in the period 1955-57 during two surveys made by Commander J.T.K Paisley and Lieutenant J.D. Winstanley on board of HMS Dalrymple. In the case of the Grand Harbour, modifications due to dredging and land reclamation in some areas is taken into account. This does not however include changes in connection with the extension of the cruise liner quay at Pinto Wharf.

3.4.2 Description of the embayments

Mellieha Bay and St. Paul's Bay (Fig. 3.8a) are two bays with an average areal extent of 5Km^2 each. The two bays have an along-axis northeastern alignment and consist of a valley-shaped sea-bed morphology with a sloping bathymetry that comprises relatively shallow areas in the inner region and maximum depths of 30m at the mouth. The bays are considered both as separate entities as well as a coupled system. The sea depth continues to increase in the open sea area adjecent to the bays, but shallows again to a minimum of about 20m over White Bank to the north of Mellieha Bay.

St. George's Bay (Fig. 3.8c) is a much smaller inlet with an axial length just under 1Km. Its along-axis direction faces approximately east. The coastal configuration is close to rectangular with a width at the mouth approximately half the bay length. The depth increases gently to about 20m at the mouth and continues to increase outside.

The Grand Harbour (Fig. 3.8b) is a narrow northeasterly oriented channel, about 3 Km long and cutting approximately perpendicular to the northward facing coastline of the island of Malta. It has a complicated coastal configuration with a curved extension at the head and a number of creek ramifications along one side of the main channel. Dredging and coastal constructions including quays, wharfs and docks have altered both its natural shape and its bathymetry such that uniformity in depth, (averaging to less than 20m) and steepness of its

edges have become more accentuated. The harbour is protected at its mouth by a breakwater so that it presents a case of a water body with a narrow connection to the open sea.

3.4.3 Application to a rectangular embayment

A simple embayment with a rectangular coast (4Km x 2Km), uniform depth (20m) and open at one of the shorter sides is taken as an example to compare the derived eigenperiods with known theoretical values. The closed boundaries are described by grid cells with a central depth set equal to zero. A node is imposed at the open end by setting zero wave amplitudes along the extreme edge of the domain. The example is used with several grid cell sizes. The calculated eigenperiods approach asymptotically the theoretical values as the grid resolution is increased. As expected, the greatest effect is on the gravest mode. At a grid cell size of 50m the gravest mode period is within 1.5% of the theoretical value. At double the grid size the difference is close to 6%. The main reason for this is that the effective position of the boundaries cannot be determined better than half the grid size. The grid size thus limits the accuracy to which the actual dimensions of the embayment can be expressed as a finite number of grid cells. This restriction is superceeded by utilising a sufficiently high resolution.

3.4.4 Test case on the Grand Harbour

The method is here applied to the Grand Harbour which is discretised into grid elements with a size of 40m. The outermost part of the breakwater at its mouth is assumed to be connected to the mainland so that the secondary opening of the breakwater is ignored. An area slightly beyond the mouth of the harbour is included in order to account for the misalignment of the two breakwater arms.

The principal eigenperiods and corresponding eigenvectors are plotted in Fig. 3.21. The eigenperiods are listed in Table 3.5. In these figures the spatial description of each eigenvector field is shown by contours joining points of equal amplitude. Prior to contouring, the amplitudes are normalised separately for each subplot. The colourbar used in the contour plots ranges from deep red (normalised height = +1) to deep blue (normalised height = -1).

Table 3.5 *Eigenperiods of the normal modes of oscillation in the Grand Harbour*

Mode	0	1	2	3	4	5	6	7	8	9	10	11
Period /minutes	22.9	10.4	7.3	6.3	5.4	4.2	4.0	3.3	3.1	3.0	2.6	2.5

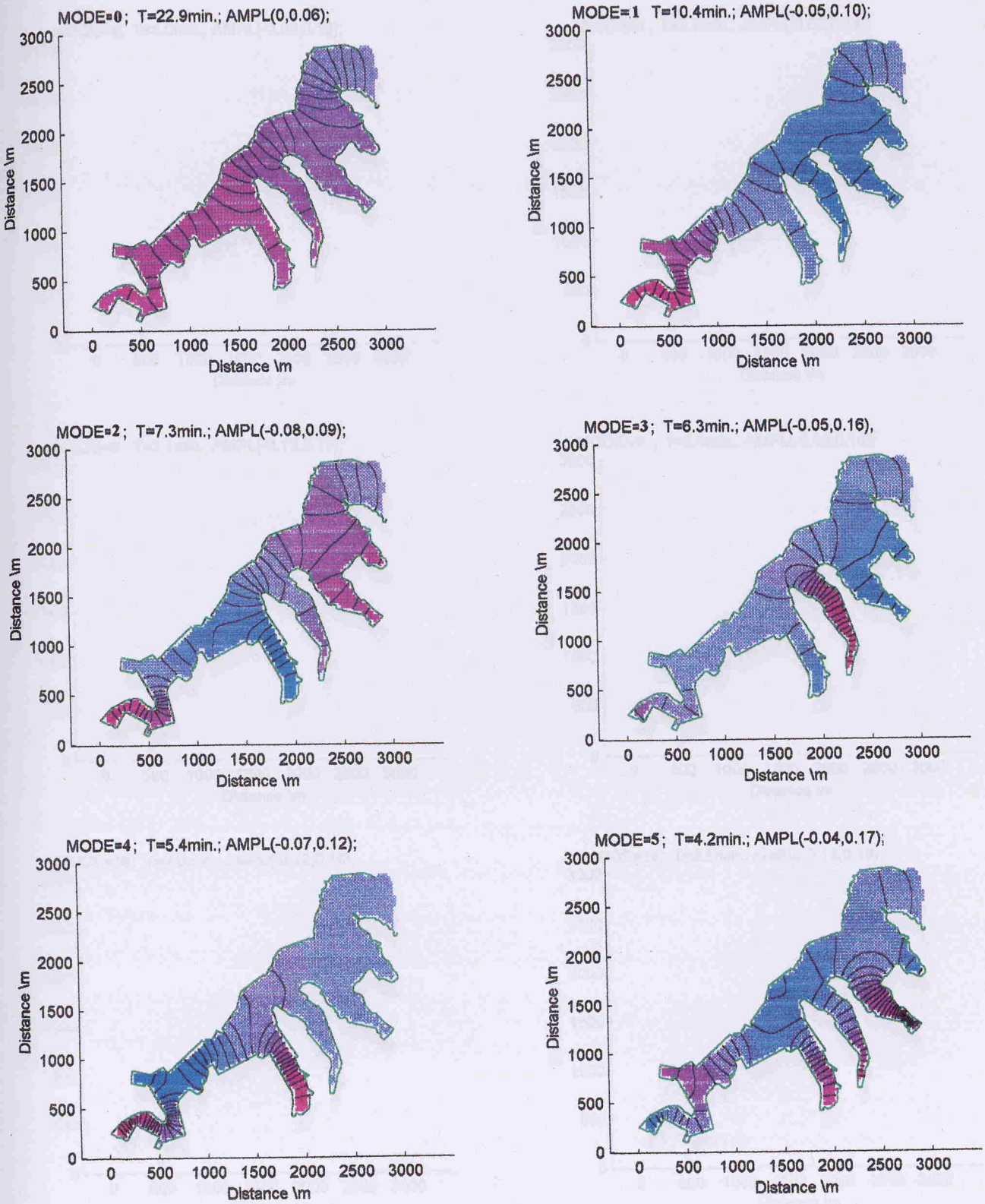

Fig. 3.21 Contour plots of eigensolutions for the Grand Harbour.
Contours join points with equal eigenvector amplitudes and are plotted at equal intervals spanning the indicated range of amplitudes. The range of amplitudes for each mode is indicated at the top of each subplot. The colourbar spans from deep blue to deep red and represents amplitudes in the range [-0.15,0.15].

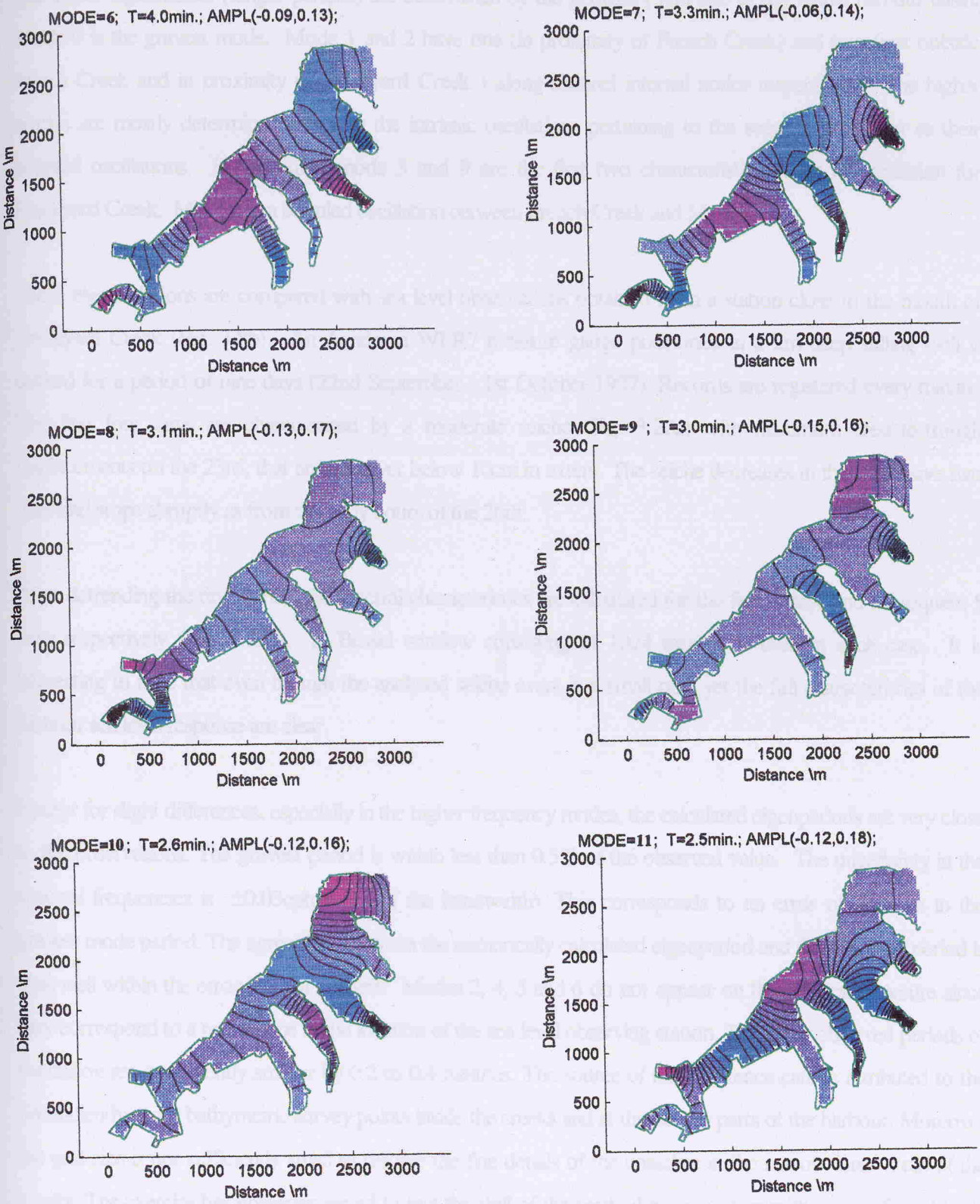

Fig. 3.21 (cont.) Contour plots of eigensolutions for the Grand Harbour.
Contours join points with equal eigenvector amplitudes and are plotted at equal intervals spanning the indicated range of amplitudes. The range of amplitudes for each mode is indicated at the top of each subplot. The colourbar spans from deep blue to deep red and represents amplitudes in the range [-0.15,0.15].

The lower eigenmodes (longer periods) are determined by the geometry and size of the whole harbour basin. Mode 0 is the gravest mode. Mode 1 and 2 have one (in proximity of French Creek) and two (just outside Marsa Creek and in proximity of Dockyard Creek) along-channel internal nodes respectively. The higher modes are mostly determined either by the intrinsic oscillations pertaining to the separate creeks or to their coupled oscillations. In particular, mode 3 and 9 are the first two characteristic modes of oscillation for Dockyard Creek. Mode 4 is a coupled oscillation between French Creek and Marsa Creek.

These eigensolutions are compared with sea level observations obtained from a station close to the mouth of Dockyard Creek (Fig. 3.8b). An Aanderaa WLR7 pressure gauge positioned in a 2m deep stilling well is utilised for a period of nine days (22nd September - 1st October 1997). Records are registered every minute. The first four days are characterised by a moderate seiche (Fig. 3.22a) with maximum crest-to-trough displacements on the 23rd, that are however below 10cm in extent. The seiche decreases in the successive two days and stops abruptly as from the early hours of the 26th.

After detrending the time series, the spectral characteristics are calculated for the first 4 days and subsequent 5 days respectively (Fig. 3.22b). A Bessel window consisting of 1024 records is used in each case. It is interesting to note that even though the analysed seiche event is a small one, yet the full characteristics of the harbour sea level response are clear.

Except for slight differences, especially in the higher frequency modes, the calculated eigenperiods are very close to the observations. The gravest period is within less than 0.5% of the observed value. The uncertainty in the spectral frequencies is $\pm$0.03cph (i.e. half the bandwidth). This corresponds to an error of $\pm$0.2min in the gravest mode period. The agreement between the numerically calculated eigenperiod and the observed period is thus well within the error limit of analysis. Modes 2, 4, 5 and 6 do not appear on the spectral signature since they correspond to a nodal zone at the location of the sea level observing station. The other observed periods of oscillation are consistently smaller by 0.2 to 0.4 minutes. The source of this difference can be attributed to the insufficiently dense bathymetric survey points inside the creeks and at the deeper parts of the harbour. Moreover the grid size is not sufficiently small to resolve the fine details of the coastline in the narrow inner areas of the creeks. The exercise has however served to test the skill of the method even in cases with a complicated basin morphology.

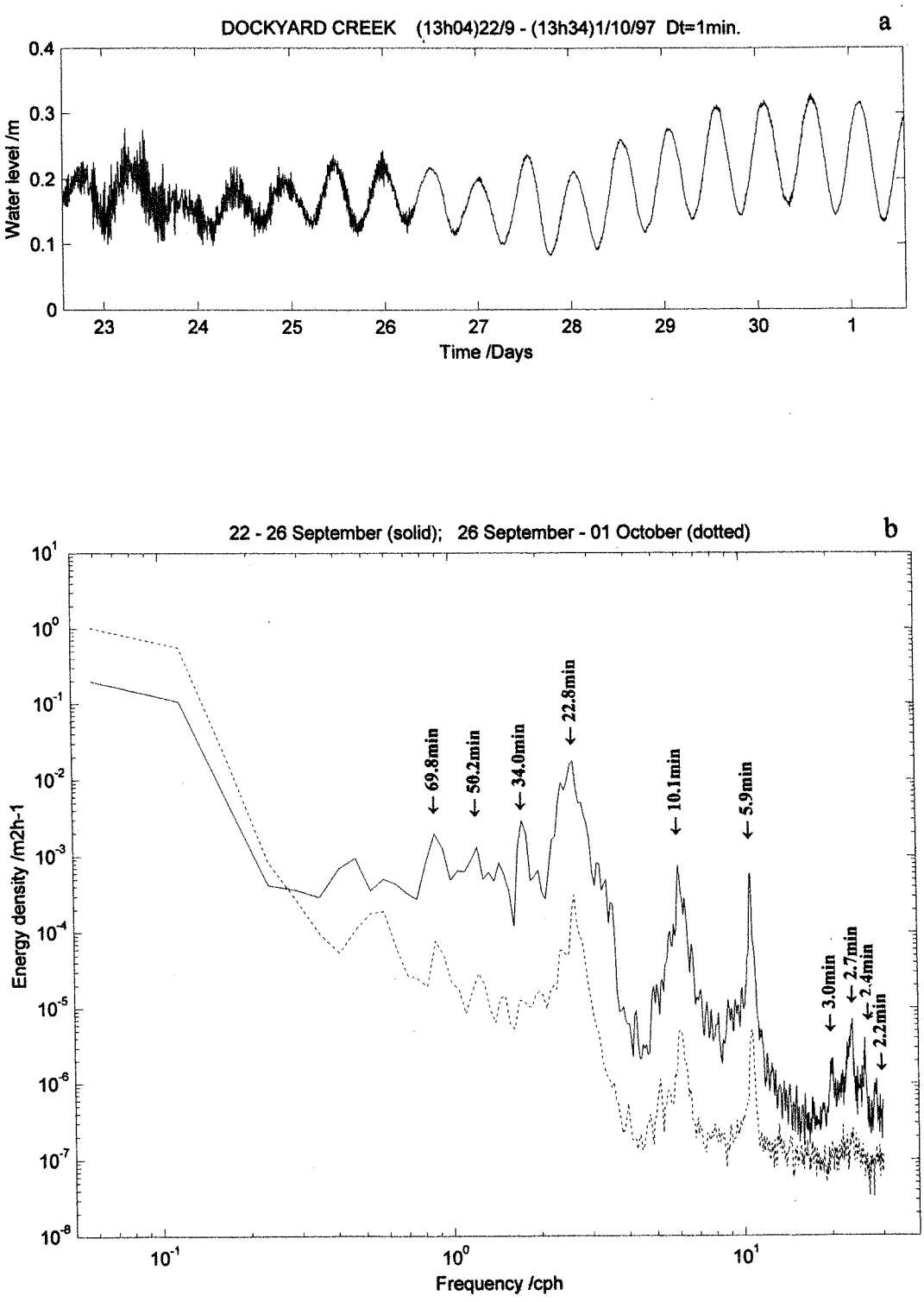

Fig. 3.22 (a) Time series of water elevation in Dockyard Creek, Grand Harbour; (b) Spectral plots for water elevation in the period 22 - 25 September (solid), and (26 September - 1 October (dotted). The 95% confidence factor, for 18 degrees of freedom is 6.1 dB (B_{min}=0.57; B_{max}=2.2).

On the basis of this analysis we obtain several interesting highlights on the characteristics of the sea level oscillations in the harbour. The predominant energy bearing maximum in the harbour is due to the gravest mode. The next two higher frequency energy peaks are at least an order of magnitude less. With its narrow mouth, the main oscillations in the harbour thus occur at spectral frequencies that are all related to the intrinsic modes of the harbour itself. Moreover, the response of the harbour is very steady in time. The characteristic frequencies are in fact maintained throughout the observation period, and under different situations of both weak and relatively stronger seiching.

The Q-factor for the gravest mode of oscillation is equal to 14. The other modes have also relatively high values of Q, which indicates that incident long waves from the open ocean can be resonantly amplified within the harbour. At the further higher frequency end of the spectrum, energy peaks with periods of the order of 2 - 3min can be enhanced during seiching. Range action in the harbour creeks can thus be a potential problem. These high frequency harbour oscillations are linked to the occurrence of surf beats in the coastal area outside the harbour (Darbyshire, 1963). The harbour offers protection from the direct exposure to swell and surf beats, but those frequencies that are in near-resonance to the harbour modes can still penetrate and become enhanced in the harbour.

The spectrum inside the harbour is thus determined mainly by the intrinsic oscillations of the corresponding water areas and not by the characteristics of the source. Nonetheless one should note the presence of long period waves with a frequency lower than the gravest mode. These waves are an expression of co-oscillations with the shelf area beyond the harbour. The harbour is thus unscreened from the influence of waves at these frequencies. The associated sea level oscillations occur with the same phase throughout the extent of the harbour. Contrary to the harbour eigenfrequencies, the relative distribution of energy at these longer period oscillations is not very steady in time, and is dictated by the spectrum outside the harbour.

3.4.5 Application to embayments with a wide open mouth

The method is applied to the three bays separately and to Mellieha Bay and St. Paul's Bay as a system of coupled embayments. The domain is discretised into equal grid cells. In all cases the calculation is repeated with a coarser grid size. No relevant differences are obtained if allowance is made to the fact that a larger grid size deteriorates the correct representation of the coastal details.

The open mouth of each basin can be treated by assuming a node at the boundary between the basin and the adjacent sea. This implies that any standing wave pattern in the basin is assigned zero amplitude anywhere beyond the boundary. Such an assumption is however inappropriate especially in the case of a wide-mouthed basin. This so-called end effect is here taken into account by extending the open boundary to some distance beyond the actual basin mouth, so that a piece of the adjacent ocean is included in the domain. Determining the portion of ocean area that should be appended to the basin is arbitrary and greatly depends on the shape and size of the basin opening as well as on the bathymetric relief in the adjacent ocean. Too large a portion introduces unreal extra modes external to the basin. On the other hand, if the open boundary is put too close to the mouth the end correction is underestimated and the periods of the lower frequency modes do not agree with observations. The appropriate position of the limiting boundary is ascertained after several trials. The main criterion used is that the open boundary should follow closely the amplitude contours in its vicinity.

3.4.6 Application to St. George's Bay

The eigenperiods are calculated for three different open boundary positions. In all cases the grid size is 20m. In the first case (SG1) a straight boundary across the mouth of the bay is used. In the other two cases, a curved open boundary joining the two bay promontaries is positioned into the adjacent sea area, at a distance from the mouth of approximately a quarter the size of the bay (SG2), and the same extent of the bay (SG3) respectively. The results of the computations are summarised in Table 3.6. The eigenplots for SG3 are given in Fig. 3.23.

Although the size of the opening is comparable to the bay dimensions, there is practically no difference between the eigenperiods in the three cases. The characteristic bay oscillations are thus intrinsic to the bay itself and do not involve, to any significant extent, the water body outside the bay. This is different from the case of Mellieha Bay and St. Paul's Bay which have wider connections to the open sea (refer section 3.4.7). The influence of the adjacent sea on the gravest and higher bay modes are thus dictated by the actual size of the open mouth and by

Table 3.6 *Eigenperiods of the normal modes of oscillation in St. George's Bay*

Mode	0	1	2	3	4
SG1 (bay only)	5.90	2.51	1.97	1.73	1.39
SG2 (bay+small adjacent sea area)	6.08	2.67	1.97	1.92	1.43
SG3 (bay+large adjacent sea area)	6.09	2.69	1.97	1.96	1.47

Period in minutes

the bathymetric relief at and adjacent to the mouth, and not by the bay shape or the relative extent of the opening with respect to the bay dimensions.

The first two modes, with zero and one internal nodes respectively, consist of oscillations along the major axis of the bay. The gravest mode consists of a quarter wave oscillation with a displacement node close to the mouth of the bay and highest amplitudes that are primarily confined within the inner 2/3 of the bay. This mode is observed as a very evident energy peak in the records measured by a coastal water level recorder placed at approximately 1/3 the bay length from its head (Fig. 3.8c). The first mode has a nodal line in close proximity to the sea level gauge position and does not thus appear in the observations. For the higher modes, lateral oscillations are induced. Mode 2 is a cross-oscillation of the very inner shallow area of the bay. The rest of the modes are mixed and involve longitudinal oscillations along the narrower middle part of the bay together with lateral movements in the wider outer bay area, especially on the short protrusion on the eastern promontary.

3.4.6.1 Comparison with observations

The sea level observations used in this section refer to the period (6:11GMT) 11/4/96 to (5:20GMT) 20/4/96 made by an Aanderaa WLR7 bottom pressure recorder (refer section 4.3.2) at an open sea station (Pembroke Station, PEMB) in a depth of 29m and at a position 1Km to the north of the mouth of the bay (35° 56.26'N; 14° 29.58'E). A further set of measurements refer to a simultaneous pair of bottom pressure recordings (again using Aanderaa WLR7 instruments) covering the period (9:11GMT) 17/1/97 to (1:50GMT) 1/2/97, with one station (SGMTH) positioned in a depth of 17m at the mouth of the bay (35° 55.8'N; 14° 29.7'E), and another (SGOFF) positioned offshore (35° 55.8'N; 14° 30.3'E) at about 1Km to the east of the bay mouth in a depth of 50m. Bottom pressure fluctuations (in mb) are translated into level variations (in cm) by a direct equivalence (refer section 4.3.2.1). In both cases the coastal station (SG) is an Endeco Type 1029 differential pressure gauge. Coastal sea level observations are adjusted for the effect of atmospheric pressure as described in section 4.3.2.2. The 50m bathymetric contour narrows down considerably in the proximity of the the bay, starting from an average distance of 5 Km normal to the main shoreline in front of Mellieha Bay, to 2Km further east and narrowing to less than 1Km in front of the Grand Harbour. Unfortunately the offshore instrument developed a time synchronisation fault in data recording on the second day and only the initial limited set of observations are useful.

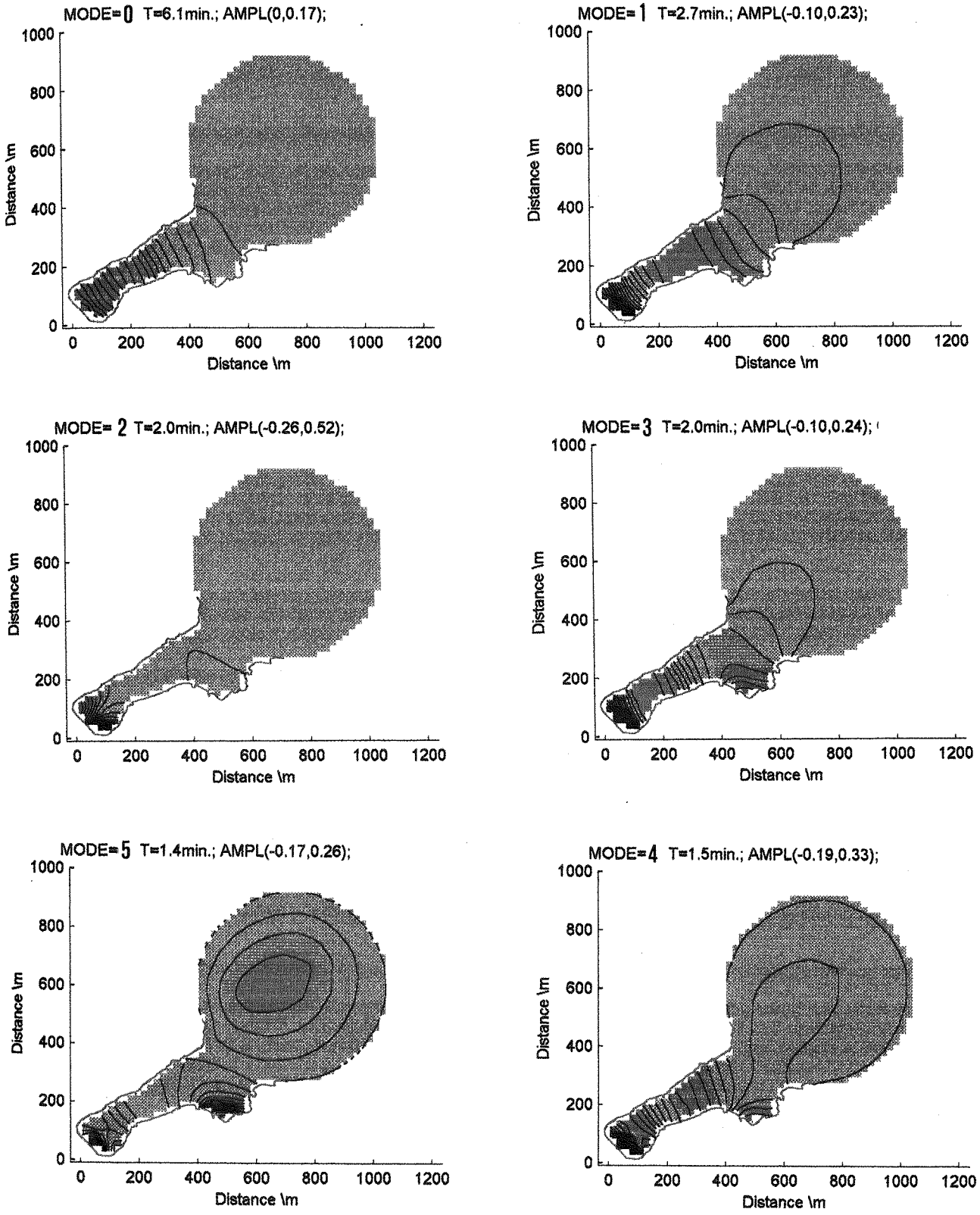

Fig. 3.23 Amplitude distribution of bay oscillations in St. George's Bay.
Contours join points with equal eigenvector amplitudes and are plotted at equal intervals spanning the indicated range of amplitudes. The range of amplitudes for each mode is indicated at the top of each subplot. The colourbar spans from deep blue to deep red and represents amplitudes in the range [-0.4,0.4].

During the set of observations in January 1997, parallel atmospheric pressure recordings are obtained at a nearby location set up in Valletta (35° 54.1'N; 14° 30.8'E). The pressure at MSL is added to the recordings of the coastal station in order to obtain the adjusted sea level. This renders the coastal sea level measurements compatible for comparison with those at the non-coastal bottom pressure stations. As expected this correction does not however influence the higher frequency signals (T < 30 minutes). The correction is however necessary for the longer periods. The observations are subsequently high pass filtered (utilising the filter described in Chapter 2, Section 2.4.5, with a 50% attenuation at f = 5 cycles/day and cut-off at f = 10 cycles/day) and the cross-spectra calculated by utilising a Bessel window of length 512 minutes and 50% overlap. The spectra thus cover a range from $0.4h^{-1}$ (limited by the filter) to $30h^{-1}$ (half the sampling frequency).

The analysis of the January 1997 recordings is done in two segments of 4.5 days each. There is no particularly strong seiching event in any of the two segments. The response of the bay to incident long period waves is however well typified by these observations. During the first segment there is no energy in the incident spectrum beyond f = 10cph. The simultaneous length of records for the three stations SGOFF, SGMTH and SG in Fig. 3.24a illustrates the development of the long period waves as they reach the bay. The sea level in the bay typically co-oscillates to the longer period undulations in the open sea without amplification. The coherence between the three recordings at these lower frequencies is remarkable (Fig. 3.25a). A very well defined and regular oscillation with the characteristic 6-minute period is however established inside the bay. The power amplification at this period is very sharp and evident.

3.4.6.2 Surf beat activity

During the second segment of recordings, the response is complicated by the presence of an anomalous band of higher frequency waves centred around T = 3 minutes (Fig. 3.25b). These shorter waves are particularly intense on 26/27th January. Their presence at the mouth of the bay and their rather random nature is illustrated in Fig. 3.24b which contrasts with the much smoother trace on 17/18 th January in Fig. 3.24a. Their average maximum height (crest-to-trough amplitude) at the sea level gauge location inside the bay is around 4cm. Their occurrence appears to coincide to periods of high surface waves impinging on the coast from the first quadrant, but no records of sea surface waves activity are available for a quantitative study. Darbyshire & Darbyshire (1964) report similar observations in Table Bay Harbour on the west coast of Cape Peninsula. They refer to the presence of such short period seiching in the harbour as range action, and attribute their origin to surf beats

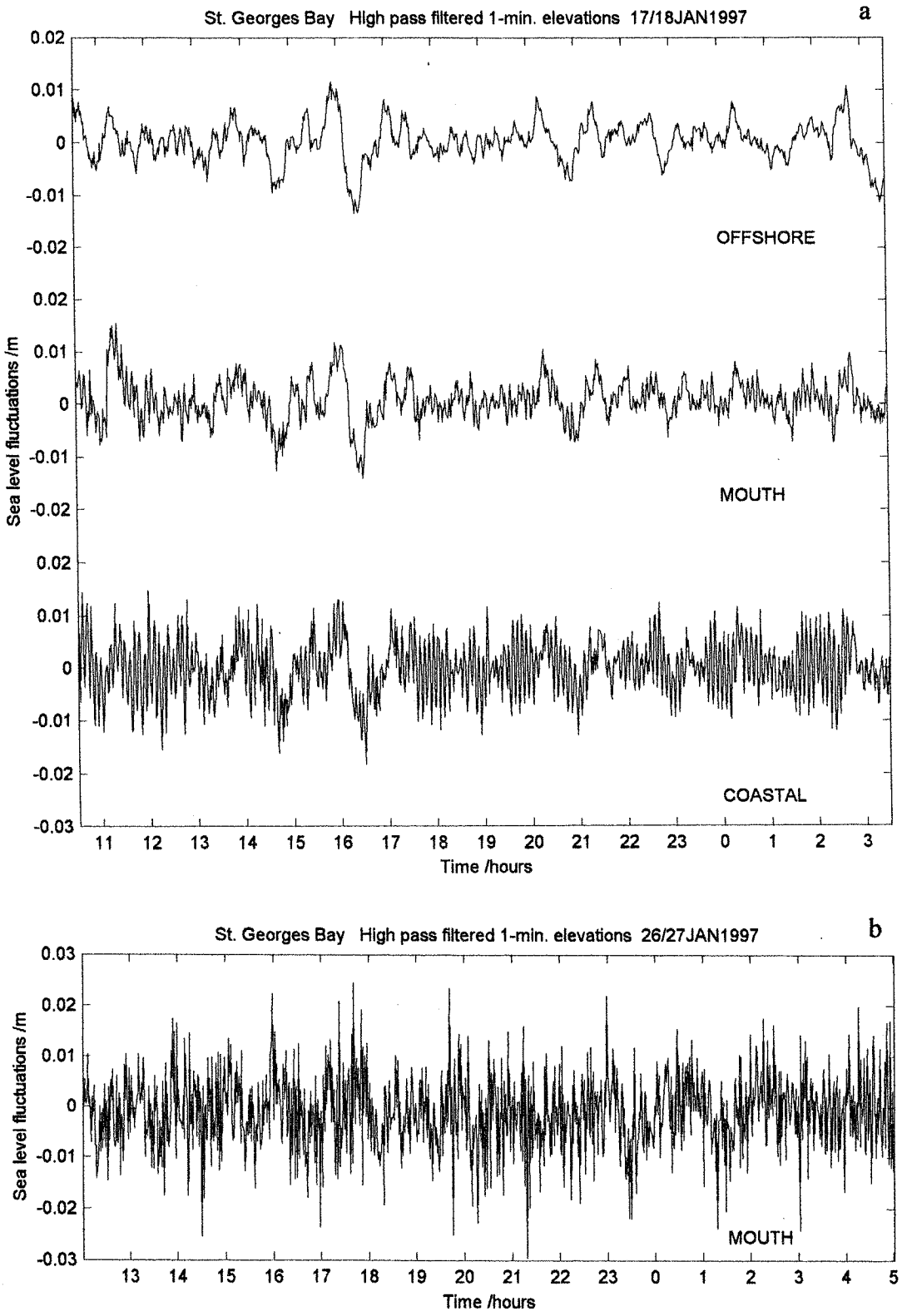

Fig. 3.24 Time series of simultaneous water level observations sampled every minute in St. George's Bay (a) from (10h29GMT) 17/1 - (03h49GMT) 18/1/97 at the coastal station, at the bay mouth (SGMTH, 35°55.79'N; 14°29.66'E) and at the offshore station (SGOFF, 35°55.82'N; 14°30.30'E), and (b) from (12h00GMT) 26/1 - (05h20GMT) 27/1/97 at the bay mouth (SGMTH) .

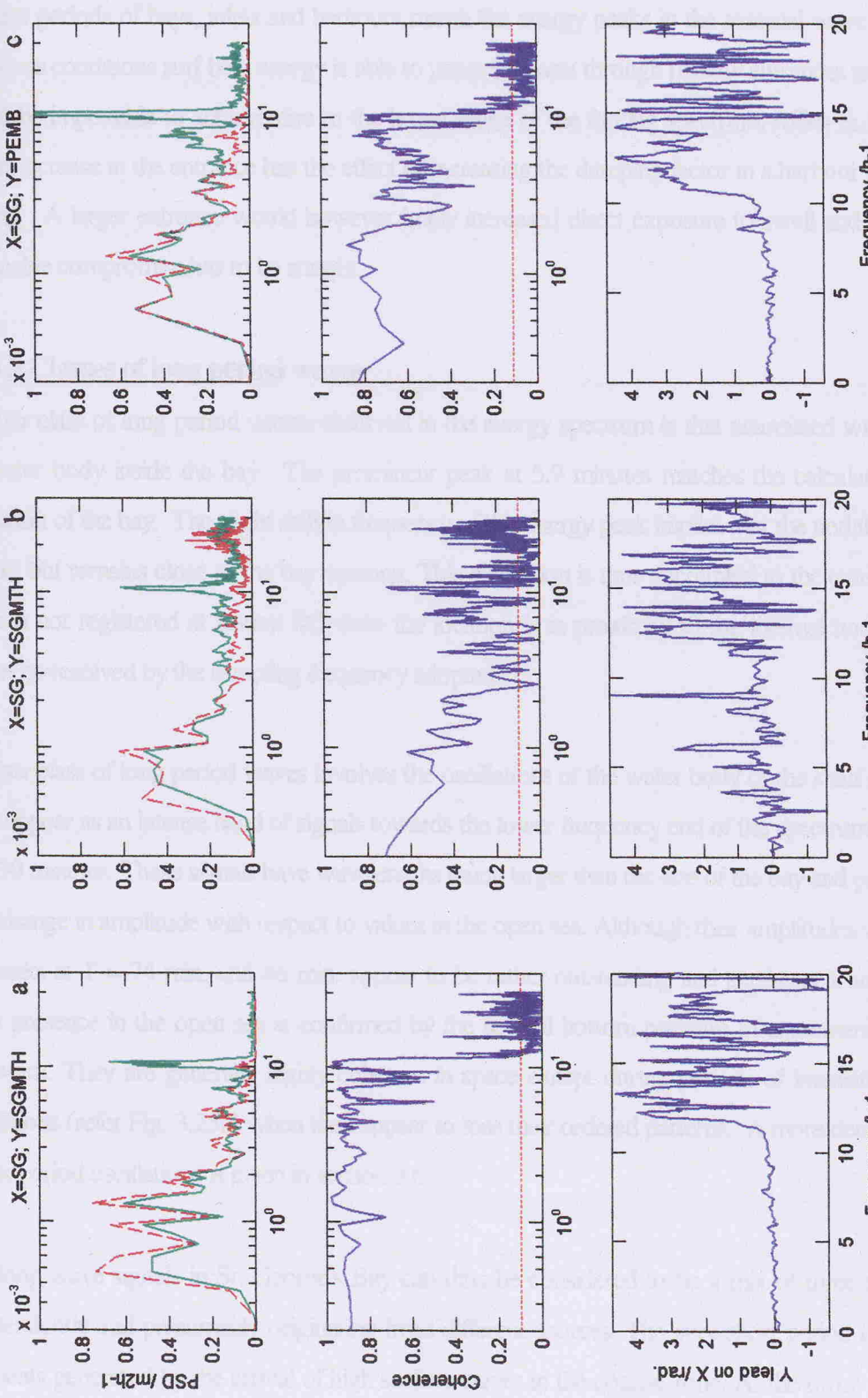

Fig. 3.25 Power spectral density, coherence and phase plots between 1-minute sampled high pass filtered water elevations in St. George's Bay (10h10GMT)17/1 - (02h43GMT)23/1/97 (a) and from (08h24GMT) 23/1 - (23h11GMT) 27/1/97 (b) at the coastal station (green) and the bay mouth (red), and the coastal station (green) and Pembroke offshore station (red) from (07h10GMT)11/4 - (04h11GMT)20/4/96 (c).
The 95% confidence level for the coherence estimate is 0.1; The 95% confidence factor, for 60 degrees of freedom is 0.29 dB (B_{min}=0.72; B_{max}=1.4).

(refer 3.1.4). The magnitude of these high frequency oscillations is dependent on the fine structure of the surf beat spectrum as well as on the wave direction. Range action can indeed be problematic in cases where the resonant periods of bays, inlets and harbours match the energy peaks in the external wave spectrum. In near-resonance conditions surf beat energy is able to penetrate even through narrow entrances and mismatching may indeed be impossible to achieve due to the broad range of the forcing spectrum. Miles & Munk (1961) found that an increase in the entrance has the effect of increasing the damping factor in a harbour and thus to suppress ranging. A larger entrance would however imply increased direct exposure to swell and surf beats, so that a reasonable compromise has to be sought.

3.4.6.3 Classes of long period waves

Another class of long period waves observed in the energy spectrum is that associated with the oscillations of the water body inside the bay. The prominent peak at 5.9 minutes matches the calculated gravest mode of oscillation of the bay. The slight shift in frequency of this energy peak implies that the nodal position can change in time, but remains close to the bay opening. This oscillation is thus uncoupled to the external ocean. The first mode is not registered at station SG since the location is in proximity to the internal node. The other modes cannot be resolved by the sampling frequency adopted.

Another class of long period waves involves the oscillations of the water body of the shelf area outside the bay. They appear as an intense band of signals towards the lower frequency end of the spectrum, with periods higher than 30 minutes. These signals have wavelengths much larger than the size of the bay and penetrate the bay with little change in amplitude with respect to values in the open sea. Although their amplitudes vary from day to day, the peaks at T = 74 min. and 46 min. appear to be rather outstanding and persistent from this set of records. Their presence in the open sea is confirmed by the several bottom pressure measurements undertaken during this work. They are generally highly coherent in space except during periods of intensified higher frequency oscillations (refer Fig. 3.25b) when they appear to lose their ordered patterns. A more detailed analysis of these longer period oscillations is given in section 3.6.

The long wave signals in St. George's Bay can thus be considered to be a mix of three types, each behaving independently and presumably originating from different sources. The very short period oscillations consist of surf beats generated by the arrival of high surface waves in the coastal zone. At the other end of the spectrum,

the longer period waves are an expression of waves on the continental shelf. In addition, the characteristic eigenoscillations occur as a resonant response of the bay.

3.4.7 Application to Mellieha Bay and St. Paul's Bay

The eigenperiods for Mellieha Bay are calculated for three different open boundary positions. In all cases the grid size is 40m. In the first case (MEL1) a straight boundary across the mouth of the bay is used. In the other two cases, a curved open boundary joining the two bay promontaries is positioned into the adjacent sea area, at a distance from the mouth of approximately a quarter of the size of the bay (MEL2), and the same extent of the bay (MEL3) respectively. The same exercise is repeated with St. Paul's Bay (PL1/2/3). The two bays are also considered together and their combined eigensolutions are calculated both with a small (MP1) and larger (MP2) adjacent sea area. The results of the computations are summarised in Table 3.7. The eigenplots for MEL2/3 and MP1 are given in Fig. 3.26 and Fig. 3.27 respectively.

Table 3.7

Eigenperiods of the normal modes of oscillation in Mellieha Bay and St.Paul's Bay

Mode	0	1	2	3	4	5	6	7
MEL1 (Bay only)	14.3	6.9	5.0	4.6	4.5	4.1	3.6	3.4
MEL2 (+ small adjacent sea area)	16.4	8.3	6.0	5.0	4.5	4.3	3.9	3.7
MEL3 (+ large adjacent sea area)	16.8	8.9	6.5	5.3	4.9	4.5	4.3	3.9
PL1 (Bay only)	14.8	8.8	5.7	5.3	4.0	3.9	3.5	3.3
PL2 (+ small adjacent sea area)	15.8	9.4	6.1	5.4	4.3	4.0	3.7	3.3
PL3 (+ large adjacent sea area)	16.1	9.6	6.2	5.4	4.6	4.0	3.9	3.5
MP1 + small adjacent sea area)	16.4	16.1	9.8	8.2	6.5	6.2	5.7	5.2
MP2 (+ large adjacent sea area)	17.7	16.4	10.4	9.3	7.2	6.4	5.7	5.6

Period in minutes

3.4.7.1 Normal mode oscillations in Mellieha Bay

The patterns of the eight gravest normal modes of Mellieha Bay (MEL3) are shown in Fig. 3.26. The gravest normal mode has a period of 16.4min and consists of an oscillation with the same phase throughout the bay, maximum amplitude at the closed end and a displacement node in the area beyond the open mouth. The first mode with a period of 8.3min has an internal node in the central area of the bay. These two first modes are both purely longitudinal in nature and with a strong coupling to the adjacent ocean. The next mode has two internal nodes and develops a transverse character towards the open end of the bay where it intensifies against the eastern promontary.

The inner nodal line is close to the tide gauge location and this mode is thus not expected to produce a signature on the sea level spectrum observed at this station. Mode 3 is very similar to mode 2 except that amplitudes within the bay are much less pronounced so that the mode is basically an intrinsic oscillation of the outermost secondary inlet adjacent to St. Paul's Islands. The same applies to mode 6. Mode 4 is a purely transverse mode whereas mode 5 and 7 each present patterns composed from a mix of longitudinal and transverse oscillations. Note that where the water depth becomes shallower the wavelengths tend to get shorter and oscillation magnitudes tend to grow. Short wavelength oscillation modes thus tend to appear in the shallow bay areas. These short wavelength modes may not however be physically feasible under natural conditions since attenuation effects are, in general, significant in shoaled areas. These modes may hence not appear in observations.

3.4.7.2 Normal mode oscillations in St. Paul's Bay

The first few eigenperiods for St. Paul's Bay are compared with those of Mellieha Bay in Table 3.7. The gravest periods of oscillation are very close which shows that the fundamental mode of oscillation is mainly dictated by the length and along-axis bathymetric slope, both of these quantities being very similar in the two bays. Mode 1 is very much influenced by the coastal configuration. In the case of St. Paul's Bay this mode is basically an intrinsic oscillation of the rectangular interior area of the bay. The first four modes are basically longitudinal with intensifications inside Mistra Bay. Modes 4-7 are a composition of longitudinal and transverse oscillations. The higher modes become more decoupled from the adjacent ocean. Mode 5 is dominated by a cross-bay oscillation in the wider outer part of the bay. Mode 7 is dominated by an intense transverse oscillation at the head of the bay.

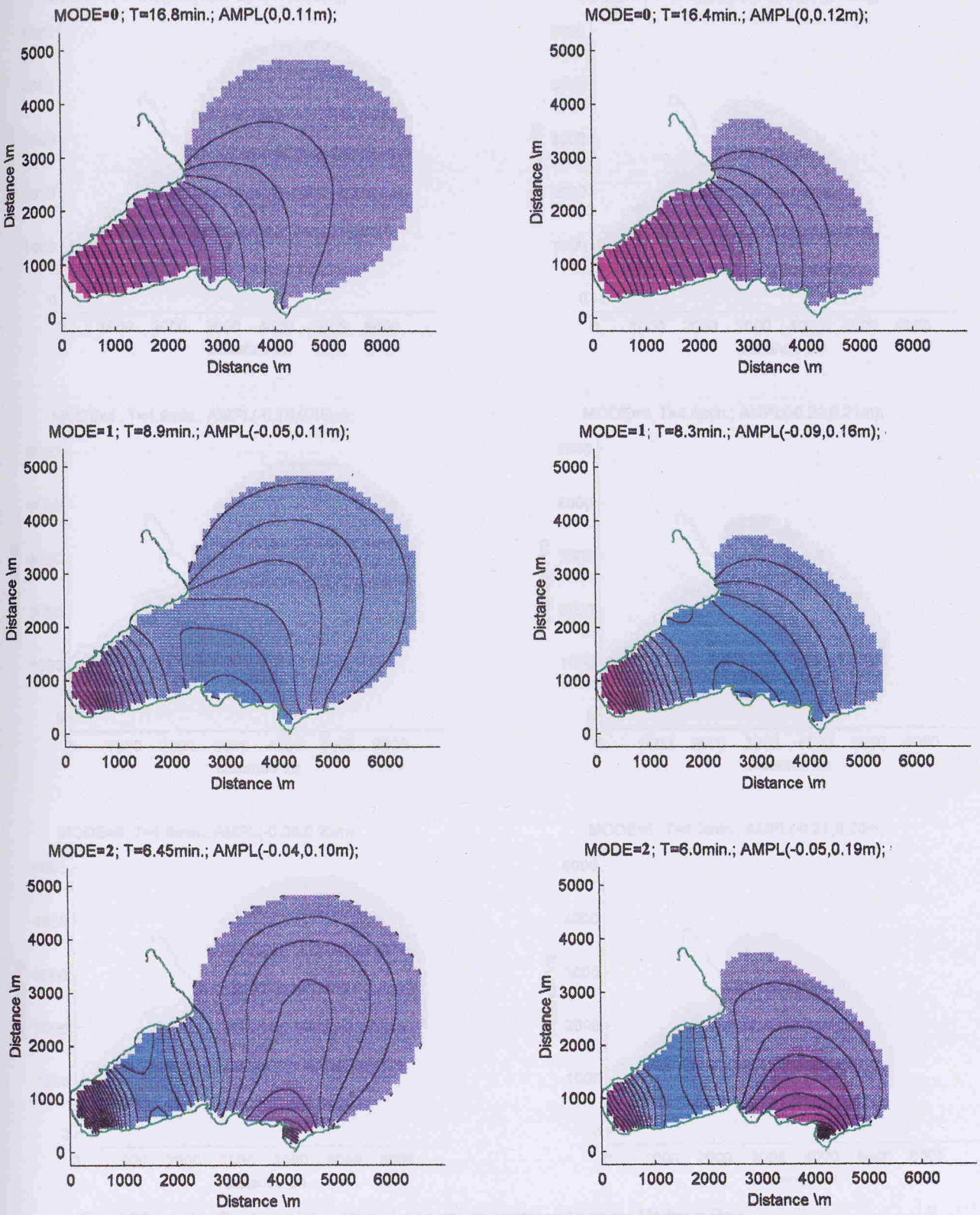

Fig. 3.26 Contour plots of the eight gravest eigensolutions for Mellieha Bay (cont. overleaf).
Contours join points with equal eigenvector amplitudes and are plotted at equal intervals spanning the indicated range of amplitudes. The range of amplitudes for each mode is indicated at the top of each subplot. The colourbar spans from deep blue to deep red and represents amplitudes in the range [-0.2,0.2].

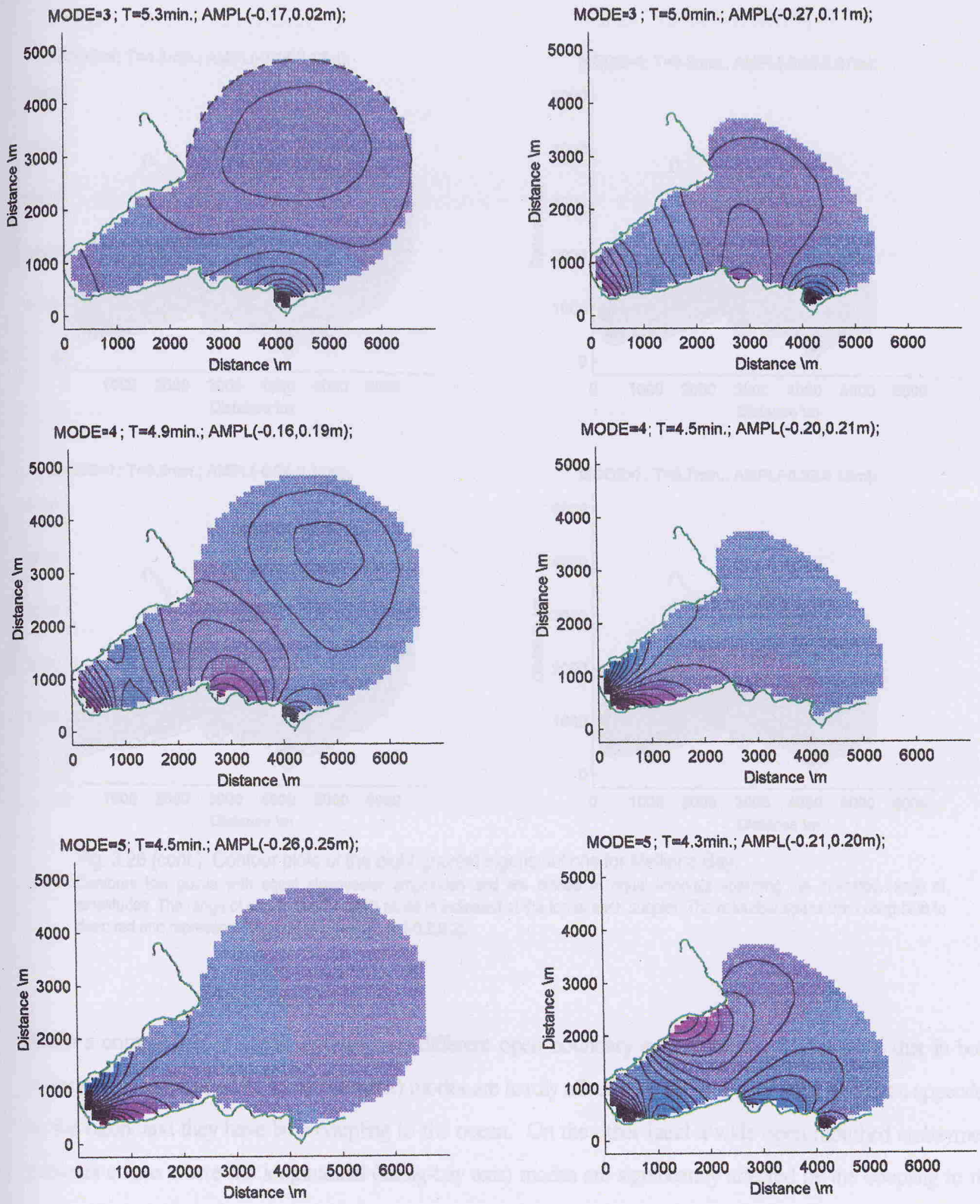

Fig. 3.26 (cont.) Contour plots of the eight gravest eigensolutions for Mellieha Bay.

Contours join points with equal eigenvector amplitudes and are plotted at equal intervals spanning the indicated range of amplitudes. The range of amplitudes for each mode is indicated at the top of each subplot. The colourbar spans from deep blue to deep red and represents amplitudes in the range [-0.2,0.2].

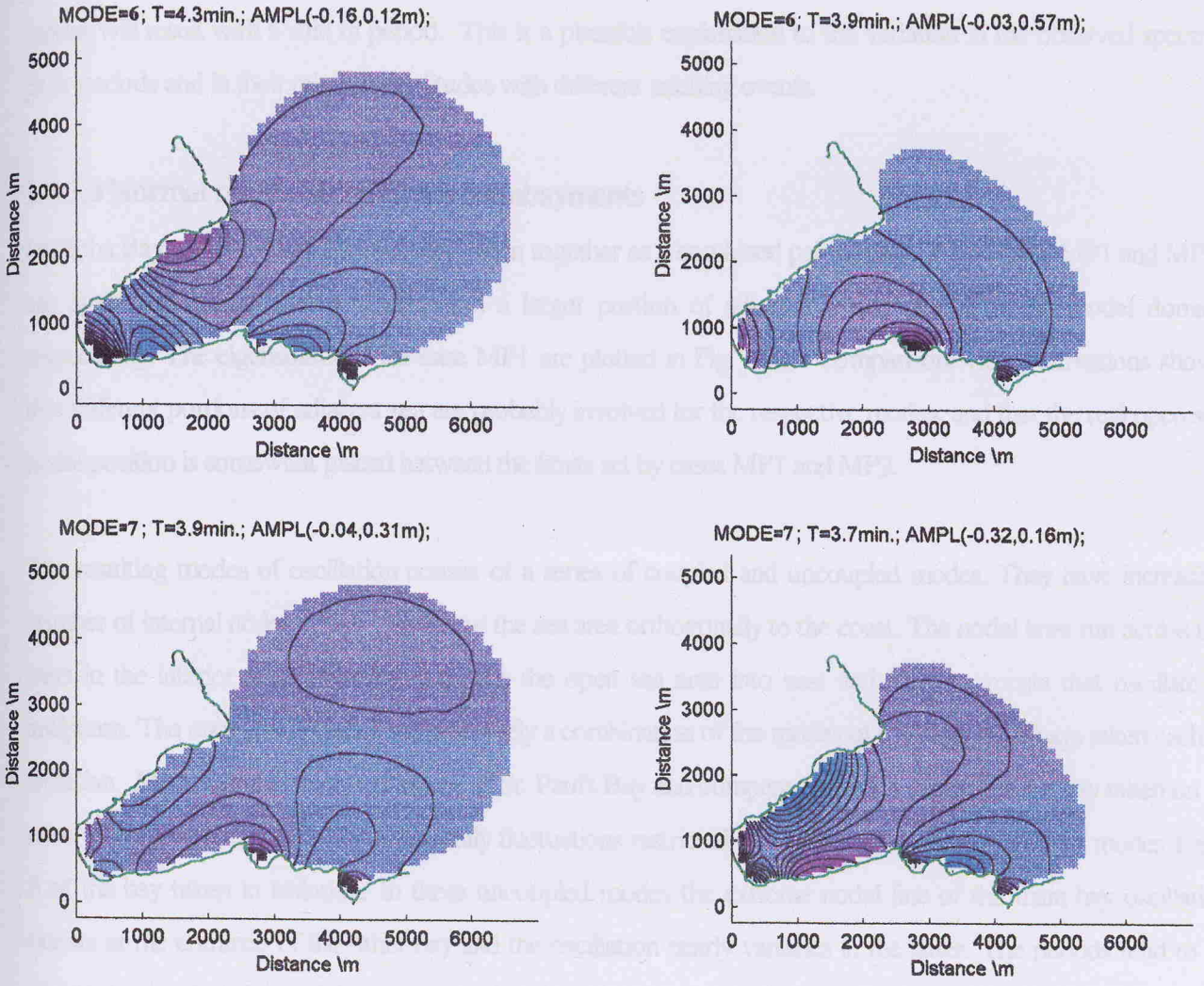

Fig. 3.26 (cont.) Contour plots of the eight gravest eigensolutions for Mellieha Bay.
Contours join points with equal eigenvector amplitudes and are plotted at equal intervals spanning the indicated range of amplitudes. The range of amplitudes for each mode is indicated at the top of each subplot. The colourbar spans from deep blue to deep red and represents amplitudes in the range [-0.2,0.2].

From a comparison of eigensolutions with different open boundary configurations, it is noticed that in both embayments the transverse (cross-bay axis) modes are hardly affected by the extent of adjacent ocean appended to the basin, and they have little coupling to the ocean. On the other hand a wide open mouthed embayment presents a case where the longitudinal (along-bay axis) modes are significantly affected by the coupling to the ocean. Their periods depend on the portion of ocean that is included in the calculations. The effects of the open end are most significant for the fundamental normal mode because it has the largest wavelength. If the forcing

agent responsible for these oscillations excites different extents of the adjacent open sea areas, coupled bay modes will result with a shift in period. This is a plausible explanation to the variation in the observed spectral peak periods and in their relative amplitudes with different seiching events.

3.4.7.3 Normal modes of the coupled embayments

Mellieha Bay and St. Paul's Bay are next taken together as a combined pair of bays. Two cases, MP1 and MP2, are again considered with a smaller and a larger portion of adjacent ocean added to the model domain respectively. The eigensolutions for case MP1 are plotted in Fig. 3.27. Comparison with observations shows that different portions of adjacent sea are probably involved for the respective modes, and that the real open sea nodal position is somewhat placed between the limits set by cases MP1 and MP2.

The resulting modes of oscillation consist of a series of coupled and uncoupled modes. They have increasing number of internal nodes which tend to cut the sea area orthogonally to the coast. The nodal lines run across the bays in the interior areas, whereas they cut the open sea area into east and west segments that oscillate in antiphase. The uncoupled modes are effectively a combination of the modes of the respective bays taken each in isolation. Modes 2 and 6 are oscillations of St. Paul's Bay and compare to modes 1 and 3 of the bay taken on its own. Similarly modes 3 and 7 are basically fluctuations restricted to Mellieha Bay and compare to modes 1 and 3 of the bay taken in isolation. In these uncoupled modes the extreme nodal line of the main bay oscillation occurs at the entrance of the other bay and the oscillation nearly vanishes in the latter. The periods tend to be slightly higher than those of the corresponding single bay mode.

Coupled modes result from a combination of a Mellieha Bay mode and a St. Paul's Bay mode which have nearly equal periods. Modes 2 of the two separate bays give rise to coupled modes 4 and 5. Similarly modes 1 of the separate bays result in the two gravest coupled modes of oscillation 0 and 1. These two longer period modes present an interesting case of coupled oscillations between two adjacent bays. They consist of a phasic oscillation with highest amplitudes in St. Paul's Bay (mode 0) and an anti-phasic oscillation with approximately equal amplitudes in the two bays (mode 1). Given the close values of the periods of the two modes, they will be expected to give rise to a beating effect between the two bays when the amplitudes of the modes are comparable. This would result in an alternate reinforcement and attenuation of the seiches in the bays, with

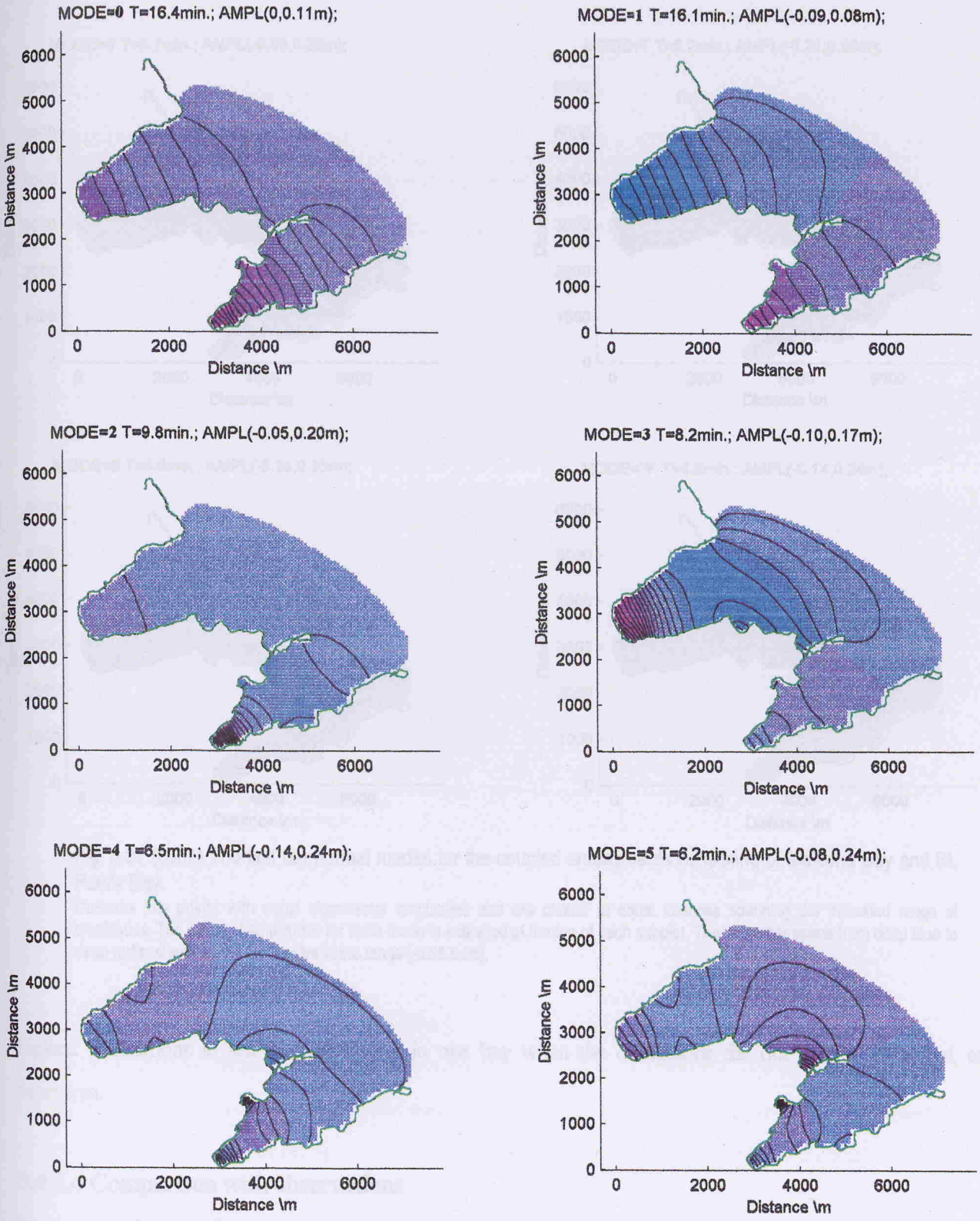

Fig. 3.27 The first ten normal modes for the coupled embayments consisting of Mellieha Bay and St. Paul's Bay (cont. overleaf).

Contours join points with equal eigenvector amplitudes and are plotted at equal intervals spanning the indicated range of amplitudes. The range of amplitudes for each mode is indicated at the top of each subplot. The colourbar spans from deep blue to deep red and represents amplitudes in the range [-0.25,0.25].

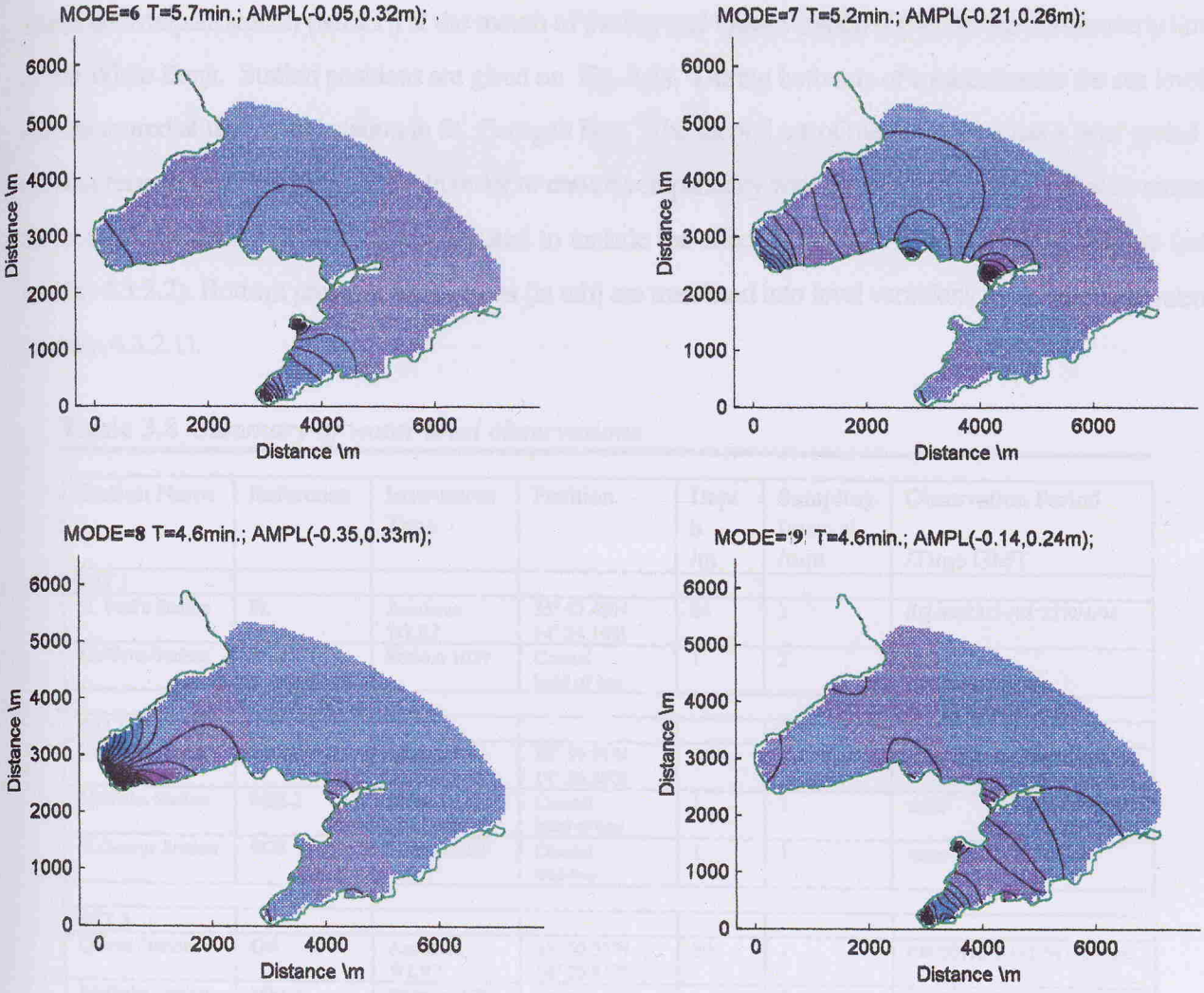

Fig. 3.27 (cont.) The first ten normal modes for the coupled embayments consisting of Mellieha Bay and St. Paul's Bay.

Contours join points with equal eigenvector amplitudes and are plotted at equal intervals spanning the indicated range of amplitudes. The range of amplitudes for each mode is indicated at the top of each subplot. The colourbar spans from deep blue to deep red and represents amplitudes in the range [-0.25,0.25].

highest fluctuations in sea level occurring in one bay when the oscillations die out in the other bay, and viceversa.

3.4.7.4 Comparison with observations

Three sets of sea level observations are used. Details are summarised in Table 3.8. The first set consists of simultaneous measurements in St. Paul's Bay and Mellieha Bay. The second and third sets focus on Mellieha

Bay and consist of measurements at the coast in conjunction with recordings at two respective offshore stations. These are Melpaul station (MELP) at the mouth of the bay and Qawra station (QW) on the northeasterly limits of the White Bank. Station positions are given on Fig. 3.8a. During both sets of measurements the sea level is also measured at the coastal station in St. George's Bay. The second set of measurements has a brief period of missing records on 20 th May 1996. In order to ensure compatibility with the offshore bottom pressure records, the coastal sea level observations are adjusted to include the effect of changes in atmospheric pressure (refer section 4.3.2.2). Bottom pressure fluctuations (in mb) are translated into level variations by a direct equivalence (section 4.3.2.1).

Table 3.8 *Summary of water level observations*

Station Name	Reference	Instrument Type	Position	Depth /m	Sampling Interval /min	Observation Period /Time GMT
SET 1						
St. Paul's Station	PL	Aanderaa WLR7	35° 57.45'N 14° 24.16'E	24	2	(07:44)23/3-(08:22)9/4/96
Mellieha Station	MEL1	Endeco 1029	Coastal head of bay	1	2	same
SET2						
Melpaul Station	MELP	Aanderaa WLR7	35° 59.21'N 14° 24.56'E	44	1	(16:02)16/5-(16:31)25/5/96
Mellieha Station	MEL2	Endeco 1029	Coastal head of bay	1	1	same
St.George Station	SG2	Endeco 1029	Coastal mid-bay	1	1	same
SET 3						
Qawra Station	QW	Aanderaa WLR7	35° 59.35'N 14° 25.81'E	30	1	(08:50)10/9-(11:54)30/9/96
Mellieha Station	MEL3	Endeco 1029	Coastal head of bay	1	1	(16:16)12/9-(11:54)30/9/96
St.George Station	SG3	Endeco 1029	Coastal mid-bay	1	1	same

3.4.7.5 Analysis of observation sets 2 and 3

The time series plot of sea levels for the observation set 2 (Fig. 3.28) show a seiching event of moderate intensity on 21/22 May. Maximum amplitudes inside Mellieha Bay are around 15cm and coincide to a corresponding increase in sea level activity at MELP where fluctuations are however only 3cm in amplitude. During observation set 3 several large amplitude sea level oscillations events are registered (Fig. 3.29). The strongest event on 18th September is relatively brief in duration, with oscillations reaching a maximum of 22cm in amplitude. The corresponding signals on the shelf at Qawra station are at least an order of magnitude less in

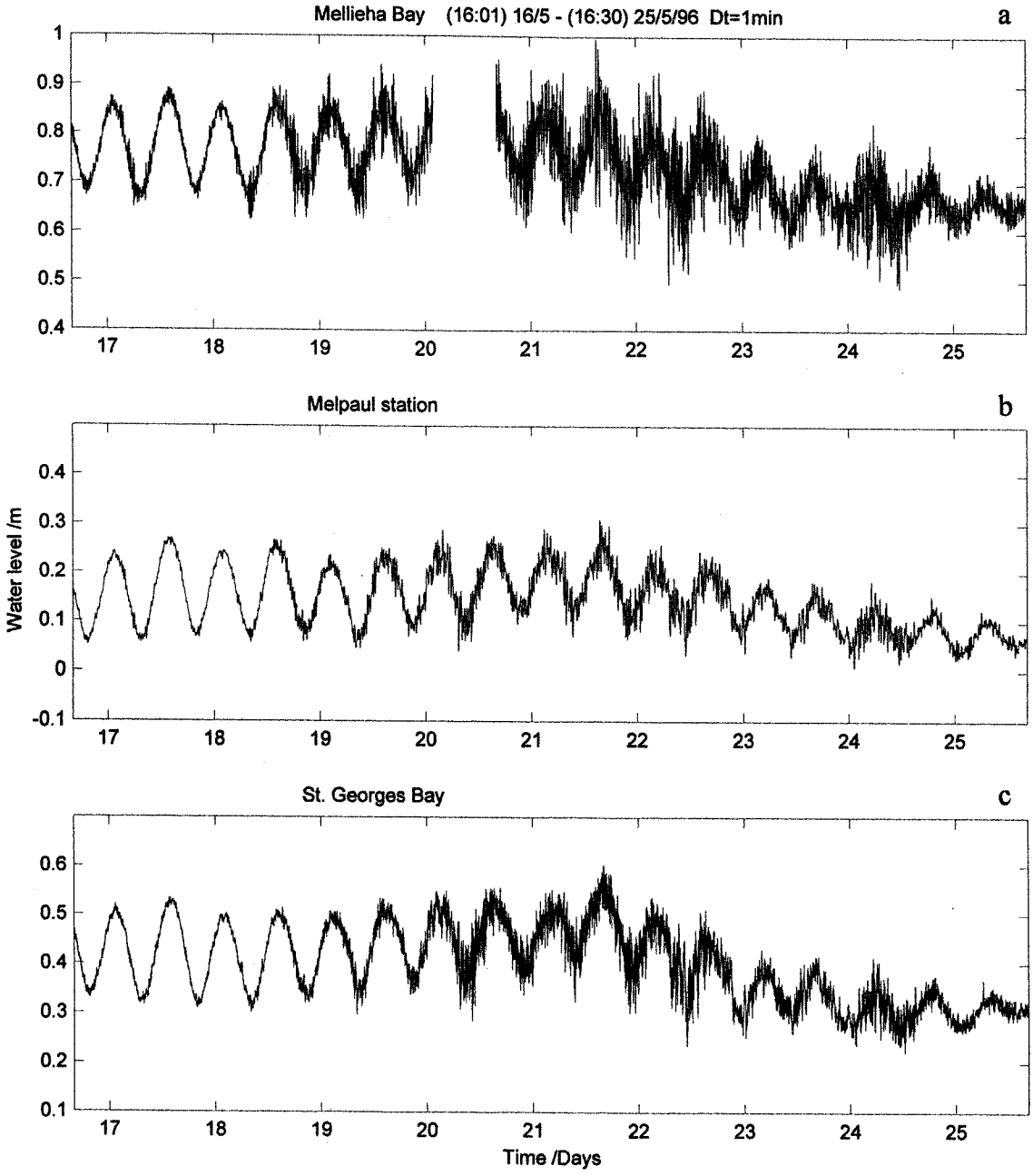

Fig. 3.28 Time series of simultaneous water level observations sampled every minute in (a) Mellieha Bay, (b) Melpaul station (MELP, 35°59.21'N; 14°24.56'E), and (c) St. George's Bay from (16h01GMT) 16/5 - (16h30GMT) 25/5/96.

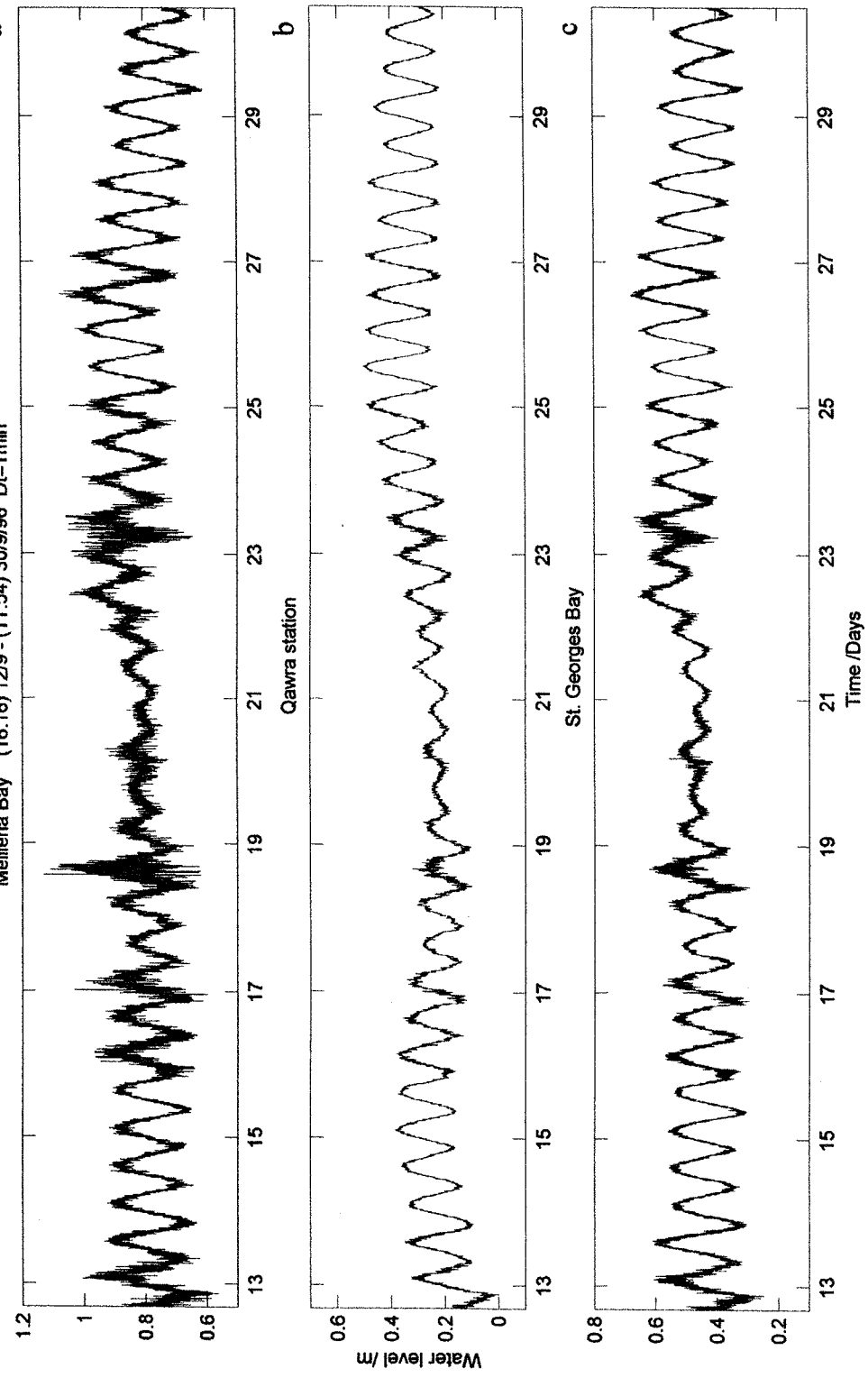

Fig. 3.29 Time series of simultaneous water level observations sampled every minute in (a) Mellieha Bay, (b) Qawra station (QW, 35°59.35'N; 14°25.81'E), and (c) St. George's Bay from (16h16GMT) 12/9 - (11h54GMT) 30/9/96.

amplitude. A simultaneous increase in sea level activity is registered in St. George's Bay at all the events. This coincidence in the recordings supports the hypothesis that the sea levels in the embayments are linked by a larger scale open ocean phenomenon.

The spectral characteristics of the sea level oscillations at the stations are determined from two data segments, each 4608 records long, and comprising respectively the two seiching events mentioned above. The time slots are (17h19GMT) 20/5 - (22h07GMT) 23/5/96 for set 2 and (00h00GMT) 16/9 - (04h48GMT) 19/9/96 for set 3. Cross-spectral computations are performed on the detrended, high pass filtered series by means of the fast fourier transform procedure, and utilising a Kaiser-Bessel spectral window of 512 records with 50% overlapping. For each observation set, the cross-spectra among the three stations are calculated for three separate station pairs. The spectra are presented in Fig. 3.30 (a) for set 2, and Fig. 3.30 (d) for set 3, with green for the Mellieha coastal station (MEL2/3), dashed blue for the St. George coastal station (SG2/3), and dotted red for the offshore stations (MELP and QW).

The relationship between pairs of records is further analysed in terms of coherence, phase difference and the admittance function. Coherence is plotted for station pairs Mellieha/Melpaul (cyan) and St.George/Melpaul (dotted, blue) in (b), and for Mellieha/Qawra (cyan) and St.George/Qawra (dotted, blue) in (e). The phase lead of Melpaul station and of Qawra station with respect to Mellieha station are plotted in (c) and (f) respectively. The phase relationship gives information on the modal structure of the oscillations and allows the identification between bay modes, shelf modes, standing waves and travelling waves. Coherence gives a measure of the extent to which two signals are physically related and thus determines the level significance of any information derived from the phase plots. The admittance function gives the amplification factor of coherent waves between two station pairs.

For each set, the spectra at all three stations are practically identical for periods greater than about 40min. The most consistent peak at these lower frequency signals is that at T = 46min. The other long wave signal is less steady and fluctuates at around T = 74min. For periods lower than 40min the energy inside Mellieha Bay is greater than outside with a conspicuous maximum at T = 16.6min that corresponds to the fundamental mode of the bay. In narrow and long bays, the longitudinal mode of longest period is generally superior. This is found to also apply in this case of wide open mouthed bays like Mellieha Bay and St. Paul's Bay where the amplification

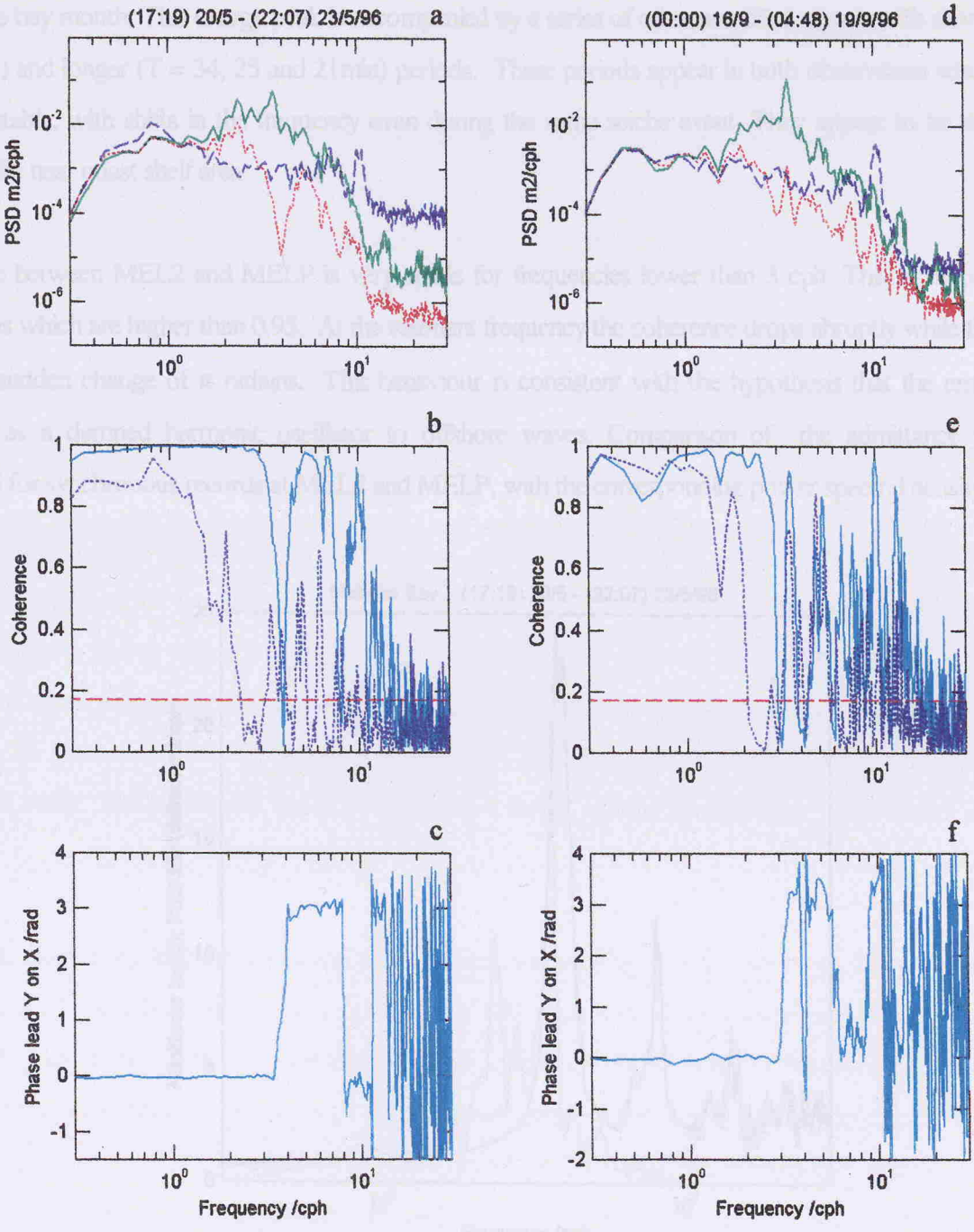

Fig. 3.30 Power spectral density, coherence and phase plots between 1-minute sampled high pass filtered water elevations in Mellieha Bay (green), Melpaul station (dotted, red), and St. George's Bay (dashed, blue) for observations from (17h19GMT)20/5 - (22h07GMT) 23/5/96 (a)-(c), and in Mellieha Bay (green), Qawra station (dotted, red), and St. George's Bay (dashed, blue) for observations from (0hGMT)16/9 - (4h48GMT)19/9/96 (d)-(e).
In (b) coherence is plotted for signals X=Mellieha and Y=Melpaul (cyan), and X=St.George and Y=Melpaul (dotted, blue). In (c) phase plot is drawn for signals X=Mellieha and Y=Melpaul.
In (e) coherence is plotted for signals X=Mellieha and Y=Qawra (cyan), and X=St.George and Y=Qawra (dotted, blue). In (c) phase plot is drawn for signals X=Mellieha and Y=Qawra.
The 95% confidence level for the coherence is 0.17. The 95% confidence with 34 d.o.f. is 0.42dB (B_{min}=0.65; B_{max}=1.7).

factor for the gravest mode is at least one order of magnitude higher than that of the next mode. The observed period of the gravest bay mode agrees with the eigenperiod computed for the case of a nodal curve situated well outside the bay mouth. This energy peak is accompanied by a series of other amplified signals with shorter (T = 13.9, 11.1) and longer (T = 34, 25 and 21min) periods. These periods appear in both observation sets, but are not very stable, with shifts in the frequency even during the same seiche event. They appear to be related to waves in the near coast shelf area.

The phase between MEL2 and MELP is very stable for frequencies lower than 3 cph. This is supported by coherences which are higher than 0.95. At the resonant frequency the coherence drops abruptly while the phase suffers a sudden change of π radians. This behaviour is consistent with the hypothesis that the embayment responds as a damped harmonic oscillator to offshore waves. Comparison of the admittance function, calculated for synchronous records at MEL2 and MELP, with the corresponding power spectral density plot at

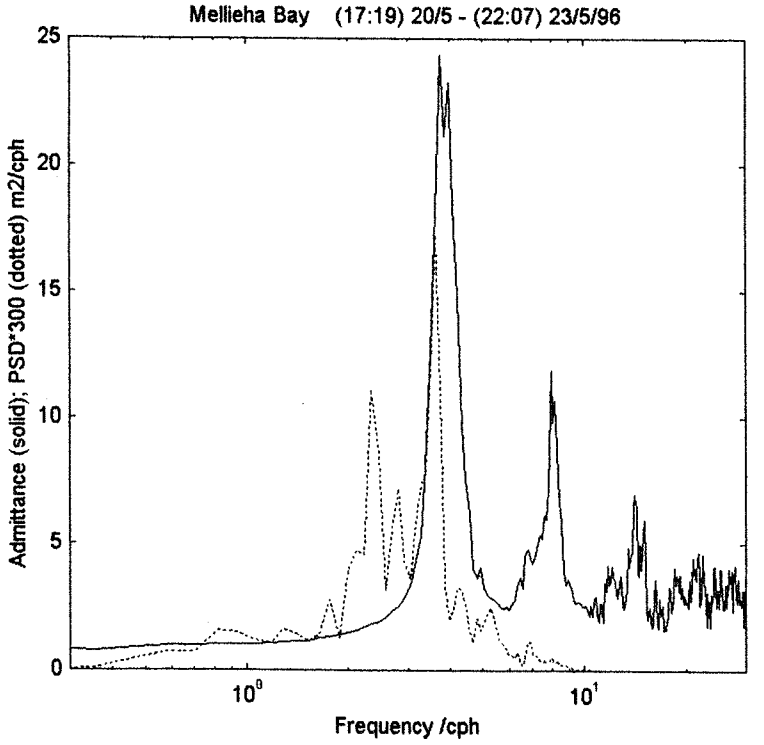

Fig. 3.31 Admittance function (solid) calculated from synchronous records at Mellieha and Melpaul stations from (17:19GMT) 20/5 - (22:07GMT) 23/5/96, and the power spectral density plot at Mellieha (dotted) for the same period.
The 95% confidence factor, for 34 degrees of freedom is 0.42 dB (B_{min}=0.65; B_{max}=1.7).

MEL2 yields important information on the instrument position with respect to the nodal position of the fundamental mode. The frequency f of the admittance peak coincides with that of the π phase change, but not with the resonant frequency f_o unless the instrument happens to be located exactly at the true nodal position. If the instrument is closer to the head of the bay than the nodal curve, then at the resonant frequency f_o , the movement of the water level at the station position would be in phase with that at the head of the bay, but the π phase change and hence the admittance peak occurs at $f > f_o$. The shift of the main admittance peak at frequency f toward higher frequencies with respect to the resonant frequency f_o (Fig. 3.31) confirms that the nodal position is further out from the bay mouth than the location of Melpaul station.

The peaks at T = 8.6min and 6.0min at the Mellieha station during the 21/22 May event are well evidenced by the high coherence at these two frequencies. They correspond to the first and second bay modes. Mode 1 is longitudinal, but mode 2 has a transverse character at the mouth of the bay. The phase relationships (Fig. 3.30c) at these two frequencies present abrupt changes of π radians which coincide to consistent drops in coherence. This is compatible to the spatial characteristics of these two bay modes. The admittance between this pair of stations supports further evidence in favour of a resonant coupling between the bay modes and the open sea waves. The admittance function is close to 1 at low frequencies, but increases to very sharp peaks in coincidence to the abrupt phase changes at the bay mode frequencies. There is no such increase in the amplification factor for a shelf mode. The admittance function thus gives a simple method of identifying between bay and shelf modes.

The cross-spectral results between Qawra and Mellieha stations (Fig. 3.30d-f) are more difficult to interpret. Qawra station is positioned further away from the bay with respect to Melpaul station and the structure of the longwave spectrum becomes more complex away from the coast. In the range of frequencies lower than the gravest mode the coherence remains high and the phase stays around zero at all frequencies. An identical behaviour is noted from a comparison of sea level records at Qawra and St.George's Bay stations (phase not shown). This result rules out the presence of travelling waves in the open sea, at least in the stretch of sea close to these stations. Such waves would in fact give rise to a phase difference that changes continuously with frequency and at a rate that depends on the phase speed of the waves. The open sea area adjacent to the embayments appears instead to be dominated by signals that have a standing wave character. Beyond f = 3cph the coherence drops to low values, but rises sharply at a few frequencies.

It is interesting to note the distinct energy peaks that characterise both offshore spectra at these frequencies. These peaks appear at the same frequencies as those observed at the coastal stations. At Qawra station, one such energy peak is even obtained at the fundamental Mellieha bay mode. These frequencies are marked by well-defined sharp rises in coherence to values well above the 95% significance level. These high coherence levels extend to St. George's Bay and thus give an idea of the spatial scales that pertain to these signals. These results imply that shelf modes in near-resonance to the embayments can lead to an amplification of the bay oscillations by a double-resonance effect (Rabinovich, 1993). This mechanism appears to apply to all the principal bay modes in both Mellieha Bay and St. George's Bay.

Differences between the coherence and phase plots for the two observation sets close to the fundamental Mellieha Bay mode deserve further attention. In the frequency slot between 2.5cph and 5cph, the coherence of MELP with respect to MEL2 decreases gradually to a minimum at $\approx$ 4cph and then increases again. The variation in the coherence of QW with respect to MEL3 in the same frequency interval is different. The coherence decreases abruptly to a minimum at $\approx$ 3cph, increases to a high level $\approx$ 3.5cph (the resonant frequency) and then dips again at $\approx$ 4cph. Very sharp phase jumps are associated with these two coherence minima. This behaviour can be explained if QW is positioned more distant from the bay mouth with respect to the nodal position of the fundamental bay mode, but closer to shore with respect to nodal position of the shelf mode. It is also noted that the phase relationship, relative to Mellieha station, at T = 8.6 min and 6.0min (bay modes 1 and 2) for QW is inverted with respect to that for MELP. At MELP, the 8.6 min/6.0 min signal is in antiphase/phase with the Mellieha coastal station, whereas at QW it in phase/antiphase. This further implies a direct coupling between the bay modes and the shelf modes. A different preferential excitation between these two bay modes is also noted for different seiche events. Their magnitude inside the embayments thus appears to depend on the nature of the long waves in the outer ocean.

Some additional higher frequency peaks at T = 4.0, 2.7 and 2.2min at the coastal Mellieha station are more difficult to explain. They are about two orders of magnitude weaker in amplitude compared to the fundamental mode, but they are very consistent in occurrence. They appear to represent inner bay longitudinal uncoupled higher modes of oscillation. This can only be confirmed by simultaneous measurements inside the bay.

The sea level signals at St. George's Bay are also a mix of shelf and bay modes. Compared to Mellieha Bay, the offshore bathymetry outside this bay is steeper and monotonic. The spectrum is much more uniform with a basically equal distribution of energy in the frequencies lower than 6 cph. Beyond this frequency amplification occurs particular at the fundamental bay mode (f = 10cph) and in the range f = 6-9cph. Amplification factors are however smaller than in Mellieha Bay, this being partly due to the position of the gauge at approximately the middle of St. George's bay. The sea level activity at the higher frequencies is particularly pronounced as already described in section 3.4.6.2. No signals emerge above the white noise levels at these frequencies. From the results presented in section 3.4.6, the lower frequency signals (f less than about 5 cph) inside the bay are very representative, in both phase and magnitude, of the signals outside. Comparison of SG2 with MELP, and SG3 with QW at these frequencies is thus very useful. In both cases, coherence remains high (Fig. 3.30b,e) and the phase (not shown) is very stable at zero for all the lower frequencies. A main drop in coherence occurs at around f = 1.5cph, with an associated phase switch of π radians. In the frequency slot 3 - 4cph, the phase returns to zero in association to a rise in coherence. At around 4cph the coherence drops again and the signals return in antiphase.

These characteristics of the offshore waves confirm the occurrence of standing wave motions on the shelf and in the near coastal area. Their variability in both magnitude and spectral characteristics depends on the different horizontal scales of influence involved in the forcing mechanisms that trigger these motions (atmospheric origin but also wind waves). When these offshore waves are in near resonance to the bay modes, they give rise to large amplitude oscillations in the embayments. The open sea long period standing wave motions thus appear to be associated with leaky waves arriving from the outer shelf areas. The results do not however exclude the possibility that edge waves form also a part of the offshore wave field. The profile of the higher edge wave modes normal to the coast are very similar to those of normal incident leaky waves with the same frequencies (Kovalev et al., 1991). A denser array of offshore and alongshore instruments would indeed be necessary in order to isolate the two types of waves (Guza & Inman 1975). Further analysis on the contribution of these two types of waves to the large amplitude bay oscillations is left to the modelling exercise in Chapter 5. The offshore long period waves can also be the near coast expression of broader standing wave patterns over the wider shelf area joining the Maltese Islands to Sicily. Insight on the triggering of coastal seiches by shelf resonances is given by an analysis of measurements made during the Malta Channel Experiment in section 3.6.3.3.

The spectral characteristics of the seiche oscillations are also studied during periods of low ('background') activity. Fig. 3.32 compares pairs of observations, each of 4068min duration, and selected during moderate and weak seiching conditions respectively. It is seen that the same spectral energy structure is maintained during periods of weak seiching. Only the energy levels are different. The admittance functions are moreover identical for both 'background' and stronger seiching. This implies that the same mechanisms apply. At the offshore stations, the spectral energy increases over practically the full range of frequencies during the seiching events, thus confirming further the existence of open sea surface waves at the same time that large sea level oscillations are observed in the bay.

3.4.7.6 Analysis of observation set 1

This set of observations is characterised by a period of strong seiching on 27th March. Slightly weaker and shorter duration seiching events (of just about 15 and 10 hours respectively) are recorded on 30th March and 2nd April. Oscillations with a period of 16.6min are clearly identified during all the events in Mellieha Bay, with a maximum amplitude of 0.6m on 27th March. Similar oscillations occur simultaneously with a very close period, but 2/3 in amplitude, in St. Paul's Bay.

Results of cross-spectral analysis between simultaneous sea level recordings for the full 17 day interval in the two bays indicate very close synchronisation at all signals with periods greater than 20min. The correlation is very high and energy is mainly concentrated at selected frequencies of 34, 28, 25.5 and 21.5min (Fig. 3.33). These periods are all longer than the gravest modes of the bay and are associated to shelf modes. They share a good part of the energy in both bays.

Coherence drops for frequencies higher than 3cph. The energy peak at T = 16.6min is the gravest mode (zero mode of free oscillations) in Mellieha Bay. The frequency resolution is not sufficient to resolve the fine structure of nearby peaks. In the same range of frequencies a pair of close peaks occur in St. Paul's Bay at T = 16.4 min and 15.2min. The signals in the two bays at 16.4min are well correlated, have identical intensities and bear an opposite phase. This signal appears to be an expression of the antiphasic coupled bay oscillation. On the other hand, the signal at T = 15.2min is intrinsic to St. Paul's Bay and not significantly correlated to Mellieha Bay. The gravest mode oscillations of the separate bays thus appear to coexist with the coupled bay mode.

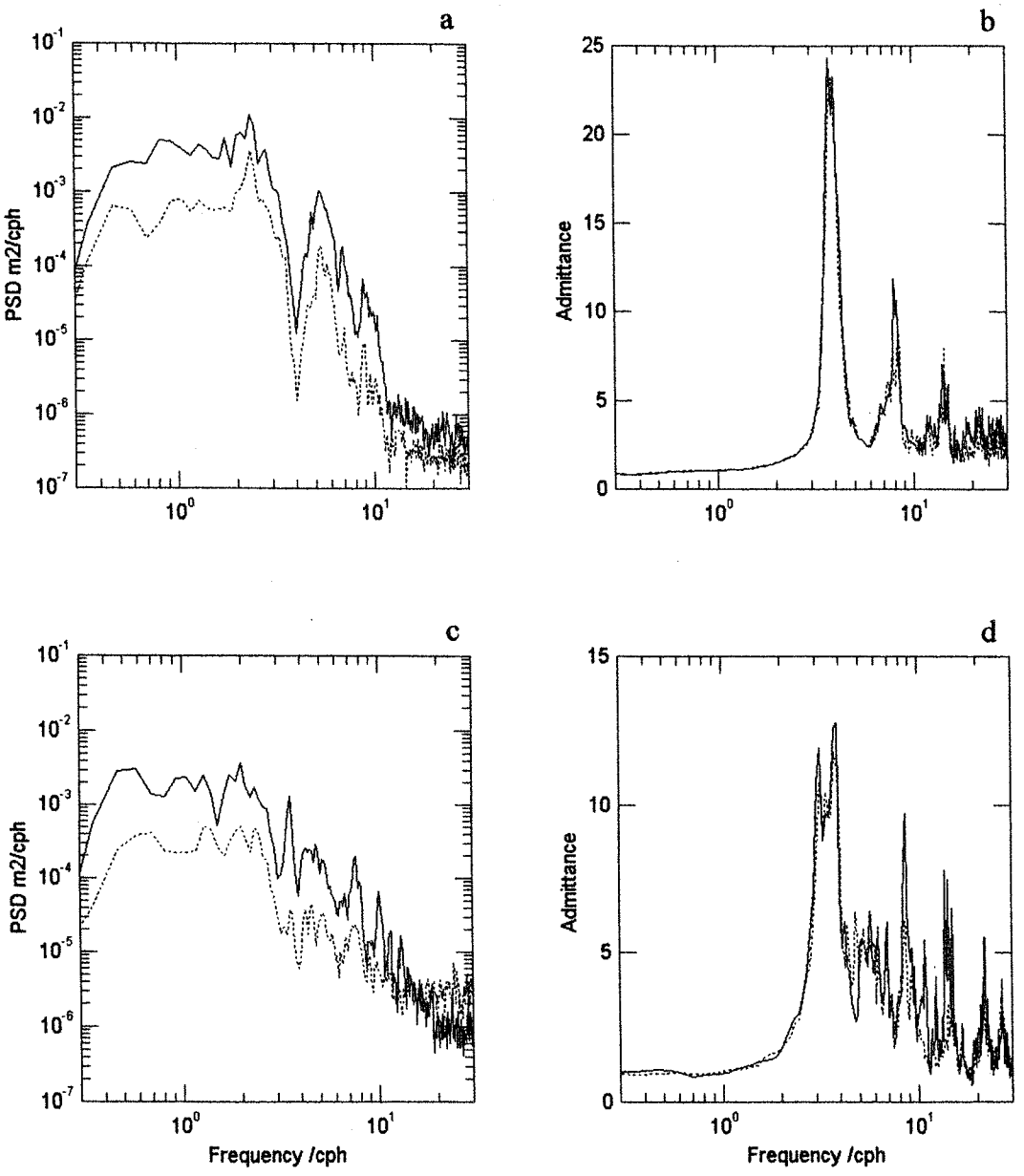

Fig. 3.32 Comparison of power spectral density and admittance function at Melpaul station (a,b) and Qawra station (c,d) during separate periods of moderate (solid) and weak (dotted) seiche oscillations. Admittance is calculated with respect to the coastal station in Mellieha Bay. The periods of observations are: (17h19)20/5 - (22h07)23/5/96 (solid) and (17h01)16/5 - (21h49)19/5/96 (dotted) for Melpaul station; (08h00)16/9 - (04h48)19/9/96 (solid) and (06h07)27/9 - (10h55)30/9/96 for Qawra Station.

Spectra are calculated with 34 degrees of freedom. The 95% confidence factor is 0.42 dB (B_{min}=0.65; B_{max}=1.7).

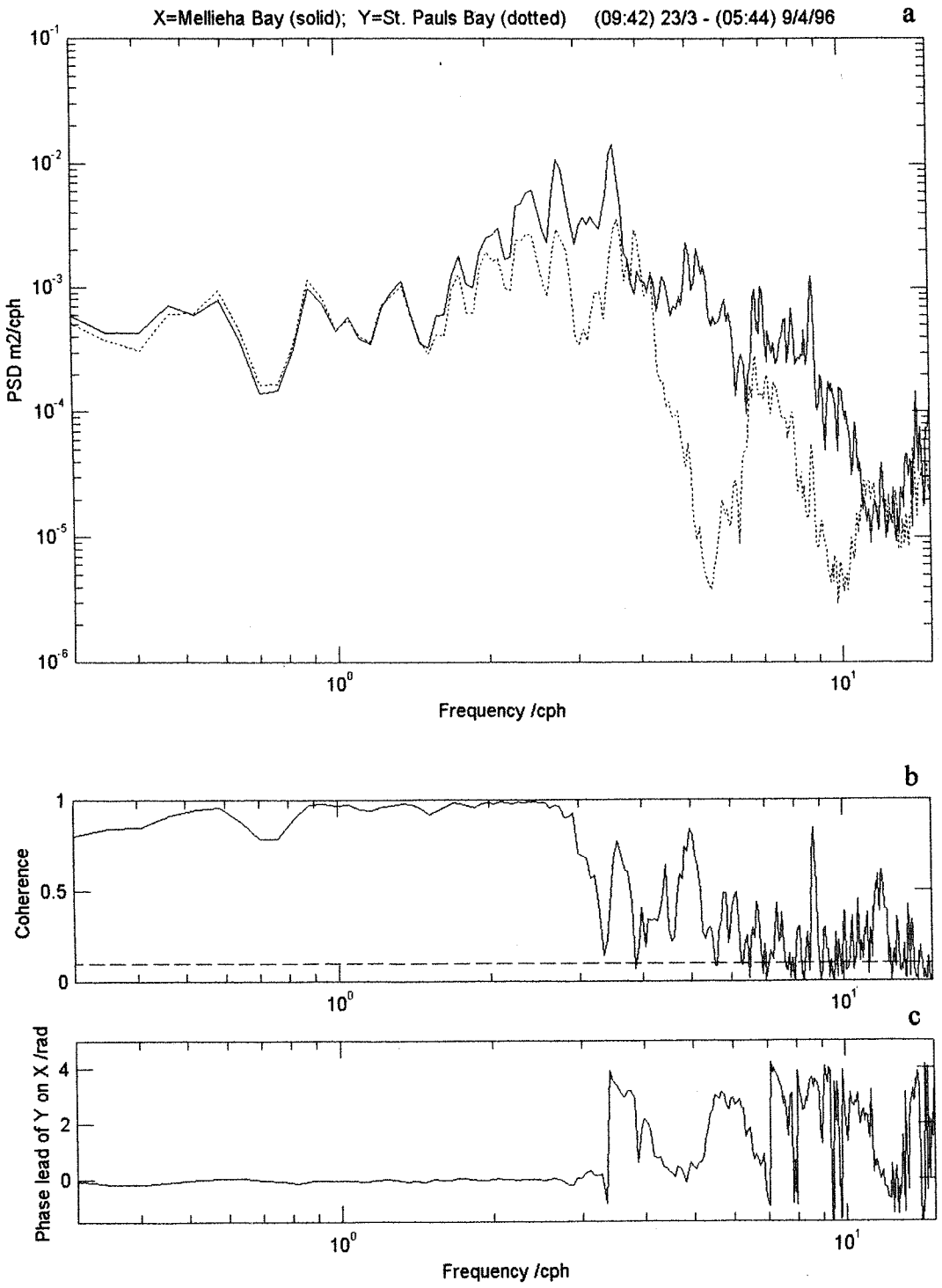

Fig. 3.33 Power spectral density (a), coherence (b) and phase (c) plots between 2-minute sampled high pass filtered water elevations in Mellieha Bay (solid) and St. Paul's Bay (dotted) for observations from (07h44GMT) 23/3 - (08h22GMT) 9/4/96.
The 95% confidence level for the coherence estimate is 0.07.
The 95% confidence factor, with 94 degrees of freedom is 2.5 dB (B_{min}=0.76; B_{max}=1.35).

Other important energy peaks at around T = 12min are shelf modes. Correlation between the two bays at this period is high and the phase is zero. The corresponding energy in St. Paul's Bay is however very low. The peak at T = 8.8min corresponds to an abrupt change in phase. It appears to be the 1st longitudinal mode intrinsic to Mellieha Bay. At T = 6.7min the two bays are again well correlated and in antiphase at the station positions. This signal can be attributed to a coupled bay mode. More detailed measurements are however necessary to identify the exact nature of these higher frequency modes.

The question of the combined or selective occurrence of the intrinsic fundamental bay modes with respect to the antiphasic coupled bay mode is of greater interest. The coexistence of the two types of oscillations can lead to detectable single bay or intra-bay beat phenomena when amplitudes are comparable and frequencies sufficiently close. Coupled oscillations in adjacent bays have been studied by Nakano & Fumijoto (1987) utilising hydraulic model techniques. They found that when a pair of coupled bays is excited by a single wave (such as a tsunami), the mode of oscillation of the seiches occurring in them changes in time. Initially the co-phasic oscillation prevails. Thereafter the co-phasic and antiphasic modes come closer in amplitude and the oscillations are characteristed by a beat phenomenon. Subsequently the oscillations are replaced by the antiphasic mode. Once the antiphasic mode is attained, it is then maintained. This behaviour is attributed to the different energy dissipation rates, by wave scattering and friction, associated to the modes.

The temporal development of these modes in Mellieha Bay and St. Paul's Bay are studied by dividing the spectrum into selected frequency segments. The signals in each segment are isolated from the rest by applying an 8th order Chebysev bandpass filter (refer Chapter 2, section 2.2.4.5). Three segments are chosen (I) from 0.1 to 0.15cph, (II) from 0.15 to 0.2cph, and (III) from 0.2 to 0.3cph. The higher frequency segment III is the one of most interest because it contains the signals under major investigation. It is subsequently further subdivided into two sub-segments, IIIa from 0.2 - 0.26cph containing energy peaks at T = 16.6 and 16.4 min., and IIIb from 0.25 - 0.29cph containing energy peak at T = 15.2 min.

Fig. 3.34 gives a comparative time series plot, at Mellieha Bay (solid) and St. Paul's Bay (dotted), of the three isolated signal components (I, II and III) during the seiche event on 27th March. It is interesting to note that at the two respective lower frequency slots the signals in the two bays retain synchronisation and change intensity together throughout the observation period. Their magnitudes are modulated in bursts. Intensification in one

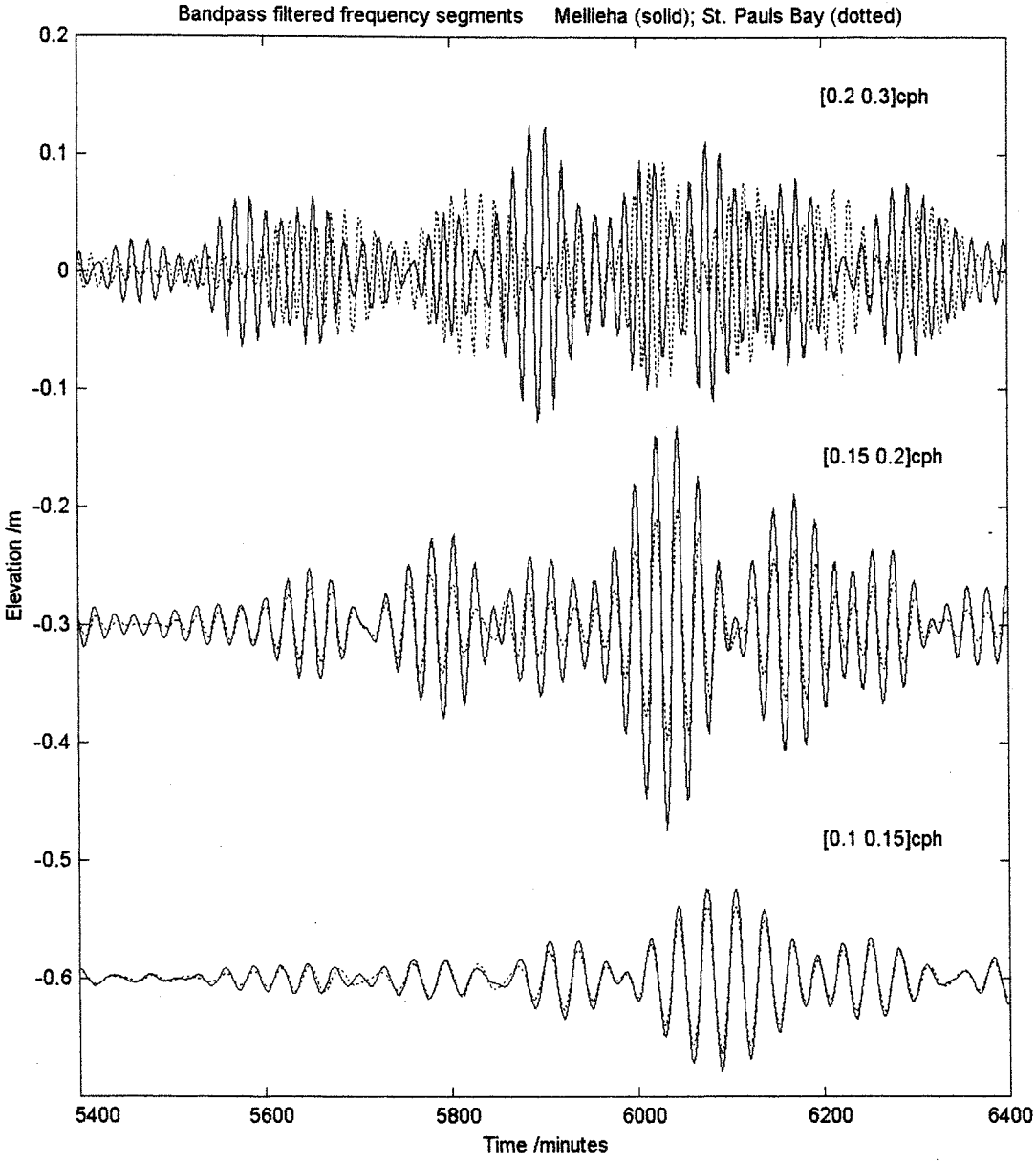

Fig. 3.34 Comparative time series plot, at Mellieha Bay (solid) and St. Paul's Bay (dotted), of the three bandpass signal components during the seiche event on 27th March.
Frequency segments are (I) from 0.1-0.15 cph, (II) from 0.15-0.2 cph, and (III) from 0.2-0.3cph.

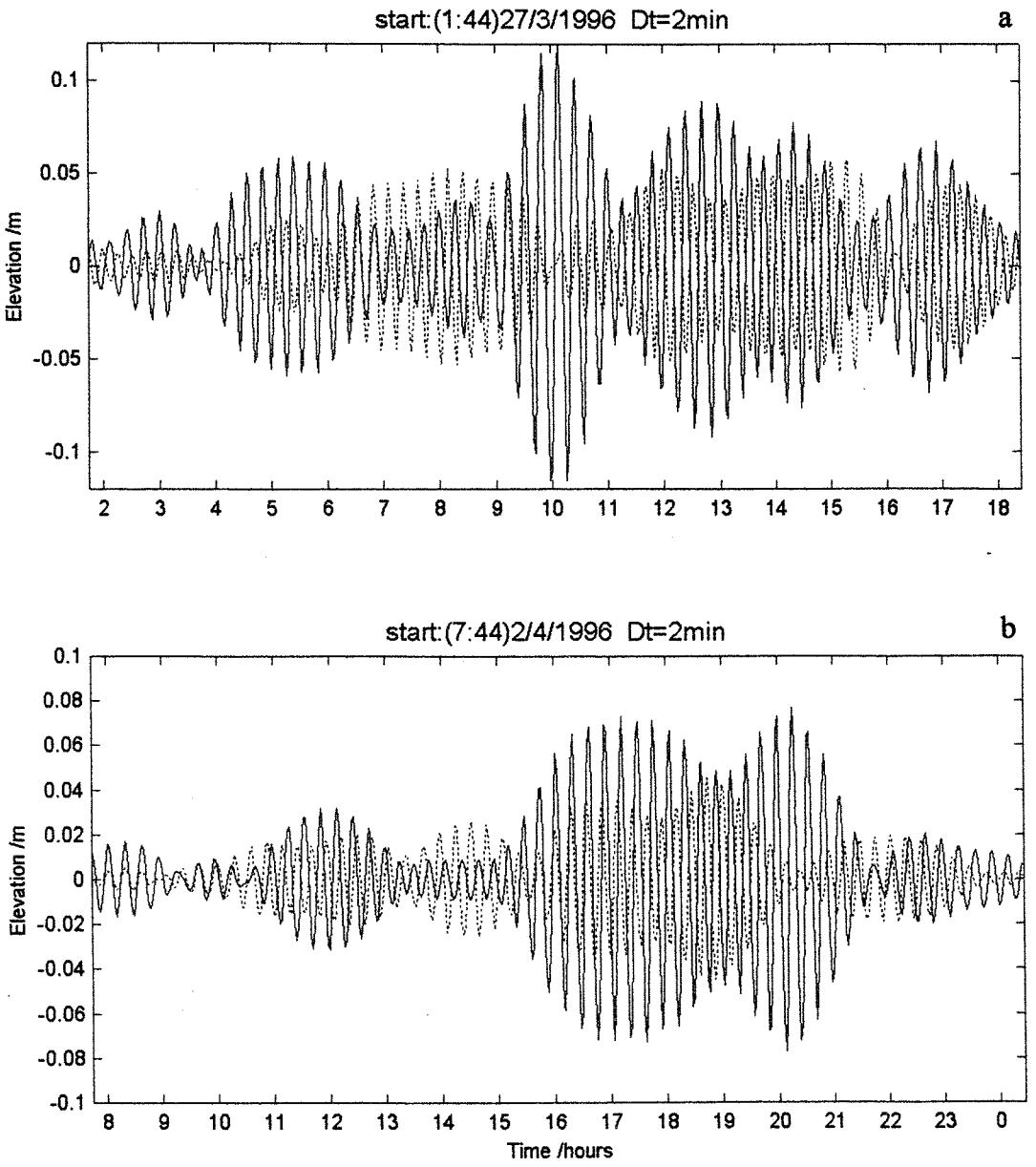

Fig. 3.35 Comparative time series plot, at Mellieha Bay (solid) and St. Paul's Bay (dotted), of the bandpass signal component (f=[0.2 - 0.26] cph) during the seiche events on 27th March, 1996(a) and 2nd April, 1996 (b).

segment does not however correlate with that in other segments so that signals have a separate response to the forcing which appears to be intermittent, variable in intensity and different for the different frequency segments. The situation is more complicated for frequency segment III. The signals in the two bays do not now maintain the same phase relationship and a beating effect between close frequencies is evident. Fluctuations in the amplitude of the oscillations succeed one another, but it is impossible to ascertain the extent of amplitude modulation by the beating effect from that related to the inherent variation in the forcing agent. A finer separation of signals in this segment is thus necessary. Results plotted in Fig. 3.35 compare the signals in the two bays for sub-segment IIIa during the seiche events on 27th March and 2nd April respectively. The changing phase relationship between the two bays can now be studied in greater detail. In particular, it is noted that the sea level fluctuations in the bays tend to be in antiphase during sustained periods with large amplitude oscillations. Amplitudes tend to be generally stronger in Mellieha, but can alternate at times. The largest oscillations in Mellieha Bay are attained when those in St. Paul's Bay die out; these oscillations do not however persist for long and get very quckly attenuated in a matter of a few subsequent oscillations. The presence of the nearby bay appears thus to be essential for maintaining oscillations in the two bays.

3.5 Seiche-induced currents in Mellieha Bay

3.5.1 Order of magnitude of seiche currents

High frequency, large amplitude sea level fluctuations can have associated horizontal motions that can be a damage potential on moored vessels. Ship loading/unloading operations can be delayed or even potentially hazardous. Constricted flow at harbour entrances also results in strong reversible currents that can be detrimental to navigation.

Taking the example of the Grand Harbour, with a narrow opening to the adjacent sea, we can estimate the magnitude of this seiche-induced flow. If the profile of the uninodal standing wave oscillation is taken to be sinusoidal with wavelength λ and swing height H, then the volume of water that must flow in half a period across a vertical line through the nodal point at the mouth of the harbour is $H\lambda/2\pi$. The time average horizontal velocity $<V>$ is obtained on dividing by the time T/2 of one half period and the average cross-sectional area,

namely the depth d. On using the shallow water wave propagation relation, the maximum velocity at the nodal point is then given by $V_{max} = \pi\langle V\rangle/2 = H\lambda/(2Td) = (H/2)\sqrt{(g/d)}$, where d is the average depth of the basin.

Taking H = 0.25m, d = 18m as typical values for the Grand Harbour, and assuming the constriction at the harbour mouth to be half the extent of the average harbour width, then the actual value of V_{max} is expected to be $0.37ms^{-1}$.

The horizontal particle excursion at the harbour mouth is given by $\langle V\rangle T/2 = H\lambda/2\pi d = (HT/2\pi)\sqrt{(g/d)} \approx 41m$. By proportion the excursion at the middle of the harbour is expected to be 20m. Thus although the maximum velocity is not excessively high, the large horizontal motion could create difficulties.

3.5.2 Measurement of seiche currents

3.5.2.1 The data set

An ENDECO/YSI tethered-type current meter is used to measure seiche-induced subsurface currents in Mellieha Bay. The instrument is deployed within the embayment at a station located at 35^0 58.8'N, 14^0 22.8'E where the total depth is 28m (refer to Fig. 3.36). Measurements consist of the vector averaged sea current and

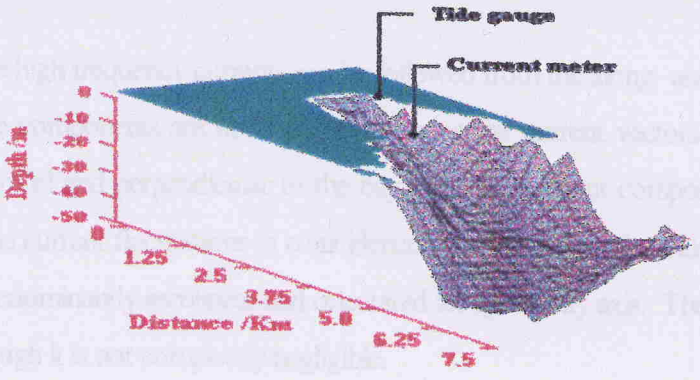

Fig. 3.36 Bathymetry of Mellieha Bay and positioning of instruments

temperature sampled every 2 minutes at 13m from the surface and cover the period 16:04GMT 25th July - 07:52GMT 30th July 1994. Sea level is also measured every 2 minutes at the coastal station situated at the head of the embayment. Meteorological parameters, including wind, surface pressure and air temperature are measured at the nearby Ramla tal-Bir station.

3.5.2.2 Analysis of currents

The current meter measures the total current which consists of a background current upon which the seiche induced currents are superimposed. The background current is predominantly established by wind-induced effects as well as by the interaction of the bay circulation with the open sea. In general this background circulation predominates and completely masks the seiche currents. During strong seiching events the associated movement of the oscillating water body in the bay can however produce significant currents. In the case of Mellieha Bay these seiche currents have the same frequency of the sea level oscillations (with a period of around 20 minutes) and can usually be easily detected as very rapid fluctuations in the current stick plots. The stick plot in Fig. 3.37 shows an example when the seiche currents become important and the current switches direction very rapidly in a matter of a few minutes. These currents are aligned in parallel to the bay axis along a NE - SW direction and are therefore an expression of the sloshing water movement in the bay. The current vectors in one half-cycle are not parallel to those in the next half cycle since a background current across the bay is superimposed during this particular interval.

The incidence of these high frequency currents can be followed from the along- and cross-bay axis components of the currents. These components are obtained by resolving the current vectors along orthogonal directions N65°E and S25°E parallel and perpendicular to the bay axis. The current component plots in Fig. 3.38 show clearly the onset of the current fluctuations in coincidence with the sea level oscillations on the 26th July. The seiche currents are predominantly rectilinear and orientated along the bay axis. Their component across the bay is less important although it is not completely negligible.

In order to better study the seiche currents it is important to isolate them from the background component. This is done by high pass filtering each of the resolved current component time series. A Vercelli filter with 48 weighting coefficients and a cut-off period of 34 minutes is used. The recombination of the high pass filtered components returns the seiche current vectors.

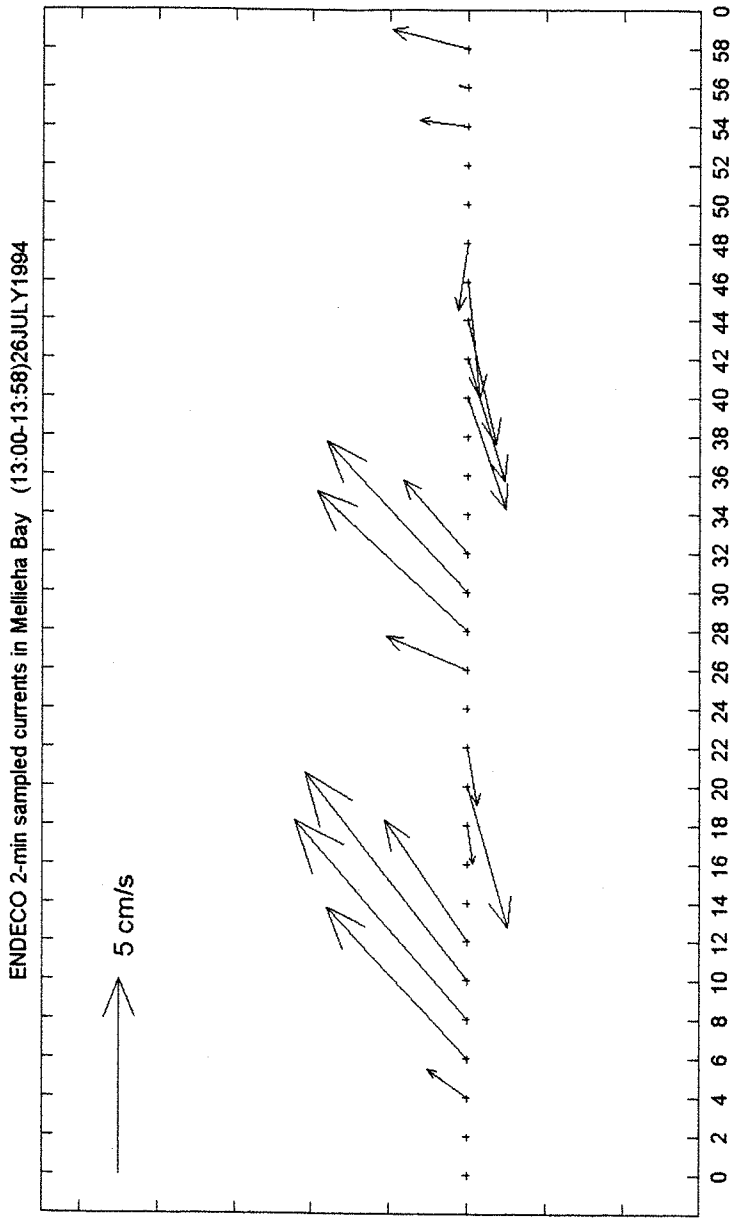

Fig. 3.37 Current stick plot of 2-minute sampled subsurface sea currents observed in Mellieha Bay at a depth of 11m from the water surface.

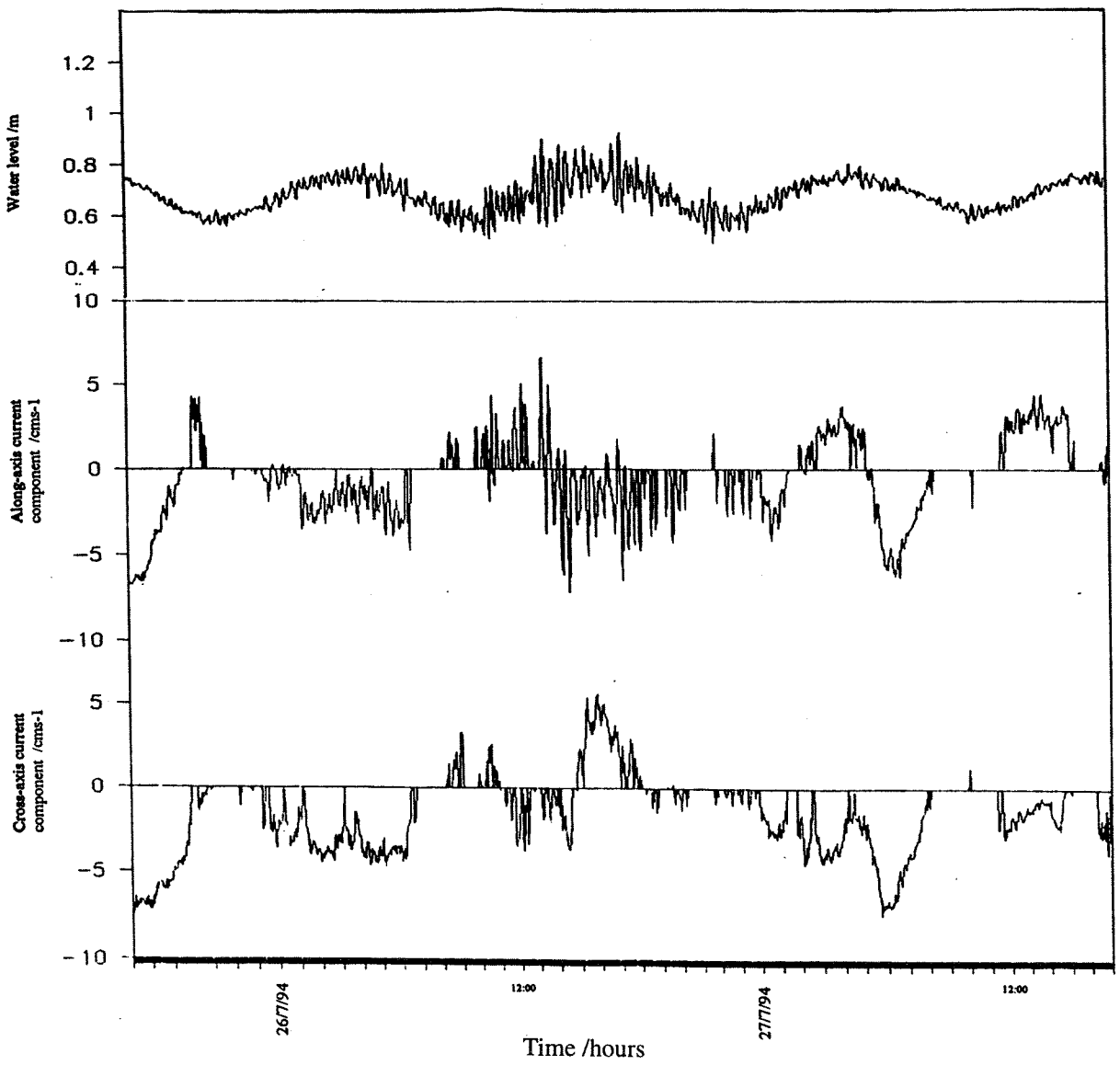

Fig. 3.38 Time series plot of (a) 2-minute sampled water elevation in Mellieha Bay, (b) and (c) 2-minute sampled subsurface current components resolved along/across the bay axis. Values span the period from 17:00GMT 25th November - 17:00GMT 27th November, 1994.

3.5.3 Estimation of seiche-generated currents from sea level data

The seiche-induced currents can be related to the sea level oscillations by means of a 1D model. Suppose that the sea level η is measured by a coastal gauge at the head of the bay (origin O in Fig. 3.39). These sea level oscillations follow the movement of the sloshing water in and out of the embayment. A one dimensional model is proposed to estimate the along-axis barotropic currents associated to this movement. Currents in the along-

axis direction are calculated at X at distance x_o from O. The bay is assumed to have constant width. The distance x from the origin O is measured along the 'talweg'; the depth D is taken to be the crossectional average orthogonal to the 'talweg'.

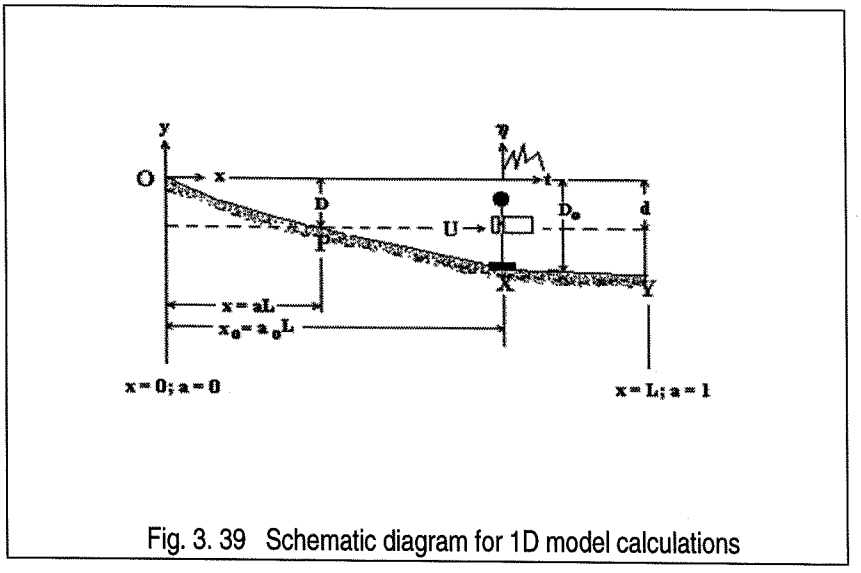

Fig. 3. 39 Schematic diagram for 1D model calculations

Suppose that the water body is oscillating at its gravest mode with period T_o. The position of the displacement node which marks the boundary between the water body in the bay and the open sea is not known a priori. The position of X with respect to this boundary is thus described by a non-dimensional distance $a_o=x_o/L$, where L is the hypothetical distance of the open boundary from O.

The elevation along the bay axis is also assumed to follow a sinusoidal profile with a maximum amplitude at the head and zero displacement at the open boundary. The elevation η at O is an expression of the instantaneous displacement of the vertical oscillation at O. If the free surface along the bay is assumed to retain a sinusoidal profile in time, the instantaneous displacement at any position a (= x/L) will be given by $y(a,t) = \eta(t)\mathrm{Cos}(\pi a/2)$. The excess volume of water $V(a_o,t)$ at time t which has accumulated behind point X is given in dimensional form and for unit cross-bay width by:

$$V(a_o,t) = L\int_0^{a_o} y\,da = \frac{2\eta L}{\pi}\left[\mathrm{Sin}(\pi a/2)\right]_0^{a_o} = \frac{2\eta L}{\pi}\mathrm{Sin}(\pi a_o/2). \qquad (3.19a)$$

Now if d is the average depth of the embayment along the 'talweg', then

$$\sqrt{(gd)} = 4L/T_o \Rightarrow L = (T_o/4)\sqrt{(gd)},$$

hence

$$V(a_o, t) = \frac{\eta(t) T_o \sqrt{gd}}{2\pi} \mathrm{Sin}(\pi\ a_o / 2). \qquad (3.19b)$$

The instantaneous flow of water across unit bay width at X is

$$\frac{dV(a_o, t)}{dt} = \frac{T_o \sqrt{gd}}{2\pi} \mathrm{Sin}(\pi\ a_o / 2) \left(\frac{d\eta(t)}{dt} \right)_o \qquad (3.20a)$$

where the subscript in $\left(\frac{d\eta(t)}{dt} \right)_o$ is included to indicate that the rate of sea level change is measured at the origin.

If D_o is the depth at $a = a_o$, the barotropic current U (+ve in the +ve x-direction) is given by

$$-\frac{dV}{dt} = UD_o. \qquad (3.20b)$$

Hence

$$U = -\frac{T_o \sqrt{gd}}{2\pi\ D_o} \mathrm{Sin}(\pi\ a_o / 2) \left(\frac{d\eta(t)}{dt} \right)_o. \qquad (3.21)$$

If the elevation η is measured as a discrete signal with sampling frequency $1/\Delta T$, $d\eta/dt$ can be expressed in finite difference form as $\frac{\eta(t+\Delta t) - \eta(t-\Delta t)}{2\Delta t}$.

The model is applied to the observations in the period 12:00GMT - 15:00GMT 26th July 1994. T_o is obtained from an inspection of the average period of the water level oscillations during this period. The value $T_o = 16.8$

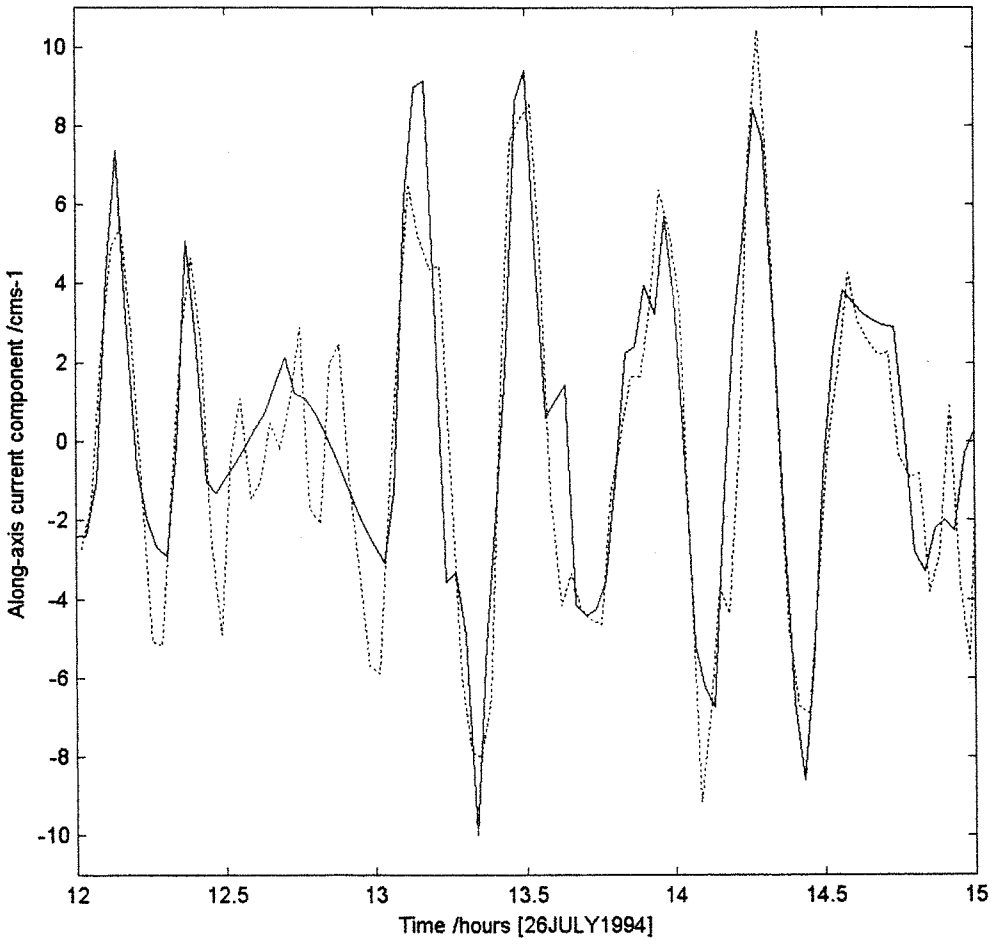

Fig. 3.40 Comparison of observed (full) and calculated (dotted) along-axis current component in Mellieha Bay. The observed currents are high pass filtered values. The calculated currents are derived from sea level observations by a 1D model (T_o=16.8min.; d=20m; D=28m) which assumes a sinusoidal water surface profile and a constant wave celerity $c=4L/T_o=\sqrt{(gd)}$.

minutes is adopted. The average depth is taken to be 20m while the total depth at the current meter station is taken as D = 28m. The sea level time series is used to obtain 2-minute values of $-\frac{T_o\sqrt{gd}}{2\pi\ D_o}\left(\frac{d\eta(t)}{dt}\right)_o$. These values are compared with the filtered along-axis current observations. The correlation estimated is found to be very high (r = 0.865) which shows the efficiency of the model. A regression analysis between U and

$-\frac{T_o\sqrt{gd}}{2\pi\ D_o}\left(\frac{d\eta(t)}{dt}\right)_o$ gives the optimal value of $Sin(\pi\ a_o / 2)$ as 1/1.96. This implies that $a_o = 0.34$ and hence that $L = x_o/0.34$. This result confirms that the seiche oscillations are not confined to the interior of Mellieha Bay, but that they actually involve a much larger water body which extends well beyond the promontaries of the bay. This water body is about three times the size of the bay and includes the deeper basin between the mouth of the bay and the White Bank to the northeast of the bay.

Fig. 3.40 compares the depth-averaged along-axis seiche current component derived by the above model (with a_o set equal to 0.34) to the observed high pass filtered currents. The correspondence confirms the validity of the model which can thus be used to predict seiche currents from observations of sea level on the coast. In particular it is interesting to note that moderate seiche amplitudes of just 15cm can generate quite strong seiche currents which peak up to 10 cms^{-1}. This shows the potential hazard of these seiche induced currents even in the case of a wide mouthed embayment such as Mellieha Bay.

3.6 Phenomenology of the longer period oscillations

3.6.1 Data sets used for the study

The long wave field in the offshore region to the north of Malta is investigated by means of two sets of data. Station positions for these sea level measurements are shown in Fig. 3.41.

The first set is intended to study signals in the immediate vicinity of the island. The measurements cover a period of 8 days (14h21GMT 7th May - 14h18GMT 15th May 1996) with simultaneous 1-minute sampled observations at the coastal gauges in Mellieha Bay and St. George's Bay, and at an open sea station by a bottom pressure Aanderaa WLR7 gauge on Munxar reef on the northeastern tip of Malta (depth = 20m; position = 35° 51.10'N; 14° 35.65'E). Mellieha and Munxar stations are at the extreme ends of the island at a separation of about 25 Km; St. George's station is approximately in the middle at about 15Km from Munxar station. During these observations, long period waves with crest-to-trough amplitudes exceeding 13cm (the largest recorded at an offshore station) were observed at Munxar station.

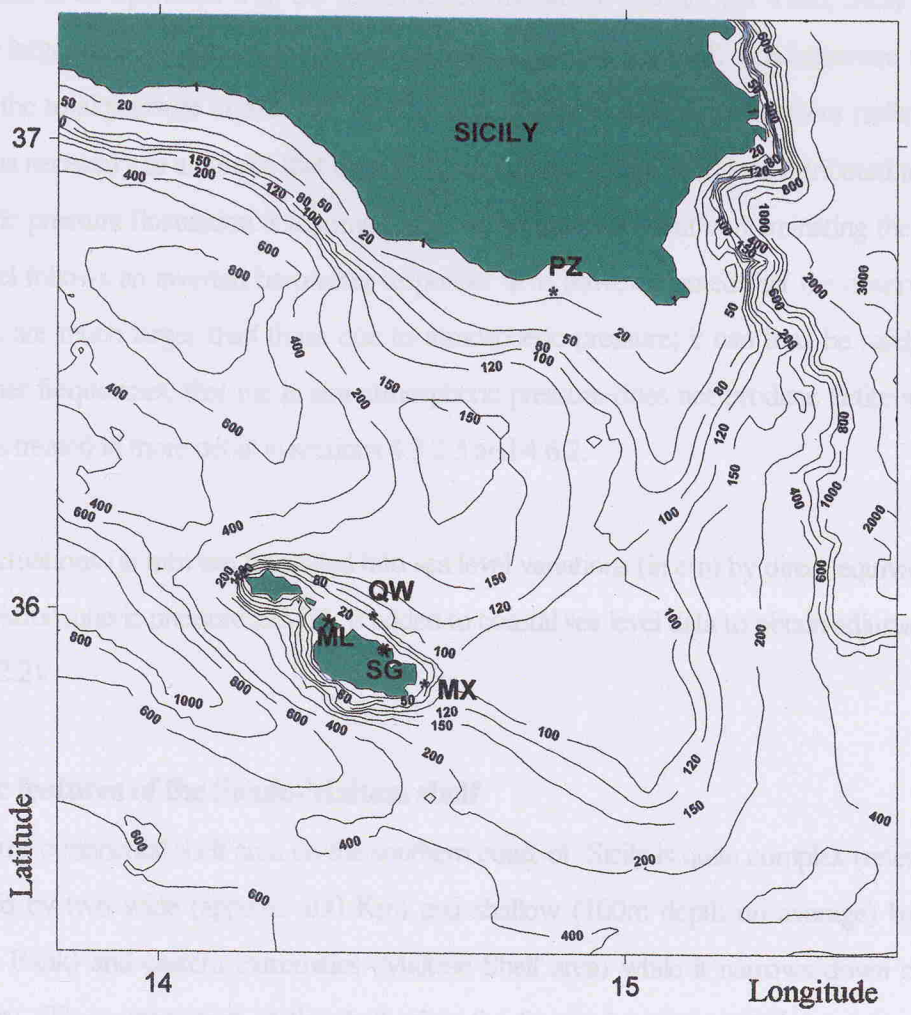

Fig. 3.41 Seabed topography of the Siculo-Maltese continental shelf. Depths are in meters. Station positions for sea level measurements are indicated by a small asterisk in the open sea and by a larger asterisk on coast.
(ML=Mellieha Bay; SG=St. George's Bay; MX=Munxar; QW=Qawra; PZ=Pozzallo).

The second set consists of simultaneous bottom pressure recordings at Qawra Station outside Mellieha Bay (depth = 30m; position = 35° 59.35'N; 14° 25.81'E) and at Pozzallo on the southern coast of Sicily (depth = 18m; position = 36° 42.21'N; 14° 50.12'E). Pozzallo station is approximately to the north of Qawra station at a separation of about 100Km across the whole shelf area. These measurements span a period of 20 days (8h50GMT 10th September - 11h54GMT 30th September 1996) and were collected during the Malta Channel

Experiment carried out in co-operation with the Italian CNR Institute at Mazara del Vallo, Sicily. They are intended to study the larger scale oscillations on the Siculo-Maltese continental shelf. It is important to note that the gauges measure the total pressure exerted by both the water column and the atmosphere (refer Chapter 4 section 3.2). It is thus necessary to ascertain that the recorded oscillations can be indeed attributed to the water body. An atmospheric pressure fluctuation is automatically compensated without contaminating the recordings provided the sea level follows an inverted barometer response. It is however noted that the observed bottom pressure fluctuations are much larger than those due to atmospheric pressure; it can thus be safely assumed, especially at the higher frequencies, that the in situ atmospheric pressure does not produce fictituous sea level signals. This aspect is treated in more detail in sections 4.3.2.3 and 4.6.2.

Bottom pressure fluctuations (in mb) are translated into sea level variations (in cm) by direct equivalence (refer to section 4.3.2.1). Atmospheric pressure at MSL is added to coastal sea level data to obtain adjusted sea levels (refer to section 4.3.2.2).

3.6.2 Topographic features of the Siculo-Maltese shelf

The topography of the continental shelf area on the southern coast of Sicily is quite complex (refer Fig. 3.41). The shelf is bounded by two wide (approx. 100 Km) and shallow (100m depth on average) banks on the western (Adventure Bank) and eastern extremities (Maltese Shelf area) while it narrows down considerably along its middle part. The eastern part of the shelf takes the form of an interrupted continental shelf and resembles a large roughly square bank with the Maltese Islands residing on the southernmost extremity. To the west and southwest the shelf overlooks the Central Mediterranean basin with an average depth of 500m, while on its eastern extremity it deepens abruptly into the deep Ionian Sea with a very sharp escarpment (known as the Malta Escarpment). The shelf topography is characterised by a plateau in its middle part, with an average depth of 150m. The shelf is flanked by a submarine ridge which protrudes as a submerged extension of Cape Passero and embraces the shelf area along the eastern and southern perimeter. The Maltese Islands represent the emerged part of this ridge while the Hurds Bank to the northeast of Malta shallows to a depth of just over 50m.

3.6.2.1 Influence of topography on the long period wave period

The seabed topography of the Malta Channel is thus characterised by significant reversals of the bottom slope. The theoretical investigation of barotropic trapped waves on the continental shelf is hence rather difficult.

Indeed the complex topography and the variable width of the shelf limit does not allow the utilisation of the classic dispersion relations that apply to monotonic depth profiles with constant alongshore characteristics. Moreover the presence of isolated bottom slope reversals introduces separate sets of trapped wave modes with energy concentration over the regions of reversed slope, and with a direction of propagation opposite to that of the wave modes established against the main shelf slope from the mainland. The Maltese archipelago rises from a submarine ridge and long wave energy can be guided along the ridge (Munk & Arthur, 1952) possibly leading to trapped waves in the form of island modes (Mysak, 1979). The islands are also situated in close proximity to the shelf break where focussing and guiding of the shelf modes occurs. These shelf modes are moreover modified by diffraction and refraction as they impact the island system. Closer to the coast, any small portion of the island can be regarded as straight locally and hence the long period wave field is expected to be influenced by the local bathymetry. In particular, the irregularities in the width of the bottom contours are expected to influence the energy spectrum of the standing wave motions in the nearshore area. The sea level signals, particularly on the northern coast, therefore consist of an expression of both the larger scale shelf modes and the smaller scale and more localised near field long period wave systems.

3.6.3 Description of the long period wave field in the Malta Channel

The long wave structure of sea level oscillations in the region is typically characterised by (a) forced motions, (b) free long waves propagating along the shelf, and (c) eigenoscillations of individual coastal areas including embayments and inlets. The bay oscillations have already been treated in previous sections and concern signals with periods lower than 20 minutes. Long waves with longer periods are however also persistent and rise above the background levels during seiching events. Their periods normally range from 20 minutes to a few hours. Main signals with periods 3.7, 2.2, 1.7, 1.1 hours, and 58, 46, 34.3, 29.5, 27.7, 25.1, 21.2 minutes were identified from the general analysis in Chapter 2 (section 3.4.2). The bays are shallow coastal indentations with shapes that do not permit natural resonant periods to match these values. This shows that these oscillations concern a larger water body.

3.6.3.1 General description of long waves on a continental shelf

The typical lengths of these lower frequency long waves are in the order of tens of kilometers and are compatible to the characteristic widths of continental shelves. The constructive interference between incident waves of appropriate dimensions from the deeper ocean with waves reflected from the coast can thus lead to

standing wave patterns corresponding to the well-known leaky modes and trapped modes (also called edge waves) of waveguide theory (MUNK et. al, 1964). These oscillations can develop on the continental shelf as well as in more restricted coastal areas provided that appropriate bottom slope conditions apply.

Leaky modes re-radiate energy into the deep sea. Along a coast with uniform alongshore bathymetry their alongshore wavelengths are usually long in comparison with the offshore wavelengths. For a particular frequency they have a continuous spectrum of alongshore wavelengths. Any angle of approach is possible, that for normal incidence corresponding to a standing wave system normal to the shore. An antinode is required at the shore and a node at the shelf edge. In the case of a shelf with constant alongshore characteristics, width L and a montonic depth profile d(x), where x is the distance normal to the coast, the fundamental period is given by $T = 4\int_0^L \frac{dx}{\sqrt{gd}}$. Other possible modes are given by the odd harmonics T/3, T/5, etc. For other angles of incidence the resonant frequencies become slightly higher and the amplification is less. Leaky waves do not however necessarily require a shelf break and can occur over smaller areas and close to shore. In the case of a plane coast with a linear sloping bathymetry $d(x) = \alpha x$, the leaky waves normal to the coast are described by the expression (Lamb,1932)

$$\eta(\omega, x) = A\boldsymbol{J}_o(\chi) = A\boldsymbol{J}_o(\sqrt{4\omega^2 x / g\alpha})$$

where $\omega = 2\pi / T$ is the angular frequency, A is the amplitude at the coast, $\boldsymbol{J}_o$ is the zeroth order Bessel function of the first kind and g is the acceleration due to gravity. The function $\boldsymbol{J}_o$ has zeros when its argument $\chi_K = 2.405, 5.520, 8.654$, etc. and maxima at $\chi_M = 3.832, 7.016, 10.174$ etc. At any offshore position, distant X from the coast, standing waves with frequencies $\omega_K = \chi_K\sqrt{(g\alpha/4X)}$ thus exist for which $\boldsymbol{J}_o = 0$ represents a nodal line parallel to the coastline. At frequencies $\omega_M = \chi_M\sqrt{(g\alpha/4X)}$ antinodes are obtained. The theoretical spectral energy distribution for this linear slope model (proportional to $\boldsymbol{J}_o^2$) thus consists of peaks at frequencies ω_M and troughs at ω_K.

In the case of trapped modes the energy is channelled by the bathymetry and remains on the shelf. The waves propagate in a direction parallel to the coast and energy is totally internally reflected at the continental slope. For a straight continental shelf of uniform width and constant depth falling vertically at the shelf edge to a flat bottomed ocean, amplitudes decrease exponentially seawards. Only certain angles of incidence are permissible.

At glancing incidence, a lower cut-off frequency occurs in each mode corresponding approximately to periods of infinity, T/2, T/4, T/6, etc. where $T=4L/\sqrt{(gh)}$, and the waves are thus non-dispersive. Their offshore wavelengths have the same scale as their offshore wavelengths. For a given frequency and bottom slope the alongshore wavelengths have a discrete spectrum, so that only certain wavelengths are permitted. For a wave of a given frequency on a continental shelf with no longshore variations, trapped modes always have shorter alongshore wavelengths compared to those of leaky modes. This may not however apply in the case of a more complicated bathymetry with both cross-shore and alongshore variations. Moreover if the depth at a distance from the coast tends to a constant value, the trapped modes leak some energy to infinity, although the consequent rate of decay may be exceedingly slow (Longuet-Higgins, 1967). With a real bathymetry the transition between leaky and trapped modes is thus much more tenuous than the idealised case.

The initial energy of these long period shelf oscillations may be absorbed from radiation of the same frequency incident from the adjacent deeper sea areas. It may alternatively be derived from a sharp pulse such as due to a travelling pressure disturbance. In the case of the Maltese shelf area, there is evidence (refer Chapter 4) in favour of the dependence of long waves in the sea on pressure fluctuations in the atmosphere. The passage of a pressure disturbance is responsible for the resonance generation of shelf modes (Kulikov & Schevchenko, 1992); it can also generate a whole range of more localised sea level signals in the medium range of frequencies. The periods of these shelf oscillations are dependent on both the period range in the pressure wave spectrum as well as on the bottom relief.

3.6.3.2 Analysis of the nearshore observations - set I

Using the results of cross-spectral analysis of various pairs of coastal and bottom pressure stations from the two sets of observations described above, it is possible to examine the wave structure in the medium range frequency band in the vicinity of the Maltese Islands. At these frequencies the signals inside the embayments are well representative, in phase as well as magnitude, of the corresponding oscillations in the adjacent open sea. This is deduced from the analysis in previous sections (3.4.6.3 and 3.4.7.5).

The plots presented in Fig. (3.43a-e) refer to the stations in the first set of observations along the northern coast of Malta. They represent the characeristics of the long wave field averaged over the whole observation period which includes periods of both calm and enhanced oscillations. A first inference from the energy spectra is the

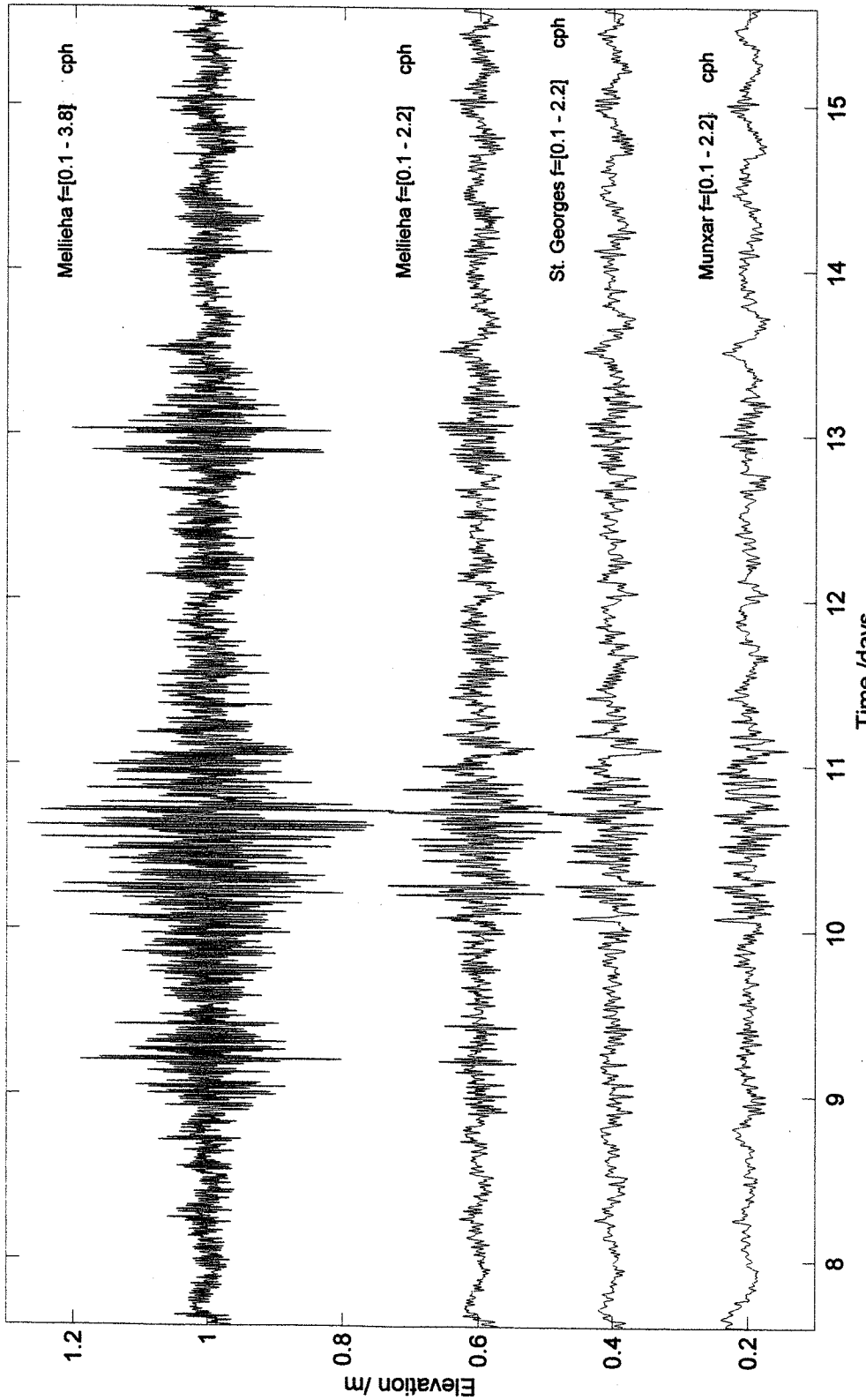

Fig. 3.42 Time series of bandpass filtered water level observations in Mellieha Bay, St. George's Bay and Munxar offshore station in the period (14h21) 7th May to (14h18) 15th May, 1996. Two overlapping bands of frequencies are plotted for comparison in Mellieha Bay. Plots are displaced for better visualisation.

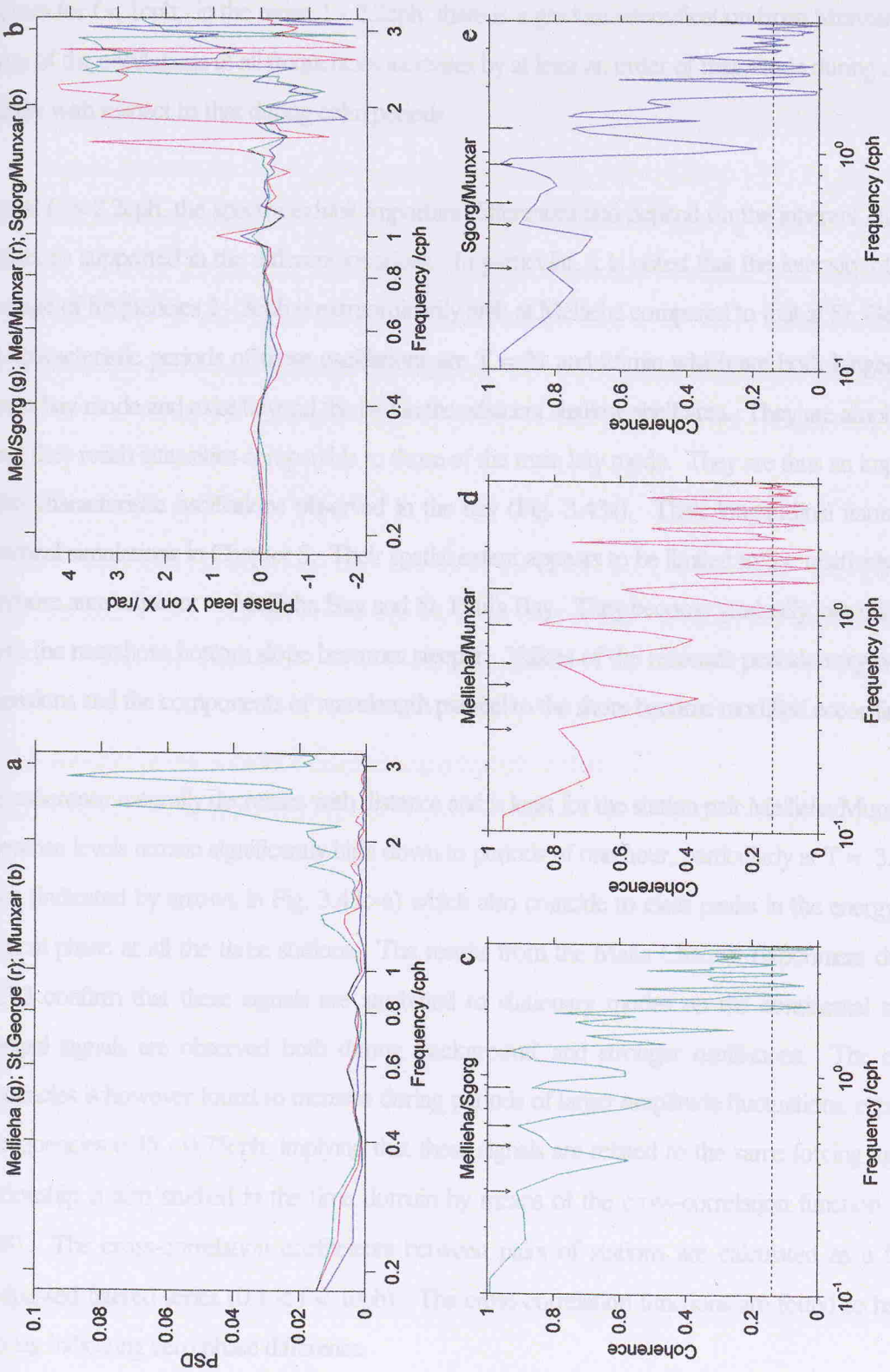

Fig. 3.43 Cross-spectral analysis of 1-minute sampled water level observations in Mellieha Bay, St. George's Bay and Munxar offshore station in the period (14h21) 7th May to (14h18) 15th May, 1996. Power spectral density in (a) is calculated over 43 d.o.f with a 95% confidence factor of 3.7 dB (B_{min}=0.73; B_{max}=1.7). The 95% confidence level for the coherence estimate is 0.14.

similarity of signals registered at the three stations with frequencies lower than 2.2cph. Fig. 3.42 compares the bandpass filtered time series ($0.1 < f < 2.2$cph) at the three stations. The spectra have the same intensity and structure for $f < 1$cph; in the range 1 - 2.2cph there is a gradual intensification from Munxar to Mellieha. The energy of the oscillations at all frequencies increases by at least an order of magnitude during events of enhanced intensity with respect to that during calm periods.

Beyond $f = 2.2$cph, the spectra exhibit important differences and depend on the inherent eigenstructure of the oscillations supported in the different locations. In particular, it is noted that the intensity of the oscillations in the range of frequencies 2 - 3cph is extraordinarily high at Mellieha compared to that at St. George and Munxar. The characteristic periods of these oscillations are $T = 21$ and 25min which are both longer than those of the gravest bay mode and exist beyond the bay in the adjacent shallow shelf area. They are amplified inside the bay where they reach intensities comparable to those of the main bay mode. They are thus an important component of the characteristic oscillations observed in the bay (Fig. 3.43a). Their longitudinal nature is confirmed by numerical simulations in Chapter 5. Their spatial extent appears to be limited to the relatively wide and shallow nearshore area adjacent to Mellieha Bay and St. Paul's Bay. They become gradually less important further east where the nearshore bottom slope becomes steeper. Values of the resonant periods vary with these changing dimensions and the components of wavelength parallel to the shore become modified accordingly.

The coherence naturally decreases with distance and is least for the station pair Mellieha/Munxar. However, the coherence levels remain significantly high down to periods of one hour, particularly at $T =$ 3.4, 2.2, 1.7 and 1.1 hours (indicated by arrows in Fig. 3.43c-e) which also coincide to clear peaks in the energy spectra and have identical phase at all the three stations. The results from the Malta Channel Experiment described in section 3.6.3.3 confirm that these signals are attributed to stationary modes on the continental shelf. These same principal signals are observed both during 'background' and stronger oscillations. The coherence at these frequencies is however found to increase during periods of larger amplitude fluctuations, especially in the range of frequencies 0.35 - 0.75cph, implying that these signals are related to the same forcing agent. Their phase relationship is also studied in the time domain by means of the cross-correlation function (Jenkins & Watts, 1968). The cross-correlation coefficients between pairs of stations are calculated as a function of lag on bandpassed filtered series ($0.1 < f < 1$cph). The cross-correlation functions are found to have a maximum at zero lag indicating zero phase difference.

Just beyond f = 1cph there is a sensible dip in coherence which coincides to a valley in the energy spectra, and to a slight variation in the phase relationship at all the three stations. It is followed by a sharp coherence peak with a period of 46min. at which the phase returns to zero. This signal is also related to resonance amplification at the nearshore shelf area of leaky waves incoming from the deeper sea. At further higher frequencies, the phase and coherence are characterised by sharp variations. When the phase shifts to 180°, the coherence falls to lower values. This low coherence implies the presence of 'trapped' waves at glancing incidence propagating parallel to the shore. At these frequencies, wavelengths become comparable or shorter than station separations. The result is that at a given station pair some wave modes are in phase while others are in antiphase, thus leading to an overall reduction in coherence at the two stations. The number of stations used in this analysis are too few in order to allow separation of leaky and trapped modes. An analysis on the lines of that adopted by Munk et. al, 1964 would require several alongshore stations at different separations.

At higher frequencies the coherence also rises above the confidence level at several small peaks. This coherent energy is related to free long waves propagating in the coastal area. They are modified by the width and mean depth of the nearshore areas as they move along the coast.

3.6.3.3 Results of the Malta Channel experiment - set II

The similarity and temporal coincidence of the bottom pressure recordings at Pozzallo and Malta is an indication that the lower frequency long wave oscillations are not related to the local topography at the respective stations, but are instead an expression of the larger scale movements of the water body over the continental shelf. The cross-spectral analysis between the two records (Fig. 3.44) shows that the principal signals at the two stations are identical, with energies being on average an order of magnitude higher in Pozzallo throughout the range of frequencies $0.4 < f < 1.1$cph. The analysis shows two main sudden variations in phase and coherence. The records are consistently in phase and highly coherent for $f < 0.7$cph. In this range of frequencies the energy spectrum carries a broad peak centred at 0.285 cph (T = 3.5h) followed by sharper and stronger peaks at T = 2.2, 1.7, 1.45h. At 0.78cph the phase changes abruptly and the signals become in antiphase between 0.8 and 1.1 cph. The strongest energy peak (with T = 1.1h) at Pozzallo is registered in this frequency range. It is accompanied by a weaker peak at T = 58min. At both these two peaks, the coherence rises to high levels. The

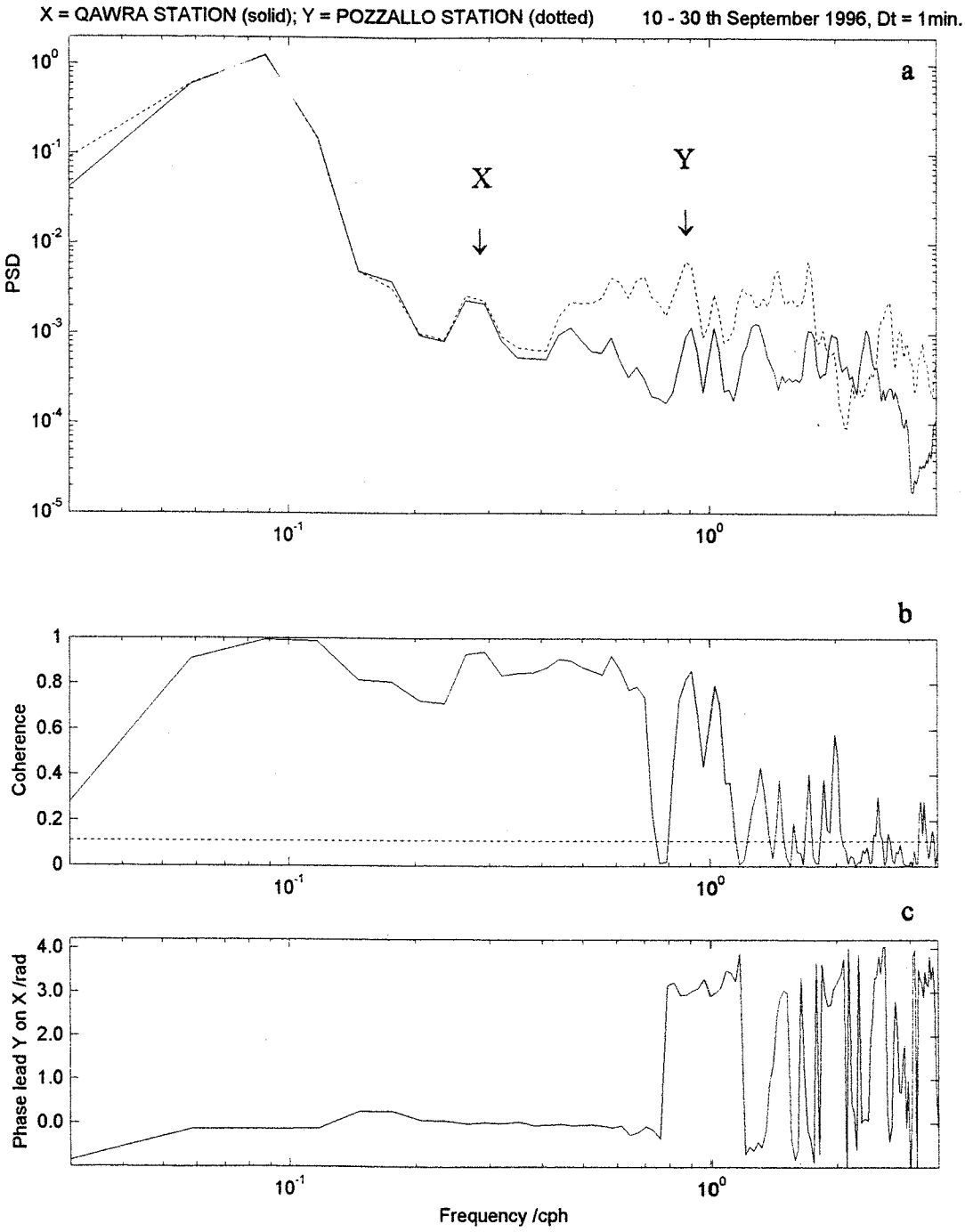

Fig. 3.44 Cross-spectral analysis of 2-minute sampled water level observations at Qawra Station (MALTA) and Pozzallo Station (SICILY) in the period (08h50) 10th September to (11h54) 30th September, 1996. Power spectral density in (a) is calculated over 54 degrees of freedom with a 95% confidence factor of 3.3 dB (B_{min}=0.7; B_{max}=1.5).
The 95% confidence level for the coherence estimate is 0.11.

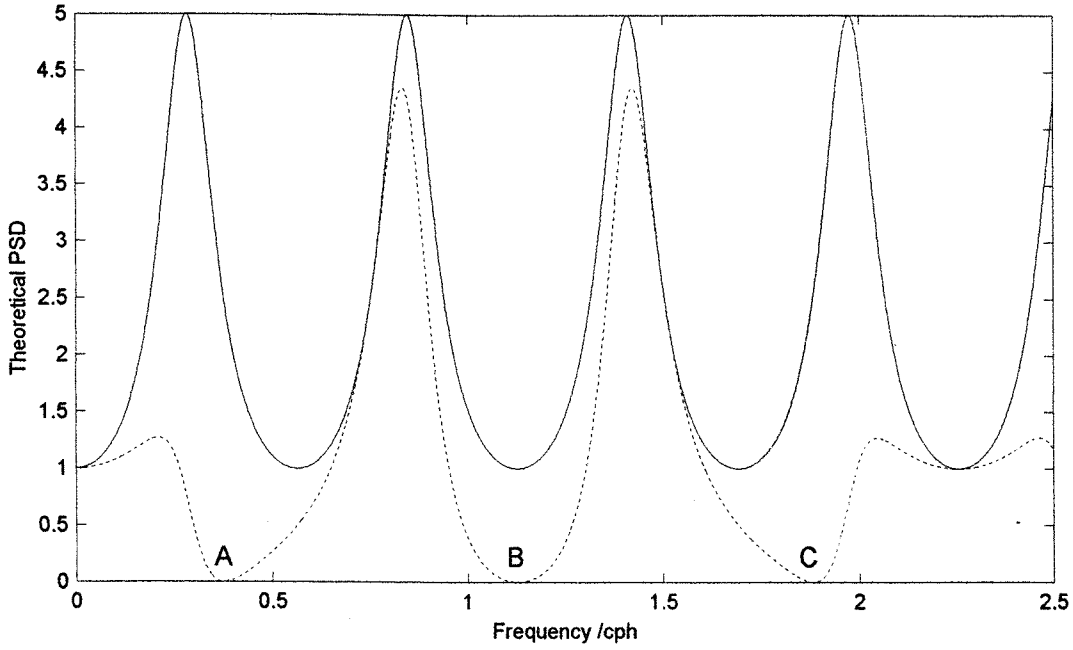

Fig. 3.45 Theoretical spectrum for a straight ledge (width = 100 Km; shelf depth = 100 m; $\gamma^2 = 5$) in the case of normal incidence. A, B and C indicate frequencies of phase reversals.

phase is reversed back to zero at 1.16cph. At each of these phase reversals the coherency dips to zero. These phase reversals between 0^o and 180^o are indicative of the occurrence of standing waves on the shelf.

These results can be tentatively explained by considering the shelf to be very simplistically represented by a straight steep coast with uniform bathymetry alongshore (y-axis) and a step cross-shore (x-axis) profile with constant width L, depth H_1 on the shelf and H_2 on the deep sea side. One possible long wave motion on this continental shelf model is a system of leaky waves normal to the shore (Snodgrass et. al, 1962) with an antinode at the shore and a node at the shelf edge. In the case of waves incident normally from the deeper ocean with an associated spectrum $S_o(f)$, the spectrum at the shoreline (x = 0) is $a^2(f)S_o(f)$, where $a^2(f) = [1 + \mathrm{Tan}^2(2\pi fL/c_1)]/[1 + \gamma^2\,\mathrm{Tan}^2(2\pi fL/c_1)]$ and $\gamma^2 = c_2/c_1$, $c_1 = \sqrt{(gH_1)}$, $c_2 = \sqrt{(gH_2)}$. The spectrum at an offshore position (x = X < L) on the shelf is $a^2(f)\mathrm{Cos}^2(2\pi fX/c_1)S(f)$. Taking a typical value for the shelf width L =

100Km and a mean depth H_1 = 100m, the theoretical spectra on the Sicilian coast (solid) and on the northern coast of Malta (dotted; with position of the island taken at X = 0.75 L) for normal incidence (from the south) are shown in Fig. 3.45 with values normalised to S(f) = 1. The signals are in phase up to A (0.37 cph), become in antiphase from A to B (1.11 cph), and return in phase from B to C (1.85 cph). The coherence (not shown) follows a negative delta function , falling to zero with a very narrow trough centred on the frequencies at each phase reversal, and is equally high on both sides. Successive spectral peaks on the Sicilian coast have also the same amplitude and occur at To = 3.55h and To/3 = 1.18h. These periods compare well to the peaks X and Y in the observed spectra (Fig. 3.44). It is also possible to account for the second phase reversal which coincides to that observed at 1.16cph. Some remarkable differences are however noted. The observed fundamental mode is weaker than the first resonance mode. The observed dips in coherence are smeared into troughs, and the coherence remains low beyond 1.2cph. The first phase is expected at a third of this frequency (f = 0.37cph) whereas it actually occurs at a much higher frequency (f = 0.78cph). The observed fundamental peaks in Malta and Sicily have also equal amplitudes which again does not agree with theory. For other angles of incidence ($\theta \neq 0$), the resonance peaks and anti-resonances shift to higher frequencies by a factor $\sqrt{(1 - \gamma^2 \sin^2\theta)}$ and the amplification at the coast is reduced. In the extreme case of glancing incidence ($\theta = 0$) this amounts to a shift of 12% in frequency which still does not account for the differences between theory and observations, especially with regard to the fundamental mode. This mode thus appears to be greatly modified by the shape and limited latitudinal extent of the shelf. The failure of the coherence to recover after the second phase reversal also suggests that the presence of multiple stationary modes is important. These modes apparently carry an appreciable fraction of in-phase energy even after most of the energy is out of phase.

The simplified model above does not thus fully apply to the shelf area between Malta and Sicily on account of the shelf's complicated bathymetry and its very abrupt termination on the east. A multi-directional distribution of incident energy from the deeper ocean may indeed partly explain the smearing of the features in the observed spectra and coherence, but the anomalous characteristics pertaining to the gravest mode should be sought in the effect produced by the coastal configuration of the northern borderland and the irregular shape of the shelf. A three-dimensional numerical modelling approach would be necessary to resolve these characteristics.

Other important intermediate energy peaks (at T = 2.2, 1.7, 1.45h and 58min) are not explained by the above model. These signals are apparently related to latitudinal stationary modes on the shelf. These modes are

attributed to the trapping of long wave energy on the shelf area as a whole as well as in localised areas along isolated features on the sea bed. One such feature is the crescentic submarine ridge which runs close to the eastern and southern perimeter of the shelf. This inner shelf ridge can act as a waveguide for long waves.

The depth profile normal to the ridge axis can be taken to be parabolic according to $H = H_o\sqrt{(1 + x^2/\alpha^2)}$, where Ho is the minimum water depth at the centre of the ridge (x = 0); at a distance $x = \alpha$ from the ridge axis the depth is $Ho/\sqrt{2}$. The lower frequency mode has a period given by $T_1 = 6.95(\alpha/\sqrt{gHo})$ (Defant, 1961, page 235) and consists of anti-phasic oscillations on opposite sides of the ridge, with a node over the ridge. On each separate side of the ridge, the oscillations remain in phase with the amplitude reaching a maximum at a distance $x \approx 2\alpha$. The next mode is shorter, with a period given by $T_2 = 3.24(\alpha/\sqrt{gHo})$, and consists of symmetrical oscillations with an antinode over the ridge, nodes at $x \approx \pm\alpha$ and antinodes at $x \approx \pm 2\alpha$. Taking $H_o = 50$m and α = 25 Km as typical values for the inner shelf ridge, the corresponding modes have periods $T_1 = 2.179$h and T_2 = 1.016h which compare well with two of the observed spectral peaks. Pozzallo and Qawra stations are on the same side of the ridge, but their longitudinal coordinates differ by 24.31' which amounts to an east-west separation of about 36 Km. This explains the phase relationship of the oscillations at the two stations which are in phase for mode T_1, but in antiphase for mode T_2.

The shelf itself can also in its totality be considered as a submerged ridge extending normal to the borderland. In this case if we take H_o = 100m and α = 60 Km, we obtain a second mode period of 1.724 h which again compares well with the observed peak at T = 1.7h. The signal at T = 1.45h is probably related to a co-oscillation of the plateau (averaging a depth of 150m) on the western flank of the shelf with the Central Mediterranean basin.

3.6.4 General conclusions

The large amplitude sea level oscillations observed on the northern coast of Malta in the long wave frequency band contain substantial energy in the range of frequencies 0.2 - 2cph. The lower frequency signals are associated to longitudinal, latitudinal and mixed stationary modes that develop on the highly irregular shaped continental shelf. The presence of these modes suggests that the Sicilian coast is a good reflector to these long waves. Their wavelengths are comparable to the shelf extent which thus modifies their characteristics from a

simple quarter-wave resonant effect. It is inferred that the observed waves are not only ones that cross the shelf from the deep sea but that comparable energy is presented in trapped waves associated to bathymetric features on the shelf.

The higher frequency coastal seiches are characterised not only by eigenmodes pertaining to inlets and bays on the coastal perimeter, but also by open sea modes in the nearshore shelf areas. This is particularly evident in the presence of coastal shallows, reefs or banks such as in the case of Mellieha Bay. The bays are in double resonance with the adjacent nearshore areas; the open coastal sea is on its own count in double resonance with the offshore deeper shelf area. It is thus inferred that the observed long period wave field in coastal areas is not simply restricted to those oscillations directly related to the deeper shelf, but that comparable energy is also present in the form of stationary coastal waves that are excited in the nearshore and inner shore areas either directly by local atmospheric disturbances or indirectly through the forcing by deeper sea waves. Both mechanisms involve a cascading effect from larger to smaller horizontal scales.

The dominant oscillations offshore of Mellieha Bay and St. Paul's Bay are found to be in the direction normal to the shelf orientation. Waves of lateral modes, such as edge waves on the shelf, become more important further east, but are not very effective in the generation of bay oscillations of longer periods.

4. Generation of extreme atmosphere-induced seiche oscillations

4.1 Atmospheric gravity waves in the Central Mediterranean

4.1.1 Introduction

Recordings of surface atmospheric pressure at the meteorological station in Ramla tal-Bir very often reveal the presence of pressure fluctuations with unusually large amplitudes of the order of a few millibars and with periods ranging from tens of minutes to a couple of hours. These pressure disturbances occur sporadically throughout the year although they tend to be more frequent during April/May and September. The data set of key meteo parameters at this station is unique for its extent as well as for its density of sampling. It has permitted the presence of these pressure disturbances in the Central Mediterranean to be confirmed. This chapter will focus on the characterisation of these pressure oscillations and on their phenomenology especially in relation to their effect on the sea surface. These pressure fluctuations are in fact found to correlate well with the occurrence of pronounced long period waves in the northern coastal area of the Maltese Islands. In particular, the long period sea level oscillations observed in Mellieha Bay and St. George's Bay are found to occur in concomitance with the occurrence of these pressure disturbances. A direct relationship between the two phenomena is thus proposed.

4.1.2 Observations of atmospheric and long period waves

In Fig. 4.1a-d the water elevation in Mellieha Bay is plotted for two separate six-day periods in September 1995 during which the sea level oscillations are intensified to large amplitudes. The traces are compared with the atmospheric pressure variations observed in the same time interval. Especially for the first segment of data, the pressure trace is unusually rugged compared to other periods when the trace is much smoother. These pressure fluctuations are believed to be the surface expression of atmospheric wave disturbances that occur as internal gravity waves on the boundary surface separating two air masses in the lower troposphere. The pressure traces typify the nature of these waves which can occur with a range of frequencies and amplitudes. The larger amplitude pressure oscillations can have a trough-to-crest extent of a few millibars and can occur as a solitary wave or as a wavetrain of several hours period. These mesoscale pressure disturbances are well reviewed in Uccellini & Koch (1987) and are known to have a significant impact on the weather.

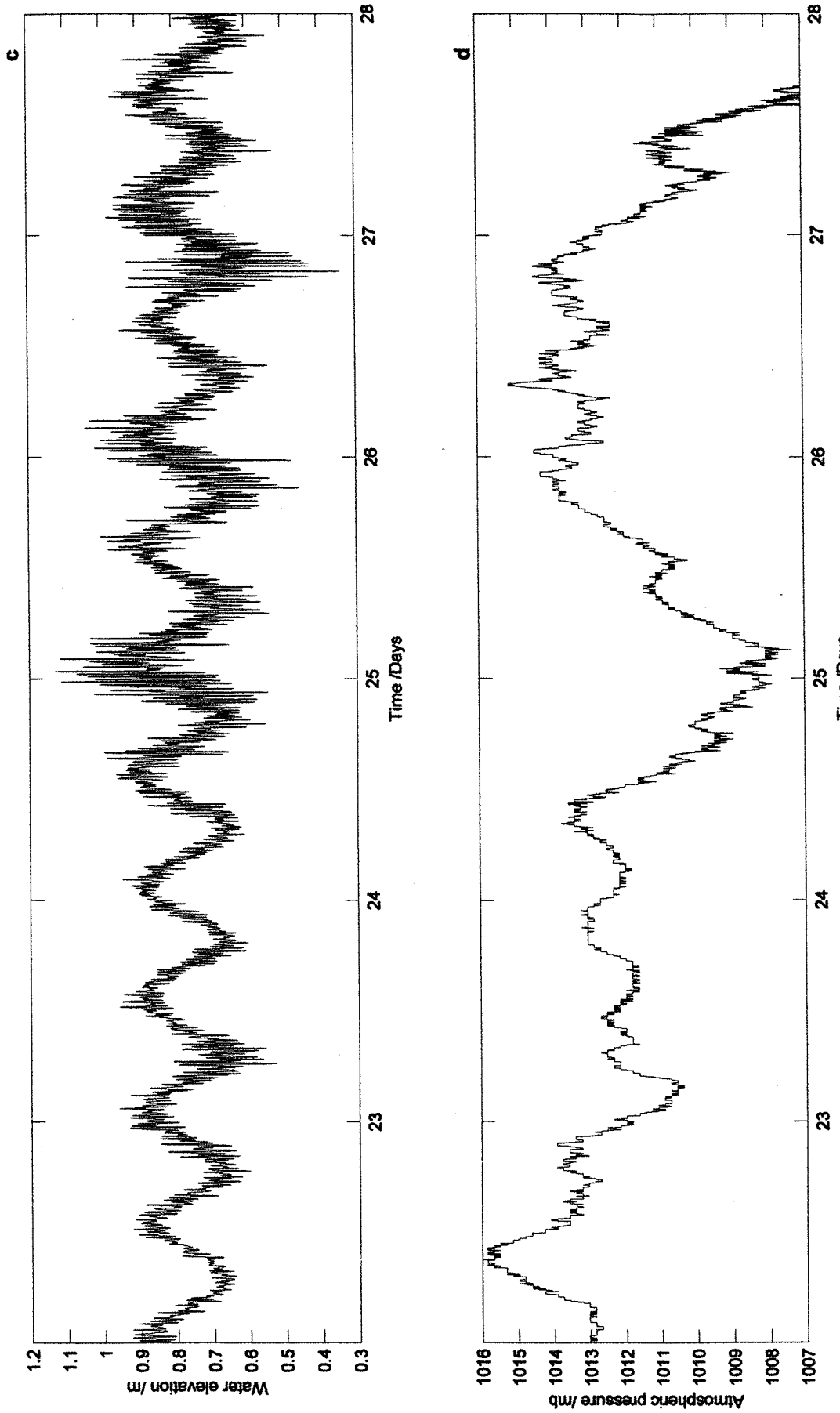

Fig. 4.1 Time series of (a) two-minute sampled sea level in Mellieha Bay from (12:00GMT) 15th September to (12:00GMT) 21st September 1995, and (b) 1-minute sampled surface atmospheric pressure at Ramla tal-Bir from (12:00GMT) 16th September to (12:00GMT) 20th September 1995.

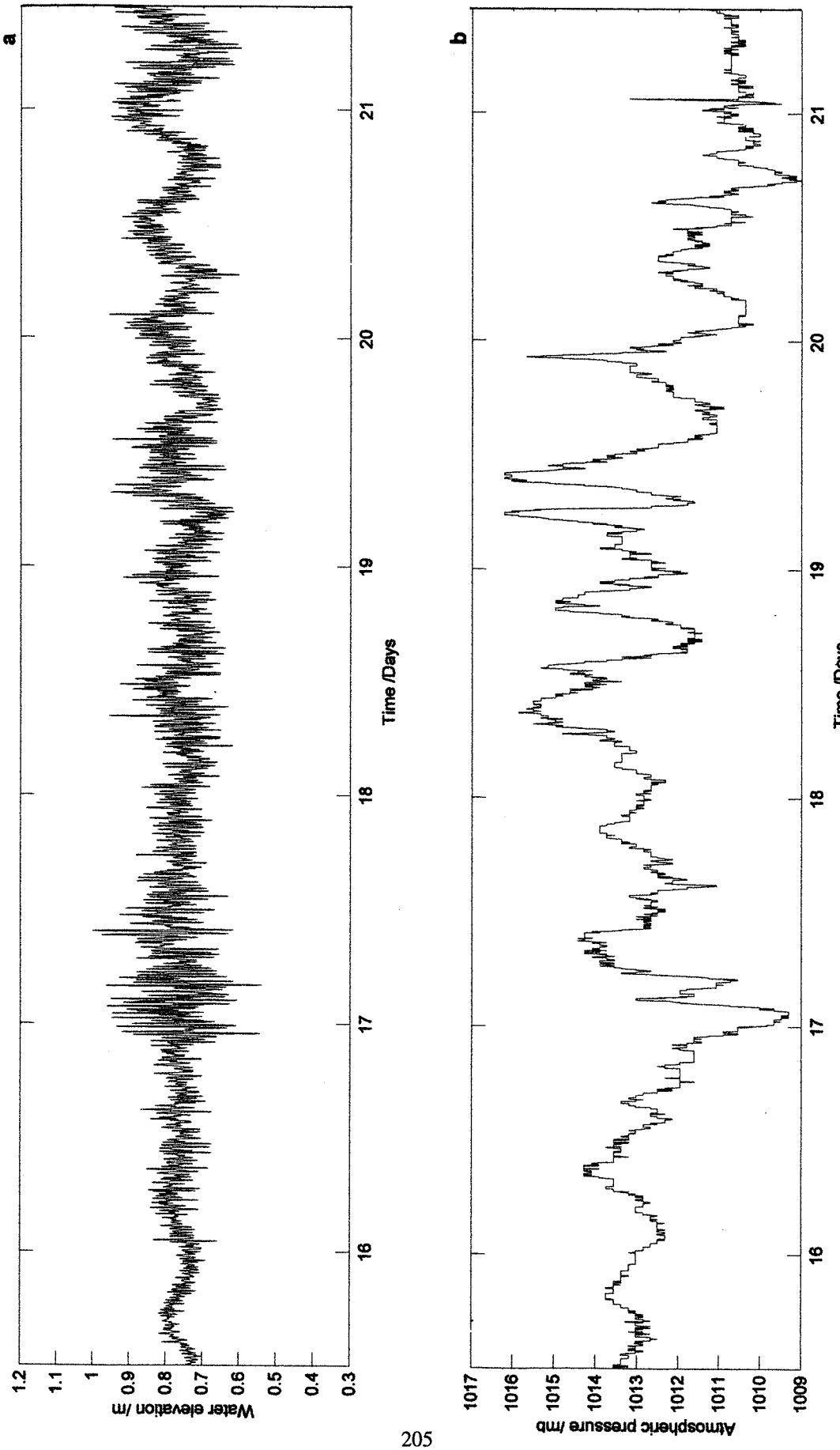

Fig. 4.1 Time series of (c) two-minute sampled sea level in Mellieha Bay from (12:00GMT) 23rd September to (12:00GMT) 29th September 1995, and (d) 1-minute sampled surface atmospheric pressure at Ramla tal-Bir from (12:00GMT) 24th September to (12:00GMT) 27th September 1995.

During September 1995, this type of wave activity is very prominent in the interval between the 17th and the 19th. The pressure trace also presents some shorter period pressure disturbances with trough-to-crest amplitudes of about 1 - 2mb and periods typically less than one hour. The presence of this second type of pressure waves triggers the occurrence of the seiching events in Mellieha Bay on the night between the 24th and the 25th, in the late hours of the 25th and the evening of the 26th September. These events are typical examples in which a correlated enhancement of the pressure signal at these periodicities is observed. There is however no simple relation between the magnitude of the air pressure fluctuations and that of the associated sea level oscillations.

4.2 Air-sea coupling in the long period frequency range

4.2.1 Historical background

The triggering of seiches by sudden changes in atmospheric pressure have long been reported by other sources. In 1908, Chrystal concluded that the sudden return to its equilibrium of a surface previously disturbed by the passage of an atmospheric disturbance over a section of a lake could in fact be the main responsible agent for the seiches of Loch Earn. Even before that, in the nineteenth century, Forel suggested that the influence of the atmospheric pressure could by far exceed the influence of the wind (Defant 1960, pg.220). Emden (1905) showed that even small quantities of energy are sufficient to cause seiches. In more recent times several workers (Darbyshire, 1963; Darbyshire and Darbyshire, 1964; Wilson 1970) have reported simultaneous recordings of unusual long wave oscillations corresponding to unusual air pressure fluctuations near Cape Town. The occurrence of large-amplitude sea level oscillations have also been reported (Ramis & Jansa, 1983; Jansa, 1986; Monserrat et al., 1991; Gomis et al., 1993;) in the Balearic Islands where they are locally known as '*rissaga*'. During tsunami monitoring measurements in the South Kuril Islands, Japan, several tsunami-like long wave trains were recorded and their origin was eventually traced to be related to atmospheric activity rather than to seismic events (Rabinovich & Monserrat, 1996).

These atmospherically induced long waves in the sea have identical properties to tsunami waves both with regard to their propagation in coastal areas as well as their amplification as they reach embayments, inlets or harbours. For this reason the term 'meteorological tsunami' has been coined to describe this phenomenon. This term was first used by Nomitsu (1935), but became widely accepted after its adoption by Defant (1961).

An understanding of the mechanism by which the atmosphere forces long waves in the ocean is however far from completely known. With their periods greater than about 2 minutes, long waves have a length that is much larger than the depth of the sea; the shallow water equations can thus be applied. Investigations concerning long waves 'trapped' on continental shelves (Snodgrass et al, 1962; Buchwald & Adams, 1968), on oceanic ridges (Buchwald, 1968), and on isolated features such as sea-mounts (Longuet-Higgins, 1967) have established the benchmarks on the propagation properties of these waves. There is however still some difficulty in understanding the mechanism by which energy is transferred from the atmosphere into long waves. The task is rendered even harder due to the fact that the effect of the wind cannot be easily isolated from that of the atmospheric pressure. Moreover atmosphere-induced long waves can be associated to a variety of atmospheric phenomena such as typhoons or strong cyclones, frontal zones, pressure jumps and trains of atmospheric gravity waves.

4.2.2 Previous studies on meteorological tsunamis

Existing studies concerning atmospherically induced sea level oscillations are mainly based on a comparison between sea level traces and simultaneous atmospheric pressure fluctuations. The traces are reported to be completely uncorrelated but periodicities of the same order are observed to be present in both. Maximum amplitudes are even shown to be often attained at about the same time, although with some lag either way. Taking the example of the Southern coast of Africa, long gravity wave height oscillations of up to 60cm with periods between 12min and 1h have been observed on tide gauge recordings in conjunction with short period (30min - 1h), small height (3mb) air pressure pulses recorded on coastal stations (Shillington, 1984). Even in the Balearic Islands, the large sea level oscillations in the Port of Ciutadella (with amplitudes of up to 1.5m and a period of about 10min) have been associated to a 10-minute gravity wave in the atmosphere (Monserrat et al., 1991). The time evolution of the energy in sea level and atmospheric pressure in the band of periods between 8.5 and 11min suggest a causal relationship between the large oscillations in the port and the pressure oscillations. Dramatic increases in both signals are reported to occur at the same time with subsequent decreases following again in parallel. The response of the port is thus attributed to a resonance between the normal mode of the port (T = 10.4min) and the pressure wave in the atmosphere. From a phase spectrum analysis between sea level and pressure, a phase change of π radians at a resonance frequency of 12min further suggests that the inlet may actually behave as a damped harmonic oscillator which is externally forced by the

atmospheric pressure oscillations. The influence of the longer periods is on the other hand restricted to just the well-known inverted barometer effect.

In their review on the generation mechanisms of meteorological tsunamis near the Balearic and Kuril Islands, Rabinovich & Monserrat (1997) investigate 13 seiche events which are found to be well correlated with significant disturbances of atmospheric pressure observed simultaneously. An essential amount of atmospheric energy at a resonance bay frequency is again quoted as being one factor that can favour seiche generation. However this energy is in general too small to suppose that the direct local bay resonance could possibly explain large seiching events. Moreover the spatial scale of coherence of strong atmospheric disturbances is much higher (by about two orders of magnitude) than the size of the bay (about 1Km in the case of the port of Cuitadella). A possible indirect generation mechanism of atmospherically induced long waves in the open sea is thus hypothesised. This mechanism consists in the generation of long waves in the open sea which subsequently force the seiches in the smaller water bodies at inlets and harbours along the coastal perimeter.

4.2.3 Mechanisms for the triggering of meteorological tsunamis

4.2.3.1 Direct generation

The question of direct or indirect generation of seiche oscillations in an embayment or inlet by atmospheric pressure disturbances is a matter that still needs clarification. In the case of what will henceforth be referred to as a 'direct atmospheric generation' mechanism, the bay oscillates as an independent water mass. The amplification of the normal mode of an embayment can be produced by a direct resonance effect with the atmospheric pressure oscillations which act as an external forcing agent. Such a mechanism would imply a high correlation between pressure and sea level especially at the resonant frequency, and a specific phase relationship similar to that of an externally forced damped harmonic oscillator. The seiching would also correspond to a natural mode of oscillation of the embayment and thus exhibit the appropriate phase differences at various points in the basin. One could also extrapolate to a situation in which the direct coupling of the atmosphere with the sea surface is not limited to the embayment but actually extends and includes a stretch of open sea as one domain. In such a circumstance the possible eigenoscillations will very much depend on the morphology of both the bay and the external sea. The atmospheric wave parameters would also have to be such as to sustain these eigenoscillations. In particular the direction of propagation would essentially have to be orthogonal to

bathymetric contours and the horizontal scales must match. The associated sea level oscillations would also be expected to have higher amplitudes inside the bay than in the open sea due to the piling up of a large volume of water in a confined space. In Chapter 3 it was shown that Mellieha Bay is characterised by such modes of oscillation with periods longer than the gravest bay mode. These oscillations are very strong and pertain to the water body composed of the bay and the immediate shelf area.

4.2.3.2 Indirect generation

The bay seiches can alternatively be triggered by an 'indirect atmospheric generation' mechanism. A two-stage mechanism can be hypothesised, consisting of (1) the atmospheric generation of offshore long period surface waves, and (2) the subsequent forcing of the embayment at its boundary with the open sea by these long waves as they propagate into the bay and feed energy to its water body. These open sea long waves can be set up from a rather localised coupling of the atmosphere with the sea in the immediate vicinity of the embayment. One can however extrapolate to a situation in which the oscillation of the whole water mass on the continental shelf between Malta and Sicily is involved and the coastal area responds as a co-oscillation. These shelf oscillations could indeed be set up by atmospheric disturbances with matching characteristics and would be expected to have much longer periods than any of the natural periods of the embayments. The sea level in an embayment at these periods would thus fall and rise almost simultaneously over its whole extent. This would be accompanied by large volumes of water sloshing alternately in and out of the embayment, and consequently giving rise to strong alternating currents at the entrance, especially if this volume is large and the entrance width is not sufficiently wide to cope with the rates of exchange.

4.2.3.3 Direct vs. indirect generation

The distinction between the direct and indirect mechanisms is difficult to discern because one mechanism does not exclude the other. In fact the natural oscillation of a bay is selectively enhanced both if the forcing comes directly from matching frequencies in the atmosphere as well as in the case of a bay response to open sea long waves that contain sufficient energy at the bay mode frequencies. The extrapolated situations mentioned in the two cases are moreover dictated by the different possible horizontal scales of the interaction. Such a range of horizontal scales will result in a merging between the possible situations described above, and effectively excludes any clear cut and distinct existence of the two situations. A study of the interaction between atmospheric pressure waves and the sea surface thus necessitates a good coverage of observations not only in

time but also in space. In particular, observations in the open sea are essential (refer section 4.6). Moreover the correlation between bay seiches and atmospheric fluctuations is expected to be significant only if the long wave generation occurs close to the embayment or if the atmospheric waves maintain their stability over sufficiently large distances. In this context it is thus highly important to study the spatial coherence of atmospheric waves (refer sections 4.4.1 and 4.4.2).

4.2.4 Important atmospheric wave parameters for seiche generation

There are some key properties of an atmospheric perturbation that dictate the efficiency of generation of meteorologically induced seiches. The intensity (amplitude) of the atmospheric pressure fluctuations associated with the perturbation is certainly one such parameter. In most cases stronger atmospheric disturbances trigger larger seiche oscillations. This cannot however be taken as a general rule. There are occasions when a pressure disturbance does not produce an associated seiching with the expected intensification. The correlation between the atmosphere and the sea surface is not straight forward and other factors besides intensity are important. These include spatial coherence, the direction of propagation and phase speed of the perturbation, and the spectral energy distribution characterising the atmospheric pressure field.

4.2.5 Response of the sea surface to atmospheric pressure variations

When the air pressure exerts a force on the sea surface it causes the water to deviate from its normal position of equilibrium. This water surface deformation will be retained as long as the force remains. In a most simplistic form one can therefore imagine that when the force subsides or ceases completely, the water surface will tend to regain its former state of equilibrium. In the absence of significant friction this restoration is accompanied by undulations whose period coincide to the natural period of free oscillations of the water body. This is what happens in the case of a pressure pulse which effectively carries with it a wide range of signals in the frequency domain. For a flat bottomed, shallow water and unbounded sea, the amplification of open sea surface waves depends only on the phase speed of atmospheric waves. In the case that the atmospheric waves are non-dispersive, the amplification is furthermore expected to be the same at all frequencies. When the disturbing force is periodic, forced oscillations are established with a period equal to that of the forcing signal. The amplitude will be maximal when the condition of resonance applies, in which case the period of the force matches one of the eigenmodes of oscillation of the water body.

4.2.5.1 Case of an ideal ocean

A formal mathematical treatment of the forcing can be expressed in terms of the equations of motion and continuity. In an ocean of uniform depth H, changes in atmospheric pressure at the surface produce depth-independent horizontal pressure gradients and currents. If the pressure variations Δp are small enough, the linearised form of the shallow-water wave theory can be applied. If friction is neglected:

$$u_t - fv + g(\tilde{\eta})_x = 0; \qquad v_t + fu + g(\tilde{\eta})_y = 0 \tag{4.1a}$$

$$(Hu)_x + (Hv)_y + \eta_t = 0 \quad \Rightarrow \quad (Hu)_x + (Hv)_y + \tilde{\eta}_t = \phi_t \tag{4.1b}$$

where η is the observed water elevation and $\tilde{\eta}$ is the adjusted sea level defined as $\tilde{\eta} = \eta + \phi = \eta + \Delta p / \rho g$, where ϕ is the static sea level and gives the atmospheric pressure perturbation Δp in Nm^{-2}, expressed as an equivalent height of water in meters (refer also to section 2.4.1.1). Writing 4.1b in terms of the adjusted sea level $\tilde{\eta}$, has the effect of transferring the forcing term from the momentum equation to the continuity equation. Physically this means that the effect of the forcing is equivalent to the situation in which fluid of the same density is added to the sea at a volume rate per unit area of ϕ. This formulation is very convenient because the effect of precipitation and evaporation can be easily incorporated in the equation of continuity as an addition/removal of mass. In such a case the forcing term on the left hand side of 4.1b would read $\frac{\partial}{\partial t}\left(\phi + \int (P-E)\mathrm{d}t / \rho\right)$. This means that for a depression of say 1mb corresponding to a negative value of ϕ equal to 1cm, it would require 1cm of precipitation to cancel out its effect.

4.2.5.2 Case of a stepped bathymetry

Another important result is derived in the case of H being piecewise constant. Elimination of u and v from 4.1a,b then yields:

$$gH\nabla^2(\eta + \phi) = \eta_{tt} \tag{4.2a}$$

The equilibrium solution in the case of a stationary atmospheric pressure distribution corresponds to the adjusted sea level being constant: $\eta + \phi = const.$ $\quad u = v = 0.$ (4.2b)

This implies that under the action of friction, the sea surface topography will tend to restore to an inverse barometer response.

4.2.5.3 Case of a uniform canal

In the case of an infinitely long and uniform canal without friction, the response takes the form of a Kelvin wave so that for $\phi = 0$ the complete solution is

$$v = 0 \text{ and } \eta = \pm\frac{cu}{g} = \exp(\frac{\pm fy}{c})F(x \pm ct), \qquad (4.3a)$$

where F is an arbitrary function of $(x \pm ct)$ and $c = \sqrt{gH}$ is the phase speed of long waves in the canal.

If the atmospheric pressure disturbance is in motion and can be represented by a wave travelling with a velocity V in the positive direction of the canal, the solution in the absence of friction, according to Proudman (1929) is given by:

$$\phi = -c^2 \exp(\frac{-fy}{V})F(x - Vt) \qquad (4.4a)$$

$$v = 0 \qquad (4.4b)$$

$$\eta = \frac{c^2 u}{Vg} = \frac{c^4}{c^2 - V^2} \exp(\frac{-fy}{V})F(x - Vt) = \frac{-\phi}{1 - V^2/c^2} \qquad (4.4c)$$

An accompanying free wave is thus set up that travels on the sea surface in the same direction of the pressure wave. This solution applies only to the somewhat special pressure disturbance described by $F(x - Vt)$. Equation 4.4c also applies in the open sea. When $V << c$ the inverted barometer effect applies, but when V is close to c, the so called 'Proudman resonance' (Rabinovich, 1993) occurs and η can attain large amplitudes. In the case of the continental shelf between Malta and Sicily, the depth is approximately 100m so that long waves propagating on the shelf have phase speeds around $31 ms^{-1}$. This is very close to the speed of atmospheric disturbances and the conditions of resonance can thus be easily attained.

Hibiya & Kajiura (1982) give a somewhat different formulation for the resonant interaction between an atmospheric disturbance and the sea surface. On the basis of an initial value problem, the amplitude of the generated sea level oscillations at resonance is given by

$$\eta = \frac{-\phi}{L_p}\frac{\chi_w}{2} \qquad (4.5)$$

where χ_w is the distance travelled over the sea by the atmospheric disturbance, $L_p = V\Delta t_p$ is the spatial scale of the frontal side of the disturbance (i.e. the distance between the disturbance maximum and the undisturbed

surface), and Δt_p is the corresponding temporal scale. The ratio $\frac{-\phi}{L_p}$ is effectively the atmospheric pressure gradient. According to this theory, the long period wave amplitudes would be expected to increase linearly with time, and to depend directly on the pressure gradient and on the travel distance. Taking the example of a very typical pressure disturbance with an amplitude of 2mb and a spatial scale of 30Km (i.e. a pressure gradient of (1/15)mb Km^{-1}), travelling from west to east along the Malta Channel shelf area (i.e. $\chi_w \approx$ 100Km), the corresponding sea level response in the open sea would be expected to be around twice the static value. The enhancement of these waves to much larger amplitudes inside the embayments can thus be only explained from a resonant response of the embayments to these open sea signals, together with effects of topographic amplification.

4.2.5.4 Case of a semi-infinite canal

Consider now the case of a semi-infinite canal with a closed boundary at x = 0 where the normal velocity component should therefore vanish. The solution for a canal that is sufficiently narrow as to be able to neglect the effect of the earth's rotation is composed of a free wave superimposed to a forced wave:

$$\phi = -F(t-x/V),\quad \eta = \frac{c^2}{c^2-V^2}\left[F(t-x/V)-\frac{V}{c}F(t-x/c)\right],$$
$$v=0,\qquad u=\frac{gV}{c^2-V^2}\left[F(t-x/V)-F(t-x/c)\right] \tag{4.6}$$

On putting x = 0 at the closed boundary, we have

$$\frac{\eta}{\phi}=\frac{-1}{1+V/c}=\text{constant} \tag{4.7}$$

This leads to the very interesting result that a strong response to a pressure wave disturbance is only expected when the wave is travelling towards the interior of the canal or bay. In fact when V > 0, so that the pressure wave travels away from the closed end, $\left|\frac{\eta}{\phi}\right| < 1$ and the amplitude of the forced wave is always smaller than the static pressure disturbance. On the other hand, when V < 0 and the pressure wave travels towards the closed end, $\left|\frac{\eta}{\phi}\right| > 1$ and the amplification can actually become very large when V approximates c. Such a situation is not atypical since the velocity of propagation of atmospheric pressure disturbances is of the order of 30ms^{-1} which compares well to the magnitude of wave speeds in an ocean of depth close to 100m. Since pressure

disturbances travel predominantly from west to east, one would therefore expect a favourable response in bays that have a latitudinal orientation and closed at the east.

4.2.5.5 Case of a rectangular shelf

Buchwald and De Szoeke (1973) have addressed the problem of the response of a rectangular shelf to a pressure disturbance travelling with constant speed V in the longshore direction. The origin is taken to lie on the coast which is represented by x = 0. In the region $0 < x < L$ the depth is H_1 so that the shelf has a uniform width L. In the region $x > L$, the depth is H_2, $H_2 > H_1$. If η_1 and η_2 are the surface displacements in the shelf and ocean regions respectively, the corresponding equations of motion from (4.2a) can be expressed in non-dimensional co-ordinates ($x^* = x/L$; $y^* = y/L$; $t^* = t(gH_1)^{1/2}/L$):

$$\nabla^2\eta_1 - (\eta_1)_{tt} = -\nabla^2\phi \quad \text{for } 0 < x < 1, \text{ and } \nabla^2\eta_2 - \frac{1}{\gamma^2}(\eta_2)_{tt} = -\nabla^2\phi \quad \text{for } x > 1 \qquad (4.8a)$$

where $\gamma^2 = H_1 / H_2 > 1$ and the asterisks denoting non-dimensional quantities are for convenience dropped. The boundary condition is that of zero normal velocity at the coast so that

$$(\eta_1 + \phi)_x = 0 \text{ at } x = 0 \qquad (4.8b)$$

The continuity of surface displacement and mass transport at the shelf break

$$\Rightarrow \eta_1 = \eta_2, \quad \text{and} \quad (\eta_1 + \phi)_x = \gamma^2(\eta_2 + \phi)_x \text{ at } x = 1 \qquad (4.8c)$$

Free waves

In the absence of atmospheric forcing, ϕ = constant and the solution takes the form of free waves given by $\eta_j = A_j(x)\exp[i(ky - \omega t)]$, with $j = 1$ and 2, where $c = \omega / k$. The superposition of incident and reflected waves on the shelf gives rise to stationary wave patterns along the x-axis (Snodgrass et al., 1962). The resulting free waves take the form of leaky modes when $c > \gamma$ and of trapped modes when $\gamma > c > 1$.

For the leaky modes $A_1(x) = A \cos\varepsilon \cos m_1 x$; $A_2(x) = A \cos m_1 \cos[m_2(x-1) + \varepsilon]$, where $m_1 = \omega \cos\theta_1 = k \cot\theta_1$; $m_2 = (\omega/\gamma)\cos\theta_2 = k \cot\theta_2$. A is an arbitrary constant, $\tan\varepsilon = (m_1 \tan m_1)/(\gamma^2 m_2)$ and m_1, m_2 are the non-dimensional alongshore wavenumbers. These equations represent long waves incident at an angle ($\pi/2 - \theta_2$) to the shelf break with reflection and refraction at x = 1, (the angle of refraction θ_1 on the shelf is given by Snell's Law: $\sin\theta_2 = \gamma \sin\theta_1$) and subsequent reflection at x = 0.

For the trapped modes, there is total internal reflection at x = 1 and

$A_1(x) = A \cos mx$; $A_2(x) = A \cos m\, e^{-r(x\,1)}$ with $r > 0$.

Here m, ω and k are related by the dispersion relation

$$m \tan m = \gamma^2 r \qquad (4.9)$$

where $m^2 = \omega^2 - k^2$ and $r^2 = k^2 - \omega^2/\gamma^2$.

These solutions are trapped on the shelf and the wave amplitudes decay exponentially with increasing offshore distance x. The trapped modes are described in detail by Snodgrass et al. (1962) and Buchwald (1968). They consist of the discrete solutions of (4.9), each corresponding to a separate mode j = 1,2,3..., (with values of m in the sub-intervals $m = (\pi/2)\mu + (j\text{-}1)\pi$, $0 \le \mu < 1$) and described by a separate dispersion curve in ω-k space. These curves are bounded by the lines $\omega = k$ and $\omega = \gamma k$.

Forced waves

In the case of a harmonic pressure disturbance travelling with speed V, in the range $[1, \gamma]$, parallel to the coast, the line $\omega = Vk$ intersects the dispersion curves at points with $k_j = [\theta + (j\text{-}1)]\pi / |V^2 - 1|^{1/2}$, where $0 \le \theta = \tan^{-1}\{\gamma^2 |1 - V^2/\gamma^2|^{1/2} / |V^2 - 1|^{1/2}\} < \pi/2$ and $\omega_j = V k_j$. The intersection points give the conditions for resonance and large amplitude waves on the sea surface are thus achieved only when there is a very strict matching of both wave speed and wavelength with that of the shallow water edge waves supported by the shelf (Buckwald & De Szoeke, 1973).

If the disturbance is in the form of a sudden jump in pressure, travelling with a speed in between the speeds of long waves on the shelf and in the ocean, the direct response of the sea surface to the front is accompanied by forced edge waves trapped on the shelf. The group velocity of these edge waves is less than their phase velocity so that once the energy is imparted to the waves it then travels more slowly than the disturbance and takes the form of a wake trailing behind the moving air pressure front.

For the rectangular shelf model the amplitudes of the excited waves are only relevant at or near resonance. In the case of a more realistic shelf bottom with an exponential profile $h(x) = H \exp\left\{\frac{2a}{L}(x - L)\right\}$ the conditions are less stringent. Here x signifies cross-shelf distance, L is the shelf width, H is the deep ocean depth, and a is

a constant related to the depth h_o at the coast ($\exp(2a) = H / h_o$). Following Viera & Buchwald (1982) the pressure front triggers a wake of comparatively large edge waves behind it provided that $\exp(-a) \leq \frac{V}{\sqrt{gH}} \leq 1$.

Numerical experiments with a travelling pressure pulse show that the forced edge wave phase velocity is always the same as that of the forcing, but the two wavenumbers need not necessarily match (Shillington & Van Foreest, 1986). In the absence of a matching between the wavenumbers of the forcing with the zero-mode edge wave, higher mode edge waves are excited instead. In the case of longshore topographic variations frequency is conserved for free waves, while for forced waves, there is an adjustment in both frequency and wavenumber such that the phase speed of the edge waves remain conserved.

4.3 Observations of atmospheric activity

4.3.1 Previous studies

Knowledge on the generation mechanism of long period sea level oscillations by atmospheric pressure forcing is mainly limited by the lack of observational data. The most important simultaneous recordings of long period sea surface waves and atmospheric pressure are those conducted in the region of Ciutadella Harbour, Balearic Islands in 1989/90 (Monserrat et al., 1991), on the southwestern shelf of Kamchatka in 1987/88 (Kovalev et al., 1991) and later in the region of Shikotan Island, in the South Kuril Islands (Rabinovich et al. 1993, Djumagaliev & Rabinovich, 1993).

4.3.2 The observations in Malta

In order to study in detail the points discussed in section 4.2 above, the observations from an intensive data collection campaign organised as part of this work, from early September to mid-December 1996, is used. This consists of high-quality records of sea level (coastal and offshore) and atmospheric pressure at a number of locations.

The present set of simultaneous field measurements of atmospheric pressure, air temperature and sea level in Malta, in addition to the permanent and longer term measurements of meteorological parameters at Ramla tal-

Bir Station and of sea level at the coastal station in Mellieha Bay, is the first of its kind for the Central Mediterranean area. It is moreover much longer than that obtained in other areas. Table 4.1 presents the general information on the additional digitised recordings of atmospheric pressure collected at the Valletta, Luqa, Attard and Marsaxlokk stations and of sea level in St. George's Bay and bottom pressure at the offshore Qawra Station. The intensive set of atmospheric pressure observations made in the period November - December 1996 is intended to study the characteristics of atmospheric waves and their impact on the sea level. The atmospheric pressure data sets consist of simultaneous measurements at three different locations in addition to those at Ramla tal-Bir. After November the pressure gauge at Luqa is transferred to Attard.

The bottom pressure and temperature measurements at Qawra Station consist of 1-minute sampled recordings made by an Aanderaa WLR7 pressure gauge during two successive deployments. The 33 minute gap of data

Table 4.1 *Additional recordings of sea level and meteorological parameters in Malta*

STATION NAME	PERIOD OF MEASUREMENT (parameters)	SAMPLING INTERVAL (minutes)	COMMENTS
Water level recordings			
St. George's Bay (coastal)	04APR96 - 27MAY97	1.0/2.0	complete set except for a short gap in December 1996
Qawra Station (offshore)	(08h50) 10SEP96 - (11h54) 30SEP96 (bottom pressure)	1.0	complete set
Barographs			
Valletta Station	(16h04) 01NOV96 - (17h26) 09APR97 (air pressure)	0.5	small gap of 931 minutes from (21h35) 3DEC - (12h47) 4DEC larger gap of 3dys 13.1hrs from (21h09) 2JAN - (10h14) 6JAN
Luqa Station	(10h10) 07NOV96 - (13h12) 26NOV96 (air pressure & temperature)	0.5	full
Attard Station	(07h01) 05DEC96 - (09h12) 14DEC96 (air pressure & temperature)	1.0	full
M'Xlokk Station	(12h24) 11SEP96 - (22h36) 28SEP96	1.0	contains short gaps of a few minutes on 18th, 21st, 22nd and 23rd due to electricity cuts
	(09h30) 18OCT96 - (20h25) 10DEC96	0.5	full

between the two sets of measurements is linearly interpolated to produce a combined data series consisting of 28985 records covering the period 08h50GMT (10/9/96) to 11h54GMT (30/9/96). The station is positioned at 35° 59.350'N and 14° 25.806'E in a total water depth of 30m. The station location is on the NE extremity of the White Bank and is therefore a very representative position to obtain information on long period wave incidence on the northwestern approaches to Malta. Since the horizontal scale of variation of the atmospheric pressure and the prevailing wind is in general greater than the distance separating Qawra Station from the coastal meteorological station, it is adequate to presume that the atmospheric observations at Ramla tal-Bir are representative of the values at the open sea location. During this set of bottom pressure measurements, atmospheric pressure is also recorded at Marsaxlokk station. These measurements are treated separately in section 4.6.

The Endeco/YSI sea level gauges, and the Aanderaa atmospheric pressure sensors have already been described in sections 2.2.1 and 2.2.2. The bottom pressure gauges are of the Aanderaa WLR7 type. The pressure sensor in this instrument is based on a pressure controlled oscillator with a frequency 36-40khz. Pressure is measured by the sensor in psi (14.5psi = 10^5Pa = 10^3mb) within a range of 0-100psi. The sensor is powered and measures continuously for 40s. The measured pressure is averaged out over this integration period, so that the effect of surface waves is eliminated, and stored in two 10-bit words. The predicted resolution of the sensor is ± 0.001% of the full range (i.e. ≈ 0.07mb). Temperature is also measured by the instrument and is based on an RC controlled oscillator where the R component is a thermistor. The resolution in this case is ± 0.04°C.

4.3.2.1 Conversion of bottom pressure recordings into level fluctuations

The minimum of the time series is first subtracted in order to obtain the changes in bottom pressure. For the purpose of a straight forward correlation between variations in elevation and pressure, it is convenient to adopt the units of elevation in centimeters and those of pressure in millibars (1mb = 100Nm^{-2} = 1hPa). Since a water elevation of 1cm can be taken, to a very good approximation, as being equivalent to a pressure of 1mb, a measurement of pressure in millibars can be translated directly into elevation in centimetres. The bottom pressure variations are thus expressed into equivalent water level variations in centimetres. These equivalent level variations do not give the real displacement of the sea water surface (refer section 4.3.2.3), but are only meant to represent the bottom pressure into a more amenable quantity of measure.

4.3.2.2 Effect of atmospheric pressure on bottom pressure recordings

Recordings of bottom pressure include the effects of both atmospheric pressure variations as well as of changes in the density profile of the water column. Such measurements need therefore to be analysed with caution. The ultimate goal is that of obtaining the absolute water elevation η, defined as the water displacement of the sea surface with respect to mean sea level, situated at a constant position H above the seabed, and measured by a perfect water surface follower in the absence of any effects related to changes in atmospheric pressure. η thus carries all the contributions to the vertical changes in elevation that are intrinsic to the water body itself and includes effects such as those related to steric changes. In reality the water elevation η_{obs} registered by a surface follower carries with it the effect of the fluctuating atmospheric pressure field. The water elevation in general follows an inverse response which means that the water elevation tends to be reduced when the atmospheric pressure is on the rise while it tends to increase with an attenuation of the atmospheric pressure. The observed water elevation will in this case carry the signature of the atmospheric pressure variations Δp (in mb). Assuming that a water elevation of 1cm can be taken, to a very good approximation, as being equivalent to a pressure of 1mb, we can thus write $\eta_{obs} = \eta - \Delta p$. This implies that adding the atmospheric pressure variations (in mb) to the observed water elevation η_{obs} (in cm) gives what is known as the adjusted sea level $\tilde{\eta}$ (in cm) that expresses the absolute water elevation in the absence of effects extrinsic to the water body.

In all cases, when bottom pressure data is compared with that recorded by a coastal sea level gauge, the latter is corrected to an adjusted sea level value. Prior to these corrections the atmospheric pressure must be reduced to its value at mean sea level.

4.3.2.3 Effect of water column structure on bottom pressure recordings

In the case of a pressure gauge situated at the bottom of a water column the bottom pressure variations ΔB_p measured with respect to the mean, carry not only the contribution of the atmospheric pressure variations but also the effects of changes in the density structure of the water column above the instrument. In the case of a stratified water column where density changes occur on a time scale comparable to the water elevation signals, it is not easy to obtain the absolute water elevation from records of bottom pressure. Moreover, the corrections to be adopted need to retain those effects of density that pertain to the absolute water elevation.

The total pressure B_P (in mb) registered by the gauge can be expressed as follows:

$$B_P=(Po+\Delta p) + (H+\eta_{obs})(\rho_o + \Delta\rho_0) \qquad (4.13)$$

where Po is the mean atmospheric pressure (in mb), ρ_o is the mean density (in gm cm^{-3}) obtained as an average in the vertical ($\frac{1}{H}\int \rho \, dz$) and in time over the extent of the experiment, $\Delta\rho_o$ is the fluctuation in ρ_o, and η_{obs} is the water displacement which would be measured by a surface follower. If the relative fluctuations in density are defined by $e = \frac{\Delta\rho_o}{\rho_o}$, then $\rho_o + \Delta\rho_o = \rho_o(1+e)$. Also if B_P is expressed in terms of a mean bottom pressure $P_o+H\rho_o$ added to the bottom pressure variations ΔB_P (in mb), then from (4.13)

$$\Delta B_P = \Delta p + \eta_{obs}\rho_o(1+e) + H\rho_o e \qquad (4.14)$$

For a typical vertical density profile of the water column during Summer (refer section 4.6.2), $e \approx 10^{-3}$ and $\rho_o \approx$ 1+0.02; with η_{obs} and Δp in the range of 20cm and 5mb respectively, the term $\eta_{obs}\rho_o e$ is sufficiently small and can be neglected; also $\eta_{obs}\rho_o \approx \eta_{obs}$, and $H\rho_o \approx H$. Hence (4.14) can be simplified to:

$$\Delta B_P = \Delta p + \eta_{obs} + He, \qquad (4.15)$$

so that the bottom pressure variations can be realised as the sum of the adjusted sea level and a density term He. In the presence of a varying water density profile, e is not constant and the density term cannot thus be considered as a constant offset. It is however appropriate to make this assumption in the higher frequency band of the bottom pressure spectrum. This is further corroborated from actual measurements at Qawra station when the instrument is situated below the summer thermocline (refer to section 4.6.2).

4.3.3 Barograph station array

Fig. 4.2 gives the geographic disposition of the atmospheric pressure stations which consist of a closely spaced array in the southeastern half of Malta, and an isolated station at the northwestern tip of the island. This disposition of the stations permits the analysis of the spatial coherence of the atmospheric waves over a wide range of distances.

Table 4.2
Distances between station locations

STATION PAIRS	DISTANCE /Km
Ramla - Valletta	17.8
Ramla - Attard	13.3
Ramla - Luqa	18.2
Ramla - M'Xlokk	24.5
Valletta - Attard	6.1
Valletta - Luqa	6.3
Valletta - M'Xlokk	7.8
Attard - Luqa	5.0
Attard - M'Xlokk	11.2
Luqa - M'Xlokk	7.0

Fig. 4.2 Positions of air pressure gauges

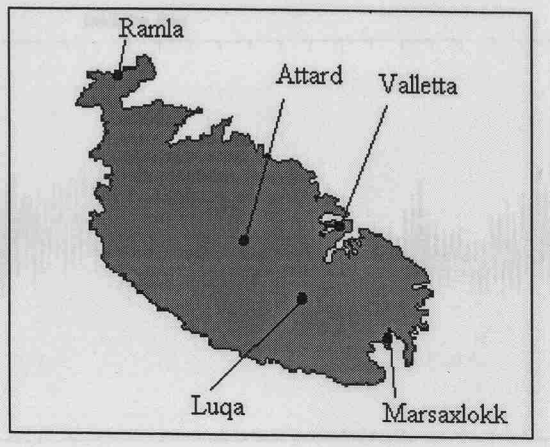

4.3.4 General description of observations

The plots of sea water elevation in Mellieha Bay and St. George's Bay (Fig. 4.3) and the corresponding comparative plots of running variance on water elevation and atmospheric pressure (Figs. 4.4 and 4.5) at the respective stations indicate the occurrence of a number of interesting events starting from the 14th of November. Four selected data intervals (Table 4.3) each 48 or 96h long are thus chosen for further analysis. Each data interval contains an interesting event of enhanced gravity-wave activity in the atmosphere with accompanying seiche excitations of the sea surface. A fifth data interval is also considered as an example with no wave activity.

During the period of measurement there were three moderate seiching events (1, 3 and 4 in Table 4.3). Each coincides to an increase in surface pressure variance, but the respective magnitude of the sea level oscillations is not proportionate to the atmospheric wave activity. Event 1 has the longest duration, spanning about 5 days, and is associated to a relatively weak air pressure variance; during this event the magnitude of the sea level fluctuations in St. George's Bay is much less compared to that in Mellieha Bay. The highest air pressure activity occurs during event 4 at Ramla tal-Bir station, but does not retain the same strength at the southernmost stations, especially in Attard and Marsaxlokk. Event 3 is particularly interesting in that it is relatively brief and sharp, occurring during a surge provoked by a major dip in barometric pressure and heavy rainfall on 1st December. Contrary to the case of the other events, the associated seiching in St. George's Bay is very strong and the maximum excursion in sea level exceeds that in Mellieha Bay. The air pressure during event 2 is as

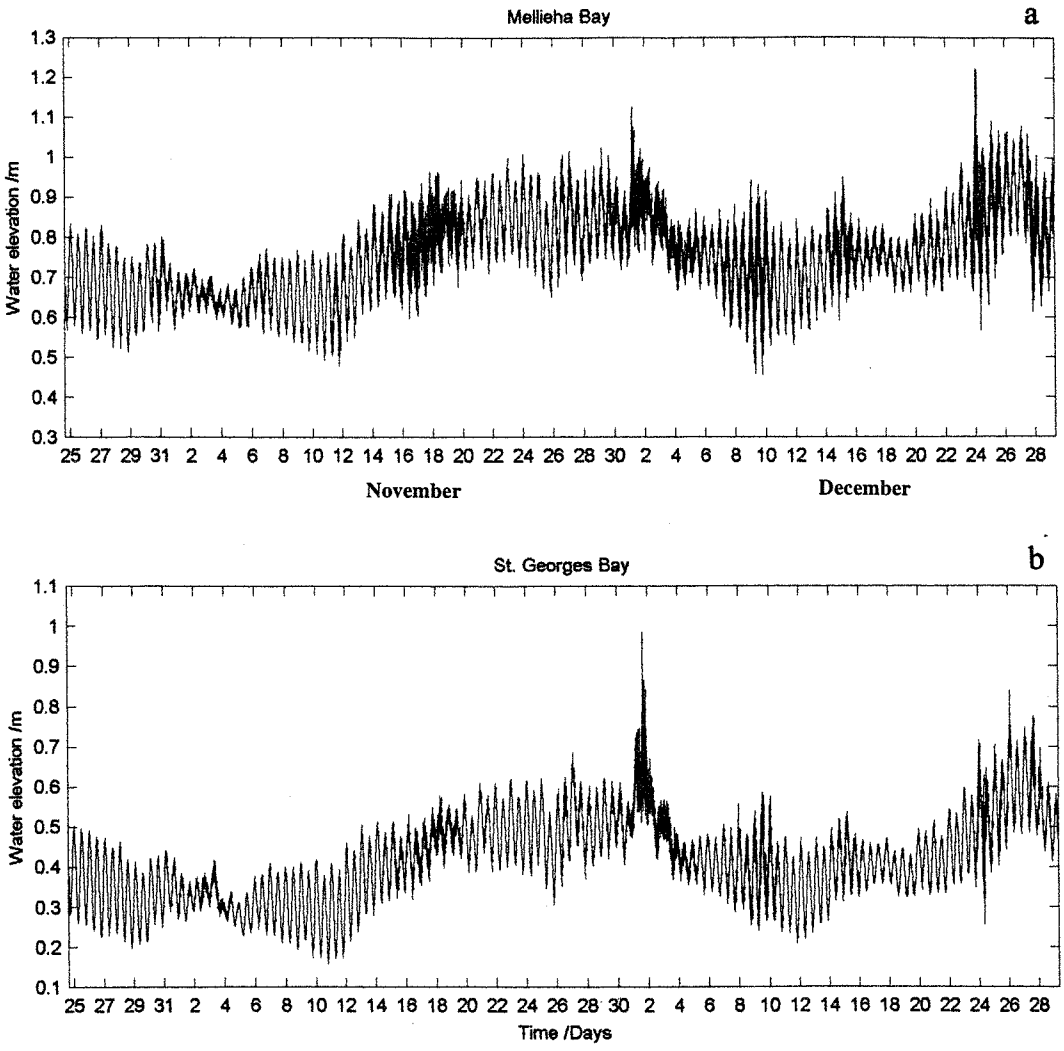

Fig. 4.3 Time series of water elevation in (a) Mellieha Bay and (b) St.George's Bay for the period (17h18)24/10/96 - (05h22)29/12/96.

strong as in event 1, but the associated seiching is significantly weaker. The mechanism which links atmospheric waves to large amplitude sea level oscillations is thus not a simple one and certainly depends on several interlinked parameters. An analysis of the four events thus serves to shed light on the possible generation of these sea level fluctuations by atmospheric waves. The period 22-23 November is included as an example of

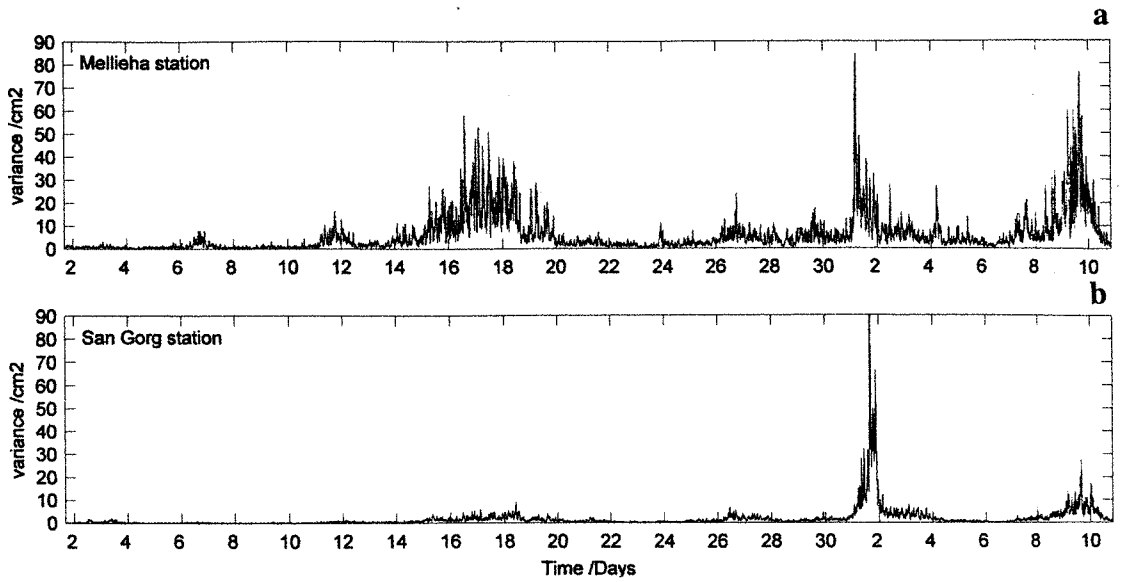

Fig. 4.4 Running variance on 2-min sampled series of water elevation in (a) Mellieha Bay and (b) St. George's Bay for the period (16h04)1/11/96 - (20h25)10/12/96.

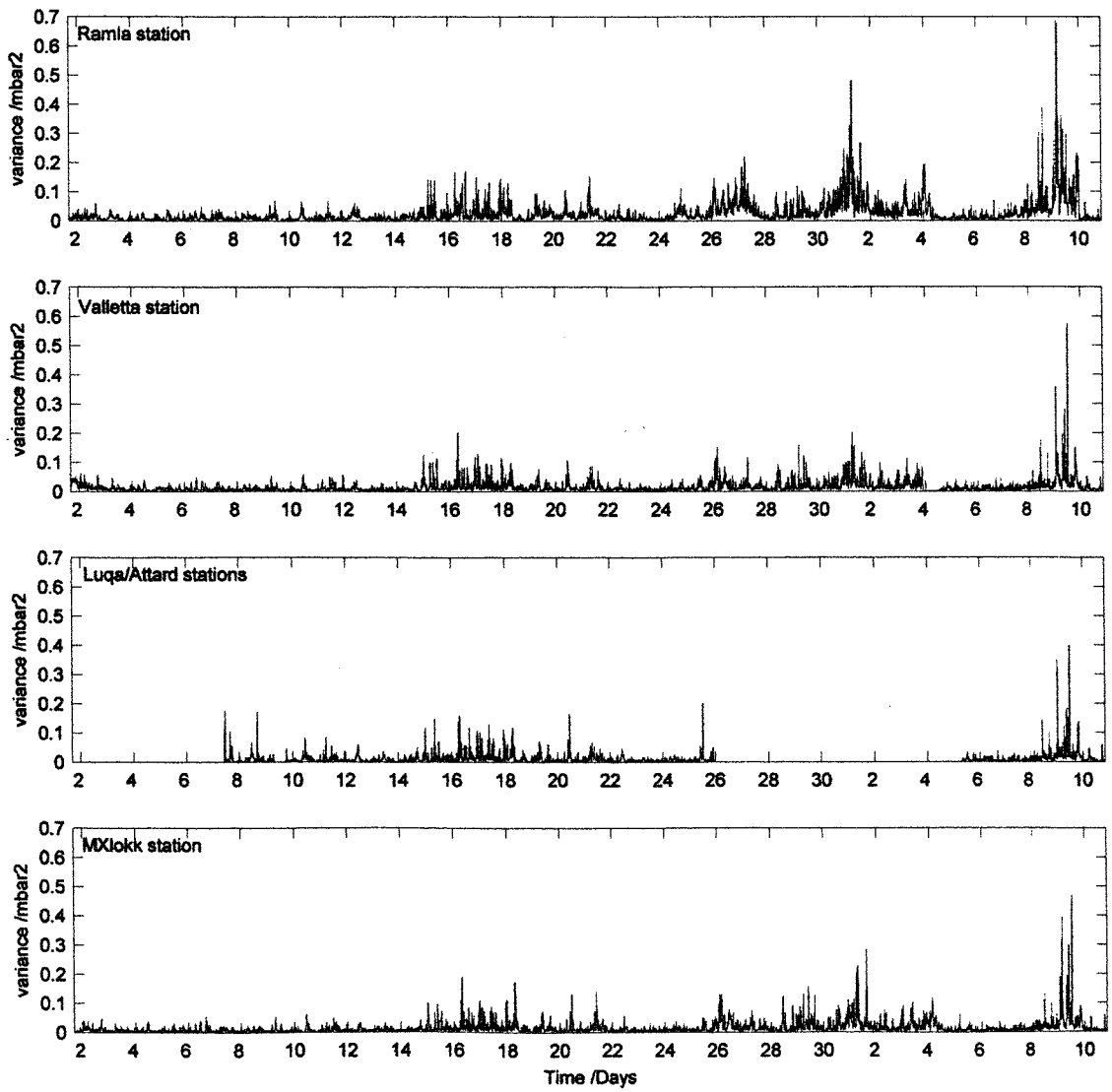

Fig. 4.5 Running variance on 2-min sampled series of atmospheric pressure in (a) Ramla tal-Bir, (b) Valletta, (c) Luqa and Attard, and (d) Marsaxlokk Bay for the period (16h04)1/11/96 - (20h25)10/12/96.

Table 4.3
The gravity-wave events selected from measurements made during Autumn 1996

	Period		Max./Average high frequency pressure fluctuations (mbar)	Max./Average sea level fluctuations (cm)	
Event Number	FROM	TO	Ramla tal-Bir	Mellieha	St. George's
1	(0h) 15 Nov.	(0h) 19 Nov.	1.0 (0.5)	23 (15)	8 (5)
2	(0h) 26 Nov.	(0h) 28 Nov.	1.0 (0.5)	15 (6)	6 (4)
3	(0h) 30 Nov.	(0h) 04 Dec.	1.25 (0.5)	29 (15)	33 (15)
4	(0h) 08 Dec.	(0h) 10 Dec.	2.0 (0.8)	28 (12)	11 (8)
5	(0h) 22 Nov.	(0h) 24 Nov.	---	8 (5)	3 (2)

All times in GMT

low atmospheric wave activity and is taken as a background reference. During these two days no sea level oscillations are registered.

4.4 Analysis of atmospheric wave activity

4.4.1 Spatial coherence of atmospheric perturbations

The station distances listed in Table 4.2 cover a range of different station pair separations between a minimum of 5Km and a maximum of 24.5Km. By means of a comparative analysis from such a wide selection of station separations, it is possible to obtain information on the spatial limits over which atmospheric waves can retain their stability.

The variation in spatial coherence is known to be a function of both period and distance. The coherence γ^2 is expected to be high for stations that are sufficiently close and for the lower frequencies; it decreases rapidly as the frequency f and station separation Π increase (i.e. $\gamma^2_{\Pi \to 0, f \to 0} \to 1$ and $\gamma^2_{\Pi \to \infty, f \to \infty} \to 0$) (Rabinovich, 1993). This dependence is typified by the coherence plots for a number of station pairs (Fig. 4.6a) calculated for the same period of time for Ramla, Valletta and Marsaxlokk stations (1st November - 10th December 1996) and for a shorter period (7 - 25th November 1996) in the case of the Valletta - Luqa stations. In each case the magnitude of the coherence function between two pressure data sets is estimated from the auto- (P_{xx}, P_{yy}) and cross-spectra (P_{xy}) by $\gamma = |P_{xy}|/(P_{xx}P_{yy})^{1/2}$. The spectra are estimated, after mean removal and linear detrending, by the Welch method using a fixed segment size of 512 records with 50% overlap of segments.

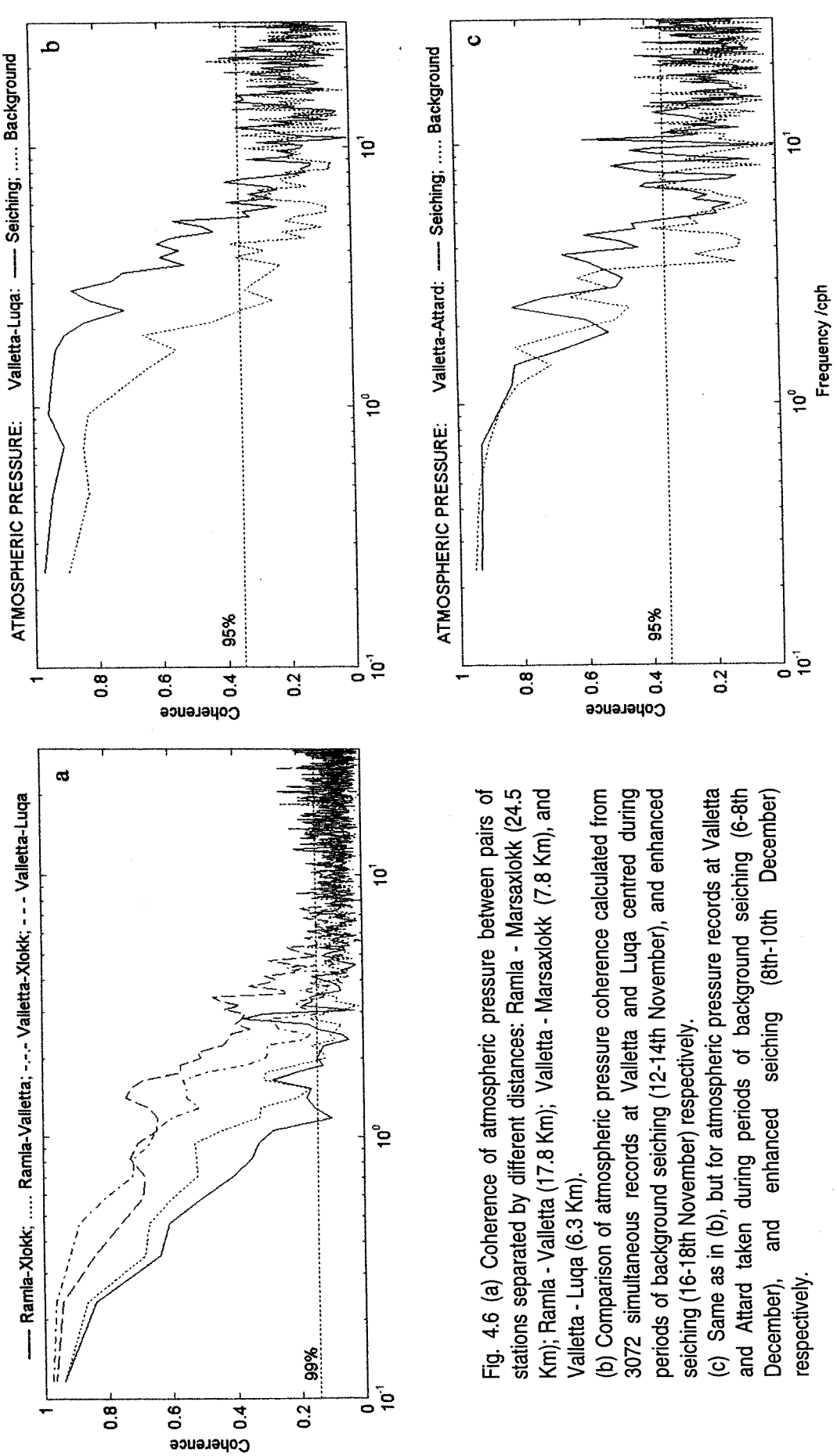

Fig. 4.6 (a) Coherence of atmospheric pressure between pairs of stations separated by different distances: Ramla - Marsaxlokk (24.5 Km); Ramla - Valletta (17.8 Km); Valletta - Marsaxlokk (7.8 Km), and Valletta - Luqa (6.3 Km).
(b) Comparison of atmospheric pressure coherence calculated from 3072 simultaneous records at Valletta and Luqa centred during periods of background seiching (12-14th November), and enhanced seiching (16-18th November) respectively.
(c) Same as in (b), but for atmospheric pressure records at Valletta and Attard taken during periods of background seiching (6-8th December), and enhanced seiching (8th-10th December) respectively.

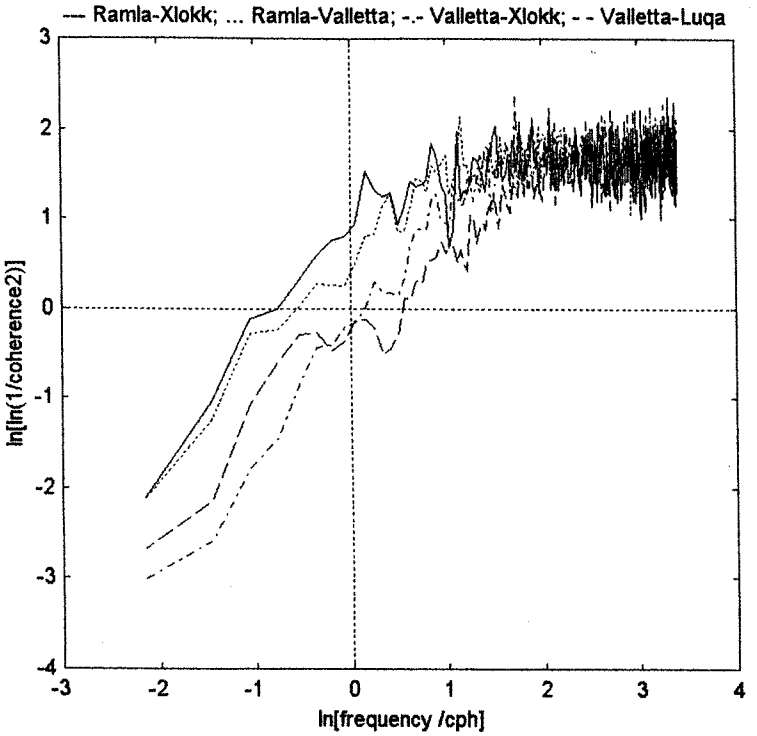

Fig. 4.7 Plot of $\ln\{\ln(1/\gamma^2)\}$ vs $\ln(f)$ constructed from the coherences in Fig. 4.6.

These results show that the coherence is indeed higher for the shorter station separations, especially for frequencies in the range of 1 - 2cph. The peak at around f = 1.7cph is noteworthy. In general the atmospheric pressure has negligible coherence for oscillations with frequencies higher than 1cph at distances greater than about 25Km. At this distance the coherence for the higher frequency background atmospheric signals is not significant. For waves with periods less than 12min, the radius of coherence is higher than the 99% significance level at only 6 Km. This agrees well with results by Herron et al. (1969) (Π = 30Km for f = 1cph; Π = 7Km for f = 6cph), but is somewhat different from one of the other few known studies on the subject by Rabinovich & Monserrat (1997) who report a much more rapid decay of spatial coherence with frequency and distance (Π = 10Km for f = 1cph; Π = 3Km for f = 6cph). One should however note that the value of the coherence greatly depends on the segment size used in the analysis. With a segment size of 256 records, the coherence estimate is indeed found to be much higher than that calculated for the same period with double the segment size. This

indicates that the temporal correlation of atmospheric pressure fluctuations at nearby stations occurs over intermittent events of limited duration.

Following Rabinovich (1993), the general character of the spatial-temporal structure of the atmospheric pressure coherence can be empirically described by an expression of the form

$$\gamma^2(f,\Pi) = \exp\{-\alpha f^{\beta}\Pi^{\nu}\} \qquad (4.16)$$

where α, ν and β are constants that are characteristic of the region. Taking logarithms on both sides, the expression takes the linear form

$$\ln\{\ln(1/\gamma^2)\} = \ln\alpha + \nu \ln\Pi + \beta \ln f \qquad (4.17)$$

For a given pair of stations (i.e. constant Π), a plot of $\ln\{\ln(1/\gamma^2)\}$ against $\ln f$ should give a straight line plot with a constant slope β. Verification with data from different station pairs shows that the relationship is approximately valid for frequencies at which the coherence is significant (Fig. 4.7). The value of β varies in the range 0.9-1.5 and thus depends, together with α and υ, on the nature of the pertinent atmospheric perturbation. At the higher frequencies, the plots converge to the point with values of $\ln f = 2$ and $\ln\{\ln(1/\gamma^2)\} = 1.5$.

4.4.2 Dependence of air-sea coupling on spatial coherence

The compatibility of the horizontal scale of an atmospheric process with the horizontal dimensions of a water body is certainly an important criterion for an effective resonant coupling between the atmosphere and the sea level. The spatial coherence of the atmosphere at the higher frequencies, as deduced from an average over the whole period of observation, may indeed appear to be too weak to sustain such a direct coupling mechanism. It should however be noted that the spatial coherence does vary in time and can occasionally improve significantly especially during strong atmospheric events.

Fig. 4.6b,c shows the contrasting atmospheric pressure coherences at chosen two-day periods with different levels of atmospheric and sea level activities. The spatial coherence is invariably low during background seiching and low atmospheric activity, but increases considerably in coincidence to the occurrence of enhanced

atmospheric activity and associated strong sea level oscillations. This observation is better studied by following the temporal evolution of the coherence.

4.4.2.1 Analysis by f-t coherence plots

The plot in Fig. 4.8 is composed of atmospheric pressure coherence estimates between two stations (Valletta and Marsaxlokk) made at successive overlapping data segments each 3072 records in length, and centred at successive central times with a separation of two days. The contour plot establishes the variability of the atmospheric coherence in f-t space. At this horizontal distance between stations (7.8Km) the coherence at the lower frequencies retains very steady and high values, but there is considerable variability in coherence at the higher frequencies. The low coherence levels centred around the 4th December are the result of a 15-hour gap in the data at the Valletta station and should not be considered. At frequencies higher than 1cph there is an evident difference in the coherence levels between relatively quiet periods and periods of higher atmospheric activity. The coherence is generally low for long intervals of time, but it occasionally and very sharply peaks to values as high as 0.6 at frequencies in the range 1 - 3cph. This is also clear in the f-t coherence plot between the more distant Valletta and Ramla stations (Fig. 4.9). These intervals of increased coherence coincide very closely with the incidence of active atmospheric events (such as during events 1 and 3) and the associated enhanced sea level oscillations. This confirms that coherence in space is an important criterion for the coupling between atmospheric pressure perturbations and the sea surface, and consequently on the triggering of meteorological tsunami.

Analysis on observations from more distant station pairs also reveals a very significant variability in the level of coherence at the lower frequencies ($f < 0.5$cph). The comparative f-t coherence contour plots for different station pairs and separations in Fig. 4.10 is useful to identify the interdependent patterns of temporal and spatial variability of atmospheric processes. The plots confirm the general decrease in atmospheric coherence with station separation, and as expected, the coherence between the more distant Ramla and Marsaxlokk stations remains quite low for frequencies higher than 0.5cph. For the lower frequencies it is however interesting to note that, in the case of the more distant station pairs (Fig. 4.10a, b), the coherence occasionally decreases to quite low levels, such as during the periods centred on the 17th and 27th November, and the 9th December. It is noted that these and other periods of reduced low frequency spatial coherence for the more distant station pairs occur in concomitance to an enhanced atmospheric pressure coherence at the higher frequencies observed

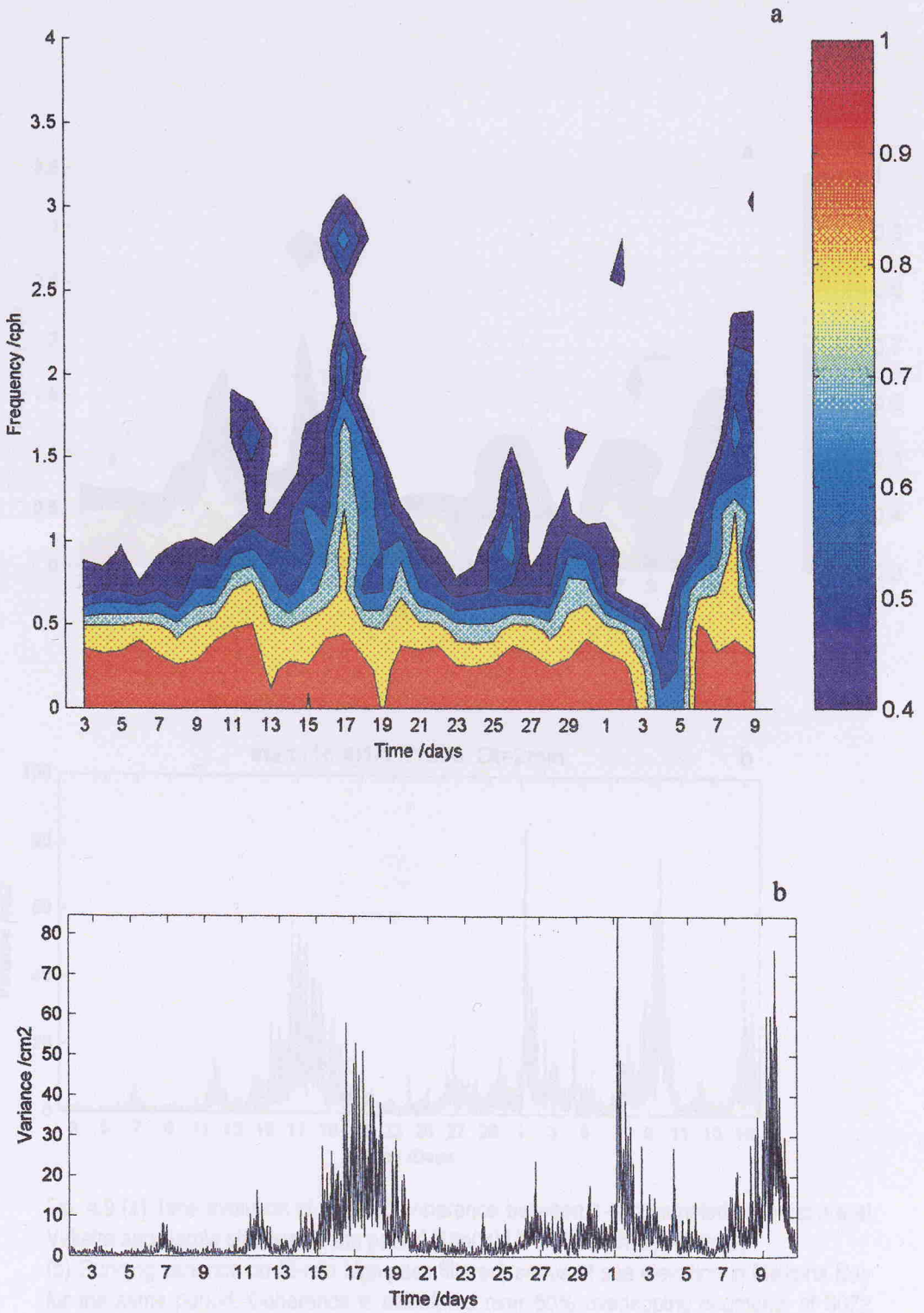

Fig. 4.8 (a) Time evolution of squared coherence between 1-min sampled air pressure at Valletta and M'Xlokk stations for the period (16h04)1/11/96 - (20h25)10/12/96;
(b) Running variance on (2-min high pass filtered) series of sea elevation in Mellieha Bay for the same period. Coherence is calculated over 50% overlapping segments of 3072 records. The 95% confidence level of γ^2 is 0.127.

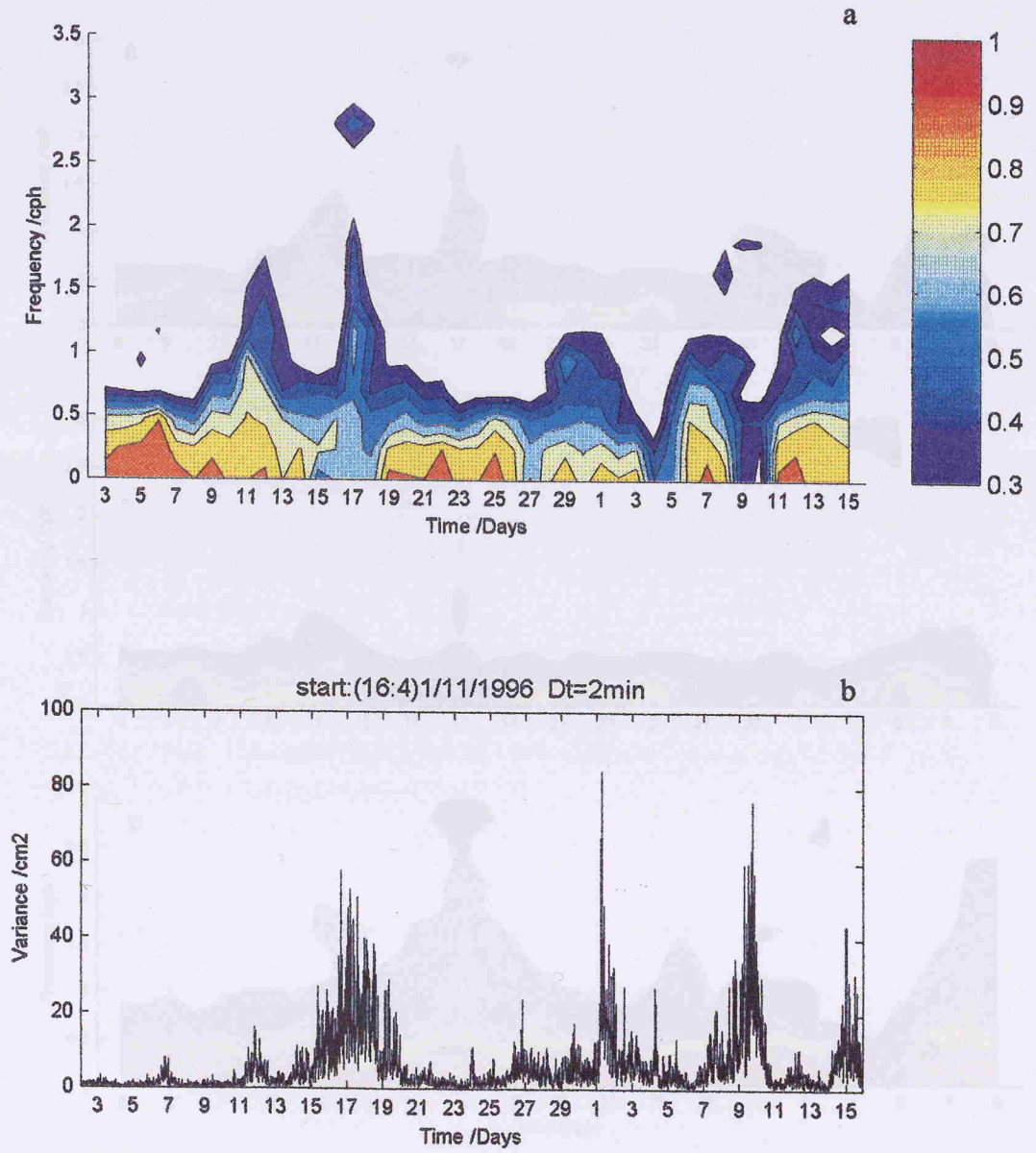

Fig. 4.9 (a) Time evolution of squared coherence between 1-min sampled air pressure at Valletta and Ramla stations for the period (16h04)1/11/96 - (09h12)14/12/96;
(b) Running variance on (2-min high pass filtered) series of sea elevation in Mellieha Bay for the same period. Coherence is calculated over 50% overlapping segments of 3072 records. The 95% confidence level of γ^2 is 0.127.

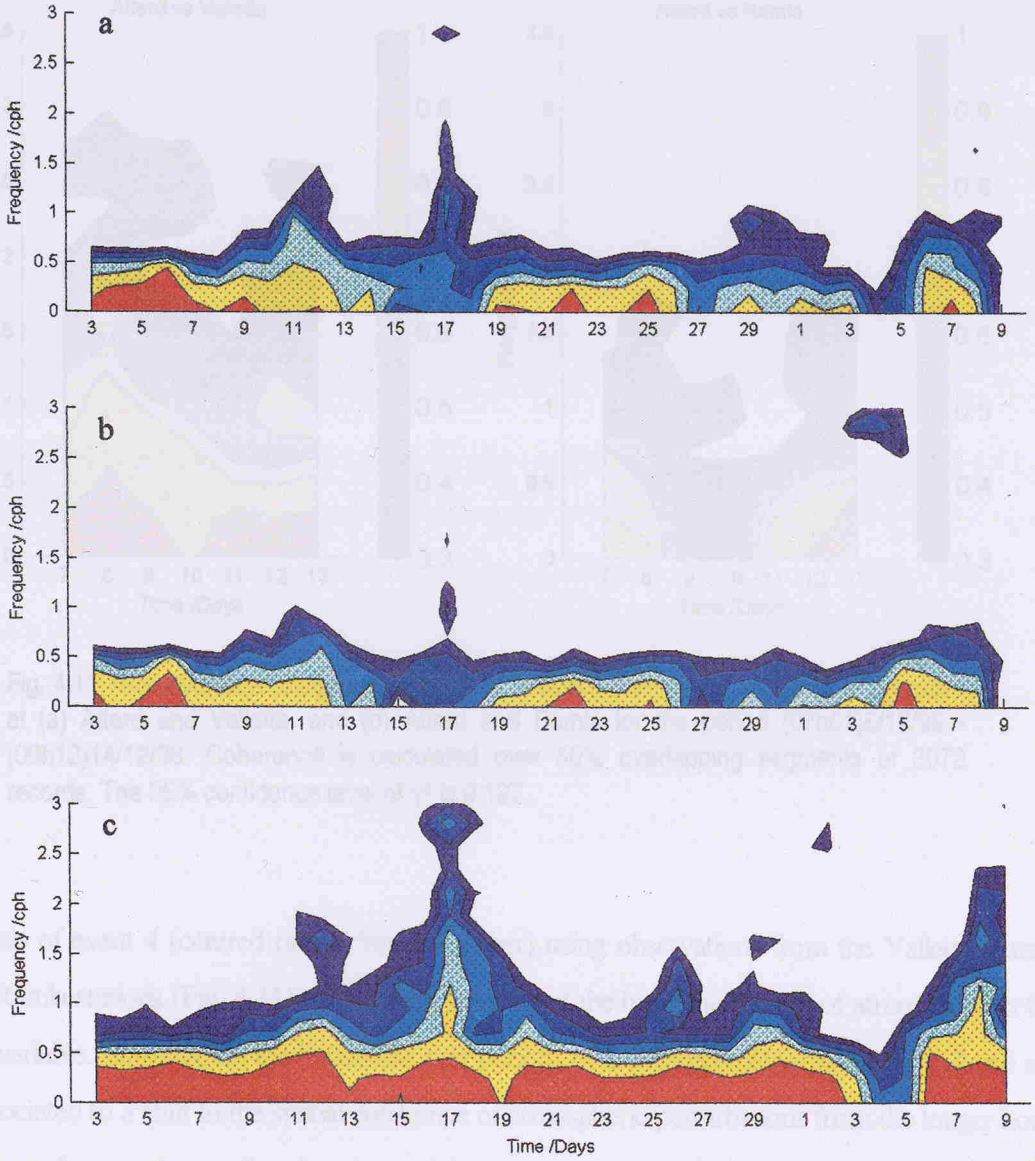

Fig. 4.10 Time evolution of squared coherence between one-minute sampled air pressure at (a) Ramla and Valletta, (b) Ramla and Marsaxlokk Bay, and
(c) Valletta and MarsaXlokk Bay for the period (16h04)1/11/96 - (20h25)10/12/96. Coherence is calculated over 50% overlapping segments of 3072 records. The 95% confidence level of γ^2 is 0.127.

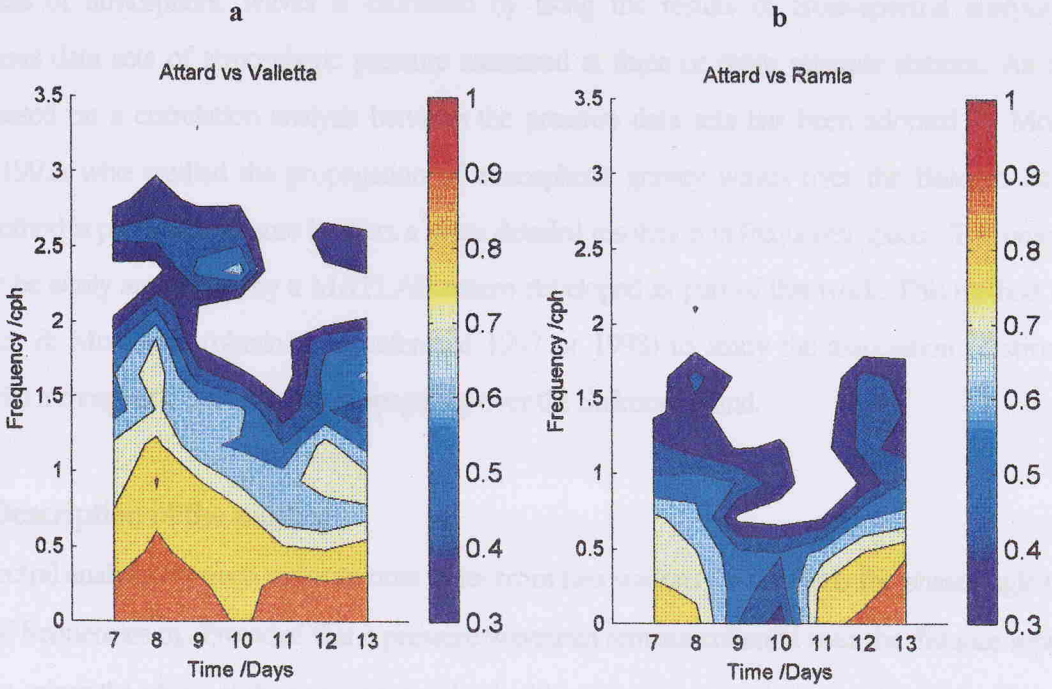

Fig. 4.11 Time evolution of squared coherence between one-minute sampled air pressure at (a) Attard and Valletta, and (b) Attard and Ramla for the period (07h01)5/12/96 - (09h12)14/12/96. Coherence is calculated over 50% overlapping segments of 3072 records. The 95% confidence level of γ^2 is 0.127.

detailed analysis of event 4 (centred on the 9th December) using observations from the Valletta, Attard and more distant Ramla stations (Fig. 4.11). This result shows that the horizontal scales of atmospheric coherence are also very variable. This favours the hypothesis that periods of intensified meteorologically induced seiching events are associated to a shift in the spatial coherence of atmospheric perturbations from the longer horizontal scales and lower frequencies to the shorter spatial scales and higher frequencies. This greater equity in horizontal spatial scales of atmospheric super-synoptic spectral components is indeed a favourable condition for the seiching of the sea surface. It is believed to be an important requisite for the atmospheric inter-spectral energy exchange and hence to an effective 'pumping' of energy in the atmosphere to frequency bandwidths that can most effeciently interact with the preferred modes of oscillation of the water body.

4.4.3 Estimation of atmospheric wave parameters

Following the method described by Likhacheva et al. (1985), the wavelength, phase speed and direction of propagation of atmospheric waves is estimated by using the results of cross-spectral analysis between simultaneous data sets of atmospheric pressure measured at three or more separate stations. An alternative method based on a correlation analysis between the pressure data sets has been adopted by Monserrat & Thorpe (1992) who studied the propagation of atmospheric gravity waves over the Balearic Islands. The former method is preferred because it offers a more detailed resolution in frequency space. The procedure can moreover be easily automated by a MATLAB macro developed as part of this work. This method is used by Rabinovich & Monserrat (obtain exact reference 1997 or 1998) to study the association of strong coastal seiches with atmospheric disturbances propagating over the Shikotan Island.

4.4.3.1 Description of the method

Cross-spectral analysis between pressure time series from two stations i and j yields the phase angle $\varphi_{ij}(\omega_n)$ at a number of frequencies ω_n. Provided that a pressure wavetrain remains coherent over the distance separating the stations, φ_{ij} gives the phase of the pressure signal at j with respect to that at i (i.e. φ_{ij} is positive if j leads i). At each frequency, the phase angle is related to the components of the wave vector $\vec{k}(\omega_n) = (k_n, l_n)$ and of the position vector $r_{ij}=(x_{ij},y_{ij})$ joining the two stations by:

$$\varphi_{ij}(\omega_n) = [\vec{k}(\omega_n) \cdot \vec{r}_{ij}] = k_n x_{ij} + l_n y_{ij} + \varepsilon_n \qquad (4.18)$$

where ε_n is the random noise component. Given three or more stations N, the wave vector $\vec{k}(\omega_n)$ is calculated by using the least squares method to minimize the expression

$$\sum_{i=1}^{N-1} \sum_{j=i+1}^{N} W_{ij} [\varphi_{ij}(\omega_n) - k_n x_{ij} - l_n y_{ij}]^2 \qquad (4.19)$$

where W_{ij} is a weighting factor that expresses the relative importance and contribution from the various possible station pairs. According to Bendat & Piersol (1986), the accuracy of the phase estimates φ_{ij} is given by

$g_{ij} = \sqrt{\frac{1-\gamma_{ij}^2}{\nu\gamma_{ij}^2}}$ and thus depends on both the coherence γ_{ij}^2 and the number of degress of freedom ν. The weighting factors W_{ij} are thus taken to be equal to the coherence γ_{ij}^2.

The minimisation of (4.19) leads to a set of simultaneous equations that are expressed by

$$\begin{pmatrix} a_{11} & a_{12} \\ a_{21} & a_{22} \end{pmatrix} \begin{pmatrix} k_n \\ l_n \end{pmatrix} = \begin{pmatrix} b_1 \\ b_2 \end{pmatrix} \qquad (4.20a)$$

where $a_{11} = \sum_{i=1}^{N-1} \sum_{i=j+1}^{N} x_{ij}^2$, $a_{12} = a_{21} = \sum_{i=1}^{N-1} \sum_{i=j+1}^{N} x_{ij} y_{ij}$, $a_{22} = \sum_{i=1}^{N-1} \sum_{i=j+1}^{N} y_{ij}^2$,

and $b_1 = \sum_{i=1}^{N-1} \sum_{i=j+1}^{N} \gamma_{ij}^2 \varphi_{ij} x_{ij}$, $b_2 = \sum_{i=1}^{N-1} \sum_{i=j+1}^{N} \gamma_{ij}^2 \varphi_{ij} y_{ij}$. (4.20b)

The solution of (4.20a) leads to a determination of the wavenumber $\vec{k}_n = \vec{k}(\omega_n) = (k_n, l_n)$ and hence to the wavelength $\lambda_n = 2\pi/|\vec{k}_n|$ and the phase speed $U_n = \omega_n\lambda_n/2\pi$. The direction of propagation θ_n, expressed as an angle increasing clockwise with respect to North, is given by:

$\theta_n = 0^o + \tan^{-1}|k_n/l_n|$, for $k_n > 0$ and $l_n > 0$; $\theta_n = 360^o - \tan^{-1}|k_n/l_n|$, for $k_n < 0$ and $l_n > 0$;
$\theta_n = 180^o + \tan^{-1}|k_n/l_n|$, for $k_n < 0$ and $l_n < 0$; $\theta_n = 180^o - \tan^{-1}|k_n/l_n|$, for $k_n > 0$ and $l_n < 0$.

and indicates the direction towards which the wave is moving.

4.4.3.2 Application to selected events

The method is applied to five selected data intervals in Table 4.3. For each data interval three stations with an approximately equidistant triangular disposition in space are selected. Where more than three stations are available for a given period, the analysis is carried out on a selection of other station triplets. If a data interval is treated as a single set the analysis gives an average for the whole event and the non-stationary character of the disturbance cannot be evidenced. In order to obtain information on the temporal evolution of the wave characteristics, each data interval is thus treated by obtaining wave estimates at subsequent computatation

subintervals consisting of 1024 data points each (approximately 8.5h for a sampling interval of 30s). Successive subintervals are shifted by 50% overlap (512 data points) with respect to one another. For a data interval of 2 days this yields 11 subintervals with a central time separation of 512 data points.

Each subinterval is analysed by overlapping spectral segments each 256 data points in length. This yields a spectral resolution of $\Delta f = 0.4688$cph. The first 17 frequency bands, each of width $0.4688h^{-1}$, and with central frequencies given by

$$f_n = 0.4688(n-1)\ h^{-1} \qquad n = 2, \ldots\ldots, 18$$

cover a range of frequencies 0.4688 to $7.9688h^{-1}$ (i.e. 128 to 7.5min). Estimates for higher frequencies are not sufficiently reliable.

The validity of the estimates is limited by the distance between the instruments. Atmospheric waves do not generally maintain their coherence over distances greater than about half a wavelength (De Maria et al., 1989) unless their energy is channelled close to the surface by some trapping mechanism (Lindzen & Tung, 1976). As already verified in section 4.4.1, the coherence between two stations deteriorates very quickly with distance, and the wave properties calculated by the method described above are only reliable for the lower frequencies at which the coherence is sufficiently significant. The following criterion is thus adopted :

$$\gamma_{ij}^2\ (\omega_h) \geq 0.4 \qquad (4.21)$$

On the other hand, if two stations are too close, the finite sampling interval ΔT and the effects of the instrumental noise put a limit on the smallest phase difference that can be detected and on the highest frequencies that can be resolved. Taking the example of three stations, suppose (x_i, y_i), i=1,2,3 are the position co-ordinates of the respective stations. φ_{12} , φ_{13} , φ_{23} are the phase differences between the respective station pairs. If the phase difference in more than one station pair is too close to zero, that is

$$|\varphi_{ij}(\omega_h)| < \omega_h \Delta T \text{ for more than one } (i,j) \text{ pair} \qquad (4.22)$$

the phase measurements are not considered to be accurate enough to give a reliable estimate of the wave speed. Furthermore if (k , l) are the wavenumbers along the respective co-ordinate axis and a wavelike disturbance f(ωt-kx-ly) passes across station 1 and subsequently across station 2, it follows that

$$f(\omega t - kx_1 - ly_1) = f(\omega t - kx_2 - ly_2 + \varphi_{12})$$

This implies that

$$kx_1 + ly_1 = kx_2 + ly_2 - \varphi_{12}. \qquad (4.23a)$$

Similarly

$$kx_1 + ly_1 = kx_3 + ly_3 - \varphi_{13} \qquad (4.23b)$$

and

$$kx_2 + ly_2 = kx_3 + ly_3 - \varphi_{23}. \qquad (4.23c)$$

(4.23a) - (4.23b) + (4.23c) yields

$$\varphi_{12} - \varphi_{13} + \varphi_{23} = 0 \qquad (4.24)$$

so that the three phase differences are not completely independent and for consistency (4.24) should also hold. A second quality control criterion is thus applied and estimates for which

$$|\varphi_{12} - \varphi_{13} + \varphi_{23}| > \pi/10 \qquad (4.25)$$

are rejected. In such cases the disturbances do not have significant energy and are relatively short-lived so that they do not remain coherent during the time taken to travel between the masts.

The MATLAB macro developed for these estimates also handles these criteria. If any of the criteria (4.21), (4.22) and (4.25) are not satisfied, the estimates are automatically rejected.

For each event and at each frequency band, the above procedure yields a set of valid estimates from a number of subintervals (up to a maximum of 11). The mean of the estimates for a given event and frequency band give an indication about the variation of the wave characteristics with time. The standard deviation of the estimates gives the spread of the results and provide a useful measure of the uncertainty of the mean.

4.4.3.3 A note on wave directions around north

In the calculation of the mean and standard deviation of wave direction particular attention is necessary in cases where values are scattered about both sides of the northern direction. If some values are slightly greater than 0° while others are slightly less than 360°, the true mean will be clearly near to 0°, but a simple average may lead to an erroneous answer close to 180°. A solution to this problem is proposed by Rees & Mobbs (1988).

Suppose that $\{\theta_i, i = 1,2,3.....n\}$ is the series of wave directions. For each value θ_i, a set of modified wave directions θ_i^j are calculated by:

$$\theta_i^j = \mathrm{mod}([\theta_i + 360(j-1)/M], 360), \quad j = 1,2,3...M \tag{4.26}$$

This yields n sets of modified directions, each containing M values. Intermediate mean values $<\theta^j>$ are next calculated:

$$<\theta^j> = \frac{\sum_{i=1}^{n} \theta_i^j}{n}. \tag{4.27}$$

The corrected mean intermediate values $<\theta_c^j>$ are obtained by:

$$<\theta_c^j>= \mathrm{mod}([<\theta^j>+360(j-1)/M],360), \quad j=1,2,3...M \tag{4.28}$$

This yields M corrected values out of which at least two should be identical and the rest have all different values. The value of the identical terms gives the mean wave direction $<\theta>$.

Taking any one of these identical terms in (4.28), if the j index is J, then the standard deviation σ is calculated by:

$$\sigma = \sqrt{\frac{\sum_{i=1}^{n} \left(\theta_i^J - \langle\theta^J\rangle\right)^2}{(n-1)}} \,. \tag{4.29}$$

A MATLAB macro is written to automise the calculations by this method.

4.4.3.4 Analysis of results

A separate analysis is carried out for each event. In each case the wavelength, phase speed and direction of propagation of atmospheric waves are estimated, as explained in section 4.4.3.1, at successive subintervals of 1024 records shifted by one hour with respect to one another. Where four simultaneous data records are available, the estimates are repeated by using different sets of station triangular arrays. Table 4.4 gives, for each frequency band, event and station array, the number of subintervals at which all quality controls are satisfied. Ramla station is located almost in line to the Valletta and Marsaxlokk stations and its position is thus not very ideal for estimating wave parameters. The distance of separation with respect to the southernmost stations is also longer. These two factors must be taken into consideration when the analysis makes use of the observations at Ramla station. Data from Ramla station is however essential in order to assess the horizontal coherence of atmospheric waves. Unfortunately, the events 2 and 3 occurred in a period when both the Attard and Luqa stations were inoperative; in these two cases the analysis is carried out by making use of the Ramla station. The wave parameters are plotted against frequency. Their temporal development is investigated by following their variation at successive subintervals. The plots of the pressure time series in Ramla tal-Bir station are used to present the main phenomenology of surface atmospheric pressure fluctuations at each event.

Table 4.4

Number of subintervals fulfilling the quality criteria at each frequency band and for respective events

Central frequency $f_n = 0.4688(n-1)$ cph	Number of valid subintervals						
Frequency band number (n)	EVENT 1	EVENT 1	EVENT 2	EVENT 3	EVENT 4	EVENT 4	EVENT 5
2	95	61	14	36	39	25	46
3	94	49	8	15	32	26	25
4	87	42	0	4	36	18	4
5	70	21	1	2	29	17	0
6	52	12	0	0	21	3	0
7	46	13	1	3	10	4	0
8	19	12	0	1	5	1	0
9	12	0	0	0	5	0	0
10	14	1	0	2	9	0	0
11	12	1	0	0	2	1	2
12	1	0	0	0	2	0	0
13	0	0	0	0	1	0	0
14	0	0	0	0	8	0	0
15	0	0	0	1	2	0	0
16	0	1	0	0	0	0	0
17	0	0	0	0	0	0	0
18	1	0	0	0	3	0	0
STATIONS	Valletta Luqa MXlokk	Valletta Luqa Ramla	Valletta MXlokk Ramla	Valletta MXlokk Ramla	Valletta Attard MXlokk	Valletta Attard Ramla	Valletta Luqa MXlokk
Total number of subintervals	97	97	49	97	49	49	49

The plots are drawn for separate 48 hour intervals. The trend in the measurements is removed before plotting and the time series in a plot does not match at the end with the beginning of the following plot. Furthermore the power spectra for each event give the distribution of the wave energy at frequencies higher than 0.2cph. In all the spectral plots the spectrum for event 5 is included for comparison as a background.

EVENT 1

This event is analysed by means of 11520 data points taken at 0.5 minute intervals (4 days) starting at 00:00 GMT 15th November, 1996. Pressure data series from the stations at Ramla tal-Bir, Valletta, Luqa and Marsaxlokk are used. Fig. 4.12a shows the surface pressure data series at Ramla tal-Bir. Two distinct data intervals characterise this set of observation. Relatively large amplitude pressure oscillations reaching up to 1.5

mbar and with periods close to 4 hours are the dominant feature in the first two days (15/16th November). They are replaced by much higher frequency fluctuations during the last two days (17/18th November) and especially in the early hours of 18th November during the passage of a pressure low. The power spectrum density plot (Fig. 4.12b) shows that the intensification in the atmospheric wave activity during the second half of the study period does not occur at a selected set of discrete frequencies, but covers a wide band from 5 to 20 cph. This atmospheric activity diminishes considerably towards the end of the 18th November.

The sea level oscillations have a very similar development in time (Fig. 4.5). Seiching intensifies in the early morning of the 15th November and remains at this level of activity throughout the day. Seiching continues to build up during the 16th November and retains the attained intensification up to the early hours of 18th November when the seiching is reduced to the levels of the first day of the event. This level is retained until the late hours of the 19th November when the seiching is gradually attenuated to background levels.

The variations in the surface pressure field should also be considered in association to the changes in the synoptic weather situation during the period. The contrast between an extensive low pressure area spanning from Algeria in the south up to Germany in Western Europe, and a high pressure system over Russia and the Ionian Sea gives rise to a warm and dry southerly current over the Maltese Islands in the first half of the 15th November. In the upper atmosphere the contact of warm air with the underlying cooler and humid air over the Western Mediterranean basin results in the generation of a large area of high clouds covering Algeria and the Central Mediterranean. The surface cyclonic circulation centred over the Balearic Islands remains quasi-stationary on the 16th November and the situation of high and medium cloud cover remains throughout the day. In the upper layer a strong southwesterly current is registered. Closer to the surface a southeasterly fluctuating current is established and drives an inflow of dry and warm air over the relatively cooler and humid underlying air mass from the west. After a brief period of attenuation, this southeasterly current becomes stronger and persistent on the 17th November which is characterised by intermittent showers. During this day the low pressure system over Central Europe favours the penetration of cooler air into the Western Mediterranean with the associated instability reaching up to the Central Mediterranean area. This situation persists until the early hours of the 18th November when the southeasterly wind builds up to a strong breeze. Towards noon of the 18th November, a weak cold front travels over the Maltese Islands. This front does not

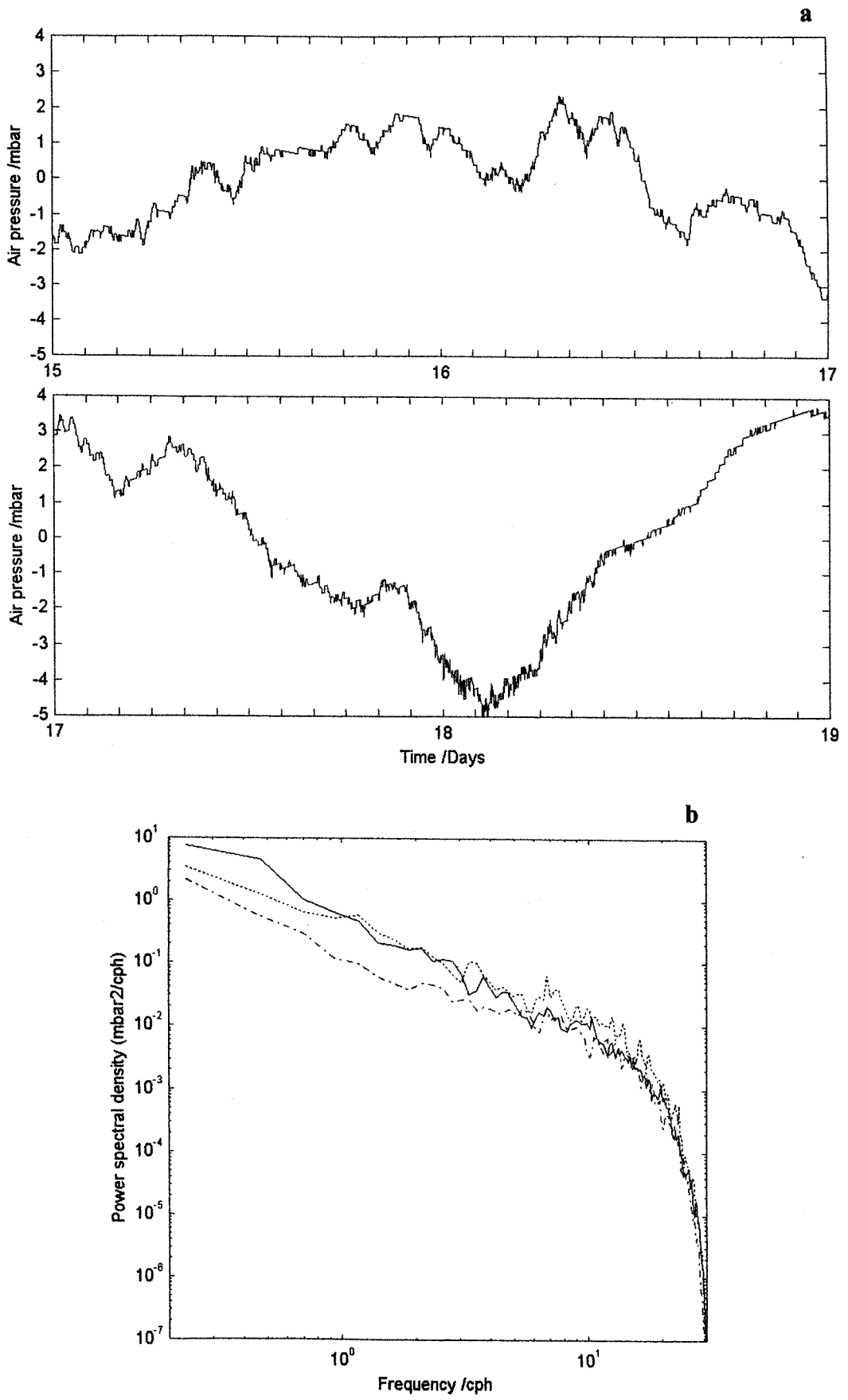

Fig. 4.12 (a) Time series of surface air pressure data at Ramla tal-Bir (15-18 November, 1996); (b) Power spectral density plot of surface air pressure at Ramla tal-Bir for the period 15/16 (solid), and 17/18 November, 1996 (dotted). The background spectrum for event 5 (dashed) is included for comparison. The 95% confidence factor, for 22 d.o.f. is 4.33 dB ($B_{min} = 0.59$; $B_{max} = 1.6$).

carry any bad weather with it, and its only effect is an abrupt change in the wind direction which veers from the west. The atmospheric wave activity stops immediately with this change in the synoptic situation.

The wave parameter estimates at each frequency band for the full 4-day period are summarised in Fig. 4.13 for the array composed of Valletta, Luqa and Marsaxlokk (VLM-array). Fig. 4.14 and 4.15 show the variation in time of the wave parameters for the respective frequency bands. For this event the number of subintervals fulfilling the quality control criteria described above is exceptionally high (Table 4.4). The lower frequencies remain coherent practically throughout the four days. At the higher frequencies (n = 4,5,6 and 7) it is interesting to note that the coherence improves in coincidence to the intervals of enhanced seiching. In particular, the frequency signals at bands n = 8 and 9 (i.e. at f ≅ 4cph) become particularly consistent from mid-day of the 16th to the late morning of the 18th November (Fig. 4.14 and 4.15).

The wavelength clearly decreases with frequency and is of the order of a few tens of kilometers for the higher frequencies. The magnitude of the wavelength is very steady in time at these frequencies. The variation in the wavelength at the lower frequencies is probably an artefact of the measurements which are taken at relatively close stations. With the exception of the transient signals at frequency bands with n higher than 12, there is little dependence of the phase speed or the wave direction on frequency. On average the phase speed is 40 ms^{-1} and the wave direction is towards N80°E.

The physical properties of the atmospheric waves are also investigated by using the observations at the Valletta, Luqa and Ramla stations (VLR-array). The distance separating the Ramla station from the Valletta-Luqa station pair in this array is more than twice that for M'Xlokk station in the VLM-array. As expected, the subintervals that qualify the quality controls are less in number even at the lower frequencies (Table 4.4). For the first seven frequency bands, the mean results are however very similar to those for the VLM-array (Fig. 4.16). It is noteworthy that on the 15th and 18th November, the criteria for the VLR-array are not satisfied even at the lowest frequency bands. The criteria are mainly satisfied during the 16th and the 17th of November, which coincides with the time of strongest seiching. Coherence at these frequencies has thus a greater spatial extent during sustained seiching.

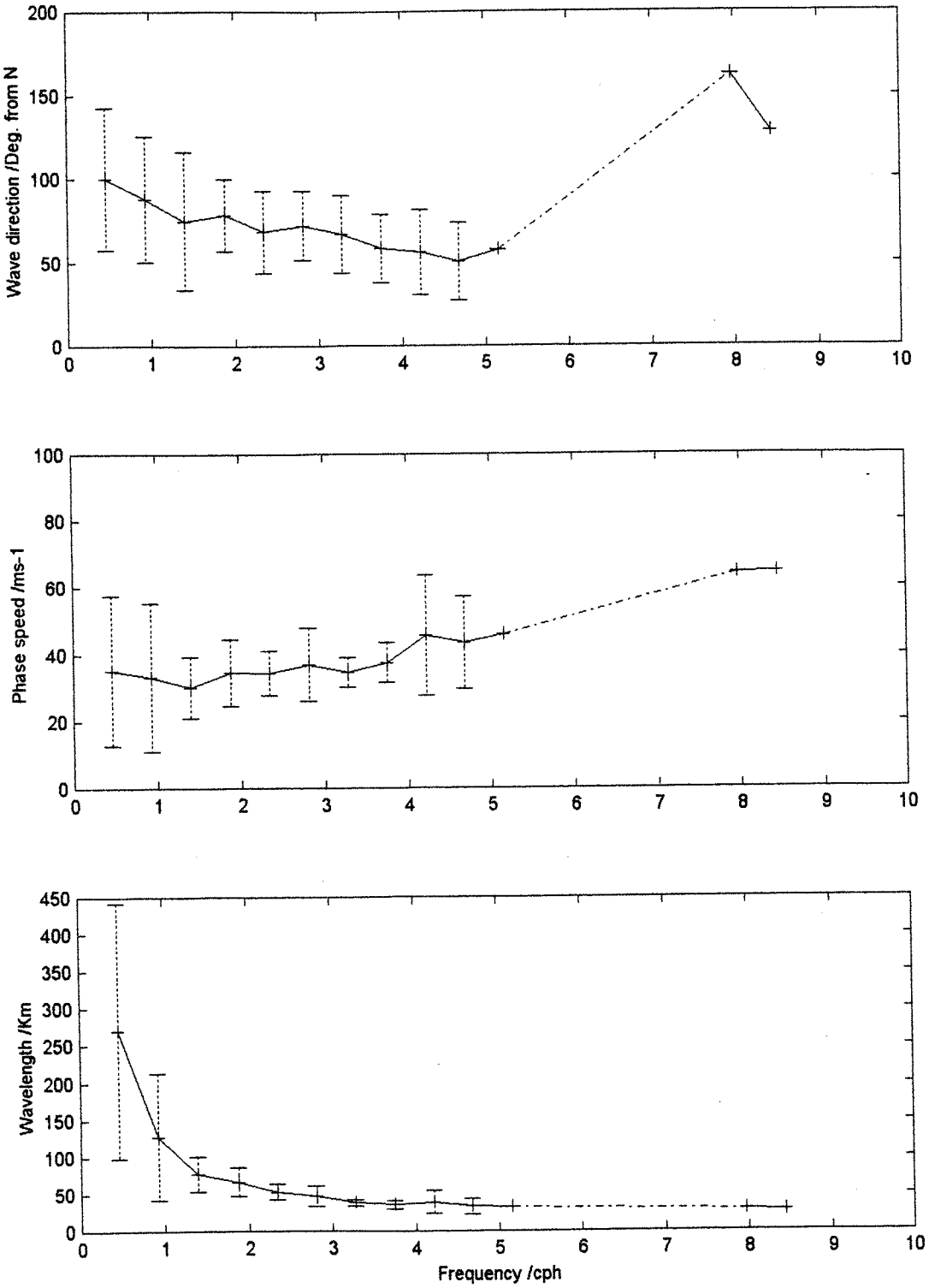

Fig. 4.13 Frequency dependence of (a) direction, (b) phase speed, and (c) wavelength for atmospheric waves during event 1, estimated from observations at Valletta, Luqa and Marsaxlokk stations.

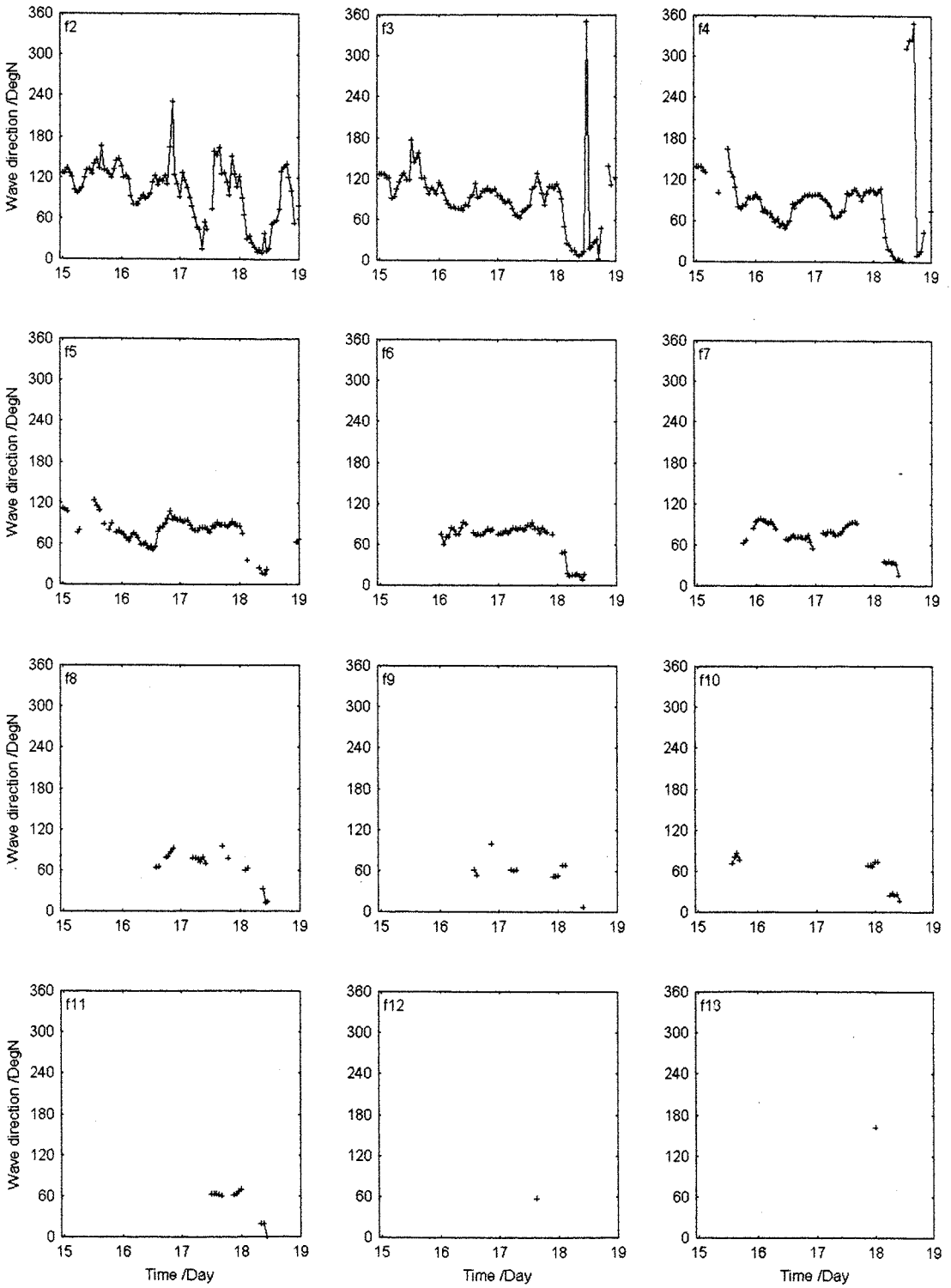

Fig. 4.14 Temporal development of atmospheric wave directions estimated for event 1 at separate frequency bands f2 - f13 from observations at Valletta, Luqa and Marsaxlokk stations.

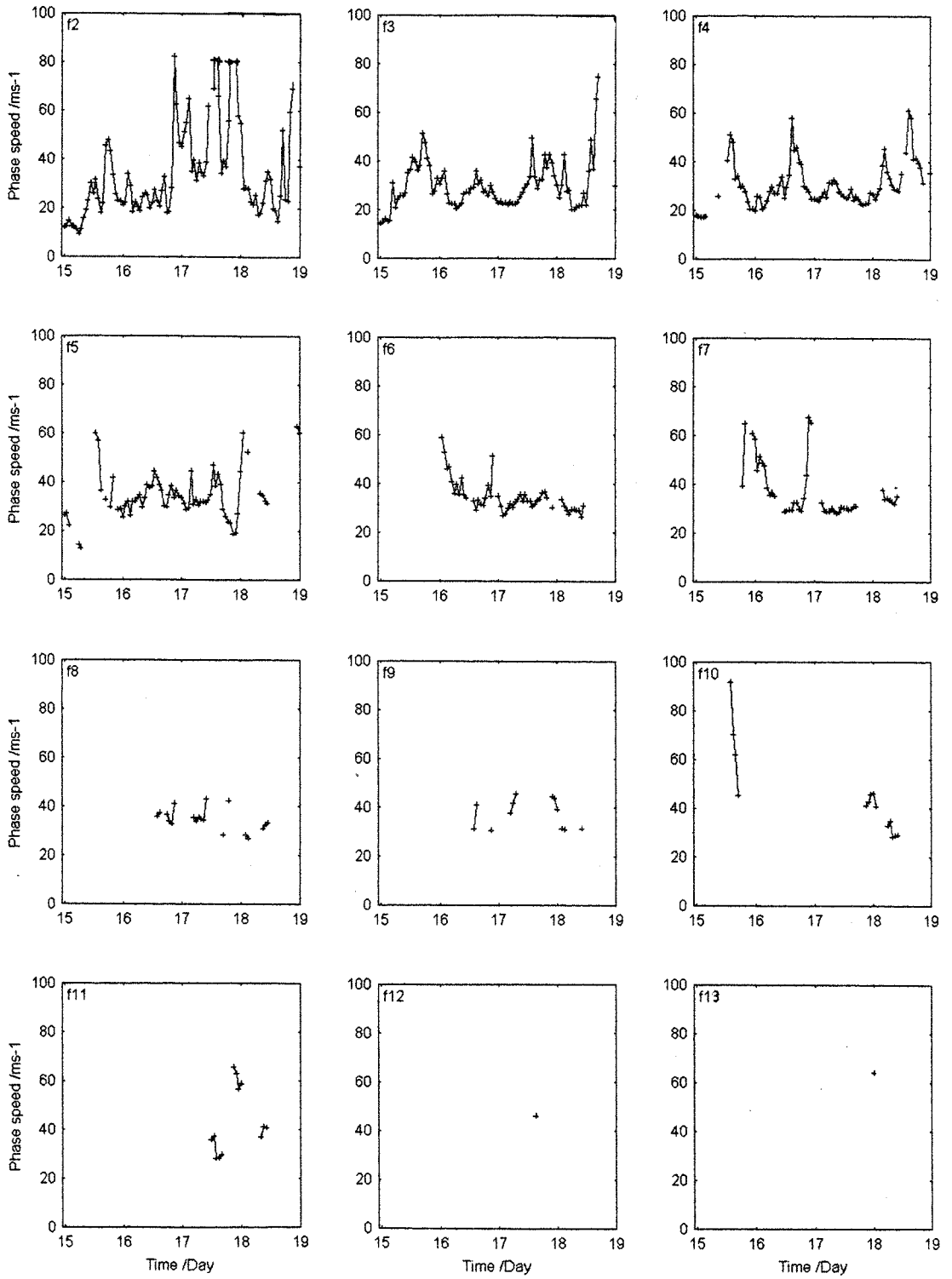

Fig. 4.15 Temporal development of atmospheric wave phase speeds estimated for event 1 at separate frequency bands f2-f13 from observations at Valletta, Luqa and Marsaxlokk stations.

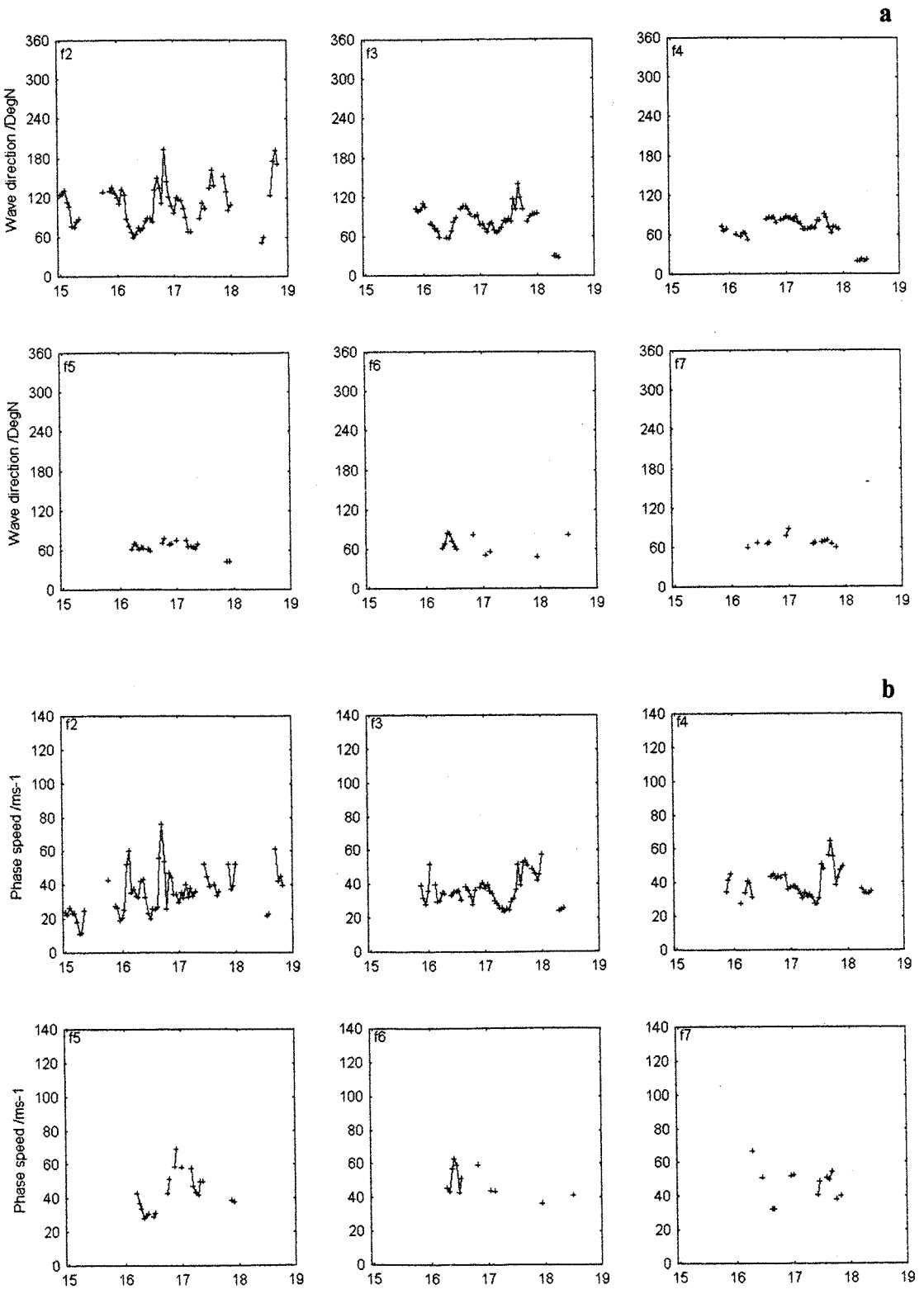

Fig. 4.16 Temporal development of atmospheric wave (a) directions and (b) wave speeds estimated for event 1 at separate frequency bands f2 - f7 from observations at Valletta, Luqa and Ramla stations.

Upon comparing the temporal analysis of the respective VLR- and VLM-arrays, it is also interesting to note that, at all the major frequency bands, the time variations of the atmospheric wave directions are very well correlated so that wave propagation occurs in the same direction over considerable horizontal extents. This correspondence does not apply to phase speed which has a more rapid evolution as the waves propagate in space. The direction of propagation of the atmospheric waves do not bear a relation to the direction of the surface wind. The propagation of the lowest frequencies (n = 2,3,4) fluctuates around an average direction directed towards ESE (note that wind direction is taken as that from which the wind blows whereas the direction of propagation of the atmospheric waves is that along which the wave is moving). The next frequency bands (n = 5,6,7,8) have a more stable direction of propagation directed along ENE. This direction is very closely orthogonal to the northern coast of Malta and is in line to the axis of Mellieha Bay, pointing away from its head towards the open sea.

EVENT 4

The synoptic weather pattern during event 4, is similar to that of event 1. During the two-day period between 00:00 GMT 8th December to 00:00 GMT 10th December 1996 the surface synoptic situation presents a complex surface cyclonic circulation over Spain, extending over Algeria and Tunisia, and reaching up to the Maltese Islands, which is blocked to the northeast by a high pressure over Eastern Europe (refer to Fig. 4.27, section 4.4.3.5). The low pressure system is accompanied by a frontal zone running from the Pyrenees, extending over Italy and swerving over the Central Mediterranean. The resulting strong southeasterly current is accompanied by high and medium cloud cover and loads the atmosphere with fine Saharian dust particles that renders the sky reddish in colour especially during sunset and sunrise, and comes down with the drizzling rain. On the 9th of December, the southeasterly surface current peaks to 17ms^{-1} in the first half of the day. It becomes also considerably more humid and an average rainfall of around 20mm is registered. After sunset the southeasterly current weakens very quickly and is replaced on the 10th December by a surface southwesterly wind.

Compared to event 1 the energy of the atmospheric waves is considerably higher at all frequencies (Fig. 4.17b). The spectrum again does not present any significant peak, but the lower frequency pressure excursions are particularly strong during this event. The surface pressure time series (Fig. 4.17a) presents some sharp and large amplitude fluctuations of the order of a couple of millibars especially at 14:00 GMT on the 8th December and

during the first half of the 9th December. The sea level responds again in synchronisation to the atmospheric perturbations. The seiche in both Mellieha Bay and St. George's Bay starts to intensify from around noon of 8th December, with maximum fluctuations throughout the 9th and subsequent attenuation in the early hours of 10th December.

The wave parameters are estimated for both the Valletta-Attard-Marsaxlokk station array (VAM) and the Valletta-Attard-Ramla (VAR) array, using 5760 half-minute (2 days) observations of surface pressure in each case. The estimates from the two arrays agree well and only the results from the VAM-array are presented here since a greater number of subsections satisfy the criteria for this array. The wavelength decreases and becomes more steady with frequency (Fig. 4.18). On the other hand there is considerable variability in wave speeds which fluctuate in time without any particular common pattern of variation between frequency bands (Fig. 4.20). The wave direction is very consistent for the duration of the two-day period (Fig. 4.19), with a predominant propagation along N65°E at all the frequency bands, except for f2 and f3 in the early hours of the 8th December when the direction veers more towards the SSE. It is also important to note that close to midnight between the 8th and the 9th December, in coincidence with the intensification of the sea level oscillations, there is an evident enhancement of the coherence at the higher frequency bands, especially in the range f8 to f12. The higher frequency wave activity during seiching events was also noted during event 1. Unfortunately it cannot be verified from wave parameter estimates for events 2 and 3 when station distances were too long to detect the smaller horizontal scales of coherence of the higher frequencies. During this interval one also notes that the lower frequency bands, especially f3 to f5, no longer satisfy the quality criteria. This observation favours the hypothesis expounded in section 4.4.2 that shorter scale and higher frequency atmospheric signals tend to become preferentially more organised during periods of optimal coupling with the sea surface. The shift of energy to the higher frequencies and the improved spatial coherence at these frequencies during meteorologically induced seiching events is thus usually accompanied by a general contraction of the circle of spatial coherence at the lower frequency bands.

EVENT 3

Event 3 comprises the period 00:00 GMT 30th November to 00:00 GMT 4th December 1996 with 11520 data points of surface atmospheric pressure at 0.5 minute intervals. During event 3 the sea level oscillations in Mellieha Bay have a range of only 5cm during 30th November, but build up very quickly in the early morning

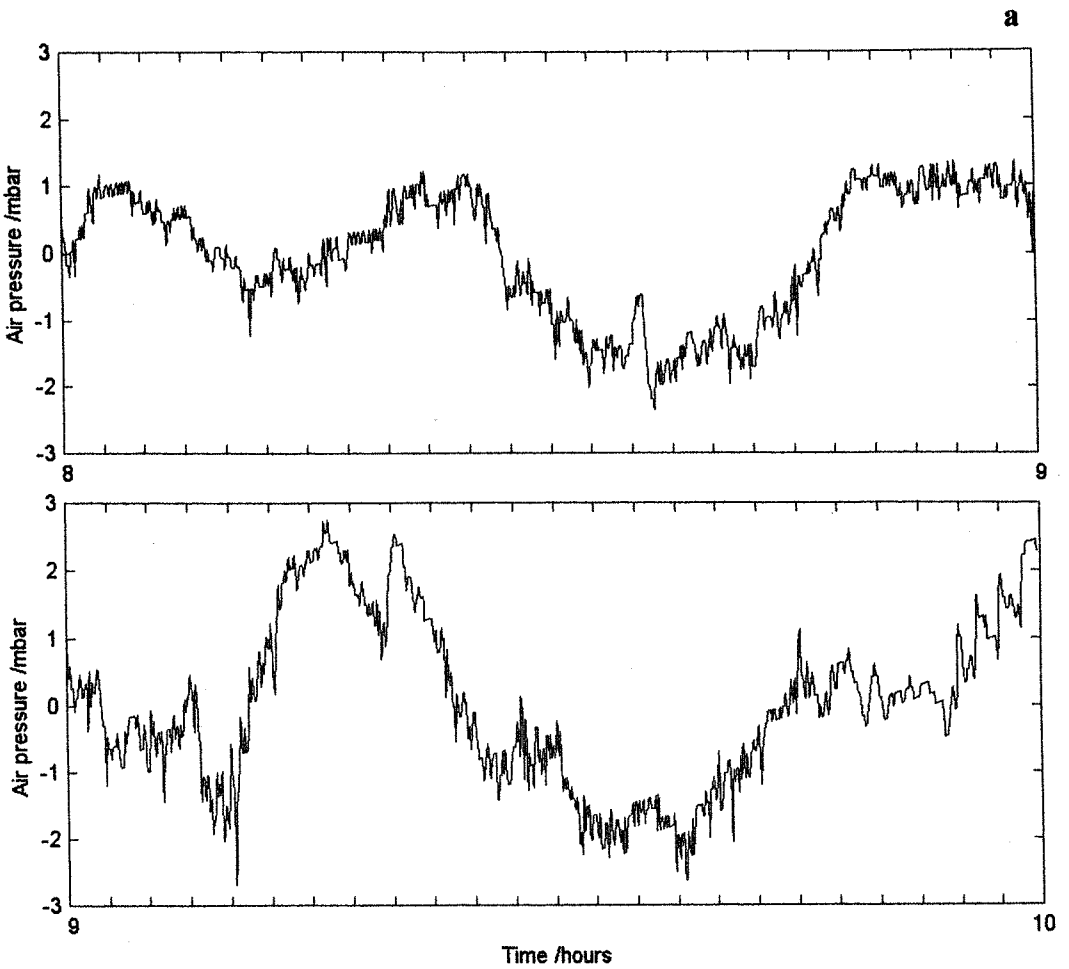

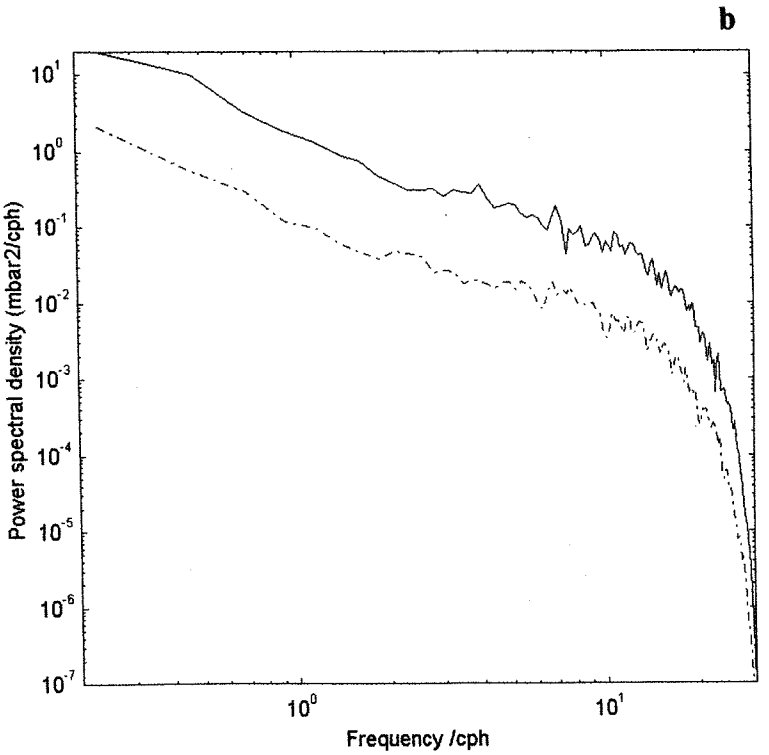

Fig. 4.17 (a) Time series of surface air pressure data at Ramla tal-Bir (8/9 December, 1996);
(b) Power spectral density plot of surface air pressure at Ramla tal-Bir for the period 8/9 December 1996 (solid). The background spectrum for event 5 (dashed) is included for comparison. The 95% confidence factor, for 22 d.o.f. is 4.33 dB ($B_{min} = 0.59$; $B_{max} = 1.6$).

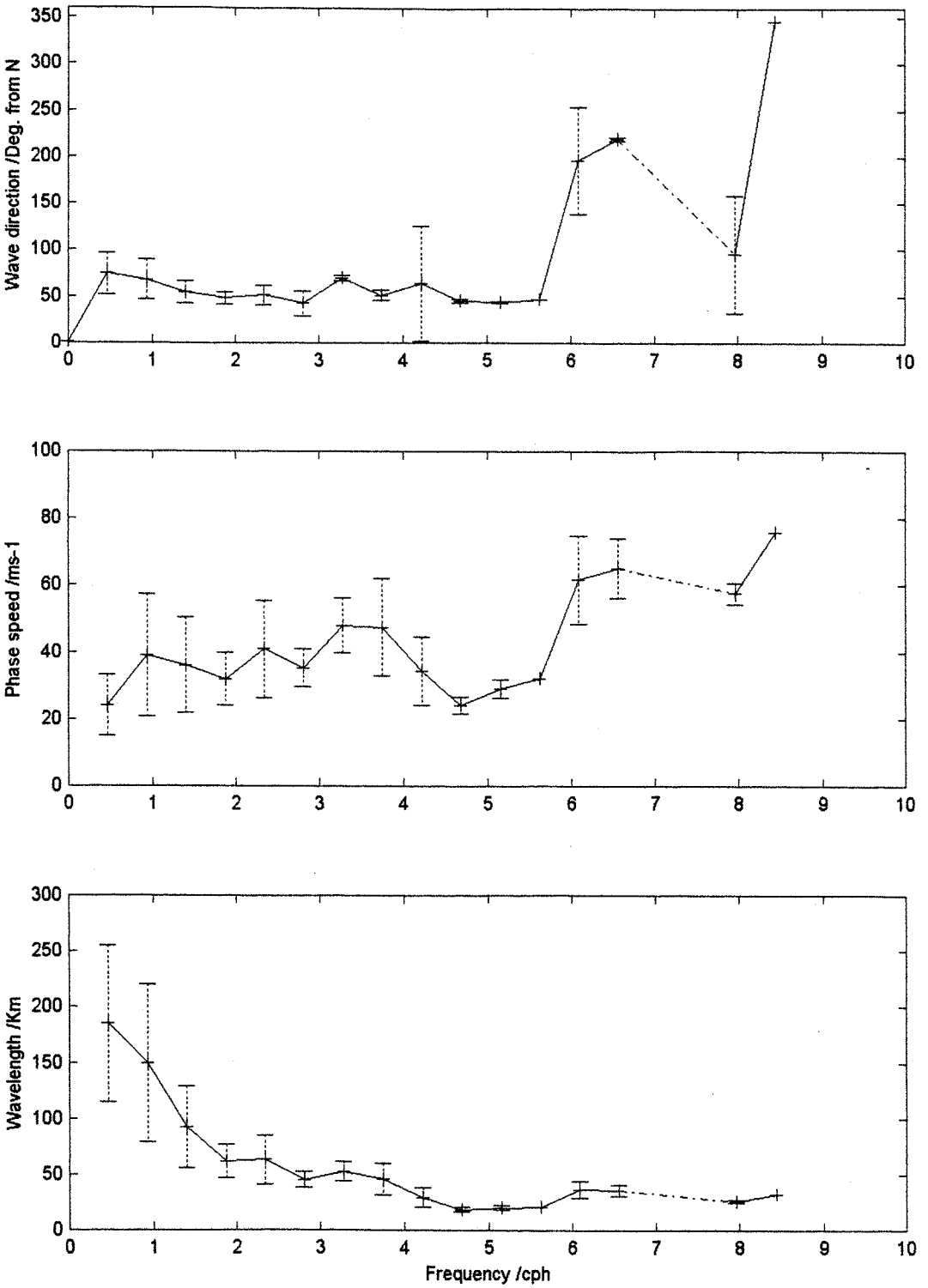

Fig. 4.18 Frequency dependence of (a) direction, (b) phase speed, and (c) wavelength for atmospheric waves during event 4, estimated from observations at Valletta, Attard and Marsaxlokk stations.

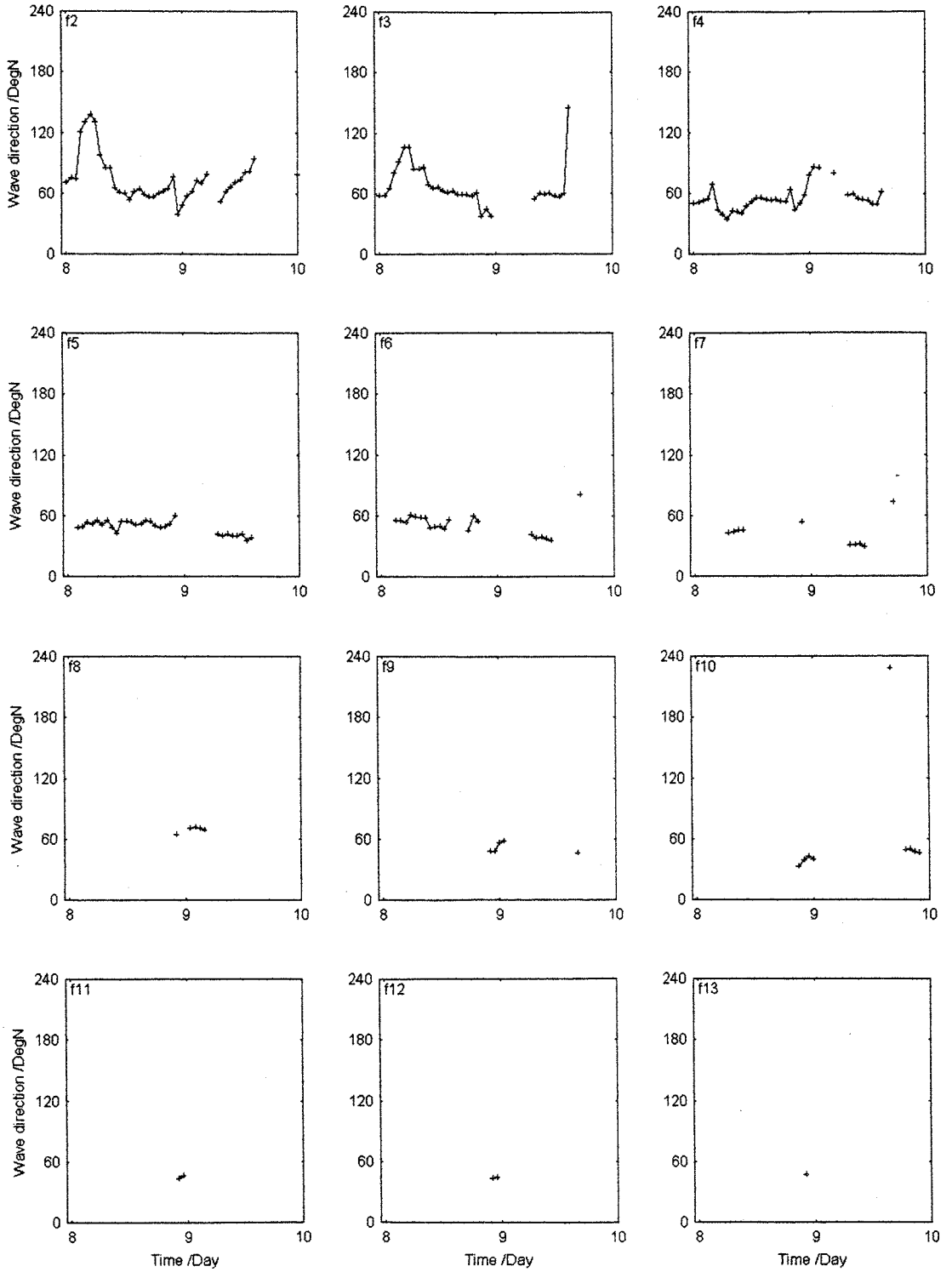

Fig. 4.19 Temporal development of atmospheric wave directions estimated for event 4 at separate frequency bands f2 - f13 from observations at Valletta, Attard and Marsaxlokk stations.

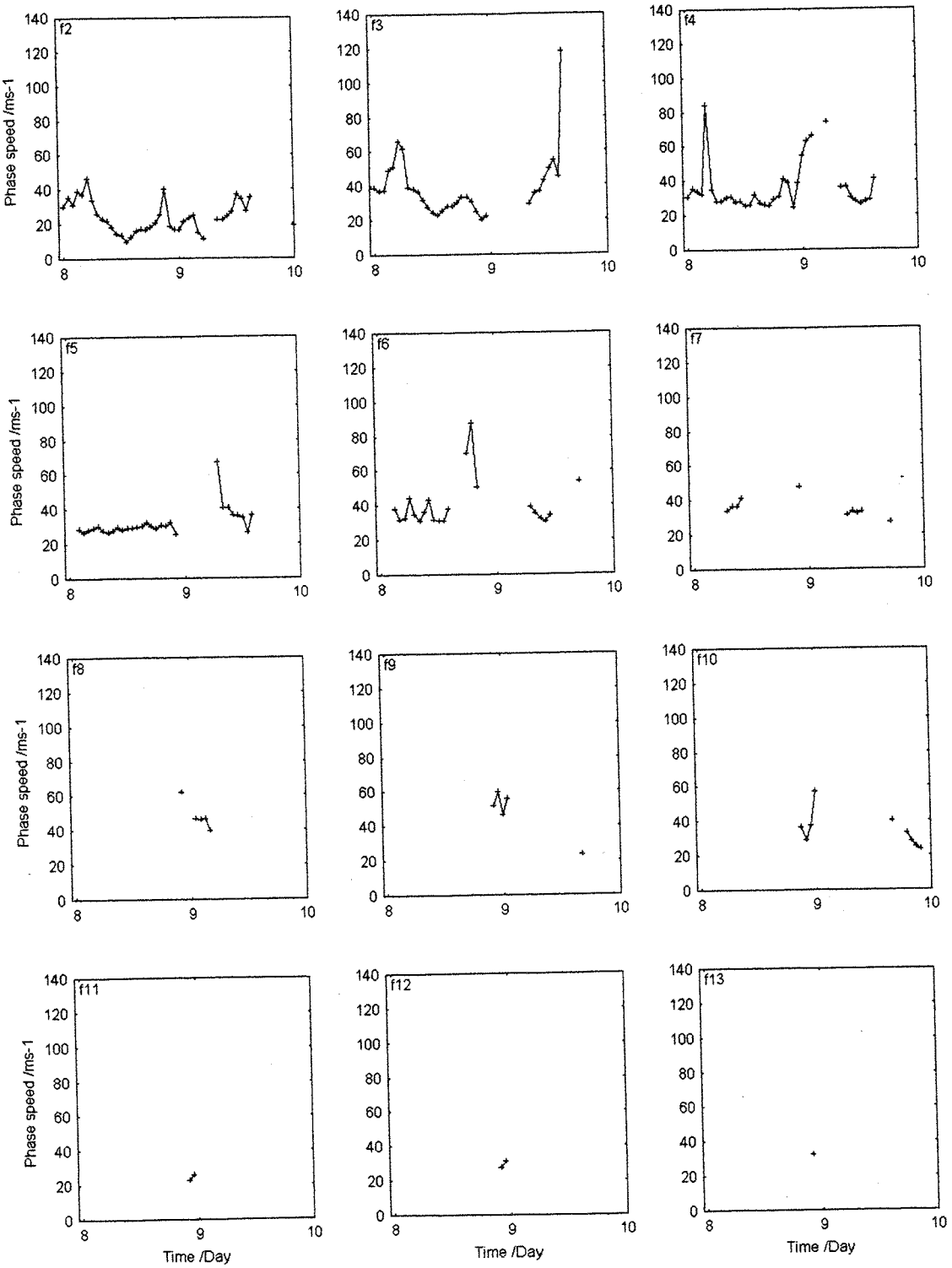

Fig. 4.20 Temporal development of atmospheric wave phase speeds estimated for event 4 at separate frequency bands f2 - f13 from observations at Valletta, Attard and Marsaxlokk stations.

of the 1st of December, reaching to a maximum range of 29cm. The sea level activity is reduced on the 2nd and is considerably attenuated by noon of the 3rd December. In St. George's Bay the sea level oscillations are exceptionally high during this event. The maximum range is 33cm in the afternoon of the 1st December. The variation in sea level activity follows very much the same pattern as in Mellieha Bay, but the strongest fluctuations in St. George's Bay occur somewhat later with respect to Mellieha Bay, during a second intensification period in the afternoon of the 1st December.

Event 3 corresponds to a period in which the meteorological situation is completely different from that of events 1 and 4. A cyclonic circulation travels from the Tyrrhenian into the Adriatic Sea and subsequently further south over Reggio Calabria. The associated strong westerly and northwesterly currents bring down cold and unstable air from over the British Isles, which penetrates into the Central Mediterranean causing bad weather and appreciable precipitation especially during the period between the evening of the 30th of November and the early hours of the 2nd of December. The sea is very rough from the northwest, particularly on the 1st December. The wind strength reaches its maximum in the first hours of the 1st of December and the atmospheric pressure dips by 6mb with a sudden rise at around 3.5h GMT in conjunction to the swift passage of a cold front over the Maltese Islands. A surge in sea elevation is registered at both Mellieha Bay and St. George's Bay during this drop in barometric pressure. The mean sea water level remains anomalously high throughout the subsequent 24 hours, and peaks again (particularly at St. George's Bay) at about 18:00 GMT on 1st December. This behaviour of the sea elevation is not related to an equivalent change in the mean atmospheric pressure recordings, and is probably caused by water run-off draining into the embayments and remaining trapped by the strong wind-induced southeasterly currents in the open sea.

The atmospheric pressure recordings during this event are characteristed by a sensible increase in energy at all frequencies (Fig. 4.21), in particular during the 1st of December which coincides with an intensification of the sea level oscillations. At each frequency band the atmospheric activity is about an order of magnitude higher than background levels. The energy in the frequency range 6 to 10cph is the highest registered from all the five events and could well explain the exceptional seiching in St. George's Bay in the first half of the 1st December. The intensified seiching in St. George's Bay in the afternoon of the same day is however attributed to surf beats (refer to section 4.5.2). The main difference with respect to events 1 and 4 is that the quality controls are fulfilled with some consistency in time only for f2 and f3 during the 30th of November and the first hours of 1st

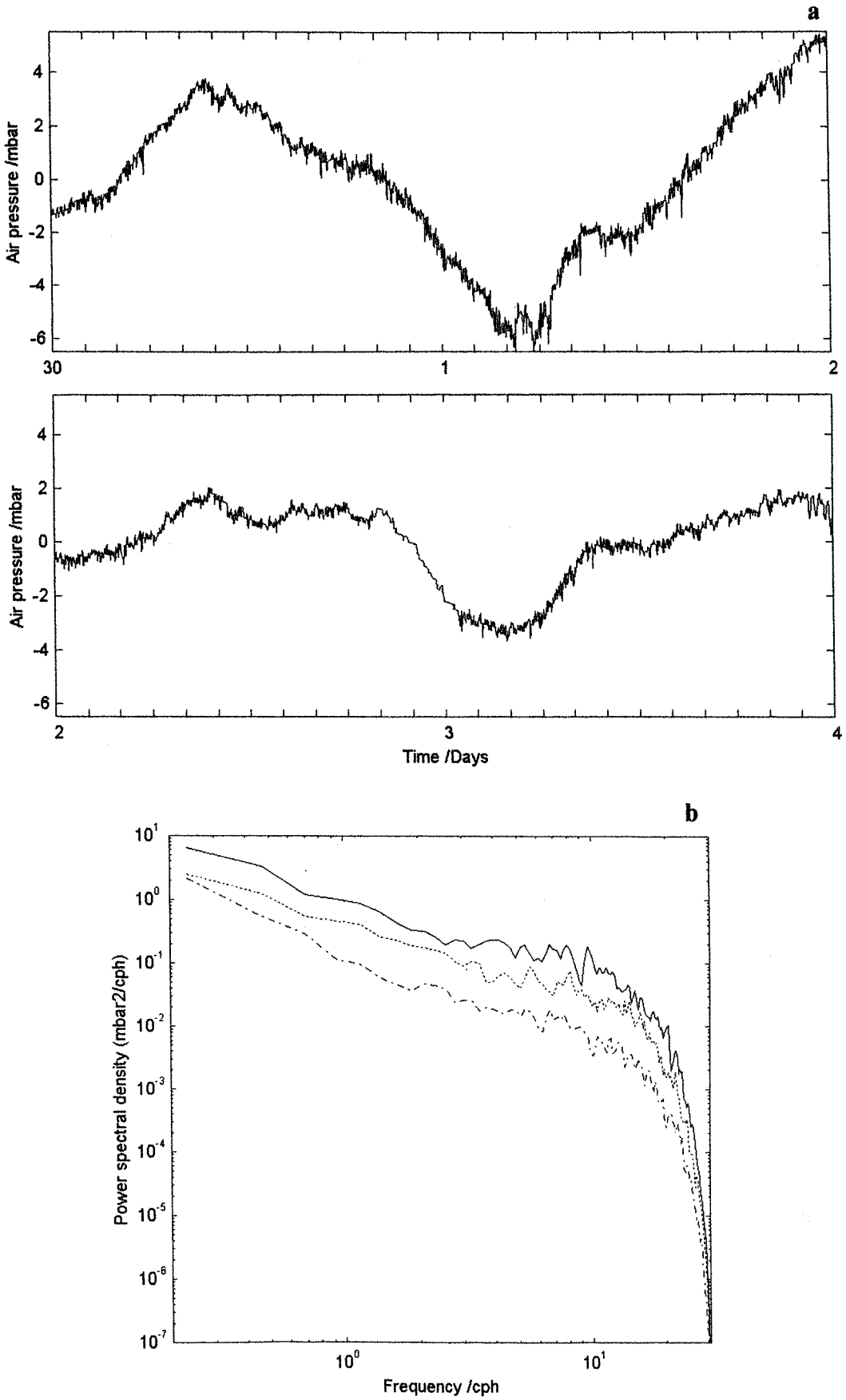

Fig. 4.21 (a) Time series of surface air pressure data at Ramla tal-Bir (30 Nov.-3 Dec., 1996);
(b) Power spectral density plot of surface air pressure at Ramla tal-Bir for the first two days (solid), and remaining two days (dotted). The background spectrum for event 5 (dashed) is included for comparison. The 95% confidence factor, for 22 d.o.f. is 4.33 dB ($B_{min} = 0.59$; $B_{max} = 1.6$).

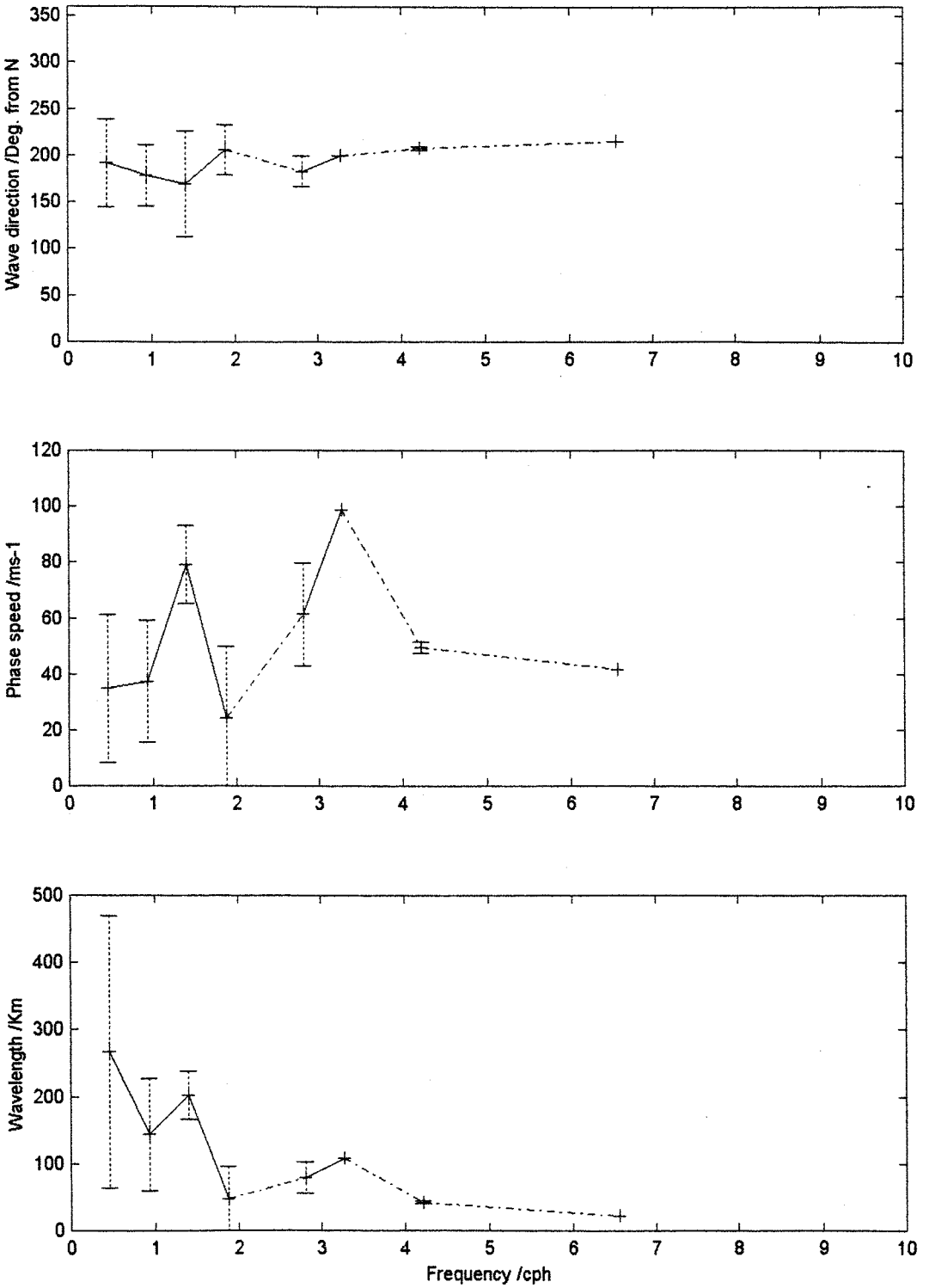

Fig. 4.22 Frequency dependence of (a) direction, (b) phase speed, and (c) wavelength for atmospheric waves during event 3, estimated from observations at Ramla, Valletta and Marsaxlokk stations.

December, and for f2 prior to and after midnight of the 2nd December. In the remaining time intervals separating these data segments, the coherence between the pressure signals is below levels of significance even at these lower frequencies. Unfortunately the air pressure data for this event is available only at Ramla, Valletta and Marsaxlokk stations which are at relatively large distances of separation and in a very close to rectilinear disposition. This can lead to an overestimation of wave speeds especially when the direction of propagation is aligned to the three stations. It is moreover impossible to ascertain the range of spatial coherence pertaining to this event. Fig. 4.22 shows the mean results for wavelength, phase speed and direction of propagation of the atmospheric waves during this event. Even in this case the wavelength clearly decreases with frequency. The mean wave direction is along 200° from north which is different from that of the surface wind. As in the case of event 1, the atmospheric waves again propagate approximately orthogonal to the northern coast of Malta, but the direction is now towards the coast and into the bays.

EVENT 2

Event 2 presents very similar meteorological conditions as those for event 3. The first half of the 26th November is characterised by a strong southwesterly wind. A warm front moves over the Maltese Islands at around 06GMT. This is followed by a front of cold air which reaches the area in the early afternoon. This system of fronts is associated to a cyclone over Southern Italy. A large extent of cloud formation moves from the west ahead of the front, reaching the Central Mediterranean and making the early hours of the afternoon very wet. The passage of the front brings with it a change in the wind direction which turns into northwesterly. This surface wind blows strongly with peaks of 15 ms^{-1} and is sustained by the contrasting low over eastern Europe and the high over the Atlantic and northwest Africa. The wind continues to blow from the same direction but gradually attenuates starting from noon of the 27th November. The surface pressure recordings at Ramla station (Fig. 4.23a) have again a relatively high variance with pressure fluctuations occurring mainly in the time interval from late evening of the 26th to noon of the 27th November. The higher frequency signals again have a wide band spectrum (Fig. 4.23b) and the same intensity as in the case of events 1, 3 and 4; the major difference is that they are considerably attenuated or disappear completely at the Valletta and Marsaxlokk stations. The energy of the surface pressure at these two latter stations is more than an order of magnitude smaller (Fig. 4.24). Consequently the wave parameter estimates qualify the quality criteria only at a few subsections (Table 4.4), mainly in the two lower frequency bands and restricted to the first hours of the 26th November (Fig. 4.25). This lack of coherence explains the reduced response of the sea surface which has a

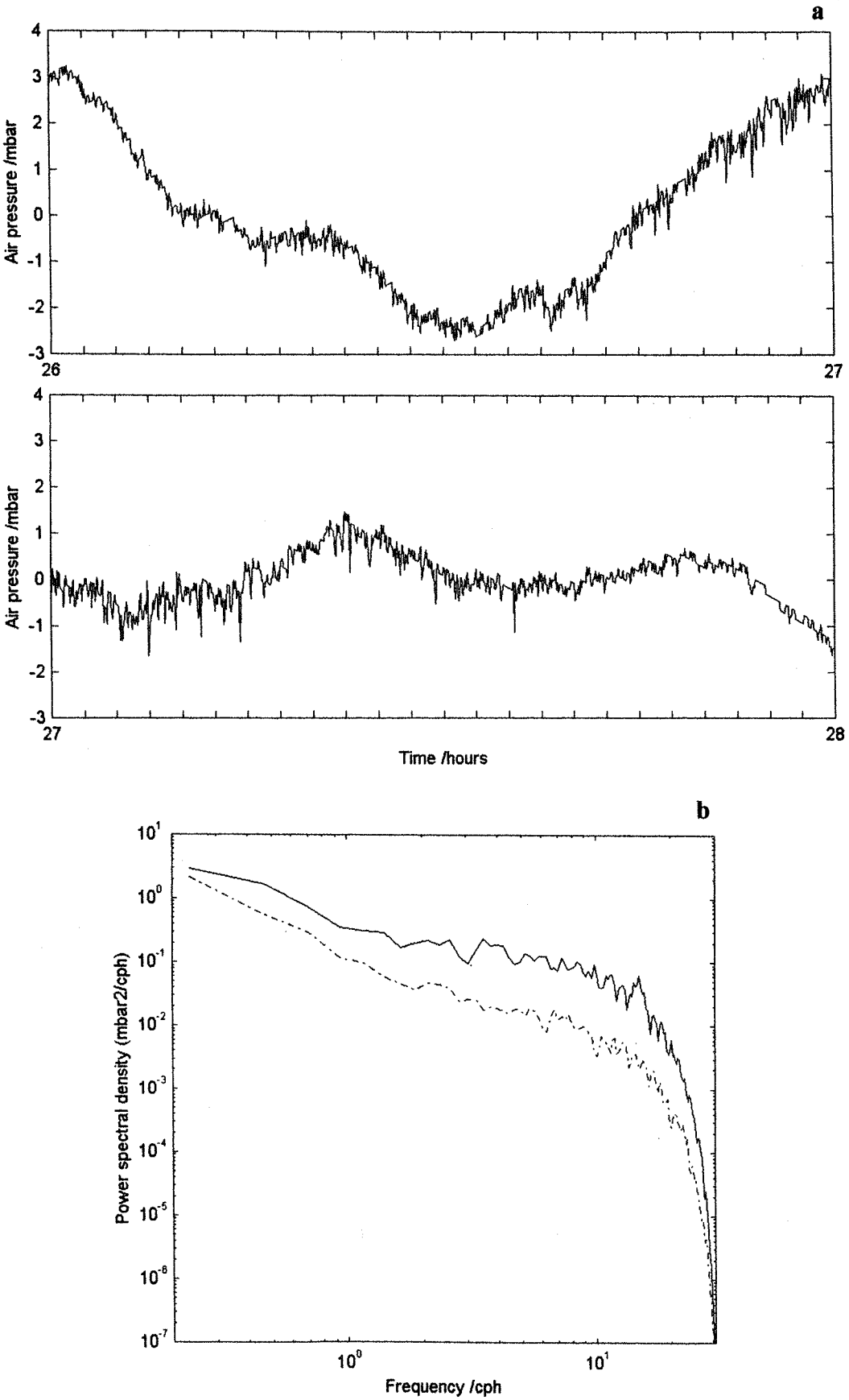

Fig. 4.23 (a) Time series of surface air pressure data at Ramla tal-Bir (26/27 November, 1996); (b) Power spectral density plot of surface air pressure at Ramla tal-Bir for the two days (solid). The background spectrum for event 5 (dashed) is included for comparison. The 95% confidence factor, for 22 d.o.f. is 4.33 dB ($B_{min} = 0.59$; $B_{max} = 1.6$).

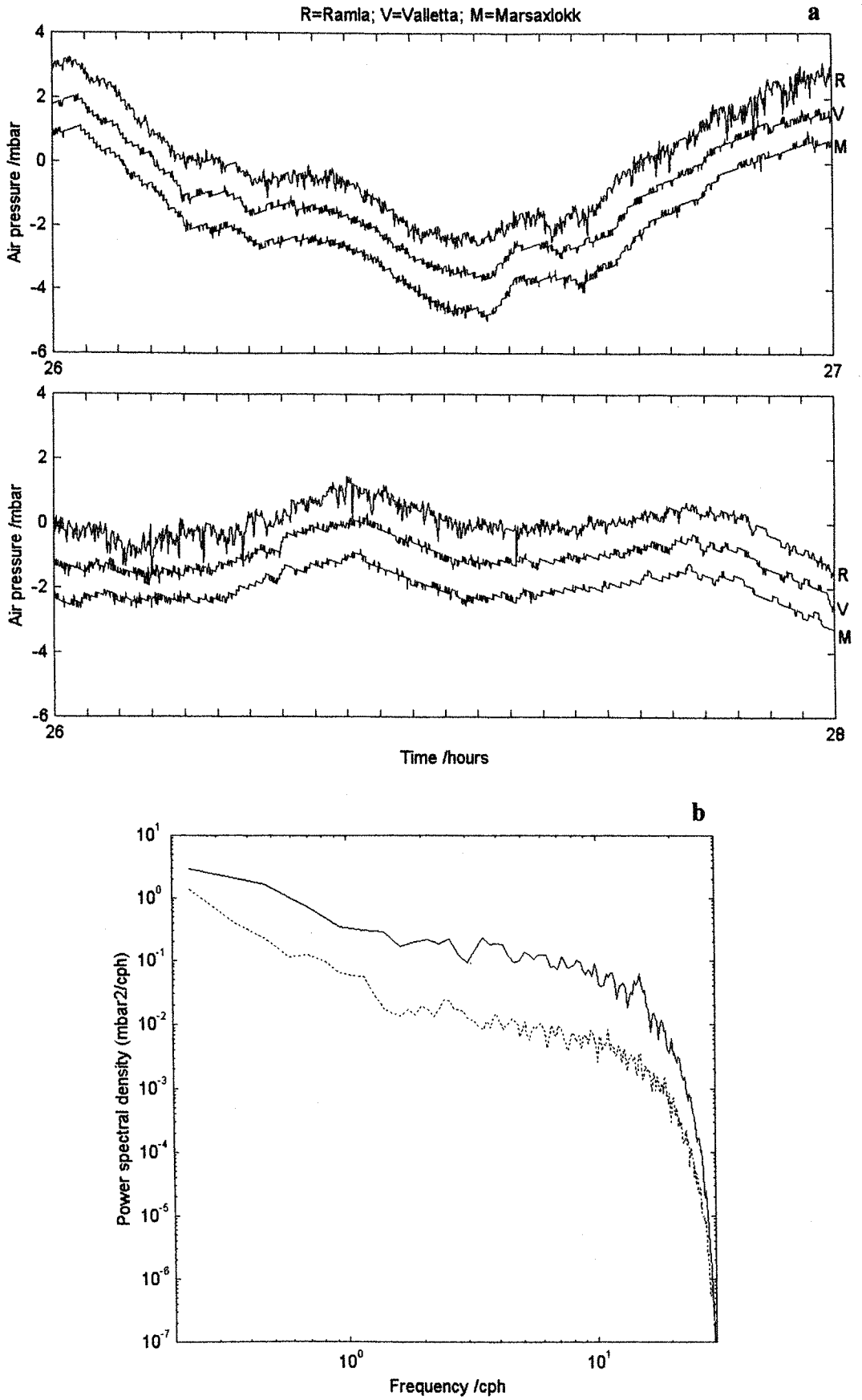

Fig. 4.24 (a) Comparative time series of surface air pressure at Ramla tal-Bir (R), Valletta (V) and Marsaxlokk (M) stations (26/27 November, 1996); plots are displaced for better visualisation. (b) Power spectral density plot of surface air pressure at Ramla tal-Bir (solid) and Valletta (dotted) for the same two days. The 95% confidence factor, for 22 d.o.f. is 4.33 dB ($B_{min} = 0.59$; $B_{max} = 1.6$).

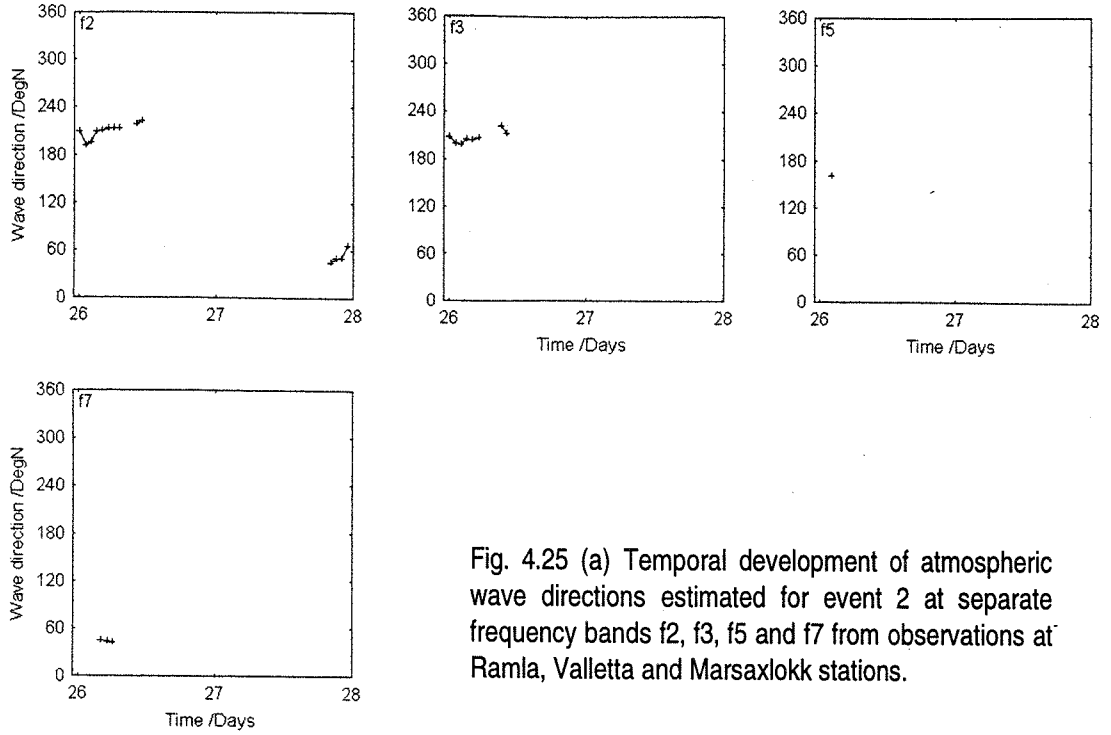

Fig. 4.25 (a) Temporal development of atmospheric wave directions estimated for event 2 at separate frequency bands f2, f3, f5 and f7 from observations at Ramla, Valletta and Marsaxlokk stations.

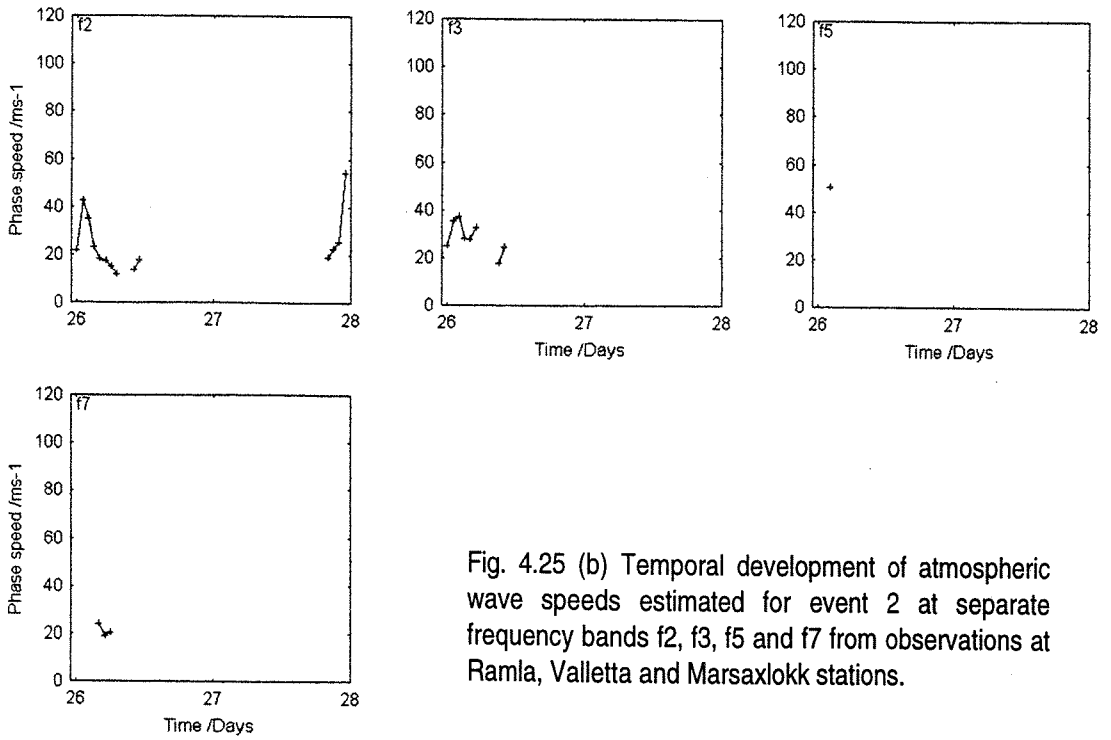

Fig. 4.25 (b) Temporal development of atmospheric wave speeds estimated for event 2 at separate frequency bands f2, f3, f5 and f7 from observations at Ramla, Valletta and Marsaxlokk stations.

much lower variance compared to events 1, 3 and 4. Referring to Fig. 4.4, the sea level variance in Mellieha Bay for event 2 is considerably lower than that for event 1, even though the surface pressure variance for the two events has the same order of magnitude. This event is interesting in that it portrays a situation in which the area of coherence of atmospheric activity is centred to the west of the island and reaches only marginally the station array. The sea level oscillations in this case thus result from a non-local response of the sea surface to atmospheric gravity waves and are, to a greater extent, related to the incidence of long period waves of a more distant origin.

EVENT 5

Event 5 covers the period 00:00 GMT 22nd November to 00:00 GMT 24th November 1996 and is chosen as

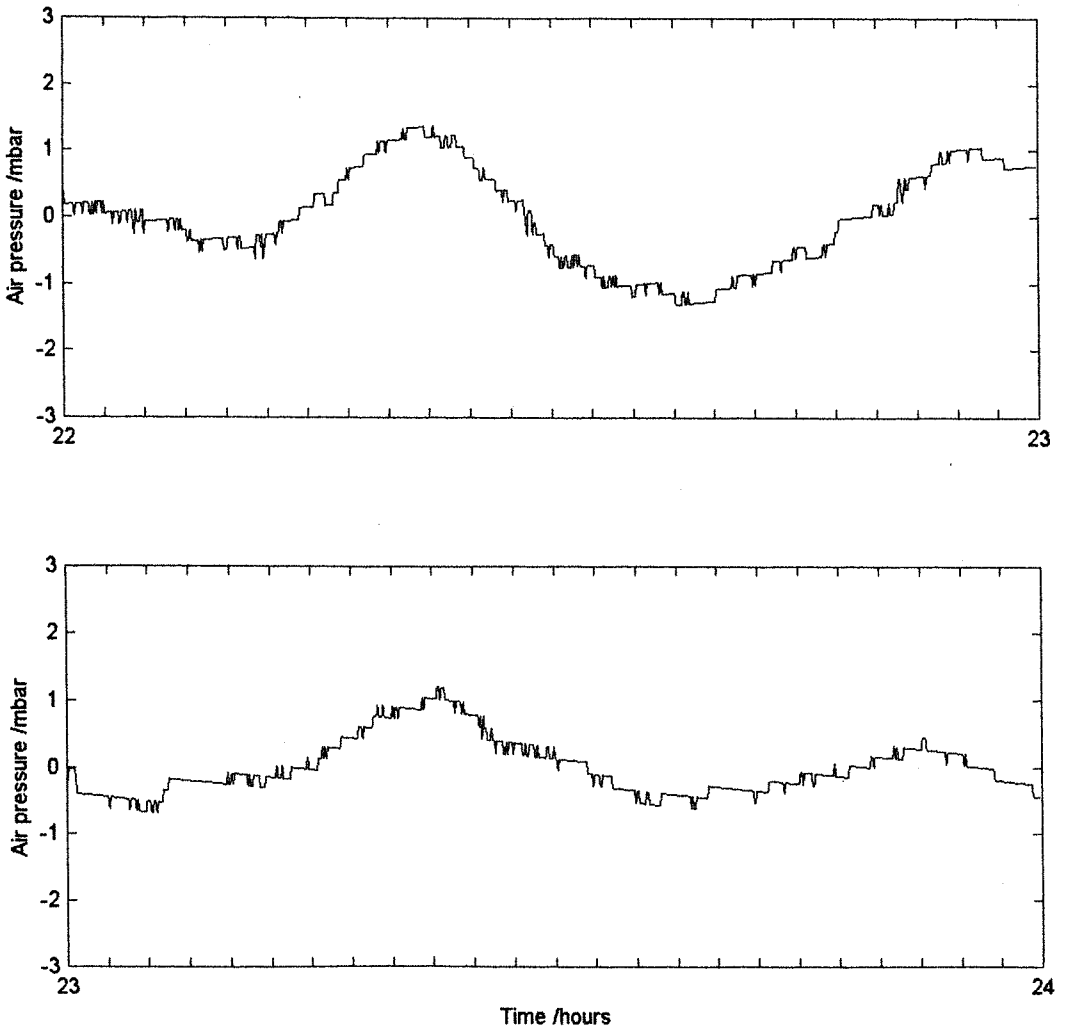

Fig. 4.26 Time series of surface air pressure data at Ramla tal-Bir (22/23 November, 1996).

an example of a period with very low sea level variance at both Mellieha Bay and St. George's Bay. The range of the sea oscillations during these two days is considered to represent the background levels. The synoptic situation is very different from the other events and is characterised by a high pressure over North Africa, which maintains fine and hot weather over the Central Mediterranean area with a moderate to weak westerly to southwesterly current. Compared to the other events, the surface pressure time series is very smooth (Fig. 4.26) and the spectral energy at all the frequency bands is the lowest registered during the whole period of measurements. This spectrum is superimposed for comparison on the surface pressure spectral plots for events 1, 2, 3 and 4 (Figs. 4.12, 4.17, 4.21 and 4.23). As expected, in the estimation of the atmospheric wave parameters from half-minute observations during the two days the quality criteria are satisfied only for the two lower frequency bands. This analysis confirms that at least for the events considered in this study, the presence of high frequency and spatially coherent pressure fluctuations in the atmosphere are essential for the occurrence of large amplitude sea level oscillations in the coastal area of the Maltese Islands. The fact that during background seiching the spatial coherence at the low frequencies f2 and f3 is often significant implies that the background signal is related to these frequencies. It may also be related to long period waves originating from a non-local remote site or from long period energy residing on the continental shelf.

4.4.3.5 Relation to the synoptic setting

The results presented in the previous section confirm the relation, observed on several other occasions, between mesoscale atmospheric gravity waves and the high frequency sea level oscillations. It is also possible to identify the most common synoptic-scale settings which favour the occurrence of these atmospheric waves, and to hypothesise on the most probable generation mechanisms.

The synoptic situation associated with events 1 and 4 typifies the most common meteorological conditions that can sustain atmospheric waves. This is presented in Fig. 4.27 which gives the surface and upper air synoptic analysis during event 4 at 12GMT on 9th December 1996. The situation during event 1 is similar. These conditions are also similar to those reported by Ramis & Jansa (1983) and Monserrat et al. (1991) during periods of atmospheric wave activity over the Balearic Islands.

At the surface a cyclonic circulation over the Western Mediterranean and Northwest African coast contrasts with a high pressure over eastern Europe. A moderate pressure gradient exists over the Central Mediterranean and the surface wind is weak to moderate from the east or southeast. At 850mb the baroclinicity over the Central Mediterranean is high with appreciable temperature gradients. This results from the interaction of a

warm and dry air tongue that comes up over the Gulf of Sirte by warm advection from the African mainland, often carrying suspended Saharian dust, with an underlying cooler and more humid air from the west. The two air masses are separated by a temperature inversion near the surface. At higher levels the cyclonic circulation is centred further south over Algeria while a ridge is situated over the Ionian Sea and the southern part of Italy. The vertical structure in the lower troposphere is accompanied by a strong wind shear which veers from a southeasterly current below the inversion to a strong southwesterly flow above it. This wind shear coincides to a layer of small Richardson number at around 800mb. The upper air southwesterly flow over the Central Mediterranean is maintained throughout the troposphere. At 500mb it reaches values of 55 and 45 knots at Tunis and Tripoli respectively. At 300mb the flow reaches 85 knots and is aligned to the jet stream. The radiosonde upper air profile available at Tripoli during event 4 (Fig. 4.28) confirms these chacteristics. The station in Tripoli is probably the most representative of the situation over the Maltese Islands. The temperature inversion is in fact less pronounced in Tunis and disappears at Trapani. These two stations must be outside the region of atmospheric wave generation. Unfortunately the upper air data in the region are very irregular and no radiosonde measurements are undertaken in Malta or on the southern Sicilian coast. It is thus impossible to make a detailed analysis of the upper air profiles.

The main characteristics of the atmosphere's vertical structure are however sufficiently apparent. During events 1 and 4 they are consistent with what Gedzelman & Rilling (1978) propose as being the most favourable for the occurrence of atmospheric gravity waves in the lower troposphere. Basically the conditions consist of a layer with stable stratification (i.e. higher potential-temperature gradients associated to a temperature inversion) close to the surface, an overlying layer with weak static stability (i.e. low Richardson number) and strong wind shear, together with an almost adiabatic middle troposphere. These atmospheric conditions (i) support a gravity wave source mechanism by vertical shear instability (e.g. Kelvin-Helmholtz instability) as suggested by Uccellini & Koch (1986), and (ii) at the same time permit the waves to be ducted over considerable distances away from their original starting points by the trapping of energy between the surface and the inversion (Lindzen & Tung, 1976). It is interesting to note that although the favourable upper air conditions to gravity wave generation may not necessarily be identical to those which are ideal for wave ducting, the need for a level with a small Richardson number is a common factor for both. A Richardson number less than 0.25 in fact provides the essential reflecting property at the top of the wave ducting layer for an effective propagation of the pressure wave. In other publications dealing with atmospheric waves generated by dynamic instability of the wind profile

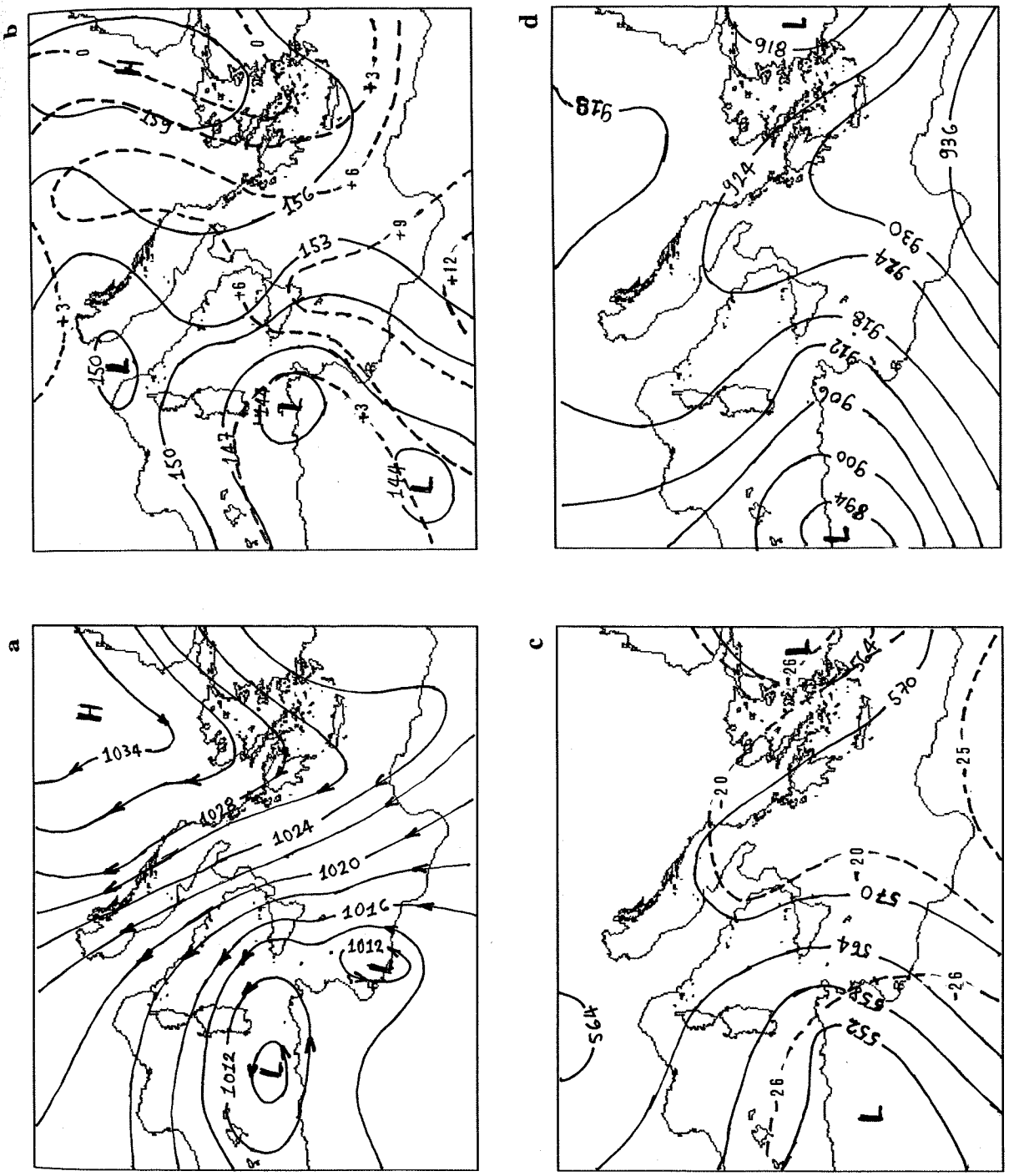

Fig. 4.27 Synoptic analysis at 1200GMT on 9th December, 1996 at (a) surface, (b) 850mb, (c) 500mb and (d) 300mb. Solid curves in (b - d) are contours of geopotential height. Dashed curves in (b) and (c) are isotherms in °C. (Reproduced from charts by the Meteorological Office in Luqa, Malta).

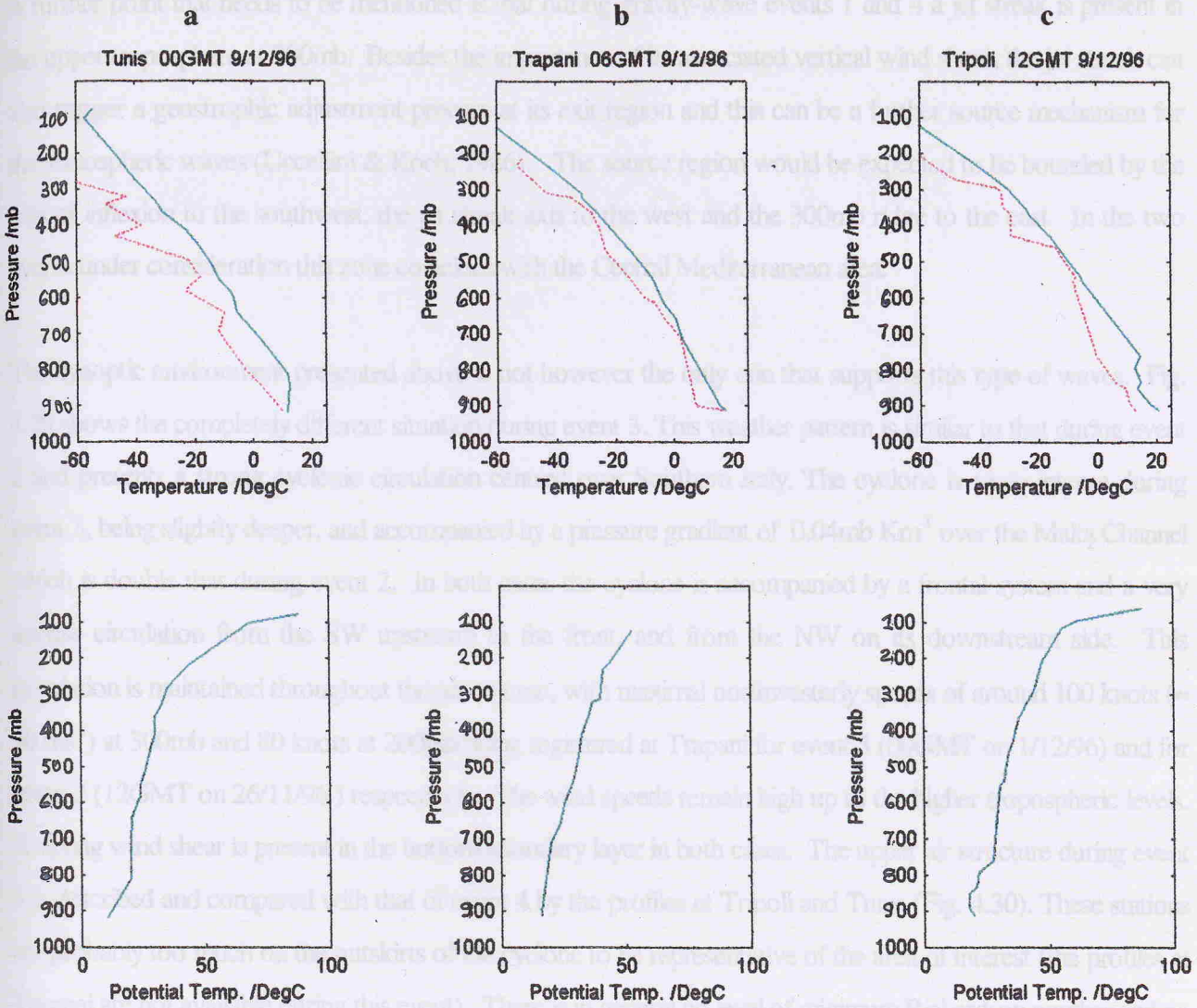

Fig. 4.28 Radiosonde upper air profiles during event 4 taken at (a) Tunis (00GMT); (b) Trapani (06GMT); and (c) Tripoli (12GMT) on 9th December 1996.

(Keliher, 1975; Gedzelman & Rilling, 1978; Stobie et al., 1983; Monserrat & Thorpe, 1991) the wave speeds and direction are found to match with those of the wind at the level of minimum Richardson number. Waves are also non-dispersive. The results for events 1 and 4 presented in section 4.4.3.4 confirm that this is also applicable to Malta. The observed pressure waves have directions along ENE (± 15°), and are thus in alignment to the upper level wind; their phase speed is also practically identical at all frequency bands. The only argument against dynamic stability seems to the broad spectrum of the observed waves.

A further point that needs to be mentioned is that during gravity-wave events 1 and 4 a jet streak is present in the upper troposphere at 300mb. Besides the importance of its associated vertical wind shear, the jet streak can also trigger a geostrophic adjustment process at its exit region and this can be a further source mechanism for the atmospheric waves (Uccellini & Koch, 1986). The source region would be expected to be bounded by the axis of inflexion to the southwest, the jet streak axis to the west and the 300mb ridge to the east. In the two events under consideration this zone coincides with the Central Mediterranean area.

The synoptic environment presented above is not however the only one that supports this type of waves. Fig. 4.29 shows the completely different situation during event 3. This weather pattern is similar to that during event 2 and presents a strong cyclonic circulation centred over Southern Italy. The cyclone is more intense during event 3, being slightly deeper, and accompanied by a pressure gradient of 0.04mb Km^{-1} over the Malta Channel which is double that during event 2. In both cases the cyclone is accompanied by a frontal system and a very intense circulation from the SW upstream to the front, and from the NW on its downstream side. This circulation is maintained throughout the air column, with maximal northwesterly speeds of around 100 knots ($\approx$ 50 ms^{-1}) at 300mb and 80 knots at 200mb being registered at Trapani for event 3 (00GMT on 1/12/96) and for event 2 (12GMT on 26/11/96) respectively. The wind speeds remain high up to the higher tropospheric levels. A strong wind shear is present in the bottom boundary layer in both cases. The upper air structure during event 3 is described and compared with that of event 4 by the profiles at Tripoli and Tunis (Fig. 4.30). These stations are probably too much on the outskirts of the cyclone to be representative of the area of interest (the profiles at Trapani are not available during this event). There is in general no level of minimum Richardson number and no significant inversion layer at these two stations.

The main difference between the two events is in the front speed V as it sweeps from west to east along the Malta Channel. From an estimation based on the sequence of synoptic charts it is found that V $\approx$ 60Kmh^{-1} (= 17ms^{-1}) for event 3 whereas V $\approx$ 40Kmh^{-1} (= 11ms^{-1}) for event 2. This difference has an important bearing on the response of the shelf to the passage of the front. If an exponential profile $h(x) = H \exp\left\{\frac{2a}{L}(x - L)\right\}$ is assumed for the Siculo-Maltese shelf area, where x signifies cross-shelf distance, L ($\approx$ 100Km) is the shelf width, H ($\approx$ 500m) is the deep ocean depth, and a is a constant related to the depth h_o at the coast ($\exp(2a) = H / h_o \approx 25$), then following Viera & Buchwald (1982) the pressure front should trigger a wake

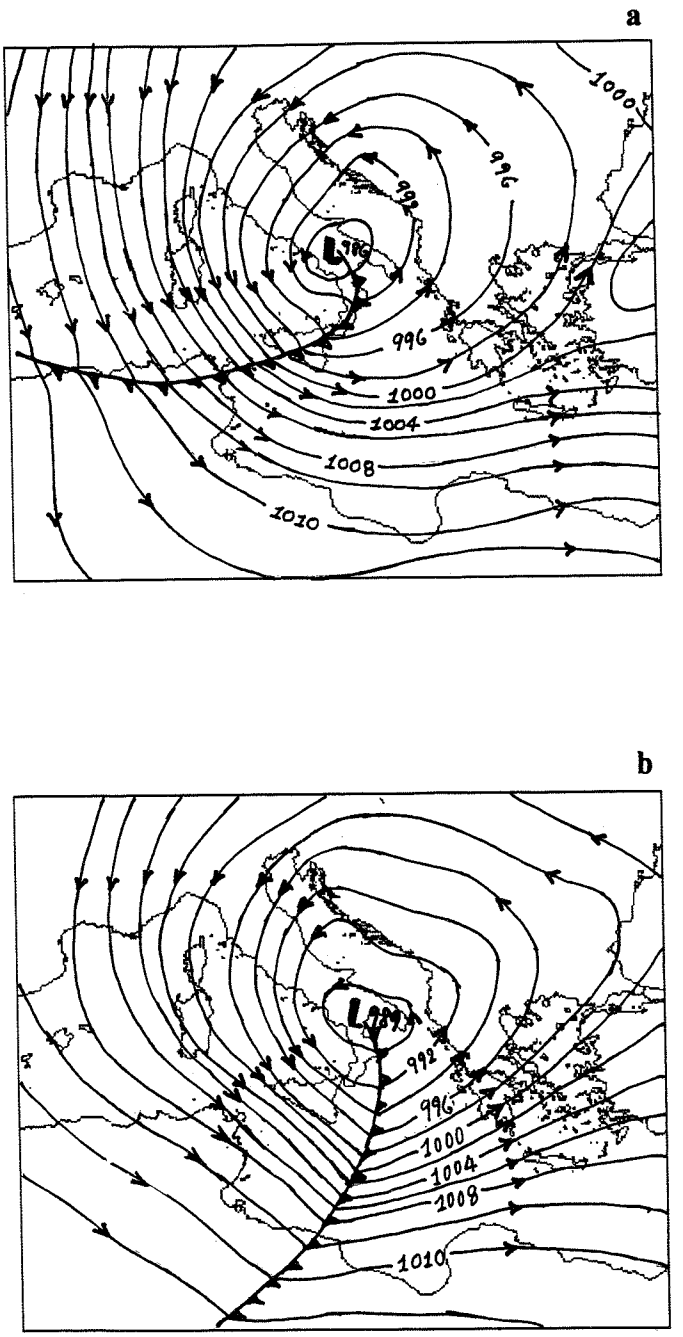

Fig. 4.29 Surface synoptic analysis at 00GMT and 06GMT on 1st December, 1996. (Reproduced from charts by the Meteorological Office in Luqa, Malta).

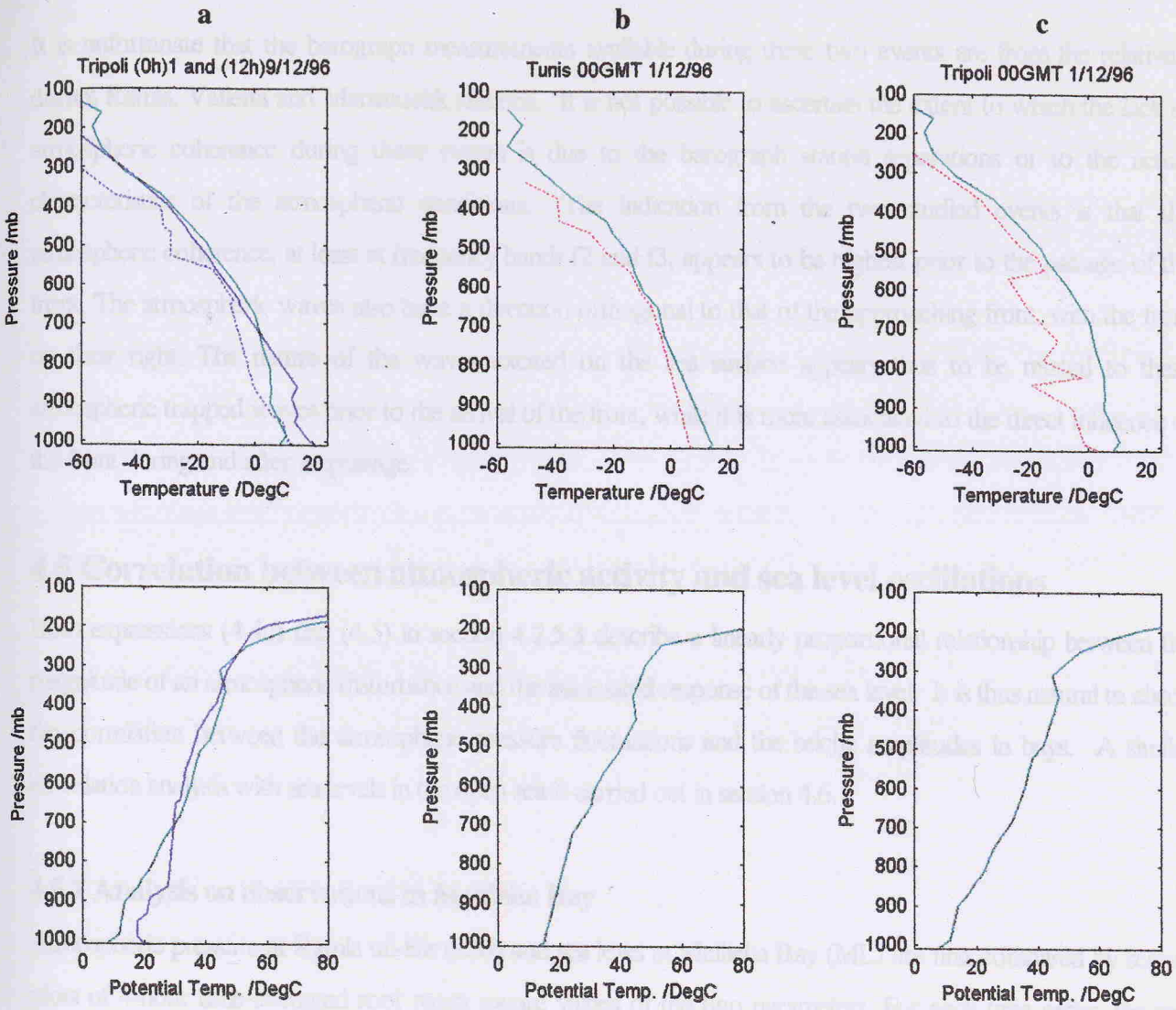

Fig. 4.30 Radiosonde upper profiles during event 3 taken at (b) Tunis (00GMT) and (c) Tripoli (00GMT) on 1st December 1996. In (a) the profiles at Tripoli during event 3 (in green) are compared with those during event 4 (in blue).

of comparatively large edge waves behind it provided that $\exp(-a) \leq \frac{V}{\sqrt{gH}} \leq 1$ (refer section 4.2.5.4). The upper limit on V is around $70ms^{-1}$ which is very fast for a pressure front. The lower limit in this case is $14ms^{-1}$ which means that while the front speed was within limits during event 3, it was not during event 2. This may explain the much lower sea level activity registered during event 2.

It is unfortunate that the barograph measurements available during these two events are from the relatively distant Ramla, Valletta and Marsaxlokk stations. It is not possible to ascertain the extent to which the lack of atmospheric coherence during these events is due to the barograph station separations or to the actual characteristics of the atmospheric conditions. The indication from the two studied events is that the atmospheric coherence, at least at frequency bands f2 and f3, appears to be highest prior to the passage of the front. The atmospheric waves also have a direction orthogonal to that of the approaching front, with the front on their right. The nature of the waves excited on the sea surface appears thus to be related to these atmospheric trapped waves prior to the arrival of the front, while it is more associated to the direct influence of the front during and after its passage.

4.5 Correlation between atmospheric activity and sea level oscillations

Both expressions (4.4c) and (4.5) in section 4.2.5.3 describe a linearly proportional relationship between the magnitude of an atmospheric disturbance and the associated response of the sea level. It is thus natural to check the correlation between the atmospheric pressure fluctuations and the seiche amplitudes in bays. A similar correlation analysis with sea levels in the open sea is carried out in section 4.6.

4.5.1 Analysis on observations in Mellieha Bay

Atmospheric pressure at Ramla tal-Bir (RM) and sea level at Mellieha Bay (ML) are first compared by scatter plots of 4-hour time-averaged root mean square values of the two parameters. For each time series, the rms values are computed over 4-hour detrended and overlapping segments with a 2-hour shift. These rms values are calculated for the whole measurement period (27th October to 17th December 1996). The scatter plots in Fig. 4.31 are for the whole 53 day period in (a), for the first 18days when seiche activity is low and close to background values in (b), and for the rest of the period (14th November to 16th December) characterised by a succession of seiching events in (c). Scatter plots for the separate seiching events 1, 3 and 4 are compared in Fig. 4.31(d - e). The spread of the points in these plots shows that the correlation between the atmospheric pressure fluctuations and the sea level oscillations in the bay is not a simple one. The overall correlation estimate $r_{(RM\text{-}ML)}$ of 0.57 is significant but not very high. Indeed a higher correlation between seiche intensity and atmospheric pressure would be expected in the case of a linear response of the bay to atmospheric pressure. The correlation estimate tends to be higher during intensified seiching events with values of 0.71 and 0.62 for

events 3 and 4 respectively; it is however only 0.42 for event 1. This implies that the amplitudes of the seiches must be related to other atmospheric wave parameters besides intensity (such as direction of propagation relative to the coastline, spectral content and spatial coherence). Low correlation values can however also result from the fact that other generation mechanisms besides that related to atmospheric pressure waves could be in action.

The correlation is insignificant ($r_{(RM-ML)} < 0.1$) during the weak seiching period (Fig. 4.31b). This confirms that background seiching is not directly related to the local atmospheric pressure field, but is to a greater extent driven by long waves incident from a distant source. This does not however exclude the importance of other factors which can also contibute on a more localised scale, such as the wind through its direct forcing effects on the sea surface during gusts, or indirectly by the wind induced sea gravity waves. The regression estimates ($3.5 \leq \sigma_{ML(cm)}/\sigma_{RM(mbar)} \leq 39$) for the whole period of observation (a) between the two parameters also establish the range of scatter of the points, and provide the upper and lower bounds of the relative rms magnitudes of sea level oscillations (in cm) in the bay with corresponding rms pressure fluctuations (in mb). Stronger atmospheric disturbances tend to generate larger sea level oscillations. With respect to the 'quieter' period (b), the maximum density of scatter points during the seiching period (c) is also centred on higher rms values of both pressure and sea level. There is however a tendency for the rms sea level amplitudes to become saturated at the larger rms amplitudes of pressure (Fig. 4.31c).

There are also differences in the relationship between the two parameters from one seiching event to another (Fig. 4.31(d - f)). Event 1 is characterised by a higher ratio of sea level/pressure rms magnitudes so that pressure fluctuations tend to produce larger sea level amplitudes with respect to events 3 and 4. The correlation estimate during event 1 is however weaker and the spread of the scatter points is higher. In section 4.5.3 it is shown that for this event the pressure energy from frequencies higher than band f6 is also particularly low and in fact lower than that in any of the other events 2,3 and 4. The atmospheric activity during this event is however maintained over a longer period of approximately 6 days. This factor together with the favourable direction of propagation of atmospheric waves along 80° on average could make up for the lower atmospheric pressure energies. The correlation is highest in the case of event 3 for which $r_{(RM-ML)} = 0.71$ and the linear fit $\sigma_{ML} = 7.55\sigma_{RM} + 0.99$ can be applied. The correlation estimate restricted to 1st December reaches 0.860 with a linear fit described by $\sigma_{ML} = 7.26\sigma_{RM} + 1.82$.

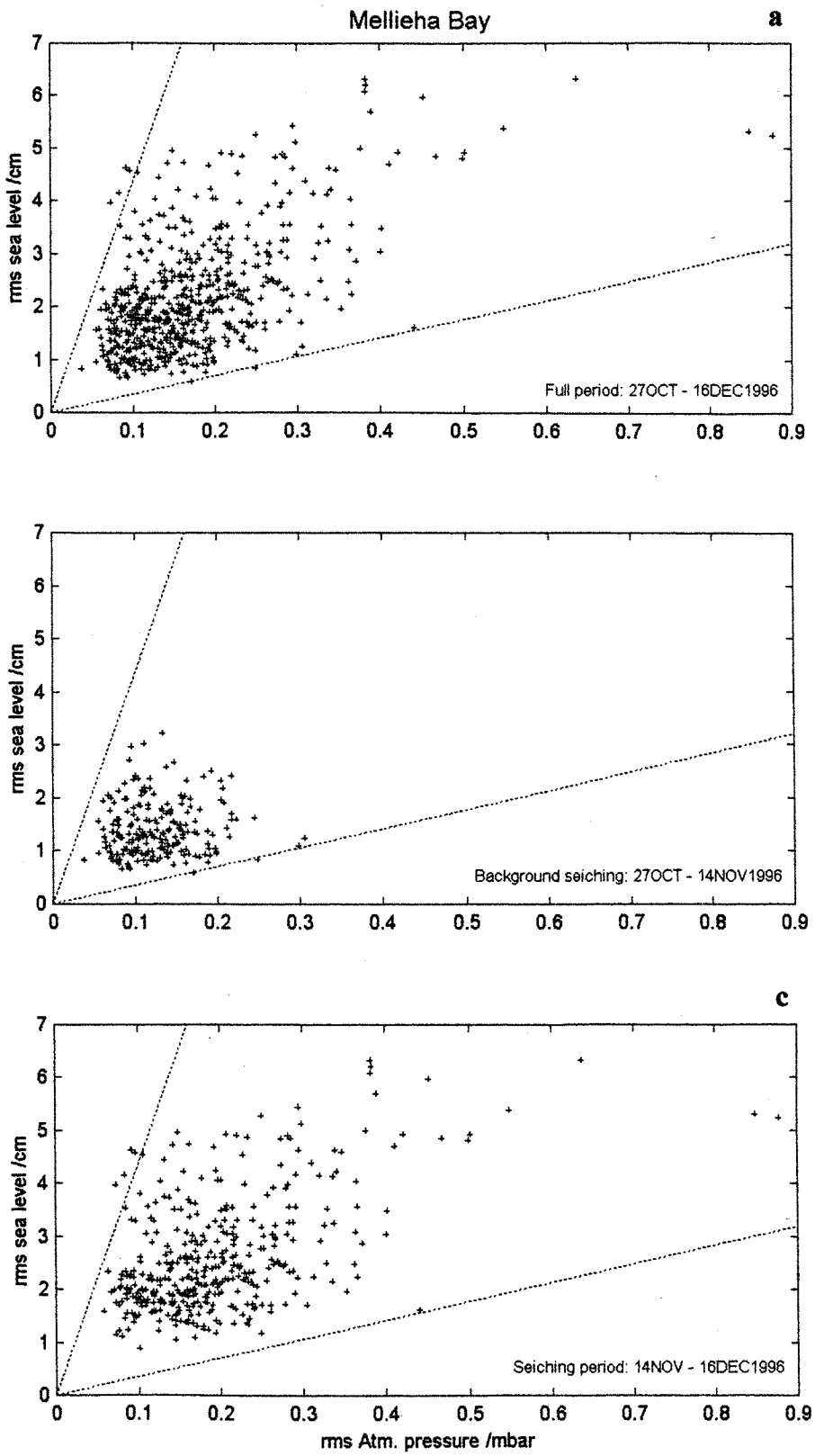

Fig. 4.31 Scatter plots between rms sea level (cm) in Mellieha Bay and rms atmospheric pressure (mb) at Ramla tal-Bir (a) for the period 27/10/96 - 16/12/96, and for data segments referring to a period of background seiching (b), a period of moderate seiching (c).

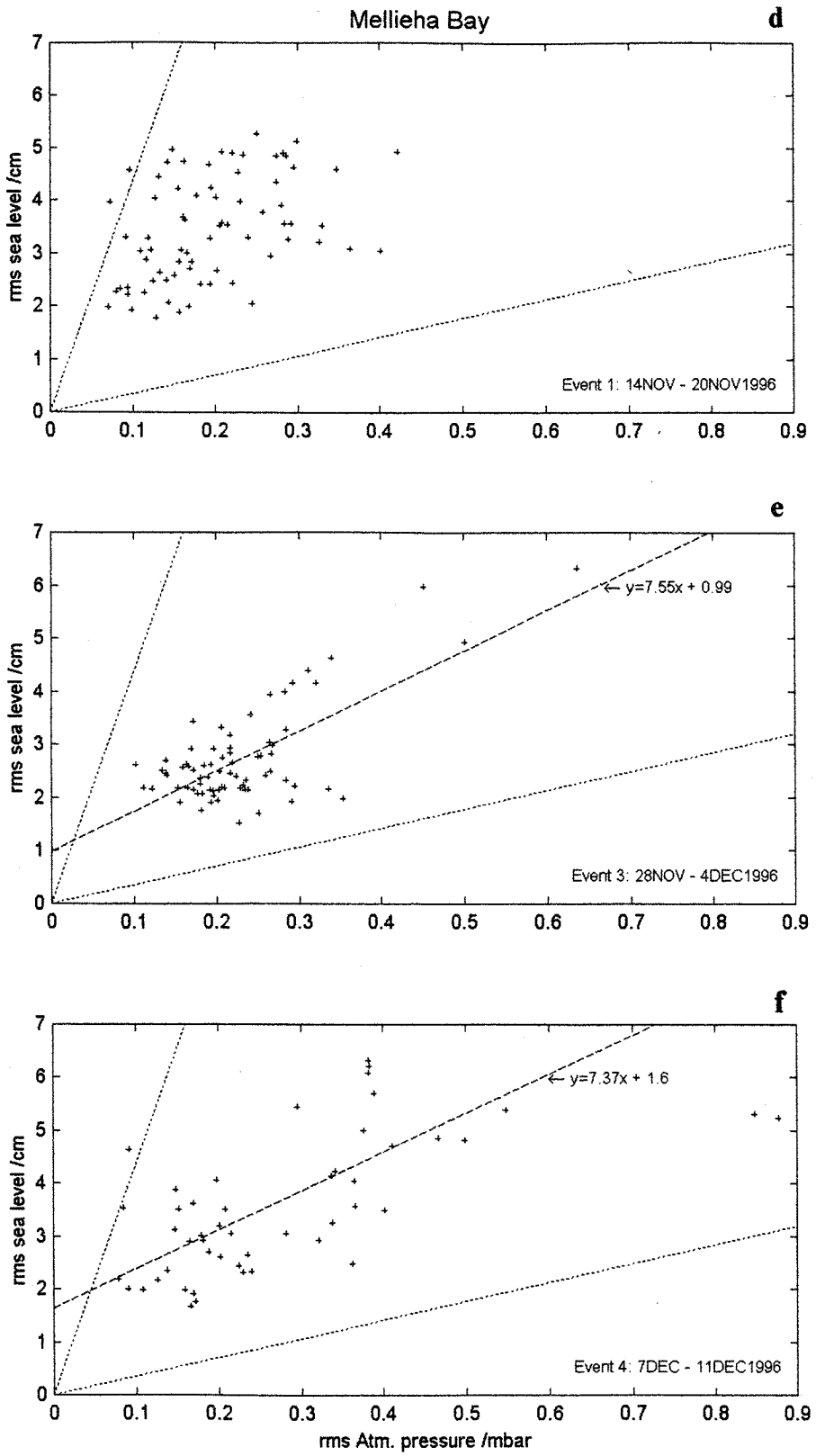

Fig. 4.31 Scatter plots between rms sea level (cm) in Mellieha Bay and rms atmospheric pressure (mb) at Ramla tal-Bir for data segments referring to event 1 (d), event 3 (e), event 4 (f).

The constant term in the linear fit expression has an important physical explanation. This constant term appears consistently in all the regression analysis performed on other parts of the observation series. It shows that seiches in Mellieha Bay exist even in the absence of atmospheric oscillations. This further confirms that other factors besides atmospheric pressure fluctuations can be responsible for the sea level oscillations in the bay.

4.5.2 Analysis on observations in St. George's Bay

It is useful to repeat the same analysis at another location in order to identify any common patterns. This is done for a set of observations of sea level in St. George's Bay and atmospheric pressure at the nearby Valletta station, covering the period 2nd November to 15th December 1996. The relation between rms sea level and rms atmospheric pressure for St. George's Bay is found to be essentially identical to that for Mellieha Bay. The scatter plot (not shown) has a similar distribution of points. It is again bounded by limiting regression lines of essentially the same magnitudes ($2.4 \leq \sigma_{SG(cm)}/\sigma_{VT(mbar)} \leq 35$) for the whole period of observation), but the main accumulation of points is shifted to slightly lower rms sea level values with respect to Mellieha Bay. The correlation estimates between the 2-hourly root mean square magnitudes of sea level and atmospheric pressure for St. George's Bay/Valletta are however consistently lower than those for Mellieha Bay/Ramla (Table 4.5). These considerations imply that while the same mechanisms are responsible for the generation of seiches in the two bays, their relative importance is not necessarily the

Table 4.5
Correlation estimates between rms sea level (cm) and rms atmospheric pressure (mbar)

	OBSERVATIONS			EVENTS		
	Full period	low seiche	strong seiche	1	3	4
Ramla/ Mellieha	0.574	0.083	0.528	0.416	0.710	0.644
Valletta/ St. Georges	0.382	0.024	0.365	0.262	0.277	0.629

same. Other factors, besides that of forcing by mesoscale atmospheric pressure disturbances, must thus contribute to the excitation of sea level oscillations. The results also show that seiching characteristics can be very different from one bay to another as well as in the same bay at different times.

The lower correlation estimates in St. George's Bay imply that these alternative generation mechanisms must be more important in this bay with respect to Mellieha Bay. The smaller size of St.George's Bay needs also to be taken into consideration. The natural frequency of oscillation of St. George's Bay (approximately 10 cph) is about three times that of Mellieha Bay. The water body involved in this oscillation does not extend much beyond the entrance of the bay (refer to section 3.4.6). Considering the overall smooth and montonic decrease of the spectral content of atmospheric pressure fluctuations with increasing frequency, one would thus expect the relative role of atmospheric pressure in seiche generation in St. George's Bay to also decrease on account of the bay's higher gravest mode frequency. Other factors can however make up for this effect. There is evidence of short period waves ($T \approx 3$min) in St. George's Bay that result from surf beats. Surf beats are particularly active during high surface wind waves at coastal areas with narrow bathymetric contours such as on the southeastern coast of the island. The range of surf beat periods (generally classified to be of the order of minutes) includes all the natural periods of oscillation of the bay's water body and the value of the period of maximum energy in the surf beat spectrum will no doubt favour different bay modes at different times. Bottom friction with the shallow bathymetry of the bay and the restriction imposed by its relatively narrow entrance will tend to attenuate surf beat activity inside the bay with respect to the open coast outside. This applies for all periods except those in near-resonance where maximum amplitude response is thus obtained. The net result is that those waves whose periods are favoured by the dimensions of the bay will be effectively enhanced. It is noteworthy to remember here (refer section 3.4.6) that the sea level gauge position coincides with the displacement node of the first mode of the bay, and so the observations do not reveal the oscillations at this mode. The higher rms sea level values in St. George's Bay can however be quite confidently attributed to instances when high surface waves impinge on the northeastern coast of Malta. Their magnitude is dependent on the fine structure of the consequent surf beat spectrum and on the wave direction. Unfortunately surface wave height data is not available for a quantitative analysis, but particularly on 1st December, the seiching from noon onwards has no direct relation to atmospheric pressure and is certainly caused by surf beats. If the scatter points from 1200GMT - 2200GMT of 1st December are ignored, the correlation estimate for event 3 indeed improves appreciably to 0.433. The correlation estimate restricted to the first half of the same day rises to 0.756 with a linear fit described by $\sigma_{SG} = 4.09\sigma_{VT} + 2.06$.

In contrast to Mellieha Bay, the rms sea level in St. George's Bay is particularly low during event 1. The correlation is also very low. This weak dependence of sea level on atmospheric pressure is probably related to

the spectral energy content of the barometric pressure around 10 cph which is recorded to be the lowest compared to the other events (refer to Fig. 4.12, section 4.4.3.4). The situation is different during event 4; the atmospheric pressure energy is enhanced over a wide band of frequencies and the correlation is exceptionally higher at both bays. The direct influence of the atmospheric pressure fluctuations on the sea surface thus seems to be important at least during event 4.

4.5.3 Frequency dependence of the coupling between atmospheric pressure and sea level

The analysis in the previous section does not completely answer the question on the direct resonance generation by atmospheric waves. Further insight into this problem can be obtained by looking for commonalities in the temporal development of atmospheric and sea level activity. The relation between the presence of atmospheric gravity waves and sea level oscillations is here investigated by studying the evolution in time of the spectral content of pressure and sea level for each of the frequency bands f2 (128min) to f13 (10.66min) described in section 4.4.3.2. The data set covering the full period of observations is analysed at each of a number of moving data segments 512 minutes long. The first segment is centred at time 00:00 GMT of 27th October 1996. The last segment is centred at time 00:00 GMT 17th December 1996. Successive data segments are displaced such that the separation between central times is 4 hours. Pressure is expressed in millibars while sea level is converted to decimeters. The spectral contents for each data segment are estimated by using a window size of 64 min with 50% overlapping resulting in 30 degrees of freedom. The results of the analysis are used to calculate the spectral energy at each of the frequency bands. The time series of spectral band energies are presented in Fig. 4.32. In order to better visualise the comparison, the same scale is used for the plots at the respective frequency bands. Also, the sea level spectrum is expressed in squared decimeters and pressure in squared millibars. This means that the plotted spectral energy for sea level should be multiplied by a factor of 100 in order to obtain a 1:1 correspondence with magnitudes of the spectral energy in the atmospheric pressure.

Fig. 4.32 shows the considerable changes in spectral content of the two parameters with time. The temporal development of the energy occurs as a succession of reinforcements which result in a series of peaks. All the events 1 to 4 discussed above are reproduced in this analysis with evident peaks in energy in both the pressure and sea level. A further event (henceforth referred as event 6) is also registered between the 14th and 16th December. Fig. 4.32 shows clearly how the energy remains low for most of the time before an event starts, then it gradually increases and reaches a maximum during the event for both the sea level within the embayment

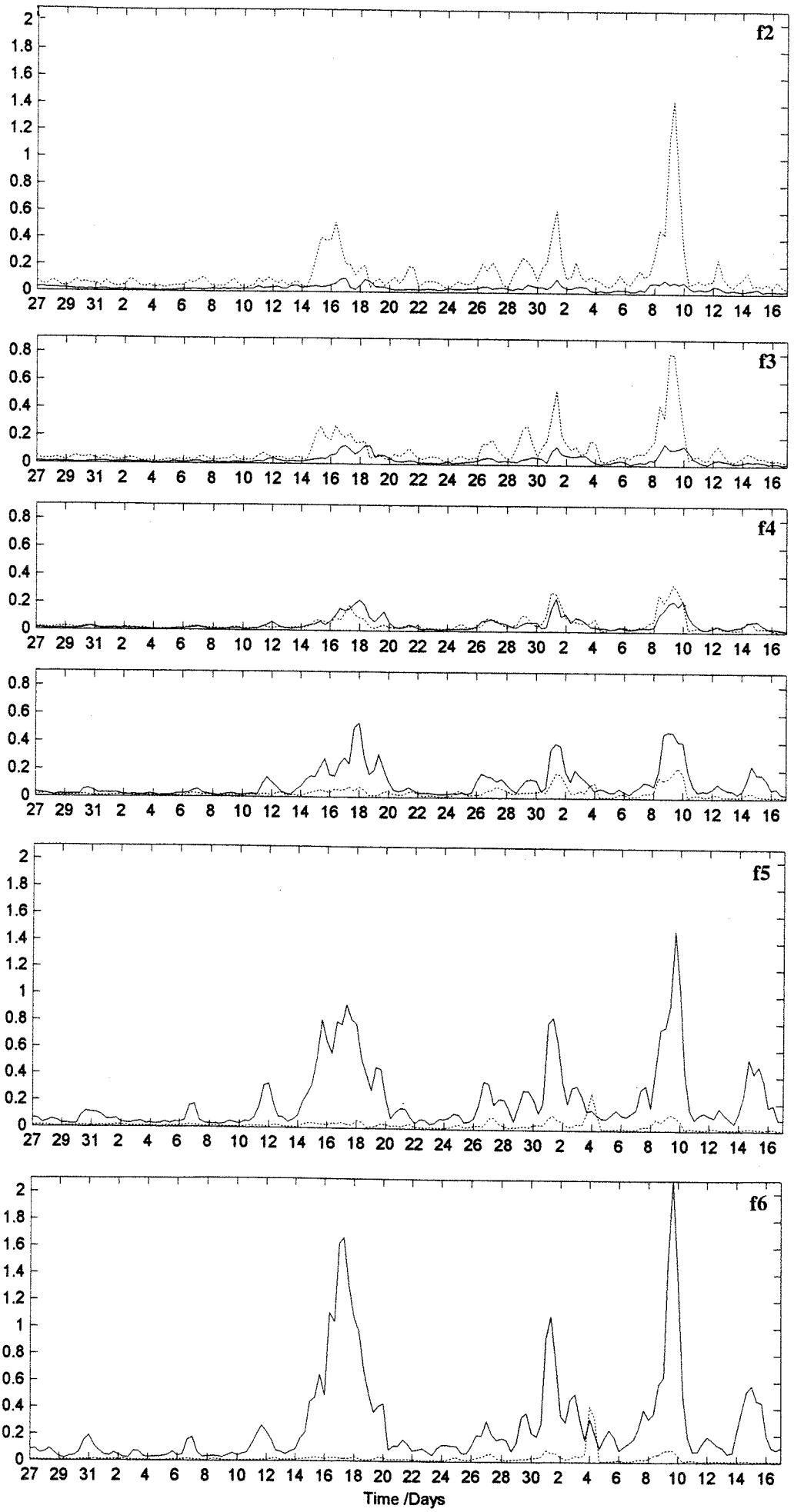
Pressure (dotted) in mb² h; Sea level (solid) in dm² h
f2
f3
f4
f5
f6
27 29 31 2 4 6 8 10 12 14 16 18 20 22 24 26 28 30 2 4 6 8 10 12 14 16
Time /Days

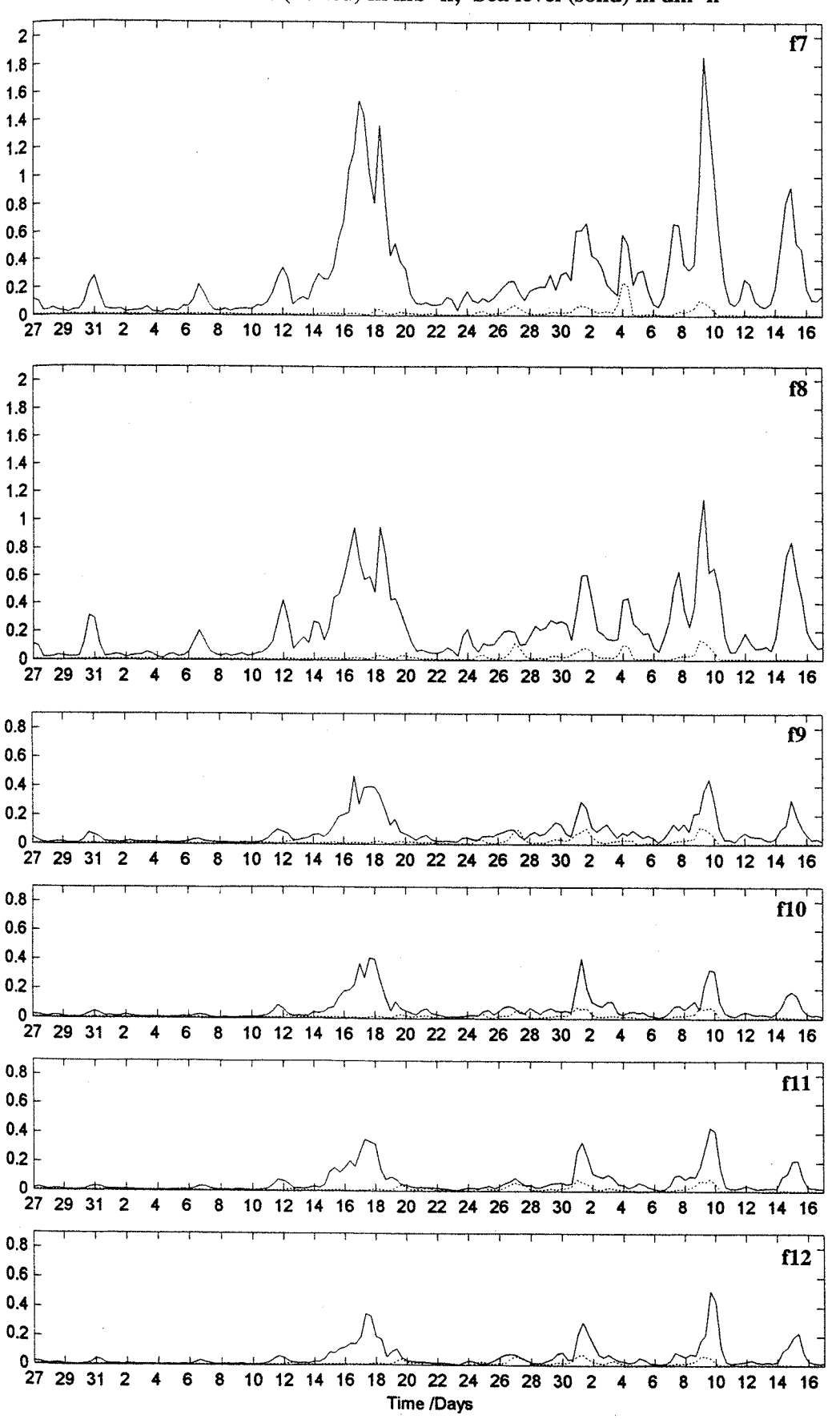

Fig. 4.32 Running spectrum at 4-hour intervals for sea level (dm) in Mellieha Bay (solid) and atmospheric pressure (mb) at Ramla tal-Bir (dotted) calculated for spectral bands f2 - f13 for the period 26/10/96 - 17/12/96. Spectra are calculated over data segments of 512min with 30 d.o.f. The 95% confidence factor, is 4.5dB ($B_{min} = 0.63$; $B_{max} = 1.8$).

and the air pressure, slowly decaying afterwards until it reaches background levels. There is also a great difference in the mean energy variance between the days preceeding and those following the 14th November. At all frequency bands and for both pressure and sea level, the 14th November represents a date of demarcation between a period of low activity when the spectral plots are low and flat, and a subsequent more energetic period with an almost uninterrupted succession of peaks in both parameters. These results confirm the causal relationship between the sea level oscillations in the embayment and the atmospheric wave activity.

A closer analysis shows that there are some important differences between the two parameters. Atmospheric pressure carries most of the energy in the lower frequency bands f2 and f3. The energy decreases very quickly with frequency. The sea level has maximum energy at the three frequency bands f6, f7 and f8 (central periods of 25.6, 21.3 and 18.3 minutes respectively). This frequency range includes the main modes of oscillation of Mellieha Bay. In contrast, the energy of the atmospheric pressure at these frequency bands is at least an order of magnitude less than the maximum. This consideration would seem to exclude a major direct and simple coupling between atmospheric gravity waves and the sea level in the embayment. A correlation between the spectral components of the two parameters at the respective frequency bands further supports this assertion. This analysis is covered in section 4.5.4.

An analysis of Fig. 4.32 further reveals the detailed temporal development of the spectral energy composition of the atmosphere and the sea level at the respective events. Some common generalities apply especially to events 3 and 4 during which the atmospheric energy at bands f2 and f3 is particularly high. This atmospheric energy content decreases with frequency but retains a base value of about $0.1 mb^2h$ for all bands higher than f6. On the other hand the atmospheric pressure energy during event 1 carries very low values from band f7 and higher. For all these three events it seems that the presence of relatively higher atmospheric energy content at the lower frequency bands is in fact a prerequisite for a stronger interaction with the sea and consequently larger amplitude sea level oscillations. This indication is corroborated by the situation in event 2 during which the sea level oscillations remain low even though the atmospheric energy in the frequency bands f6 and higher has a magnitude equivalent to that during the main seiching events 3 and 4. The reason seems to be related to the comparatively weaker energy content at the lower frequency bands during this event. Similarly on the 4th December, a sharp peak in atmospheric pressure energy occurs principally at frequency bands f6 to f8, but is not accompanied by an enhancement of lower frequency energy. Event 6 is to some extent an exception to this

general pattern in the sense that moderate sea level oscillations occur during this event even though atmospheric pressure is low at all the frequency bands. This event does not seem to be related to local atmospheric activity and is probably triggered by a remote source. Unfortunately the lack of observations at a sufficient number of stations does not permit a detailed study of this event.

Furthermore it is noted that the band energy peaks may not necessarily be coherent and often occur with a time shift between one frequency band and another. For example the sea level band energy for event 1 decreases on the 17th November for frequency bands f2 and f3, and mainly for f8 and f9, whereas it peaks on the same day for all the other frequency bands. These considerations, in addition to the above, may imply that the sea level activity at a particular frequency band may in fact be related to the atmospheric energy at a different frequency band. This can have very important implications as discussed later in section 4.5.5 where a cascading energy mechanism is hypothesised.

4.5.4 Correlation analysis between the spectral contents of atmospheric pressure and sea level

The spectral decomposition of atmospheric pressure and sea level at each of the 4-hour overlapping segments calculated in section 4.5.3 can also be used to correlate the two parameters at each frequency band separately. The quantity $\langle\sigma_j\rangle = \sqrt{[\Delta f_j\ S(f_j)]}$, calculated for each central frequency f_j , gives the standard deviation at the particular frequency band. In this expression $S(f_j)$ is the spectral density at the particular frequency band, and Δf_j is the spectral frequency resolution. This quantity will henceforth be referred to as the 'band deviation'. For each frequency band f_j and at each 4-hour overlapping segment, the band deviation $\langle\sigma_j\rangle$ is calculated independently for both sea level and atmospheric pressure. This results in a time series of 4-hour band deviations for the respective parameters. The simultaneous evolution of the band deviations of sea level and atmospheric fluctuations in Mellieha Bay is thus obtained at each frequency band. This allows a correlation analysis on the same lines of that carried out in sections 4.5.1 and 4.5.2, but applied to each frequency band separately.

The results for frequency bands f2 $\rightarrow$ f13 are depicted in Fig. 4.33 by means of scatter plots between band deviations for sea level (in cm) and for atmospheric pressure (in mb). The scatter of the points shows a marked dependence on frequency. The most interesting feature in the plots are the high correlations especially at the lower frequency bands (i.e. frequency in the range 0.5 to 2 cph) with maximum correlation values reaching

higher than 0.8. The regression slope is a measure of the ratio of the relative magnitudes of sea level to atmospheric pressure band deviations. The height of sea water equivalent to 1mb pressure is only approximately 1cm, so that the high regression slopes cannot be accounted for by the statical effect of the pressure fluctuations. The slopes also rise consistently with frequency so that the response of sea level to atmospheric pressure fluctuations at the lower frequency bands is smaller by a factor of about 5 when compared to the value at the resonant frequencies (f7 and f8). It must however be pointed out that the sea level observations used in this analysis were taken inside the bay and therefore carry the superimposed effect of the topographic amplification. The influence of this effect may very well override and mask the component of the sea level oscillations that is effectively related to the coupling with the atmospheric pressure. This effect can only be eliminated by measurements in the open sea (refer section 4.6).

One further notes that the ratio of the relative magnitudes of sea level to atmospheric pressure band deviations tend to follow the same changes with frequency over the full range of pressure amplitudes and including in particular the lower amplitudes. This implies that the response of the sea to atmospheric pressure activity is not simply restricted to the larger amplitude fluctuations but actually extends even to weaker fluctuations. Hence the same mechanisms seem to apply down to small magnitudes.

The frequency dependence of the correlation estimates can furnish important indications on the nature of the pressure-sea level coupling. In the case of a linear response of the bay oscillations to external forcing, a higher correlation between seiche intensity and atmospheric energy would be expected specifically at the resonant frequencies of the bay. The general correlation estimates between the band deviations of the two parameters averaged over the whole observation period (51 days) and calculated at the different frequency bands (Fig. 4.34) do not confirm this result. The correlation is in fact lowest for frequencies in the range 2.5 to 6 cph which include the gravest mode frequency of the bay. The more specific frequency dependence of the correlation on an event by event basis is analysed in the subplots of Fig. 4.34. The correlation is insignificant during weak seiching periods (Fig. 4.34b). It increases considerably during seiching events but with no particular preference at the resonant frequencies. There are also differences between events. The correlation is very high at all the plotted frequencies during event 3 which has a short but intense duration (Fig. 4.34e). During event 4 the correlation drops considerably at the higher frequencies. Event 1 has on the other hand an anomalously low correlation at most frequencies especially in the range 3 to 9cph. These differences result from the dependence

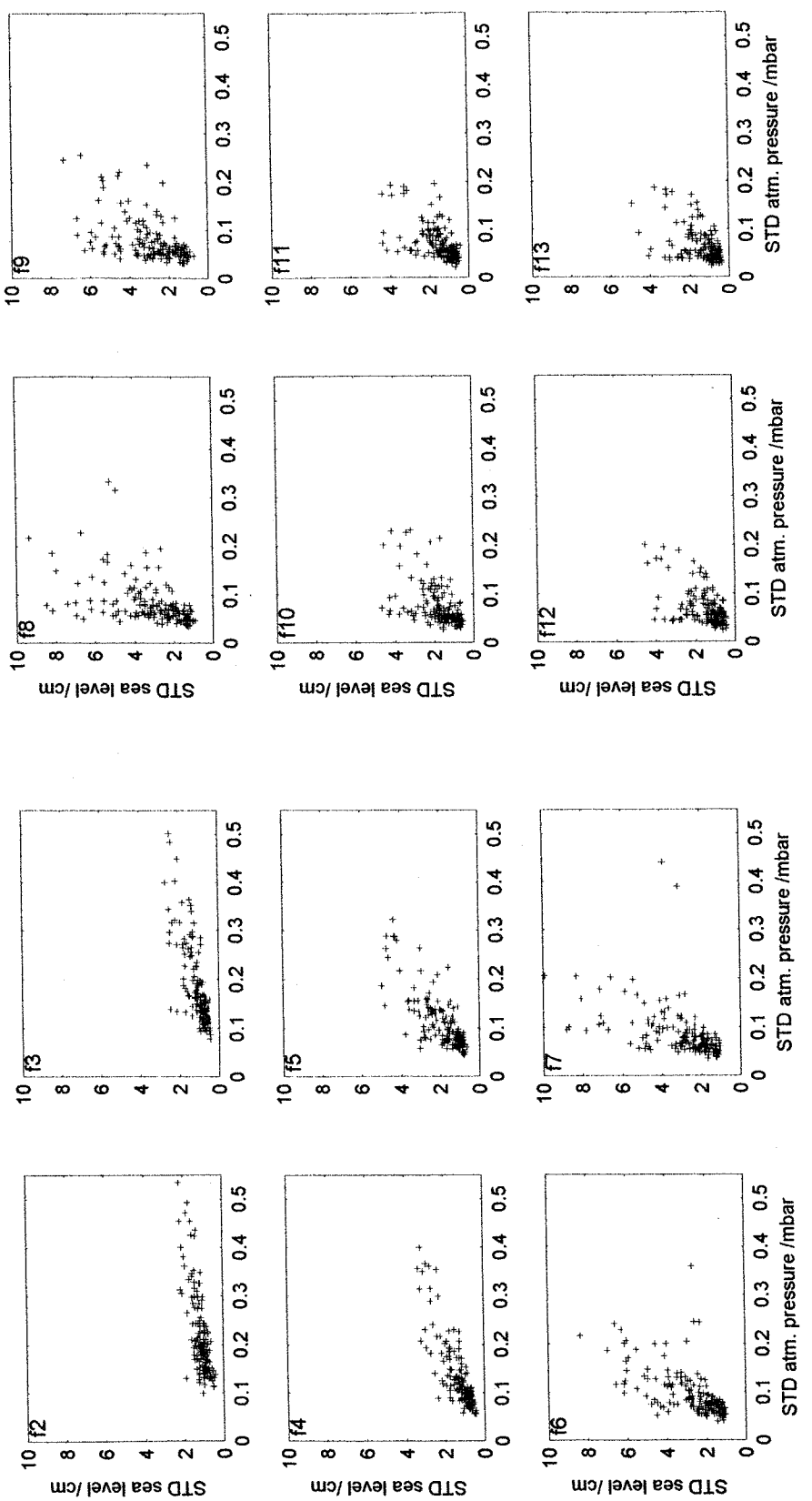

Fig. 4.33 Scatter plots between band deviations calculated at 4-hour intervals for sea level (cm) in Mellieha Bay and atmospheric pressure (mb) at Ramla tal-Bir at spectral bands f2 - f13 for the period 26/10/96 - 17/12/96.

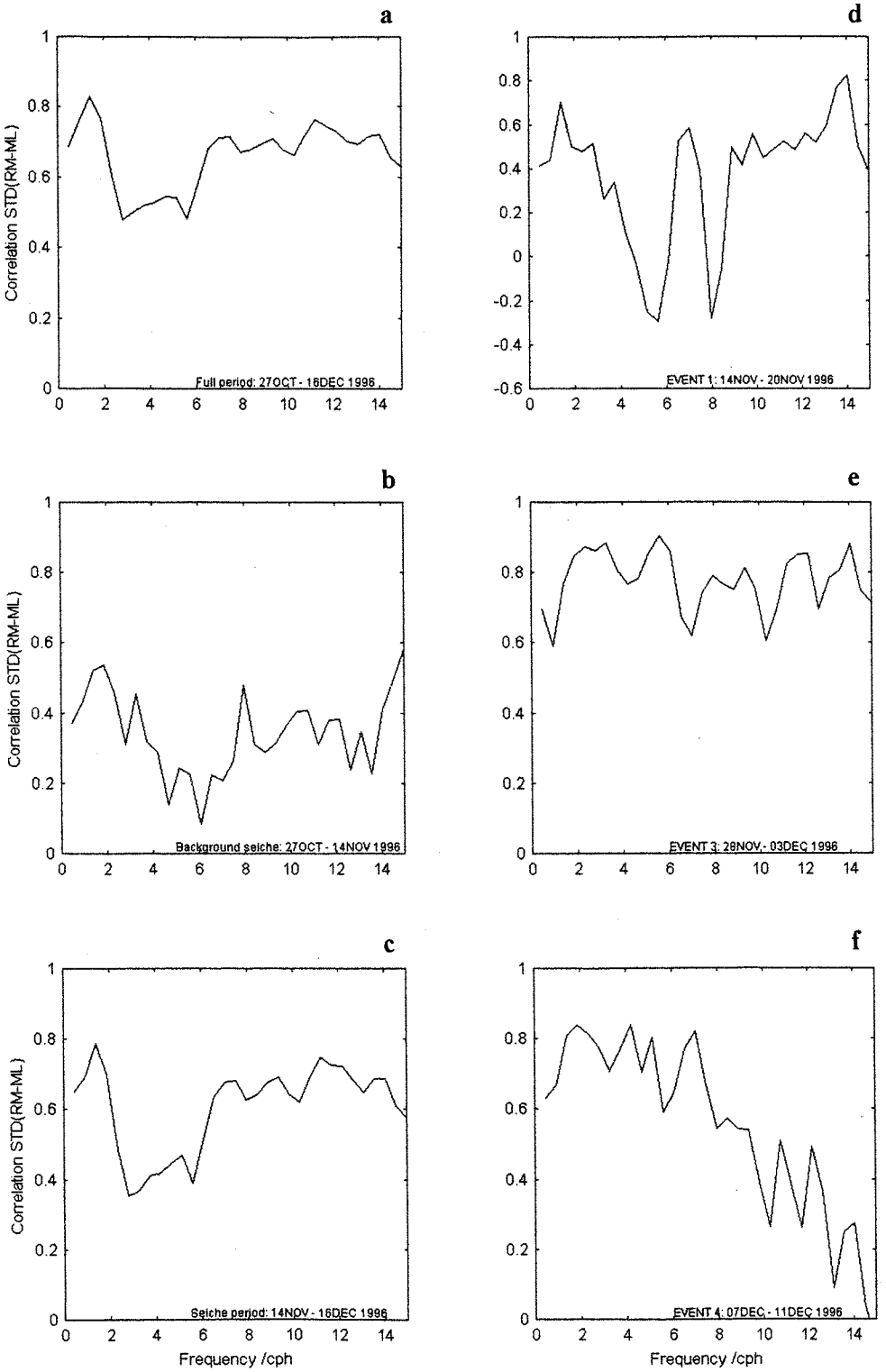

Fig. 4.34 Frequency dependence of correlation estimates between band deviations for sea level (cm) in Mellieha Bay and atmospheric pressure (mb) at Ramla tal-Bir (a) for the period 26/10/96 - 16/12/96, and for data segments referring to a period of background seiching (b), a period of moderate seiching (c), event 1 (d), event 3 (e), event 4 (f).

of the character of the air pressure-sea level interaction on multiple actors and confirm that it is not simply the magnitude of the atmospheric fluctuations that dictates the character of the interaction.

4.5.5 Cascading energy hypothesis

In section 4.4.2.1 it was already mentioned that the presence of atmospheric pressure energy in the sub-resonance lower frequency bands seems to be essential for inducing large amplitude sea level oscillations. This consideration is taken up again in this section with a focus on the interdependence of the energy content between different frequency bands as well as on the possible interchange of energy between frequency bands. The time series of frequency band energy contents obtained in section 4.5.3 are used. The temporal correlations between atmospheric pressure band spectral energies against the corresponding energy contents at two selected frequency bands, f2 (full curve) and f6 (dotted curve) respectively, are calculated. The contrasting results for two different periods of observations are displayed in Fig. 4.35. During weak seiching periods (Fig. 4.35b) the higher frequency band atmospheric pressure signals retain a level of correlation between themselves, but their correlation with the lower frequency band signals is well below significance. The situation is completely different during strong seiching periods. The typical plot in Fig. 4.35a refers to the period 28th November to 3rd December, which includes event 3. There is in this case a very high correlation in time between the atmospheric energy content at the lower frequency bands and those at the higher frequencies. This means that

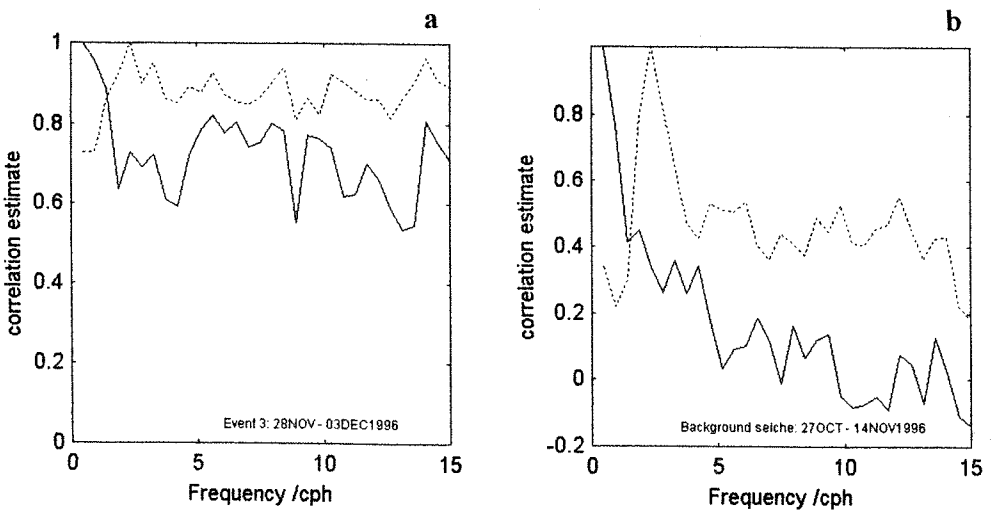

Fig. 4.35 Correlation estimates between band atmospheric pressure spectral energy content and pressure spectral energy at frequency bands f2 (solid) and f6 (dotted). The correlation is calculated for a period including a seiching event in (a), and during background seiching in (b).

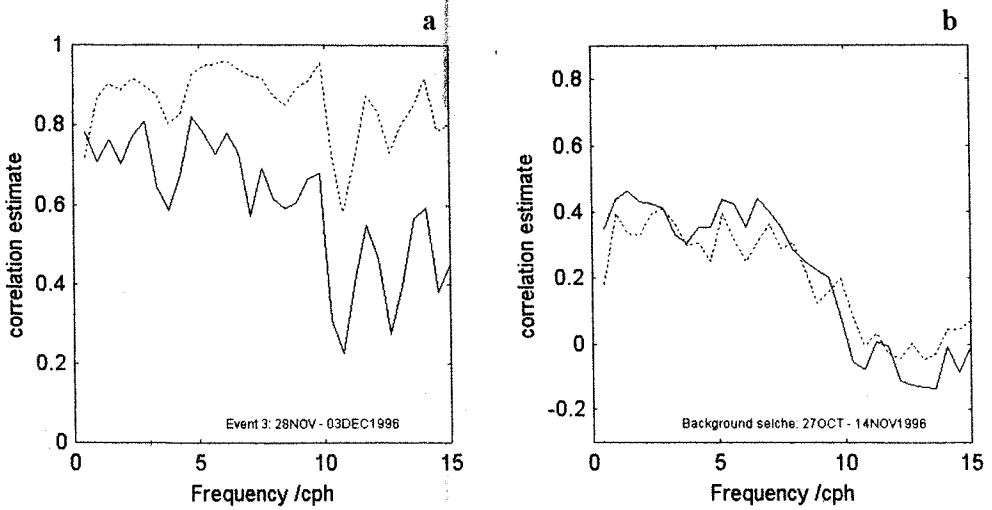

Fig. 4.36 Correlation estimates between band sea level spectral energy content and pressure spectral energy at frequency bands f2 (solid) and f6 (dotted). The correlation is calculated for a period including a seiching event in (a), and during background seiching in (b).

the temporal development of the higher frequency band energies follows very closely that occurring in the lower frequency bands. This phenomenology of the atmospheric pressure field applies to the full range of frequency bands and thus demonstrates the wide band character of the atmospheric energy.

The same temporal correlation analysis is also applied to compare spectral energies of sea level with those of atmospheric pressure. Fig. 4.36 gives the correlation in time between sea level band spectral energies and the energy content of atmospheric pressure at selected frequency bands f2 and f6. These correlations are equivalent to a combination of the correlations between pressure in Fig. 4.35 and between pressure and sea level. They are however plotted explicitly in order to confirm that during the seiching periods the high correlation between sea level and pressure is not simply restricted to equivalent frequency bands. The lower frequency atmospheric pressure fluctuations are indeed related to the higher frequency sea level signals at least as much as they are to those at the equivalent frequencies. The coupling between the atmospheric pressure fluctuations and the sea level oscillations does not therefore simply involve a one-to-one transfer of energy between corresponding frequencies, but actually appears to result from intra-band exchanges of energy from the lower to the higher frequency bands.

These results indicate that the triggering of large amplitude sea level oscillations by atmospheric activity is probably related to conditions which are favourable to a wide band energy cascading process whereby lower frequency energy is 'pumped' to the higher frequencies, including the resonant frequencies. It is not clear whether this energy cascading process occurs in the atmosphere or whether it forms part of the air pressure-sea level coupling mechanism. Upon considering the spectral characteristics of the atmospheric disturbances discussed in section 4.4.3.4 it would probably be more appropriate to put more weight on the former hypothesis. The energy redistribution can however be inherent to the coupling.

The interaction of the atmosphere with the sea occurs over a wide range of spatial scales. Very often atmospheric disturbances are in the form of a pressure jump which is very sharp in the time domain, and contains a wide band of energy in the frequency domain. The associated sea level oscillations thus cover a range of temporal and spatial scales. These larger scale motions that are triggered on the shelf will subsequently drive the smaller scale and more localised oscillations so that energy will tend to become organised into the higher frequencies before becoming dissipated. Long waves can also be generated by the scattering of a moving surge sea level displacement by bottom and coastline irregularities (Kulikov & Schevchenko, 1985). In these mechanisms a transfer of energy from the lower to the higher frequencies is involved. Energy can however also be channelled in the opposite direction. In the presence of an intense source it is not uncommon for energy involved with high frequency and small scale motions to be transferred to lower frequency and larger scale movements. For example, modulated wave groups incident from a distant storm are known to induce low frequency long wave motion close to the shore (Gallagher, 1971). In this case energy is transferred from short gravity waves to larger scale motions. In combination, the mechanisms described above are therfore expected to result in a 'pumping' of energy into the middle long wave frequency bands both from the higher and from the lower frequency bands.

When an eigenfrequency falls within this preferred frequency band the response of the sea is then expected to be more vigorous. This broad band energy pumping mechanism can thus explain situations of large amplitude seiches reported in the literature. One such case is that of the 'rissaga' waves observed on the 10-11th August 1989 in Ciutadella harbour in the Balearic Islands, with wave heights of more than 1m which were generated when the most energetic atmospheric waves had a typical period of about one hour; that is approximately six times larger than the resonance period of the inlet (Rabinovich & Monserrat, 1998).

4.6 Analysis using offshore measurements

This section makes use of the bottom pressure recordings made at the offshore Qawra Station from 10th to 30th September 1996 (refer section 4.3.2). The analysis is intended to confirm the atmospheric origin of seiches by analysing the long period waves in the offshore area, prior to their modification as they propagate towards shore.

4.6.1 Presentation of the data set

Fig. 4.37(a - c) shows the time series of bottom pressure (converted to cm according to section 4.3.2.1) at Qawra station, of the surface atmospheric pressure at Ramla tal-Bir station (corrected to MSL), and of bottom temperature. Although the higher frequency sea level fluctuations are smaller than those registered inside Mellieha, a number of seiching events of relatively short duration can easily be discerned. The strongest wave is registered on 12th September with a peak-to-peak excursion of 13cm. The relative magnitudes of the seiching events can be followed from the running variance plot in Fig. 4.39c.

The atmospheric pressure record (Fig. 4.37c) shows the characteristic low frequency cycling of highs and lows which alternate one another every 2-3 days. The relatively deep cyclone on the 22nd of September is associated to an extensive low pressure circulation on the eastern part of Italy that only marginally affected the Central Mediterranean. The cyclone was preceeded by a moderate but consistent current from the ESE which persisted for 18 hours and kept the air temperature some 5°C higher than the mean for this period of the year. The subsequent flow of cool air driven over the Central Mediterranean from Germany caused some instability with associated rain over the Maltese Islands.

As expected, the semidiurnal variation in atmospheric pressure reaches its maxima at approximately 06h-07h and 20h-21h local time each day with peak-to-peak amplitudes of the order of 1.5-2mb; an additional peak at mid-day is not uncommon. The atmospheric pressure trace is otherwise relatively smooth except for occasional rapid and large amplitude fluctuations such as on the 12th (afternoon), on the night between 16th and 17th, and on the 18th and 20th (morning).

The bottom temperature is characterised by strong diurnal fluctuations which are associated to internal waves.

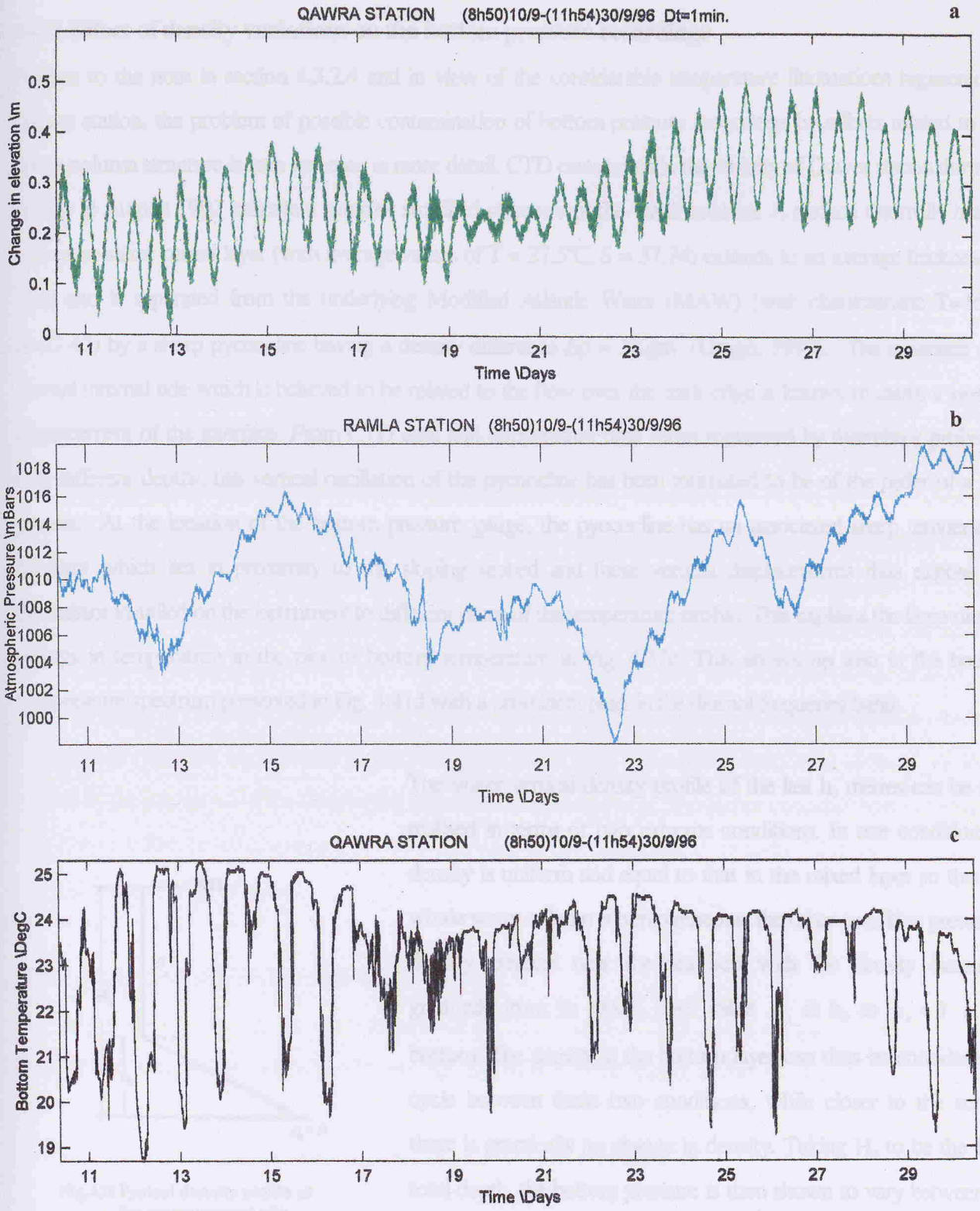

Fig. 4.37 Time series of 1-minute sampled (a) bottom pressure recordings (converted into equivalent sea level fluctuations) at Qawra Station, (b) atmospheric pressure at Ramla tal-Bir Station, and (c) bottom temperature at Qawra Station, for the period (08h50)10/9/96 - (11h54)30/9/96.

4.6.2 Effect of density variations on the bottom pressure recordings

Further to the note in section 4.3.2.4 and in view of the considerable temperature fluctuations registered at Qawra station, the problem of possible contamination of bottom pressure recordings by effects related to the water column structure is here revisited in more detail. CTD casts taken in the vicinity of Qawra station during a survey in August 1992 indicate a summer stratified structure of the water column. A surface thermally heated and more saline mixed layer (with average values of T = 27.5°C, S = 37.74) extends to an average thickness of 20m and is separated from the underlying Modified Atlantic Water (MAW) (with characteristic T=16°C, S=37.45) by a sharp pycnocline having a density difference $\Delta\rho \approx 3 Kgm^{-3}$ (Drago, 1997). The existence of a diurnal internal tide which is believed to be related to the flow over the shelf edge is known to cause a vertical displacement of the interface. From CTD data and temperature time series registered by thermistor probes at two different depths, this vertical oscillation of the pycnocline has been estimated to be of the order of a few metres. At the location of the bottom pressure gauge, the pycnocline has an associated sharp temperature gradient which lies in proximity to the sloping seabed and these vertical displacements thus expose the thermistor installed on the instrument to different slices of the temperature profile. This explains the large diurnal swings in temperature in the plot of bottom temperature in Fig. 4.37c. This shows up also in the bottom temperature spectrum presented in Fig. 4.41d with a prominent peak in the diurnal frequency band.

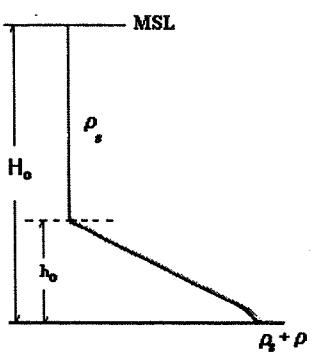

Fig.4.38 Typical density profile at the measurement site

The water vertical density profile of the last h_o metres can be thus realised in terms of two extreme conditions. In one condition the density is uniform and equal to that in the mixed layer so that the whole water column is homogeneous; the other condition presents a density gradient near the sea bed with the density increasing gradually from its mixed layer value ρ_s at h_o to $\rho_s + \hat{\rho}$ at the bottom. The density in the bottom layer can thus be considered to cycle between these two conditions, while closer to the surface there is practically no change in density. Taking H_o to be the fixed total depth, the bottom pressure is then shown to vary between the values:

$B_P = H_o\ \rho_s g$ and

$$B_P = \rho_s\, g\, (H_o - h_o) + \int_0^{h_o} \rho\, g\, dz = \rho_s\, g H_o + h_o g \hat{\rho}/2.$$

Taking $h_o \approx 10$m and $\hat{\rho} \approx 3 Kgm^{-3}$, the effect on B_P is equivalent to 15mm. This may be expected to explain an extra contribution to the diurnal signal in the bottom pressure time series in addition to the K1 astronomical tide. In reality this contribution may be effectively counterbalanced by the sea level variations that accompany internal waves and which, according to theory (Millot & Crepon, 1981), are in opposition to the associated density variations. It is thus hard to quantify with accuracy the net effect of these density variations on the bottom pressure tidal signals.

In this study we are however more concerned with bottom pressure signals in the higher frequency bands. Focussing on the bottom temperature time series reveals several events of high frequency variations with crest-to-crest magnitudes in the range of 1-3°C. If the associated density variation ($\approx 1.5 Kgm^{-3}$) were to affect the whole extent of the water column (30m depth), the effect on bottom pressure would be of the order of 4.5mb, which is equivalent to a significant sea level variation of 4.5cm. From a visual inspection between the bottom temperature and pressure time series, there is no evidence of any such significant (opposite) relationship between the variations present in the two series. This is further confirmed from the lack of any coincidence between surges in the time series of running variance of the respective parameters. This is an indication that the temperature variations are restricted to the bottom boundary layer and probably associated to sharp gradients caused by the interaction of the thermocline with the sloping bathymetry. The higher frequency bottom pressure variations can thus be safely assumed to be an expression of real oscillations at the surface and not a signature of water column density variations.

4.6.3 Analysis of the offshore sea level data

Spectral analysis on the high-pass filtered series of the Qawra sea level is carried out using a Bessel window of 8192 minute-sampled records with 50% overlap. The most relevant feature in this spectrum (Fig. 4.41a) is the occurrence of considerable energy in the long wave lower frequency band (LLB) in the range 0.2-8cph.
The time evolution of the sea surface oscillations is studied by spectrographic techniques. The analysis consists in computing the segmented discrete-time Fourier transform (DFT) of the signal using a sliding window of 512 sampling points, which is moved in steps across the whole extent of the time series. Each DFT gives 257 spectral estimates at equally spaced central frequencies in the range of 0-30cph. The window is applied to

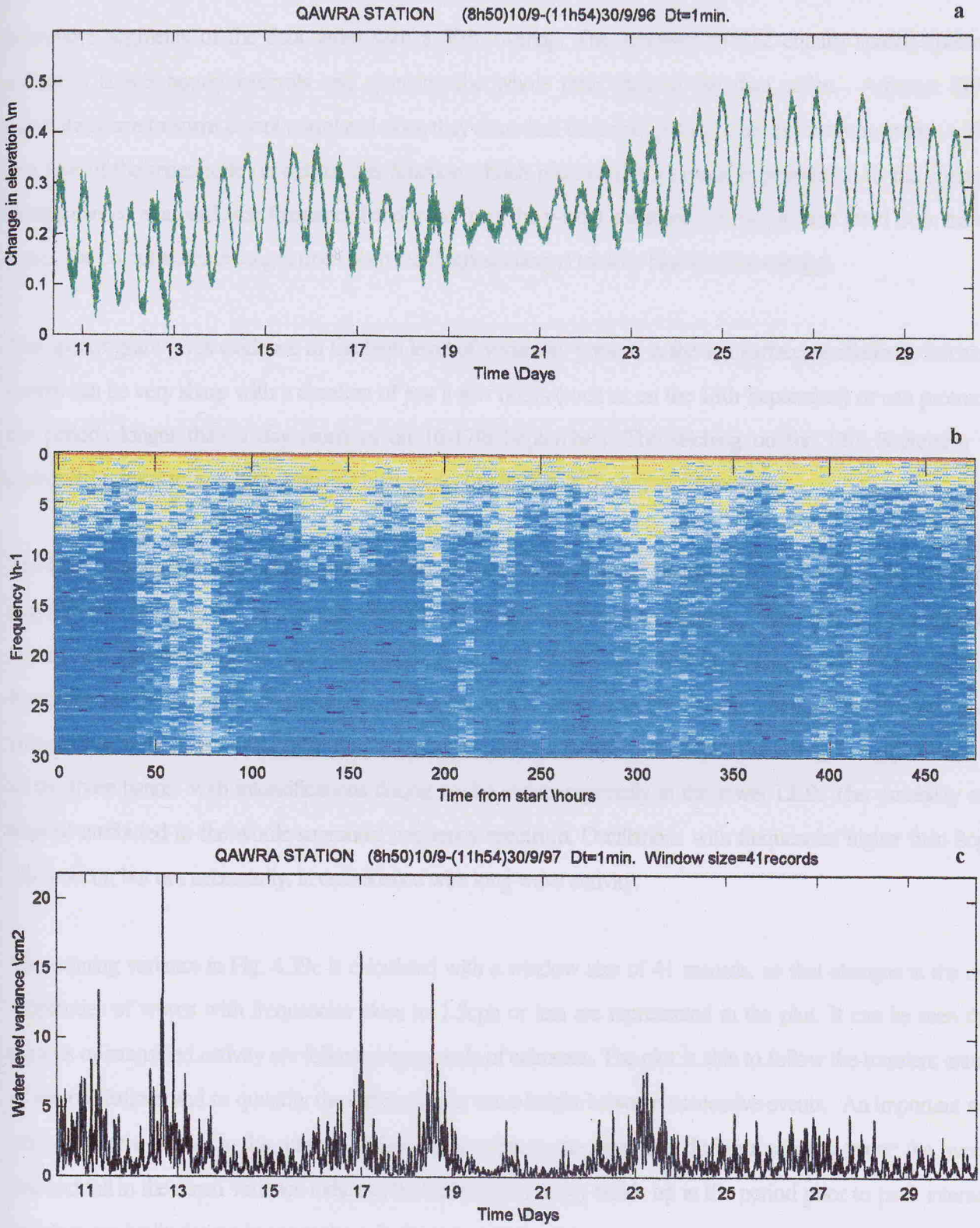

Fig. 4.39(a) Time series of 1-minute sampled bottom pressure recordings (converted into equivalent sea level fluctuations), (b) spectrogram calculated over 50% overlapping data segments of 512 records each, and (c) running variance calculated with a window size of 41 records, at Qawra Station for the period (08h50)10/9/96 - (11h54)30/9/96.

successive segments of the data series with a 50% overlap. This amounts to 112 equally spaced spectral estimates at 4.3 hourly intervals and spanning the whole time span of the data series. Adjacent DFT calculations are to some extent correlated since they share half their data points. The spectrogram in Fig. 4.39b is a plot of the magnitude (in dB) of this function. Each pixel carries a colour in proportion to the spectral energy carried at a particular frequency band (read from the y-axis) and a selected slot in time (read from the x-axis). The colour scheme ranges from deep red (highest energy) to deep blue (lowest energy).

The spectrogram gives evidence to the high level of variability present in the sea surface oscillations. Seiching events can be very sharp with a duration of just a few hours (such as on the 18th September) or can protrude for periods longer than a day (such as on 16-17th September). The seiching on the 13th September is particularly characterised by a relatively high content of energy at the higher frequencies.

The band structure of the spectrogram presents clear horizontal lines of demarcation, at f = 3cph and f = 8cph respectively, which divide the energy field into three distinct frequency stripes. Tidal and lower frequency signals are unresolved. The first two frequency stripes divide the LLB band into the lower LLB with frequencies in the range 0.2-3cph and an upper LLB with a higher frequency range 3-8cph. The third frequency stripe refers to the long wave higher frequency band (LHB) in the range 8-30cph. The energy is higly variable in all the three bands with intensifications during seiche events especially in the lower LLB. The variability can thus be attributed to the whole supratidal frequency spectrum. Oscillations with frequencies higher than 8cph often occur, but not necessarily, in coincidence with long wave activity.

The running variance in Fig. 4.39c is calculated with a window size of 41 records, so that changes in the rms amplitudes of waves with frequencies close to 1.5cph or less are represented in the plot. It can be seen that periods of intensified activity are followed by periods of calmness. The plot is able to follow the transient nature of the oscillations and to quantify the differences in wave height between successive events. An important and very consistent feature in the running variance plot refers to the symmetry during a seiching event; the overall rise and fall in the mean variance indicates how the wave energy builds up in the period prior to peak intensity and then gradually decays in approximately the same extent of time.

The distribution of energy in frequency and time space is next analysed. Fig. 4.40a,b show the development in time of the mean energies in the lower LLB, the upper LLB and the LHB bands, and of the relative percentage

energy between the three bands. The highest share of energy is carried by the lower LLB band both during seiche intensification as well as during periods of relative calm. The variable nature of the seiching events is noted. During the three events (marked E1) on the 18th, 20th and 23rd September, the intensification comprises the three bands with an energy distribution shifted towards the lower frequencies.

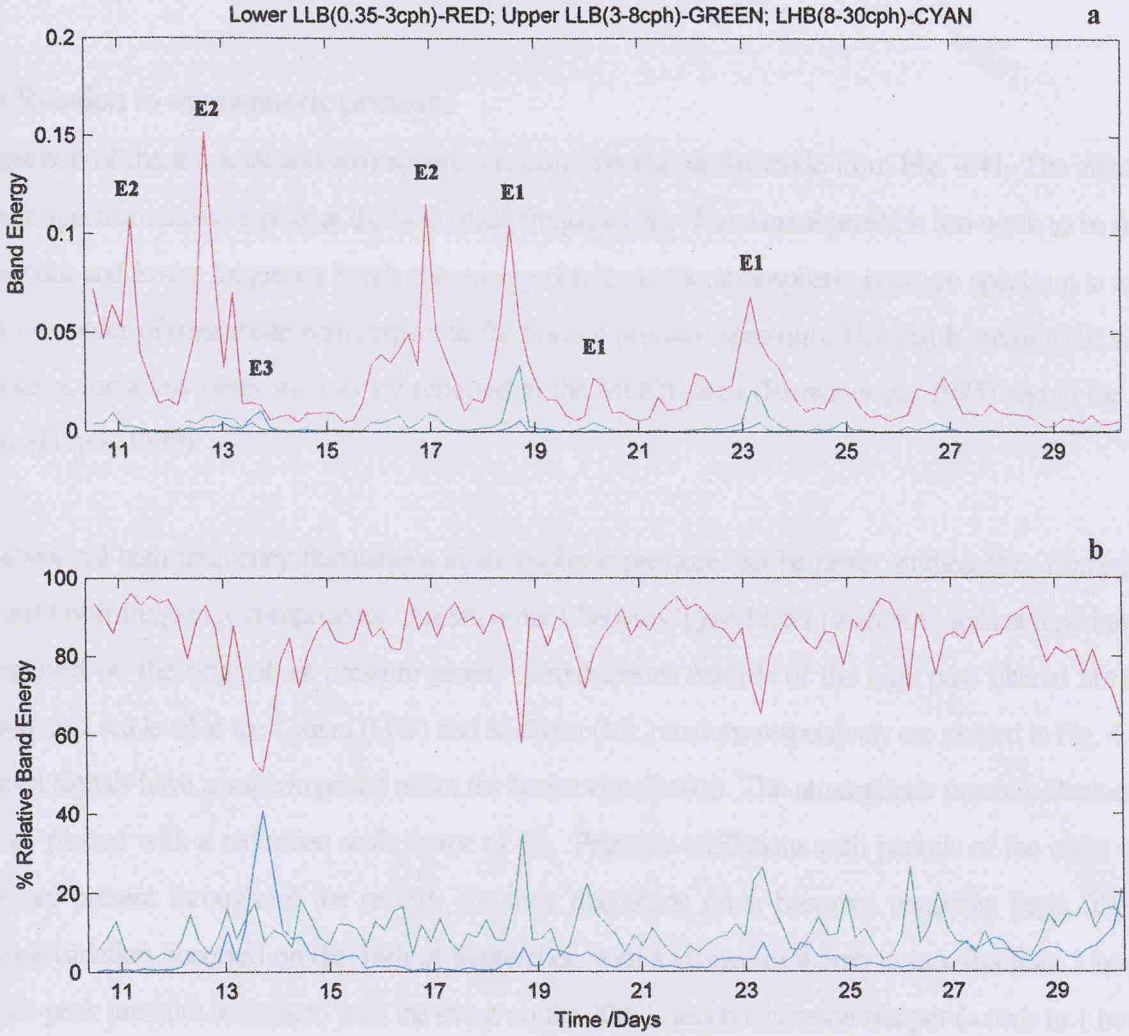

Fig. 4.40 (a) Time evolution of the seiche energy in the lower LLB (0.35 - 3cph, in red), upper LLB (3 - 8cph, in green) and LHB (8 - 30cph, in cyan) bands calculated over 50% overlapping segments each of length 512 records, at Qawra Station for the period (08h50)10/9/96 - (11h54)30/9/96.

(b) Variability of the relative distribution of the seiche energy in the lower LLB, upper LLB and LHB bands for the same period as in (a).

The events on the 11th, 12th and 16/17th (marked E2) are almost exclusively dominated by energy in the lower LLB. The event on the 13th (marked E3) is unique and carries the signature of enhanced oscillations in the LHB band while the energy in the lower LLB is in this case no longer predominant. This event coincides to a period of strong winds and rough sea state. This method of analysis can be used to classify the different types of seiching phenomena. Most importantly it shows that the bulk of the long wave energy is predominantly in the lower LLB band. It is therefore in this frequency band that we should particularly look for a correlation between activity in the atmosphere and that at the sea surface.

4.6.4 Relation to atmospheric pressure

Comparison of the sea level and atmospheric pressure spectra can be made from Fig. 4.41. The atmospheric pressure spectrum shows a peak at the twice daily frequency S_2. The diurnal period is too weak to be resolved. In the tidal and lower frequency bands the energy density in the atmospheric pressure spectrum is lower by about one order of magnitude with respect to the bottom pressure spectrum. This result seems to be a general one except for a few cases such as are reported in the MODE area (Brown et al., 1975) and in the Gulf of Alaska (Hayes, 1979).

The abnormal high frequency fluctuations in atmospheric pressure can be better studied after filtering off the tidal and lower frequency components. An 8th order Chebysev Type I filter (with 50% gain at a period of 10h) is employed on the original air pressure series. Simultaneous records of the high pass filtered atmospheric pressure and sea level at the Qawra (QW) and Mellieha (ML) stations respectively are plotted in Fig. 4.42. The sea level signals have a superimposed offset for better visualisation. The atmospheric pressure fluctuations (in mb) are plotted with a reduction scale factor of 10. Pressure oscillations with periods of the order of a few hours are present throughout the record, but their magnitude often becomes unusually large. The largest pressure variation occurred on the 18th of September, with a change of 4.5mb in just less than 3 hours. The peak-to-peak pressure associated with the event on the 20th is less but is much sharper ($\approx$ 3mb in 1 hour). The main feature emerging from this figure is the similarity between the records. The atmospheric pressure oscillations and the seiching events are clearly related and become enhanced together.

Fig. 4.43 shows the event on the 18th September in more detail. The larger pressure disturbance in the early morning has a most energetic period of approximately 4h; it is preceeded by a smaller wave with half the period

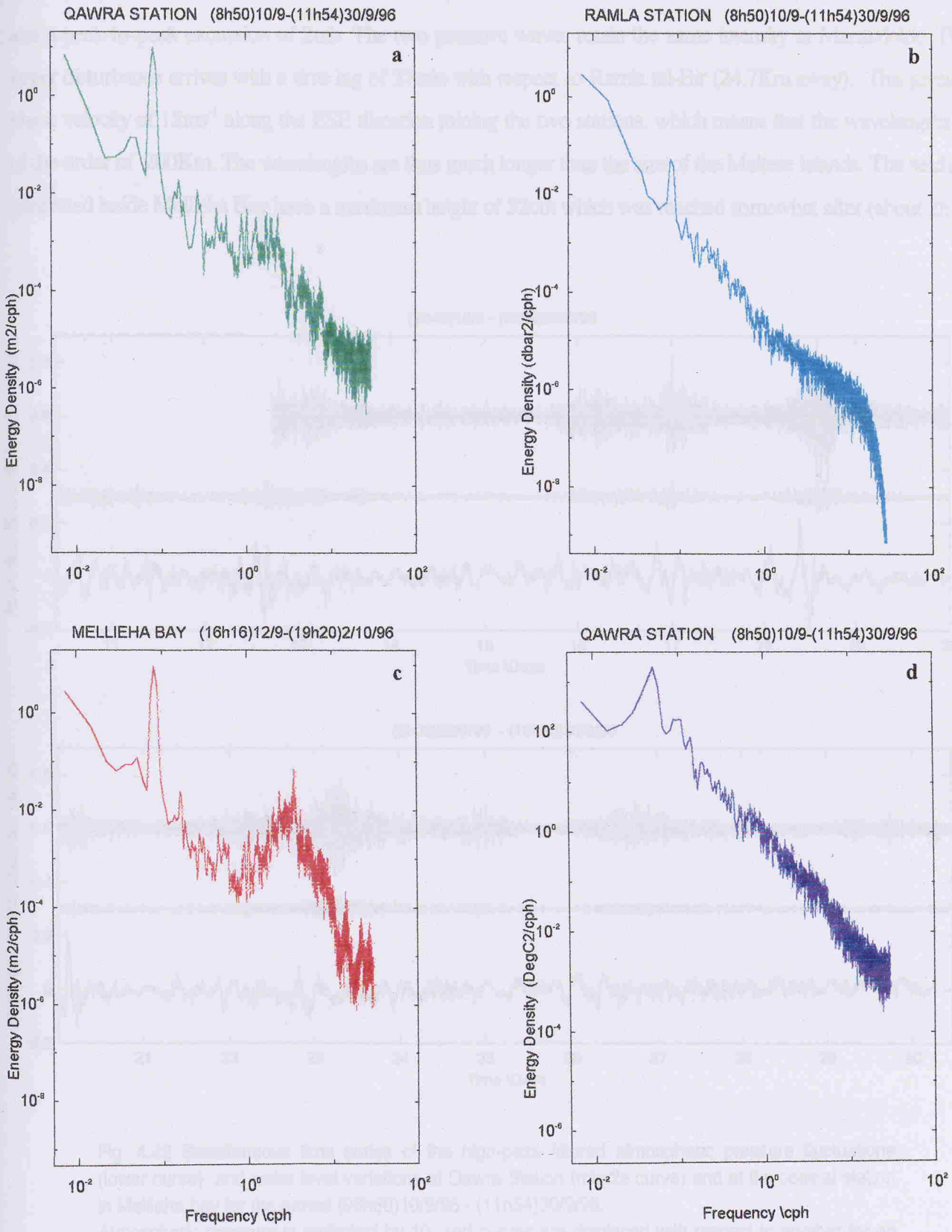

Fig. 4.41 Spectra of (a) bottom pressure variations (expressed into equivalent change in sea level), (b) Atmospheric pressure at Ramla tal-Bir, (c) sea level at the Mellieha Bay coastal station, and (d) bottom temperature at Qawra Station for the period (08h50)10/9/96 - (11h54)30/9/96.
The 95% confidence factor, for 26 d.o.f. is 4.6dB (B_{min} = 0.62; B_{max} = 1.8).

and a peak-to-peak excursion of 2mb. The two pressure waves retain the same intensity at Marsaxlokk. The larger disturbance arrives with a time lag of 27min with respect to Ramla tal-Bir (24.7Km away). This gives a phase velocity of 15ms^{-1} along the ESE direction joining the two stations, which means that the wavelengths is of the order of 200Km. The wavelengths are thus much longer than the size of the Maltese Islands. The seiches generated inside Mellieha Bay have a maximum height of 52cm which was reached somewhat after (about 2h

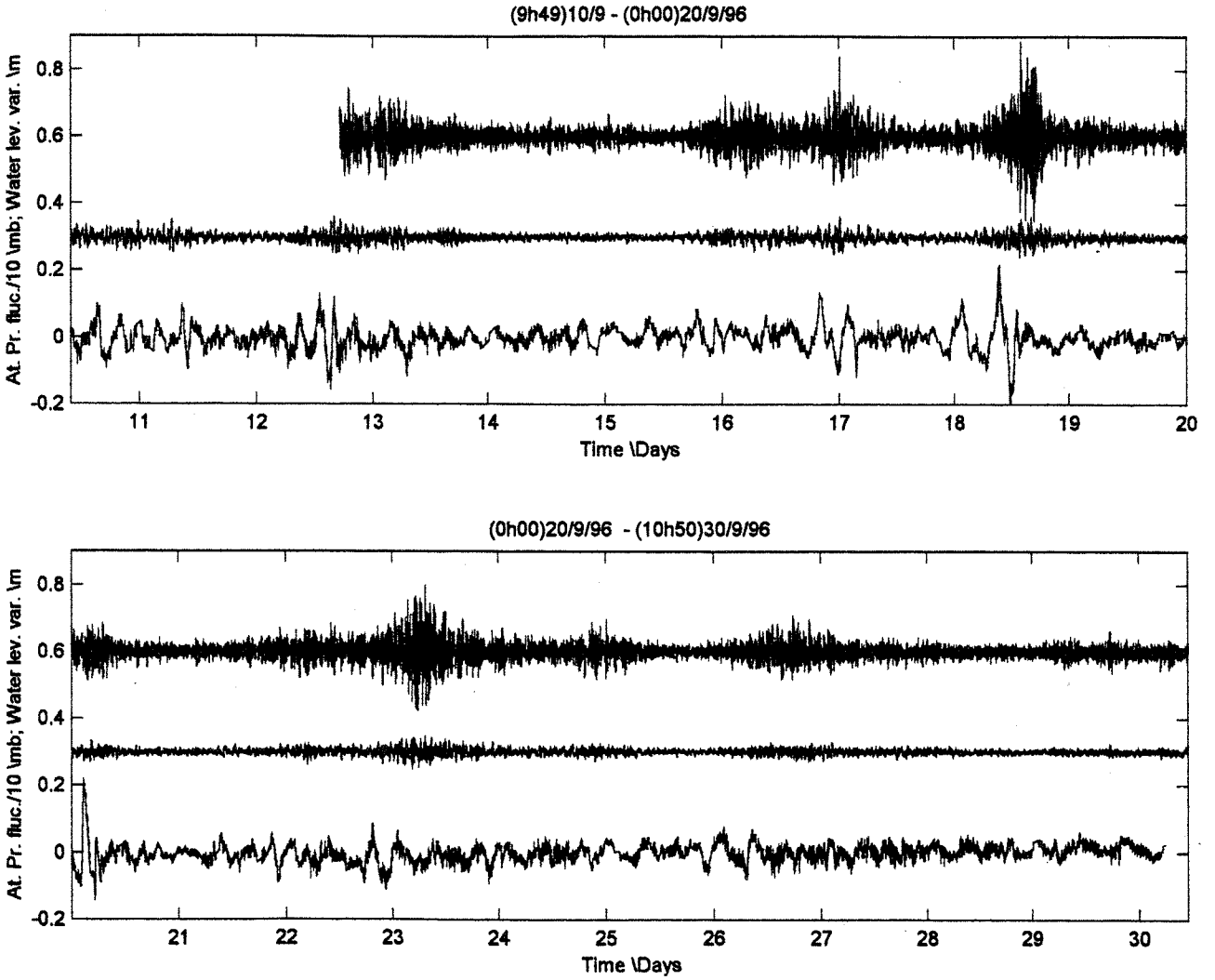

Fig. 4.42 Simultaneous time series of the high-pass filtered atmospheric pressure fluctuations (lower curve), and water level variations at Qawra Station (middle curve) and at the coastal station in Mellieha bay for the period (08h50)10/9/96 - (11h54)30/9/96.
Atmospheric pressure is multiplied by 10, and curves are displaced with respect to another for an improved visualisation.

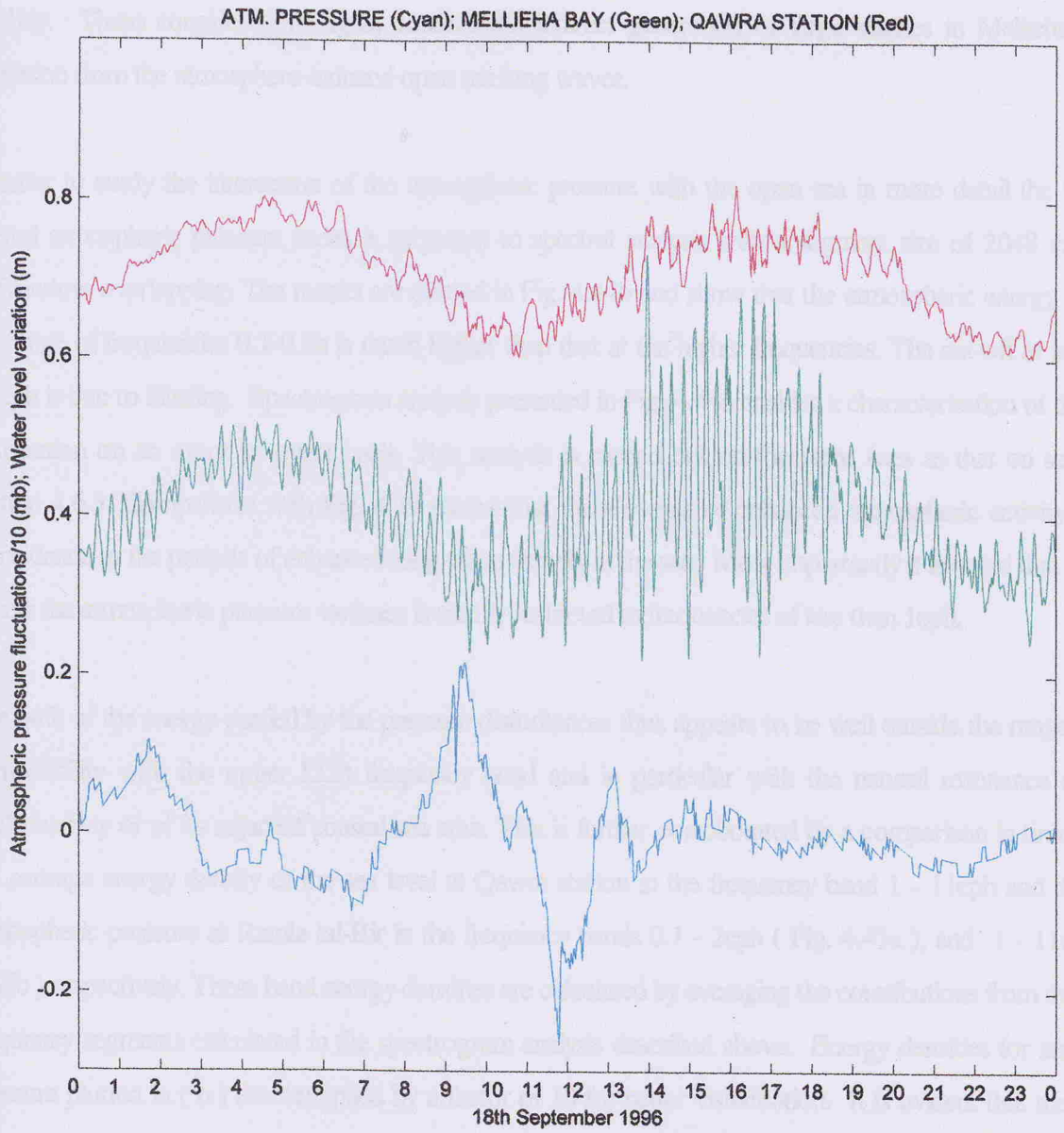

Fig. 4.43 Atmospheric pressure record at Ramla tal-Bir after high-pass filtering (half-gain at T = 10h) and sea level records at the coastal station in Mellieha Bay and the open sea Qawra station during the seiche event on 18th September 1996. Pressure values are reduced by a factor of 10 and traces are plotted with a different offset for better visualisation.

later) the second pressure pulse. A simultaneous intensification of the sea level at Qawra station is noted. The wavelength of the atmospheric disturbance is much larger than the size of the bay and a direct generation of the seiches is thus excluded. The dominant atmospheric periods are also much longer than the resonant periods of the bay. These considerations again confirm the indirect generation of large seiches in Mellieha Bay by excitation from the atmosphere-induced open sea long waves.

In order to study the interaction of the atmospheric pressure with the open sea in more detail the high pass filtered atmospheric pressure series is subjected to spectral analysis with a segment size of 2048 values and halfwindow overlapping. The results are plotted in Fig. 4.44b and show that the atmospheric energy carried in the range of frequencies 0.1-0.5h is much higher than that at the higher frequencies. The cut-off at around f = 0.1cph is due to filtering. Spectrogram analysis presented in Fig. 4.44a enables a characterisation of the energy distribution on an event by event basis. This analysis is carried out on the same lines as that on sea level in section 4.6.3. Comparison with Fig. 4.39 shows that these events of enhanced atmospheric activity occur in coincidence to the periods of enhanced long wave activity in the sea. Most importantly it is noted that for all the events the atmospheric pressure variance is mainly restricted to frequencies of less than 1cph.

The bulk of the energy carried by the pressure disturbances thus appears to be well outside the range of direct compatibility with the upper LLB frequency band and in particular with the natural resonance modes of Mellieha Bay or of its adjacent coastal sea area. This is further corroborated by a comparison in time between the average energy density of the sea level at Qawra station in the frequency band 1 - 11cph and that of the atmospheric pressure at Ramla tal-Bir in the frequency bands 0.1 - 2cph (Fig. 4.45a), and 1 - 11cph (Fig. 4.45b) respectively. These band energy densities are calculated by averaging the contributions from the relevant frequency segments calculated in the spectrogram analysis described above. Energy densities for atmospheric pressure plotted in (b) are multiplied by a factor of 10 for better visualisation. It is evident that the sea level activity in the upper LLB is well correlated to the atmospheric energy in the lower frequency band (Fig. 4.45a). For all the major events of intensified seiching there is a corresponding atmospheric maximum. The energy peaks in pressure tend to preceed those of elevation. The overall correlation estimate is 0.85. On the other hand the correlation between the sea level activity in the upper LLB with the atmospheric energy at the higher frequencies is only 0.64. The relative increase of atmospheric energy at the resonance bay frequencies is too low to suppose a relevant contribution of direct resonance to the generation of the seiches. This agrees with the

results discussed in the previous sections, namely that the effectiveness of seiche generation depends on the content of atmospheric energy over a band of frequencies which may include, but is not restricted to the natural eigenfrequencies of the sea. A mechanism is hypothesised to be in place which 'pumps' energy into this band of frequencies.

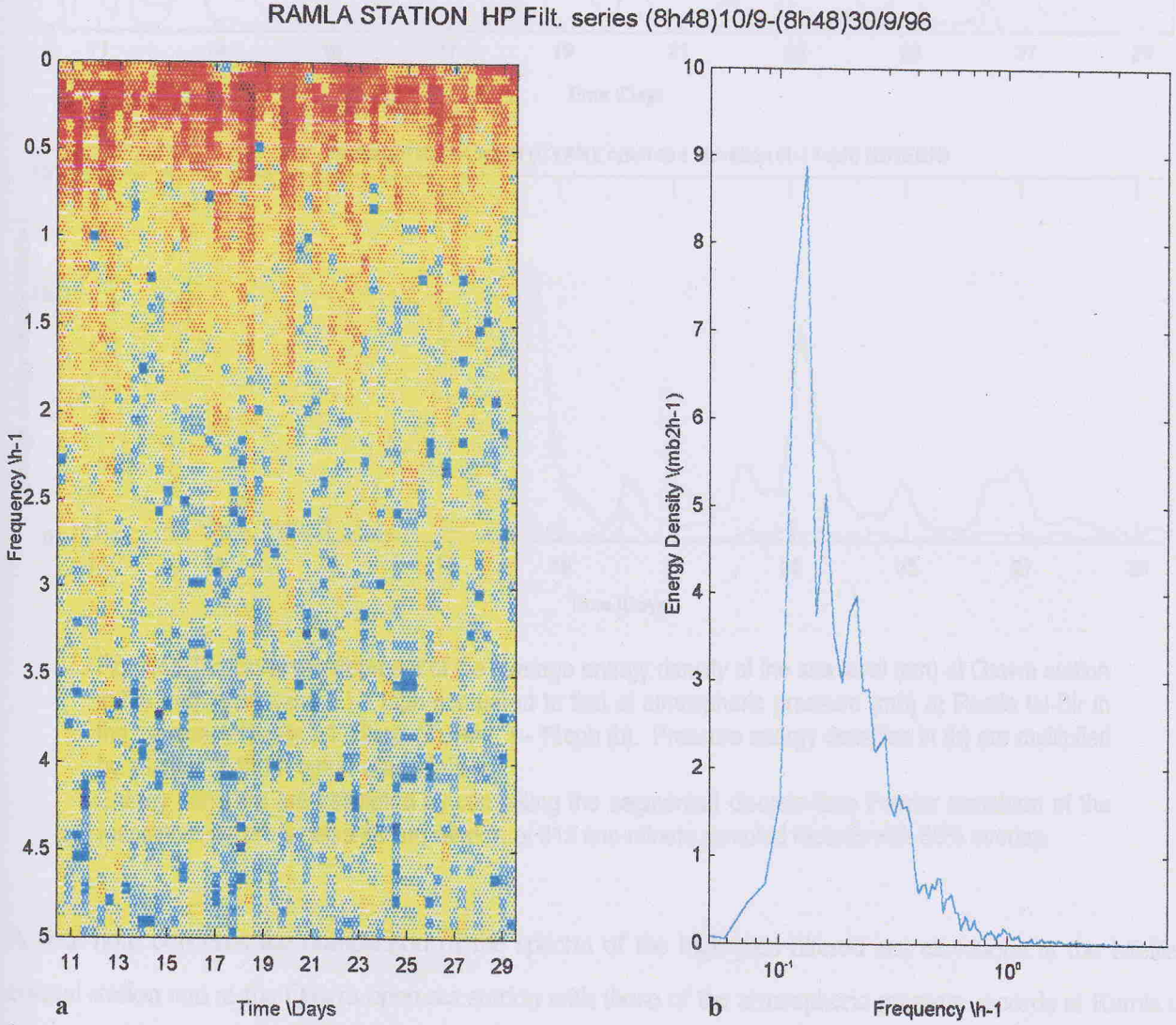

Fig. 4.44 (a) Spectrogram fluctuations calculated over 50% overlapping data segments of 512 records each, and (b) spectrum calculated with 54 degrees of freedom and a 95% confidence factor of 3.3dB (B_{min} = 0.7; B_{max} = 1.5), of the high-pass filtered atmospheric pressure at Ramla tal-Bir station for the period (08h50)10/9/96 - (11h54)30/9/96.

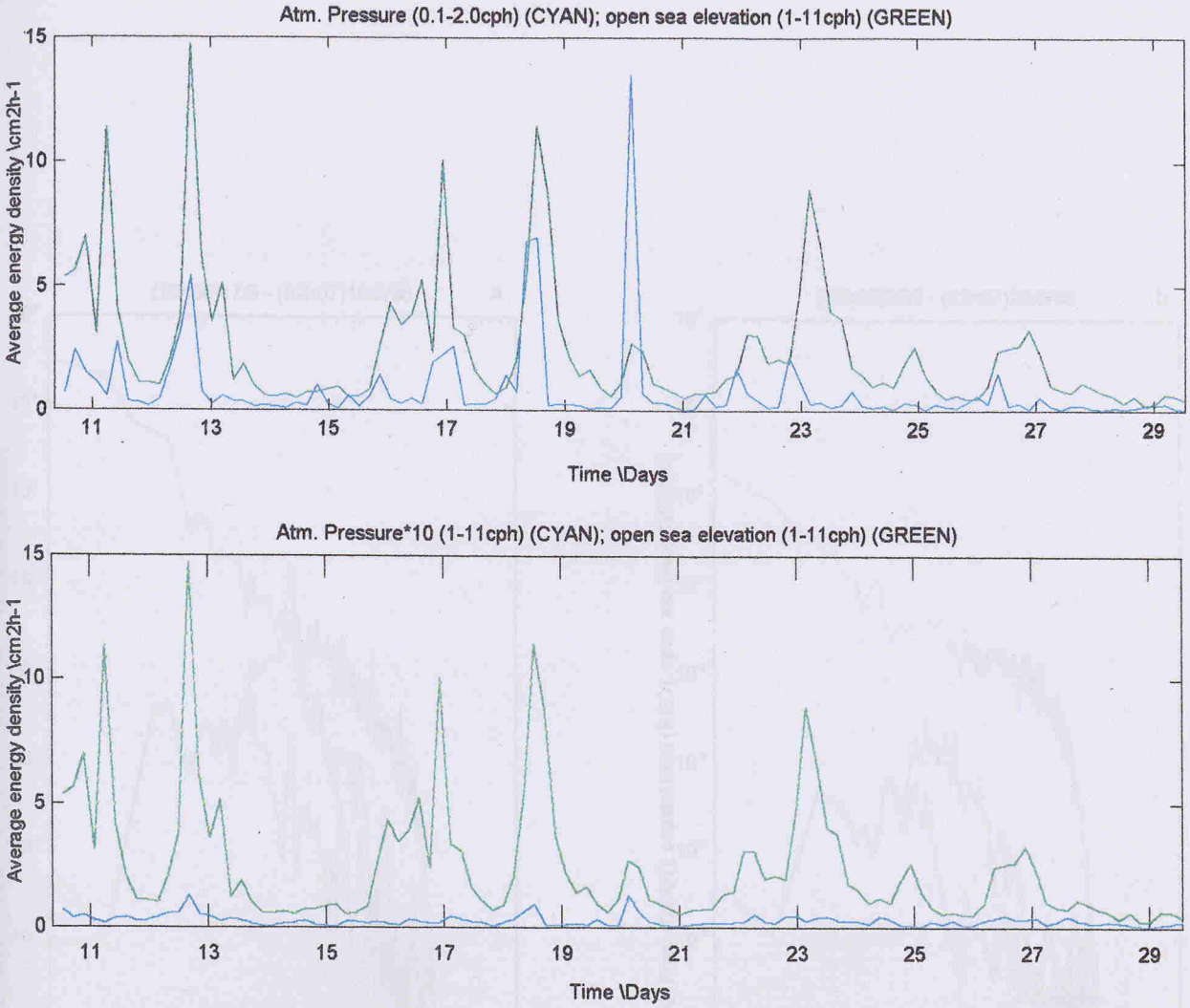

Fig. 4.45 Temporal development of the average energy density of the sea level (cm) at Qawra station in the frequency band 1 - 11cph compared to that of atmospheric pressure (mb) at Ramla tal-Bir in the frequency bands 0.1 - 2cph (a), and 1 - 11cph (b). Pressure energy densities in (b) are multiplied by a factor of 10 for better visualisation.
Energy densities are estimated by computing the segmented discrete-time Fourier transform of the respective signals using a sliding window of 512 one-minute sampled records with 50% overlap.

A final note concerns the comparison of the spectra of the high-pass filtered sea elevations at the Mellieha coastal station and at the Qawra open sea station with those of the atmospheric pressure records at Ramla tal-Bir for equal respective periods from (i) (16h00)17/9/96 to (02h07)19/9/96 during a seiche event (Fig. 4.46a), and (ii) (16h00)27/9/96 to (02h07)29/9/96 during background oscillations (Fig. 4.46b). The direct correlation between the atmospheric pressure and the sea level is confirmed to be below the significant level even during the seiching period (Fig. 4.47). Apart for their differences in energy (at least an order of magnitude higher

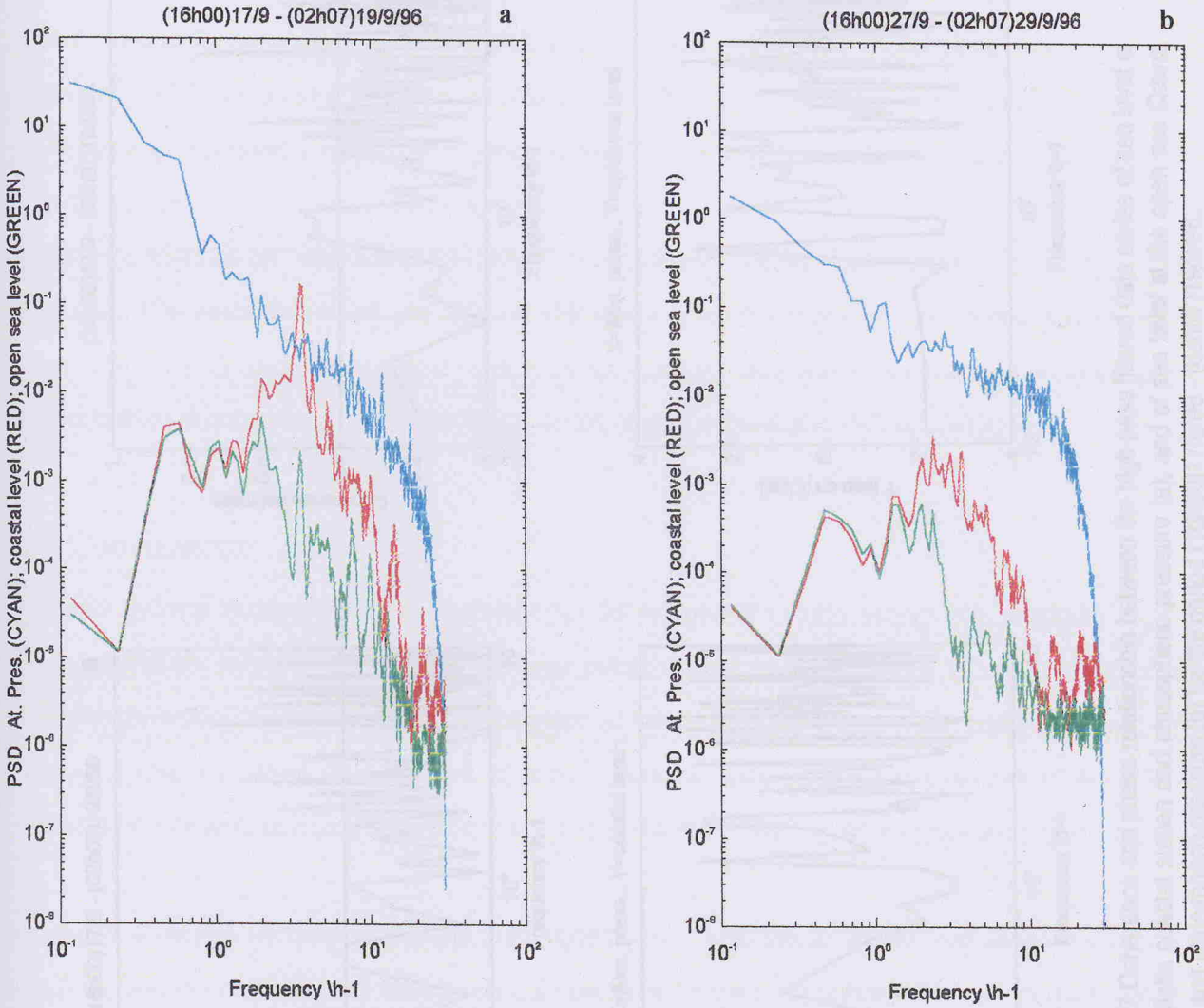

Fig. 4.46 Comparative spectra of high-pass filtered data series of sea level (m) at the Mellieha coastal station (red), sea level at the Qawra open sea sation (green), and atmospheric pressure (mb) at Ramla tal-Bir for the periods (a) (16h00)17/9/96 - (02h07)19/9/96 during a seiche event, and (b) (16h00)27/9/96 - (02h07)29/9/96 during background oscillations.
Spectrum for sea level is in m^2/cph; spectrum for atmospheric pressure is in mb^2/cph.
The 95% confidence factor, for 14 d.o.f. is 7.1dB (B_{min} = 0.54; B_{max} = 2.8).

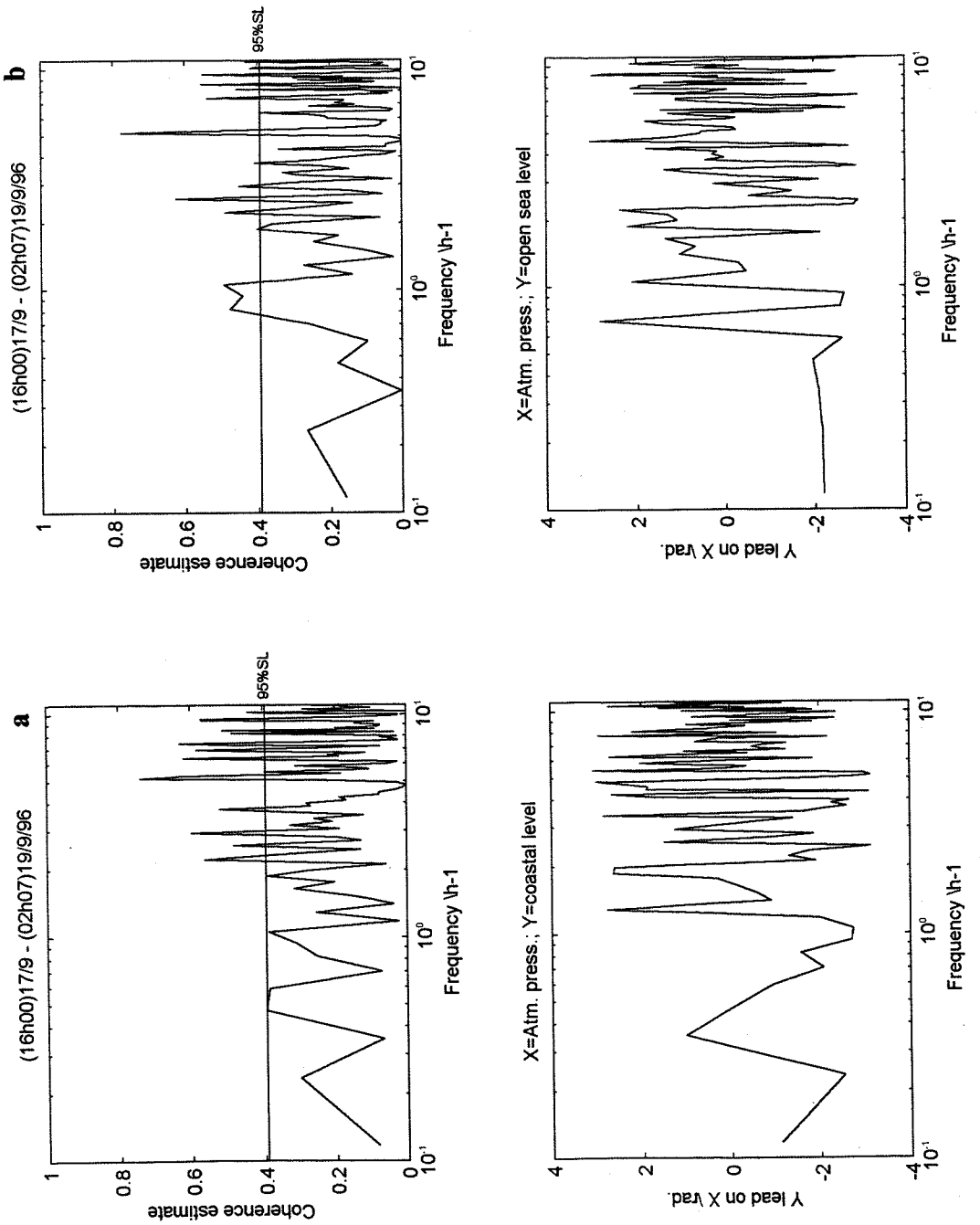

Fig. 4.47 Coherence and phase relationship between the high-pass filtered data series of sea level at the Mellieha coastal station and atmospheric pressure (a), and of sea level at the open sea Qawra Station and atmospheric pressure (b) for the period (16h00)17/9/96 - (02h07)19/9/96. The 95% confidence level of γ^2 is 0.393.

during seiching), the sea level spectra show that waves in the frequency range of 2 - 11cph undergo, as expected, the same amplification process upon reaching the embayment. These characteristics are determined by the topographic features of the coastal area. There is however a remarkable difference in the atmospheric pressure spectral shapes. During the 'quite' period the atmospheric energy density fits closely an inverse power relationship ($\approx \omega^{-1.2}$) with frequency. On the other hand the spectral slope is much steeper during the active period and a $\omega^{-2.0}$ power relationship is followed, which better agrees with results generally observed in the atmosphere. Most importantly it is noted that the open sea level spectrum follows in parallel to these changes in the frequency dependence of the atmospheric energy. This implies that the response of the sea to the atmosphere has a strong local component and occurs over a broad band of frequencies. When this band of frequencies matches the eigen-characteristics of a coastal area the response of the water body is greatly amplified. This interaction of the sea with the atmosphere is moreover present even during periods of lower levels of activity. Although background oscillations are generally attributed to remote long wave activity, the local effect of the atmosphere appears to be also an important component in their occurrence.

4.7 Conclusions

The data analysed in this chapter has confirmed that the occurrence of large seiches (the '*milghuba*' waves) in the northwestern coast of Malta are to a large extent caused by the presence of atmospheric pressure disturbances which travel in the lower troposphere as trapped gravity waves. The main advantage of the analysis is that it is based on a long set of densely sampled, simultaneous measurements of sea level and atmospheric pressure, including observations in the open sea and on land by an array of barographs.

Although a definite correlation between time variations of atmospheric activity and longwave intensity is testified, there is an unexpected lack of spectral coherence between the atmospheric and the long period sea waves. The amplitude of the sea level oscillations tends to be higher in relation to the strength of atmospheric disturbances which generate them, but this is not always the case. The heights of seiches generated by disturbances with similar intensities can be very different. Moreover different nearby coastal areas may respond differently to the same atmospheric disturbance. The energy transfer between the atmosphere and the sea is thus far from trivial and involves an interplay of several conditions. This is investigated by analysing a number of seiche events in terms of their relation to atmospheric wave properties. Spatial coherence of the atmospheric

waves over a wide band of frequencies is a necessary prerequisite. In particular the coherence at the higher frequencies is observed to increase during seiche intensification periods. The propagation of atmospheric waves parallel to the direction of maximum bathymetric gradients and the matching of their phase speeds with that of long waves in the adjacent open sea areas appear also to be other important factors.

Furthermore the spectral energy content of the pressure disturbance strongly dictates the nature of its interaction with the sea surface. The additional energy is mainly in the frequency band 0.1 - 2cph and decreases rapidly with frequency. The air-sea coupling does not appear to be related to any particular single frequency. Although the atmospheric energy content at the resonant eigenfrequencies can enhance seiche amplitudes by a direct resonance mechanism, this energy is in general too small for this factor to be a prevailing one. When in action this interaction involves a larger water body than that of the bay itself and includes the adjacent shelf areas. A wide-band frequency coupling is thus proposed in which the effectiveness of seiche generation depends on the distribution of atmospheric energy at a band of frequencies, in particular from 0.1 - 2cph, rather than on the total energy of the atmospheric distrubances.

The air-sea interaction appears also to be characterised by an energy redistribution process which occurs both in the atmosphere and in the sea. An energy 'pumping' process is proposed to be in action whereby energy is channelled to a preferred band of frequencies both from the higher and the lower frequencies. Cases of extraordinary seiches in embayments result when the eigenfrequencies coincide to this preferred frequency band. This 'pumping' of energy can occur by a number of mechanisms. Non-linear interactions such as that of gravity waves during intense events typify the transfer of energy from higher frequency and smaller scale motions to lower frequency and larger scale movements. The lower frequency resonances generated on the shelf can trigger and sustain the more localised resonant seiches in coastal areas representing a case in which the transfer of energy is in the opposite direction, that is towards higher frequencies.

The most common synoptic-scale environment within which mesoscale atmospheric waves generated by dynamic instability, can be maintained for several cycles is found to be characterised by a low and strong inversion and a nearly unstable, strongly sheared and very dry layer above it. The vertical wind shear is often associated with a jet streak in the upper troposhere, which can furnish by a geostrophic adjustment process an alternative source of energy for the atmospheric waves. Atmospheric activity is also frequent prior to the

passage of frontal systems. It is thus no coincidence that local fishermen link the *'milghuba'* to a forecast of northwesterly winds. Energetic seiches however occur also during the summer months when they are more rare and of shorter duration, often consisting only of a few oscillations. Although occurring during periods of fine weather, these seiches are again associated with the presence of strong transient pressure disturbances.

The same atmospheric pressure forcing mechanisms appear to be in place over a wide range of levels of activity. Although the nature of the interaction is complex there seems to be a uniformity spanning from the most extreme events to the lowest amplitude 'background' oscillations. Other sources of energy are however not excluded. Some seiching events which cannot be related to atmospheric pressure variations are instead attributed to rapid excursions of the wind vector. During 'quiet' periods the effect of atmospheric pressure forcing is low and the oscillations are predominantly characterised by these alternative sources; these include effects by the wind, wind waves, internal waves as well as by long waves incident from remote regions.

The results of this chapter have again confirmed the two-way mechanism by which the coastal sea level responds to signals generated in the open sea. In particular it is seen that the different reaction in different basins to similar forcing demonstrates a significant influence of the local topography. In the next chapter numerical model applications are used to simulate the dynamics of the seiches in coastal embayments and their forcing by the open sea long wave field.

5. Seiche dynamics in coastal embayments

5.1 General aims and description

The study of the response of Mellieha Bay and St. Paul's Bay to offshore disturbances is made by using a high-resolution numerical depth-averaged model. The two embayments are in close proximity to one another and their oscillations are mutually inter-dependent. They also present a case of wide-open mouthed bays that are not easy to model. Contrary to the case of narrow-mouthed bays and harbours, there are only a limited number of numerical studies concerning embayments with a wide connection to the open sea, for example Nakamura (1987) and Rabinovich & Monserrat (1998). These applications utilise the linear two-dimensional shallow-water equations.

In this study the more robust Princeton Ocean Model developed by Blumberg & Mellor (1987) is utilised. This is a primitive equation, finite difference, time-dependent, and free surface coastal ocean circulation model. The model is here applied in two-dimensional form and non-linear terms in the momentum equations are retained. The study is intended to obtain a dynamical understanding of the seiche oscillations that can be supported in these two adjoining coastal embayments. The seiche-induced currents are comparable to the circulation caused by the direct influence of the wind, and they thus play an important role in the flushing of the embayments. The dependence of the resonant periods and the admittance function on the coastal geometry, bay and shelf bathymetry, as well as on bay orientation with respect to the incident disturbances are assessed. The results of these numerical model experiments are compared with observations. They essentially explain the non-linear behaviour of the bay response to long waves propagating in the open sea, and supply further insight on the possible triggering by atmospheric disturbances.

5.2 Model application

5.2.1 Model domain

The domain consists of the two small coastal embayments, Mellieha Bay and St. Paul's Bay, and the stretch of open sea in the immediate vicinity of the embayments (Fig. 5.1). The two embayments cover a total area of about 5 Km^2 with a average depth of 25m in each. The open sea area measures 4.8 Km in the offshore direction

and 7.2Km alongshore. The bottom topography is complicated by a comparatively extensive bank which shallows to less than 20m depth. The 3-D view of the bottom topography (Fig. 5.2b) depicts the steep gradients on the promontaries, and the comparatively deeper water basin confined between the two embayments and the bank. Beyond this bank the depth contours are fairly uniform in the alongshore direction and follow the general ESE alignment of the islands. The maximum depth at the northernmost point of the domain is 70m.

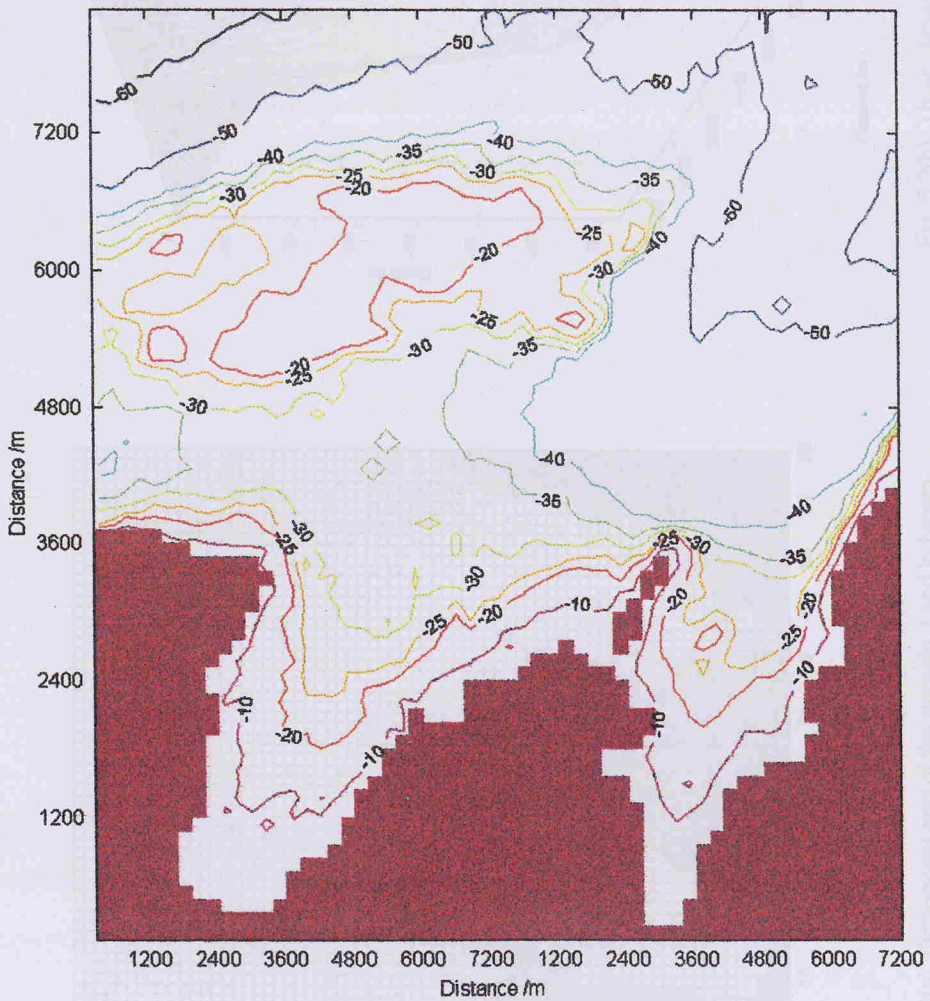

Fig. 5.1 Bathymetric contour map of the modelled area.

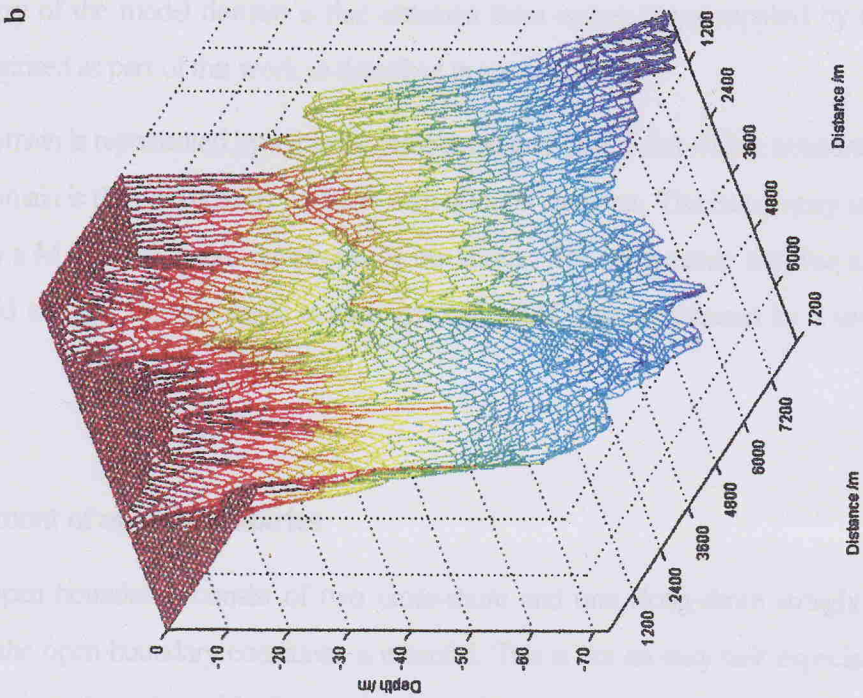

Fig. 5.2(b) Three-dimensional view of the bottom topography.

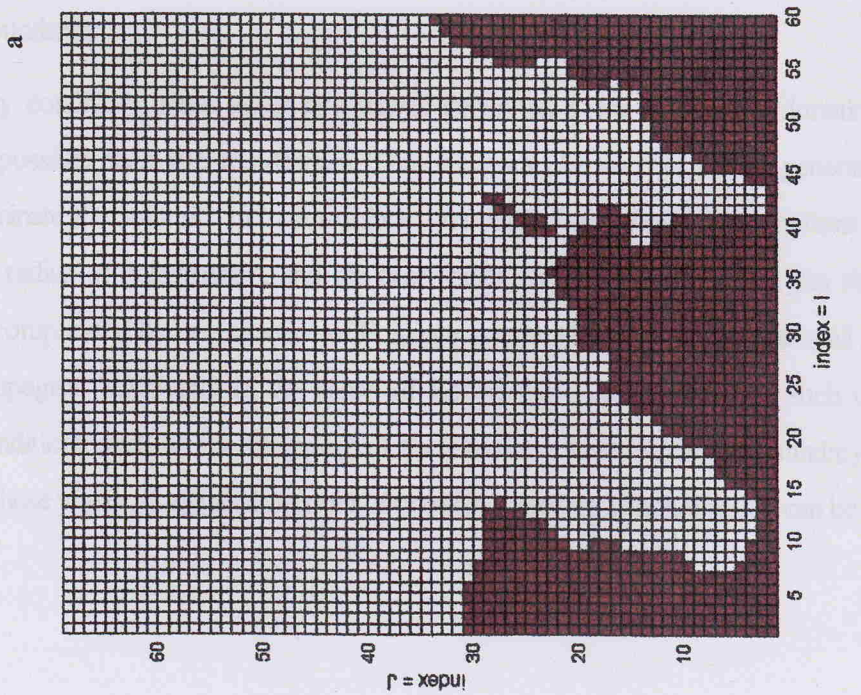

Fig. 5.2(a) Orthogonal grid of the domain. Land in brown.

5.2.2 Model bathymetry and grid

The bathymetry of the model domain is that obtained from survey maps supplied by the UK Hydrographic Office, and digitised as part of this work as described in section 3.4.1.

The model domain is represented by a regular orthogonal grid (Fig. 5.2a) with a horizontal resolution of 120m. The whole domain is thus covered by a matrix with 60 x 69 elements. The bathymetry is sub-sampled onto the model grid by a MATLAB macro developed by the author. The bathymetric data has a higher resolution than the model grid and the average depth at each grid cell could thus be obtained by a simple weighted average procedure.

5.2.3 Treatment of open boundaries

The model open boundaries consist of two cross-shore and one along-shore straight segments. A proper treatment of the open boundary conditions is essential. This is not an easy task especially in applications with more than one open boundary. Ideally one should apply a larger model domain with subsequent nesting to the higher resolution model. Such a modelling effort would however require a robust computational setup and is beyond the scope of the present work. A solution is thus sought with the most appropriate conditions on the three open boundaries.

The boundary conditions must allow any waves generated inside the model domain to exit with as little reflection as possible back into the domain. They must also be such as not to generate any spurious effects which contaminate the solution. In high resolution models where alongshore variations are of the order of or less than the radius of deformation, and the time scales are of the order of or less than 1/f, the problem is furthermore complicated by the presence of Poincare' waves which can propagate in all directions. They can in particular propagate 'backward' in the sense of Kelvin wave propagation. In such circumstances ordinary boundary conditions such as the clamping of the elevation at an upstream boundary will lead to spurious reflection of these waves. A detailed account of possible boundary conditions that can be used is given in section 5.4.3.

5.3 Description of the Princeton Ocean Model

5.3.1 Model equations

The numerical model is adapted from the Princeton Ocean Model (POM) and is used to simulate the forcing inside the embayments due to relatively high frequency sea level seiche oscillations incident from the open sea. The model is used in a version for application to 2-D depth-averaged non-linear horizontal flow.

The basic equations are the shallow water equations. Suppose that an orthogonal Cartesian co-ordinate system is adopted with x increasing eastward, y increasing northward and z increasing vertically upwards. The free surface is then located at $z=\eta(x,y,t)$ and the bottom is at $z=-H(x,y)$. If $\vec{u}$ is the horizontal velocity vector with components (u,v), $\rho(x,y,z)$ is the in situ density and ∇ is the horizontal gradient operator, the continuity equation is:

$$\rho_t+\nabla.(\rho\ \vec{u})=0 \tag{5.1}$$

where the subscript x denotes partial differentiation with respect to the x-coordinate. For a system with no sources of mass and for which the density gradient terms ρ_x , ρ_y , ρ_z can be neglected unless multiplied by the gravitational acceleration term g , and (5.1) reduces to:

$$\nabla.\vec{u}+w_z=0 \tag{5.2}$$

The Reynolds momentum equations are:

$$u_t+\vec{u}.\nabla u+wu_z-fv=\frac{-p_x}{\rho_o}+\left(K_M\,u_z\right)_z+F^{(x)} \tag{5.3}$$

$$v_t+\vec{u}.\nabla v+wv_z+fu=\frac{-p_y}{\rho_o}+\left(K_M\,v_z\right)_z+F^{(y)} \tag{5.4}$$

where, ρ_o is the reference density, K_M is the vertical eddy diffusivity (vertical kinematic viscosity) of turbulent momentum mixing, f is the Coriolis parameter and p is the pressure at depth z , expressed by

$$p=P_{atm}+\rho_0\,g\eta+g\int_z^0\rho\,(x,y,z',t)dz' \tag{5.5}$$

and P_{atm} is the atmospheric pressure. Subgrid scale processes that are not resolved by the model grid are represented by the terms $F^{(x)}$ and $F^{(y)}$ and can be parametrised in terms of the horizontal diffusivity (horizontal kinematic viscosity in m^2s^{-1}) A_M according to:

$$F^{(x)} = \left(2A_M u_x\right)_x + \left(A_M\left(u_y + v_x\right)\right)_y \tag{5.6a}$$

$$F^{(y)} = \left(2A_M v_y\right)_y + \left(A_M\left(u_y + v_x\right)\right)_x \tag{5.6b}$$

In the case where the free surface elevation and the volume transports are required it suffices to consider a 2D numerical simulation. Equations (5.2)-(5.4) are thus integrated over the depth thereby loosing the definition of all vertical structure. If $D = (H + \eta)$ is the instantaneous total depth and $UD = \int_{-H}^{\eta} u\, dz$, $VD = \int_{-H}^{\eta} v\, dz$ are the depth averaged horizontal fluxes, the equations of motion take the form:

$$\eta_t + (UD)_x + (VD)_y = 0 \tag{5.7}$$

$$(UD)_t + \left(U^2 D\right)_x + (UVD)_y - f\,VD + gD\eta_x - D\overline{F}_{(x)} = -\overline{wu}(surf) + \overline{wu}(bot) \tag{5.8}$$

$$(VD)_t + \left(V^2 D\right)_y + (VUD)_x + f\,UD + gD\eta_y - D\overline{F}_{(y)} = -\overline{wv}(surf) + \overline{wv}(bot) \tag{5.9}$$

where

$$D\overline{F}_{(x)} = \left(2A_M (UD)_x\right)_x + \left(A_M\left((UD)_y + (VD)_x\right)\right)_y \tag{5.10a}$$

$$D\overline{F}_{(y)} = \left(2A_M (VD)_y\right)_y + \left(A_M\left((UD)_y + (VD)_x\right)\right)_x \tag{5.10b}$$

$-\overline{wu}(surf) = K_M U_z|_{z=\eta} = \frac{\tau_{ox}}{\rho_o}$ and $-\overline{wv}(surf) = K_M V_z|_{z=\eta} = \frac{\tau_{oy}}{\rho_o}$ are the wind stress components at the free surface,

$-\overline{wu}(bot) = K_M U_z|_{z=-H} = \frac{\tau_{bx}}{\rho_o}$ and $-\overline{wv}(bot) = K_M V_z|_{z=-H} = \frac{\tau_{by}}{\rho_o}$ are the bottom stress components at the seabed. $\vec{\tau}_o = (\tau_{ox}, \tau_{oy})$ is the surface wind stress vector, and $\vec{\tau}_b = (\tau_{bx}, \tau_{by})$ is the bottom frictional stress.

All density variations are neglected since their effect on water elevation and phase are negligible (Blumberg, 1977).

5.3.2 Finite Difference Formulation

The governing equations form a set of simultaneous partial differential equations which can only be solved by numerical computation methods using discretised equations on a grid. A finite difference is used with grid space increments of Δx and Δy along the Cartesian axes. The staggered Arakawa C grid is employed in which $\eta_{i,j}$ and $D_{i,j}$ are defined at the centre of the grid cell (i, j), while the east-west, $U_{i,j}$, and the north-south, $V_{i,j}$, velocity components are respectively placed at distances $\Delta x / 2$ and $\Delta y / 2$ to the east and south of $\eta_{i,j}$. This type of grid is very effective for high resolution models (Batteen & Han, 1981). The coastal boundaries of the domain are chosen such that a north-south boundary coincides with the U points, and an east-west boundary coincides with the V points.

The leapfrog technique is used for time stepping while the terms involving spatial gradients are centre differenced. The diffusion terms are evaluated at the previous time level in order to avoid computational instabilities.

To write equations (5.7)-(5.10) in finite difference form, it is best to define the following sum and difference operators:

$$\overline{F(x,y,t)}^{(x)} = \frac{F\left(x+\frac{\Delta x}{2},y,t\right)+F\left(x-\frac{\Delta x}{2},y,t\right)}{2}$$

$$\delta_{(x)}[F(x,y,t)] = \frac{F\left(x+\frac{\Delta x}{2},y,t\right)-F\left(x-\frac{\Delta x}{2},y,t\right)}{\Delta x} \qquad (5.11a,b)$$

Hence

$$\delta_{(x)}\overline{F(x,y,t)}^{(x)} = \frac{F(x+\Delta x,y,t)-F(x-\Delta x,y,t)}{2\Delta x} \qquad (5.11c)$$

and upon applying the commutative and distributive properties

$$\overline{F(x,y,t)}^{(x,y)} = \overline{\overline{F(x,y,t)}^{(x)}}^{(y)} = \overline{\overline{F(x,y,t)}^{(y)}}^{(x)} \qquad (5.11d)$$

F is here representing any function of the discrete variables $x, y,$ and t. Similar operators are defined for variables y and t.

Equations (5.7)-(5.10) can thus be expressed in finite difference form as follows for the continuity equation:

$$\frac{\eta^{n+1}-\eta^{n-1}}{2\Delta t}+\delta_{(x)}\left(\overline{D}^{(x)}U\right)+\delta_{(y)}\left(\overline{D}^{(y)}V\right)=0 \qquad (5.12)$$

and for the momentum equations:

$$\frac{\left(\overline{D}^{(x)}U\right)^{n+1}-\left(\overline{D}^{(x)}U\right)^{n-1}}{2\Delta t}+\delta_{(x)}\left(\overline{\overline{D}^{(x)}U}^{(x)}\overline{U}^{(x)}\right)+\delta_{(y)}\left(\overline{\overline{D}^{(y)}V}^{(x)}\overline{U}^{(y)}\right)-f\overline{\overline{V}^{(y)}D}^{(x)}$$

$$+g\overline{D}^{(x)}\delta_{(x)}\eta-\overline{F_{(x)}}^{n-1}=-\overline{wu}(surf)+\overline{wu}(bot) \qquad (5.13a)$$

$$\frac{\left(\overline{D}^{(y)}V\right)^{n+1}-\left(\overline{D}^{(y)}V\right)^{n-1}}{2\Delta t}+\delta_{(x)}\left(\overline{\overline{D}^{(x)}U}^{(y)}\overline{V}^{(x)}\right)+\delta_{(y)}\left(\overline{\overline{D}^{(y)}V}^{(y)}\overline{V}^{(y)}\right)+f\overline{U^{(x)}D}^{(y)}$$

$$+g\overline{D}^{(y)}\delta_{(y)}\eta-\overline{F_{(y)}}^{n-1}=-\overline{wv}(surf)+\overline{wv}(bot)$$

(5.13b)

where the cumbersome but straightforward formulation of the horizontal viscosity and diffusion is intentionally omitted. The finite difference equations presented above are second order accurate in space and time and conserve energy and momentum.

5.3.3 Stability constraints

The separation of solutions at odd and even time steps introduced by the leapfrog timestep is removed by applying a weak filter (Asselin, 1972). The filter smooths the solution at each time step according to:

$$F_s^n=F^n+\frac{\alpha}{2}\left(F^{n+1}-2F^n+F_s^{n-1}\right),$$

where $\alpha=0.05$ and F_s is a smoothed solution. This technique introduces less damping than either the Euler-backward or forward stepping techniques (Blumberg & Mellor, 1987).

In practice a non-zero horizontal diffusivity A_M is required in order to suppress any small scale computational noise from leading to numerical instability of the model.

5.4 Formulation of the boundary conditions

Appropriate conditions have to be applied to the field equations (5.8)-(5.10) at the boundaries of the computational domain.

5.4.1 Surface and bottom boundaries

At the free surface, the momentum flux by the wind is formulated by:

$$\left[\overline{wu}(surf),\overline{wv}(surf)\right]=-\frac{\vec{\tau}_0}{\rho}=-C_D|\vec{W}|\vec{W} \qquad (5.14)$$

where $\vec{W}$ is the wind vector, and C_D is a drag coefficient.

At the bottom, the 'no slip' condition can be applied and the velocity may be put equal to zero at a height z_o from the seabed, where z_o is the local bottom roughness. The bed shear may alternatively be determined by matching velocities with the logarithmic law of the wall. The velocity at the bottom boundary layer is thus assumed to follow the logarithmic distribution for turbulent flow

$$\vec{U}(z = \Delta z - H) = \frac{\vec{\tau}_b}{\kappa u_{tb}} \ln(\Delta z / z_o) \tag{5.15}$$

where κ is the von Karman constant and u_{tb} is the friction velocity associated with the bottom frictional stress $\vec{\tau}_b$. Specifically, this means that the bed friction is formulated upon a quadratic dependence of bottom drag given by

$$[\overline{wu}(bot), \overline{wv}(bot)] = -\frac{\vec{\tau}_b}{\rho} = -\lambda |\vec{U}_b| \vec{U}_b \tag{5.16}$$

where $\lambda = \dfrac{\kappa^2}{[\ln\{(H + z_b) / z_o\}]^2}$.

z_b and $\vec{U}_b$ are the grid point and corresponding velocity in the grid point closest to the bottom. In the 2D mode $\vec{U}_b$ is taken as the depth averaged velocity. The value of κ is taken to be 0.4; the value of 0.01m is adopted for z_o.

5.4.2 Closed boundaries

At the coastal perimeter with no inflow or outflow the normal component of the volume fluxes *UD* and *VD* is suppressed. In POM these lateral boundary conditions are handled automatically by the land and sea masks. The landward tangential velocities in the horizontal friction terms are also set to zero by these masks.

5.4.3 Open boundary conditions (OBCs)

The open boundary is a fictitious border connecting the computational domain to the open sea. This boundary is indispensable for reasons of computational economy, but it is often problematic to specify adequate conditions

on it which are both physically and numerically valid. A most convenient condition which is often adopted is one which allows the free radiation to the open sea, without back reflection, of any signal reaching the open boundary from inside. Details on open boundary conditions are treated in the next section.

5.4.4 Formulation of open boundary conditions

An ideal open boundary condition is one which renders the computational boundary transparent to disturbances originating in the interior of the regular domain without disturbing or deteriorating the interior solution (RØed & Cooper, 1986). Along an open boundary the solution is unknown and must be assumed or extrapolated from the interior solution. The optimal formulation of the open boundary conditions is even more important in the present application which presents one alongshore and two cross-shore open boundaries which are necessary to limit the extent of the domain in the open sea. The present work is not directly intended to test OBC performance. Nonetheless a number of OBCs were tested in order to quantify the sensitivity of the simulation results to the different OBCs. The testing of OBC performance could involve many permutations of different conditions with effects of different bottom frictions, different topographies, different open boundary location as well as grid size and time step. The performance may indeed vary from one coastal model to another so that an OBC may be tailored to fit one application, but may not necessarily perform equally well in a different model (Chapman, 1985). The testing was thus restricted to one simple domain consisting of a narrow channel closed at one end and connected to an open stretch of sea with the same depth. The domain is forced from the north by a regular sinusoidal signal with a frequency close to the fundamental mode of the channel. Model outputs are then compared.

5.4.4.1 Comparison of open boundary conditions

The applied OBCs are basically all derived from the radiation condition which for a variable ϕ is defined by:

$$\frac{\partial \phi}{\partial t} \pm c^* \frac{\partial \phi}{\partial n} = 0 \qquad (5.17)$$

and describes the advection of a disturbance through the boundary at a phase speed of c* normal to the boundary. The variable ϕ can be taken as the elevation or velocity. The upper/lower sign applies to an eastern/western boundary. Following Miller & Thorpe (1981), the condition is expressed in numerical form by using a forward-in-time, upstream differencing:

$$\phi_B^{N+1} = \phi_B^N - \left(\frac{c^* \Delta t}{\Delta n}\right)\left(\phi_B^N - \phi_{B\mp1}^N\right) \qquad (5.18)$$

where N denotes the time level, B is the boundary grid point, B∓1 is one grid point in from the boundary and Δn is the grid spacing normal to the boundary.

The proper choice of c* will minimise the reflection of the disturbance back into the domain. In common model applications the governing equations are non-linear and complex so that c* is not known a priori. In such circumstances the classical gravity wave Sommerfeld radiation condition (Sommerfeld, 1949), with a fixed phase speed $c^* = \sqrt{gH}$, is not adequate. Heaps (1973) expressed the gravity wave radiation condition in terms of the depth-averaged velocity U normal to the boundary and the elevation η as

$$U \mp \eta \sqrt{g / H} = 0 \qquad (5.19)$$

which allows the propagation of energy outwards from the interior of the model domain in the form of simple progressive waves. This condition has been widely used in barotropic ocean models.

Orlanski (1978) first proposed the 'floating phase speed' method in which c^* is determined every time step by measuring the phase speed of disturbances just prior to their encounter with the boundary. Thus $c^* = \mp\left[\frac{\partial \phi / \partial t}{\partial \phi / \partial n}\right]_{B\mp1,N-1}$ is evaluated by using the solution from a previous time step and one grid point inside the boundary B. The value of c^* is restricted to remain within the range $0 \le c^* \le \Delta x/\Delta t$. When $c^* < 0$ at a western boundary (or $c^* > 0$ at an eastern boundary), c^* is set equal to zero so that the boundary condition does not use information outside the integration domain and information is inhibited from entering the domain. For stability reasons an upper bound on the value of c^* is also necessary.

In the Implicit Orlanski Scheme, c^* is expressed by

$$c^* = \frac{\Delta n}{\Delta t} \frac{\phi_{B\mp1}^{N-1} - \phi_{B\mp1}^{N+1}}{\phi_{B\mp1}^{N+1} + \phi_{B\mp1}^{N-1} - 2\phi_{B\mp2}^{N}}, \text{ and}$$

$$\phi_B^{N+1} = \left[\frac{1-\mu}{1+\mu}\right]\phi_B^{N-1} + \left[\frac{2\mu}{1+\mu}\right]\phi_{B\mp1}^{N} \qquad (5.20)$$

$$\text{where } \mu = \begin{cases} 1 & \text{if} \quad c^*\Delta t/\Delta n \geq 1 \\ c^*\Delta t/\Delta n & \text{if} \quad 0 < c^*\Delta t/\Delta n < 1. \\ 0 & \text{if} \quad c^*\Delta t/\Delta n \leq 0 \end{cases}$$

An alternative choice when $c^* > 0$ is to put $\mu = 1$ (Camerlengo & O'Brien, 1980) or $\mu = (\Delta t/\Delta n)\sqrt{(gH)}$ so that only the extreme values of phase speed are used. Mathew et. al (1996) further propose the use a modified form of the Heaps radiation condition with the phase speed specified by the Orlanski method. This condition was found to be particularly effective at an off-shore open boundary in the numerical simulation of open coast surges.

Miller & Thorpe (1981) suggest several other schemes of higher order accuracy to calculate c^*. In particular, they formulated a forward in time method that has an optimised truncation error and uses fewer time levels according to:

$$c^* = \frac{\Delta n}{\Delta t}\frac{\phi_{B\mp1}^{N} - \phi_{B\mp1}^{N-1}}{\phi_{B\mp2}^{N-1} - \phi_{B\mp1}^{N-1}}, \text{ and}$$

$$\phi_B^{N+1} = [1-\mu]\phi_B^{N} + \mu\phi_{B\mp1}^{N} \qquad (5.21)$$

This condition has been applied successfully in the formulation of the conditions at the three open sea boundaries of a reduced-gravity model of a bay (Greatbatch & Otterson, 1991).

5.4.4.2 Errors related to open boundary conditions

The use of open lateral boundary conditions is however accompanied by the generation of errors at the boundaries. The growth of these errors which propagate into the interior domain is attributed to the feedback of these enhanced disturbances to the boundaries and thus leading to a runaway error growth (Hedley & Yau, 1988). These errors are particularly problematic in limited area models. The origin of these errors lies in the

inaccurate estimation of c*. These errors are particularly large in the calculation of boundary tendencies when the horizontal gradients are very close to or equal zero. The fixed phase scheme leads to systematically overestimated values of c*. This can lead to a total loss of stability. The floating scheme overestimates c* as often as it underestimates it, but the asymmetry in the estimates leads to an overall underestimation which a consequential artificial reduction in the dynamics of the modelled domain (Klemp & Wilhelmson, 1978). Hedley & Yau (1988) reduce these errors by implementing a restriction on the lower bound of c*. When c* is less than a predetermined positive value c_{min} ($< \Delta n/\Delta t$), it is set equal to c_{min} . This implies that when c* is negative, its value is not set to zero, but is instead put equal to a minimum phase speed c_{min}. With this provision the boundary condition becomes a fixed phase type for slowly propagating disturbances, whereas the floating scheme is actually used for faster travelling disturbances. This hybrid scheme was found to be superior to the fixed and floating phase speed schemes particularly in the case of a severly truncated domain (Hedley & Yau, 1988).

5.4.4.3 Application of sponges

A boundary condition which has been found to be most transparent to waves consists of a sponge combined with a radiation condition (Israeli & Orszag, 1981). The sponge layer is a region of increasing bottom friction at the outer edge of the model domain, and its function is to damp out the waves and disturbances generated in the interior. The absorbing boundary can be applied by the Orlanski radiation condition at the outer edge of the sponge (Chapman, 1985). This kind of sponge has been found to be very effective in barotropic coastal models dealing primarily with wave propagation and no wind forcing. But the performance of a boundary condition may vary with the kind of model application and no single condition is expected to fare equally well in the separate applications. For example, Chapman (1985) reports that sponges are not an ideal choice in the case of domains forced by the wind.

5.5 Formulation of the friction term

In the original POM code the friction terms in the momentum equations are expressed by an explicit scheme. When the model is applied in 2D mode, the term $\lambda|\vec{U}|(U, V)$ is defined by $CBC * \sqrt{UAB^2 + VAB^2} * (UAB, VAB)$ where **CBC** is the Fortran variable assigned to λ , and

UAB, VAB are the depth averaged velocity components at $t - \Delta t$. According to Goto & Ogawa (1997) such a scheme can be a source of instability. An implicit scheme is thus adopted such that

$$\lambda|\vec{U}|(U, V) = CBC * \sqrt{UAB^2 + VAB^2} * \left(\frac{UAB + UAF}{2}, \frac{VAB + VAF}{2} \right) \quad (5.22)$$

where UAF and VAF are the depth averaged velocity components at $t + \Delta t$.

The finite difference formulation of this scheme is explained below.

In subroutine **ADVAVE**, the variable **WUBOT** is defined as follows:

```
WUBOT(I,J)=-0.5E0*(CBC(I,J)+CBC(I-1,J))*SQRT(UAB(I,J)**2
+(.25E0*(VAB(I,J)+VAB(I,J+1)+VAB(I-1,J)+VAB(I-1,J+1)))**2),
```

and similarly for **WVBOT**.

In each external integration **UAF** is subsequently calculated according to the **U**-momentum equation as follows:

```
      DO J=2,JMM1
      DO I=2,IM
      UAF(I,J)=ADX2D(I,J)+ADVUA(I,J)
     1  -ARU(I,J)*.25*( COR(I,J)*D(I,J)*(VA(I,J+1)+VA(I,J))
     2        +COR(I-1,J)*D(I-1,J)*(VA(I-1,J+1)+VA(I-1,J)) )
     3        +.25E0*GRAV*(DY(I,J)+DY(I-1,J))*(D(I,J)+D(I-1,J))
     4        *( (1.E0-2.E0*ALPHA)*(EL(I,J)-EL(I-1,J))
     4        +ALPHA*(ELB(I,J)-ELB(I-1,J)+ELF(I,J)-ELF(I-1,J)) )
     5        +DRX2D(I,J)
     6        +ARU(I,J)*( WUSURF(I,J)-(WUBOT(I,J)*(UAB(I,J)/2.0)) )
      ENDDO
      ENDDO
```

```
      DO J=2,JMM1
      DO I=2,IM
      UAF(I,J)=
     1     ((H(I,J)+ELB(I,J)+H(I-1,J)+ELB(I-1,J))*ARU(I,J)*UAB(I,J)
     2      -4.E0*DTE*UAF(I,J))
     3     /((H(I,J)+ELF(I,J)+H(I-1,J)+ELF(I-1,J))
     4      -(2.0*DTE*WUBOT(I,J)))*ARU(I,J)
      ENDDO
      ENDDO
```

where

H is the bottom depth;

EL is the surface elevation as used in the external mode;

ELF is the surface elevation at time $t + \Delta t$;

ELB is the surface elevation at time $t - \Delta t$;

DTE is the external time step;

ADVUA is the sum of the second, third and fifth terms in the U-momentum equation;

ADX2D is the vertical integral of the horizontal advection and diffusion terms;

DRX2D is the vertical integral of the x-component of the internal baroclinic pressure gradient;

COR is the Coriolis parameter;

ARU is the cell area centred on the variables **T**, **U** and **V**;

WUSURF is the momentum flux at the surface;

ALPHA (=0.225) is a constant used to weight average the sea level.

VAF is similarly calculated according to the **V**-momentum equation.

5.6 Model output visualisation

The model code is adapted in order to generate time series of the total kinetic energy in the domain **EKK**, of sea elevation **EL**, and the depth-averaged velocities **UA** and **VA** at selected points in the domain. The variation of **EKK** with time is important to assess the stability of the model and the manner it reaches steady state. The time series of the other variables is used for cross spectral analysis of the results.

The code also generates an output of **EL**, **UA** and **VA** over the full domain at selected times of integration. In order to visualise this output a MATLAB macro was developed. This macro automates the reading of the fields from the output file and generates synoptic maps of the domain with layers of the selected fields in an interactive manner. The plots include contours of elevation with an adjustable colour palette, 2D feather plots of the current vectors with adjustable scales.

5.7 Model application 1: Co-oscillation of an idealised narrow closed channel with the open ocean

In order to test the robustness and skill of the Princeton Ocean Model in simulating the propagation of long period waves in shallow coastal embayments, the 2D POM model (MODE=2) is first applied to several idealised model experiments with a known analytic solution.

The first experiment consists in the forced oscillation of a uniform narrow channel with the open sea. In general, a co-oscillation of an embayment with the open sea should be studied with (i) friction and other dissipative terms included; (ii) reflection at the closed end, and (iii) radiative damping at the opening. In this case the third factor is not included, the effect of the earth's rotation is neglected, dissipative terms are excluded and bed friction only is considered. The sea level oscillations in the embayment can thus be represented by the linear shallow water equations and have the character of a progressive wave. The effect of friction causes the abrupt change of phase of π radians at a displacement node to be replaced by a gradual change in phase.

In this particular example the channel is taken to have a length L of 3.18Km (along the y-axis), a width of 0.6 Km, is closed at one end (y = 0), and has a uniform depth of 40m. Although the analytical solution can considered to be one-dimensional, the numerical solution is obtained by treating the problem in two dimensions. The water elevation η is forced at the open end by a sinusoidal signal ($\eta\ (y = \mathrm{L}) = \eta_o\ e^{i\sigma t}$) with angular frequency σ and amplitude η_o .

5.7.1 Analytic solution

In a shallow domain the current intensity is expected to be almost uniform with depth, steep gradients developing only near the sea bed. The equations of motion can thus be simplified by integrating vertically. The non-linear terms are removed. Their exclusion does not modify the original harmonics, but account of double interactions and of net displacements out of oscillatory movements is lost.

The linearised depth-averaged long wave equations of motion are therefore adopted, namely:

$$\begin{aligned} \partial U/\partial t &= -g\,\partial \eta/\partial x - rU \\ \partial V/\partial t &= -g\,\partial \eta/\partial y - rV \\ \partial \eta/\partial t + H\partial U/\partial x + H\partial V/\partial y &= 0 \end{aligned} \qquad (5.23)$$

in which $\vec{U} = (U, V)$ is the depth averaged horizontal velocity field, **H(x,y)** is the depth, g the acceleration due to gravity, and the frictional terms are expressed by the linear friction coefficient **r**. The boundary conditions to be satisfied are:

$$\eta\,(y = L) = \eta_o \quad \text{and} \quad V(y = 0) = 0$$

CASE 1

In the case of a narrow channel with constant depth (i.e. $H(x, y) = h$), the resulting solution is:

$$\eta = \eta_o \frac{\cos[k'' y]}{\cos[k'' L]} e^{i\sigma t} \qquad (5.24a)$$

$$V = \frac{gk''\eta_o}{\sigma(1 - ir/\sigma)} \frac{\sin[k'' y]}{\cos[k'' L]} e^{i(\sigma t - \pi/2)} \qquad (5.24b)$$

where $k'' = \frac{\sigma}{\sqrt{gh}} \sqrt{(1 - ir/\sigma)}$.

CASE 2

In the case of a bathymetry with constant slope (i.e. $H(x, y) = \frac{y}{L} h_o$, where h_o is the depth at the open mouth of the channel), the solution is

$$\eta = \eta_o \frac{J_o(2s\sqrt{y})}{J_o(2s\sqrt{L})} e^{i\sigma t} \qquad (5.25a)$$

$$V = -i\eta_o \sqrt{\frac{g}{(1-i(r/\sigma))h_o}} \frac{J_1(2s\sqrt{y})}{J_o(2s\sqrt{L})} e^{i\sigma t} \qquad (5.25b)$$

where $s = \sigma\sqrt{\frac{L(1-i(r/\sigma))}{gh_o}}$ and J_o and J_1 are Bessel functions of the first kind with zero- and first- order respectively.

5.7.2 Numerical solution (case 1)

The grid cell is chosen with size 120m x 120m so that the computational domain, including the masked borders, is represented by a matrix with 7 x 31 elements (**IM** x **JM**). The basin is represented by a width of 5 and a length of 30 grid cells respectively. The code is adapted so that only the linear terms are retained. Two versions of the code are used with (i) an explicit and (ii) an implicit formulation of the friction terms as described in section 5.5. The linear friction coefficient is taken equal to 0.001. Model runs are also made without friction (**r** = 0). The horizontal diffusivity is taken to be zero. The forcing at the open boundary is specified by an elevation condition η=BC, where BC is a sinusoidal input signal with fixed period (**PER**) and amplitude (**AMP**). This open boundary condition is formulated by:

ELF(I, JM-1) = AMP*SIN(2.*PI*TIMES/PER)

ELF(I, JM) = ELF(I, JM-1)

VAF(I, JM) = VAF(I, JM-1)

UAF(I, JM) = 0

where **TIMES** is the time from start.

5.7.3 Results (case 1)

Model runs are conducted with forcing periods in near-resonant as well as non-resonant conditions. When the bed friction is taken into account, the explicit formulation of the friction terms gave consistently slightly lower amplitudes with respect to theory. The highest discrepancy of about 5% occurs near resonance. On the other

hand the results agree perfectly with theory when the implicit formulation is utilised. This formulation is henceforth retained in all model applications described in this study.

5.7.4 Numerical solution (case 2)

The same computational domain is used with **IM**=7, **JM**=31and same grid size as in case 1. The only difference is that the topography changes linearly along the channel. The depth at the head is 2m because of the staggered grid, while the depth at the mouth is 40m with **H(JM) = H(JM-1)**. Thus the bottom slope is constant and equal to $\partial h / \partial x = 1.36$ except at the head and mouth. For the analytical analysis, the bottom slope is however assumed constant over the whole channel with little imposed error. In all model runs the linear friction coefficient is taken as r = 0.001. The modes of oscillation of the basin are known from the turning points of $\eta = \eta(\sigma)$ in (5.25a). The gravest mode is at $T_0 \approx 900$s while the other resonances occur at T_1 slightly less than 400s, $T_2 \approx 250$s and $T_3 \approx 180$s. Model runs for co-oscillations in both near-resonant and non-resonant conditions are conducted.

5.7.5 Results (case 2)

Both the elevation and the along channel velocity are reproduced perfectly by the model at forcing periods away from resonance. Fig. 5.3a,b compares the simulated elevations with theory at the forcing periods of 800s and 200s respectively. The model results are presented (in green) as superimposed horizontal profiles of elevation taken every fixed number of integrations. The enveloping curves (in blue) give the theoretical maximum elevations at increasing distance from the closed end of the channel. These results show that the model description of the channel oscillations are satisfactory even at near-resonant frequencies.

5.8 Model application 2: Rectangular harbour coupled to the open sea

A domain consisting of a stretch of open coast interrupted by a harbour in the form of a narrow rectangular inlet (Fig. 5.4) is considered in this section. The inlet has a uniform depth H_1 with an unrestricted access to a semi-infinite non-rotating sea of constant depth H_2. It has length L along the x-axis and width W << L along the y-axis. The closed end is at x = 0, while the open end lies between the points (L,-W/2) and (L,+W/2). The open sea is represented by the semi-infinite plane x > L.

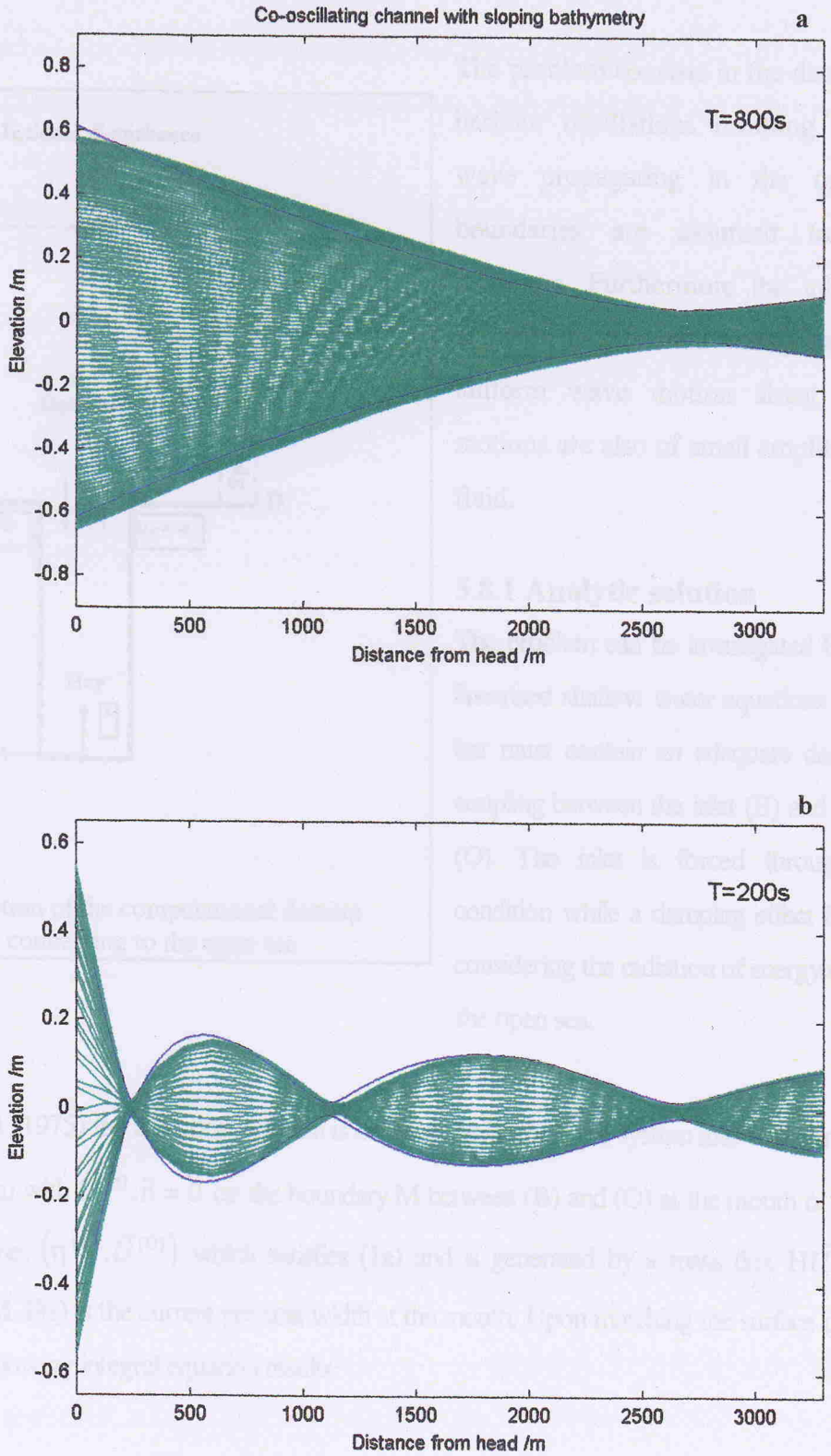

Fig. 5.3 Comparison of simulated (green) and analytical (blue) elevations for a co-oscillating narrow channel with sloping bathymetry. Simulated elevations are plotted every 4s. Theoretical elevations are plotted as maximal amplitudes.

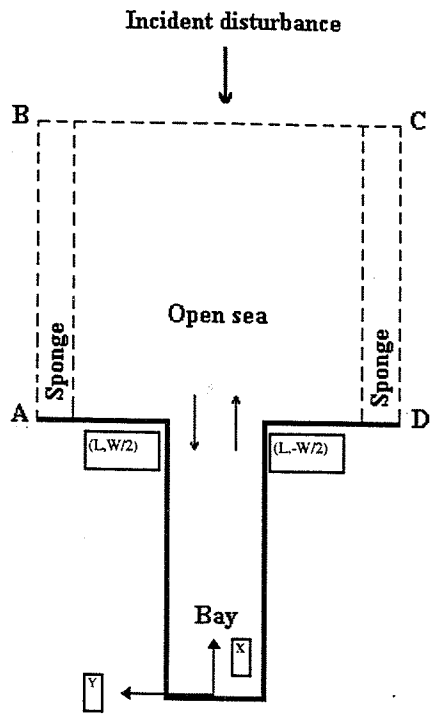

Fig. 5.4 Description of the computational domain for a bay connecting to the open sea

The problem consists in the description of the harbour oscillations resulting from a plane wave propagating in the open sea. All boundaries are assumed to be perfect reflectors. Furthermore the inlet entrance is assumed to be small enough as to ensure a uniform wave motion along it. All wave motions are also of small amplitude in an ideal fluid.

5.8.1 Analytic solution

The problem can be investigated by means of the linearised shallow water equations of motion (1a), but must contain an adequate description of the coupling between the inlet (B) and the exterior sea (O). The inlet is forced through a boundary condition while a damping effect is introduced by considering the radiation of energy from the inlet to the open sea.

Following Garrett (1975) the analytical solution is obtained by dividing the system into two parts: $(\eta^{[B]}, \vec{U}^{[B]})$ which satisfies (1a) with $\vec{U}^{[B]}.\vec{n} = 0$ on the boundary M between (B) and (O) at the mouth of the inlet as well as on the coastline; $(\eta^{[O]}, \vec{U}^{[O]})$ which satisfies (1a) and is generated by a mass flux $H\vec{U}^{[O]}.\vec{n} = F(s)$ at position s along M. F(s) is the current per unit width at the mouth. Upon matching the surface displacements at the mouth, the following integral equation results:

$$\int_M G_B(\mathbf{x},s)F(s)ds = \eta_O(\mathbf{x}) - \int_M G_O(\mathbf{x},s)F(s)ds \qquad (5.26)$$

where $G_B(\mathbf{x},s)$ and $-G_O(\mathbf{x},s)$ are the Green's functions describing the response, in B and O respectively, to a unit mass flux out of B across M at s. $\eta_O(\mathbf{x})$ is the wave field which would exist in the open sea in the absence of the harbour; the second term on the right of (5.26) is the response of the open sea , in the form of scattered waves, to the oscillating mass flow at the mouth.

The solution of (5.26) can be greatly simplified by employing the equivalent electrical circuit method first developed by Miles (1971, 1974) and subsequently modified by Garrett (1975). The method consists in evaluating a weighted integral of (5.26). Define F(s) = *I* f(s), such that $\int_M f(s)ds = 1$. *I* is here the total volumetric flow through the mouth. In an electrical analogy it represents the current. f(s) is a current distribution function along the boundary M. Upon multiplying (5.26) by the f*(s'), the complex conjugate of f(s), and integrating over the width of the mouth, we obtain at the mouth of the inlet itself:

$$V_B = I\, Z_B = V_O - I\, Z_O, \tag{5.27a}$$

where $V_B = \int_M \eta\ (s)f^*(s)ds$ and $V_O = \int_M \eta_O(s)f^*(s)ds$ (5.27b)

are the averaged elevations and may be considered as analogous to voltages, while

$$Z_{B,O} = \iint_M f^*(s)G_{B,O}(s,s')f(s')ds'ds \text{ are the impedances of B and O} \tag{5.27c}.$$

With (5.27a,b), applying values at the inlet mouth, $Z_B = V_B / I = \eta_M / WHv_M$. On substituting for η_M and v_M from (5.24a) and (5.24b), we get an expression for the harbour impedance

$$Z_B = ik''\frac{\cot[k''L]}{\sigma W} \tag{5.28}$$

which is thus purely reactive.

For a friction free open sea, the Green's function for wave radiation due to a time harmonic current source at the mouth and with spatial form $u(0,y) = \delta(y-s)/H_2$ is given by (Miles, 1971):

$$G = -\frac{\sigma}{2gH_2} H_0^{(2)}\left(\frac{\sigma R}{\sqrt{gH_2}}\right) \tag{5.29}$$

where $R = \left[(x-L)^2 + (y-s)^2\right]^{1/2}$ and $H_0^{(2)}$ is a zeroth order Hankel function describing the outward phase propagation. Assuming that the inlet opening is much smaller than the length of the scattered wave, Hankel's function can be approximated by (Abramowitz & Stegun, 1965)

$$H_0^2\left(\frac{\sigma R}{\sqrt{gH_2}}\right) \approx \left[1 + \frac{2i}{\pi}\left\{\ln\left(\frac{\sigma R}{\sqrt{gH_2}}\right) + \gamma\right\}\right] \tag{5.30}$$

where γ = Euler's constant = 0.5772.

Taking the trial function f(s) = 1/W, the ocean impedance results from (5.27c) into

$$Z_O = \frac{\sigma}{2gH_2}\left[1 - \frac{2i}{\pi}\left\{\ln\left(\frac{\sigma W}{2\sqrt{gH_2}}\right) + \gamma - 1.5\right\}\right] \tag{5.31}$$

The response of the inlet as a function of frequency is calcuated by using (5.28) and (5.31) in $I = \frac{V_O}{Z_O + Z_B}$ (5.32). In the case of an open sea wave, with frequency σ, incident towards the inlet from a direction perpendicular to its mouth, the sea level oscillations in the open sea take the form of a standing wave, and $V_O = a_O e^{i\sigma t}$ where a_O is the amplitude of the open sea wave if the mouth of the inlet were closed. The amplitude of the response is then given by the magnitude of $(Z_B + Z_O)^{-1}$, while the phase is given by $\tan^{-1}\left(\frac{-\mathrm{Im}(Z_B + Z_O)}{\mathrm{Re}(Z_B + Z_O)}\right)$. The profiles of along-axis velocity and elevation inside the inlet are given by:

$$U(x,t) = \frac{a_o}{H_1 W} \frac{\sin(k''x)}{\sin(k''L)} \frac{e^{i\sigma t}}{(Z_B + Z_o)} \qquad (5.33a)$$

$$\eta\ (x,t) = -\int H_1 U_x dt = \frac{a_o}{\sqrt{gH_1}\, W} \frac{\cos(k''x)}{\sin(k''L)} \frac{ie^{i\sigma t}}{(Z_B + Z_o)} \qquad (5.33b)$$

The amplification factor **A** is defined as the ratio of the standing wave amplitudes inside and outside the harbour. **A** can be defined at any point in the harbour and is derived from (5.33b) in the general form as:

$$\mathbf{A} = \frac{\eta\ (x)}{a_o} = \frac{\cos(k''x)}{\sqrt{gH_1}\, W \sin(k''L)\ \left|(Z_B + Z_o)\right|} \qquad (5.34)$$

The resonant frequency is that which minimizes the denominator in (5.32). At resonance, when $Z_B = 0$, the magnitude of the response is entirely controlled by the radiative impedance and infinite amplitudes are thus prevented. The role of the radiation is similar to that of damping by friction. The location of the resonance peaks is also shifted from the free modes towards smaller frequencies.

5.8.2 Numerical solution

In this test model the domain is discretised into a regular orthogonal grid with a cell size of 120m so that the resolution exactly matches that proposed for the actual model implementation on Mellieha Bay and St. Paul's Bay. The inlet has a size of 30 x 5 cells. The open sea area extends symmetrically on both sides of the inlet to a total size of 35 by 30 cells in the alongshore and cross-shore directions respectively. The depth of the inlet is taken as 40m, while the open sea area has a uniform depth of 100m. The linear bottom friction coefficient is 0.001 inside the inlet and zero outside.

As discussed in section 5.4.4, the open boundary conditions have to be selected with caution. The forced elevation is applied at the offshore boundary. The input signal consists of a sinusoidal variation of elevation with a prescribed amplitude and period. The signal has a uniform phase along the boundary so that the incidence is normal to the boundary. An implicit formulation of the friction terms in the momentum equations is again adopted as in section 5.5. Non-linear terms and the effect of the earth's rotation are furthermore excluded.

Several types of boundary conditions are tested on the two cross-shore boundaries. None of the radiation boundary conditions mentioned in section 5.4.4 gave adequate results when applied on their own. In particular, the Heaps radiation condition underestimated the elevations, whereas the Implicit Orlanski scheme introduced considerable noise in the solution. When these conditions are however replaced by two sponge barriers on the east and west open boundaries, the simulation is found to resemble the theoretical solution very closely. At each sponge area, which is five grid cells thick, the coefficient of friction increases linearly from 0 to 0.15. A radiation condition with the phase speed determined by the Implicit Orlanski scheme is applied at the outer extreme edge of each sponge. The sponge areas serve to dissipate outgoing wave energy radiated from the harbour which would otherwise remain in the main basin and distort the amplification factor. This method resembles the employment of energy dissipators on the side walls of wave basins in physical modelling applications to study long wave propagation.

The effectiveness of the model is assessed in the next section. This is done by checking that the response of the harbour to the excitation is independent of the incident wave height. The frequency response of the harbour should also be a smooth curve, free from multi-resonance spikes (Ippen & Raichlen, 1962). The open sea standing waves in the northernmost parts of the domain should furthermore have uniform wave heights along the x-direction.

5.8.3 Results

5.8.3.1 Dependence on incident amplitude

From (34), the amplification factor **A** should be invariable to changes in the incident wave amplitudes. A verification of this condition is obtained by repeating the simulation in three separate runs with incident sinusoidal signals having the same frequency (T = 600s) but different amplitudes of 0.1m, 0.2m and 0.3m. The simulated amplification factors at three reference points inside the harbour are checked to comply to this condition (Table 5.1). The skill of the model to reproduce the expected theoretical response of the harbour is also remarkable. The comparison between the theoretical and modelled amplification factors is limited by the resolution, but the difference is less than 5%. It must however be noted that a slight discrepancy is observed in the maximal positive and negative displacements of the water level. The amplitude is consistently greater during the half-cycle when the water level moves below the level of zero displacement. At the head of the inlet, where this effect is most pronounced, the discrepancy however amounts to only 1.2%.

Table 5.1 *Theoretical vs modelled amplification factors for three different incident amplitudes*

Amplification factor A	RUN 1	RUN 2	RUN 3	Theoretical
at head of inlet	4.863	4.864	4.864	4.873
at mid-distance	3.267	3.267	3.265	3.195
close to mouth	1.298	1.298	1.299	1.229

5.8.3.2 Frequency response

The model is tested to assess its skill to simulate the harbour response to incident waves of varying periods. The response is measured in terms of the amplification factor, measured at the head of the inlet, and is verified in both the near-resonant and non-resonant conditions.

In such studies the incident disturbance is traditionally taken in the form of a solitary sinusoidal wave which propagates into the domain and sets the water body into oscillation. The spectral signatures of the numerically simulated sea levels at one or more selected points in the inner basin are then compared with observed elevations. The procedure is repeated with different incident frequencies. Such a method has been widely used in the study of the response of harbours and inlets to tsunami waves.

The waves which induce resonant conditions in actual harbours do not however consist of regular wavetrains with discrete periods. The incoming waves are better regarded as a combination of random waves with different periods and amplitudes. The incident disturbance on the northern open boundary is thus better simulated by a continuous power spectrum (Djumagaliev et. al.,1995). The input function is assumed to have a constant phase along this boundary so that the direction of incidence is taken to be orthogonal to the boundary. An auto-regressive model of the first order is used. The model is expressed by the process:

$$\eta(t) + a_1\eta(t-1) + \ldots\ldots + a_{na}\eta(t-na) = \varepsilon(t) \qquad (5.35)$$

where η is the modelled signal (in this case sea elevation), the noise $\varepsilon(t)$ is defined to be a random signal with a normal distribution, and a_i are positive parameters in the range [0,1]. Up to first order all the coefficients vanish except for a_1. The spectrum of this process is

$$S_\eta = \frac{1}{[1 - a_1 \cos(\omega\ \Delta t)]^2 + a_1^2 \sin^2(\omega\ \Delta t)} \qquad (5.36)$$

where Δt is the discrete time step and ω is the angular frequency. This spectrum decreases monotonically up the Nyquist frequency ω_N and the higher frequency components of the signal are suppressed. When (1-a) << 1 and $\omega << \omega_N$, the spectrum takes the form

$$S_\eta = \frac{1}{(1 - a_1)^2 + a_1^2 (\omega\ \Delta t)^2}.$$

For $\omega >> \frac{1-a}{\Delta t}$, this spectrum decreases as ω^{-2} and thus resembles the observed dependence of open sea long waves on frequency (Efimov et. al, 1985). In this application the value of a_1 is -0.96 and the incident disturbance is calculated at intervals of 30 seconds.

In the simulations the same harbour dimensions are retained as in section 5.7, with a narrow mouth of just 5 grid cells. At the mouth the depth changes abruptly from 40m inside the harbour to 100m outside. The numerical integrations are carried out every 0.5s, and the incident wave amplitude is updated at each time step. The model is run for 1.2 days. The numerical output is stored at 1-minute intervals. The amplification factor is calculated as the root-mean-square amplitude of the spectrum at the head of the harbour with respect to the incident spectrum. The results are summarised in Fig. 5.5 which compares the frequency dependence of the amplification factor, measured at the head of the inlet, with the theoretical response curve. The agreement between the theoretical and the numerical response is considered to be sufficiently good on considering the tough geometry application to which the model is submitted. The model amplitudes at resonance are consistently lower than the theoretical values, particularly at the fundamental mode. This is probably a result of energy dissipation at the coastal boundaries due to imperfect reflection. Even small deviations from perfect boundary reflections

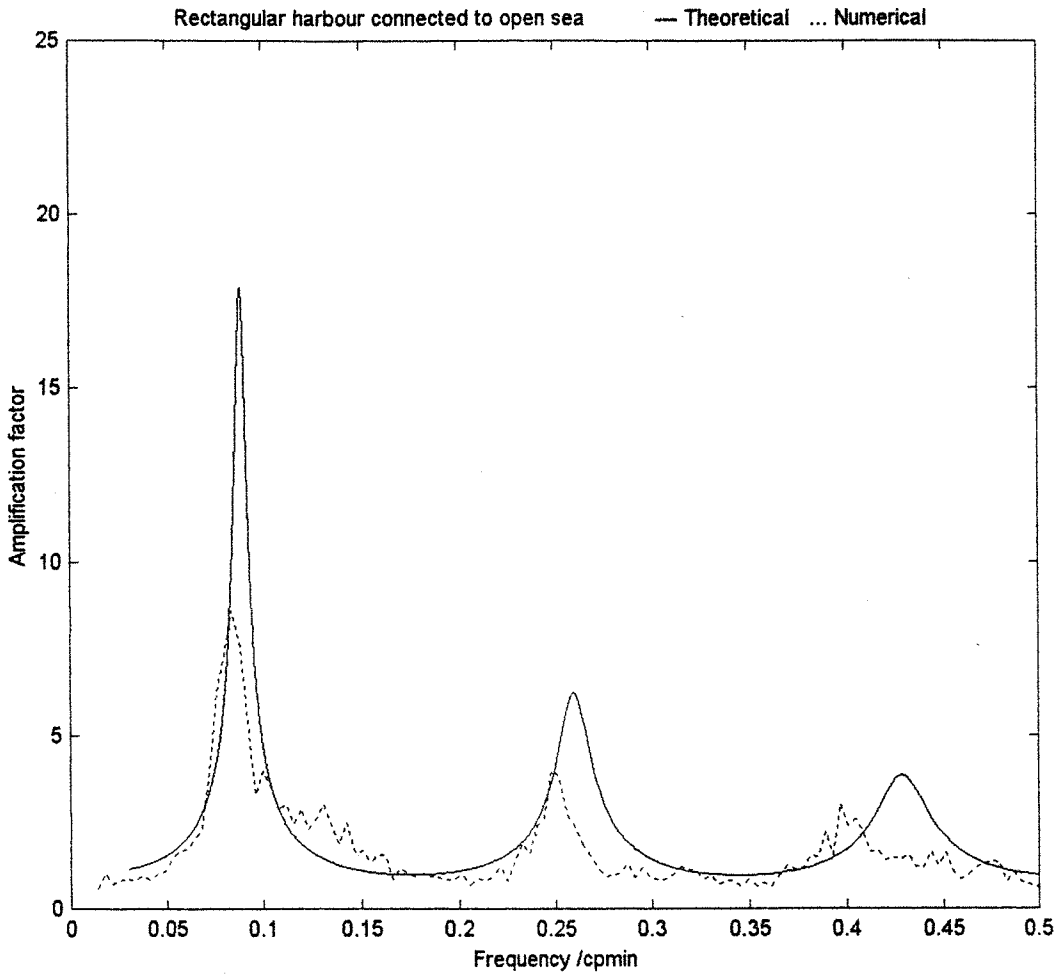

Fig. 5.5 Theoretical (solid) and simulated (dotted) frequency response curves for a narrow harbour (uniform depth = 40m) connected to a frictionless, non-rotating open sea area (constant depth = 100m).

can cause large changes in resonant amplification (Ippen & Goda, 1983; Kostense et al., 1986).

The simulated resonant periods are also shifted towards higher values with respect to theory, especially at the higher modes. The discrepancies are mainly related to the weak grid resolution at the narrow mouth and are expected to be lower in the case of a wider mouth. Furthermore it should be noted that the fundamental

resonant peak of the theoretical frequency response curve of this harbour is so sharp that its half-power width of about 0.008 min^{-1} is comparable to the spectral resolution of 0.0039 min^{-1}.
Another point in case to mention is that the adopted input function does not have a smooth spectral signature and may thus carry unrepresentative energy estimates at crucial frequencies.

5.8.3.3 Analysis of flow patterns

The change in the incident wave height and the pattern of propagation of the incident wavefronts before reaching the harbour mouth can also have a substantial effect on the amplification factor. The simulated wave patterns in the open sea and harbour at two instances during ebb (t = 0 and t = 0.3T) are shown in Fig. 5.6a,b. The coloured contours join points of equal elevation with deep red denoting peak positive elevations and deep blue denoting peak negative elevations respectively. These patterns apply to the case in which the open sea wave is incident from the north with a fixed period of 600s. The patterns during flood are identical except that the elevations and flow are reversed.

As expected, the wave motion is one-dimensional inside the harbour and has a purely standing wave character. At this forcing period a displacement node exists in the interior at about y = 2L/3. The incident signal resembles closely the standing wave characteristics, and wave fronts are close to plane parallel at the northernmost boundary. In the vicinity of the harbour, the flow is influenced by the oscillating flux at the mouth. and the waves assume a two-dimensional pattern.

At t = 0 (Fig. 5.6a) the elevation inside the harbour attains its maximum displacement, while the incident sinusoidal disturbance is close to its peak displacement below the mean level. The flow field is thus very weak. At t = 0.3T (Fig. 5.6b), just beyond a quarter of a cycle later, the sea level is close to its undisturbed level throughout the domain and the flow is at its peak with currents of the order of 20 cms^{-1} at the mouth of the harbour. This pattern is reversed with perfect symmetry half a cycle later.

With the tests described above, the model is thus found to describe adequately the coupling between a harbour and an adjacent deeper open sea area. The model thus qualifies for application to real domains.

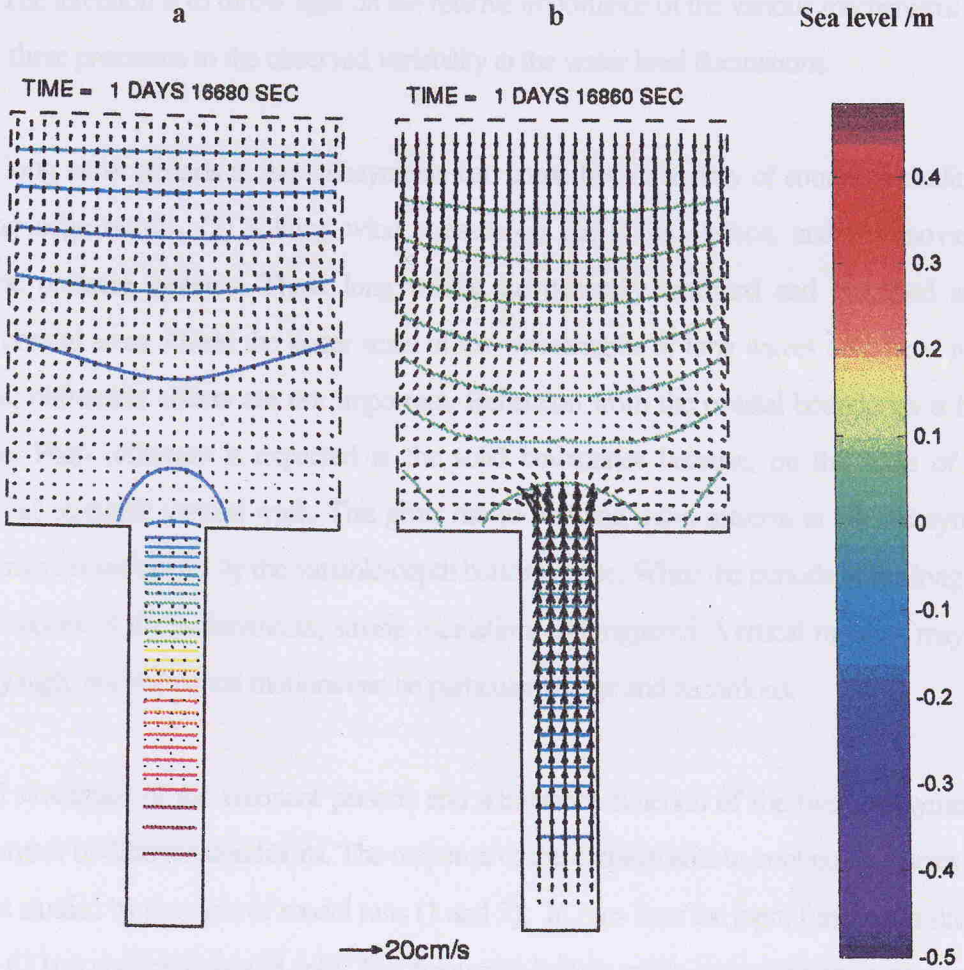

Fig. 5.6 Flow patterns in the case of a narrow harbour (depth = 40m) connected to a frictionless, non-rotating open sea (depth = 100m) and with a sinusoidal disturbance (period = 600s) incident from the north.
(a) Peak elevation inside harbour;
(b) Flow out of the harbour during ebb.
The colorbar applies to the contours of equal elevation in metres.

5.9 Numerical modelling of coastal embayment response to long waves

This section describes the application of the two-dimensional POM to the coupled bay system composed of Mellieha Bay and St. Paul's Bay in order to simulate the long wave oscillations in the embayments. The model runs are aimed to study the possible generation mechanisms for the strong seiche oscillations that occur in the two bays. The intention is to throw light on the relative importance of the various mechanisms that are in action and to link these processes to the observed variability in the water level fluctuations.

Energy at long wave periods in the embayments can come from a variety of sources including (1) longshore-propagating edge waves, (2) shifting wind stresses on the water surface, and (3) moving or fluctuating atmospheric pressure systems. These long waves are generally modified and amplified as they enter the shallower coastal areas. Given the larger scale of the wavelengths of long waves compared to the embayment dimensions, diffraction effects are not important. Reflection from the coastal boundaries is however of great importance. High reflection is expected at the solid boundaries because, on the scale of long waves, the boundaries all resemble vertical walls. This gives rise to standing wave patterns in the embayments. The waves are furthermore transformed by the variable-depth bottom shape. When the periods of the long waves match the resonance modes of the embayments, strong oscillations are triggered. Vertical motions may not generally be excessively high, but horizontal motions can be particularly large and hazardous.

Numerical simulation of the resonant periods and admittance function of the two embayments is carried out under a number of different conditions. The response of the embayments to continuous waves incident from the open sea is studied by two sets of model runs (1 and 2). In runs 1a-c the input function is sinusoidal with fixed amplitude (0.1m) and frequency (3 cph). This frequency is close to the expected first resonant mode. In runs 2a-c an input random function is applied; this is composed from an auto-regressive model of the first order (as described in section 5.8.3.2) which suppresses the high frequency components. By this method a numerically simulated time series of sea level inside the domain can be obtained. In runs 1a and 2a, the waves are incident into the domain from an along-bay axis direction and are assumed to have the same phase along the outermost open boundary. In runs 1b and 2b the waves enter the domain from the left cross-shore open boundary. In runs 1c and 2c the waves enter the domain from the right cross-shore open boundary. Their direction of incidence is

perpendicular to these boundaries, and incident wavefronts are assumed to have the same phase along the cross-shore boundary.

In these runs the non-linear terms of the momentum equations are included and the Coriolis factor is taken to be constant with its value at 36° latitude. Bottom friction is applied by means of a quadratic drag formulation.

A zero-flow condition is assumed at the coast. As described in section 5.4.4.3, a boundary condition consisting of a sponge with an Orlanski radiation condition at the outer edge can be used on the two cross-shore open boundaries in the case of tests 1a and 2a. Other possible alternative conditions are however tested. The simpler and less computationally demanding Heaps radiation condition is found to practically give identical results in the embayments. This boundary condition is thus adopted at the cross-shore open boundaries in the model runs described below. For runs 1b and 2b, a zero gradient condition on EL and VA at the alongshore open boundary, and a Heaps radiation condition on the right cross-shore open boundary are found to be adequate.

5.9.1 Response to a sinusoidal wave

5.9.1.1 Model run 1a: Normal incidence

Fig. 5.7a,b shows the long wave patterns and flow in the two bays at times separated by 0.3T (T=1200s) for the case of normal incidence from the northern boundary. Fig. 5.7a corresponds to a time just after highest sea level displacement in the embayments. Fig. 5.7b corresponds to a time close to maximum ebb flow when the sea level is nearly at its undisplaced position. Once the model reaches steady state conditions, the patterns are repeated with reversed elevations and flow directions in each successive half-cycle.

The longitudinal oscillation is predominant at this forcing period and water sloshes in and out of the bays in an along-bay axis direction. The displacement of the sea level is highest at the head of the bays. The highest sea level at the head of Mellieha Bay is 0.6m while that in St. Paul's Bay is 0.45m. The amplification factor is thus higher in Mellieha Bay. The oscillations in the inner areas of the two bays practically occur in phase. The sea level displacement diminishes gradually with along-bay axial distance from the bay head. There are no mesh points in the domain with permanently zero displacement, as would be expected in the case of a simple co-oscillation with no friction. The nodal zone extends instead over a region well beyond the promontaries of the bays and delimits the area of transition between the incident waves and the inner shelf oscillations. In the case of a bay with a wide open mouth, such as Mellieha Bay, it thus becomes evident that the resonant modes actually

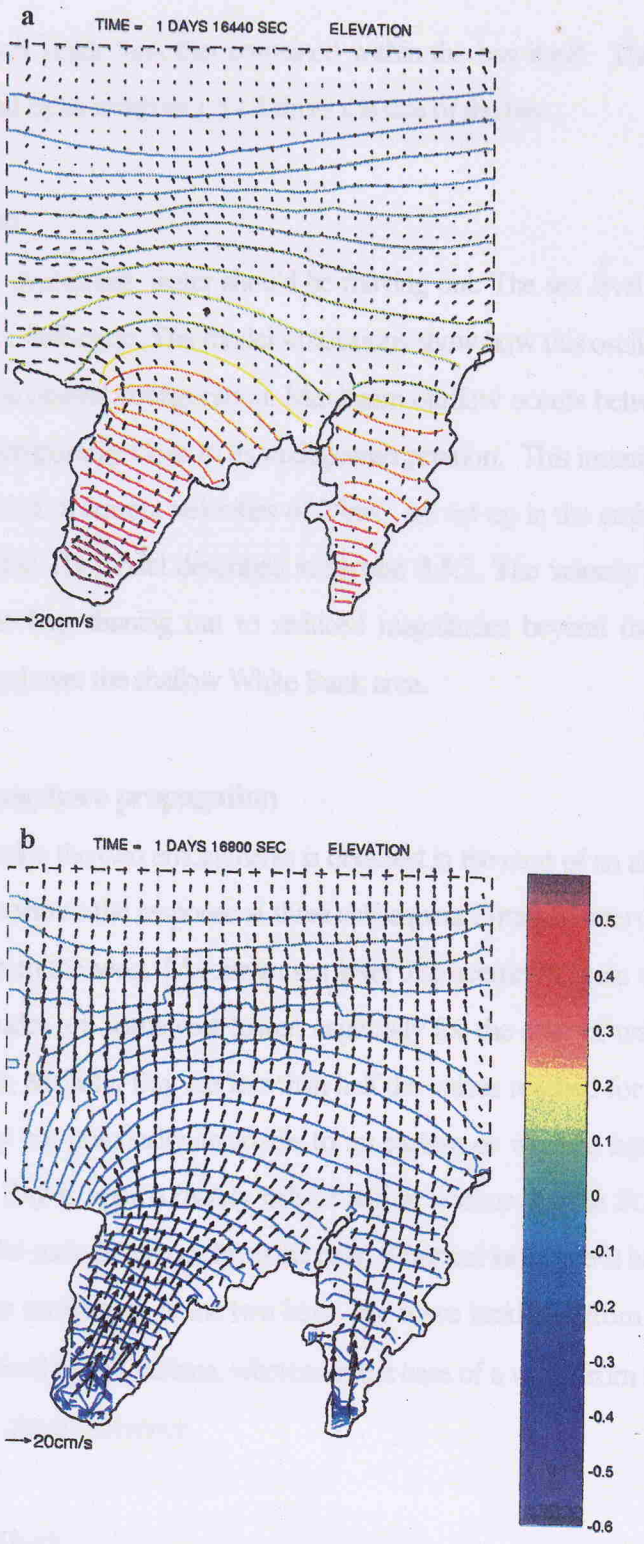

Fig. 5.7 Snapshots of water elevation and flow patterns for run 1a, (a) at time close to maximum sea level displacement in the embayments, and (b) at 0.3T (T = 1200s) later and close to maximum ebb flow. Forcing is produced by a sinusoidal signal (T = 1200s; A=0.1m) incident from the open sea in an along-bay axis direction.
Elevation is measured in meters and is its magnitude for each contour is described by the colorbar. Sea current is measured in cms^{-1}.

involve a water body that is much larger than that contained within the bay itself. The nodal area is in fact located offshore from the bay head by as much as 1.5 - 2 times the size of the bay.

5.9.1.2 Flow patterns (run 1a)

When the sea level in the bays is decreasing, water should be moving out. The sea level increases again as the water flows back in the successive half-cycle. The model simulations show how this oscillatory flow is modified by the bottom topography and the coastal configuration. Maximum outflow occurs between times of high and low water when the sea level is temporarily close to its undisplaced position. This instant is shown in Fig. 5.7b during maximum ebb flow. Maximum current velocities of $25ms^{-1}$ are set up in the embayments and compare well with values obtained from the 1D model described in section 3.5.2. The velocity field is predominantly aligned along the axis inside the bay, fanning out to reduced magnitudes beyond the bay mouth. Further offshore the flow is again enhanced over the shallow White Bank area.

5.9.1.3 Model runs 1b,c: Alongshore propagation

A very similar forced response inside the two embayments is obtained in the case of an along-shore input signal incident from the left. Fig. 5.8a-c shows the response at three subsequent 2-minute intervals for a near-resonant sinusoidal signal (T = 1200s) from the west. Maximum sea level displacements again occur in the innermost parts of the bays but the amplitudes are somewhat lower, especially for the case of wave incidence from the west when sea level excursions in Mellieha Bay are less than half the values reached for normal incidence. Sea level excursions in St. Paul's Bay are practically invariable to an eastern or western input signal; on the other hand, the response in Mellieha Bay is approximately halved and is weaker than in St. Paul's Bay when the forcing wave is from the west. The main difference from the case of normal incidence is however the occurrence of a phase difference between the oscillations of the two bays. For wave incidence from the west, the sea level fluctuations inside Mellieha Bay lead by $\pi/3$ radians, whereas in the case of a wave from the east, St. Paul's Bay leads by approximately the same phase difference.

5.9.1.4 Flow patterns (runs 1b,c)

The sea level displacements decrease gradually away from the embayments until the wave patterns merge into the open sea wavefronts propagating in the alongshore direction. It is interesting to note how the standing wave oscillations in each embayment are set up in phase to waves in the open sea. High water in the embayment

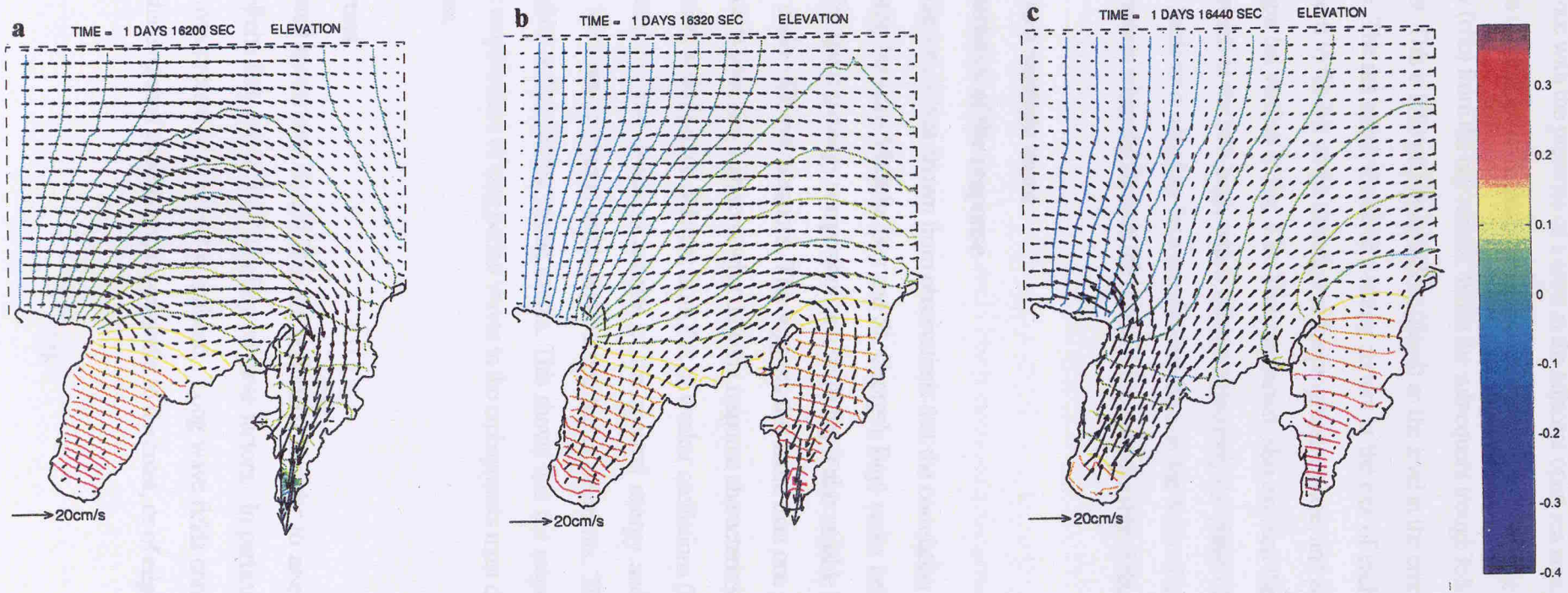

Fig. 5.8(a)-(c) Snapshots of water elevation and flow patterns at 2-minute intervals for the case of a sinusoidal signal (T = 1200s; A=0.1m) incident from the left (run 1c).
Elevation is measured in meters and its magnitude for each contour is described by the colorbar.
Sea current is measured in cms^{-1}.

occurs in coincidence with the presence of a crest in the adjacent open sea area. At this instant the flow into the embayment is at its minimum. At the next quarter cycle the open sea wave is at its undisturbed level and there is maximum outflow (ebb) from the bay mouth. When the subsequent trough follows in the open sea area, the sea level is at its lowest. This is followed by an inflow (flood) as the level in the embayment rises to maximum in the next quarter cycle. The net effect is that of a rotary current at the exit of each bay. The rotation is clockwise where the coastline is to the left of the direction of the progressive wave, and is alternatively anticlockwise for a coastline to the right (as verified in Fig. 5.8). This mechanism also explains the phase discrepancy between the standing wave systems in the two bays, which follow respectively the phase of the open sea wave. This phase difference further leads to a coupling between the two bays in the form of an oscillating flux. This flux is a maximum at the instants when the flows in the two bays are opposite (Fig. 5.8a,c).

5.9.2 Response to a random wave

5.9.2.1 Characteristics of the response

In the previous chapters, it was shown from observations that the correlation between oscillations in different embayments (notably between Mellieha Bay and St. George's Bay) varies between cases of strong and weak seiching events. The spectral energy composition at a single bay is also variable in time and energy peaks tend to shift in frequency under different situations. This suggests that more than one generating mechanism can be in action at any instant in time, and with somewhat different response characteristics. In particular, the triggering of strong seiching events is likely to be different from that of weaker oscillations (Rabinovich & Monserrat, 1998). This is corroborated by time evolution analysis of the spectral energy and admittance function made on simultaneous sea level measurements inside and outside the embayments. The admittance function varies in time, reaching highest values during strong events. This shows that the response of the embayments is non-linear and that the amplification of long period waves in the embayments must depend on the nature of the wave field in the open sea.

5.9.2.2 Model runs

The depth-integrated model runs 2a and 2b,c are performed in order to assess the dependence of the seiche oscillations in Mellieha Bay and in St. Paul's Bay on these factors. In particular, the dependence on different boundary long waves present on the shelf is analysed. Long wave fields consist of either leaky waves which take the form of standing shelf oscillations perpendicular to the coast, or of edge waves trapped on the shelf and

propagating parallel to the coast. These two situations are simulated by applying a continuous source of random waves entering the model domain either from the north (model run 2a) or the east/west (model runs 2b,c) boundaries respectively.

In these runs an external time step of 0.5 seconds is again used. As in the previous model applications, the domain is represented by a regular orthogonal grid with a mesh size of 120m. Depths less than 2m are considered as land. Bottom friction is applied by means of a quadratic drag formulation. In the model results presented below the horizontal diffusion is taken equal to $50m^2s^{-1}$. The experience gained from the previous applications on the most adequate conditions on the open boundaries is utilised. The same boundary conditions as those adopted above are again used. The sea level is stored every minute at selected mesh points in the domain.

5.9.2.3 Sensitivity tests

The bottom roughness parameter z_0 is assumed to be horizontally homogeneous and equal to 1cm. Oey et al. (1985) reported low sensitivity of long wave response to variations in z_0. Indeed long waves are expected to interact more strongly than short waves with the bottom, but model results are found to be only mildly sensitive to the choice of z_0. For run 2a, amplitudes are only increased by 4% when z_0 is reduced to 0.2cm.

The amplification of the long period waves is however found to be sensitive to the value of the horizontal diffusion coefficient A_H. Non-zero values of A_H are necessary in order to ascertain computational stability. A number of tests are carried out in order to check the dependence of the model output on this parameter. Different fixed values of A_H are applied in separate model runs with the same random signal incident from the outermost boundary. The amplitudes and power spectral densities at selected grid points from the separate runs are then compared. The results show that the amplitude of the simulated oscillations increase with smaller values of A_H, but the relative distribution of spectral energy is practically unaffected. The optimal values of A_H are in the range 50 - 100 m^2s^{-1}. The change in power spectral densities with A_H in this range is 16%.

5.9.2.4 Model results

The response of the embayments is measured by means of the power amplification factor which expresses the relative rms spectral magnitude of the water level or current velocity variation at any two grid points in the

model domain. The station pair in Mellieha Bay is chosen with one point on the coast at the head of the bay with I = 7 and J = 6 (coinciding to the location of the coastal station in the bay), and a second one at an open sea location just outside the mouth with I = 29 and J = 38. The gains, coherences and phase lags for these pair of stations are used to compare the numerical computations with direct observations. The open sea level observations are taken from MELPAUL station (refer section 3.4.7.4), with a sampling interval of one minute, and cover the period 16h02 16/5/96 to 16h31 25/5/96. The station coincides to the mesh point I = 29 and J = 38 in the model domain.

The skill of the model in reproducing the results of direct observations is presented in Figures 5.9 and 5.10 for the case of normal incidence (run 2a). The frequencies of peaks and troughs in the observed energy amplification spectra, and the coherences and phase differences between the bay and the open sea location are well predicted especially for the fundamental and first resonance modes. The main maxima of the amplification factor curve, the troughs in coherence and the phase jumps of 180° correspond well to the resonant periods. The amplification of the fundamental mode is however slightly underpredicted. This is rather unexpected in view of the neglect by the model of energy losses at the coast. The neglect of these losses due to incomplete reflection at the coastal boundaries are thus more than compensated by the effects of the applied bottom friction and horizontal diffusion parameter values. But the main cause of the discrepancy is probably due to the erroneous model depths at the very shallow areas of the Bay (especially at the relatively extensive inner beach area) where a number of mesh points with depths less than 2m are considered as land by the model.
The spectral plots at the head of Mellieha Bay and St. Paul's Bay for the three model runs 2a,b,c are plotted together in Fig. 5.11a-d. The model reproduces very well the main long wave characteristic frequencies of oscillation of the two bays as described in Chapter 3. The complex multiple-peak structure observed from measurements is also reproduced by the numerical computations.

The series of peaks P (25.5min.; 21min.) and Q (11.5min.) are predominant in run 2a. They are greatly attenuated or completely suppressed in runs 2b. These peaks are associated to standing wave oscillations extending over the shelf. They have the same phase in both bays. The generation of these leaky modes is favoured by energy entering the domain towards the bays from an along-bay axis direction and thus enhancing the coupling between the bay and the shelf modes.

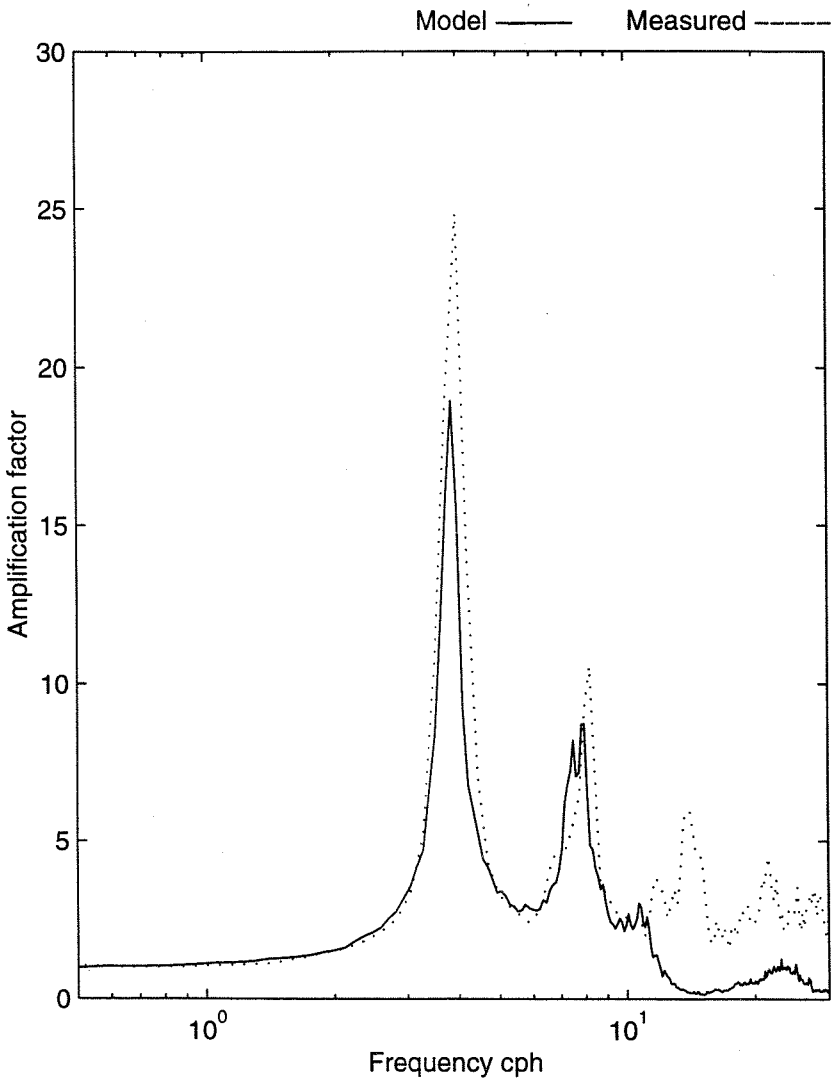

Fig. 5.9 Comparison between modelled (solid line) and observed (dotted line) amplification factor at the head of Mellieha Bay (output) with respect to a position just beyond its open mouth (input).
The mesh point at the head of the bay mouth corresponds to I = 7 and J = 6; that at the mouth corresponds to I = 29 and J = 38.
The observations (20-25th May, 1996) refer to MELPAUL station (36° 59.2' N; 14° 27.6' E) described in Chapter 2, Section 4.7.4
The 95% confidence factor, for 18 degrees of freedom is 6.1 dB (B_{min}=0.57; B_{max}=2.2).

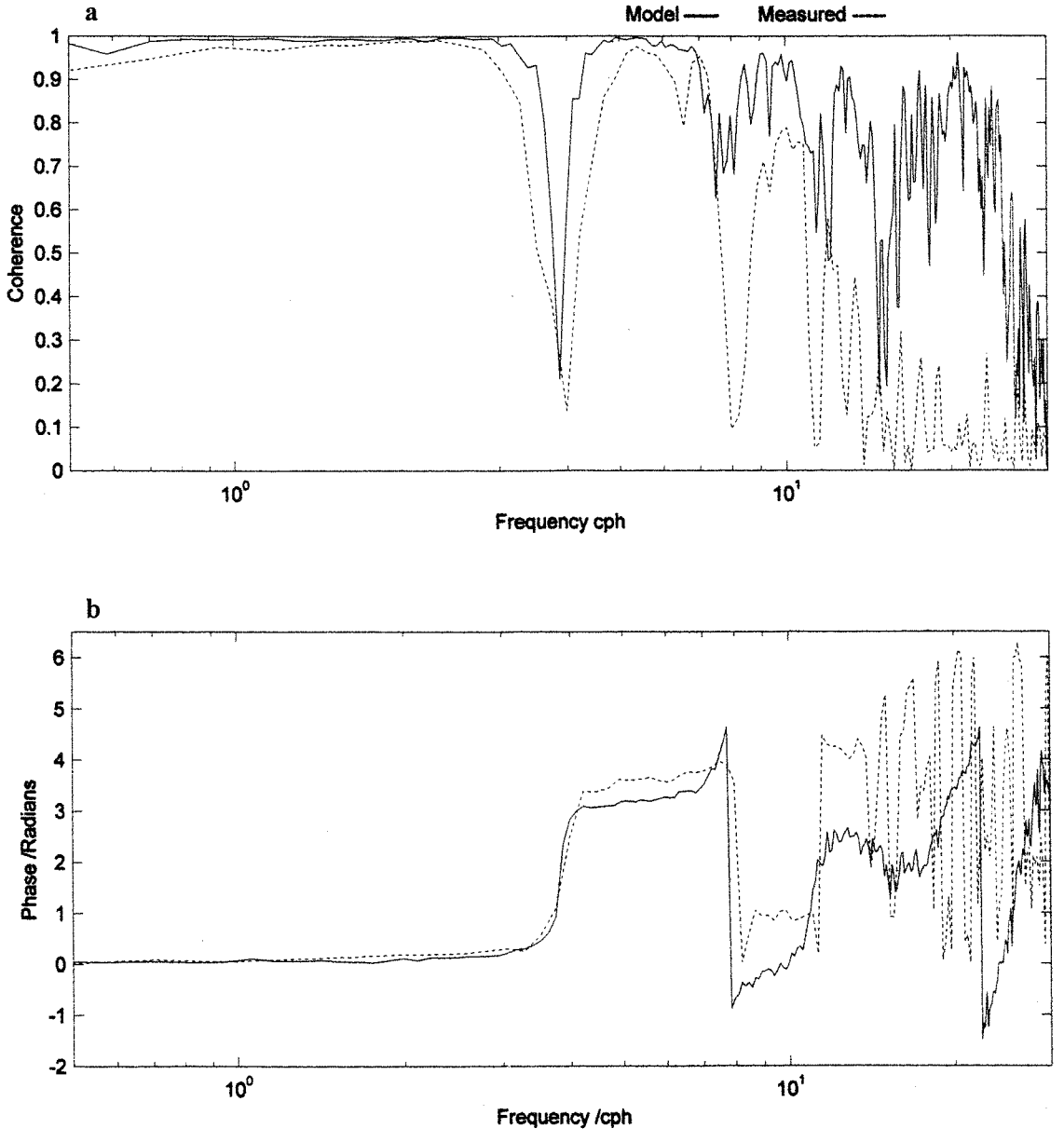

Fig. 5.10 Modelled (solid line) and observed (dotted line) coherence and phase lag between records at the head of Mellieha Bay (output) with respect to a position just beyond its open mouth (input).
The mesh point at the head of the bay mouth corresponds to I = 7 and J = 6; that at the mouth corresponds to I = 29 and J = 38.
The observations (20-25th May, 1996) refer to MELPAUL station (36° 59.2' N; 14° 27.6' E) described in Chapter 2, Section 4.7.4
With 18 degrees of freedom the level at which the coherence is significant at the 95% confidence level is equal to 0.28.

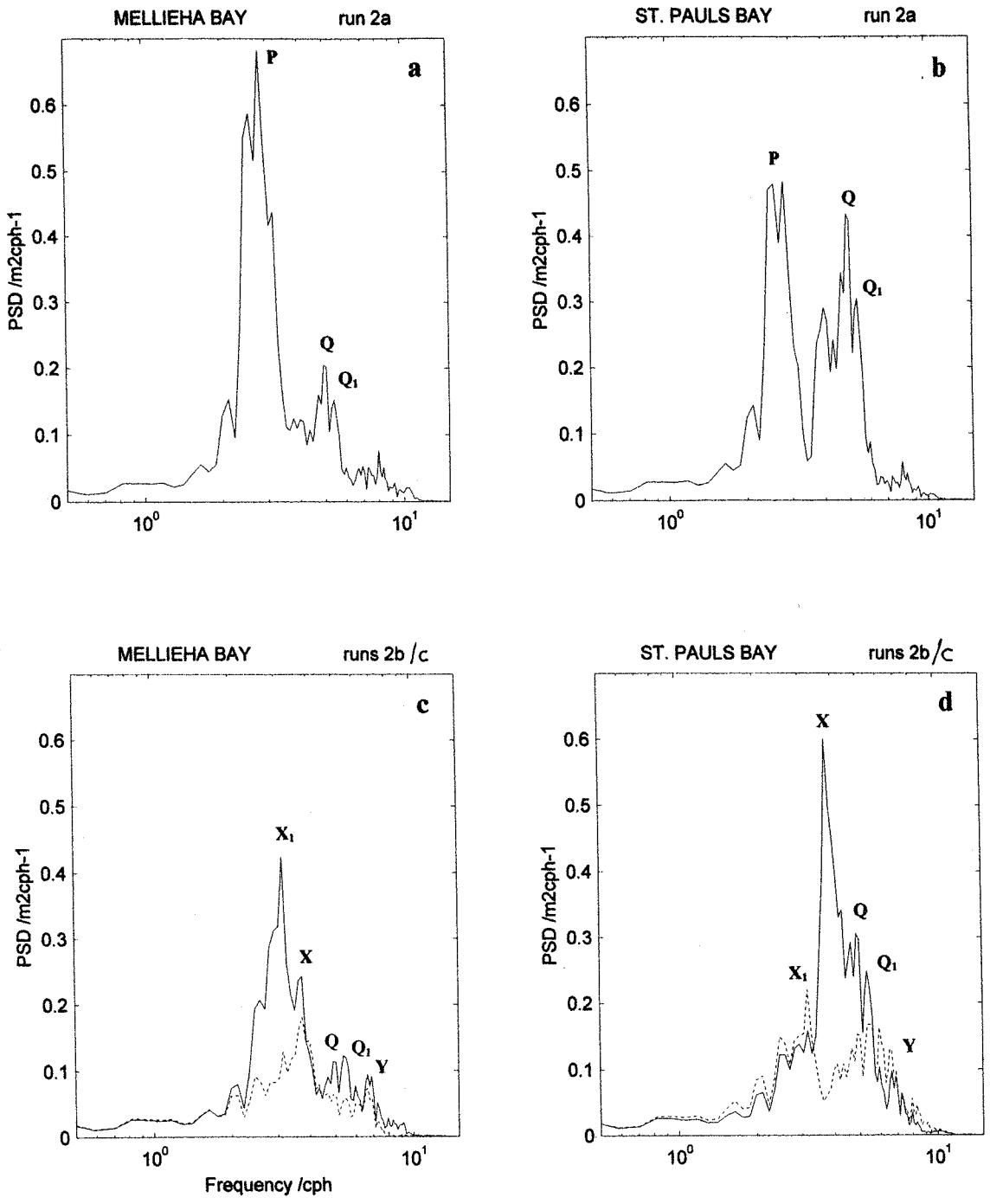

Fig. 5.11 Spectral plots for modelled elevations at a mesh point (I = 7 ;J = 6) inside Mellieha Bay for (a) run 2a with cross-shore random signal, and (b) for runs 2b,c with alongshore random signal from right (solid) or left (dotted).
Spectral plots for modelled elevations at a mesh point (I = 42;J = 4) inside St. Paul's Bay for (c) run 2a with cross-shore random signal, and (d) for runs 2b,c with alongshore random signal from right (solid) or left (dotted).
The 95% confidence factor, for 18 degrees of freedom is 6.1 dB (B_{min}=0.57; B_{max}=2.2).

The spectra for runs 2b,c are characterised by a different set of peaks. The energy of the bay oscillations is also considerably lower in the case of an alongshore open sea wave especially when the incidence is from the left. The bays are excited both as a coupled system as well as isolated basins. In both cases, the eigenfrequencies depend on the extent of the water body that is influenced by the oscillation. This water body includes the immediate basin outside the open mouth of the bays. The results confirm that the frequency response of the embayments depends on the direction of incidence of the alongshore open sea wave. The peaks X (16.2min.) and Y (8.9min.) correspond to coupled bay eigenmodes. A phase difference in excess of $\pi/2$ radians characterises the associated water level displacements at the two bay heads at these frequencies. These two seiche modes constitute the main response of the bay to an alongshore wave from the left. When the open sea wave travels in the opposite direction the leaky modes X1 (19min.) in Mellieha Bay, and to a lesser extent Q (11.5min.), Q1 (11.2min.) in St. Paul's Bay are intensified instead.

5.9.2.5 Simulated flow patterns

The model simulations permit a detailed analysis of the spatial characteristics of the oscillations and of the correlated flow patterns. This is important in clarifying the mechanisms of propagation and transformation of the waves as they reach the embayments. The model results are displayed in two types of graphic output. The first type of output is the conventional 'snapshot' of the entire model domain at a particular time step, as already utilised in previous sections. The second output is in the form of a PSD frequency-space (f-s) diagram. The model output produces a time series of sea elevation at selected grid points along a chosen transect which in this case consists of a segment along the bay axis, joining to a second segment with constant index I, inside and outside the bay respectively (TR1 and TR2 in Fig. 5.12). The power spectral density is calculated at each point along the transect on the assumption that the discrete values of the elevation can be treated as a time series of a stationary Gaussian process. In the f-s diagram, the space axis represents the J index of each point on the transect, the ordinate is the frequency in intervals of $1/(2\Delta T)$ cph, where ΔT is the sampling interval (= 1minute). The plotted quantity along the z-coordinate represents the PSD at each transect point and frequency. Dark red signifies a high PSD value (crest) while dark blue signifies a low PSD value (trough).

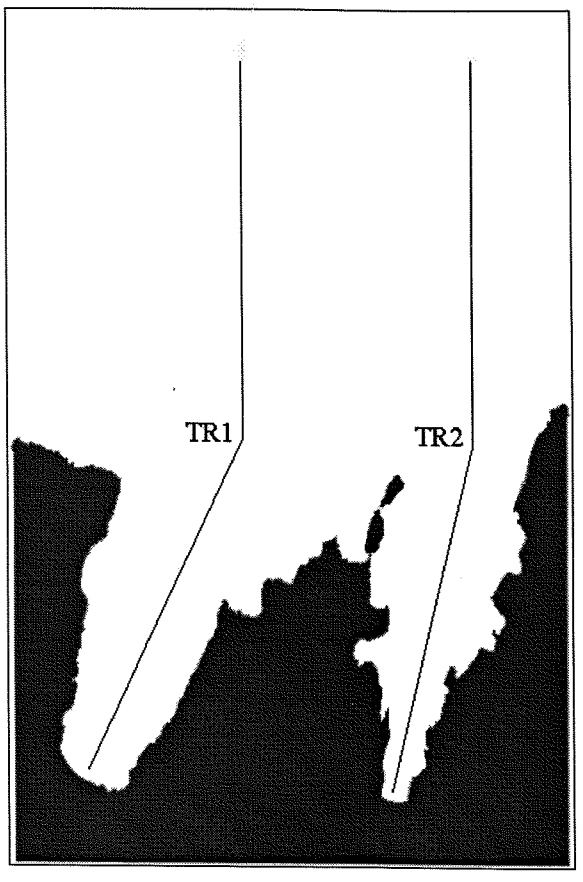

Fig. 5.12 Transects for model output

ELEVATION AND FLOW PATTERNS

Fig. 5.13a-d shows four consecutive snapshots of the elevation and current vector fields at 2 minute intervals. These plots refer to a random signal from the north (run 2a). In combination they give a temporal dimension to the water movements. The contours join points of equal instantaneous elevation. The colorbar covers the range indicated at the top of each figure, with deep red denoting the higher sea level displacements and deep blue denoting the lower levels. The 30 contour levels used for each plot are spread equally over the range of sea levels. The sea level gradients are thus evidenced in the plots by the spatial concentration of contuors.

The complex structure of the oscillations is revealed in these figures and often leads to opposite currents even within the bays themselves (Fig. 5.13a). Notwithstanding the random nature of the incident wave, the time evolution of the water movements shows some regular patterns within the bays. The water body responds to a number of superimposed modes of oscillation which in combination give rise to the complex elevation and current field. These modes consist of (i) inner bay oscillations which are predominantly axial to the bays, (ii) basin wide oscillations which comprise the full extent of the basin (including the area immediately outside the bays) and consist of both along-bay and cross-bay components, as well as (iii) leaky modes established by the coupling of the bays with the outer shelf area. Coupling between the two bays is not well evidenced in this circumstance and the response in the bays is predominantly that of two separate basins. In St. Paul's Bay the oscillations occur predominantly along the bay axis and the flow is basically axial. In Mellieha Bay the cross-bay oscillations are particularly evident across its wide mouth and a cross-bay current component exists in

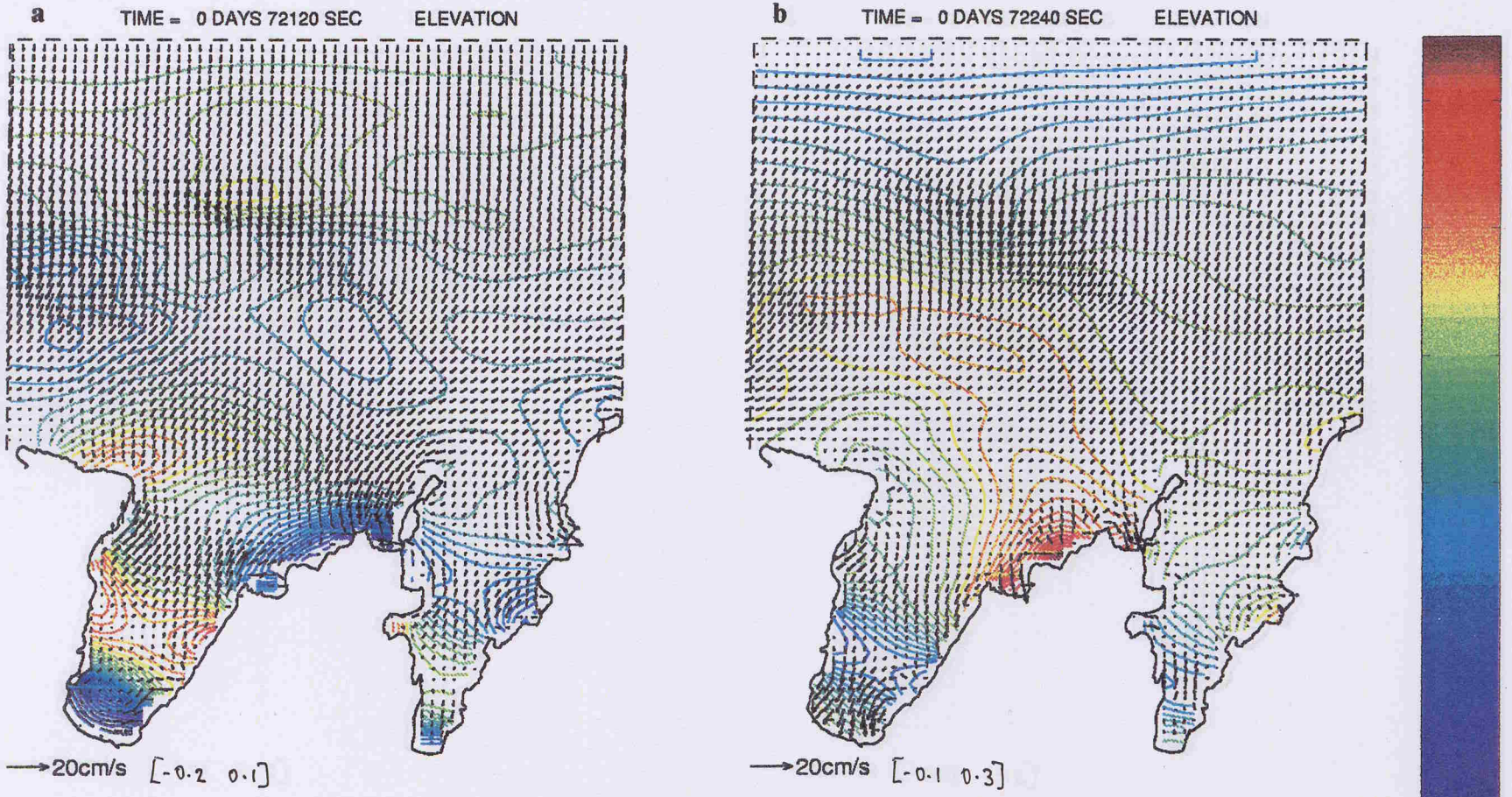

Fig. 5.13(a)-(b) Snapshots of water elevation and flow patterns at two minutes interval for run 2a. Forcing is produced by a random signal (A_{rms} = 0.1m) incident from the open sea in an along-bay axis direction.
Elevation is measured in meters and its magnitude for each contour is described by the colourbar.
The range of elevations is indicated separately for each plot. Sea current is measured in cms^{-1}.

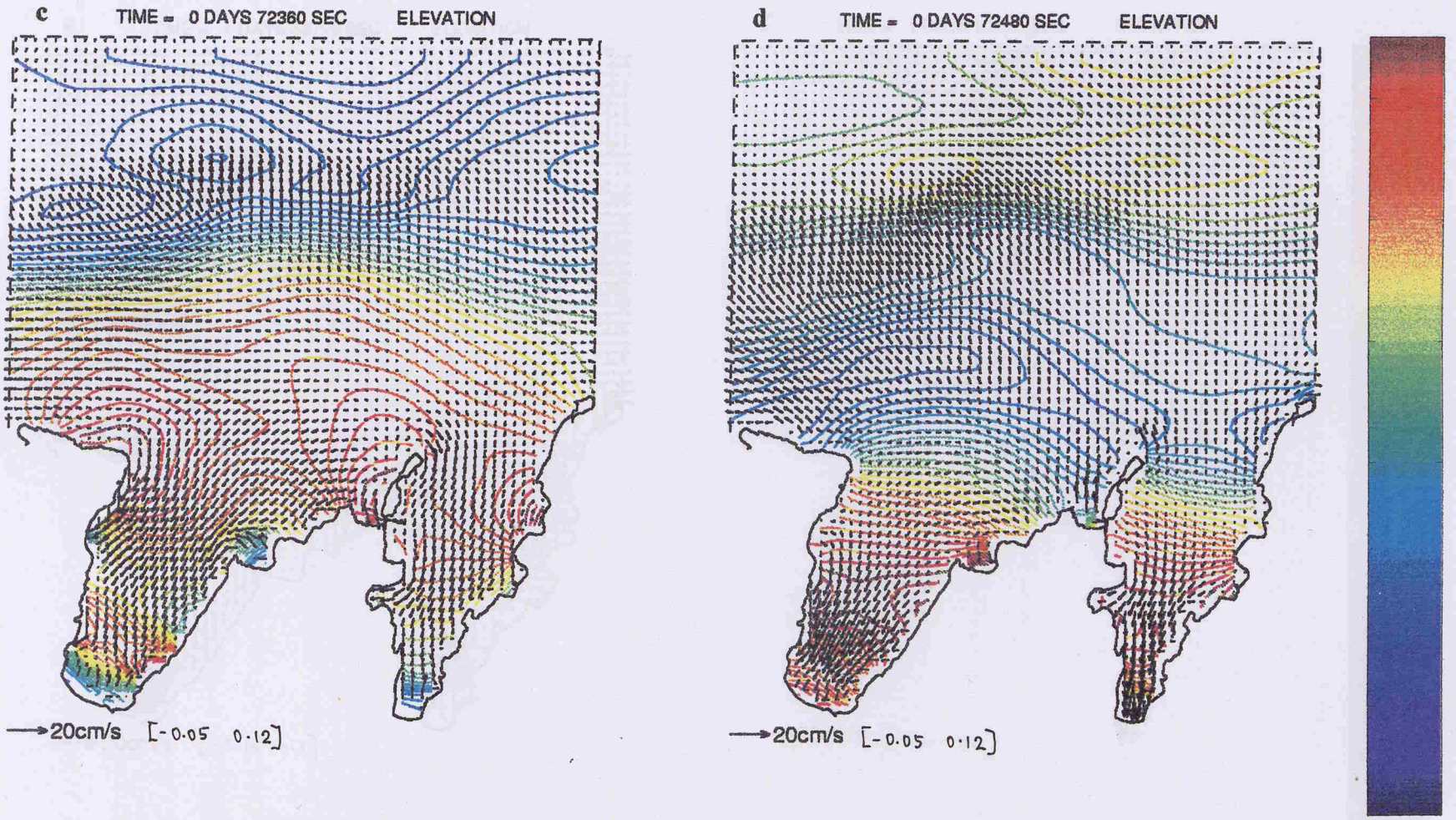

Fig. 5.13(c)-(d) Snapshots of water elevation and flow patterns at two minutes interval for run 2a. Forcing is produced by a random signal (A_{rms} = 0.1m) incident from the open sea in an along-bay axis direction.
Elevation is measured in meters and its magnitude for each contour is described by the colourbar.
The range of elevations is indicated separately for each plot. Sea current is measured in cms^{-1}.

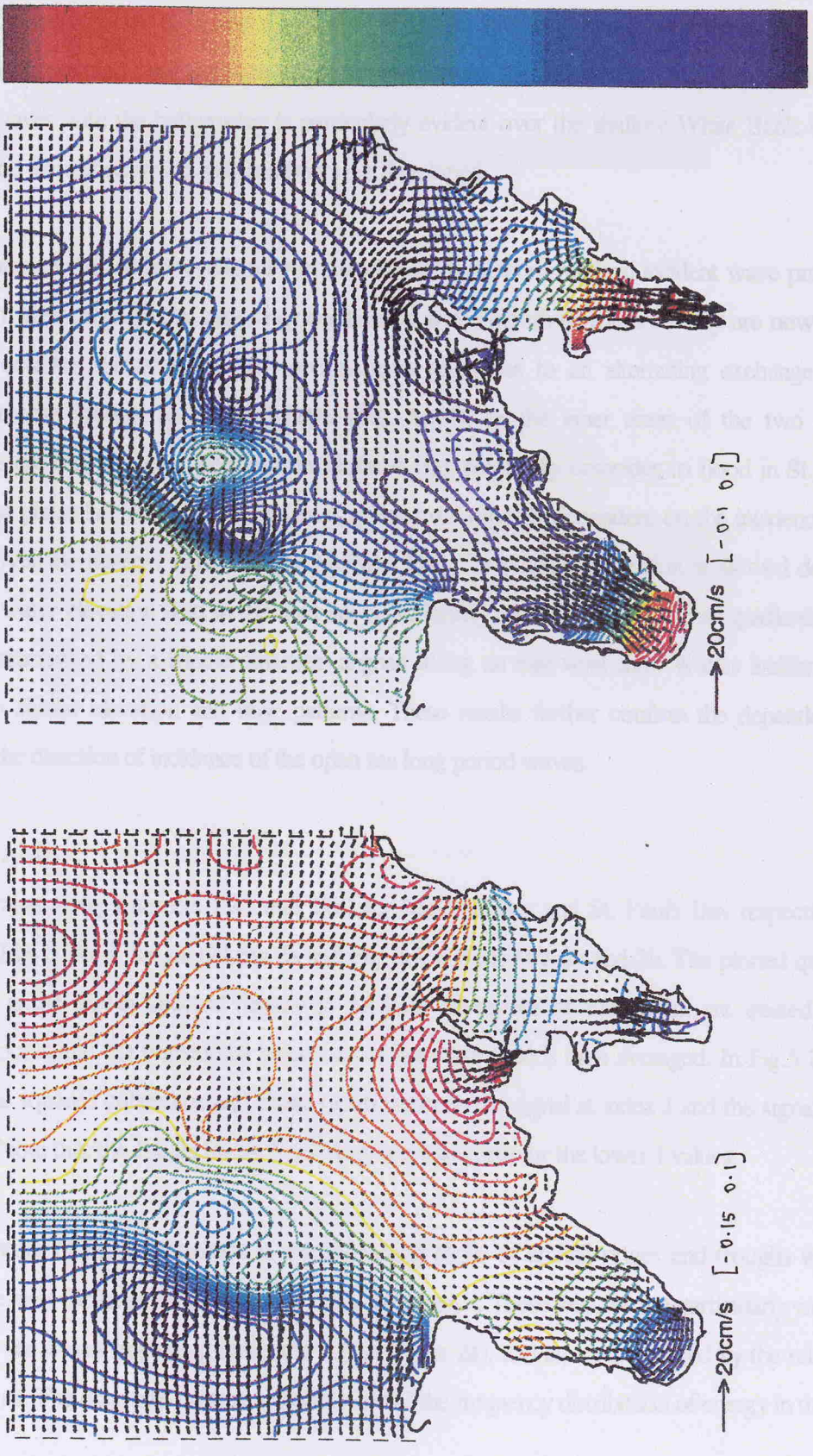

Fig. 5.13(e)-(f) Snapshots of water elevation and flow patterns at five minutes interval for run 2b. Forcing is produced by a random signal (A_{rms} = 0.1m) moving in an alongshore direction from the west.
Elevation is measured in meters and its magnitude for each contour is described by the colourbar.
The range of elevations is indicated separately for each plot. Sea current is measured in cms^{-1}.

association to an oscillation between the western bay promontary and the outer eastern flank of the bay. The latter piece of shore consists moreover of a number of smaller inlets at which there is a tendency for waves to be amplified and for coupled oscillations to occur between them. In the open sea, the interaction of the incident long period waves with the bathymetry is particularly evident over the shallow White Bank where steep sea level slopes and intensified seiche-induced flows are developed.

Fig. 5.13e,f present the model results for run 2b with an alongshore random incident wave propagating in the open sea from west to east. The cross-bay oscillations at the mouth of Mellieha Bay are now enhanced (Fig. 5.13e). The coupling between the two embayments gives rise to an alternating exchange flow which is particularly intense around St. Paul's Islands (Fig. 5.13f). In the inner areas of the two bays, sea level displacements are out of phase. Ebb flow in Mellieha Bay practically coincides to flood in St. Paul's Bay and viceversa. The phase lag between the two bays is however strongly dependent on the incidence of the forcing wave field. Over the shallow bank outside Mellieha Bay, the wave propagation is slowed down and spatial scales of the water elevation field in the area are considerably reduced. The sea level gradients and associated flows are characterised by a tripole structure aligned along an east-west axis. Waves incident from the east produce very similar elevation and flow patterns. These results further confirm the dependence of the bay response on the direction of incidence of the open sea long period waves.

F-S DIAGRAMS

The f-s diagrams along transects TR1 and TR2 for Mellieha Bay and St. Paul's Bay respectively are plotted separately in Fig. 5.14a-f for model run 2a and Fig. 5.15a-b for runs 2a and 2b. The plotted quantity along the z-coordinate is the power spectral density in decibels. Elevations at each point are treated as a stationary stochastic process and the transitional behaviour of the wave field is time averaged. In Fig.5.14c-f the plotted quantity is the squared coherence and phase (lead) between the signal at index J and the signal at the origin of the transect. Note that the J scale for St. Paul's Bay is not uniform for the lower J values.

The main feature of the f-s diagrams is the alternating series of arched ridges and troughs which tend to be parallel to the axes for large values of index J and frequency f. These features are particularly well defined in the case of open sea waves impinging along the bay axis (run 2a), and are corroborated by the relevant coherence and phase plots. The diagrams portray a spatial view of the frequency distribution of energy in the model

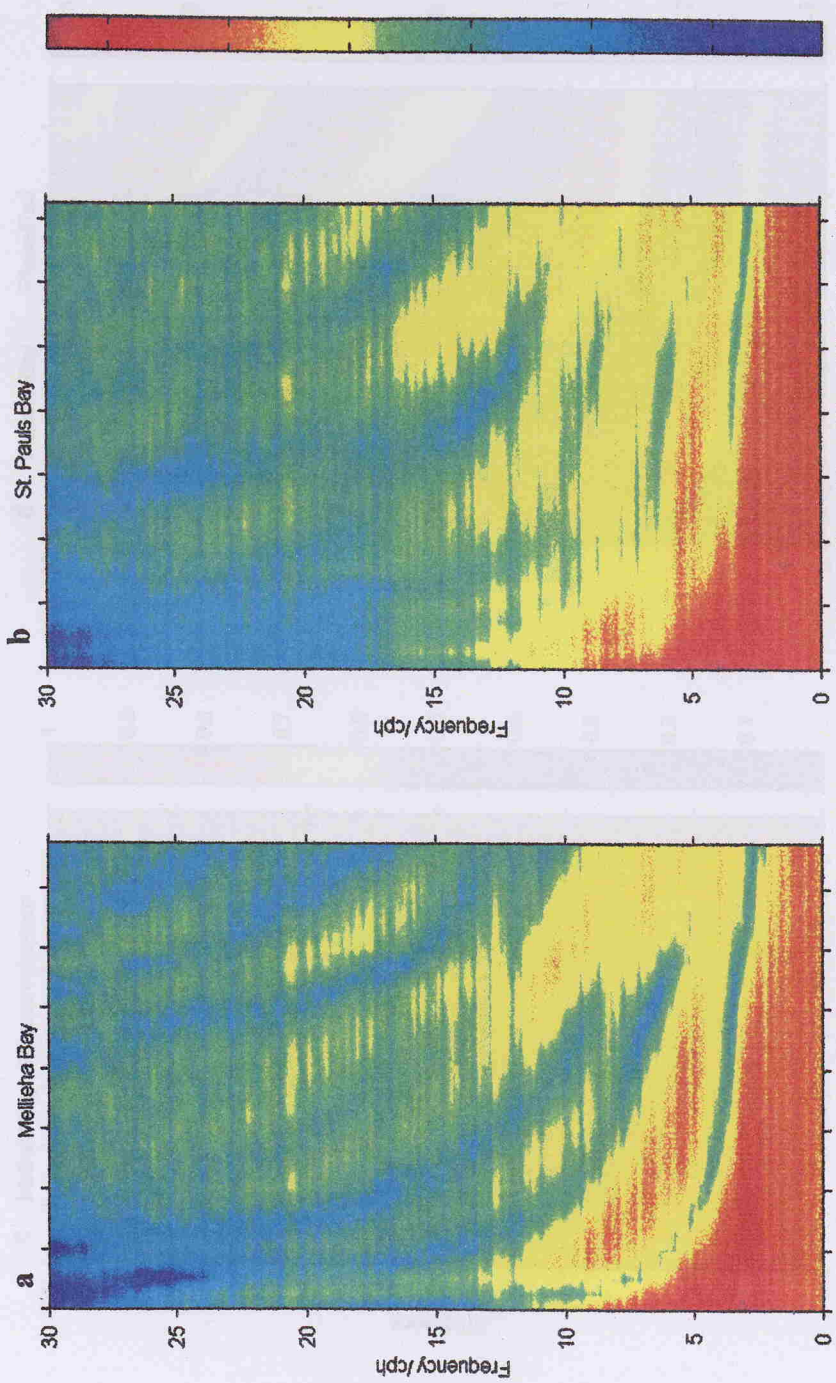

Fig. 5.14 PSD in decibels plotted in frequency-space for (a) Mellieha Bay and (b) St. Paul's Bay in the case of run 2a. The J index for space runs over the transects TR1 and TR2 in Fig. 5.12. Maximum/minimum PSD values used in the colorbar are denoted next to each plot.
The power spectral densities are calculated with 18 degrees of freedom and a 95% confidence factor of 6.1 dB (B_{min}=0.57; B_{max}=2.2).

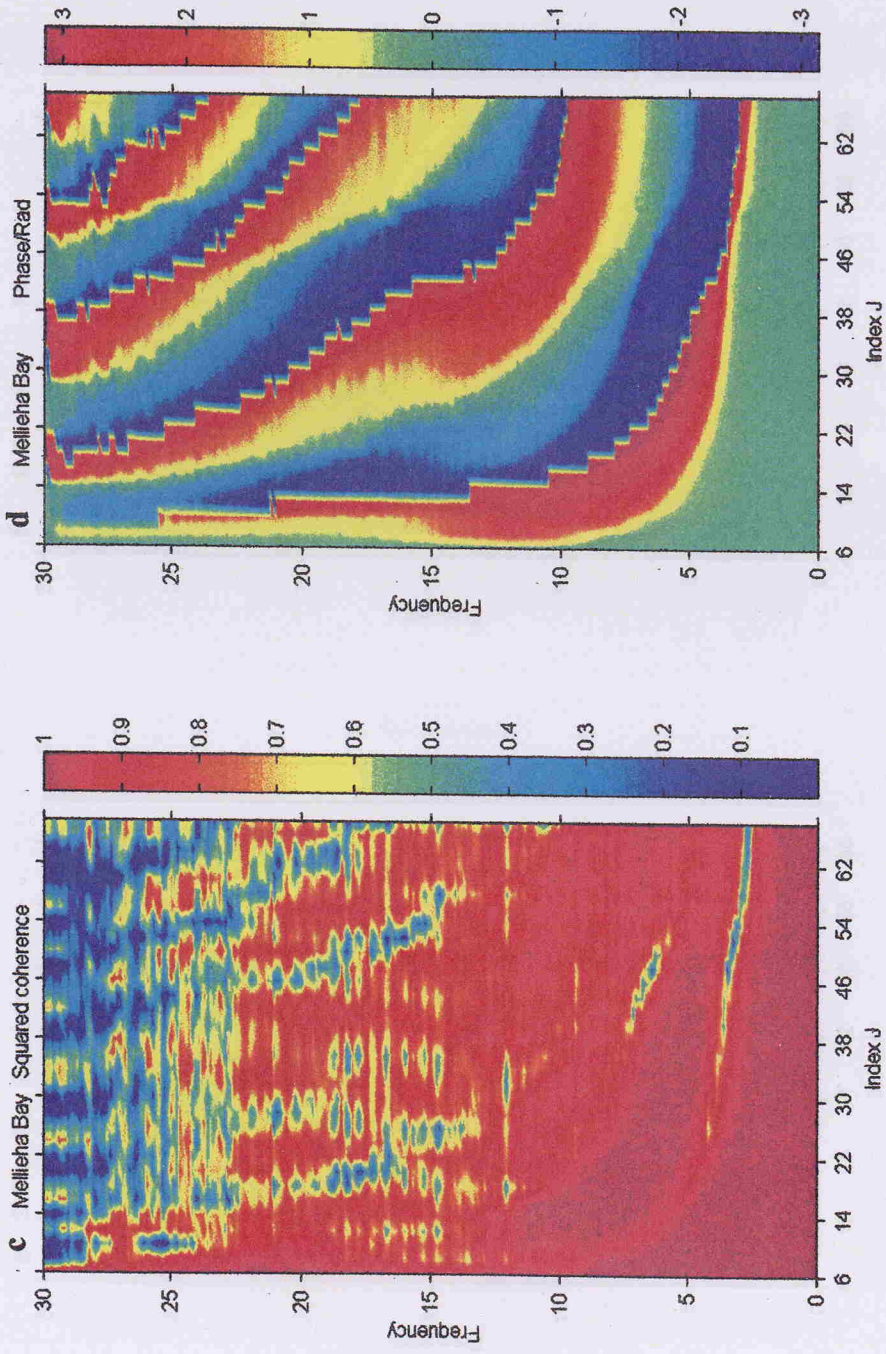

Fig. 5.14 (c) Squared coherence and (d) phase for Mellieha Bay in the case of run 2a, plotted in frequency-space. The J index for space runs over the transects TR1 and TR2 in Fig. 5.12. With 18 degrees of freedom the level at which the coherence is significant at the 95% confidence level is equal to 0.28.

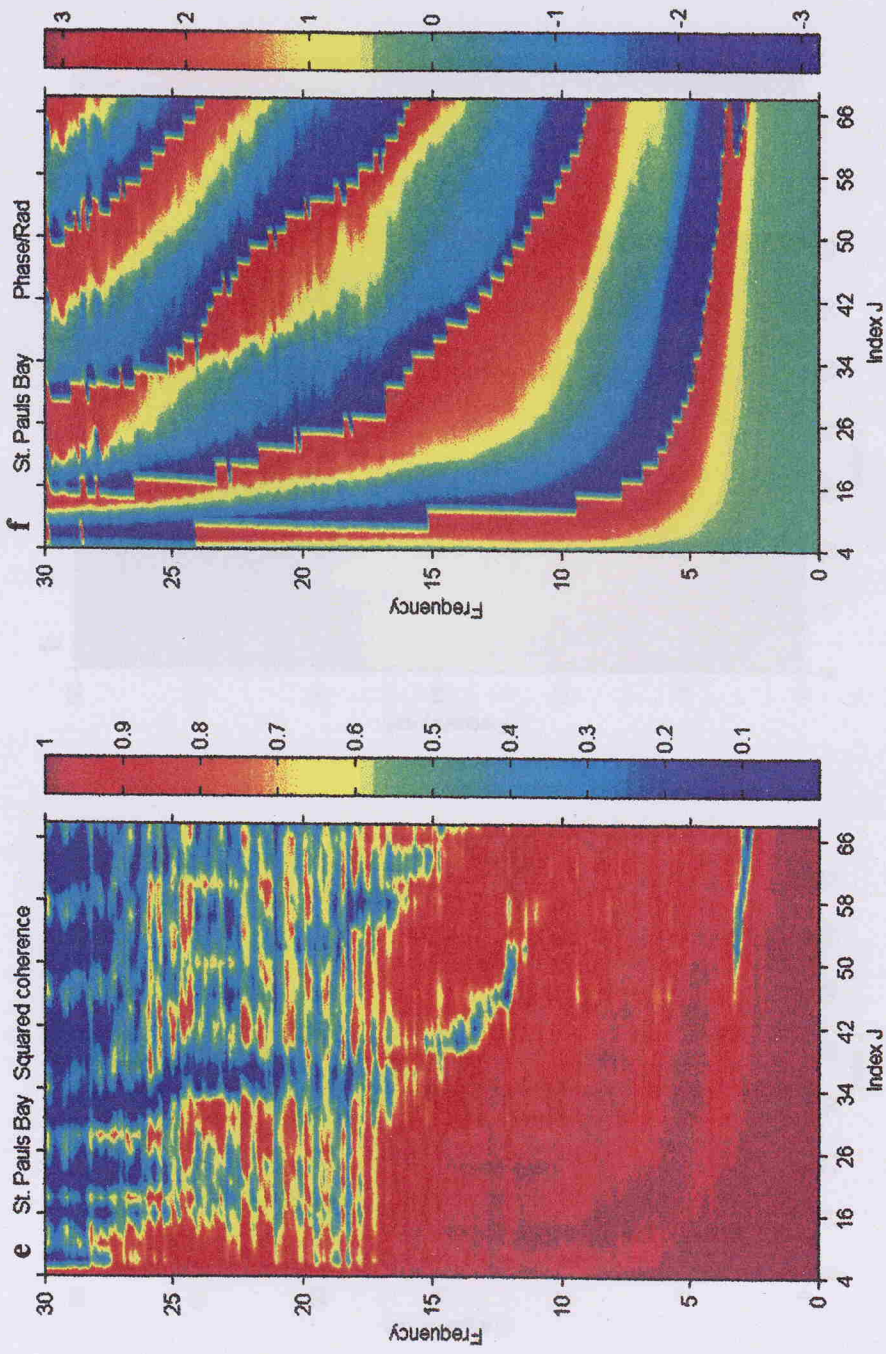

Fig. 5.14 (e) Squared coherence and (f) phase for St. Paul's Bay in the case of run 2a, plotted in frequency-space. The J index for space runs over the transects TR1 and TR2 in Fig. 5.12.
With 18 degrees of freedom the level at which the coherence is significant at the 95% confidence level is equal to 0.28.

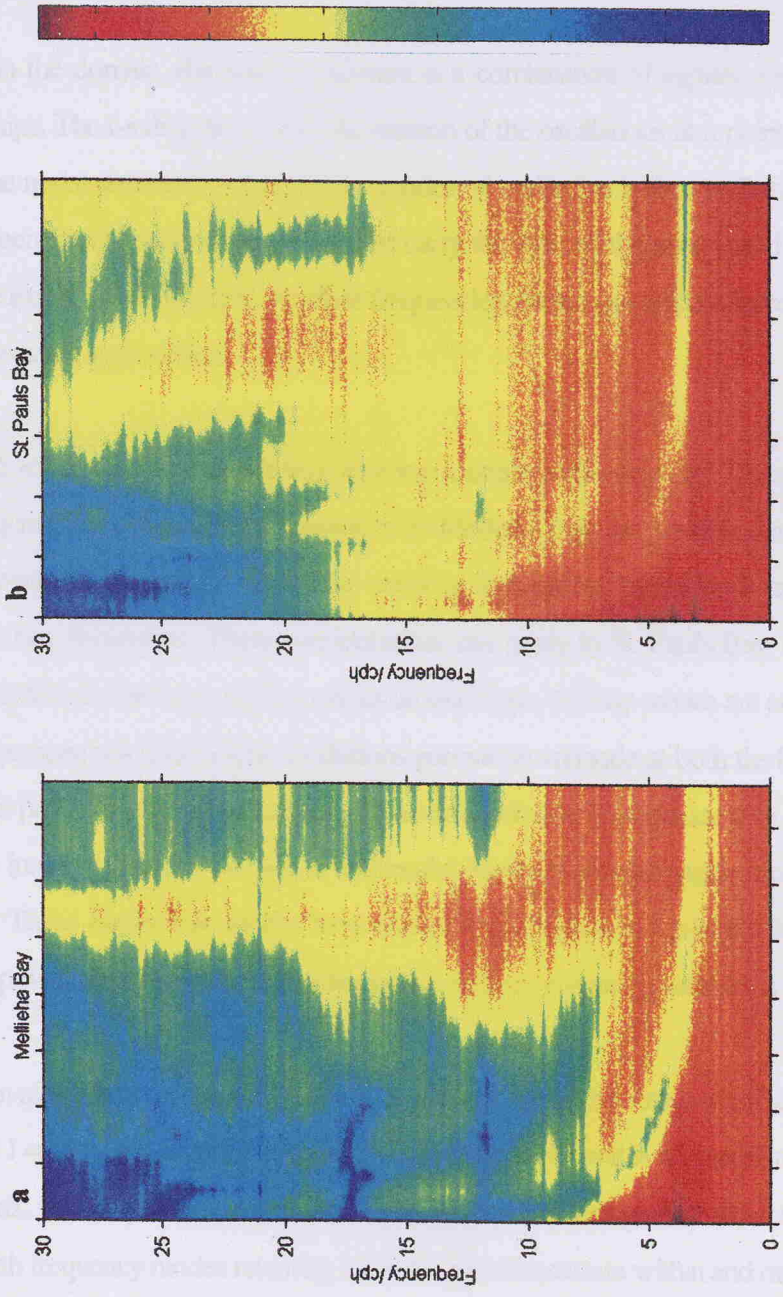

Fig. 5.15a,b PSD in decibels plotted in frequency-space for (a) Mellieha Bay and (b) St. Paul's Bay in the case of run 2b. The J index for space runs over the transects TR1 and TR2 in Fig. 5.12. The range of PSD values spanning the colorbar is denoted next to each plot.
The power spectral densities are calculated with 18 degrees of freedom and a 95% confidence factor of 6.1 dB (B_{min}=0.57; B_{max}=2.2).

domain. It is important to note that the colorbar of PSD values is specific to each plot and ranges from the maximum PSD (deep red) to minimum PSD (deep blue). This is necessary in order to optimise colour contrast. These maximum/minumum PSD values are denoted in decibels next to each plot. Comparisons between f-s diagrams should thus be done with caution.

At each point in the domain, the water oscillation is a combination of signals with different frequencies and phase relationships. The f-s diagrams show the relation of the oscillations at a point with that at other points in the domain. The nodal structure of the various modes of oscillation is thus well evidenced by these diagrams. The lower frequencies (f less than about 2.5 cph) carry the bulk of the energy and oscillations retain the same phase along the extent of the transect. At these frequencies, there is an evident increase of the power density as the inner bay areas are approached.

In the range $2.5 < f < 4$ cph the oscillations develop a single nodal structure. The position of the node moves closer to the bay mouth with increasing frequency. In Mellieha Bay, the predominant mode at T = 21minutes (P in Fig. 5.11) extends up to index J = 50. This confirms that the oscillation involves a water body that extends well beyond the bay dimensions. These considerations also apply to St. Paul's Bay, even though the aperture of the bay is slightly less. In the range of frequencies around 5cph, the bay modes are coupled to the standing wave oscillations in the open sea area. These oscillations present an antinode at both the head of the bay as well as at around J = 34 in proximity to the bay mouths. These antinodes are in antiphase (Fig. 5.14d). As we go to higher frequencies the inner bay modes develop a multinodal structure which is again clearly coupled to the adjacent open sea area. These higher bay modes have similar wavelengths and energies in St. Paul's Bay. The trend shows that the power density for the higher frequency region decreases gradually in the interior of the bays.

In the case of an alongshore open sea wave (Fig. 5.15 for run 2b), the streak of enhanced power spectral density centred around J = 50 runs across the full spectrum of frequencies and is attributed to the amplification of waves over White Bank. For frequencies lower than 7cph, the f-s diagrams present the same general characteristics as in the above with frequency modes retaining the same spatial structure within and outside the bays. The selective frequency distribution of energy within the embayments is however somewhat altered (as explained in section 5.9.2.4) and amplification ratios in the embayments with respect to the open sea wave are considerably reduced especially in St. Paul's Bay.

5.9.2.6 Summary of model comparison with observations

It is of course unrealistic to pretend a complete correspondence between model results and observations since the adoption of a simple incidence of energy from a single direction in the model cannot realise the real, complex wave field in the open sea. This limitation is particularly evident at the higher frequencies. The relatively high coherence, and the generally linear variation of phase at these frequencies (refer to Fig. 5.10) are in fact connected to the presence of a consistent progressive wave component in the open sea area. This problem can only be overcome by the use of nested models in which the nearshore model is forced by a larger area model. In such an application the solution domain is composed of (1) a high resolution near-region that encompasses the embayments, and (2) the immediate open sea area, together with a lower resolution far-region that extends over the shelf area. The solutions in the two sub-domains are coupled by matching solutions and applying appropriate conditions at the artificial boundary joining them.

The numerical simulations in this study have however succeeded to model the response of two coupled wide-mouthed embayments in detail. The simulations have also highlighted and confirmed a number of important points relating to the character of seiches in the two embayments.

1) The model results demonstrate that the specific topographic features of a basin plays a determining role in the transformation and amplification of long waves near the coast. Long narrow inlets, or relatively wide-mouthed bays, can both act as local resonators to incoming long waves. The most energetic frequencies for narrow-mouthed basins during seiching events are very similar to those for ordinary background waves and correspond to the eigen-frequencies of these basins. In the case of wide-mouthed basins like Mellieha Bay and St. Paul's Bay, the two-way coupling with the open sea area is more important and there is a greater variability in the spectral response. It is however noted that the seiche oscillations are dominated by the fundamental and the first bay modes even in the case of wide-mouthed open basins.

2) The higher frequency seiches involve the isolated motion of the inner shallow bay area, whereas the lower frequency oscillations consist of a coupled motion of the interior of the bay with the deeper open sea areas. The coupling between the two embayments is confirmed by the common spectral peaks of the two embayments as well as an analysis of the phase and spatial wave patterns. The coupling between the embayments is further complicated by the morphology of the sea bottom which presents a comparatively extensive bank in the

immediate offshore area outside Mellieha Bay. The water body that is set in motion is thus not simply confined to the interior of the bays, but actually extends well beyond the bay promontaries.

3) The results support the hypothesis of a two-step generation mechanism for strong seiching events and show that water level oscillations in the embayments result from a response of the embayments to wave structures in the adjacent open sea area. The direct forcing of seiche oscillations in the embayments is unlikely. The intensity and spectral character of the sea level oscillations in the embayments are found to be greatly dependent on the nature and incidence of the long period open sea waves. Leaky waves reaching the embayments along the cross-shore direction (run 2a) are more effective in forcing strong water level oscillations. Weaker oscillations occur in the case of eastward propagating alongshore waves.

4) The model can be easily adapted for transport studies of contaminants and general flushing characteristics in the embayments. This is explained in detail in section 5.10. The model applications in this section can be extended to include not only the seiche-induced flow but also the effects of the mean circulation in the bays. In particular, the results show the effectiveness of the Princeton Ocean Model in describing the response functions of water level and current velocities in the embayments to an offshore disturbance. This has important applications particularly in estimating the amplification of incoming waves in tsunami prediction and protection.

5.10 Seiche-induced flushing in coastal embayments

5.10.1 Water quality problems in the bays

Both Mellieha Bay and St. Paul's Bay are very popular touristic areas and anthropogenic pressures on the water quality in the embayments is problematic especially during summer. The two bays are used for bathing, berthing and mooring of fishing and pleasure boats, as well as for fish-farming activities. The surrounding coastal areas are also heavily developed especially in the case of St. Paul's Bay. Water quality management programs are thus necessary in order to assess the pollution loading in the coastal embayments especially in view of the intensive and multiple use of the coast. If pollutant concentrations are allowed to increase above critical levels, then the result is sub-standard water quality as characterised by a reduction in dissolved oxygen and the presence of algal blooms. A quantitative knowledge on the flushing mechanisms pertaining to the two embayments is thus necessary in order to assess their carrying capacity and sustainable exploitation.

Wind and waves are important factors in flushing out pollutants from the bays especially during storms. The alternating diurnal alongshore currents outside the embayments and density differences have also an effect on the exchange of water between the embayments and the open sea. During milder periods of calm wind conditions other factors such as the seiche-induced motions in the embayments become important. The action of the seiche in mixing and flushing bay water is similar to the effect of the tidal exchange between semi-enclosed coastal areas (such as gulfs, inlets or harbours) and the open sea in tidally dominated environments.

The sloshing of water into and out of the embayments during seiche oscillations can drastically dilute the contaminated bay water with clean open sea water. In the case of wide open-mouthed embayments, the seiching exchange is predominantly caused by the horizontal flows associated with the seiche. The depth-averaged mathematical model described above is thus adequate to consider the seiching exchange mechanism of horizontal circulation in the two embayments. The model utilises the seiche-induced hydrodynamics in Mellieha Bay and St. Paul's Bay to quantify the effect of seiching on the flushing characteristics of the embayments in terms of an exchange coefficient with the open sea and the degree of mixing. The effect of turbulent diffusion is parametrised by combined depth averaged dispersion and diffusion coefficients which are used in the two-dimensional advection-diffusion equation.

5.10.2 Exchange index of the bays

Enclosed basins like bays have much more water quality problems than open sea coasts since the water exchange is restricted. According to Murakami (1993), a parameter that is used to indicate the level of enclosure of a coastal embayment is

$$E.I. = \frac{\sqrt{S_a}\,D}{WD_o} \tag{5.37}$$

where E. I. is the enclosure index, S_a is the horizontal areal extent of the embayment, W is the width of the connection to the open sea, D is the mean depth of the embayment and D_o is the mean depth at the entrance. For an enclosed sea, E.I. > 2 while for an open sea E.I. < 1. Intermediate values qualify for a semi-enclosed sea.. E.I. = 1 corresponds to the case of a square embayment with uniform depth and open along one side.

Table 5.2 *Enclosure index for Mellieha Bay and St. Paul's Bay*

	S_a/Km^2	D/m	W/m	D_0/m	E.I.
Mellieha Bay (total)	6.422	16.1	3000	28	0.49
Mellieha Bay (inner)	2.160	11.0	1500	15	0.72
St. Paul's Bay (total)	3.874	15.3	1500	30	0.67
St. Paul's Bay (inner)	1.166	6.6	1000	10	0.72

According to this index (refer to Table 5.2), neither Mellieha Bay nor St. Paul's Bay can be classified as enclosed coastal areas, and flushing of the embayments should not therefore be excessively problematic except for the inner areas of the bays. The inner bay regions considered in this estimate are the same as those depicted in Fig. 5.16.

5.10.3 Transport mechanisms and parametrisation

This section draws the basic elements necessary for an assessment on the effect which seiches can have on the transportation of resuspended debris or of contaminants that can accidentally become released in the embayments. Knowledge on the incidence of seiches, and on the associated dispersion characteristics of the sea water can throw light on how to best control sources of pollution in order to minimise risks on other entities operating in the area.

The problem of interest concerns the spreading of suspended particulate matter or dissolved constituent, released continuously or sporadically at a point or restricted area, and subsequently transported by the sea currents. Similar to the case of momentum transport in coastal geophysical domains, this transport of particulate matter in the sea can be assumed to be essentially horizontal in the far field. In close proximity to the source the three-dimensional nature of the phenomenon may indeed be important, but at a sufficient distance away from the source, the horizontal component of the transport mechanism prevails over the vertical. In the case of suspended particles in the presence of a homogeneous water column, it may thus be assumed that the concentration C(x,y,t) can be represented by a depth-mean value. In the presence of stratification, strong buoyancy effects may constrain the transport to occur along a surface or interfacial layer and the concentration can be defined with respect to a specific layer thickness and depth. In both these cases the 2D treatment of the transport is adequate.

It is also important to note that the transport process is governed by two main physical mechanisms, namely advection and diffusion. Advection results from the entrainment of the suspended particles in the local flow which results in a transport along the trajectory and with the velocity of the water (assuming a negligible resistance to the flow). On the other hand, diffusion occurs even in the absence of a flow and results, in the case of laminar flow, from the motions at molecular level that cause a gradual and continuous increase of the area around the source occupied by the particles. In the case of turbulent flow, the nature of the diffusion process is no longer restricted to the molecular motions and the entrainment of suspended mass in turbulent eddies becomes the predominant mechanism for the spreading of the particles. In the sea, it is the latter diffusion process that is most important, and the related rate of diffusion, according to the Boussinesq approximation, is described by what is known as the Eddy Diffusion coefficient K which is several orders of magnitude greater than the molecular diffusion coefficient. The proportion by which the two mechanisms of advection and diffusion contribute to the transport of the suspended particles is quantified through the Peclet number $P_e=UL/K$, where U (ms^{-1}) is the characteristic velocity of the transporting fluid and L (m) is a characteristic length of the flow domain. Values of P_e, $o[P_e]>1$ imply a dominance of advection over diffusion.

Finally, it is also necessary to distinguish between the cases of conservative (passive) and non-conservative (active) transport of constituents in the sea. If the total mass of the advected-diffused constituent is not altered during its transport, then it is characterised as a conservative one. Otherwise, if physical, chemical or biological processes occur along with its transport resulting in a decrease or increase of its initial mass, the constituent is then characterised as a non-conservative one. In the case of suspended particles, the gradual settlement back to the sea bed is equivalent to a decay of the original suspended mass of sediment.

5.10.4 Estimation of seiche flushing times by the box model

5.10.4.1 Single box model

In order to estimate integral time scales that apply to the physical transport processes of the embayment as a whole, the simple well-mixed box model approach can be adopted. The embayment is considered as a single water body of volume V, that is continuously flushed by a flux Q (m^3s^{-1}) through its boundary with the open sea. The mixing processes in the embayment are assumed to be strong enough to quickly distribute any

substance introduced in the basin over all of its volume. The water exchange with the open sea is then given by

$$\frac{dC_n}{dn} = -\frac{QC_n}{V} \tag{5.38}$$

and can thus be characterised by the exchange coefficient E (Falconer, 1984) defined by:

$$E = 1-\left(C_n / C_o\right)^{1/n} \tag{5.39}$$

where C_o is the initial spatial average concentration of a passive tracer, and C_n is the spatial average concentration after n exchange cycles. In our application, each seiching oscillation can be taken as a cycle of water movement into and out of the embayment. This coefficient is a measure of the renovation rate and depends on the seiche range and the harbour geometry. Dependence on seiche range is monotonous but not linear. Concerning the geometry, the entrance size, depth and orientation, as well as the influence of the external geometry are important. The exchange coefficient can be used as a parameter for assessing the contribution of the seiche on the flushing and water quality characteristics of the embayment. An estimate of E can be obtained from the slope (= log(1-E)) of the linear plot $\log(C_n/C_o)$ against n.

On the basis of E it is also possible to calculate the handling capacity of an embayment to sources of pollution. In the case of a continuous discharge of pollution of concentration C_p, at a rate Q_p, the equilibrium concentration C_{eq} inside the embayment is given by

$$C_{eq} = \frac{C_p Q_p T}{EV} \tag{5.40}$$

where V is the bay mean water volume and T is the seiche period.

The box model concept can also be used to obtain an estimate of the flushing time scale on the basis of the seiche prism. The seiche prism is defined as the amplitude V_s with which the bay mean water volume V

oscillates during a seiche cycle. If the volume introduced during inflow, $2V_s$, is assumed to completely mix with the low seiche volume V- V_s, the flushing time τ_o for the embayment is given by

$$\tau_o = \frac{V - V_s}{2V_s} T \tag{5.41}$$

This gives a lower bound to τ_o since the inflow volume is in general not completely mixed with the full bay water body. Takeoka (1984) expresses the flushing characteristics in terms of an averaged residence time τ_d expressed by

$$\tau_d = \int_0^{\infty} C(t)dt / C_o \tag{5.42}$$

5.10.4.2 Application to Mellieha Bay and St. Paul's Bay

On the basis of r.m.s transports simulated by model run 2a, for an incident random signal with an r.m.s amplitude of 0.1m, the box model method is used to estimate the exchange coefficients and flushing parameters for Mellieha Bay and St. Paul's Bay. The initial concentration within the representative box is assumed to be uniform, whereas the concentration outside is zero. The estimates are presented in Table 5.3. The parameters for the inner bay regions (M_1 and P_1 respectively) are calculated from an exchange with the outer and deeper part of the bay which are in this case assumed to be clean waters. The exchange volumes across the respective boundaries of the inner and full bay regions (Fig. 5.16) are obtained from the numerically modelled results (run 2a). Each seiche cycle is on average taken to be equivalent to 20 minutes. From a comparison between expressions (38) and (39), $\ln(1 - E) = -Q / V$, from which E can be estimated.

These results show that a moderate seiching event produces a major contribution in the flushing of the two embayments even in cases where the duration of the event is less than one day. The flushing characteristics for the two bays are very similar. The water body in Mellieha Bay is about twice that in St. Paul's Bay, but the greater exchange with the outer open sea permits the flushing rates to be nearly the same in the two bays. The inner parts of the embayments are shallow and represent only a small volume of the respective bay water body.

Table 5.3 *Flushing characteristics for Mellieha Bay and St. Paul's Bay*

	Mean basin volume /x10^{6}m^3	Exchange volume / x10^{6}m^3	Exchange coefficient E	Residence time τ_d /seiche cycles
Mellieha Bay (total)	103.4	1.12	0.0107	93
Mellieha Bay (inner)	23.6	0.66	0.0272	37
St. Paul's Bay (total)	59.1	0.72	0.0120	83
St. Paul's Bay (inner)	7.7	0.30	0.0381	26

(1 seiche cycle ≈ 20 minutes)

They are relatively well flushed by the seiches which can reduce contamination at an e-folding rate (time to reduce the average concentration to 1/e of its initial value) of less than 12 hours.

5.10.4.3 Double box model

In a more refined manner, time scales may differ appreciably at different positions in the bay. For this purpose the box model concept can be extrapolated by dividing the bay into a number of interconnected segments each of which is coupled by flux exchanges with the adjacent segments. This method can be usefully applied to estimate the seiche-induced flushing of contaminants originating at different parts of the two bays.

The two embayments are each divided into two segments, with mean volumes V_1 and V_2, and tracer concentrations C_1 and C_2 respectively (Fig. 5.16). The flux exchange between the two segments is Q_1 (m^3s^{-1}). The exchange with the open sea is Q_o (m^3s^{-1}). Assuming a well mixed system, with no internal sources or sinks, the mass balance between the segments leads to the set of simultaneous equations:

$$V_1 \frac{dC_1}{dt} = Q_1(C_2 - C_1) \qquad (5.43a)$$

$$V_2 \frac{dC_2}{dt} = Q_1(C_1 - C_2) + Q_0(C_0 - C_2) \qquad (5.43b)$$

where C_o is the tracer concentration in the open sea, assumed to be constant. Knowing V_1, V_2, Q_1 and Q_o, these equations can be solved, with appropriate initial conditions, to give the time evolution of C_1 and C_2.

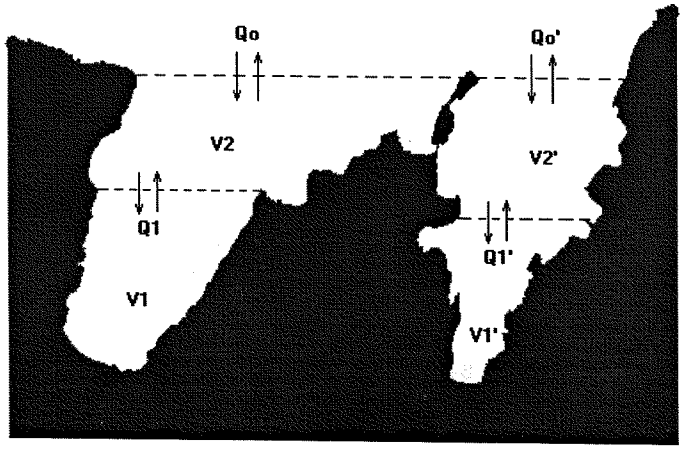

Fig. 5.16 Segments of Mellieha Bay and St. Paul's Bay considered for the two-box model.

This has been done using values of Q_1 and Q_o as in Table 5.3 derived from the hydrodynamical model (run 2a). Three cases are considered: (1) with initial concentrations of 100 units in each segment; (2) with an initial concentration of 100 units in the inner segment and nil concentration in the intermediate segment, and (3) with an initially clean sea in the inner segment and maximum initial concentration in the intermediate segment only. In all cases the outer sea is assumed to retain nil concentration so that any contamination flowing out of the bays is dispersed and never returns back into the bays.

The results of the analysis (Fig. 5.17a-c) indicate a very effective diminuition of contamination that originates in the inner parts of the embayments (case 2). This is due to the seiche-induced flow exchange with the deeper outer segment of the bays where the contaminant is able to spread and become quickly diluted. The e-folding

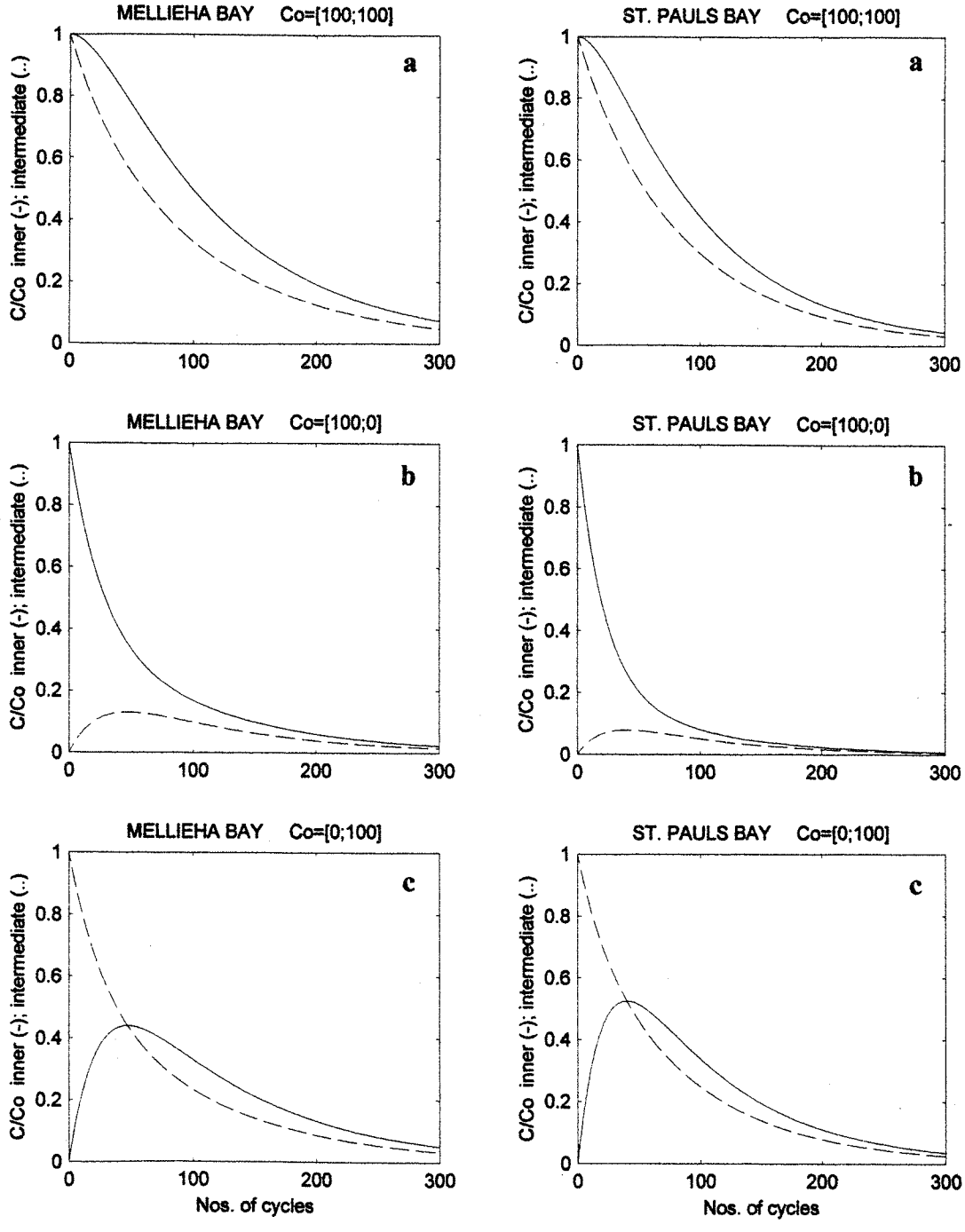

Fig. 5.17 Application of the 2-box model in Mellieha Bay and St. Paul's Bay with initial maximum concentration C_o, (a) in both inner and intermediate segments (case 1), (b) in the inner segment only (case 2), and (c) in the intermediate segment only (case 3). The normalised concentrations C/C_o are plotted as a solid/dashed curve for the inner/outer segments.

dilution times for the inner bay areas are of the order of 18h and 11h in Mellieha Bay and St. Paul's Bay respectively.

When the receiving intermediate bay segment is already contaminated (case 1), the flushing is much slower and agrees with rates determined by the one-box model. The worst conditions occur when the contamination originates in the intermediate segments (case 3). The results show that the seiche-induced horizontal advection causes a considerable transport of contaminants into the inner bay areas where relative concentrations can reach values close to 45% in Mellieha Bay and 55% in St. Paul's Bay respectively. These conditions are of greater detriment to the water quality in the bays because the contamination in the inner bay areas takes even longer to be flushed out than in the case 2 when the contamination source originates from the inner bay area itself. Hence mixing caused by the seiche oscillations is of benefit in diluting contaminants originating in the inner bay areas, but tends to deteriorate conditions when the contamination comes from the outer bay areas.

5.10.5 Mathematical advection-diffusion transport model

The box model is underpinned by a number of simplifications. Mixing is assumed to be under the exclusive control of advective processes. Outgoing contaminants are also assumed to be diluted quickly enough and a return back into the bay is excluded. A numerical contamination transport model is thus applied in this section to study the seiche-induced flushing characteristics of Mellieha Bay in greater detail. The model calculates the two-dimensional depth-averaged concentration field as it evolves in time under the influence of the seiche-induced bay oscillations and of the correlated mixing and exchange with the open sea water. The model supercedes the box model calculations in that it provides a spatial and temporal coverage of the concentration field, thus enabling a concentration control at specific positions within the bay. Moreover the model takes into consideration both the advection and diffusion effects on the transport. It can also be applied to situations in which contaminant discharge is confined to localised sources.

5.10.5.1 Formulation of the model

The governing differential equations used in the mathematical model consist of the time-dependent, depth-averaged, non-linear equations of mass and momentum describing the fluid motion in the horizontal plane, together with an advection-diffusion equation describing the conservation of mass of suspended/dissolved matter during its motion. The momentum equations are solved by means of the finite difference formulation

used in POM, with the effects of the earth's rotation and bed friction included as described in section 5.3.1. The advection-diffusion model is written in terms of a scalar function C(x,y,t) which describes the concentration as a mass of suspended/dissolved matter in unit volume of sea water. A 2D depth-averaged horizontal transport is adopted so that complete mixing throughout the depth of flow is assumed. In the presence of turbulent flow, Fick's Law and the Boussinesq approximation are assumed to apply. The model equation is thus expressed as:

$$\frac{\partial C(H+\eta)}{\partial t}+\frac{\partial (CU(H+\eta))}{\partial x}+\frac{\partial (CV(H+\eta))}{\partial y}=\frac{\partial}{\partial x}\left((H+\eta)K_x\frac{\partial C}{\partial x}\right)+\frac{\partial}{\partial y}\left((H+\eta)K_y\frac{\partial C}{\partial y}\right) \qquad (5.44)$$

where K_x and K_y are the horizontal diffusion-dispersion coefficients and (U,V) are the depth averaged velocity components of the flow field. The boundary conditions completing the model are those of free transmission at an open boundary, that is

$$\frac{\partial}{\partial n}\left(K\frac{\partial C}{\partial n}\right)=0 \qquad (5.45)$$

where n is the unit vector normal to the boundary. At the closed boundaries the normal velocity components and the advective and diffusive transport was put equal to zero.

5.10.5.2 Solution by a finite differences scheme

This mixed (hyperbolic + parabolic) partial differential equation is solved numerically by a finite difference scheme which utilises the Alternating Directions Implicit technique. According to this method the solution advances from time level N to N+1 using an implicit scheme along y and explicit along x, while alternately from N+1 to N+2, it uses an implicit scheme along x and explicit along y. For a domain composed of IM grid cells along x and JM grid cells along y, this technique leads to the solution of IM algebraic systems in JM unknowns when advancing from N to N+1, and to the solution of JM systems in IM unknowns when advancing from N+1

to N+2 time levels. The finite difference formulation is implemented with all terms being fully centred in both space and time, and takes the form:

$$\begin{aligned}
&\left[C(H+\eta)\right]_{ij}^{n+1} = \left[C(H+\eta)\right]_{ij}^{n} - \frac{\Delta t}{2\Delta x}\left(\left[CU(H+\eta)\right]_{i+1j}^{n} - \left[CU(H+\eta)\right]_{i-1j}^{n}\right) \\
&-\frac{\Delta t}{2\Delta y}\left(\left[CV(H+\eta)\right]_{ij+1}^{n+1} - \left[CV(H+\eta)\right]_{ij-1}^{n+1}\right) \\
&-\frac{\Delta t K_x}{\Delta x^2}\left(\left[C(H+\eta)\right]_{i+1j}^{n} - 2\left[C(H+\eta)\right]_{ij}^{n} + \left[C(H+\eta)\right]_{i-1j}^{n}\right) \\
&+\frac{\Delta t K_y}{\Delta y^2}\left(\left[C(H+\eta)\right]_{ij+1}^{n+1/2} - 2\left[C(H+\eta)\right]_{ij}^{n+1/2} + \left[C(H+\eta)\right]_{ij-1}^{n+1/2}\right)
\end{aligned} \tag{5.46a}$$

$$\begin{aligned}
&\left[C(H+\eta)\right]_{ij}^{n+2} = \left[C(H+\eta)\right]_{ij}^{n+1} - \frac{\Delta t}{2\Delta x}\left(\left[CU(H+\eta)\right]_{i+1j}^{n+2} - \left[CU(H+\eta)\right]_{i-1j}^{n+2}\right) \\
&-\frac{\Delta t}{2\Delta y}\left(\left[CV(H+\eta)\right]_{ij+1}^{n+1} - \left[CV(H+\eta)\right]_{ij-1}^{n+1}\right) \\
&-\frac{\Delta t K_x}{\Delta x^2}\left(\left[C(H+\eta)\right]_{i+1j}^{n+3/2} - 2\left[C(H+\eta)\right]_{ij}^{n+3/2} + \left[C(H+\eta)\right]_{i-1j}^{n+3/2}\right) \\
&+\frac{\Delta t K_y}{\Delta y^2}\left(\left[C(H+\eta)\right]_{ij+1}^{n+1} - 2\left[C(H+\eta)\right]_{ij}^{n+1} + \left[C(H+\eta)\right]_{ij-1}^{n+1}\right)
\end{aligned} \tag{5.46b}$$

The stability of the numerical computations is controlled by:

$$U_{max}\frac{\Delta t}{\Delta x} < 1 \text{ and } K_{max}\frac{\Delta t}{(\Delta x)^2} < 0.5 \tag{5.47}$$

This does not however eliminate the propagation of errors deriving from numerical diffusion and the validity of the solution has to be ascertained by the choice of the right computational scheme.

The numerical code was written in Fortran 77 as part of this work and incorporated into the POM model.

5.10.5.3 The horizontal dispersion coefficients

The validity of these solutions relies on the values of the horizontal dispersion coefficients. These dispersion coefficients are related to the horizontal scale of the process that they represent and are difficult to quantify on a theoretical basis. Ideally they should be measured by, for example conducting dye studies. These coefficients are however related to the time and length scales of the largest unresolved motion and their order of magnitude can be estimated by dimensional relations extended from 3D turbulence theory (Okubo, 1980). If l denotes the length scale of mixing ($l \approx$ grid size) and ε the rate of energy cascade in the corresponding scale range, then

$$K \approx \varepsilon^{1/3} l^{4/3} \qquad (5.48)$$

This estimate is based on the assumption of (1) vertical homogeneity in a thin layer where the suspended constituent is confined, (2) horizontal homogeneity over some region embodying the dispersion patch, and (3) horizontal isotropy along an axis moving with the centre of the patch. These assumptions lead to symmetrical theoretical solutions that may not seem realistic, but which nevertheless give an ensemble estimate that is a reliable indication of the extent and rapidity of the dispersion (Bowden, 1972).

According to (5.48), the appropriate value of ε for the scale of motions with l in the range 100m - 1km is 10^{-8} m^2s^{-3}, which gives values of K in the range 1 - 22 m^2s^{-1}. Following Falconer (1984) the depth averaged dispersion coefficients are expressed by:

$$K_x = \frac{\lambda^{1/2} D(k_1 U^2 + k_2 V^2)}{(U^2 + V^2)^{1/2}} \ (m^2s^{-1}); \qquad K_y = \frac{\lambda^{1/2} D(k_1 V^2 + k_2 U^2)}{(U^2 + V^2)^{1/2}} \ (m^2s^{-1}) \qquad (5.49)$$

where according to Elder (1959) $k_1 = 5.93$ and $k_2 = 0.23$. These values of K are within the range expressed above. $D = H + \eta$ and λ is defined by (5.16).

5.10.5.4 Model runs

In all the model runs, initial conditions need to be specified for the water elevations, velocities and concentrations at all the wet grid points in the model domain. The elevation and velocity fields are first

established from a preliminary warming up phase of the hydrodynamical model. The advection-diffusion model is subsequently initiated from a specific starting concentration field of the conservative tracer.

In all the model runs applied below, the hydrodynamical field is established for the case of a random signal with an r.m.s amplitude of 0.1m, incident into the domain from an along-bay axis direction. The same model specifications as in run 2a, section 5.8, are utilised. The grid size is 120m, the integration time step for the momentum equations is 0.5s, bottom friction is expressed by a quadratic drag formulation and the horizontal kinematic diffusivity A_M is taken equal to $50m^2s^{-1}$. The tracer concentration field is integrated every 60s. The overall runtime is 2 days. The resulting concentration field is stored every half an hour for the whole domain and every 1 minute at selected grid points.

In run 1, an initial uniform tracer concentration field with a value of 100 units is assumed throughout Mellieha Bay. The concentration is set to zero in the rest of the model domain. The flushing of the bay is compared with that predicted by the box model. In run 2, a continuous source is positioned on the western flank of Mellieha Bay; the tracer concentration is set to 100 at a patch of selected grid points in order to study the effect of such a source on the water quality in the rest of the bay.

5.10.5.5 Model results for run 1 (Discrete source)

The rate at which the average tracer concentration in Mellieha Bay decreases with time is shown by the dashed curve in Fig. 5.18. These results are best described by an exponential curve fit of the form

$$C = C_o \exp(-At^B) \qquad (5.50)$$

where A and B are constants. A plot of $\ln(\ln(C/C_o))$ against $\ln(t)$ is in fact a perfect straight line giving values of $A = 0.074\ hr^{-1}$ and $B = 0.85$. On the basis of one cycle being equivalent to 20 minutes, the average residence time τ_d is calculated to be 66 cycles.

The flushing rate of the bay can alternatively be expressed in terms of the e-folding time which equals 76 cycles. These values are slightly higher than those estimated by the single box model which takes into account only the

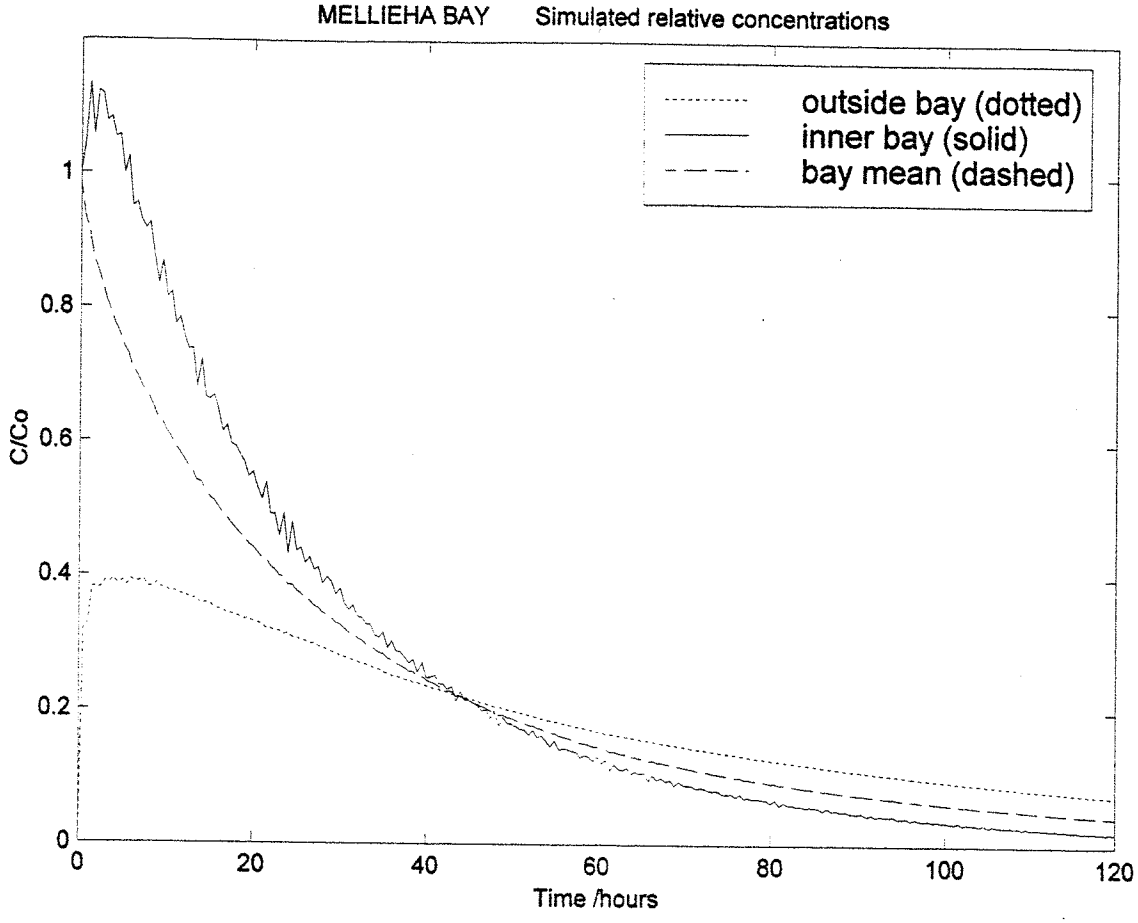

Fig. 5.18 Comparison of the decay curves of normalised concentration in Mellieha Bay simulated by model run 1. Values are time-averaged over a period of 5 minutes. The dashed curve refers to the normalised concentration averaged over the full bay area; the solid and dotted curves refer to the normalised concentrations at grid point (I = 12; J = 8) inside the bay and at grid point (I = 29; J = 28) outside the bay respectively.

advective mixing. This shows that the effect of dispersion is an important factor in the flushing of contaminants from the embayment.

Fig. 5.18 also shows the variation of the relative tracer concentration at a point inside (I = 12; J = 8) and outside (I = 29; J = 28) the bay respectively. It is interesting to note that the concentration in the inner bay areas tends to increase initially, but subsequently continues to decrease monotonically, with values becoming eventually even

lower than in the rest of the bay or its immediate vicinity after about 42 hours. The normalised concentration outside the bay initially increases very quickly to a maximum of about 0.4. Thereafter it decreases slowly, remaining however higher than the bay average concentration values. This results from the fact that once the contaminant has reached the open sea, the reduced seiche-induced advective mixing becomes less efficient in diluting the contaminant.

The full spatial distribution of the concentration field in the model domain is retrieved every half an hour, and it is possible to follow its evolution in time. For the case of run 1 snapshots at 6, 12, 24 and 36 hours from the start are presented in Fig. 5.19. The concentration field is represented by a normalised value (in the range 0 to 1) with respect to the initial value of 100 units which uniformly covers the full extent of the embayment. The initial line of demarcation between polluted and clear water runs across the mouth of the bay from the western bay promontary to the outermost point of St. Paul's Islands. The colourbar attributes the higher concentrations to red and the lower concentrations to blue. Clear waters are shown in a deep blue colour.

As expected the concentrations are initially diluted quickly at the outer bay area where there are the higher concentration gradients. Flushing is more effective along the western flank of the bay where the seiche currents are more intense. At six hours from start, the concentration within the rest of the embayment is however still higher than 0.7 and close to its initial value in many parts of the bay. Thereafter the reduction in tracer concentration is consistent in time. The changes are practically uniform throughout the bay, but some spatial variation in the flushing of the embayment is evident. The deeper areas of the bay are relatively better flushed. On the other hand patches of remnant concentration tend to remain higher than average, especially at the outer eastern flank of the bay and the inner bay areas. These areas represent the shallower parts of the bay and comprise the small Mgiebah sandy beach and the popular Mellieha sandy beach respectively, the latter being one of the larger beaches on the island. After 12 hours, the concentration level within the bay is still high at around 55% of the initial levels. After one day the average relative concentration is below 40% although higher levels are retained in some restricted shallow areas. Levels in these areas remain around 20% even after 36 hours. The distribution of the tracer concentration outside the bay is mainly controlled by dispersion. The transport closer to the mouth of the bay tends to predominate towards east and overflows into St. Paul's Bay. Concentration levels beyond White Bank and in the vicinity of St. Paul's Bay remain below 0.05 so that one can in this case exclude any major effect of contamination in Mellieha Bay on its adjoining embayment.

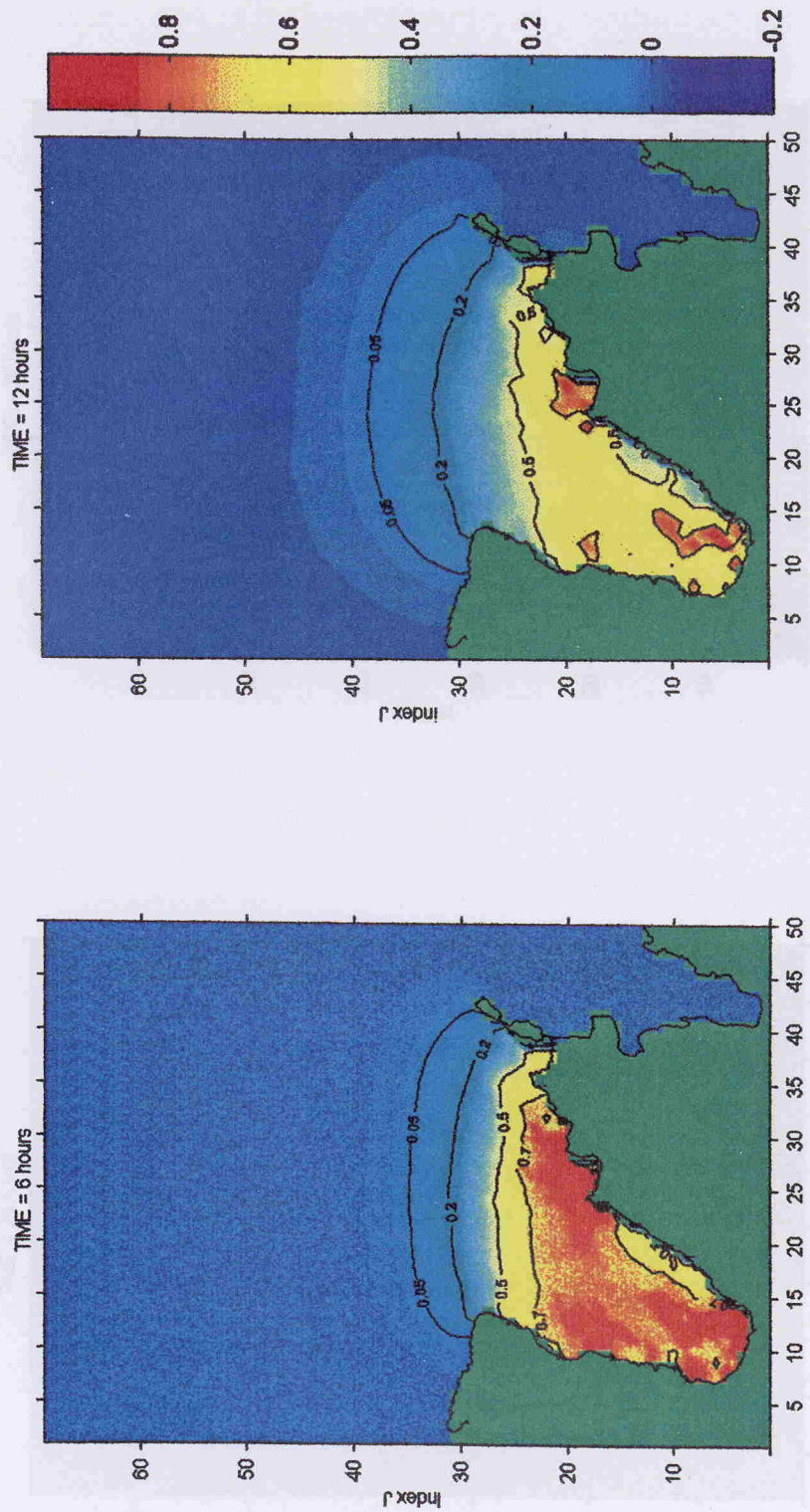

Fig. 5.19 Snapshots of the simulated relative concentration field in Mellieha Bay at time 6 and 12 hours from start. Results from model run 1. The initial field is uniformly equal to 1 throughout the embayment.

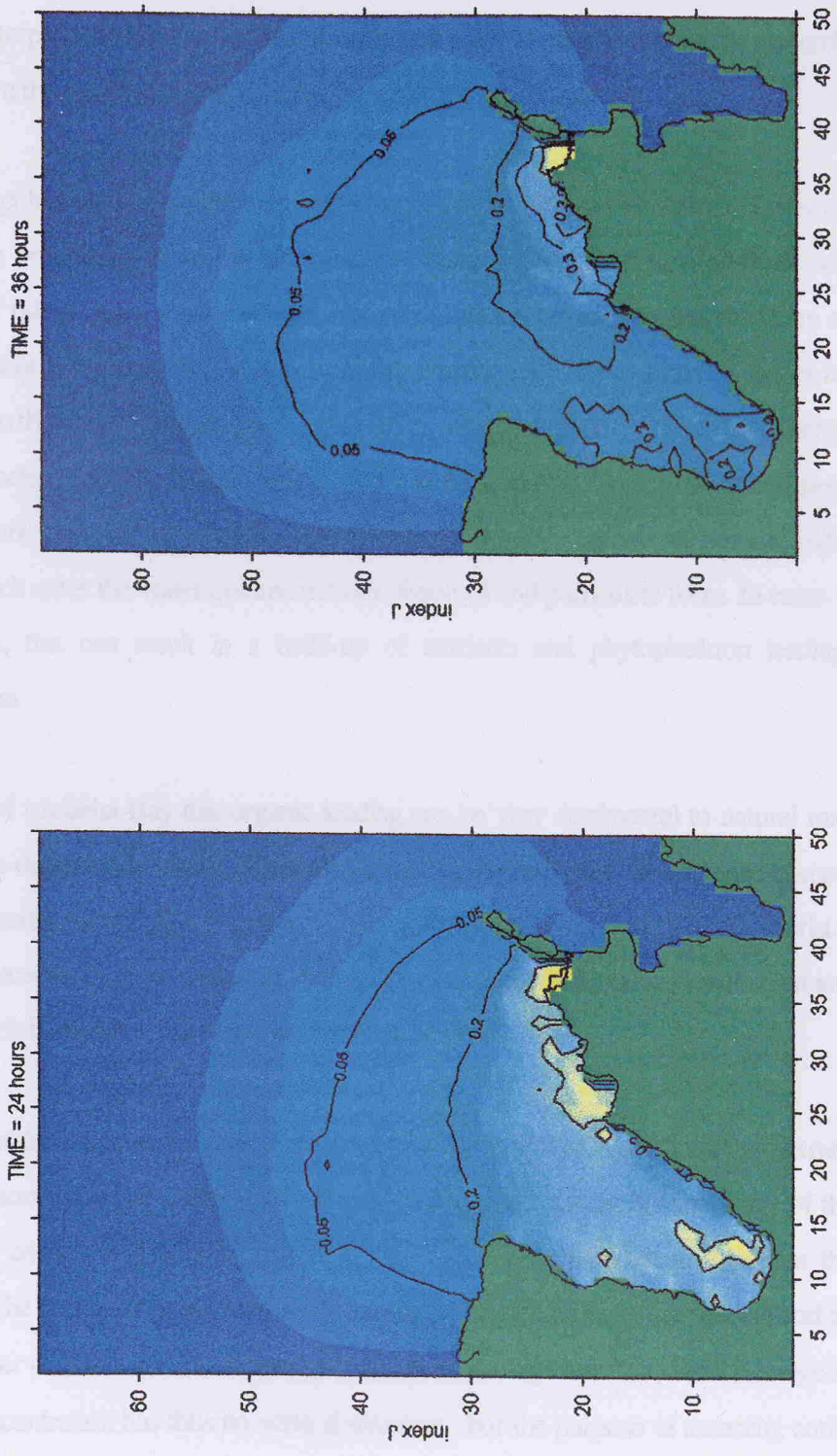

Fig. 5.19 Snapshots of the simulated relative concentration field in Mellieha Bay at time 24 and 36 hours from start. Results from model run 1. The initial field is uniformly equal to 1 throughout the embayment.

5.10.5.6 Model results for run 2 (Continuous Source)

This run simulates the impact of a continuous source of pollution inside the bay, close to its western promontary. A fishfarm comprising a number of fish cages is located at this site. It represents one of the most important enterprises in the local aquaculture industry. Given its position within the embayment, the impact of this activity on the marine environment has been a matter of dispute.

This model application is intended to quantify the influence of the seiche-induced water movements in dispersing contaminants originating from this site, and the likely impacts on other locations within the bay. Intensive cultivation of fish in cages generates large amounts of mainly organic wastes which are continually released into the environment at the cage site. Wastes from fish farming arise mainly from the faeces and excreta of the caged fish, and from the excess uneaten food. Other minor wastes include feed additives, therapeutic agents and other treatments such as anaesthetics, as well as antifoulants used on cage structures and nets (Spiteri, 1996). The most important components of these wastes are their organic carbon and nutrient (nitrogen and phosphorus) contents which enter the water column in both dissolved and particulate form. In cases where the circulation is unfavourable, this can result in a build-up of nutrients and phytoplankton leading to serious levels of eutrophication.

In the case of Mellieha Bay this organic loading can be very detrimental to natural marine biota and habitats, especially the degradation of the Posidonia Oceanica meadows that are a crucial component of the ecosystem balance and sediment stability in the bay. The impact on the water quality in this tourist valued and recreational coastal area needs also to be assessed. High levels of nutrients may indeed result in an increase in phytoplankton biomass which in extreme cases may lead to algal blooms.

The results of the model run are presented as a time series plot of normalised concentration (with respect to the value at the source) at three sites within the bay in Fig. 5.20, and as 2D snapshots of the concentration field at times 6, 12, 24 and 36 hours from start in Fig. 5.21. It is important to highlight the 2D character of this simulation. The source is assumed to have a constant concentration in the vertical and the transport is assumed to occur under the influence of a barotropic current in a completely mixed and homogeneous water column; the resulting concentration has thus no vertical structure. For the purpose of assessing contaminant loads, the time evolution of the concentration field is not as important as its longer term development. The swiftly alternating

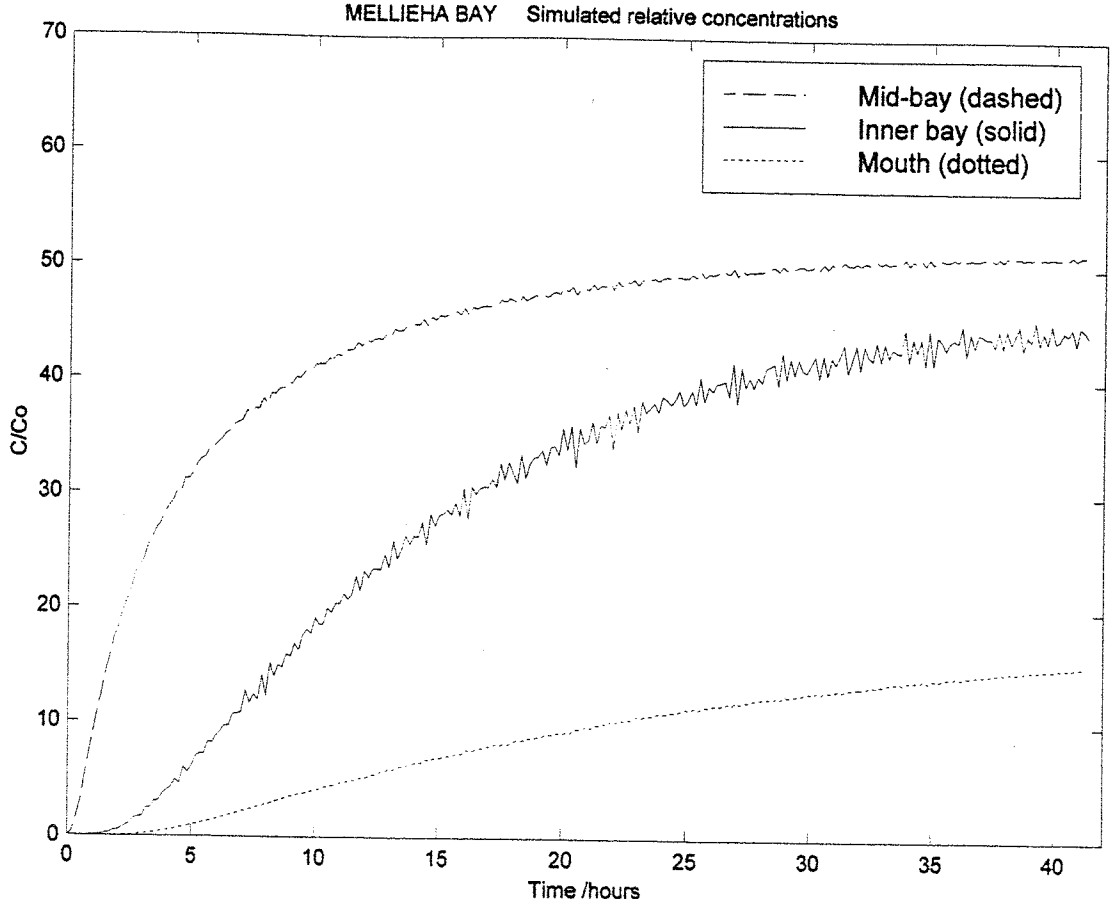

Fig. 5.20 Time series of relative concentration in Mellieha Bay simulated by model run 2 for a continuous source on the western flank of the bay. Values are time-averaged over a period of 5 minutes. The solid curve refers to the relative concentration at grid point (I = 12; J = 8) in the inner part of the bay; the dashed and dotted curves refer to the relative concentrations at grid point (I = 16; J = 16) and at grid point (I = 24; J = 26) situated in the middle and mouth of the bay respectively.

seiche-induced currents are able to percolate the contaminants both towards the inside of the bay as well as away into the open sea. Outside the bay the concentration level is still on the increase after 42 hours of simulation, whereas in the inner bay areas a steady state condition is reached. The impact on the water quality on the eastern flank and inner beach areas of the bay thus remains finite, with upper bound levels of concentration of about 40% that at the source. The results of the model thus show that the seiche-induced

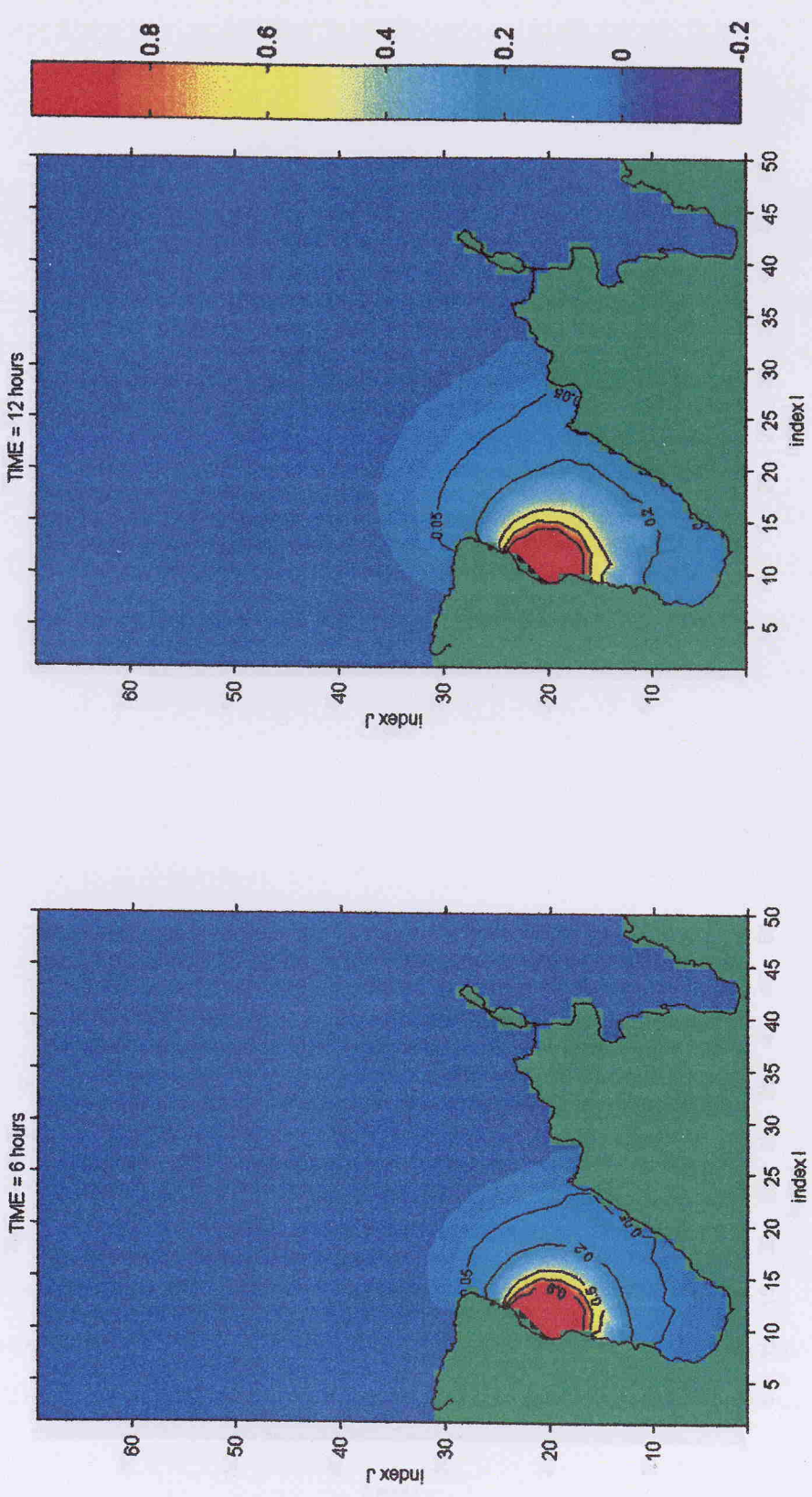

Fig. 5.21 Snapshots of the simulated relative concentration field in Mellieha Bay at time 6 and 12 hours from start. Results from model run 2 with a continuous source (concentration = 1) at the western flank of the bay.

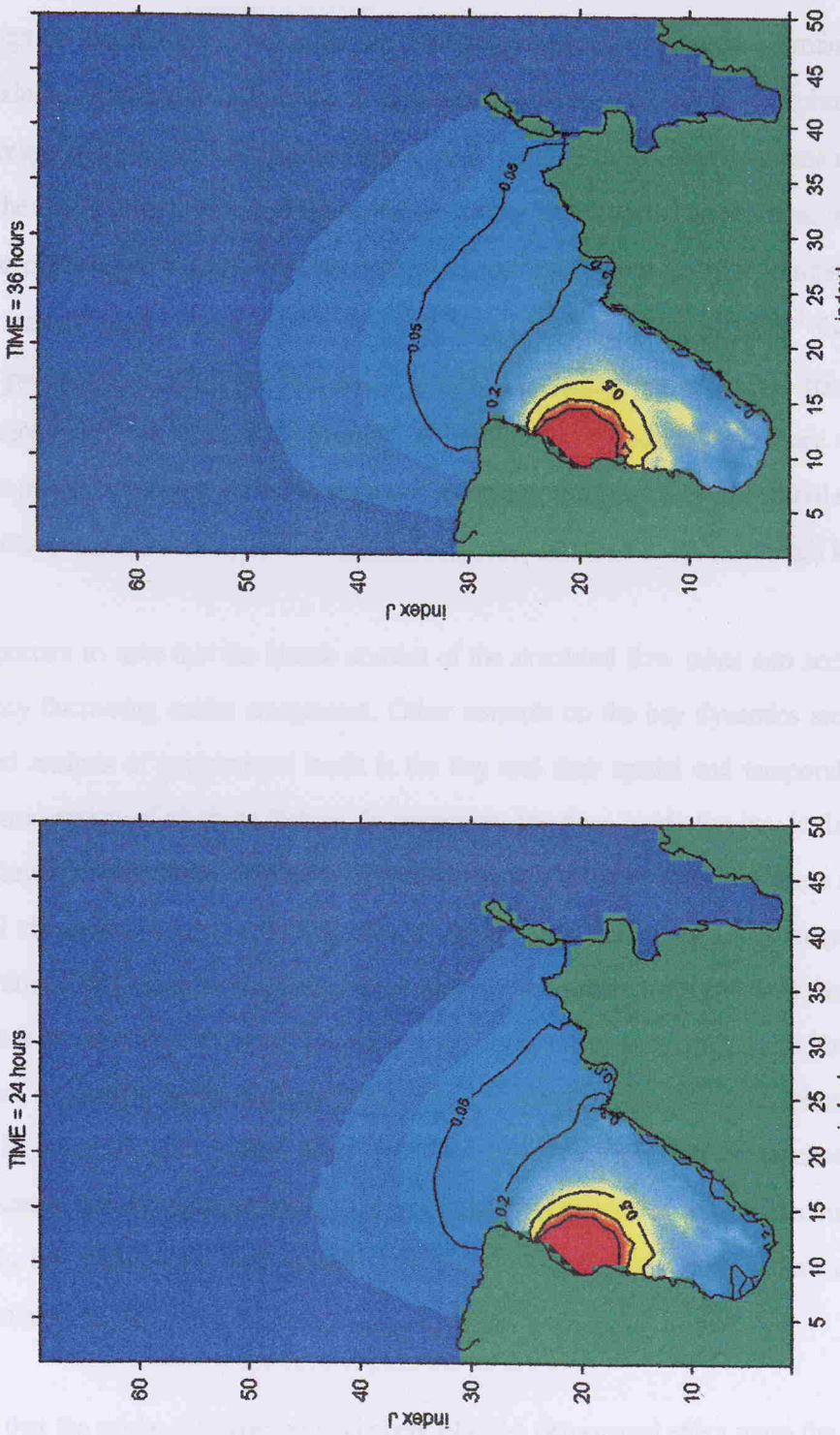

Fig. 5.21 Snapshots of the simulated relative concentration field in Mellieha Bay at time 24 and 36 hours from start. Results from model run 2 with a continuous source (concentration = 1) at the western flank of the bay.

flushing of contaminants into the open sea is able to compensate for any accumulation of contaminants within the interior of the bay.

On the assumption that nutrient levels in the bay are entirely derived from the fish farming activity and that only the seiche-induced flushing is in action, a nitrate-nitrogen and phosphate-phosphorus level of 22.5μgL^{-1}/0.75μgL^{-1} respectively at the source (these are typical averages from monthly values reported by monitoring activities of the local Aquaculture Centre) would, according to the model simulations, result in a concentration of 9μgL^{-1} for nitrates and 0.3μgL^{-1} for phosphates at the beach area. Local investigations of inshore waters indicate that nutrient levels exceeding thresholds of 60μgL^{-1} for nitrates and 3μgL^{-1} for phosphates would be expected to produce associated environmental problems including eutrophication (personal communication, Prof. V. Axiak, Dept. of Biology, University of Malta). The simulated levels are thus well below these thresholds. In reality the situation is however much more complex than this. Terrestrial run-off following heavy rainfall and resuspension of bottom sediments by rough seas can lead to sporadic high levels of nutrients in the area.

It is also important to note that the kinetic content of the simulated flow takes into account only the relatively high frequency fluctuating seiche component. Other controls on the bay dynamics are however in action. A more detailed analysis of contaminant loads in the bay and their spatial and temporal variability would thus require a consideration of all these factors. In particular, the flow inside the bay is forced by the alternating alongshore flow (predominantly diurnal) outside the bay, as well as by the wind stress and density differences. The residual circulation is thus a combination of agents that dictate its lower frequency component. The advective action of this residual circulation can prolong or accentuate the flushing of the embayment depending on whether it is directed into or out of the embayment. In any of these circumstances, the effect of the seiche on a contaminant originating within the bay would be to repeatedly slosh the contaminant to and fro inside the embayment for a considerable number of cycles before the contaminant actually reaches the open sea. This will inevitably disperse the contaminant within a bigger volume of sea water and, depending on the position of the source within the embayment, will detrimentally affect a bigger water body before definitively entering the circulation outside the bay.

This implies that the seiche can have both a beneficial and a detrimental effect upon the water quality inside the bay. It is certainly crucial for the flushing of the bay during calm periods. The enhanced rates of spread of

source will affect the opposite flank of the bay and the inner bay areas by a 20% relative rise in concentration after about 12 hours. Sporadic events of increased contamination can thus very quickly affect other parts of the bay. The seiche enhances dispersion so that the mixing processes in action will affect larger bodies of water. Consequently concentrations would tend to remain low and steady state situations can be attained as in the case of the simulation above. On the other hand, if the contaminants are able to reach the bottom before complete decomposition or flushing, a larger seabed area is affected. This implies a larger area of impact on the seabed from waste feed and fish faeces around the cages.

The model also indicates that the control station used in the array of sampling sites utilised by the national aquaculture authorities in the monitoring of the environmental impact of the fishfarm activity should be well away from the fishfarm site. The currently adopted distance of 100m is inadequate.

6.0 General conclusions and recommendations for future work

When this thesis was first planned activities in the field of oceanography were non-existant in Malta. Adequate structures had to be established by the author in order to undertake this study. This consisted in the installation of a permanent sea level and meteorological stations as well as the purchase of other oceanographic equipment and computing facilities mainly through funding by the UNESCO Participation Programme 1993/94, the Malta Council for S&T, the University of Malta and the Oil Division in Malta. This setup became the basis of what today is the Physical Oceanography Unit at the IOI-Malta Operational Centre within the University of Malta.

The work is based on data collected between June 1993 and December 1996. In addition to the results presented in this thesis other important complementary activities have been undertaken. These include a number of oceanographic surveys and a programme of long term sub-surface current measurements. The work has also involved the writing of an extensive set of computer programs (mainly in Fortran and MATLAB) relating to the actual analysis of the data as well as to its management, quality checking and pre-processing.

6.1 Conclusions

More than 60% of the sea level variance in Malta is of non-tidal origin. The residual sea level spectrum is dominated by energy inputs from the synoptic and the planetary wave scales. Analysis of the data by means of a multiple regression model confirms the predominant contribution of atmospheric pressure in determining the variability of the sea level for frequencies lower than 0.75cpd. The mid-synoptic frequency range is an exception where the unexplained variance rises to 30%. The pressure coefficient is exceptionally low at a frequency close to 0.12cpd at which the variability is mainly explained by the alongshore wind component. The direct wind effect is otherwise generally much smaller than that of barometric pressure. In the upper synoptic frequency range ($0.3 < f < 0.5$ cpd) the response is very close to isostatic, with an average gain of 0.7. At other frequencies the overall response is however non-isostatic implying that other factors besides mesoscale atmospheric pressure disturbances contribute to the sea level variability. It is not easy to identify the physical processes responsible for such a response. Discrepancies from the inverse barometer effect are associated with

local effects as well as with indirect, non-local factors pertaining to the larger scale dynamics of the Strait of Sicily and the control of the strait on exchange by sub-basin differences.

A novel method based on the wavelet transform is successfully used to study decompositions of the sea level signal and the dependence of their variability in time on one or more correlated parameters. The analysis describes the intermittent nature of the sea level response to the weather variables. The position and extent of the frequency range at which the response approximates to the inverted barometer effect is found to depend on the amplitude of the atmospheric pressure fluctuations. During the stronger pressure variations, the inverted response of the sea level occurs at practically the full range of synoptic frequencies and even lower.

Strong seasonal non-eustatic changes in the mean sea level show a major maximum towards the last months of the year which is typically followed by a sharp fall to a minimum in February/March. These variations can reach peak-to-trough values of up to 0.35m. Besides the usual steric and direct meteorological effects, this variability is attributed to adjustments in the mass balance of the whole Mediterranean basin.

Long period waves with periodicities ranging from a few minutes to several tens of minutes are observed throughout the year on the northern coastal area of the Maltese Islands. These coastal seiches, locally known as '*milghuba*', resemble closely tsunamis in character, but result predominantly from meteorological forcing rather than seismic events. These waves are present uninterrupted on the sea level trace and during 'quiet' periods they characterise the 'background' oscillations. Occasionally the '*milghuba*' intensifies to large amplitude fluctuations reaching up to 1m in extent. These events of enhanced seiching are triggered by mesoscale atmospheric gravity waves which occur in association to the passage of frontal disturbances or during particular synoptic settings characterised by an inversion near the surface, and by dynamic instability and vertical wind shear in the middle troposphere.

The coupling between the atmospheric waves and the sea surface is broad-banded and depends primarily on the distribution of energy in the band of frequencies ranging from 0.1 to 2cph. The interaction occurs without the need of a direct matching of the atmospheric signals with the eigenmodes of the coastal area. Besides the amplitude of the atmospheric wave, spatial coherence, the matching of phase speeds with the underlying sea and the propagation along directions orthogonal to bathymetric contours are other important properties favouring

the coupling. The air-sea interaction is also characterised by an energy redistribution process whereby energy is 'pumped' to a preferred band of frequencies both from the lower and from the higher frequencies. This underlies the indirect nature of long wave generation by the atmospheric forcing. Extreme oscillations in coastal inlets and embayments occur when their resonant frequencies fall within this preferred frequency band.

The seiche oscillations in the embayments are thus not forced by direct resonance but occur in response to sea level fluctuations originating in the open sea. The long wave field carries the signature of both local and remote signals, and consists of a combination of signals with a cascading influence from the regional scale to the shelf scale and down to higher frequency coastal scale oscillations. The natural modes of oscillation of Mellieha Bay, St. Paul's Bay, St. George's Bay and the Grand Harbour are investigated by developing an efficient and accurate method consisting in numerically solving the Helmholtz equation by transformation into an eigenvalue problem. The seiches excited in the wide open mouthed Mellieha Bay and the nearby St. Paul's Bay consist of separate and coupled modes, and pertain to a water body that extends into the adjacent open sea area. Overtones are more evident in the narrow mouthed Grand Harbour, which indicates the influence of nonlinearity. Oscillations with frequencies lower than the eigenmodes of Mellieha Bay are attributed to the resonant oscillations of the outer shelf. Periods higher than 1h are an expression of the forced motions and free long waves propagating on the continental shelf area joining Malta to Sicily. This is confirmed by simultaneous measurements made across the shelf during the Malta Channel Experiment.

A statistical analysis on seiche excursions shows that the response of Mellieha Bay close to its gravest mode can be described by a narrow banded process following the Weibull distribution. The Weibull exponent depends on the size of the seiche and can be used to classify seiches. The statistical incidence of large seiches is found to be higher than that given by a Rayleigh distribution.

The free surface, non-linear Princeton Ocean Model (POM) in 2D mode is used to simulate the transformation and dynamics of long waves approaching Mellieha and St. Paul's Bays. Bottom topography and coastal configuration play an important role in the amplification of the incident waves as they enter the embayments. The model can be used for the zoning of coastal areas to long wave response. In the case of Mellieha Bay the response function is high not only in the inner bay areas but even in the smaller inlets on the eastern promontary. The simulations show that the seiche oscillations are dominated by the fundamental and first bay mode even in

the case of wide-mouthed open basins. The intensity and spectral character of the sea level oscillations inside the embayments are found to be greatly dependent on the nature and incidence of the long period waves in the open sea. Standing oscillations generated along the cross-shore direction on the shelf (leaky waves) are more effective in forcing the extreme oscillations in the embayments rather than edge waves propagating alongshore.

The very short period of the '*milghuba*' implies that the seiche-induced barotropic currents can be very strong. Direct measurements of seiche currents inside Mellieha Bay show that they can be well estimated from sea level data. The seiche dynamics and impact on the flushing of Mellieha Bay are studied by means of an advection-diffusion scheme implemented within POM. While the swiftly alternating seiche-induced currents constitute one of the important mechanisms for the flushing of the bay, the repeated sloshing of a contaminant leads to a more widespread dispersion inside the embayment, and detrimentally affects a bigger water volume before its definite release into the open sea.

6.2 Future work

Island scale sea level studies

The focus in this study has been on the sea level variability along the northern coast of Malta, facing the shelf area between the islands and the southeastern coast of Sicily. In the future it is intended to extend measurements on the southern shores and on the western coast of the sister island, Gozo, facing directly the Central Mediterranean Basin. Such observations will provide valuable information on the long wave oscillations in the central areas of the Strait of Sicily as opposed to those on the shelf area. Simultaneous measurements around the perimeter of the islands can be used to identify the presence of island-trapped sub-inertial waves. The position of the islands close to the shelf break presents a very interesting case of an island system with a very unsymmetric surrounding bathymetry which is relatively shallow on the north and northeast, but deepens very sharply to the south and southwest.

Regional scale sea level studies

It is intended to extend this study to the whole region of the Strait of Sicily. Many of the tools developed in this thesis can be directly used or adapted to apply to larger domains. The focus will be to better understand the phenomenology of the sea level variability in the region, to identify commonalities and differences in

mechanisms responsible for long wave signals that have regional scale signatures as compared to those occurring on the shelf and in the coastal areas, as well as to establish the dependencies of the latter smaller spatial scale oscillations on the regional scale dynamics and basin wide influences and controls. Such a study will undoubtedly make use of substantial modelling efforts, but will also have to rely on a more accurate bathymetry of the region and on an adequate database of hydro-meteorological data for the region that is sufficiently extensive in both spatial coverage and duration. It is envisaged that MedGLOSS will in the near future provide the framework for such observations. MedGLOSS is an IOC/CIESM programme which will establish a sea level monitoring network system for systematic measurements in the Mediterranean and Black Seas. The system will be based on the basic GLOSS requirements and methodology, aiming to provide high quality standardised data on sea level in near realtime. One of the stations in the first phase will be installed in Malta. MedGLOSS will become operative early next year and Malta is expected to become a data management node for the Central Mediterranean.

Air-sea interaction

Numerical modellers rely mainly on parameterisation techniques to empirically describe the air-sea interaction. The way forward will be to improve capabilities in the direct modelling of the physical properties dictating the interaction, especially that of atmospheric pressure disturbances on the sea level. Before this can be achieved satisfactorily the knowledge on the transient dynamics of the troposphere has to be enhanced by more frequent, regular and accurate upper air observations.

The conditions for the wave ducting of atmospheric gravity waves may not necessarily be the same as those at their source, and in this respect it is difficult to ascertain, from a single location of surface pressure measurements and of upper air soundings, whether the observations represent conditions for their optimal propagation or for their generation. This uncertainty can only be superceeded by simultaneous air profiles at an array of stations covering both the shorter and longer spatial scales. In particular, a better understanding of the phenomenology of atmospheric waves and their correlation to the sea waves needs longer term simultaneous measurements of sea level and surface pressure at a set of stations both on land and offshore.

Time series analysis and seiche prediction

In this work the application of the wavelet transform is successfully applied to analyse time series of sea elevation. It is shown that the temporal development of the sea level fluctuations can be modelled as a

superposition of wavelet decompositions of the respective dependent parameters. This opens the way to alternative methods of forecasting and hindcasting sea elevations from a knowledge of the wavelet decompositions of the dependent parameters. Following this experience, wavelet analysis in combination with neural networks will be applied in the future to study more concretely the possibility of predicting seiches on the basis of characteristic patterns in the atmospheric and sea level signals.

Impulsive type seiches

The study has left some open questions that have to be addressed in the future. One of these relates to the different character of the seiche oscillations observed during summer, which tend to have larger amplitudes and are of a much shorter duration often lasting only a few cycles. It is not clear whether these properties originate from differences in the characteristics of the atmospheric waves or whether they are related to the propagation properties and energy decay processes of the long period waves in a stratified sea. The occurrence of these impulse type seiches during calm and fine days contradicts the view expressed by Gedzelman & Rilling whereby the presence of strong low-level static stability in the atmosphere serves mainly to enhance the surface pressure amplitudes; this means that atmospheric gravity wave activity should be suppressed under fair weather conditions and enhanced when frontal surfaces (and therefore clouds and precipitation) are overhead. The larger amplitude summer seiches could result from a more spatially confined atmospheric-sea interaction, which implies that the source is closer to the observing station and therefore the signal is stronger. The propagation of the barotropic sea level signal in the thin mixed layer would be expected to dissipate its energy to an accompanying movement on the thermocline, and this can explain a faster decay of the surface expression.

Bay dynamics

The high Q-factor of the embayment indicates that the oscillations in Mellieha Bay are not significantly influenced by friction. The balance of energy of the bay oscillations with the open sea is however an aspect that needs to be examined in more detail in the future. The sea level in the embayment carries the signature of other effects beside that of the seiches; the bay dynamics is certainly dictated by the exchange of energy with the contiguous shelf. The modelling efforts in the future will be directed to simulate the circulation in 3D and include wind and wave impacts as well as the influence of the strong fluctuating currents outside the embayment.

A1. A brief description of the Wavelet Transform

A1.1 Introduction

A1.1.1 Comparison to the Fourier Transform

In conventional signal analysis the Fourier transform provides a connection between time and frequency in terms of a decomposition of harmonic waves extending over an infinite time axis. An inherent disadvantage of Fourier techniques is that the resulting frequency composition gives an average over the whole length of the signal and thus loses track of the non-stationary characteristics of the signal. This drawback can be partly overcome by adopting the Short-Time Fourier Transform (STFT) which utilises a windowing technique to span the signal in small successive sections. In STFT the window size is however fixed and it would be ideal to have a more flexible approach where the compromise between time and frequency information can be controlled.

A1.1.2 The Wavelet Transform

The wavelet transform offers the solution to this difficulty by combining a description in both time and space through the use of short wavelets instead of long waves. By means of a windowing technique on variable-sized regions, wavelet analysis provides a much more localized analysis so that an event remains connected to its time of occurrence. The method is fundamentally a decomposition technique whereby a signal is expressed in terms of a series of orthogonal basis functions $W(x)$ of finite length, called wavelets. A wavelet can be dilated, that is compressed or stretched, by means of a scaling factor **a**. At the finest scale, wavelets may be very short indeed; at a coarse scale, they may be very long. The position of a wavelet along the time axis can also be changed by a shifting factor **b**. Thus the wavelet $W(\frac{x}{\mathbf{a}} - \mathbf{b})$ is shifted by **b** along the positive x-axis and has a time span that is **a** times that of $W(x)$.

A1.2 Definition of a wavelet

A1.2.1 Wavelet families

There are several wavelet families. The simplest wavelet is discontinuous and resembles a step function (Haar, 1910) as shown in the top view of Fig. A1.1a where it is plotted over the range x=0 to 1. At higher

levels j, there are 2^j wavelets that fit in this interval. This system of numbering applies also for negative levels as shown in Fig.A1.1b. Following the conceptualisation of wavelets in its present theoretical form by the team at the Marseille Theoretical Physics Centre (Goupilland et al., 1984), and the development of methods of wavelet analysis mainly by Y. Meyer and his colleagues, several other families of wavelets have proven

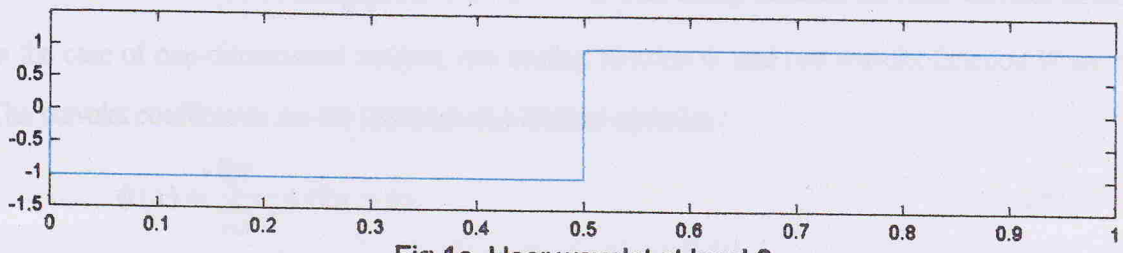

Fig.1a Haar wavelet at level 0

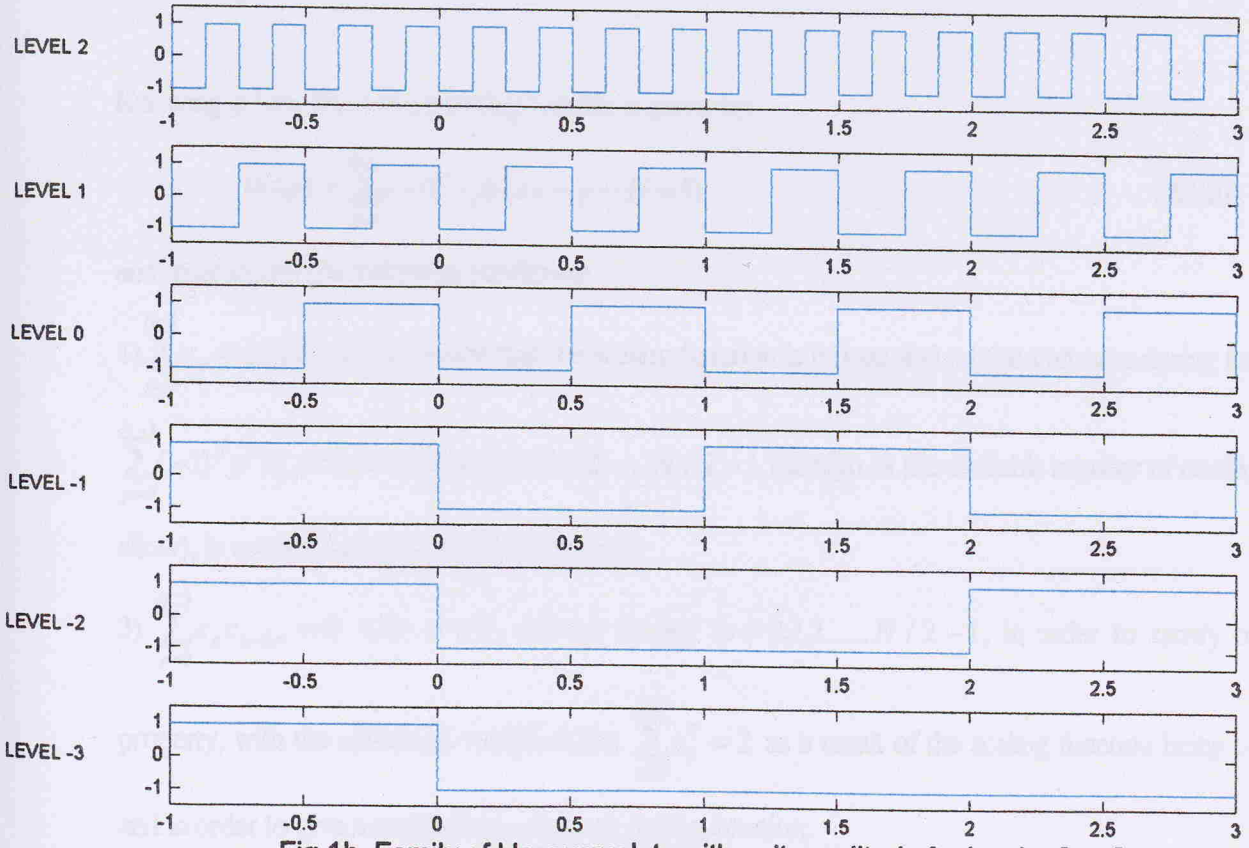

Fig.1b Family of Haar wavelets with unit amplitude for levels -3 to 2

to be especially useful. In particular, discrete wavelet analysis became possible with the advent of compactly-supported orthonormal wavelets (Daubechies, 1988).

A1.2.2 The Daubechies wavelets

The generation of orthogonal Daubechies wavelets, denoted by dbN for a given order $N = 2,4,6.....$, is based on the theory of dilation equations (Daubechies, 1990). For each wavelet order, N is the even number of wavelet coefficients $c_p,,\ p = 0 \rightarrow N-1$. This family includes the Haar wavelet written as db2. In the case of one-dimensional analysis, one scaling function ϕ and one wavelet function W are necessary. The wavelet coefficients are the solutions of a dilation equation :

$$\phi(x) = \sum_{p=0}^{N-1} c_p \phi(2x-p). \qquad \text{(A1.1)}$$

In general it is not possible to solve this equation directly to find the function $\varphi(x)$ and an iterative algorithm is necessary.

Knowing $\phi(x)$, the corresponding wavelet is given by:

$$W(x) = \sum_{p=0}^{N-1} (-1)^p c_p \phi(2x+p-N+1) \qquad \text{(A1.2)}$$

and must satisfy the following conditions:

1) $\sum_{p=0}^{N-1} c_p = 2$, in order to ensure that the scaling function is unique and retains unit area during iteration; 2) $\sum_{p=0}^{N-1} (-1)^p p^m c_p = 0$, for integer $m = 0,1,2.....N/2-1$ (as high as the available number of coefficients will allow), in order to achieve maximal accuracy;

3) $\sum_{p=0}^{N-1} c_p c_{p+2m} = 0$ with $m \neq 0$, and for integer $m = 0,1,2.....N/2-1$, in order to satisfy orthogonal property, with the additional condition that $\sum_{p=0}^{N-1} c_p^2 = 2$ as a result of the scaling function being orthogonal and in order to give a constant mean square during iteration.

A1.3 The Discrete Wavelet Transform

A1.3.1 Decomposition of a signal into wavelets

The goal of the wavelet transform is to decompose any arbitrary signal $f(x)$ into an infinite summation of wavelets at different scales. If $f(x)$ is discrete with 2^n elements and sampling interval T, so that $f_m = f(x = mT)$, $m = 0 \rightarrow 2^n - 1$, the expansion becomes:

$$f(x) = \sum_{j=-\infty}^{\infty} \sum_{k=-\infty}^{\infty} C(j,k)\ W(2^{n-j}x - k) = \sum_{j=-\infty}^{\infty} \sum_{k=-\infty}^{\infty} C(j,k)\ W_{j,k}(x) \qquad \text{(A1.3)}$$

where both the scale and translation factors are expressed on a dyadic basis with levels j ($\mathbf{a} = 2^{j-n}; \mathbf{b} = k\mathbf{a}$; $(j,k) \in Z^2$), and $C(j,k)$ are the family of wavelet transform coeffic-ients. In practice, this is equivalent to a summation of successive scans of the signal over all time by scaled and shifted versions of the wavelet.

The choice of the wavelet order depends on the amount of detail that needs to be resolved in the signal $f(x)$. The signal $f(x) = Ax$, with A =constant can be represented exactly by the db4 wavelet; if $f(x) = Ax + Bx^2$, with A, B =constants, then db6 is necessary. In general, the higher the order of the polynomial expansion of the signal, the higher also is the corresponding order of wavelet coefficients necessary to represent it with sufficient accuracy.

In expression (A1.3), the summation is carried out for both negative and positive levels j. When n-j is negative, $W(2^{-j}x - k)$ can be expressed as a sum of terms $\phi(x-k)$. Hence

$$\sum_{j=n+1}^{\infty} \sum_{k=-\infty}^{\infty} C(j,k)\ W(2^{n-j}x - k) = \sum_{k=-\infty}^{\infty} C(\phi, k)\ \phi(x-k),$$

where $C(\phi, k)$ is a new set of coefficients. The expansion in (A1.3) can thus be expressed in two parts:

$$f(x) = \sum_{k=-\infty}^{\infty} C(\phi, k)\ \phi(x-k) + \sum_{-\infty}^{n} \sum_{k=-\infty}^{\infty} C(j,k)\ W(2^{n-j}x - k) \qquad \text{(A1.4)}$$

Subject to very general conditions on $f(x)$ and $W(x)$, the wavelet series (A1.3) and (A1.4) converge and can thus provide a practical basis for signal analysis.

If the independent variable is time t and the duration of the signal is D, define the non-dimensional variable $x = t / D$. The signal $f(x)$ is now defined over the interval $0 \le x < 1$. A complication arises at the edges of this interval because some of the analysing wavelets overlap one or more edges. This problem is solved by assuming $f(x)$ to be periodic by making it to repeat itself exactly in the adjacent unit intervals. The full contribution of a wavelet to $f(x)$ can thus be obtained as a combination of 'wrapped' contributions over successive unit intervals. The wavelet expansion of $f(x)$ in the interval $0 \le x < 1$ can thus be written:

$$f(x) = a_o \phi(x) + \sum_{j=1}^{n} \sum_{k=0}^{2^{n-j}-1} a_{2^{n-j}+k} W(2^{n-j}x - k) \qquad \text{(A1.5)}$$

where

$$a_o = \int_0^1 f(x)dx \text{ and } a_{2^{n-j}+k} = 2^{n-j} \int_0^1 f(x)\ W(2^{n-j}x - k)dx. \qquad \text{(A1.6)}$$

The set of coefficients $\{a_m\ , m = 0 \rightarrow 2^n - 1\}$ constitute the discrete wavelet transform of the signal $f(x)$ and give the amplitudes of the contributing wavelets, after wrapping, to one cycle of the periodic version of $f(x)$ in the interval $0 \le x < 1$. Due to scaling $\phi(x)$ becomes a constant.

A1.3.2 Details and Approximations

Various levels of decomposition of the original signal $f(x)$ can thus be made if the set of coefficients $\{a_m\}$, $\phi(x)$ and $W(2^{n-j}x - k)$ are known. The signal can be decomposed in steps so that it can be realised as a family of hierarchically organised components. These components, known as approximations A_j and details D_j, can be obtained at each level j.

At the level j the detail D_j is the synthesis of the signal using the subset of coefficients $\{a_m\ , m = 2^{n-j} \rightarrow 2^{n-j+1} - 1\}$ with the rest of the coefficients being put to zero. That is

$$D_j(x) = \sum_{k=0}^{2^{n-j}-1} a_{2^{n-j}+k} W(2^{n-j}x - k). \qquad \text{(A1.7)}$$

The lower levels represent the finer components of the signal. Summing over j, the expression in (A1.5) can be written as $f(x) = A_n + \sum_{j=1}^{n} D_j$, and the signal is thus realised as a sum of details and an approximation $A_n = a_o \phi(x)$. If we take a reference level J, there are details associated with indices $j \le J$, corresponding

to scales $2^{n-j} \leq 2^{n-J}$ which are the fine details, and those associated with indices $j > J$ which are the coarser details. The approximation to level J of the signal $f(x)$ is the sum of the latter detail, that is $A_J = \sum_{j>J}^{n} D_j$. Details and approximations can be connected so that $f(x) = A_J + \sum_{j\leq J}^{n} D_j$. This implies that $f(x)$ is the sum of its approximations A_J and its fine details. Note that successive approx-imations are linked by $A_{J-1} = A_J + D_J$. The tree of components making up $f(x)$ is given below:

Level 1: $f(x) = D_1 + A_1$,

Level 2: $f(x) = D_1 + D_2 + A_2$,

. . . . . .

Level n: $f(x) = D_1 + D_2 + \ldots\ldots + D_n + A_n$,

where

D_1 involves coefficients $a_{2^{n-1}\to 2^n-1}$ and wavelets $W(2^{n-1}x-k)$;

D_2 involves coefficients $a_{2^{n-2}\to 2^{n-1}-1}$ and wavelets $W(2^{n-2}x-k)$;

. . . . . .

D_n involves coefficient a_1 and wavelet $W(x)$.

A1.3.3 Mallat's Algorithm

The numerical algorithm for the decomposition of an arbitrary signal $f(x)$, $0 \leq x < 1$, into its wavelet components $\{a_m\}$ was first devised by Mallat (1989). Mallat's algorithm does not require the explicit generation of $\phi(x)$ and $W(2^{n-j}x-k)$ with the subsequent evaluation of the integrals in (A1.6). The convolutions of (A1.6) are computed instead. Successive levels of $f(x)$ are filtered out by means of an ingenious sequential process, starting with the wavelets of lowest level (finest scale) and working progressively through the higher levels. With a signal of length 2^n, the discrete wavelet transform (DWT) consists of at most n stages. The first step produces, starting from $f(x)$, two sets of coefficients: approximation coefficients cA_1 and detail coefficients cD_1. These vectors are obtained by convolving $f(x)$ with a matrix L_1 to generate the approximation $\frac{1}{2}L_1 f$, and with a matrix H_1 for the detail $\frac{1}{2}H_1 f$,

both being followed by a dyadic decimation. L_1 and H_1 are effectively a low-pass and a high-pass filter respectively. The next step splits the approximation coefficients cA_1 in two parts using the same scheme, with cA_1 replacing $f(x)$, and producing cA_2 and cD_2 by matrices L_2 and H_2.

This can be repeated to cover all levels as shown in Fig.A1.2. The standard forms of L and H are:

$$L = \begin{bmatrix} c_o & c_1 & c_2 & c_3 & .... & .... & c_{n-1} & & & & \\ & & c_o & c_1 & c_2 & c_3 & .... & .... & c_{n-1} & & \\ & & & & c_o & c_1 & c_2 & c_3 & .... & .... & c_{n-1} \\ & & & & & & .... & .... & .... & .... & .... \end{bmatrix}$$

$$H = \begin{bmatrix} -c_{n-1} & c_{n-2} & -c_{n-3} & .... & -c_1 & c_o & & & & & \\ & & -c_{n-1} & c_{n-2} & -c_{n-3} & .... & -c_1 & c_o & & & \\ & & & & -c_{n-1} & c_{n-2} & -c_{n-3} & .... & -c_1 & c_o & \\ & & & & & & .... & .... & .... & .... & .... \end{bmatrix},$$

where the coefficients are those derived from the dilation equation (A1.1). The size of both L_j and H_j is 2^{j-1} x 2^j. A signal can also be regenerated from its DWT by a similar algorithm that works exactly in the reverse order.

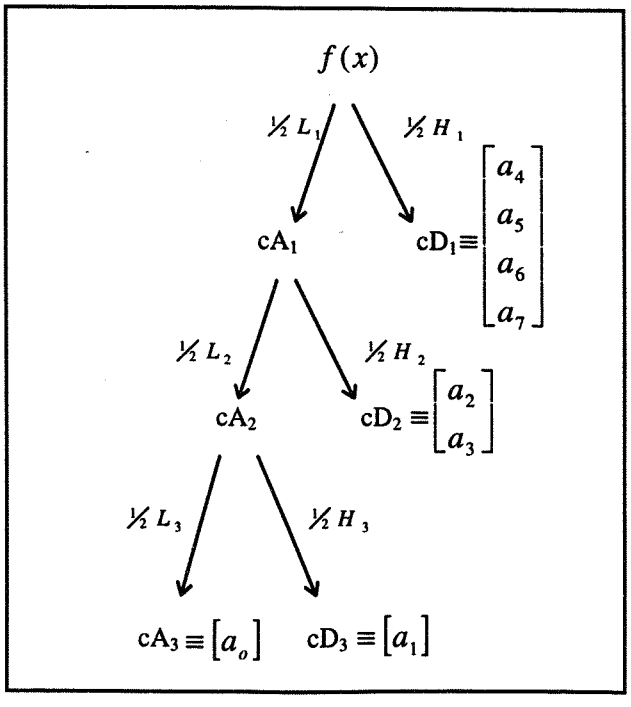

Fig. A1.2
Mallat's algorithm for the DWT of a signal with eight terms.

A1.4 The Continuous Wavelet Transform

When a signal is recorded in continuous time or on a very fine time grid, discrete wavelet analysis several levels of a decomposition are needed to reconstruct a signal satisfactorily. In such cases continuous wavelet analysis is necessary. The wavelet transform coefficients are given by:

$$C(a,b) = \int_R f(t) \frac{1}{\sqrt{a}} \psi\left(\frac{x-b}{a}\right) dt \qquad \text{(A1.7)}$$

where $a \in R^+ - \{0\}$, R = domain of real numbers, is the scaling factor, $b \in R$ is the shift factor, and ψ is a wavelet. Unlike the discrete wavelet transform, the continuous transform can operate at every scale, from that of the original signal up to some maximum scale which is determined by a trade off between the detail of analysis required and the computing power available. The continuous wavelet transform is also continuous in terms of shifting, in the sense that during computation the analysing wavelet is shifted smoothly over the full domain of the original signal. In the case of a continuous wavelet transform applied to a sampled signal, $a = 2^j T$ and $b = kT2^j$, $(j,k) \in Z^2$, so that the fine structure of a and b is in this case limited by the sampling interval T.

A2. Response of a linear time invariant system

A2.1 Mathematical description of a linear system

Following the practice in random vibration theory, a vibratory system may be considered to have a number of inputs $x_1(t)$, $x_2(t)$, $x_3(t)$, etc. which constitute the excitation and a number of outputs $y_1(t)$, $y_2(t)$, $y_3(t)$, etc. which constitute the response. The physical laws which express the relationship between input and output are generally in the form of highly coupled nonlinear differential equations. Fortunately, many physical systems exhibit a linear behaviour around an operating point within some range of the variables. This permits a description of such physical systems by linear approximations. The advantage in the case of a linear system is that the response to each input variable can be considered separately. Each response variable y(t) is thus related to the excitation by a linear, constant coefficient ordinary differential equation of the form:

$$\begin{aligned} a_n y_1^{(n)} + a_{n-1} y_1^{(n-1)} + \ldots\ldots + a_1 y_1^{(1)} + a_0 y_1 = \{ & \left[b_r x_1^{(r)} + b_{r-1} x_1^{(r-1)} + \ldots\ldots + b_1 x_1^{(1)} + b_0 x_1 \right] \\ & + \left[c_s x_2^{(s)} + c_{s-1} x_2^{(s-1)} + \ldots\ldots + c_1 x_2^{(1)} + c_0 x_2 \right] \\ & + \left[d_t x_3^{(t)} + d_{t-1} x_3^{(t-1)} + \ldots\ldots + d_1 x_3^{(1)} + d_0 x_3 \right] \\ & + \ldots\ldots\ldots\ldots\ldots\ldots\ldots\ldots\ldots\ldots\ldots\ldots \} \end{aligned} \qquad \text{(A2.1)}$$

where superscripts denote the order of differentiation with respect to time. On the basis of the principle of superposition, if $y_1(t)$ and $y_2(t)$ are the responses of the system to two separate excitations, then the response to the combined excitations is $y_1(t) + y_2(t)$. This result greatly simplifies the problem because the full response at an output from the excitation at several inputs can be worked out as a combination of the separate responses at this output from each of the single inputs. A multiple input-output system can thus be realised as a combination of single input-output systems.

A2.2 Single input-output system

With one input and one output the right hand side of (A2.1) will consist of just one bracketed set of terms:

$$a_n y^{(n)} + a_{n-1} y^{(n-1)} + \ldots\ldots + a_1 y^{(1)} + a_0 y = \left[b_r x^{(r)} + b_{r-1} x^{(r-1)} + \ldots\ldots + b_1 x^{(1)} + b_0 x \right] \qquad \text{(A2.2)}$$

The Laplace transform $\mathcal{L}$ can be used to obtain an input-output description of such a linear, time-invariant (LTI) system. The Laplace transform F(s) of a function f(t) with $t \in [0,\infty]$ is defined by $F(s)=\mathcal{L}\{f\}(s)=\int_0^\infty e^{-st} f(t)dt$. If $Y(s) = \mathcal{L}\{y\}(s)$ and $X(s) = \mathcal{L}\{x\}(s)$, then taking the Laplace Transform on both sides of (A2.2) and assuming zero initial conditions results in:

$$\frac{Y(s)}{X(s)} = H(s) = \frac{b_r s^r + b_{r-1}s^{r-1} + \ldots\ldots + b_1 s + b_0}{a_n s^n + a_{n-1}s^{n-1} + \ldots\ldots + a_1 s + a_0} \qquad \text{(A2.3)}$$

The Laplace transform of y(t) is thus the product of the transfer function $H(s)$ and the Laplace transform of x(t). Hence y(t) can be obtained from the convolution $(h \bullet x)(t)$, where h is the inverse Laplace transform of H. $h(t) = \mathcal{L}^{-1}\{H\}(t)$ is called the Impulse Response Function. The impulse response function h(t) gives the response at time t to a unit impulse or 'hammer blow' applied at time t = 0, that is the response after a delay of duration t. It follows that h(t - ν) gives the response at time t to a unit impulse applied at time t = ν, that is the response after a delay of duration t - ν.

Assuming zero initial conditions, the output y(t) will be given by :

$$y(t) = (h \bullet x)(t) = \int_{-\infty}^{t} h(t-\nu)x(\nu)d\nu \qquad \text{(A2.4)}$$

Physically this means that an arbitrary input function can thus be considered as a composition of a continuous series of impulses. The 'impulse' corresponding to the input x(t) between the time limits ν and $\nu + d\nu$ has the magnitude $x(\nu)d\nu$. The response at time t to this 'impulse' alone is just the fraction $x(\nu)d\nu/1$ of the response to a unit impulse at time t = ν, which is h(t - ν). The response at time t is thus $h(t - \nu)x(\nu)d\nu$. The integral in (A2.4) sums all such elemental contributions to give the total response at time t.

A2.2.1 Case of a harmonic signal

In the case of a deterministic (non-random) input such as a constant amplitude harmonic signal $x(t) = x_o e^{i\omega t}$ applied to an LTI system, multiplication of (A2.4) by $e^{i\omega t}$ and integrating on both sides (with the introduction of the unit step function u(t - ν) which equals 1 for $\nu \le t$ and equals zero for $\nu > t$) yields

$$\frac{1}{2\pi}\int_{-\infty}^{\infty} y(t)e^{i\omega t}dt = \frac{1}{2\pi}\int_{-\infty}^{\infty}\left\{\int_{-\infty}^{t} h(t-v)x(v)dv\right\}e^{i\omega t}dt$$

$$= \frac{1}{2\pi}\int_{-\infty}^{\infty}\left\{\int_{-\infty}^{\infty} u(t-v)h(t-v)x(v)dv\right\}e^{i\omega t}dt,$$

The LHS of the equation is the Fourier transform $Y(\omega)$ of the output. Upon exchanging integrals, the RHS of the equation can be written

$$= \frac{1}{2\pi}\int_{-\infty}^{\infty} x(v)\left\{\int_{-\infty}^{\infty} u(t-v)h(t-v)e^{i\omega t}dt\right\}dv$$

$$= \frac{1}{2\pi}\int_{-\infty}^{\infty} x(v)\left\{\int_{v}^{\infty} h(t-v)e^{i\omega t}dt\right\}dv$$

since u(t-v) is zero for $t<v$. Letting $a = t - v$, the integral within the bracketed terms becomes $e^{-i\omega v}\int_0^{\infty} h(a)e^{-i\omega a}da = e^{-i\omega v}H(\omega)$, where $H(\omega)$ is the complex frequency response function of the system evaluated at the angular frequency ω. Hence the final result is obtained:

$$H(\omega) = \int_0^{\infty} h(t)e^{-i\omega t}dt \qquad \text{(A2.5a)}$$

and

$$Y(\omega) = \frac{H(\omega)}{2\pi}\int_{-\infty}^{\infty} x(v)e^{-i\omega v}dv = H(\omega)X(\omega) \qquad \text{(A2.5b)}$$

This means that the Fourier transforms of the input and the output are related by the frequency response function $H(\omega)$. The nature of this relationship is explained by the fact that when a linear system is subjected to a steady state harmonic excitation at frequency ω, it responds with a steady harmonic output at the same frequency. For an aperiodic input signal, frequency components $X(\omega)d\omega$ in the frequency band ω to $\omega+d\omega$ in the input will correspond to components $Y(\omega)d\omega$ in the same frequency band in the output.

In the case of the harmonic input $x(t) = x_o e^{i\omega t} = X(\omega)d\omega\, e^{i\omega t}$, the corresponding harmonic output would thus be given by $y(t) = Y(\omega)d\omega\, e^{i\omega t} = H(\omega)X(\omega)d\omega\, e^{i\omega t}$. In these expressions either the real part or the imaginary part of the right-hand side of the equations is understood. The magnitude of $H(\omega)$ gives the ratio of the amplitudes of y(t) and x(t). Its argument gives the phase angle between y(t) and x(t). The quantity x_o need not necessarily be real. Its magnitude gives the amplitude of x(t) while the magnitude of $H(\omega)x_o$ gives the amplitude of y(t).

A2.2.2 Example of a harmonic oscillator

The single degree-of-freedom mechanical oscillator depicted in Fig. A2.1 is a very useful example. The equation of motion is $My^{(2)} + Cy^{(1)} + Ky = x = x_o e^{i\omega t}$, where M is the mass of the oscillating body, C is the linear damping coefficient and K is the spring constant. Putting $y(t) = H(\omega)x_o e^{i\omega t}$ gives:

$$(-\omega^2 M + i\omega\, C + K)H(\omega)e^{i\omega t} = e^{i\omega t}$$

$$\Rightarrow \quad H(\omega) = \frac{1}{-\omega^2 M + i\omega\, C + K} = a(\omega) - b(\omega).$$

The output is $y(t) = y_o e^{i(\omega t - \varphi)}$, where the amplitude ratio $\frac{y_o}{x_o} = |H(\omega)| = \frac{1}{\sqrt{(K-\omega^2 M)^2 + \omega^2 C^2}}$,

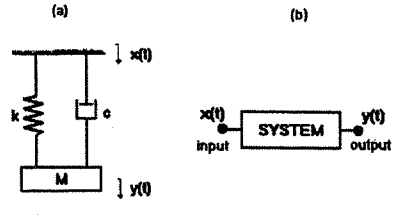

Fig. A2.1 Mechanical oscillator with one degree-of-freedom and the equivalent representation as a system with one input and one output.

and the phase angle φ is given by $Tan\varphi = \dfrac{b(\omega)}{a(\omega)} = \dfrac{\omega\, C}{K - \omega^2 M}$. The resonant frequency is $\omega_o = (K/M)^{1/2}$.

The response of the oscillator is often described in terms of the power amplification factor $A^2(\omega)$ and the normalised impedance $Z(\omega)$ which are defined by

$$A(\omega)^2 = \frac{1}{|Z(\omega)|^2} = \frac{{y_o}^2}{{x_o}^2} = \frac{1}{\left[1 - \left(\dfrac{\omega}{\omega_o}\right)^2\right]^2 + \dfrac{1}{Q^2}\left(\dfrac{\omega}{\omega_o}\right)^2} \qquad \text{(A2.6)}$$

where $Q = \omega_o M/C$ is the dissipation factor. $1/Q$ is thus a linear measure of the damping in the system.

As shown in Fig. A2.2, the power amplification factor increases from unity at $\omega = 0$ to a maximum Q^2 at $\omega = \omega_o$ and then decreases monotonically to zero for infinite frequency. Assuming $Q >> 1$, the half-power points are given by $\omega = \omega_o(1 \pm 1/2Q)$. The relative bandwidth is defined as the difference between these two frequencies divided by ω_o, and is thus $1/Q$. Close to the resonance frequency the amplification factor can be approximated by:

$$A(\omega_0)^2 \approx \frac{1}{4\left[1 - \left(\dfrac{\omega}{\omega_o}\right)\right]^2 + \dfrac{1}{Q^2}} \quad \Rightarrow \quad \frac{A(\omega_0)^2}{A(\omega)^2} \approx 1 + 4Q^2\left[1 - \left(\frac{\omega}{\omega_o}\right)\right]^2 \qquad \text{(A2.7)}$$

The problem of a basin or harbour connected directly to the open sea by means of an aperture is analogous to this example. The response of a harbour which is excited by the long wave signals in the open sea is of course more complicated. The harbour is a system with many degrees-of-freedom and the amplification factor given by (A2.6) is an oversimplification. But if the resonance of any particular mode is sufficiently sharp, the behaviour of the amplification factor in the neighbourhood of resonance can be expressed by (A2.7) (Miles & Munk ,1961).

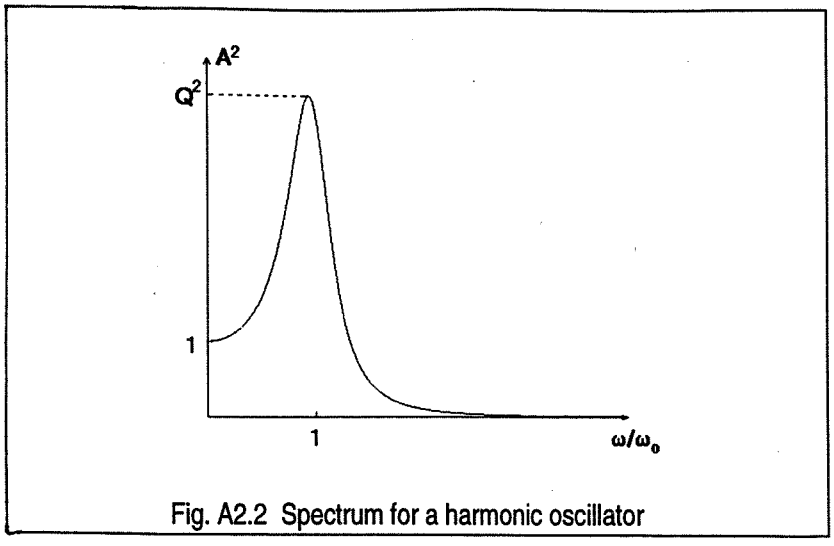

Fig. A2.2 Spectrum for a harmonic oscillator

A2.2.3 Generalisation to multi-frequency signals

In reality, the input signal is not monochromatic but consists of an infinite number of superposed harmonic components of different amplitudes with random phase. The input signal is thus usually represented by a wave spectrum $S_x(\omega)$ that is peaked at the dominant period of the waves. These spectra vary from region to region of the sea and are characteristic of the local wave regime. The characteristics of the excitation are modified by the response of the system which, in electrical engineering terms, acts as a filter. Following Newland (1993), the response spectrum $S_y(\omega)$ in the case of a single input is thus given by

$$S_y(\omega) = H^*(\omega)H(\omega)S_x(\omega) = |H(\omega)|^2 S_x(\omega) \qquad \text{(A2.8a)}$$

The generalisation to N inputs is expressed as

$$S_y(\omega) = \sum_{r=1}^{N}\sum_{s=1}^{N} H_r^*(\omega)H_s(\omega)S_{x_r x_s}(\omega) \qquad \text{(A2.8b)}$$

where $S_{x_r x_s}(\omega)$ are the cross-spectral density terms between inputs x_r and x_s and $S_{x_r x_r}(\omega) = S_{x_r}(\omega)$ is the autospectrum for input x_r. For uncorrelated inputs the cross-spectral density terms are all zero and

$$S_y(\omega) = \sum_{r=1}^{N} |H_r(\omega)|^2 S_{x_r}(\omega) \qquad \text{(A2.8c)}$$

The theory above implies that the response of a system can be obtained by means of a statistical analysis based on a frequency response function (or the corresponding transfer function). The frequency response function converts the input wave spectrum into a response output spectrum of wave heights inside the basin. Integration of the spectra with respect to the frequency gives the mean squared value (i.e. the variance σ^2) of the random variable under consideration

$$\sigma_y^2 = \langle y^2(t) \rangle = \lim_{T\to\infty} \frac{1}{T} \int_{-T/2}^{T/2} y^2(t)dt = \int_0^{\infty} S_y(\omega)d\omega \qquad \text{(A2.9)}$$

The quantity $\langle y^2(t) \rangle$ associated to a narrow frequency interval ω to $\omega + d\omega$ is simply $S_y(\omega)d\omega$.

This approach can be applied to the linear response of a coastal embayment or basin that is excited by a random input signal from the open sea. If the basin is realised as a composition of spatial elements then the response at each element i will be different. The spectrum at each element can thus be related to the same input by

$$S_{y_i}(\omega) = |H_i(\omega)|^2 S_x(\omega) \qquad \text{(A2.10)}$$

where $H_i(\omega)$ is the frequency response function for the i th element.

This formulation is very important. It signifies that the hydrodynamic response of a basin can be analysed by utilising the tools of modern control system analysis and design.

REFERENCES

Airy G.B., 1878, On the tides in Malta, *Phil. Trans. R. Soc. London*, 169, 123-138.

Astraldi M., C. Galli, C. Gasparini, E. Lazzoni and G.M.R. Manzella, 1987, The Janus Experiment, *Istituto Dinamica Grandi Masse, S. O. Technical Report* TR140, 40pp.

Batteen M.L. and Han Y.-J., 1981, On the computational noise of finite-difference schemes used in ocean models, *Tellus*, 33, 387-396.

Bendat, J.S and A.G. Piersol, 1986, Random data analysis and measurements procedures, *J. Wiley, NY*, 566p.

Blumberg A.F., 1977, The influence of density variations on estuarine tides and circulations, *J. Estuarine and Coastal Marine Science,* 3, 123-126.

Blumberg A.F., 1977, Numerical tidal model of Chesapeake Bay, *J. Hydraul. Div.*, 103, 1-10.

Blumberg A.F. and G.L. Mellor, 1987, A description of a three-dimensional coastal ocean circulation model, *In: Three-Dimensional Coastal Ocean Models,* Vol. 4, ed. by N. Heaps, pp. 208, AGU, Washington, D.C.

Bowden K.F., 1972, Measurements of diffusion in the sea, *Mémoires Société Royale de Liége*, 6e série, tome II, pp.79-89.

Bowen A.J. and R.T. Guza, 1978, Edge waves and surf beat, *J. Geophys. Res.*, 83, 1913-1920.

Brown W., W.H. Munk, F.E. Snodgrass, H. Mofjeld and B. Zettler, 1975, MODE bottom experiment, *J. Phys. Oceanogr.*, 5, 75-85.

Buchwald V.T., 1968, Long waves on oceanic ridges, *Proc. R. Soc.*, A 308, 343-358.

Buchwald V.T. and J.K. Adams, 1968, The propagation of continental shelf waves, *Proc. R. Soc.*, A 305, 235-250.

Buchwald V.T. and R.A. de Szoeke, 1973, The response of a continental shelf to a travelling pressure disturbance, *Aust. J. Mar. Freshwater Res.*, 24, 143-158.

Camerlengo A.L. and O'Brien J.J., 1980, Open boundary conditions in rotating fluids, *J. Comput. Physics*, 35, 12-35.

Candela J., C. Winant and A. Ruiz, 1990, Tides in the Strait of Gibraltar, *J. Geophys. Res.* Vol. 95, No. C5, 7313-7335.

Candela J., 1991, The Gibraltar Strait and its role in the dynamics of the Mediterranean Sea, *Dynamics of Atmospheres and Oceans*, 15, 267-299.

Candela J. and C. J. Lozano, 1994, Barotropic response of the Western Mediterranean to observed atmospheric pressure forcing, In: *Seasonal and Interannual Variability of the Western Mediterranean Sea, Coastal and Estuarine Studies*, Vol. 46, Ed.: P.E. La Violette, pp325-359, AGU, Washington D.C.

Carrier G.F., R.P. Shaw and M. Miyata, 1971, The response of narrow mouthed harbours in a straight coastline to periodic incident waves, *J. Appl. Mech.*, 38, Series E, No.2, 335-344.

Chapman D.C., 1985, Numerical treatment of cross-shelf boundaries in a barotropic coastal ocean model, *J. of Phys. Oc.*, Vol. 15, 1060-1075.

Chrystal G., 1904, some results in the mathematical theory of seiches, *Proc. Roy. Soc. Edinb.*, 25, 325.

Chrystal G., 1905a, Some further results in the mathematical theory of seiches, *Proc. Roy. Soc. Edinb.* 25, 637.

Chrystal G., 1905b, On the hydrdynamical theory of seiches, *Trans. Roy. Soc. Edinb.*, 41, 599.

Chrystal G., 1908a, Investigation of the seiches of Loch Earn by the Scottish Loch Survey, Part III, *Trans. Roy. Soc. Edinb.*, 46(3), 455-517.

Chrystal G., 1908b, An investigation of the seiches of Loch Earn, Part IV, Effect of meteorological conditions upon the denivellations of lakes, *Trans. Roy. Soc. Edinb.*, 46, No.20.

Colucci P. and A. Michelato, 1976, An approach to the study of the 'Marrubbio' phenomenon, *Bollettino di Geofisica Teorica ed Applicata*, V13(69), p3-10.

Crepon M., 1965, Influence de la pressione atmosphérique sur le niveau moyen de la Méditerranée occidentale et sur le flux á travers le détroit de Gibraltar, *Cahiers Océanographique*, 17, 15-32.

Crepon M., 1975, Sea level, bottom pressure and geostrophic adjustment, *Memoirés Societé Royale du Science de Liége*, 6(10), 43-60.

Darbyshire M., 1963, Long Waves on the Coast of the Cape Peninsula, *Deutsche Hydrographische Zeitschrift*, Band 16, 167-185.

Darbyshire J. and M. Darbyshire, 1964, Range action in Table Bay Harbour, *The South African Journal of Science*, Vol. 60, No. 6, 173-182.

Daubechies I., 1987, Orthonormal bases of wavelets with finite support - Connection with discrete filters, *Proc. Int. Conf. on Wavelets*, Marseille, published as pages 38-66 of Wavelets, Time-frequency Methods and Phase Space, J.M. Combes, A. Grossmann and Ph. Tchamitchian (eds.), Springer-Verlag, Berlin, 1989.

Daubechies I., 1988, Orthonormal bases of compactly supported wavelets, *Comm. Pure and Applied Maths*, Vol. XLI, pp.909-996.

Daubechies I., 1990, The wavelet transform, time-frequency localization and signal analysis, *IEEE Trans. On Information Theory*, Vol. 36, 961-1005.

Defant A., 1961, Physical Oceanography, Vol.2, Oxford, Pergamon Press.

DeMaria M., J.M. Davies and D.M. Wojtak, 1989, Observations of mesoscale wave disturbances during the genesis of Atlantic Lows Experiment, *Mon. Weather Rev.*, 117, 826-842.

Djumagaliev V.A. and A.B. Rabinovich, 1993, Long wave investigations at the shelf and in the bays of the South Kuril Islands, J. Korean Soc. Coastal and Ocean Eng., 5, 318-328.

Djumagaliev V.A., Rabinovich A.B. and Fine I.V., 1995, Theoretical and experimental estimation of transfer pecularities of the Malokurilsk Bay coast, the Island of Shikotan, *Atm. Oc. Phys.*, Vol. 30, No. 5, 680-686.

Drago A. F., 1997, Hydrographic Measurements in the North Western Coastal Area of Malta, *Xjenza, Journal of the Malta Chamber of Scientists,* Vol.2, No.1, pg 6-14.

Drago A. F. and S. Ferraro, 1996, Oscillazioni del livello del mare nel Porto di Malta, In: *Proceedings of the XI Congress of the Italian Association of Limnology and Oceanography,* Sorrento, 1994, 235-246.

Efimov V.V., 1985, Waves in boundary regions of the ocean, 280 pp., Gidrometeoizdat, Leningrad.

Elder J.W., 1959, The dispersion of marked fluid in turbulent shear flow, J. Fluid Mech., 5, Part 4, 544-560.

Emden R., 1905, Der Energiegiehalt der Seiches, *Jr. Sankt Gallischen naturw*, Ges.

Falconer R. A., 1984, A mathematical model study of the flushing characteristics of a shallow tidal bay, *Proc. Instn. Civ. Engrs.*, Part 2, 77, 311-332.

Forel F.A. 1892, "Le Leman (Collected Papers)", 2 vols., Rouge, Lausanne, Switzerland.

Gallagher B., 1971, Generation of surf beat by non-linear wave interactions, *J. Fluid Mechanics*, 49, 1-20.

Garrett, C.J.R., 1975, Tides in Gulfs, *Deep Sea Res.*, 22: 23-35.

Garrett C. and B. Toulany, 1982, Sea Level Variability due to meteorological forcing in the Northeast Gulf of St. Lawrence, *Journal of Geophysical Research*, 87(C3), 1968-1978.

Garrett C., 1983, Variable sea level and strait flows in the Mediterranean: a theoretical study of the response to meteorological forcing, *Oceanologica Acta*, Vol.6, No.1, 79-87.

Garrett C. and F. Majaess, 1984, Nonisostatic response of sea level to atmospheric pressure in the Eastern Mediterranean, *Journal of Physical Oceanography*, 14, 656-665.

Garrett C., A. Bormans and K. Thompson, 1990a, Is the exchange through the Strait of Gibraltar maximal or sub-maximal? In: *The Physical Oceanography of sea straits*, Pratt L.J. ed., Kluwer Academic Publ., Boston: 271-294.

Garrett C., K. Thompson and W. Blankchard, 1990b, Sea level flips, *Nature*, 3482: 292.

Gedzelman S.D. and R.A. Rilling, 1978, Short period atmospheric gravity waves: a study of their dynamic and synoptic features, *Mon. Weather Rev.*, 106, 196-210.

Geller R.J., Noak R.M., and Fetter A. L., 1985, Normal mode solutions for absorbing boundary conditions, *Geophs. Res. Lett.* 12,145-148.

Giese G.S. and R.B. Hollander, 1987, The relation between coastal seiches at Palawan Island and tide-generated internal waves in the Sulu Sea, *J. Geophys. Res.*, 92(C5), 5151-5156.

Giese G.S., R.B. Hollander, J.E. Fancher and B.S. Giese, 1982, Evidence of coastal seiche excitation by tide-generated internal solitary waves, *Geophys. Res. Lett.*, 9,1305-1308.

Giese G.S., D.C. Chapman, P.G. Black and A.J. Fornshell, 1990, Causation of large-amplitude coastal seiches on the Caribbean coast of Puerto Rico, *J. Phys. Oceanog.*, 20(9), 1449-1458.

Giese G.S. and D.C. Chapman 1993, Coastal seiches, *Oceanus*, 38-46.

Giese G.S., D.C. Chapman, M. Garcies, D. Gomis and S. Monserrat, 1994, Large amplitude harbor seiches in the Western Mediterranean, part 2, Generation by tide-generated internal waves, *EOS Tran.*, AGU, 75(3), Ocean Sci. Meet. Suppl., 61.

Gill A. E. and P. P. Niiler, 1973, The theory in the seasonal variability in the ocean, *Deep Sea Research*, 20, 141 - 177.

Godin G., 1972, *The Analysis of Tides*, University of Toronto Press, Canada, 264 pp.

Godin G. and L. Trotti, 1975, Trieste water levels 1952-1971: A study of the tide, mean level and seiche activity, *Environment Canada, Fisheries and Marine Services*, Miscellanous Special Publication 28, 23p.

Goldsmith V., 1990, Non-eustatic sea level changes from Mediterranean tide gauges, In: R. Paepre et al. (eds.), *Greenhouse Effect, Sea Level and Drought*, 145-152, © 1990 Kluwer Academic Publishers, Netherlands.

Goldsmith V. and M. Gilboa, 1987, Mediterranean sea level changes from tide gauge records, *Proc. 20th Int. Coastal Eng. Conf. A.S.C.E.*, N.Y., pp. 223-231.

Gomis, D., Monserrat S., and Tintore' J., 1993, Pressure-forced seiches of large amplitude in inlets of the Balearic Islands, J. Geophys. Res., 98, 14437-14445.

Goto C. and Ogawa Y., 1997, Numerical method of tsunami simulation with the leaf-frog scheme, *IUGG/IOC Time Project, IOC Manuals and Guides* No. 35, UNESCO.

Goupilland P., A. Grossmann and J. Morlet, 1984, Cycle-octave and related transforms in seismic signal analysis, *geoexploration*, Vol. 23, pp85-102.

Grace S. F., 1931, Historical review of dynamical explanations of the tides of the Mediterranean, the Baltic Sea, the Gulf of Mexico and the Arctic Ocean, *Publication Scientifique, Assoc. d'Oceanographie Physique* 1, 15-26.

Greatbatch R.J. and Otterson T., 1991, On the formulation of open boundary conditions at the mouth of a bay, *J. Geo. Res.*, Vol. 10, C10, 18431-18445.

Guza R.T. and D.C. Inman, 1975, Edge waves and beach cusps, *J. Geophys. Res.*, 80, 2997-3012.

Haar A., 1910, Zur Theorie der orthogonalen Funktionensysteme, *Math. Ann.*. Vol.69, 331-371.

Heaps N.S., 1973, Three dimensional numerical model of the Irish Sea, *Geophy. Journ. R. Astro. Soc.*, 35, 99-120.

Hedley M. and Yau M.K., 1988, Radiation boundary conditions in numerical modelling, *Mon. Wea. Rev.*, Vol. 116, 1721-1736.

Herron T. J., I. Tolstoy and T. W. Kraft, 1969, Atmospheric pressure background fluctuations in the mesoscale range, *Journal of Geophysical Research,* 74, 1321-1329.

Hibiya T. and K. Kajiura, 1982, Origin of 'Abiki' phenomenon (a kind of seiches) in Nagasaki Bay, *J. Oceanogr. Soc. Japan*, 38, 172-182.

Hidaka K., 1936, Application of Ritz Variation Method to the Determination of Seiches in a Lake, *Mem. Imp. Mar. Obs. Kobe*,6, No.2.

Hibiya T. and K. Kajiura, 1982, Origin of 'Abiki' phenomenon (a kind of seiches) in Nagasaki Bay, *J. Oceanogr. Soc. Japan*, 38, 172-182.

Honda K., T. Terada, Y. Yoshida and D. Isitani, 1908, An investigation on the secondary undulations of oceanic tides, *J. College Sci.*, Imp. Univ. Tokyo.

Hutchnance J., 1986, The subtidal behaviour of the Celtic Sea - III. A model of shelf waves and surges on a wide shelf, *Cont. Shelf Res.* 5, pp 347-377.

Hwang Li-San and E.O. Tuck, 1970, On the oscillations of harbors of arbitrary shape, *J. Fluid Mechanics*, 42, Part 3, 447-464.

IOC, UNESCO, 1985, Manual on sea level measurements and interpretation, *Intergovernmental Oceanographic Commission, Manuals and Guides*, No. 14, 71.

Ippen A.T. and Raichlen F., 1962, Wave induced oscillations in harbours: the problem of coupling of highly reflective basins, *Hydrodyn. Lab., Mass. Inst. of Tech.*, Tech. Report No. 49.

Ippen A.T. and Goda Y., 1963, Wave induced oscillations in harbours: the solution for a rectanguar harbour connected to the open sea, *Hydrodyn. Lab., Mass. Inst. of Tech., Cambridge, Mass.*, Tech. Report No. 59, pp. 1-90.

Israeli M. and Orszag S.A., 1981, Approximation of radiation boundary conditions, *J. Comput. Phys.*, 21, 251-269.

Jansa A., 1986, Marine response to mesoscale-meteorological disturbances: The June 21, 1984, event in Cuitadella (Menorca) (in Spanish), *Rev. Meteorol.*, 7, 5-29.

Jenkins J.M. and D.J. Watts, 1968, Spectral analysis and its applications, Holden Day, San Francisco.

Keliher T.E., 1975, The occurrence of micro-barograph gravity waves compared with the existence of dynamically unstable wind shear layers, *J. Geophys. Res.*, 80, 2967-2976.

Klemp J.B. and Wilhelmson R.B., 1978, The simulation of three-dimensional convective storm dynamics, *J. Atmos. Sci.*, 35, 1070-1096.

Koninklijk Netherlands Meteorological Institute, 1957, *Middellanse Zee*, (The Mediterranean Oceanographic and Meteorological Data).

Kostense J.K., Meijer K.L., Dingemans M.W., Mynett A.E. and Vah den Bosch P., 1986, Wave energy dissipation in arbitrary shaped harbours of variable depth, *Proc. Int. Coastal Eng. Conf.*, 20th, 2002-2016.

Kovalev P.D., A.B. Rabinovich and G.V. Shevchenko, 1991, Investigation of long waves in the tsunami frequency band on the southwestern shelf of Kamchatka, *Natural Hazards*, 4, 141-159.

Kulikov E. A. and G.V. Shevchenko, 1992, The resonant generation of shelf waves by a moving cyclone, *Sov. J. Phys. Oceanogr.*, Vol.3, No.5, pp 331-341.

Lacombe H., P. Tchernia, C. Richez and L. Gamberoni, 1964, Deúxieme Contribution á l'étude du régime du détroit de Gibraltar (travaux de 1960), *Cahiers Océanographique*, 16, 283-314.

Larnicol G., P. Y. Le Traon, N. Ayoub and P. De Mey, 1995, Mean Sea Level and Surface Circulation Variability of the Mediterranean Sea from 2 Years of TOPEX/POSEIDON Altimetry, *J. Geophys. Res.*, Vol. 100, No. C12, 25,163-25,177.

Lascaratos A. and M. Gacic, 1990, Low frequency sea level variability in the northeastern Mediterranean, *J. Phys. Oceanogr.*, 20, 522-533.

LeBlond P. H. and L. A. Mysak, 1978, *Waves in the Ocean*, Elsevier Scientific, 602pp.

Le Traon P.Y. and P. Gauzelin, 1997, Response of the Mediterranean Mean Sea Level to Atmospheric Pressure Forcing, *J. Geophys. Res.*, Vol. 102, No. C1, 973-984.

Levyant A.S., B.I. Rabinovich and A.B. Rabinovich, 1994, Computation of seiche oscillations in seas of arbitrary configuration (exemplified by the Caspian Sea), *Oceanology*, Vol. 33, No. 5, 588-598.

Likhacheva O.N., A.B. Rabinovich and A.V. Fine, 1985, Analysis of the atmospheric pressure field over the sea of Okhotsk and the northeastern Pacific Ocean, In: *Theoretical and Experimental Investigations of the Long Wave Processes, Vladivostok, USSR, Academy of Sciences*, 144-157.

Lindzen R.S. and K. K. Tung, 1976, Banded convective activity and ducted gravity waves, *Mon. Weather Rev.*, 104, 1602-1617.

Longuett-Higgins M S and Stewart R W, 1962, Radiation Stress and mass transport in gravity waves with application to 'surf beats', *J. Fluid Mech.*, 13, 481.

Longuet-Higgins M.S., 1967, On the trapping of wave energy round islands, *J. Fluid Mech.*, Vol. 29 (Part 4), 781-821.

Loomis H.G., 1966, Some numerical hydrodynamics for Hilo Harbor, *Institute of Geophysics, Univ. Hawaii,* HIG-66-7.

Mallat, S., 1989, A theory for multiresolution signal decomposition: The wavelet representation, *IEEE Trans. Pattern Anal. and Machine Intell.,* 11, 674-93.

Manzella G. M. R. and A. J. Elliott, 1991, EUROSPILL: Mediterranean Tidal and Residual Circulation Databases, *Marine Pollution Bulletin,* Vol. 22,No. 11,553-558.

Manzella G. M. R., G. P. Gasparini and V. Artale, 1988, Analysis of bottom pressure measurements in the Strait of Sicily, *J. Geophys. Res.*

Mathew J.P., Mahadevan R., Bharatkumar B.H. and Subramanian V., 1996, Numerical simulation of open coast surges, Part I: Experiments on offshore boundary conditions, *J. Coastal Res.*, 12, 1, 112-122.

Matuzawa T., K. Kanbara and T. Minakami, 1933, Horizontal movement of water in the tsunami of March 3, 1933, *Jpn. J. Astron. Geophys.*, 11(1), 11-16.

Meteorological Office, 1964, *Weather in the Mediterranean,* Vol I and II, 2nd edition, London M.O., 391p.

Miles J.W. and W.H. Munk, 1961, Harbor Paradox, *J. Waterways and Harbors Division, Proc. Am. Soc. Civ. Eng.*, 87,111.

Miles J.W., 1971, Resonant response of harbours: An equivalent circuit analysis, *J. Fluid Mech.*, 46, 241-265.

Miles J.W., 1974, Harbor seiching, *Ann. Rev. Fluid Mech.*, 6: 17-35.

Miller M.J. and Thorpe A.J., 1981, Radiation conditions for the lateral boundaries of limited-area numerical models, *Q. J. R. Meteorol. Soc.*, 107, 615-628.

Millot C. and Crepon M., 1981, Inertial oscillations in the Gulf of Lions, *J. Phys. Oceanogr.*, 11.

Miyata M., 1993, Island-trapped shelf waves, *La Mer,* 31: 169-178.

Molines J. M., L. Monsaingeon and C. Le Provost, 1989a, Topex/Poseidon calibration plan: Sea level variability induced by geophysical environmental parameters in the area of the nominal site of Lampedusa. A bibliographical survey, *Contract report CNES/SBS* D2921, 42pp.

Molines J. M., L. Monsaingeon and C. Le Provost, 1989b, Topex/Poseidon calibration plan, Part II: Numerical modelling and optimal instrumentation of the site, *Contract report CNES/SBS D3380,* 31pp.

Molines J. M., 1991, Modelling the barotropic tides in the Strait of Sicily and Tunisian shelf, *Oceanologica Acta,* 14, Nos 3, 241-252

Monserrat S., Ramis C., Thorpe A. J., 1991, Large amplitude pressure oscillations in the Western Mediterranean, *Geophys. Res. Lett.*, 18, 183-186.

Monserrat S and A.J. Thorpe, 1992, Gravity wave observations using an array of microbarographs in the Balearic Islands, *Q. J. Roy. Meteor. Soc.*, 117, 553-570.

Momoi T., 1970, A long wave in a rectangular bay (I), *Bull. Earthquake Res. Inst.*, Tokyo Univ., 48, 871-891.

Mosetti F., 1971, Considerazioni sulle cause dell'ácqua alta a Venezia, *Bollettino di Geofisica e Teoria Applicata,* 13, 169-184.

Mosetti F. and N. Purga, 1982, First results on long and mid-period tide distribution in Italian seas and their existence in the groundwater, *Il Nuovo Cimento,* Vol. 5 (C2): 143-148.

Mosetti F. and N. Purga, 1989, The semi-diurnal tides in the Sicily Strait, *Il Nuovo Cimento*, Vol 12C, No.3, 349-355.

Munk W.H. and R.S. Arthur, 1952, Wave intensity along a refracted ray, *Proc. Symp. on Gravity Waves, U.S. Nat. Bur. Standards*, Circular 521, pp95-108.

Munk W.H., F. Snodgrass and G. Carrier, 1956, Edge waves on the continental shelf, *Science*, 123(3187), 127-132.

Munk W. H., F. Snodgrass and F. Gilbert, 1964, Long waves on the continental shelf: An experiment to separate trapped and leaky modes, *J. Fluid Mech.*, 20 (Part 4), 529-554.

Murakami K., 1993, Water exchange in enclosed coastal seas, *Report of the Port and Harbour Research Institute*, Vol. 31, No. 5.

Murray M. T., 1964, A general method for the analysis of hourly heights of the tide, *International Hydrographic Review*, 41(2), 91-101.

Mysak L. A., 1967, On the theory of continental shelf waves, *J. Mar. Res.*, 25, 205-227.

Nakano M. and N. Fujimoto, 1987, Seiches in bays forming a coupled system, *J. of Oc. Soc. Jap.*, Vol. 43, 124-134.

Newland D. E., 1993, Random vibrations, spectral and wavelet analysis, 3rd edition, Longman, Harlow and John Wiley, New York.

Nomitsu T., 1935, A theory of tsunamis and seiches produced by wind and barometric gradient, *Mem. Coll. Sci. Imp. Univ. Kyoto*, A18(4), 201-204.

Oey L.-Y., Mellor G.L. and Hires R.I., 1985, A three-dimensional simulation of the Hudson-Raritan estuary, Part I: Description of the model and model simulations, *J. of Phys. Oc.*, 15, 1676-1692.

Okubo A., 1980, Diffusion and Ecological problems: mathematical models, Springer Verlag, Berlin, 254pp.

Orlanski J., 1978, A simple boundary condition for unbounded hyperbolic flows, *J.of Computational Physics*, 21, 251-269.

Orlic M., 1983, On the frictionless influence of planetary atmospheric waves on the Adriatic sea level, *J. Phys. Oceanogr.*, 13, 1301-1306.

Ozsoy E., U. Unluata and M. Aral, 1982, Coastal amplification of tsunami waves in the Eastern Mediterranean, *J. Phys. Oceanogr.*, 12, 117-126.

Ovchinnikov I. M., 1974, On the water balance of the Mediterranean Sea, *Oceanology, Eng. Trans.* 14, 198-202, 1974.

Palumbo A. and A. Mazzarella, 1982, Mean sea level variations and their practical applications, *J. Geophys. Res.*, 87, 4249-4256.

Papa L., 1978, A statistical investigation of low frequency sea level variations at Genoa, *Istituto Idrografico della Marina, Universita' degli Studi di Genova*, F. C. 1087, Grog. 6, 13p.

Pirazzoli P. A., 1987, Sea level changes in the Mediterranean, In: Tooley, M.J. and Sherman I. (eds.) *Sea Level Changes*, Basil Blackwell, N.Y., pp. 152 - 181.

Platzman G. W., 1972, Two-dimensional free oscillations in natural basins, *J. Phys.Oceanogr.*, 2, No. 2, 117-138.

Platzman G. W., 1975, Normal modes of the Atlantic and Indian Oceans, *J. Phys. Oceanogr.*, 5, No. 2, 114-137.

Portolano del Mediterraneo, 1950: Vol. II, Parte II.

Proudman J., 1914, Free and Forced Longitudinal tidal motion in a Lake, *Proc. Lond. Math. Soc.* (2), 14.

Proudman J., 1929, The effects on the sea of changes in atmospheric pressure, Mon. Not. R. Astr. Soc. Geophys. Supp., 2, No. 4, 196.

Pugh D. T., 1987, Tides, surges and mean sea level, John Wiley and Sons, GB.

Purga N., F. Mosetti and E. Accerboni, 1979, Tidal Harmonic Constants for some Mediterranean Harbours, *Boll. Geofis. teor. appl.*, 21, 81,72-81.

Rabinovich A. B. and A. YE. Zhukov, 1984, Tidal Oscillations on the Shelf of Sakhalin Island, *Oceanology*, Vol. 24, No. 2, 184-189.

Rabinovich B.I. and A.S. Levyant, 1990, Numerical solution of problem of computing seiches using conformal mapping RT method, In:- *Natural Catastrophes and Calamities in Far Eastern region, Vladivostok, DVOAN, SSSR*, pp 328-342.

Rabinovich A.B., V.A. Djumagaliev, I.V. Fine and Y.A. Kulikov, 1993, Analysis of weak tsunami in the region of the Kuril Islands and resonance influence of topography, *Proceedings IUGG/IOC International Tsunami Symposium,* Wakayama, Japan, 95-105.

Rabinovich A. B., Monserrat S., 1996, Meteorological Tsunamis near the Balearic and Kuril Islands: Descriptive and Statistical Analysis, *Natural Hazards,* 13: 55-90.

Rabinovich A. B., Monserrat S., 1998, Generation of meteorological tsunamis (large amplitude seiches) near the Balearic and Kuril Islands, *Natural Hazards,* vol. 18, No.1, p27-55.

Rabinovich A.B. and Monserrat S., 1998, On the generation of meteorological tsunamis in the region of the Balearic Islands, Western Mediterranean, *Proceedings of the 1st International Conference on Port, Coast and Environment*, Varna, Bulgaria, 268-276.

Ramis C., Jansa A., 1983, Meteorological conditions simultaneous to sea level oscillations of great amplitude in the Western Mediterranean, (In Spanish) *Rev. Geofis.*, 39,35-42.

Rees J.M. and S.D. Mobbs, 1988, Studies of internal gravity waves at Halley Base, Antarctica, using wind observations, *Q. J. R. Meteorol. Soc.*, 114, 939-966.

RØed L.P. and Cooper C.K., 1986, Open boundary conditions in numerical ocean models, In*: J.J. O'Brien (Editor), Advanced Physical Oceanographic Numerical Modelling,* NATO ASI Series C, Vol. 186, D. Riedel Publ. Co.: 411-436.

Sanchez B. V., R. D. Ray and D. E. Cartwright, 1992, A Proudman-function expansion of the M2 tide in the Mediterranean Sea from satellite altimetry and coastal gauges, *Oceanologica Acta*, 1992, 15, 4, 325-337.

Shillington F.A., 1984, Long period edge waves off southern Africa, *Continental Shelf Res.*, Vol.3, No.4, 343-357.

Shillington F.A. and D. van Foreest, 1986, Numerical model studies of long-period edge waves, *J. Phys. Oceanogr.*, 16, 1487-1492.

Snodgrass F.E., Munk W.H., Miller G.R., 1962, Long period waves over California's continental borderland, I, Background spectra, *J. Mar. Res.*, 20, 3-30.

Sommerfeld A., 1949, Partial Differential Equations, Lect. Theor. Phys., vol. 6, 335pp., Academic, San Diego, Calif.

Spiteri D., 1996, Aquaculture and the environment, In: Marine Pollution in Malta, The problem and its management, *Proceedings Conference on the Management of Marine Contamination Hazards*, Ed.: Axiak V., 110-107.

Sterneck R., 1915, Hydrodynamische Theorie der halbtagige Gezeiten des Mittelmeeres, *S. B. Akad. Wiss. Wien, (Abt. IIa),* 124, 905.

Stobie J.G., F. Einaudi and L.W. Uccellini, 1983, A case of gravity waves-convecting storms interaction: 9 May, 1979, *J. Atmos. Sci.*, 40, 2804-2840.

Stravisi F., 1989, Fortran and basic programs for computing and plotting the astronomical tide, *Universita' degli studi di Trieste, Internal Report* FTC 89/4, 23pp.

Takeoka T., 1984, Fundamental concepts of exchange and transport time scale in a coastal sea, *Cont. Shelf Res.*, Vol. 3, 311-326

Taku T., Yoshinobu T., Masahito T., Yoshikazu U., Masayuki K., Takashi E., Yasuhiro Y, 1992, Comparison of Observed and Theoretically Calculated Seiches of Heda Bay, *Pageoph.* Vol.138, No.2.

Thompson K. and D. T. Pugh, 1986, The subtidal behaviour of the Celtic Sea - II. Currents, *Cont. Shelf Res.*, 5, pp. 321-346.

Tinti S. and D. Giuliani, 1983, The Messina Straits Tsunami of December 28, 1908: A critical review of experimental data and observations, *Nuovo Cimento*, 6C, N.4, 429-441.

Tintore' J., D. Gomis, S. Alonso, and D.-P. Wang, 1988, A theoretical study of large sea level oscillations in the western Mediterranean, *J. Geophys. Res.*, 93(C9), 10,797-10,803.

Trewartha G. T., 1962, Mediterranean Lands, In: *The Earth's Problem Climates*, Methuen and Co., London.

TSIMPLIS M. N., 1995, The Response of Sea Level to Atmospheric Forcing in the Mediterranean, *J. Coastal Res.*, 11(4), 1309-1321.

Tsimplis M. N., R. Proctor and R. A. Flather, 1995, A two-dimensional tidal model for the Mediterranean Sea, *J. Geophys. Res.*, Vol. 100, No. C8, p16223-16239.

Tsimplis M. N. and G. N. Vlakhis, 1994, Meteorological forcing and sea level variability in the Aegean Sea, *J. Geophys. Res.*, 99(C5), 9879-9890.

Uccellini L.W. and S.E. Koch, 1987, The synoptic setting and possible energy sources for mesoscale wave disturbances, *Mon. Wea. Rev.*, 115, 721-729.

Van Dorn, W.G., 1965, Tsunamis, In: *Advances in hydroscience*, Vol. 2, Academic Press, 1-44.

Viera F. and V.T. Buchwald, 1982, The response of the east Australian continental shelf to a travelling pressure disturbance, *Geophys. Astrophys. Fluid Dyn.*, 19, 249-265.

Wilson B. W., 1970, Seiches, In: *Advances in hydrosciences*, Vol.8, Ven Te Chow, editor, Academic Press, N.Y., pp. 1-94.

Wilson B.W., 1971, Tsunami-responses of San Pedro Bay and shelf, *Calif. J. Waterw. Harbors Coastal Eng. Div.*, 97(WW2), 239-258.

Wilson B.W., 1972, Seiches, In: *Advances in hydrosciences*, 8,1-94.

Wunsch C., 1972, Bermuda sea level in relation to tides, weather, and baroclinic variations, *Rev. Geophys. Space Phys.*, Vol. 10, No.1, 1-49.